https://ntrs.nasa.gov/search.jsp?R=19820018179 2020-03-21T07:36:09+00:00Z

NASA

Technical Memorandum 83848

(NASA-TM-83848) X-RAY ASTRONOMY THE 1980'S N82-26055
(NASA) 620 p HC A99/MF A01 CSCL 03A THRU
N82-26086
Unclas
G3/88 21232

X-RAY ASTRONOMY IN THE 1980'S

Edited by
Stephen S. Holt

MAY 1982
RECEIVED
NASA STI FACILITY
ACCESS DEPT.

November 1981

Proceedings of a Workshop held at the Goddard Space Flight Center
October 5, 6 and 7, 1981.

National Aeronautics and
Space Administration

Goddard Space Flight Center
Greenbelt, Maryland 20771

X-RAY ASTRONOMY IN THE 1980's

Edited by
STEPHEN S. HOLT

November 1981

Proceedings of a Workshop held at the Goddard Space Flight Center
October 5, 6 and 7, 1981.

PRECEDING PAGE BLANK NOT FILMED

PREFACE

A Workshop on X-ray Astronomy and Spectroscopy was held at the Goddard Space Flight Center on October 5 through 7, 1981, under the sponsorship of GSFC and NASA. The purpose of this workshop was to evaluate the current status of X-ray astronomy following a decade of very rewarding exploration in which it matured to the point of having comparable importance to UV, optical, IR and radio astronomy for addressing the important questions concerning the observational universe. Theorists were asked to present the status of our understanding of a wide range of problems in astrophysics, and to explore what key observational parameters in X-rays are needed to shed new light on the currently unanswered questions. Experimentalists were asked to present the latest developments in instrument design capabilities and the types of missions on which these instruments might be utilized.

After the theoretical requirements and instrument capabilities had been presented during the first two days of the Workshop, the final day of the meeting was opened up for an intensive discussion of the types of missions that should be recommended for further study. In addition to a reendorsement of the anticipated Explorer program in astrophysics, including EUVE, ROSAT and XTE, a general consensus was reached on several important issues, namely:

1. The importance of a continuing program of balloon-borne research as a cost-effective means by which studies at energies in excess of 20 keV may be performed.

2. The unique scientific opportunity presented by the Space Transportation System (STS) to develop low-cost experiments which are beyond the scope of balloon-borne capabilities, but which may not require the long exposures of a free-flyer platform. Traditional Spacelab instruments, as well as EOP and IPS-mounted experiments, are important elements in a continuing balanced program of research.

3. The highest priority moderate cost free-flyer mission is one which should be devoted to high throughput (rather than resolution) in the areas of spectroscopy, imaging and timing. We have tentatively called it HTM (High Throughput Mission). A study group should be formed to refine the mission beyond the conceptual precepts discussed at the Workshop.

It was widely felt among the participants that the above recommendations are essential to maintaining the vigor of X-ray astronomy, and hence astrophysical research, during the coming decade. A more detailed discussion of these recommendations is presented in the Summary section of this report.

Organizing Committee

G.P. Garmire

S.S. Holt

R. McCray

S. Rappaport

H. Tananbaum

TABLE OF CONTENTS

ORIGINAL PAGE IS
OF POOR QUALITY

A G E N D A

Monday October 5, 1981

Chairman, S. Holt

S. Holt	Welcome
F. Martin	Introductory Remarks
J. Linsky	Main Sequence Stars
D. Lamb	Degenerate Dwarfs and Cataclysmics
F. Lamb	Neutron Star Binaries and Bursters

Chairman, S. Rappaport

M. Shull	Supernovae and Supernova Remnants
L. Cowie	Clusters and the Interstellar Medium
A. Fabian	Galaxies and Cosmology
A. Lightman	Active Galactic Nuclei
Y. Tanaka	The Japanese X-Ray Astronomy Program
L. Culhane	The European X-Ray Astronomy Program

Tuesday October 6, 1981

Chairman H. Tananbaum

P. Gorenstein	Large Area Modular Array of Reflectors (LAMAR)
R. Catura	LAMAR with Wolter I Optics
G. Riegler	Charge Coupled Device (CCD) Development
W. Ku	Imaging Gas Scintillation Proportional Counter (GSPC)
R. Petre	Wide Field Soft X-Ray Telescope
M. Ulmer	X-Ray Imaging above 3 keV
R. Novick	Large Focussing Polarimeter
R. Proctor	Hard X-Ray Imaging
J. Grindlay	Hard X-Ray Imaging

Chairman G. Garmire

G. Vaiana	Stellar Coronal Explorer
D. McCammon	Soft X-Ray Spectroscopy of Diffuse Sources
W. Cash	Objective Relflection Grating Spectrograph
C. Canizares	Dispersive Soft X-Ray Spectroscopy
P. Serlemitsos	Broad Band X-Ray Telescope (BBXRT)
P. Meszaros	X-Ray Emission from Pulsars
G. Wunner	Emission Lines in Strong Magnetic Fields
R. Smither	Focussing Bragg X- and Gamma-Rays
R. Griffiths	Spherically Curved Imaging Spectrometer (SCIS)
G. Ricker	Hard X-Ray Detector Telescope (HXDT)
J. Matteson	10 keV - 10 MeV Spectroscopy with Germanium
D. Helfand	5 - 500 keV Spectroscopy with Germanium
R. Rothschild	Hard X-Ray Scintillator Arrays

Wednesday October 7, 1981

Chairman, R. McCray

G. Garmire	Discussion and Summary Presentations by the
S. Holt	Members of the Organizing Committee
S. Rappaport	
H. Tananbaum	
R. McCray	

PRECEDING PAGE BLANK NOT FILMED

SUMMARY

I. BACKGROUND FOR THE WORKSHOP

Opportunities for conducting X-ray astronomy observations in the immediate future appear to be quite limited. A summary of the sensitivity and spectroscopic capabilities of past and anticipated missions is given in Table 1.

TABLE I. APPROXIMATE MISSION[1] CAPABILITIES

Mission	[2]Launch	[3]log S	[4]Range	$\bar{E}$ [5]	[6]R	[7]A_{net}
UHURU	1969	0	2-10	7	3	200
HEAO-1	1977	-1	.1-3	1	2	200
			2-60	7	7	1000
			20-1000	50	5	200
HEAO-2	1978	-3	.1-3	1	100	.2
			.5-4	2	15	200
EXOSAT	1982	-2	.04-2	1	2	15
			1-50	7	5	700
			2-80	7	10	150
ROSAT	1987	-3	.1-3	1	3	300

XTE	1988	-1	2-60	7	7	5000
AXAF	1990	-5	.1-8	1	1000	2
			.5-8	7	50	100

---

[1]Representative X-ray astronomy free flyers. Past (e.g. Ariel-5, SAS-C, OSO-8) and future (Astro-B, Astro-C) missions with capabilities comparable to those indicated for missions in a similar time frame are omitted for the sake of clarity.

[2]Actual or estimated launch date

[3]S is the advertised source detection sensitivity, in units of 10^{-3} of the Crab nebula intensity

[4]Effective energy range (keV)

[5]Typical photon energy in range

[6]Resolving power ($E/\Delta E$) at $\bar{E}$

[7]Net area available for R at $\bar{E}$

Of the U.S. X-ray astronomy missions, only the X-ray Timing Explorer is currently in line for flight in the late 1980's. This mission is envisioned to have wide participation in the form of guest investigator observations. The Extreme Ultraviolet Explorer, operating at energies lower than the X-ray band, is a single institution mission and will have only limited outside activity. The Advanced X-ray Astrophysics Facility is a major U.S. program which requires congressional approval before it can be initiated. In the current climate of budget reductions in Washington, it is difficult to believe that this major new program will be started before the mid 1980's, with a launch at the end of the decade at the very earliest.

Foreign missions which appear to be coming along with a high probability for flight in this decade are: EXOSAT, ROSAT, Astro B and Astro C. another mission, X-80, is in the formative stages and will possibly fly by the end of this decade as well. Only the ROSAT mission is expected to have any substantial participation by U.S. investigators, although the other missions may be open to guest observers on a limited basis for some portion of the useful life of the various satellites.

From the above discussion it is obvious that the opportunities for U.S. investigators to participate in a flight program are very limited. Any future mission that is recommended will represent a rare opportunity. This being the case, the proposed mission must maximize the amount of science that can be accomplished; it must significantly surpass and avoid overlap with current or envisaged mission capabilities, and it should appeal to the scientific priorities of a wide sector of the astronomical community. Finally, the proposed program should be moderate in scope, costing less than a major observatory, but in the general range of current explorers such as IRAS, COBE, or XTE.

II. AN OVERVIEW OF THE WORKSHOP PRESENTATIONS

The first day of the Workshop was devoted to a scientific summary of the current status of astrophysics covering a broad spectrum of topics. Each reviewer was asked to examine his topic carefully and suggest critical X-ray observational data which would provide substantial advancements toward a better understanding of the given subject. These topics and recommendations are presented in the body of the report.

The following table summarizes the suggested observational requirements for a significant advance in each area.

TABLE II

OBSERVATIONAL REQUIREMENTS

QUESTION	OBSERVATION	"R" REQUIRED
Stellar Sources		
Temperatures	Low resolution spectroscopy	10
Geometry	Moderate resolution spectroscopy	100
Activity	Monitor soft X-ray and UV flux	
Densities	Moderate resolution spectroscopy	200
Winds?	Moderate resolution spectroscopy	200
Differences between young & old stars	high resolution spectroscopy	2500
Do hot stars have coronae?	Moderate resolution spectroscopy	200

Imaging needed to separate doubles	$\Delta\theta<0.5'$	

Degenerate Dwarfs and Cataclysmic Variables

Emission mechanism	broadband spectroscopy 0.1-100 keV temporal monitoring	3-10

Neutron Stars

Disk fed or wind fed accretion	UV/Soft X-ray spectroscopy and timing	50
Cyclotron scattering and high magnetic field effects	rapid temporal variations and hard spectra	10

Supernova Remnants

non-Sedov effects (temperature, pressure structure)	imaging spectroscopy	100
reverse shock spectroscopy		100
abundances in different parts of remnant	imaging spectroscopy	10-100

Interstellar Medium and Cluster of Galaxies

Is there a galactic halo?	arc minute resolution with large area	
ISM temperature	absorption spectra	1000
Intergalactic medium	arc minute resolution	
Galaxies	high sensitivity for diffuse emission	10
Galactic coronae	arc minute resolution spectra	100
X-ray background origin	fluctuations deep source counts	

Active Galactic Nuclei

Radiation Processes	large spectral range, high sensitivity 1 keV-10 MeV	5
Power source	temporal behavior, spectra	5
Jet structure	high resolution - arc seconds high sensitivity	

The second day of the Workshop was devoted to a discussion of instrumentation and mission concepts. These are presented in the body of the Proceedings. A general assessment of the technological advancements made since the instrument selection for the HEAO-1 and Einstein Observatory reveals that significant improvements can be made in detector efficiency, energy resolution, background reduction and sensitivity over a broad energy range. Mass production techniques for moderate angular resolution (~ 1') telescopes

have advanced to the stage where it appears feasible to construct an array of telescopes with an area an order of magnitude greater than AXAF at a moderate cost. Advances in spectrometer designs show that a one or two order of magnitude improvement in sensitivity can be achieved over the Einstein Observatory capability with comparable resolving power. At higher energy (>10 keV) several new concepts were presented to provide detectors with better angular resolution and lower backgrounds.

The overall impression gained from the many presentations was that the technology is available to make order-of-magnitude improvements over previous and currently planned missions in almost every dimension of parameter space.

III. RECOMMENDATIONS OF THE WORKSHOP

The final day of the meeting was devoted to a discussion of the strategy to carry out the programs required to achieve the scientific aims outlined in the first day's discussions and within the context of the instrumental capabilities presented on the second day. The group unanimously reendorsed the scientific merits of the X-ray Timing Explorer and the ROSAT missions. These programs should be carried out as soon as possible.

The next moderate cost free-flyer mission that should be initiated, following the XTE and ROSAT, should be a high throughput mission optimized for energies below 10 keV with a collecting area substantially greater than AXAF, and which combines the capabilities of imaging (~1 '), spectroscopy (R ~ 10-100), and timing (m sec). Such a mission received virtually unanimous support. It was recommended that a study group be formed by NASA to define this mission and to provide initial cost estimates, since it was recognized that such a program must be well defined if a moderate cost was to be credible.

Experiments which are designed for flight on the Space Shuttle constitute an effective utilization of this resource. These experiments can provide fundamentally new data on important astrophysical problems and are complementary to the ongoing program of moderate cost free-flyer missions. Important specific scientific questions can be addressed by these experiments which will fall outside the scope of the larger, long duration missions. These experiments could benefit from the EOP or GAS in many cases, as well as the IPS. More opportunities for such specialized observations using the STS should be vigorously pursued.

Finally, balloon-borne expeirments were identified as a relatively

inexpensive means for obtaining answers to key scientific questions in the energy range above 20 keV. These experiments can cost far less than experiments for the STS or for satellites. The high energy spectra of objects ranging from neutron stars and black holes to the nuclei of active galaxies represent an area in which important scientific questions remain unanswered, and support for balloon-borne experiments represents a very cost effective approach to advancing this area of astrophysics

In summary, the Workshop endorsed a pragmatic approach to near-term X-ray astronomical research. First, the continuation of a vigorous balloon-borne program is a necessary complement to the GRO at energies $\gtrsim$ 20 keV. Second, opportunities for specialized experiments afforded by the STS can be a unique inexpensive resource that should be fully exploited. The third recommendation is similarly modest in its cost implications, insofar as it singles out one area of investigation which clearly has priority over all others in the consideration of candidates for a moderate cost free-flyer mission. Purposely sacrificing resolution for throughput in a cost-constrained program, the mission may aptly be dubbed "HTM", for High Throughput Mission.

N82 26056

PRECEDING PAGE BLANK NOT FILMED

CORONAE OF NONDEGENERATE SINGLE AND BINARY STARS: A SURVEY OF OUR PRESENT UNDERSTANDING AND PROBLEMS RIPE FOR SOLUTION

Jeffrey L. Linsky[1]

Joint Institute for Laboratory Astrophysics
National Bureau of Standards and University of Colorado
Boulder, Colorado 80309

ABSTRACT

Einstein has discovered X-ray emission from stars located in nearly every portion of the HR diagram, and, as a consequence, has completely changed our understanding of stellar coronae. Despite this great accomplishment or perhaps because of it, we now recognize that there are many important unanswered questions that require the capabilities of the next generation of X-ray instrumentation. In this survey I review what Einstein has told us about the coronae of stars in different portions of the HR diagram, and how the characteristics of such coronae compare with what we now know about the solar corona. For each type of star, I then list some important unanswered questions and the generic type of X-ray instrument required to answer these questions. This survey clearly points out the critical need for a sensitive X-ray instrument with both moderate spectral resolution ($E/\Delta E$ = 100-300) and imaging ($E/\Delta E \sim 3$) capability that can monitor selected targets for long periods of time. There is also a need for high spectral resolution ($E/\Delta E = 10^3$-10^4), provided sensitivities can be improved greatly over Einstein, and near simultaneous ultraviolet spectroscopy.

I. SOME INTRODUCTORY COMMENTS

While looking through the literature in preparation for this talk, I was struck by how little we knew about stellar coronae as late as 1979. Prior to the launch of Einstein, the literature on this topic consisted of theoretical papers, most of which are now recognized to be based on false premises, X-ray flux upper limits that were not very interesting, and a few tantalizing observations by rockets and the ANS, SAS-3, and HEAO-1 satellites of nearby stars that did not adequately sample the HR diagram. Reviews of this topic prior to Einstein (e.g. Linsky 1977; Vaiana and Rosner 1978; Ulmschneider 1979; Mewe 1979) have thus become very dated with the rapid onslaught of Einstein observations.

---

[1]Staff Member, Quantum Physics Division, National Bureau of Standards.

Prior to Einstein the few detected X-ray sources among normal stars consisted of RS CVn-type binary systems (e.g. Walter et al. 1980), several nearby late-type dwarf stars like α Cen (G2V + K1V), η Boo (G0 IV), and ξ Boo A (G8 V), several M dwarf stars detected during large flares, and the puzzling detections of Vega (A0 V) and Sirius (A1V + WD). Clearly, we needed an instrument that could observe sources several orders of magnitude fainter than the HEAO-1 sky survey. To achieve this gain in sensitivity in soft X-rays, such an instrument would require a pointed telescope with imaging optics and two-dimensional detectors. The launch of Einstein (cf. Giaconni et al. 1979) in 1978 filled this need.

Among its many accomplishments, Einstein has likely had its greatest impact on stellar astronomy because it replaced a picture of stellar coronae based on a handful of detections, which were biased by the high sensitivity limit of previous surveys, with a picture based on detections of X-rays from nearly every type of star (cf. Vaiana et al. 1981). In particular, Einstein detected X-rays from stars of spectral classes O, B, and A, contrary to most previous predictions, and from stars of all ages and stages of evolution. The only region of the HR diagram from which no stellar X-rays have yet been detected is the upper right hand corner including the K-M supergiants and giants (Ayres et al. 1981). Another salient feature of the Vaiana et al. (1981) survey is that there is a factor of three hundred spread in the X-ray luminosities of late-type stars of the same spectral type and luminosity class, implying that effective temperature and gravity are not the main parameters determining the properties of stellar coronae. As we shall see, magnetic fields and stellar rotation play important roles.

While Einstein has told us a great deal about the types of stars that have hot coronae and the range in L_x for each spectral-luminosity class, it has told us very little about the important physical properties of these coronae. For example, the IPC data have so far permitted only a few crude measurements of coronal temperatures, for example, the M5.5e V flare star Proxima Centauri (Haisch et al. 1980), and temperature estimates using SSS data are available only for π^1 UMa (G0 V) (Swank 1981) and a few RS CVn-type systems and Algol (Swank et al. 1981). To my knowledge the OGS data have been used to estimate a coronal temperature for Capella (G6III + F9III) (Mewe et al. 1980), but no other nondegenerate stars or systems. Einstein lacked the sensitivity at high spectral resolution to measure coronal densities, flow velocities, and total energy output for any nondegenerate stars. Thus we can only speculate concerning the geometry, heating rates, wind acceleration mechanisms, and the mechanisms responsible for coronal variability and dynamic phenomena such as flares.

II. CRITICAL X-RAY MEASUREMENTS NEEDED TO UNDERSTAND STELLAR CORONAE

Since the purpose of this Workshop is to plan for future X-ray astronomy missions, I would like to outline what types of measurements are needed to answer the important problems of stellar coronae that Einstein could not answer. In Table 1 I list the specific measurements desired and the minimum spectral resolution ($E/\Delta E$) needed to make these measurements. I do not specify the signal-to-noise needed, but clearly spectra with insufficient

Table 1

Critical X-Ray Measurements Needed to Understand Stellar Coronae

	Generic Type of X-Ray Instrument[a]					
	Imaging Instrument	Energy Distribution Photometry	Low Resolution Spectra	Moderate Resolution Spectra	High Resolution Spectra	Ultraviolet Spectra
$\Delta E/E$	---	3	10-30	100-300	10^3-10^4	$>10^4$
Measurements						
Target Identification	✓					
Timing + Monitoring	✓					
Temperature (T)		Begin	✓			
Range of T			Begin	✓		
Emission Measure (EM)		Begin	✓			
EM(T)			Begin	✓		
Abundances			Begin	✓	✓	✓
Electron Densities (n_e)				✓	✓	✓
Flow Velocities (v)					✓	✓
Questions						
Geometry	Begin			✓	✓	
Energy Balance		Radiative loss rate			Wind loss rate	Conduction loss rate
Heating Mechanism		Begin			✓	✓
Wind Acceleration Mechanism					✓	✓

[a]The entry marked "Begin" indicates the instrument that can begin to measure the quantity of interest. A check mark indicates the instrument with lowest spectral resolution that can make the required measurement.

ORIGINAL PAGE IS
OF POOR QUALITY

signal-to-noise cannot be used to derive information requiring the full spectral resolution. The instruments listed are generic, but by energy distribution photometry I have in mind an instrument with the spectral resolution of an IPC, and by low resolution spectroscopy I have in mind an instrument with the resolution of the SSS at the high energy portion of its bandpass. Moderate resolution spectrometers could have transmission or reflection gratings, either mounted before or after the objective. In general, one would use an instrument with the lowest possible spectral resolution capable of making the necessary measurement as the throughput generally decreases with increasing spectral resolution.

The types of measurements each instrument is capable of performing are the following:

(1) Broadband imaging instruments are best suited for identification of targets, timing experiments, and monitoring of coronae for variability due to rotation of active regions on and off the visible disk, intrinsic changes in the active regions, and flares.

(2) Energy distribution photometry can give crude estimates of coronal temperatures and emission measures from hardness ratios or the distribution of flux measured in each energy bin, provided the detector is well calibrated, theoretical estimates of the continuum and line flux emitted by an optically thin plasma in steady-state equilibrium are accurate, and these assumptions are realistic.

(3) With somewhat higher spectral resolution ($E/\Delta E$ = 10-30), a capability I refer to as low resolution spectroscopy, one can more reliably estimate coronal temperatures and emission measures, provided the plasma is isothermal, or begin to determine a two-temperature fit to the temperature distribution as Swank et al. (1981) have done for the RS CVn binary systems using the Einstein SSS. Holt et al. (1979) have also shown that it is possible to estimate abundances of some elements like Mg, Si, S, and Fe using such data.

(4) Moderate resolution spectroscopy ($E/\Delta E$ = 100-300) has the capability of measuring fluxes of individual spectral lines or close blends formed over a wide range of temperatures. The power of such data has long been recognized by solar astronomers, because selected pairs of lines are often accurate temperature and electron density diagnostics. Jordan and Brown (1981) and Dere and Mason (1981) have recently reviewed the literature concerning such diagnostics.

(5) Finally, high resolution spectroscopy ($E/\Delta E = 10^3$-10^4) permits the measurement of line widths, shapes, and Doppler shifts, as well as the separation of individual lines in close blends. Such data permit the measurement of flow velocities, for example winds, in stellar coronae in the way that ultraviolet spectra from Copernicus and IUE have permitted measurements of outflow velocities in cooler plasmas.

These measurements are the necessary prerequisites for answering specific questions concerning stellar coronae such as:

(1) What is the geometry of the emitting plasma? Imaging experiments with high angular precision can begin to answer this question by identifying the X-ray source with a specific star, and by monitoring the X-ray flux variability for periodic changes due to stellar rotation and to intrinsic source changes. Such data contain crude information on the inhomogeneity of the emitting structures in a corona and their dimensions. Estimates of the volume of the emitting structures require measurements of the emission measure and the electron density, and thus require moderate or high resolution spectroscopy.

(2) What is the energy balance in a stellar corona? The radiative component of the total coronal losses can be determined directly from broadband instruments that measure the total soft X-ray flux, provided one knows the stellar distance. However, when the coronal temperature is less than about 2×10^6 K, it is necessary to estimate the extreme ultraviolet emission from the emission measure and temperature. For many stars the coronal energy losses may not be primarily in the form of X-radiation. Measurement of wind expansion losses requires a determination of the mass loss rate and coronal temperature. Since the mass loss rate is

$$\dot{M} = 4\pi r^2 \rho v$$

one requires high resolution spectroscopy to measure the expansion velocity (v) and mass density (ρ), but the radial position (r) corresponding to these quantities must be estimated theoretically. I am skeptical that X-ray instruments with resolutions of 10^3-10^4 and sufficient sensitivity to study many stars will be feasible soon, so that for the foreseeable future estimates of coronal wind expansion losses may have to be made on the basis of ultraviolet P Cygni-type profiles and microwave fluxes (cf. reviews by Cassinelli 1979, and Conti 1981). Such data may be adequate for O stars, but X-ray spectra are needed to measure the wind properties of late-type stars with hot coronae. The third important coronal loss mechanism is often thermal conduction to the transition region, which appears as ultraviolet emission line flux. Thus ultraviolet spectra are needed in addition to X-ray data to assess the total coronal energy budget of many stars.

(3) What are the important coronal heating mechanisms in different types of stars? This difficult question has not yet been answered even for the Sun (cf. reviews by Kuperus, Ionson, and Spicer 1981; Hollweg 1981; and Ulmschneider 1981). Necessary prerequisites for answering this question are estimates of the total input flux and its dissipation length together with information on whether the emitting volume is spherically symmetric or primarily in closed magnetic loops. As described below, coronal heating in the Sun is enhanced in closed magnetic loops; consequently, estimates of coronal field strengths and filling factors either from extrapolations of photospheric fields or from microwave flux measurements would be useful. These types of data, as necessary as they are, are not sufficient. To clearly identify the dominant heating mechanism in specific types of stars, we need reliable theoretical calculations that point out the unique signatures of the different possible mechanisms in X-ray and other data.

(4) What are the important wind acceleration mechanisms in different types of stars with hot coronae? This is also a difficult question because different mechanisms have been proposed (radiation pressure, momentum deposition by acoustic waves and by magnetohydrodynamic waves), and the unique signatures of these different mechanisms have not yet been worked out. Cassinelli (1979), Hearn (1981), Castor (1981), and Linsky (1981) have recently reviewed these mechanisms and the types of stars for which each may be important. Clearly it is necessary to determine empirically mass loss rates, terminal velocities, and temperatures for different types of stars, and especially how these quantities depend on stellar luminosity, gravity, effective temperature, and age. As previously noted, this is difficult because one generally needs high resolution X-ray spectra; however, for the O stars ultraviolet spectra and microwave fluxes may provide much of the necessary data to discriminate among different mechanisms.

III. WHAT WE KNOW ABOUT THE SOLAR CORONA THAT WILL LIKELY BE OF RELEVANCE TO OTHER STARS

Before proceeding to a discussion of the stellar data and the unanswered questions they raise, it is important to summarize what has been learned recently about the one stellar corona that can be studied with the necessary spatial resolution. I do not wish to imply that all stellar coronae are similar to the Sun or even that the solar corona exhibits all the physical processes that occur in stellar coronae. However, the Sun probably does provide useful prototypes of phenomena and mechanisms that we should search for on stars, but there are some types of stars like the O stars that have coronae that may be qualitatively different from the solar example. Recent reviews of phenomena and structures seen in X-ray observations of the Sun include Withbroe and Noyes (1977), Vaiana and Rosner (1978), and Webb (1981).

a) Geometry of the Solar Corona

(1) Perhaps the most basic statement that can be made about the solar corona as imaged in soft X-rays is that it is not in any way homogeneous or spherically symmetric. On the contrary, it is highly structured. Thus any theoretical model of a stellar corona that assumes spherical symmetry lacks essential physics.

(2) The basic structure in the solar corona is the closed magnetic flux tube. There are three lines of evidence that support this statement. First, soft X-ray images of the corona clearly show structures that appear to be individual loops or arcades of loops. Second, potential (i.e. force-free) extrapolations of the observed photospheric magnetic fields into the corona are nearly coincident with the observed X-ray loops (cf. Poletto et al. 1975), but the match is not precise, implying that there are electric currents in the corona. Thus the soft X-ray emission outlines the three-dimensional magnetic field structure of the corona. Third, the solar corona is a low β plasma (i.e. the thermal energy is much less than the magnetic energy), so that the plasma should be confined by closed loop structures.

(3) The solar corona has three types of regions. Active regions consist of bright loops that generally have at least one footpoint in a spot penumbra or umbra. These loops have strong magnetic fields and connect areas of opposite magnetic polarity. Quiet regions also contain closed loop structures, but the fields are weak and there are no sunspots. Finally, coronal holes are regions of very weak X-ray emission and have field lines that are open to space.

(4) In active and quiet regions essentially all of the observed X-ray emission is from the closed loops. Thus the closed loops are the solar corona, and meaningful coronal models must include a loop geometry and incorporate magnetic forces.

(5) Empirical models of coronal structures clearly show that differences in physical conditions (temperatures, densities, mass and energy flux) from point to point across the Sun appear to be intimately related to the configuration and strength of the magnetic fields, in particular whether the fields are open or closed.

(6) The structuring of the solar atmosphere into loops dominates the whole atmosphere from the chromosphere, through the transition region, and out some distance into the corona.

(7) Coronal holes are the origins of high speed wind streams (with velocities up to 800 km s^{-1}) and perhaps most of the mass loss from the Sun. The latter point is difficult to verify as coronal holes typically lie at high latitudes and wind measurements are made mostly in the ecliptic. Zirker (1981) has recently reviewed the properties of coronal holes.

(8) There is strong evidence that magnetic fields control the energy balance in loops by channeling the flow of mass and energy as well as presumably playing a major role in the heating rate (see Holweg 1981 for a recent review of this topic). Withbroe and Noyes (1977) have estimated the coronal energy budget for active regions (representative of loops with strong fields), quiet regions (representative of loops with weak fields), and coronal holes (open field regions). It is interesting that although the total coronal loss rates (presumably equal to the heating rates) are 30 times larger in active than in quiet regions, both regions are cooled primarily by conduction down to the transition region and X-radiation. For both regions the wind losses are very small, presumably because closed field lines in loops prevent the escape of plasma to space. The total loss rates for coronal holes and quiet regions are similar, but holes are cooled primarily by the solar wind flux instead of conduction down to the transition region and X-radiation. Also holes have lower temperatures, pressures, and temperature gradients than quiet and active regions.

(9) Thus the solar corona in reality consists of many loops with different physical properties that coexist due to the thermal isolation provided by closed magnetic field lines.

b) Properties of Solar Coronal Loops

(1) Individual X-ray images of the solar corona deceptively suggest that the loops are static; but on the contrary, the solar corona is always changing. The brightness of individual loops changes with time due to the filling and draining of flux tubes with changes in the heating rate and restructuring of magnetic field lines on a time scale of hours. Many loop structures, called empherical regions, appear and fade within a day. The so-called bright points are compact, high density loop structures that represent newly emerging magnetic flux. These typically survive less than a day, but even the large active region loops live for only a few days. Thus theoretical loop models that assume steady-state conditions and hydrostatic equilibrium are gross oversimplifications.

(2) When first seen in X-rays, loops are generally small, hot, dense, and bright. As they evolve, the loops generally expand, decrease in plasma temperature and density, and thus in X-ray brightness. Golub et al. (1980) presented evidence that the energy density of loops ($U_T = nkT$) is inversely proportional to the loop length (L) and age (t). They also argued that $U_T \sim \phi_T^{1.7}$, where ϕ_T is the magnetic flux, and that the gas pressure $P \sim B^{1.6}$, where B is the average longitudinal field.

(3) Observed loop lengths, $L = 10^8$-10^{10} cm, are much smaller than the solar radius, ($R_\odot = 7 \times 10^{10}$ cm) and the coronal pressure scale height ($\approx 0.23\ R_\odot$ for $T = 2.5 \times 10^6$ K). Although loop sizes form a continuous distribution, there are many more small than large loops. Loop temperatures generally lie in the small range, $T = 2\text{-}3 \times 10^6$ K, and densities lie in the much larger range, $n_e = 10^8$-10^{10} cm^{-3}. Thus loop pressures lie in the range, $P = 0.03 - 3$ dynes cm^{-2}. There is considerable evidence that individual flux tubes are isothermal, both in the longitudinal and radial directions, and that they are isobaric, consistent with their heights being smaller than a pressure scale height. There is no obvious reason why loops cannot be larger than a stellar radius or coronal pressure scale height in stars with different gravities and magnetic field configurations, but the solar data suggest that at least dwarf stars with bright X-ray emission probably have small, dense loop structures.

(4) There are several empirical scaling laws for the properties of solar coronal loops (cf. Withbroe 1981). One widely quoted law is $T_{max} = 1.4 \times 10^3\ (PL)^{1/3}$, where T_{max} is the maximum loop temperature, proposed by Rosner, Tucker and Vaiana (1978). Since solar loops have only a small range in temperature, this law implies that $P \sim L^{-1}$. Webb (1981) has pointed out that the empirical scatter about this scaling law is very large, and the assumptions of hydrostatic equilibrium, absence of flows along the loop or conductive heat flow at the bottom, and constant loop cross section made by Rosner et al. may not be valid. Recently, Serio et al. (1981) have generalized the Rosner et al. scaling law to include loops larger than a pressure scale height, and Priest (1981) has reviewed the theory of loop flows and instabilities.

(5) At present we should view recent loop models as moderately successful as they can interrelate plasma parameters within a loop in a manner consistent with observations. Such models should also be thermally stable provided that the maximum temperature occurs at the top of the loop. However, the major problem with these models is that the loop properties, in particular L_x, appear to depend only on the heating rate and not on the heating mechanism or even where in the loop the heating occurs. Thus there are no unique signatures of the heating process. Perhaps stellar observations can help. For a recent overview of heating mechanisms see Hollweg (1981) and Kuperus et al. (1981).

(6) Finally, we should ask why the range in solar loop temperatures is so small. I believe that this small range indicates that loops can easily respond to changes in the heating rate by evaporation or condensation of material at transition region temperatures ($\sim 10^5$ K) at the loop footpoints. For example, increased heating anywhere in the loop leads to enhanced conductive heating at the footpoints that evaporates transition region gas into coronal (i.e. $T > 10^6$ K) gas. This process is stable because radiative losses from the loop ($\sim n_e^2$) can then balance the increased heating with little change in temperature. Conversely, decreased heating leads to condensation of coronal gas at the footpoints, decreased radiative losses, and energy balance with little change in loop temperature. Thus stellar coronal temperatures much in excess of 3×10^6 K may indicate a very different energy balance or geometry in such coronae.

IV. DWARF STARS OF SPECTRAL TYPES F, G, K AND M

Given as background what we now know about the solar corona, I would like to survey the HR diagram and ask two questions. First, what have we learned in general about the coronae of each group of stars from Einstein and other experiments? Second, what are the important unanswered questions that could be answered by the next generation of X-ray experiments? Since I would like to compare and contrast the solar and stellar data, I will begin with the stars that are most solar-like and gradually move on to stars that have very different coronae or perhaps outer atmospheres that should not even be called coronae.

a) What We Have Learned from Einstein

(1) Einstein has detected X-rays from almost every type of star with the exception of the cool supergiants, as will be discussed below. In the first comprehensive survey of Einstein stellar observations, Vaiana et al. (1981) detected essentially all nearby F-M dwarf stars that were observed for sufficiently long times. For many of these stars the IPC count rates exceeded 0.1 counts s^{-1}, corresponding to 2×10^{-12} ergs cm^{-2} s^{-1} for the 0.25-4 keV band, and typical limiting sensitivies were 10^{-13} ergs cm^{-2} s^{-1} in 2000 second exposures. The HEAO-1 A2 experiment all sky survey was unable to detect many F-M dwarfs because its sensitivity was only $\sim 6 \times 10^{-12}$ ergs cm^{-2} s^{-1}.

(2) It is clear that the soft X-ray emission is from analogues of the solar corona rather than accretion as in the classical X-ray binary systems because both single and binary stars are soft X-ray sources, and as will be

described later, the X-ray emission from the tidally synchronous binary systems (like the RS CVn systems) is similar to that of single stars with the same rotational velocities.

(3) Perhaps the most far reaching result is that the standard stellar parameters of mass, effective temperature, and gravity, which determine where a star is located in the HR diagram, are not the most important parameters determining the soft X-ray luminosities of F-M dwarf stars and most other types of stars. There are two main reasons for this conclusion. First, the Vaiana et al. (1981) survey shows that for stars of the same effective temperature and luminosity class there is a factor of 300 spread in L_X, which could be even larger because of the sensitivity threshold of Einstein. Second, the mean value of L_X for the F, G, K, and M dwarfs is roughly $10^{28.5}$ ergs s^{-1}, independent of spectral type even though L_{bol} decreases rapidly toward the cooler stars. With appropriate hindsight we should have expected this result because the solar X-ray brightness varies greatly from point to point across the solar surface, and it is apparently controlled by the local magnetic field strength and geometry.

(4) The range in L_X observed for G-type dwarf stars is entirely consistent with the range in L_X seen in the Sun. For example, the mean value of L_X for the quiet Sun is roughly $10^{26.8}$ ergs s^{-1}, which lies close to the bottom of the distribution for early G dwarfs, whereas the value of L_X for the whole solar surface if covered with active regions ($L_X = 10^{29.3}$ ergs s^{-1}) would lie near the top of this distribution. This latter coincidence could be interpreted either that the brightest solar-type stars are covered entirely by coronal structures similar in brightness to solar plages (active regions) or that they are partially covered with superplages (regions with X-ray brightness much larger than is seen in solar active regions). The Hyades data strongly support the existence of superplages.

(5) There is convincing evidence that stellar rotation plays a critical role in determining the relative X-ray luminosity of stars with similar spectral type and luminosity class, although the functional form of this relation has not yet been decided conclusively. The importance of rotation can be seen at once by comparing three early G dwarf stars -- π^1 UMa (G0 V), α Cen A (G2 V), and the quiet Sun (G2 V). π^1 UMa is the most luminous G dwarf observed by Vaiana et al. ($L_X = 10^{29.1}$), and it is a rapid rotator for its spectral type ($v \sin i = 9$ km s^{-1}). By comparison α Cen A and the quiet Sun have low X-ray luminosities ($L_X = 10^{27.1}$ and $10^{26.8}$ ergs s^{-1}, respectively) and small rotational velocities ($v \sin i = 2$ km s^{-1}).

However, there is disagreement as to the dependence of L_X on rotational parameters for F-M dwarfs. Using HEAO-1 observations of a few single stars and RS CVn systems, Ayres and Linsky (1980) suggested that L_X/L_{bol} increases rapidly with $v \sin i$. Pallavicini et al. (1981) used the existing Einstein observations of single F7-M5 stars to show that $L_X \sim (v \sin i)^{1.9 \pm 0.5}$, independent of L_{bol} and luminosity class. This result is consistent with the X-ray surface flux being proportional to Ω^2, where Ω is the angular rotational velocity. On the other hand, Walter and Bowyer (1981) and Walter (1981) found that $L_X/L_{bol} \sim \Omega$ fairly well represents the Einstein and HEAO-1 data

for 47 RS CVn systems and 13 rapidly rotating F8-G5 dwarfs stars. Subsequently, Walter (1982) proposed that no single power law can fit the Einstein observations of single F8-G2 dwarfs including the Sun and Hyades stars, but instead two power laws are needed of the form $L_X/L_{bol} \sim \Omega^{\alpha}$ with a break near a rotational period of 12 days. It is interesting that Vaughan and Preston (1980) and Vaughan (1980) find evidence that the character of stellar dynamos changes when dwarf stars slow down to a rotational period of 12 days, which occurs at an age of about 1×10^9 yr.

(6) The age of late-type stars on the main sequence is also an important parameter, perhaps in a more fundamental sense than rotation. In the 1960s there were a number of important studies of the rotation of F and G dwarf stars by Wilson, Kraft, Skumanich, and others, who concluded that stellar rotational velocities decrease with age on the main sequence, presumably as a consequence of angular momentum loss in stellar winds. On the basis of these data, Skumanich (1972) proposed that the stellar equatorial velocity, $v \sim t^{1/2}$, where t is the age on the main sequence. Recently, rotational velocity measurements have become more precise as a result of increased throughput for high resolution spectroscopy, Fourier techniques for analyzing line profiles (cf. Gray 1976), and programs to monitor the rotational modulation of stellar active regions by observing the Ca II flux (e.g. Vaughan et al. 1981). Duncan (1981) and Soderblom (1981) showed that these new data confirm the Skumanich (1972) rotation-age correlation.

As yet there is no thorough survey of the relation of stellar X-ray luminosity or surface flux with age. However, the Stern et al. (1981) study of the Hyades cluster ($t = 10^{8.6}$) stars with Einstein clearly indicates a definite correlation of bright X-ray emission with youth. Despite their sensitivity threshold, which corresponds to a factor of 10 higher than the quiet Sun value of L_X, they detected 80% of the F and G dwarfs in the cluster. Their brightest source is 71 Tau, an F0 V star with $v \sin i = 200$ km s^{-1} and $L_X \geq 10^{30}$ ergs s^{-1}, and their brightest G star is HD 27836 (G1 V) for which $L_X = 10^{30}$ ergs s^{-1}. Since this star is about five times as bright in X-rays as the Sun would be if covered entirely by plages, it must contain flux tubes which are beyond the range of brightness, and thus presumably also of density, typically seen in the solar corona. Stern et al. (1981) have proposed, on the basis of scaling laws, that this star contains superactive regions covering about 10% of the stellar surface.

(7) By analogy with the solar corona, the F-M dwarf stars, especially the young stars with bright X-ray emission, should have strong closed magnetic field structures in their coronae. This argument is no longer speculation, but has now been confirmed by two separate lines of evidence. First, Robinson, Worden, and Harvey (1980) have measured photospheric magnetic fields in two young dwarfs, ξ Boo A (G8 V) and 70 Oph A (K0 V) by measuring line splitting in unpolarized light. For ξ Boo A, they found the field to be 2,600 ± 400 Gauss covering 30% of the surface. Marcy (1980) has detected magnetic fields in additional stars and is now studying variability and rotational modulation of stellar active regions with large magnetic fields. It is interesting that the major difference noted so far between the photospheric magnetic fields of these young stars compared to the Sun is that the strong fields cover a much larger fraction of the stellar surface.

The second type of direct evidence is observations of microwave emission from stellar coronae. Gary and Linsky (1981) detected steady 6 cm emission from χ^1 Ori (G0 V) and UV Cet (dM5.5e) with the VLA, which they interpreted as gyroresonant emission from electrons spiralling along coronal magnetic field lines. This emission is consistent with coronal fields of roughly 300 Gauss, slightly larger than the field strengths in solar coronal loops. Both stars are bright X-ray sources for their spectral types.

(8) There are as yet very few measurements of coronal temperatures for late-type dwarfs. In principle, the Einstein IPC pulse height spectra can provide crude temperature estimates, but meaningful temperatures await the reprocessing of these data. The Einstein SSS instrument has proved to be useful in estimating coronal temperatures for RS CVn systems, but so far the only coronal temperature for late-type dwarf stars obtained with the SSS is for the young G0 V star π^1 UMa, for which Swank (1981) estimated $T = 3\text{–}5 \times 10^6$ K. Haisch et al. (1980) have also estimated $T = 4 \times 10^6$ K for Proxima Centauri (dM5e) at quiescent times using IPC pulse height spectra.

b) Some Important Unanswered Questions

1. What is the range of coronal temperatures that occurs in magnetic loop structures? In particular, does the temperature increase with stellar X-ray luminosity or surface flux, and does it depend at all on spectral type among the cool dwarfs? This question can be answered with energy distribution photometry, perhaps with reprocessed Einstein IPC data, and low resolution spectroscopy (see Table 1).

2. What fraction of the coronal volume is filled with bright X-ray emitting loops for stars of different ages, spectral types, and L_X? Since the volume of the emitting region can be derived from the emission measure and electron density, this question requires moderate resolution spectra.

3. What are the evolutionary time scales of coronal loops and active regions, and what are the properties of stellar magnetic cycles and dynamos? Monitoring of stars with imaging experiments is important for studying these time scales, but such observations should be accompanied by simultaneous measurement of the stellar transition regions with ultraviolet spectroscopy, photospheric magnetic fields with optical spectroscopy, and microwave observations with the VLA.

4. What are the densities of coronal loops in different types of stars? Of specific interest is the question of whether loops in stars with large L_X are dense and small, or tenuous and large, or both. Moderate or high resolution spectroscopy is needed to measure density-sensitive line ratios in order to answer this question.

5. What mechanism or mechanisms heat coronae in late-type dwarf stars? The observational data needed to answer this difficult question cannot be predicted easily due to our lack of knowledge as to how even the solar corona is heated. My guess is that we need to know more about how the energy balance in dwarf star coronae changes with effective temperature, age, and L_X, and whether the geometry of these coronae are solar-like as we presently

believe. An understanding of the energy balance will require energy distribution photometry, high resolution spectroscopy, and ultraviolet spectroscopy (see Table 1). Also, the study of eclipsing systems with imaging experiments will provide information on where the coronal cooling occurs for comparison with theoretical models.

6. Do active dwarf stars ($L_X >> L_X(\odot)$) have hot winds and low mass loss rates like the Sun? This question might be unanswerable with foreseeable instrumental developments, but it is important to try to answer this question by searching for Doppler-shifted X-ray lines with a high throughput high resolution spectroscopic experiment.

7. What are the fundamental differences between the coronae of young and old dwarf stars. Are the differences primarily in the fraction of the coronal volume filled with loops, the loop lengths, densities, temperatures, or total coronal heating rates? Since the measurement of coronal densities is critical to answering this question, we need moderate or high resolution spectra.

8. What are the hottest dwarf stars with solar-like corona? A high throughput imaging experiment should be able to answer this question.

V. PRE-MAIN SEQUENCE STARS

Pre-main sequence (preMS) stars, including the T Tauri stars, the young stars in clusters such as Orion, and the recently identified post-T Tauri stars, probably have coronae that are qualitatively similar to the young F-M dwarfs that recently became main sequence (MS) stars. However, as we shall see, the X-ray emission from the preMS stars can be absorbed by overlying circumstellar gas.

a) What We Have Learned from Einstein

1. When detected as X-ray sources, the T Tauri and other preMS stars are the most luminous among the late-type stars that are not known to be close binaries. Since these stars are distant, the detection thresholds are large; for example, $L_X \approx 10^{30}$ ergs s^{-1} for the Taurus-Aurigae cloud and $L_X \approx 2 \times 10^{31}$ ergs s^{-1} for the Orion cloud. Nevertheless, 10 out of the 14 known T Tauri stars in the Taurus-Aurigae cloud brighter than $m_V = 13$ have now been detected as X-ray sources by Walter and Kuhi (1981), and the fainter T Tauri stars were likely not detected due to the sensitivity limit of Einstein. Feigelson and de Campli (1981) detected DG Tauri at $L_X = 8 \times 10^{30}$ ergs s^{-1}, and Gahm (1980) detected Th 12 at $L_X = 6 \times 10^{30}$ ergs s^{-1} in the Taurus-Aurigae cloud. These stars are 10^4 times more luminous than the quiet Sun. The most luminous preMS star detected so far is GW Ori ($L_X = 5 \times 10^{31}$ ergs s^{-1}) observed by Feigelson and de Campli (1981).

2. Given that the detected preMS stars are so luminous in X-rays, an important question is why many of these stars in the Taurus-Auriga and Orion clouds, primarily those with strong Hα emission and blue excess emission, are not detected as X-ray sources. Gahm (1980) argued that interstellar absorption is not the reason for the many nondetections on the basis that

RW Aurigae is a T Tauri star with extremely bright optical and ultraviolet emission lines, yet it is not a detected X-ray source despite its lying outside the dark obscuring regions of the Taurus-Aurigae cloud, and the small interstellar gas column density in its line of sight. Instead he argued that the preMS stars have hot coronae that are surrounded by extensive cool circumstellar gas envelopes that can totally absorb the X-ray emission in some cases. For example, he estimated optical depths for the RW Aurigae envelope of $\tau(0.6\ \text{keV}) \approx 72$ and $\tau(2\ \text{keV}) \approx 2$. Thus the soft X-ray emission would be totally absorbed, but this star might be a hard X-ray source. Walter and Kuhi (1981) supported Gahm's (1980) model by finding an inverse correlation among the T Tauri stars of Hα equivalent widths and X-ray fluxes. They concluded that the T Tauri stars have small solar-like coronae surrounded by extensive cool envelopes that produce the Hα emission and X-ray absorption.

3. Feigelson and de Campli (1981) observed rapid variability in the X-ray flux of the T Tauri star DG Tau. They detected no flux during the first 35 minutes of observation and then a rapid increase in flux on a time scale of 4 minutes. This rapid flare-like variability also suggests emission from a small region of high density close to the star, and like the brightest X-ray features on the Sun (the so-called bright points) could be emission from small dense loops of newly emerging magnetic flux just above the photosphere.

4. In T Tauri stars for which X-ray emission is detected, $L_X/L_{bol} \approx 10^{-4}$, which is similar to the ratio for the youngest F and G main sequence stars. By comparison $L_{H\alpha}/L_{bol} \approx 10^{-3}$, $L_{Mg\ II}/L_{bol} \approx 2 \times 10^{-3}$, $L_{Ca\ II}/L_{bol} \approx 5 \times 10^{-4}$, and $L_{Wind}/L_{bol} \approx 5 \times 10^{-3}$ for the same stars. Thus the emission from the corona is much less than from the chromosphere and/or envelope, and the radiative losses are comparable to the wind losses in T Tauri stars.

5. The coronal temperatures for T Tauri stars are poorly known, but Feigelson and de Campli (1981) estimated $T \geq 5 \times 10^6$ K for DG Tau during its flare, and Walter and Kuhi (1981) estimated $T \geq 14 \times 10^6$ K for AA Tau on the basis of IPC pulse height spectra. Estimated T Tauri coronal temperatures are likely affected by circumstellar gas absorption.

6. Recently Feigelson and Kriss (1981) and Walter and Kuhi (1981) discovered five X-ray sources that lie 1-3 magnitudes above the main sequence yet have weak Hα emission, no ultraviolet excess, and show no evidence for optical variability or winds. They therefore believe these stars to be intermediate in age between the T Tauris and main sequence stars. These stars are luminous ($L_X \approx 10^{30}$ ergs s^{-1}), and presumably have coronae similar to but more active than the stars that have recently arrived on the main sequence.

7. Three mechanisms have been proposed to explain high temperature emission from preMS stars. Ulrich (1976,1978) and Mundt (1980) studied accretion shocks, but their models typically predict $T < 3 \times 10^6$ K, which appears to be smaller than observed. Heating by shocks at the wind-interstellar medium interface was proposed by Kuhi (1964) and Ku and Chanan (1979), but the observed anticorrelation of Hα equivalent width and X-ray emission are hard to explain by this model. At present, the most plausible model appears to be that of a small corona surrounded by an extensive cool

circumstellar gas envelope. If this model is valid, as is suggested by the data, then the coronae of preMS stars are probably extreme examples of the solar corona with emission from small dense magnetic loop structures.

b) Some Important Unanswered Questions

1. What are the physical properties of the X-ray emitting regions in preMS stars: their temperatures, densities, and volumes? As previously discussed in §IV, temperature measurements require either energy distribution photometry or low resolution spectroscopy, but the latter is probably needed for these stars because one must measure both the circumstellar absorption and coronal temperature together. While in principle well-calibrated energy distribution photometry could measure both parameters, experience with the Einstein IPC points out the need for higher resolution data. Measurements of density and volume require at least moderate resolution spectroscopy.

2. What is the geometry of the emitting regions in preMS stars? I would estimate that the rotational periods for these stars probably lie in the range 3-8 days. Thus monitoring the X-ray emission from these stars for this time period with an imaging experiment should determine whether the X-rays are emitted from a few active regions or uniformly across the stellar surface, and such observations should also determine time scales for the variability of these active regions. High resolution ultraviolet spectra should also be useful in measuring the Doppler shifts of transition region emission lines from active regions and thus their location on the stellar surface, however, such measurements will be difficult because of the large line widths.

3. Various authors have estimated mass loss rates and flow velocities for the cool circumstellar gas, but there are no measurements of the outflow or infall velocities for the hot coronal gas. It is entirely possible that the X-ray emitting plasma is confined to closed magnetic loops that do not participate in the flow while the wind originates in magnetically open regions (coronal holes). Measurement of the flow velocities for coronal plasma requires high resolution X-ray spectroscopy, which may not be feasible for these stars, but similar measurements for the plasma at transition region temperatures requires high resolution ultraviolet spectroscopy, which will be feasible with Space Telescope. Even with such data, however, the interpretation will be difficult as different authors have interpreted P Cygni-type profiles for T Tauri stars as indicating mass inflow and outflow.

VI. M DWARF FLARE STARS

a) What We Have Learned from Einstein

1. Flares on the Sun have been studied extensively with instruments covering the electromagnetic spectrum, and flares on M dwarf stars have been studied at optical and radio wavelengths since 1949. While it was recognized that X-ray observations would be critical in understanding the properties of the hot plasmas in flares, sensitivity limitations precluded X-ray observations of all but the most energetic events prior to Einstein. For example,

Heise et al. (1975) detected a large flare on YZ CMi (M4.3eV) and UV Cet (M5.6eV) using the ANS satellite, and Kahn et al. (1979) detected two flares each on AD Leo (M3.5eV) and AT Mic (M4.4eV). The X-ray luminosities for the flares observed in AD Leo and AT Mic are very large, L_X = 1.3-1.6 × 10^{30} ergs s^{-1}, as much as a factor of 4000 larger than very large solar flares.

2. Einstein has now observed flares on Proxima Cen (Haisch et al. 1980, 1981), YZ CMi (Kahler et al. 1982), Wolf 630 AM and BD + 44°2051 (Johnson 1981), and perhaps other M dwarfs. Many of these observations were part of collaborative observing programs involving simultaneous optical, ultraviolet, and radio observations. As a result of the greater sensitivity of Einstein, less luminous flares can be studied in detail. For example, the flare on Proxima Centauri observed by Haisch et al. had a peak luminosity of L_X = 7.4 × 10^{27} ergs s^{-1}, comparable to a very large solar flare.

The X-ray light curve and temperatures of this flare on Proxima Centauri were in many ways similar to solar flares. For example, the temperature, as crudely estimated from IPC pulse height spectra, reached a peak of 17 × 10^6 K early in the flare and the X-ray luminosity peaked about 5 minutes after the peak temperature. Both properties are typical of solar flares. From the X-ray decay time they postulated that the flare was cooled by radiation, but simultaneous ultraviolet spectra are needed to determine the importance of conduction and expansion cooling. For the extremely luminous flare on AT Mic, Kahn et al. (1979) were able to derive a single characteristic temperature of 30±10 × 10^6 K, which is somewhat larger than the temperatures typically seen during the cooling phase of solar flares.

b) Some Important Unanswered Questions

1. We need to observe a considerable number of flares to see what ranges of temperature, X-ray luminosity, and emission measure are typical for flare events in M dwarf stars of different effective temperatures and ages. Monitoring by imaging instruments with energy distribution photometry capability is needed.

2. What are the variations of temperature, electron density, X-ray luminosity, and emitting volume as a function of time during flares? To answer this question, we need a high throughput instrument with moderate spectral resolution capability.

3. What are the turbulent and systematic mass motions during flares, and do these motions play an important role in the flare energy balance? Depending on whether the velocities are ~10^2 or ~10^3 km s^{-1}, either high or moderate X-ray spectral resolution will be needed to study the hot gas. Velocities of the cooler gas should be easily studied in the ultraviolet by the Space Telescope High Resolution Spectrograph.

4. A critical question is whether flares are cooled primarily by radiation, conduction, or expansion. This question requires simultaneous measurements by different instruments: radiative losses can be measured by X-ray energy distribution photometry, conductive losses by ultraviolet spectroscopy, and expansion losses by moderate or high resolution X-ray spectroscopy

as previously discussed. A determination of the total cooling rate determines the heating rate, and thus provides valuable information on the flare energy source.

5. Do flares occur on warmer stars? The answer must be yes because the Sun flares, but such flares are difficult to see optically because of reduced contrast with respect to the photospheric background and the probable lower frequency of flares. X-ray observations should be able to answer this question as the quiescent coronal background is generally small compared to flares even for the Sun. Monitoring of G and K dwarfs with a simple X-ray imaging experiment for long periods of time is needed to answer this question.

VII. LUMINOUS COOL STARS

a) What We Have Learned from Einstein

1. Prior to Einstein no nonbinary late-type giant or supergiant was detected as an X-ray source. Einstein detected several nonbinary G giants with L_X between 10^{28} - 10^{30} ergs s^{-1} and two early K giants, ε Sco (K0 III-IV) and α Ser (K2 III), with $L_X \approx 10^{28}$ ergs s^{-1} (Vaiana et al. 1981, Ayres et al. 1981). The latter two stars have $L_X/L_{bol} \approx 3\times10^{-8}$, which is smaller than this ratio for solar coronal holes.

2. Einstein was unable to detect X-rays from single giants cooler than about K2 III and G-M supergiants. For example, α Boo (K2 III) and α Tau (K5 III) were not detected with upper limits $L_X/L_{bol} < 3 \times 10^{-9}$, about a factor of 30 smaller than for solar coronal holes. Also the G supergiants β Aqr (G0 Ib) and α Aqr (G2 Ib) have upper limits $L_X/L_{bol} < 10^{-7}$ and the M supergiants α Ori (M2 Iab) and α Sco (M1 Ib+M) have upper limits $L_X/L_{bol} < 2 \times 10^{-9}$. These nondetections led Ayres et al. (1981) to propose a boundary in the cool portion of the HR diagram separating a region (consisting of K2-M giants and G-M supergiants) in which there is no evidence for hot coronae from a region (consisting of G-K2 giants and F-M dwarfs) in which hot coronae are usually, but not always, detected. The location of this boundary is similar to that separating regions where transition regions are or are not typically seen and where massive cool winds begin to appear.

3. At present we do not know which of several possible explanations for this boundary in the HR diagram is correct. If the nondetection of X-rays from stars cooler and more luminous than this boundary is an instrumental threshold effect, then the coronae have surface brightnesses much smaller than coronal holes. Alternatively, the coronae may be cooler than $\sim 1\times10^6$ K and the X-ray emission will be too soft for detection by Einstein. Absorption of soft X-ray emission by overlying cool circumstellar gas is a possible explanation for the lack of detected X-rays from the G-M supergiants but not the K2-M giants. Finally, these stars may not have hot coronae, but rather extended cool ($T \approx 10^4$ K) envelopes that do not emit X-rays. Ayres et al. (1981) proposed the latter explanation, but more information is needed to confirm or refute this proposal.

b) Some Important Unanswered Questions

1. Do the K2-M giants and G-M supergiants have faint coronae at 10^5 - 10^6 K? This question can be answered with ultraviolet spectra, such as from IUE and Space Telescope, or by an extremely soft X-ray or extreme ultraviolet imaging experiment. Hartmann et al. (1980, 1981) have already found that β Aqr (G0 Ib), α Aqr (G2 Ib), and α TrA (K4 III) show ultraviolet emission lines formed at 10^5 K.

2. What are the coronal temperatures for the G giants that are detected as X-ray sources? Energy distribution photometry can answer this question, and in principle recalibrated Einstein IPC pulse height spectra will provide this information on a few stars.

3. What are the electron densities and emitting volumes (i.e. loop dimensions) for the G giants? Moderate resolution X-ray spectra are needed.

4. What are the geometries of the G giant coronae? Monitoring of these stars over rotational periods with imaging experiments is needed to answer this question.

VIII. RS CVn AND RELATED CLOSE BINARY SYSTEMS

The RS CVn binary systems are detached systems with periods of 1-14 days, generally consisting of a K0 IV primary and a late G dwarf secondary star. Hall (1976, 1981) has reviewed the properties of these systems as well as the related long period systems with giant star components and the contact W UMa systems, and Popper and Ulrich (1977) have discussed their evolutionary status. The most striking peculiarity of the RS CVn systems is a migrating quasi-sinusoidal distortion in their optical light curves (Hall 1981; Rodono 1981) that is generally explained by an uneven distribution of dark, cool photospheric spots (cf. Eaton and Hall 1979). There is evidence that the chromospheric Hα and Ca II H and K emission lines are bright when the visible hemisphere shows maximum coverage by the dark spots (cf. Dupree 1981).

a) What We Have Learned from Einstein

1. Using the HEAO-1 A2 experiment, Walter et al. (1980) detected 15 out of 59 systems observed with luminosities in the range $L_X = 10^{30.5}$-$10^{31.6}$ ergs s^{-1}, and ascribed the nondetections to the sensitivity threshold of HEAO-1. As a consequence of its lower sensitivity threshold, the Einstein IPC has detected at least 47 systems with $L_X = 10^{29.4}$-$10^{31.5}$ ergs s^{-1} and $\log(L_X/L_{Bol})$ in the range -4.9 to -2.4 (cf. Walter and Bowyer 1981). Further, the L_X/L_{Bol} ratio does not depend on the gravity of the cooler star in the system (usually the more active star) over two decades in gravity.

2. Walter and Bowyer (1981) showed that $L_X/L_{Bol} \sim \Omega$, the angular velocity of the star with the most active chromosphere in the system. Since single G-type stars follow the same relationship (Walter 1981), the bright X-ray luminosity of the RS Cvn systems is not a direct consequence of

binarity, but rather a result of rapid rotation which is in turn produced by tidally-enforced synchronism of rotation and orbital motion. Rapid rotation presumably results in strong dynamo-generated magnetic fields in stars with deep convective zones.

3. HEAO-1 observations of Walter et al. (1980) and Garcia et al. (1980) indicated that RS CVn systems have rather hot, variable spectra. Subsequently, Swank et al. (1981) were able to obtain low resolution spectra of 7 RS CVn systems and Algol (a contact eclipsing system) with the Einstein SSS detector. Assuming that the X-ray emission is from an optically thin thermal plasma in collisional ionization equilibrium, they found that the spectra can be fit by two components — a warm component with $T_{warm} = 4\text{-}8 \times 10^6$ K, and a hot component with $T_{hot} = 20\text{-}100 \times 10^6$ K. The luminosities of the two components lie in the range $L_{warm} = 10^{30}\text{-}10^{31}$ ergs s^{-1} and $L_{hot} = 10^{29.3}\text{-}10^{31.3}$ ergs s^{-1}. The warm component appears not to vary, while the hot component varies by a factor of 2. The ratio L_{hot}/L_{warm} lies in the range 0.1 (for the 104^d Capella system) to 4 (for the 6.5^d UX Ari system). Since the hot components vary while the warm components do not, the two components probably originate in separate plasmas.

4. In all likelihood the emitting structures are closed magnetic loops. This hypothesis is based on solar analogy, the appearance of large dark starspot groups on the photospheres of these stars, and the inability of these stars to confine the observed hot plasma by gravity alone. Swank et al. (1981) and Walter et al. (1980) assumed the Rosner, Tucker, and Vaiana (1978) scaling law for magnetic flux tubes with the following results. If the gas pressure in the loops is roughly 10 dynes cm^{-2}, similar to the largest pressures seen in solar active region loops, then the loop sizes for the warm plasma are small compared to the stellar radii and the hot loops have sizes comparable to the binary separations. If, on the other hand, the loop pressures are ≥ 100 dynes cm^{-2}, then both the warm and hot loops are smaller than the stellar radii in scale. There is no compelling evidence yet as to which pressure is correct, but the absence of large changes in the X-ray flux from AR Lac during primary and secondary eclipse (Swank et al. 1981) suggests that the emitting regions may be comparable to the binary separation in this system. This raises the possibility of interactions between loops from the two stars, which Simon, Linsky, and Schiffer (1980) proposed as the mechanism responsible for flares in these systems.

b) Some Important Unanswered Questions

1. What are the geometries of the X-ray emitting regions in these systems? Monitoring the X-ray and ultraviolet emission during a full binary orbit with X-ray energy distribution photometry and ultraviolet spectroscopy can determine the location of the hot and warm loops and their relation to the spots. Also moderate resolution X-ray spectroscopy will permit measurements of electron densities and thus pressures and loop sizes using appropriate scaling laws. Such data will also provide information on the fraction of the available volume that is filled by loops.

2. Is the radiation in the hot component indeed thermal and why is this plasma so hot? The answer to this question will require a hard X-ray

spectroscopy instrument that can monitor these systems to study their variability time scales.

3. What are the mechanisms responsible for flares in these systems? Two kinds of observations are needed. First, we need to monitor these systems during flares with moderate resolution X-ray spectroscopy and ultraviolet spectroscopy to determine variations in the X-ray and ultraviolet fluxes, temperatures, and electron densities with time. Second, we need to determine the plasma flows, perhaps in interacting flux tubes from the two stars or other binary interactions. Such measurements require high resolution X-ray and ultraviolet spectra.

IX. HOT STARS

a) What We Have Learned from Einstein

1. Einstein discovered that the O and B stars are the brightest X-ray sources among all nondegenerate stars, despite prior predictions that these stars should not have hot outer atmospheres on the basis that they lack convective zones and thus acoustic wave heating processes should be inoperative. Harnden et al. (1979) and Seward et al. (1979) reported the initial Einstein observations of luminous O stars in the Cyg OB2 association and the region around the η Carinae nebula, finding that L_X is typically $\sim 10^{33.7}$ ergs s^{-1} for these stars. Subsequent observations of hot stars by Long and White (1980), Vaiana et al. (1981), Pallavicini et al. (1981), and Cassinelli et al. (1981) have led to the results that typical luminosities are 10^{31}-10^{33} ergs s^{-1} for the O dwarfs, 10^{27}-$10^{30.7}$ ergs s^{-1} for the B8 V- A1 V stars, $10^{31.9}$-$10^{33.6}$ ergs s^{-1} for the O supergiants and $\leq 10^{31}$ ergs s^{-1} for the late B supergiants. The reason that these stars were not observed as X-ray sources prior to Einstein is that they are generally more than 100 pc distant, especially the O supergiants, so that the apparent X-ray flux of the brightest source, ζ Pup (O4f), is only 1×10^{-11} ergs cm^{-2} s^{-1}, close to the HEAO-1 threshold.

2. Pallavicini et al. (1981) reported that $L_X/L_{bol} = 1.4 \times 10^{-7}$ for most O3-A5 stars in their sample, independent of spectral type and luminosity class. Using a sample of 21 supergiants of spectral type O4-A2, Cassinelli et al. (1981) found a similar result, $L_X/L_{bol} \approx 1.6 \times 10^{-7}$, for B1 and hotter supergiants, but this ratio is perhaps a factor of 3 smaller in the later B supergiants. The roughly constant value of L_X/L_{bol} for the hot stars suggests that only one mechanism is responsible.

3. Pallavicini et al. (1981) searched without success for any correlations between L_X or L_X/L_{bol} with rotational velocities (v sin i). Thus rotation does not play an important role in determining the X-ray emission from these stars.

4. The O and B stars, especially supergiants, exhibit rapid mass loss with rates up to $\dot{M} \approx 10^{-4.5}$ $M_\odot$ yr^{-1} and terminal velocities up to $v_\infty \approx 3500$ km s^{-1}. Cassinelli (1979), Conti (1981), Lamers (1981) and others have reviewed the properties of these winds and how they are derived from P Cygni-type line

profiles and VLA observations. Garmany et al. (1981) found that $\dot{M} \sim L_{bol}^{1.73}$, and compared this result with the predictions of radiatively driven stellar wind theory. The ratio of X-ray luminosity to the kinetic energy in the wind flow, $L_x/1/2\ Mv_\infty^2 \approx 10^{-4}$. Thus the X-rays do not drive the wind, but rather the wind could be responsible for creating the X-rays.

5. The measurement of considerable soft X-ray flux at energies below 1 keV has played a crucial role in understanding the origin of the X-rays from the hot stars. Long and White (1980) argued that the large column densities of the wind in O supergiants should absorb all the soft X-ray emission from a hot corona lying at the base of the wind as proposed by Cassinelli and Olson (1979). Thus the X-ray emitting region must be distributed throughout the wind, and Long and White (1980) proposed that both hot ($\sim 3 \times 10^6$ K) and cool ($\sim 3 \times 10^4$ K) plasma coexist in the winds of these stars. Cassinelli et al. (1981) discussed constraints on the range of hot plasma temperatures and wind column densities, assuming the hot plasma is embedded in the wind.

6. Lucy and White (1980) proposed a phenomenological theory to explain the observed X-ray emission from hot star winds. As a working premise, they accepted earlier calculations that winds driven by radiation pressure in lines are unstable, since density enhancements will feel greater acceleration than the surrounding gas and the increased velocity will result in greater acceleration as the absorption lines are Doppler-shifted into the bright stellar continuum of the star. Lucy and White (1980) proposed that this mechanism will produce density enhancements in the wind that are radiatively driven through the ambient gas and confined by ram pressure. These enhancements (the so-called blobs) will form hot bow shocks that radiate the observed soft X-rays. Cassinelli et al. (1981) discussed the validity of this mechanism and competing mechanisms for explaining the Einstein data as well as such ionization anomalies such as the O VI/O IV ratio.

b) Some Important Unanswered Questions

1. What heats the hot plasma in these stars and where is it located? In particular, is the Lucy-White mechanism valid, or can such alternative mechanisms as a hot corona near the base of the wind or spatial separation of a hot corona from the expanding cooler gas by magnetic fields (Rosner and Vaiana 1980) better explain the data? To answer this question one needs low resolution spectra to measure both the temperature and attenuation as a function of time (and thereby aspect angle due to stellar rotation) for both dwarf and supergiant O and B stars. Observing stars of different spectral types and luminosities is important because there is evidence that the X-rays are created by only one mechanism in the hot stars but the ionization state of the wind depends critically on spectral type.

2. What are the processes responsible for the ionization equilibria seen in these stellar winds, and, in particular, what is responsible for the ionization anomaly of O VI? To address this question we need to know the range of temperatures and electron densities in these winds from moderate resolution X-ray spectra as well as contemporaneous measurements of ultraviolet line profiles, especially the O IV λ1032, 1037 doublet.

3. What mechanisms are responsible for the acceleration of hot star winds? What we now know about these winds is based only on ultraviolet spectra that tell us only about the flow properties of plasma cooler than 2×10^5 K. Since hot gas may be embedded in the cooler wind and perhaps flows faster, moderate resolution X-ray spectra should be able to measure the flow properties of this component.

4. Similar types of measurements are needed to study the poorly understood winds and coronae in Wolf-Rayet stars.

ACKNOWLEDGMENTS

This work was supported in part by National Aeronautics and Space Administration grants NGL-06-003-057, NAG-8316, NAG-8334, NAG-8382, and NAG-8400 to the University of Colorado. I wish to thank Dr. R. McCray and F. Walter for carefully reading the manuscript.

REFERENCES

Ayres, T. R. and Linsky, J. L. 1980, Ap. J., 241, 279.
Ayres, T. R., Linsky, J. L., Vaiana, G. S., Golub, L., and Rosner, R. 1981, Ap. J., 250, 293.
Cassinelli, J. P. 1979, Ann. Rev. Astr. Ap., 17, 275.
Cassinelli, J. P. and Olson, G. L. 1979, Ap. J., 229, 304.
Cassinelli, J. P., Waldon, W. L., Sanders, W. T., Harnden, F. R. Jr., Rosner, R., and Vaiana, G. S. 1981, Ap. J., 250, 677.
Castor, J. 1981, in Physical Processes in Red Giants, eds. I. Iben, Jr. and A. Renzini (Dordrecht: D. Reidel), p. 285.
Conti, P. S. 1981, in Effects of Mass Loss on Stellar Evolution, eds. C. Chiosi and R. Stalio (Dordrecht: D. Reidel), p. 1.
Dere, K. P. and Mason, H. E. 1981, in Solar Active Regions, ed. F. Q. Orrall (Boulder: Colorado Associated University Press), p. 129.
Duncan, D. K. 1981, Ap. J., 248, 651.
Dupree, A. K. 1981, in Solar Phenomena in Stars and Stellar Systems, eds. R. M. Bonnet and A. K. Dupree (Dordrecht: D. Reidel), p. 407.
Eaton, J. A. and Hall, D. S. 1979, Ap. J., 227, 907.
Feigelson, E. D. and de Campli, W. M. 1981, Ap. J. (Letters), 243, L89.
Feigelson, E. D. and Kriss, G. A. 1981, Ap. J. (Letters), 248, L35.
Gahm, G. F. 1980, Ap. J. (Letters), 242, L163.
Garcia, M., Baliunas, S. L., Conroy, M., Johnson, M. D., Ralph, E., Roberts, W., Schwartz, D. A., and Tonry, J. 1980, Ap. J. (Letters), 240, L107.
Garmany, C. D., Olson, G. L., Conti, P. S., and Van Steenberg, M. E. 1981, Ap. J., 250, 660.
Gary, D. E. and Linsky, J. L. 1981, Ap. J., 250, 284.
Giaconni, R. et al. 1979, Ap. J., 230, 540.
Golub, L., Maxson, C., Rosner, R., Serio, S., and Vaiana, G. S. 1980, Ap. J., 238, 343.
Gray, D. F. 1976, The Observation and Analysis of Stellar Photospheres (New York: John Wiley), p. 392.

Haisch, B. M., Bornmann, P. L., Linsky, J. L., Stencel, R. E., and Slee, O. B. 1981, Bull. A.A.S., 13, 515.
Haisch, B. M., Linsky, J. L., Harnden, F. R., Jr., Rosner, R., Seward, F. D., and Vaiana, G. S. 1980, Ap. J. (Letters), 242, L99.
Hall, D. S. 1976, in Multiple Periodic Variable Stars, ed. W. S. Fitch (Dordrecht: D. Reidel), p. 287.
_____. 1981, in Solar Phenomena in Stars and Stellar Systems, eds. R. M. Bonnet and A. K. Dupree (Dordrecht: D. Reidel), p. 431.
Harnden, F. R. Jr., Branduardi, G., Elvis, M., Gorenstein, P., Grindlay, J., Pye, J. P., Rosner, R., Topka, K., and Vaiana, G. S. 1979, Ap. J. (Letters), 234, L51.
Hartmann, L., Dupree, A. K., and Raymond, J. C. 1980, Ap. J. (Letters), 236, L143.
_____. 1981, Ap. J., 246, 193.
Hearn, A. G. 1981, in Effects of Mass Loss on Stellar Evolution, eds. C. Chiosi and R. Stalio (Dordrecht: D. Reidel), p. 125.
Heise, J., Brinkman, A. C., Schrijver, J., Mewe, R., Gronenschild, E., de Boggende, A., and Grindlay, J. 1975, Ap. J. (Letters), 202, L73.
Hollweg, J. V. 1981, in Solar Active Regions, ed. F. Q. Orrall (Boulder: Colorado Associated University Press), p. 277.
Holt, S. S., White, N. E., Becker, R. H., Boldt, E. A., Mushotzky, R. F., Serlemitsos, P. J., and Smith, B. W. 1979, Ap. J. (Letters), 234, L65.
Johnson, H. M. 1981, Ap. J., 243, 234.
Jordan, C. and Brown, A. 1981, in Solar Phenomena in Stars and Stellar Systems, eds. R. M. Bonnet and A. K. Dupree (Dordrecht: D. Reidel), p. 199.
Kahler, S. et al. 1982, Ap. J., to appear.
Kahn, S. M., Linsky, J. L., Mason, K. O., Haisch, B. M., Bowyer, C. S., White, N. E., and Pravdo, S. H. 1979, Ap. J. (Letters), 234, L107.
Ku, W.H.-M. and Chanan, G. A. 1979, Ap. J. (Letters), 234, L59.
Kuhi, L. V. 1964, Ap. J., 140, 1409.
Kuperus, M., Ionson, J. A., and Spicer, D. S. 1981, Ann. Rev. Astr. Ap., 19, 7.
Lamers, H. J. G. L. M. 1981, in Effects of Mass Loss on Stellar Evolution, eds. C. Chiosi and R. Stalio (Dordrecht: Reidel), p.19.
Linsky, J. L. 1977, in The Solar Output and Its Variation, ed. O. R. White (Boulder: Colorado Associated University Press), p. 477.
_____. 1981, in Effects of Mass Loss on Stellar Evolution, eds. C. Chiosi and R. Stalio (Dordrecht: D. Reidel), p. 187.
Long, K. S. and White, R. L. 1980, Ap. J. (Letters), 239, L65.
Lucy, L. B. and White, R. L. 1980, Ap. J., 241, 300.
Marcy, G. W. 1980, B.A.A.S., 12, 834.
Mewe, R. 1979, Space Sci. Rev., 24, 101.
Mewe, R. et al. 1980, Smithsonian Special Report, No. 389, p. 107.
Mundt, R. 1980, Astr. Ap., 95, 234.
Pallavicini, R., Golub, L., Rosner, R., Vaiana, G. S., Ayres, T. R., and Linsky, J. L. 1981, Ap. J., 248, 279.
Poletto, G., Vaiana, G. S., Zombeck, M., Krieger, A. S., and Timothy, A. F. 1975, Solar Phys., 44, 83.
Popper, D. M. and Ulrich, R. K. 1977, Ap. J. (Letters), 212, L131.
Priest, E. R. 1981, in Solar Active Regions, ed. F. Q. Orrall (Boulder: Colorado Associated University Press), p. 213.

Robinson, R. D., Worden, S. P., and Harvey, J. W. 1980, Ap. J., 239, 961.
Rodonò, M. 1981, in Binary Stars, Maratea (Italy), in press.
Rosner, R., Tucker, W. H., and Vaiana, G. S. 1978, Ap. J., 220, 643.
Rosner, R. and Vaiana, G. S. 1980, in X-ray Astronomy, ed. R. Giaconni and G. Setti (Dordrecht: Reidel), p. 129.
Serio, S., Peres, G., Vaiana, G. S., Golub, L., and Rosner, R. 1981, Ap. J., 243, 288.
Seward, F. D., Forman, W. R., Giaconni, R., Griffiths, R. E., Harnden, F. R. Jr., Jones, C., and Pye, J. P. 1979, Ap. J. (Letters), 234, L55.
Simon, T., Linsky, J. L., and Schiffer, F. H., III. 1980, Ap. J., 239, 911.
Skumanich, A. 197?, Ap. J., 171, 565.
Soderblom, D. R. 1981, preprint.
Stern, R. A., Zolcinski, M.-C., Antiochos, S. K., and Underwood, J. H. 1981, Ap. J., 249, 647.
Swank, J. H. 1981, private communication.
Swank, J. H., White, N. E., Holt, S. S., and Becker, R. H. 1981, Ap. J., 246, 208.
Ulmschneider, P. 1979, Space Sci. Rev., 24, 71.
_____. 1981, in Solar Phenomena in Stars and Stellar Systems, eds. R. M. Bonnet and A. K. Dupree (Dordrecht: D. Reidel), p. 239.
Ulrich, R. K. 1976, Ap. J., 210, 377.
_____. 1978, in Protostars and Planets, ed. T. Gehrels (Tucson: Univ. of Arizona Press).
Vaiana, G. S. and Rosner, R. 1978, Ann. Rev. Astr. Ap., 16, 393.
Vaiana, G. S. et al. 1981, Ap. J., 245, 163.
Vaughan, A. H. 1980, Pub. A. S. P., 92, 392.
Vaughan, A. H., Baliunas, S. L., Middelkoop, F., Hartmann, L. W., Mihalas, D., Noyes, R. W., and Preston, G. W. 1981, Ap. J., 250, 276.
Vaughan, A. H. and Preston, G. W. 1980, Pub. A. S. P., 92, 385.
Walter, F. 1981, Ap. J., 245, 677.
_____. 1982, preprint.
Walter, F. and Bowyer, S. 1981, Ap. J., 245, 671.
Walter, F. M., Cash, W., Charles, P., and Bowyer, S. 1980, Ap. J., 236, 212.
Walter, F. M. and Kuhi, L. V. 1981, Ap. J., 250, 254.
Webb, D. F. 1981, in Solar Active Regions, ed. F. Q. Orrall (Boulder: Colorado Associated University Press), p. 165.
Withbroe, G. L. 1981, in Solar Active Regions, ed. F. Q. Orrall (Boulder: Colorado Associated University Press), p. 199.
Withbroe, G. L. and Noyes, R. W. 1977, Ann. Rev. Astr. Ap., 15, 363.
Zirker, J. B. 1981, in Solar Phenomena in Stars and Stellar Systems, eds. R. M. Bonnet and A. K. Dupree (Dordrecht: D. Reidel), p. 301.

N82 26057

CONTINUUM AND LINE SPECTRA OF DEGENERATE DWARF X-RAY SOURCES*

D. Q. Lamb
Harvard-Smithsonian
Center for Astrophysics

ABSTRACT

We summarize recent observations of degenerate dwarf X-ray sources, and review theoretical work on their continuum spectra and lines. We discuss some of the important unresolved issues concerning these sources, and conclude with an outline of the kinds of X-ray observations that would best advance our understanding of them.

I. INTRODUCTION

a) Historical Remarks

The first degenerate dwarf X-ray source was discovered in 1974 when Rappaport et al. (1974) detected an unexpected soft X-ray source during a brief rocket flight and deduced that the source was SS Cyg in outburst.

Two years later Berg and Duthie (1976) suggested that the cataclysmic variable AM Her was the optical counterpart of the hard X-ray source 4U1814+50. This identification was confirmed by Hearn et al. (1976), who detected AM Her in soft X rays. Soon after the optical identification, Szkody and Brownlee (1977) and Cowley and Crampton (1977) found that AM Her has a binary period of 3.1 hours. More remarkably, Tapia (1977a) discovered that the optical light from AM Her is nearly 10% circularly and linearly polarized and that the degenerate dwarf is strongly magnetic. The periods of the circular and linear polarization curves, the radial velocity curves, and the optical, soft and hard X-ray light curves are identical. Thus the rotation period of the accreting magnetic degenerate dwarf is phase-locked to the binary orbital period of 3.1 hours. Within less than a year, two other similar sources, AN UMa and VV Pup, were identified from their optical emission line spectrum and confirmed by detection of linear and circular polarization (Krzeminski and Serkowski 1977, Tapia 1977b).

Soft and hard X-rays were soon also detected from the well-known cataclysmic variables U Gem (Mason et al. 1978; Swank et al. 1978), EX Hya (Watson, Sherrington, and Jameson 1978; Cordova and Riegler 1979), and GK Per (King, Ricketts, and Warwick 1979), in addition to SS Cyg (Heise et al. 1978; Mason, Cordova, and Swank 1979).

Subsequent examination of nearby cataclysmic variables turned up many more X-ray sources. A few of these were discovered by Ariel 5 and HEAO-1, but most detections required the high sensitivity of the focusing instrument on Einstein. Other cataclysmic variables have been found by looking for the optical counterparts of faint

*This research was supported in part by NASA grant NAGW 246.

galactic X-ray sources, and this method promises to become increasingly important in the future. More than 53 of these accreting degenerate dwarf X-ray sources are now known (Cordova and Mason 1982).

Soft X-rays have also been detected from several hot (T_{eff} > 30,000 - 60,000 K) isolated degenerate dwarfs, including Sirius B (Martin et al. 1982 and references therein) and HZ 43 (Hearn et al. 1976).

b) Potential

The study of degenerate dwarf X-ray sources can provide many returns. For example, these sources afford a laboratory in which to explore the physics of hot, dense plasmas in strong magnetic fields (the parameter regime is, in fact, similar to that of interest in plasma fusion reactors). We can also learn from them a great deal about the masses, internal structure, and magnetic fields of degenerate dwarfs themselves. Potentially, the pulsing sources can provide as much information as has been obtained from the pulsing neutron star X-ray sources. Noise measurements can be used to probe the accretion process, reflection and reprocessing effects give clues to the geometry of the disk and the binary system, and time delay curves yield the parameters of the binary system and thereby lend insight into its formation and evolution.

However, because most degenerate dwarf X-ray sources were found only recently, we know very little about their X-ray properties. Only three (AM Her, SS Cyg, and U Gem) have been studied in any detail. The situation is similar in this respect to that of the stellar X-ray sources also found by Einstein (Linsky 1982). Exploration of the X-ray emission from both has only begun, and future X-ray astronomy missions must provide the data with which to understand it.

In this review, we concentrate on the soft and hard X-ray spectra produced by accreting degenerate dwarfs. We first summarize the observations in §II. We then discuss the theory of formation of the continuum spectrum in §III, and of emission and absorption lines in §IV. In §V, we mention some of the important unresolved issues. Finally, in §VI we outline the kinds of X-ray observations that would best advance our understanding of these sources. For reviews of the optical properties of cataclysmic variables, see Robinson (1976) and Warner (1976); for reviews of the X-ray observations, see Garmire (1979) and Cordova and Mason (1982). Lamb (1979) and Kylafis et al. (1980) contain earlier reviews of theoretical work.

II. OBSERVATIONAL PROPERTIES

a) Luminosities and Space Densities

Probably all cataclysmic variables are X-ray sources. The ones detected so far have X-ray luminosities $L \sim 10^{31} - 10^{33}$ ergs s^{-1}. None of the bright ($L \sim 10^{36}$-10^{38} ergs s^{-1}) galactic X-ray sources have been identified with degenerate dwarfs. Thus the known accreting degenerate dwarf X-ray sources are $\sim 10^{5}$ times fainter than, e.g., the pulsing neutron stars (Lamb 1979) but $\sim 10^{3}$ times brighter than ordinary stars (Linsky 1982).

The nearest cataclysmic variable X-ray sources lie at distances d of only 75 - 100 pc (Cordova and Mason 1982). This implies a space density $n \sim 3 \times 10^{-7}$ $(d/100\ pc)^{-3}$ pc^{-3}. Assuming a uniform distribution of sources throughout the galaxy and a galactic

volume V $\sim$ 1 x 10^{12} pc^3, the above space density implies that the total number of sources in the galaxy is N $\sim$ 3 x 10^5 (d/ 100 pc)$^{-3}$. Thus the total number of degenerate dwarf X-ray sources in the galaxy may exceed a million. This compares with a total number of bright (L $\sim$ 10^{36}- 10^{38} ergs s^{-1}) neutron star sources of $\sim$ 100.

b) X-Ray Spectra and Temporal Behavior

Among accreting degenerate dwarf X-ray sources, there are two recognized classes involving magnetic degenerate dwarfs: the AM Her stars and the DQ Her stars (Lamb 1979, Patterson and Price 1981). The remaining systems show no clear-cut manifestation of a magnetic field. However, if the past is a guide, some of these sources will be reclassified as AM Her or DQ Her stars on the basis of future observations. We may even speculate that magnetic fields are endemic in degenerate dwarfs. If so, most, perhaps all, of the other systems also contain magnetic degenerate dwarfs. However, the field strengths may be less. Below we discuss the X-ray spectra and temporal behavior of the AM Her stars, the DQ Her stars, and the other cataclysmic variables.

i) AM Her stars

Table 1 lists the seven AM Her stars that are now known and summarizes some of their properties. These stars show strong (> 10%) circular and linear polarization of their infrared and visible light, and are believed to be accreting magnetic degenerate dwarfs (Chanmugam and Wagner 1977, 1978; Stockman et al. 1977). The polarization (Tapia 1977a) of the visible light from AM Her, the prototype of this class, is shown in Figure 1. The X-ray spectra of these stars typically have two distinct components: an apparent blackbody component with T_{bb} < 100 ev and a bremsstrahlung component with T_{br} > 10 kev. The inferred blackbody luminosity is greater than the bremsstrahlung luminosity, often by a factor of 10 or more (cf. Tuohy et al. 1978, 1981; Szkody et al. 1981; Patterson et al. 1982). Figure 2 shows the soft and hard X-ray spectrum of AM Her recently constructed from HEAO-1 observations by Rothschild et al. (1981). The bremsstrahlung spectra of these sources also show strong iron line emission at $\sim$ 7 keV, as is evident in Figure 2. In these systems, the periods of the polarized light, the optical and X-ray light, and the orbital velocity curves are all the same. Thus the rotation period of the degenerate dwarf is synchronized with the orbital period of the binary system, probably due to interaction of the magnetic field of the degenerate dwarf with the companion star (Joss, Katz, and Rappaport 1979). Figure 3 shows the resulting 3.1 hour "pulse profile" of AM Her in soft X-rays (Tuohy et al. 1978).

The source EF Eri (2A0311-227) is the second most well-studied in X-rays of the AM Her stars. Figures 4 and 5 show its 1.3 hour "pulse profile" in soft X-rays (Patterson et al. 1981) and its bremsstrahlung hard X-ray spectrum (White 1981). Note again the strong iron emission line at $\sim$ 7 keV.

ii) DQ Her stars

Table 2 lists the seven systems we have classified as DQ Her stars and summarizes some of their properties. DQ Her, the prototype of this class, is believed to be an accreting magnetic degenerate dwarf (Bath, Evans, and Pringle 1974; Lamb 1974). However, it shows little, if any, polarization of its infrared and visible light (Swedlund, Kemp, and Wolstencroft 1974). This system underwent a nova outburst in 1934 and shows coherent small amplitude optical pulsations at 71 seconds, which are believed to

TABLE 1

AM HER STARS

STAR	P_b (Hours)	d (pc)[a]	L_s (10^{30} ergs s^{-1})[b]	T_{bb} (eV)	L_h (10^{30} ergs s^{-1})[b]	T_{br} (keV)	REFERENCES
EF Eri (=2A0311-227)	1.35	[100]	24	$\lesssim$80	170	18.1±3.0	8, 15, 18
VV Pup	1.67	144	160	20^{+60}_{-10}	7.0	>10	2, 7, 14
E1405-451	1.69	[100]	9.7	...	...	...	6
H0139-68	1.83	[100]	72	$\lesssim$300	...	...	1, 17
PG1550+191	1.89	[100]	...	...	...	...	10
AN UMa	1.91	[100]	0.86 33	$\lesssim$40	...	...	3, 5, 12
AM Her	3.09	75±10	45-480 21	28-40	260 480	30.9±4.5	4, 9, 11, 13, 16, 19

[a] Distances in brackets are assumed.

[b] Luminosities assume a distance of 100 pc, except for AM Her and VV Pup.

(1) Agrawal et al. (1981)
(2) Bailey (1981)
(3) Hearn and Marshall (1979)
(4) Hearn and Richardson (1977)
(5) Krzeminski and Serkowski (1977)
(6) Mason et al. (1982)
(7) Patterson et al. (1982)
(8) Patterson et al. (1981)
(9) Rothschild et al. (1981)
(10) Stockman et al. (1981)
(11) Swank et al. (1977)
(12) Szkody et al. (1981)
(13) Tapia (1977a)
(14) Tapia (1977b)
(15) Tapia (1979)
(16) Tuohy et al. (1981)
(17) Visvanathan et al. (1982)
(18) White (1981)
(19) Young and Schneider (1979)

ORIGINAL PAGE IS OF POOR QUALITY

ORIGINAL PAGE IS
OF POOR QUALITY

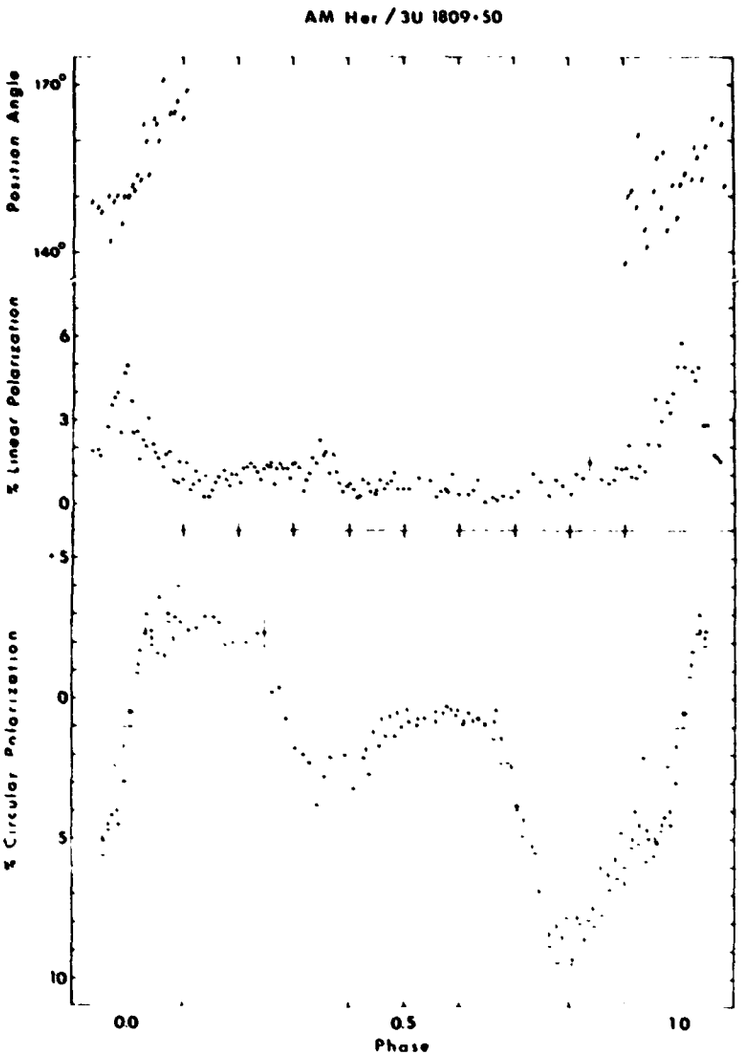

Fig. 1--Circular and linear polarization of the optical light from AM Her as a function of the phase of the 3.1 hour rotational period of the degenerate dwarf (from Tapia 1977).

ORIGINAL PAGE IS
OF POOR QUALITY

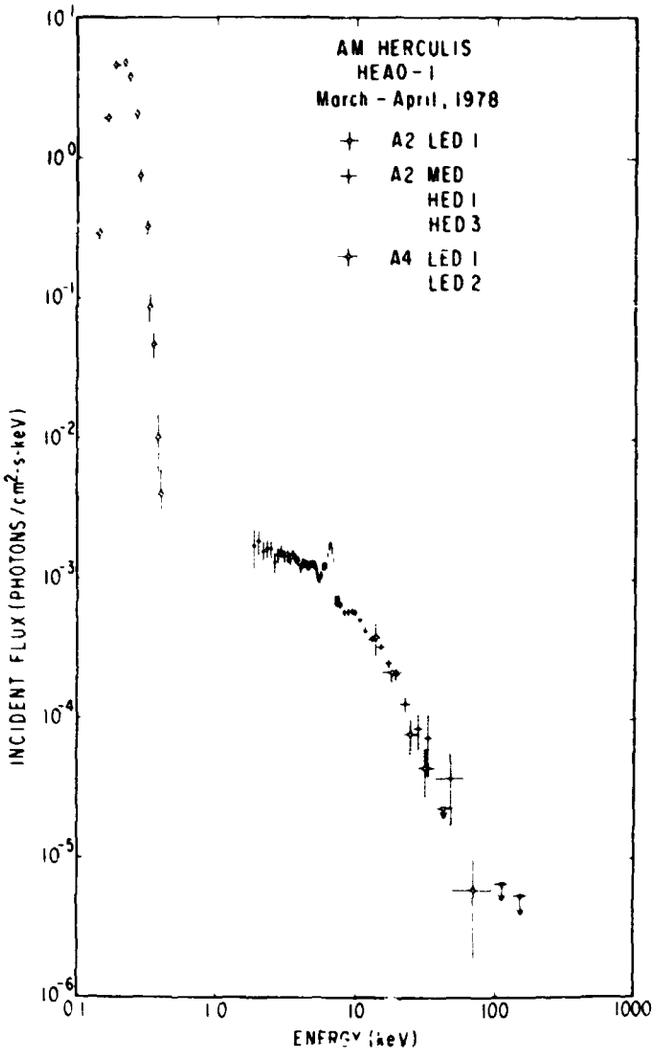

Fig. 2--Hard and soft X-ray spectrum of AM Her (from Rothschild et al. 1981). The two distinct components with T ≈ 30 keV and T < 40 eV are clearly visible.

ORIGINAL PAGE IS
OF POOR QUALITY

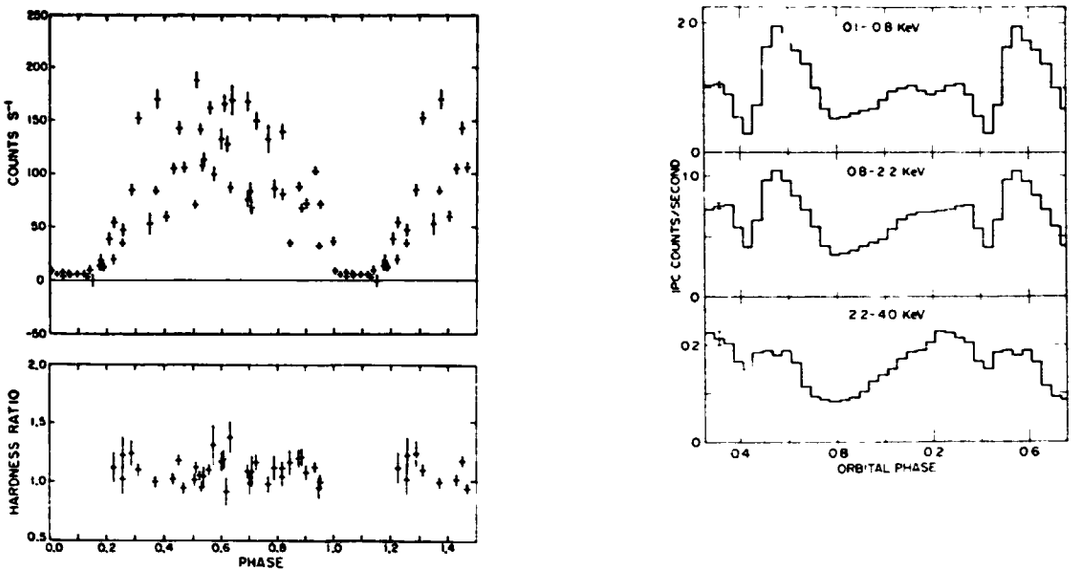

Fig. 3--Soft X-ray pulse profile and hardness ratio of AM Her as a function of the phase of the 3.1 hour rotational period of the degenerate dwarf (from Tuohy et al. 1978).

Fig. 4--X-ray pulse profile of EF Eri (2A0311-227) observed by Einstein as a function of orbital phase (or, equivalently, phase of the rotational period of the degenerate dwarf) (from Patterson et al. 1981).

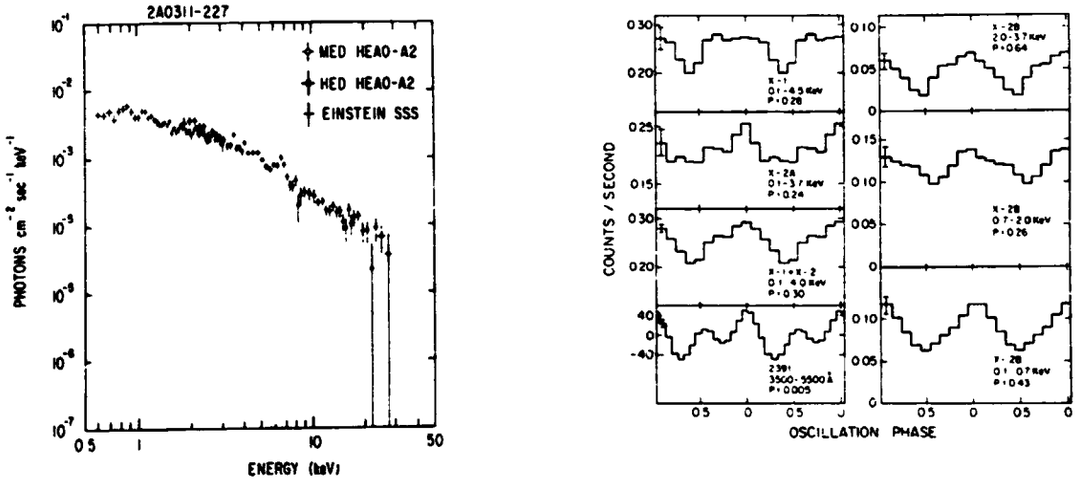

Fig. 5--Hard X-ray spectrum of EF Eri (2A0311-227) (from White et al. 1981). Note the iron emission line at ≈ 7 keV.

Fig. 6--Comparison of the pulse profile in soft X-rays and in optical light of AE Aqr through the 33 second rotation period of the degenerate dwarf (from Patterson et al. 1980).

TABLE 2

DQ HER STARS

STAR	P_b (Hours)	d (pc)[a]	P (s)	$\lvert\dot{P}\rvert^{-1}$	L_s (10^{30} ergs s^{-1})[b]	T_{bb} (eV)	L_h (10^{30} ergs s^{-1})[b]	T_{br} (keV)	REFERENCES
DQ Her	4.65	420	71.0653	1.2×10^{12}	< 2.4	...	...	...	2, 11
V533 Her	≈ 7	1000-1500	63.63307	$> 3 \times 10^{12}$	< 20-40	...	...	...	2, 5, 7
AE Aqr	9.88	84	33.076737	2×10^{13}	5.4	...	...	...	1, 6, 7, 9
EX Hya (?)	1.64	100	4021.62	2.2×10^{10}	14	570	60	≈ 5	3, 4, 15
							100	≈ 4.5	
H2252-035	3.59	[100]	805.21	$> 5 \times 10^{9}$	...	...	80	> 20	8, 10, 16, 17
H2215-086	4.03	[100]	1254.5	$> 3 \times 10^{8}$	5	...	12	≳ 10	12
							30	≳ 10	
V1223 Sgr	...	[100]	794.380	$> 5 \times 10^{9}$	...	...	100	≳ 10	13, 14

[a] Distances in brackets are assumed.

[b] Luminosities assume a distance of 100 pc if distance is unknown.

(1) Bailey (1981)
(2) Cordova, Mason, and Nelson (1981)
(3) Cordova and Riegler (1979)
(4) Gilliland (1982)
(5) Patterson (1979a)
(6) Patterson (1979b)
(7) Patterson (1982a)
(8) Patterson (1982b)
(9) Patterson et al. (1980)
(10) Patterson and Price (1981)
(11) Patterson, Robinson, and Nather (1978)
(12) Patterson and Steiner (1982)
(13) Steiner (1981)
(14) Steiner et al. (1981)
(15) Swank (1980)
(16) Warner, O'Donoghue, and Fairall (1981)
(17) White and Marshall (1981)

ORIGINAL PAGE IS
OF POOR QUALITY

represent the rotation period of the degenerate dwarf (Patterson, Robinson, and Nather 1978, and references therein). Two other members of this class are V533 Her, which underwent a nova outburst in 1963 and shows coherent small amplitude optical pulsations at 63 seconds (Patterson 1979a), and AE Aqr, which shows similar pulsations at 33 seconds (Patterson 1979b). Embarrassingly, neither DQ Her nor V533 Her have been detected in X rays (see Table 2). In the case of DQ Her, it has been suggested that the X rays are blocked by the disk because we are nearly in the orbital plane of the system, while in the case of V533 it can be argued that the system is too far away, and therefore too faint, to have been detected. Thankfully (for theorists), X rays have now been detected from AE Aqr and are pulsed with the 33 second optical period (Patterson et al. 1980). Figure 6 compares the optical and soft X-ray pulse profiles of AE Aqr.

Recently, several faint galactic X-ray sources have been identified with systems that are optically similar to cataclysmic variables. They exhibit large amplitude optical and X-ray pulsations with periods $\gtrsim$ 1000 seconds that are believed to represent the rotation period of the accreting star (Patterson and Price 1981; Warner, O'Donoghue, and Fairall 1981; White and Marshall 1981). There is controversy as to whether these X-ray sources are actually degenerate dwarfs or are neutron stars (cf. Patterson and Price 1981, White and Marshall 1981). We believe, based on their optical appearance and their X-ray to optical luminosity ratio, that they are degenerate dwarfs. They have also been called "interlopers" between the previously known DQ Her stars, with short rotation periods of 33 - 71 seconds, and the AM Her stars, with rotation synchronous with their orbital periods of 1.2 - 2.1 hours (Patterson and Price 1981). However, we believe that they should be regarded as members of the DQ Her class, in analogy with the short and long period pulsing neutron star X-ray sources, and therefore we include them in Table 2.

The source H2252-035 was the first of these systems to be optically identified (Griffiths et al. 1980). Figure 7 shows its optical light curve (Patterson and Price 1981). Clearly visible are the optical pulsations with a period of 859 seconds, which are thought to be produced by reprossessing of the 805 second X-ray pulse. Figures 8 and 9 show the pulse profile and the spectrum of the hard X-rays (White and Marshall 1981). The hard X-ray spectrum exhibits iron line emission at $\sim$ 7 keV.

Recently, a 67 minute (4022 second) periodicity has been identified in the well-studied cataclysmic variable X-ray source EX Hya (Vogt, Krzeminski, and Sterken 1980; Gilliland 1982). This period is also evident in soft X-rays but not in hard (Swank and White 1981), as shown in Figure 10. The coherence of the period over many years suggests that it may also be due to rotation of a magnetic degenerate dwarf. We have therefore included EX Hya in Table 2, but with a question mark to indicate its uncertain status.

iii) Other cataclysmic variables

Table 3 lists 10 sources selected from the remaining 44 cataclysmic variable X-ray sources currently known (Cordova and Mason 1982). Among these are the prototypical dwarf novae, SS Cyg and U Gem, which undergo outbursts every $\sim$ 100 days. During quiescence, both exhibit a hard X-ray spectrum with $T_{br} \sim 10 - 20$ keV (Mason, Cordova, and Swank 1979; Swank 1979). During outburst, the hard X-ray luminosity first increases and then decreases, the spectral temperature of the hard X-rays decreases, and an intense blackbody component with temperature $T_{bb} < 100$ eV appears in soft X-rays (cf. Mason, Cordova, and Swank 1979). Figure 11 compares the hard X-ray spectrum of SS Cyg in quiescence and in outburst with the spectrum of AM Her.

ORIGINAL PAGE IS
OF POOR QUALITY

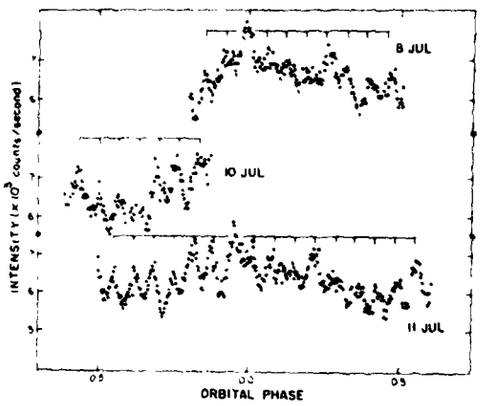

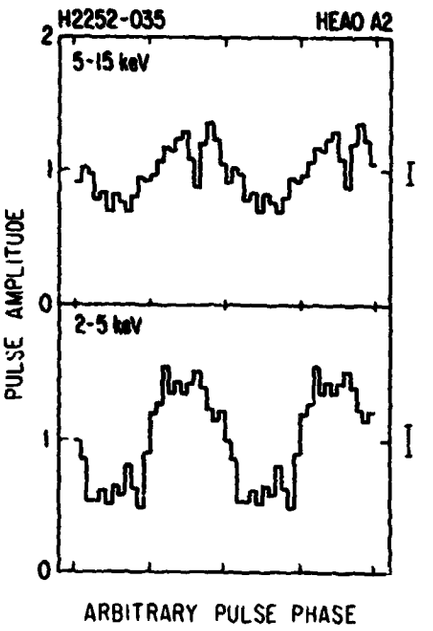

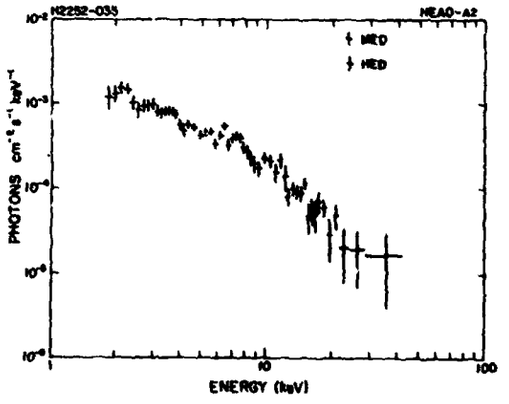

Fig. 7--Fast photometry of the optical light from H2252-035 (from Patterson and Price 1981). The 859 second pulsations, corresponding to reprocessed light from a stationary point in the binary system, are clearly visible.

Fig. 8--Hard X-ray pulse profile of H2252-035 through the 805 second rotation period of the degenerate dwarf (from White and Marshall 1981).

Fig. 9--Hard X-ray spectrum of H2252-035 (from White and Marshall 1981). The iron emission line at ≈ 7 keV is again clearly visible.

TABLE 3

SELECTED OTHER CATACLYSMIC VARIABLES (AFTER CÓRDOVA AND MASON 1982)

STAR[a]	P_b (Hours)	d (pc)[b]	P (s)[c]	L (10^{30} ergs s^{-1})[d]	T_{br} (keV)[e]	REFERENCES
WZ Sge	1.36	[100]	27.87, 28.97 (c)	6.0 (o)	[10]	14, 20
VW Hyi	1.78	[100]	24-32 (q) 88, 413 (q)	3.2 (q)	[10]	3, 7, 13
Z Cha	1.79	125±20	27.7 (c)	1.2 (o) 2.5 (q)	[10] [10]	1, 23
V603 Aql	3.33	430	...	160	[10]	2
U Gem	4.25	76±30	20-30 73-146	20 (o) 2 (q)	≈ 5 [10]	3, 5, 6, 19
UX UMa	4.72	214	28.5-30.0 (c)	2.0	[10]	1, 12
SS Cyg	6.60	125±25	8.5-10.9 (c, q) 32-36 (q)	100 (o) 410 (q)	≈ 8.5 ≈ 20	1, 4, 5, 8, 9, 11, 15, 17, 19, 21
Z Cam	6.96	[100]	16.0-18.8 (c)	1.9 (s)	[10]	18, 22
RU Peg	8.90	[100]	11.6-11.8 (c) ~ 51 (q)	23 (q)	[10]	2, 3, 16, 19
GK Per	16.43	480	~ 380 (q)	5200 (o) 130-220 (q)	[10] [10]	10, 15

[a] All stars are dwarf novae except GK Per (classical nova) and UX UMa (nova-like).
[b] Distances in brackets are assumed.
[c] Symbols "c" and "q" in parentheses denote "coherent" and "quasi-periodic", respectively.
[d] Luminosities assume a distance of 100 pc if distance unknown; the symbols "o", "q", and "s" in parentheses denote "outburst", "quiescence", and "standstill", respectively.
[e] Temperatures in brackets are assumed.

(1) Becker (1981)
(2) Becker and Marshall (1981)
(3) Cordova, Mason, and Nelson (1981)
(4) Cordova et al. (1980)
(5) Cordova et al. (1981)
(6) Fabbiano et al. (1981)
(7) Haefner, Schoembs, and Vogt (1979)
(8) Hillebrand, Spiller, and Stiening (1981)
(9) Horne and Gomer (1980)
(10) King, Ricketts, and Warwick (1979)
(11) Mason, Cordova, and Swank (1979)
(12) Nather and Robinson (1974)
(13) Patterson (1979)
(14) Patterson (1980)
(15) Patterson (1981)
(16) Patterson, Robinson, and Nather (1977)
(17) Patterson, Robinson, and Kiplinger (1978)
(18) Robinson (1973)
(19) Robinson and Nather (1979)
(20) Robinson, Nather, and Patterson (1978)
(21) Swank (1979)
(22) Swank (1980)
(23) Warner (1974)

ORIGINAL PAGE IS OF POOR QUALITY

ORIGINAL PAGE IS
OF POOR QUALITY

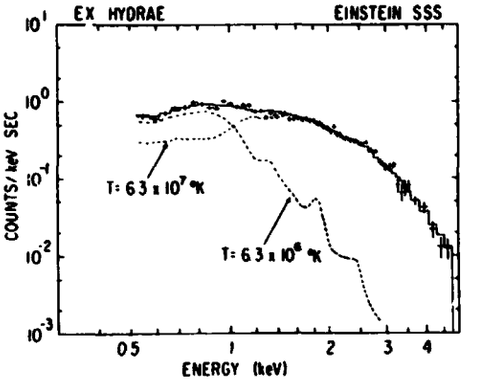

Fig. 10--Soft X-ray spectrum of EX Hydra measured by Einstein and showing the necessity of invoking at least two components (from Swank and White 1981).

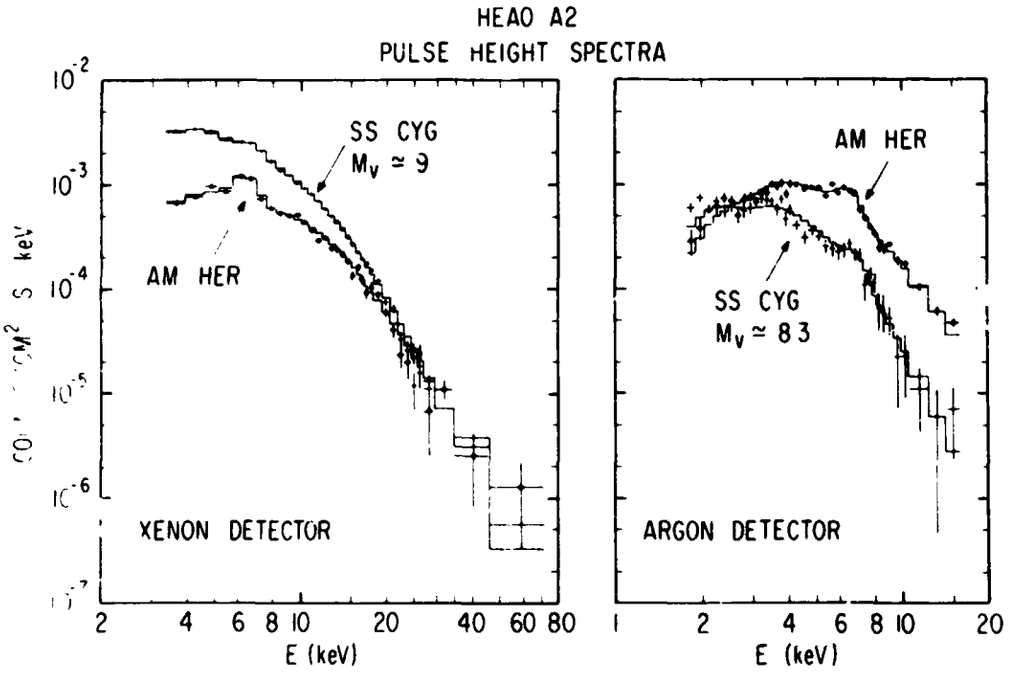

Fig. 11--Hard X-ray spectra of SS Cyg during quiescence (left panel) and during outburst (right panel) compared with the spectrum of AM Her (from Swank 1979). The presence of iron line emission at ≃ 7 keV in all spectra and the absence of low energy absorption in the spectrum of SS Cyg in outburst are evident.

The temporal behavior of the hard and soft X-ray luminosities of U Gem during an outburst is shown in Figure 12, while Figure 13 shows the way in which the hard X-ray spectrum of SS Cyg varies during an outburst.

Most of the remaining cataclysmic variables show only a hard X-ray component. It is not known whether the failure to detect a soft component during quiescence, or even during outburst in some sources, is due to its absence or due to the fact that it may have so low a spectral temperature that it is unobservable in soft X-rays.

Essentially all of the cataclysmic variables listed in Table 3 exhibit small amplitude quasi-periodic or coherent optical pulsations, usually during the onset of an outburst (Robinson 1976). Of special interest are the $\sim$ 8 - 10 second quasi-periodic pulsations in SS Cyg. They are strongly present in soft X-rays during outburst, yet their coherence persists for only 3-5 pulse periods (Cordova et al. 1980, 1981).

iv) Isolated stars

Sirius B, the first degenerate dwarf discovered, was detected as a very soft X-ray source by Mewe et al. (1975). Subsequently, very soft X rays were also detected from the hot degenerate dwarf HZ 43 (Heam et al. 1976). Both of these degenerate dwarfs are members of binaries, but the binary separations are so large that the companions are not believed to play any role in the X-ray emission. Feige 24, another hot degenerate dwarf, has been detected in the extreme UV (Margon et al. 1976); however, it was not detected by the HEAO-1 soft X-ray survey and, unfortunately, Einstein ceased operating before observations of it were carried out. Table 4 lists these three sources and summarizes some of their properties.

The emission from Sirius B, HZ 43, and Feige 24 at optical, UV, and X-ray wavelengths can be understood as photospheric emission from a hydrogen-rich [$n_{He}/n_H \sim 10^{-5}$] atmosphere with $T_{eff} \sim$ 30,000 - 60,000 K (Shipman 1976, Margon et al. 1976, Wesselius and Koester 1978, Martin et al. 1982). An upper limit in the extreme UV (200 - 800 A) for Sirius B (Cash, Bowyer, and Lampton 1978) appeared to conflict with photospheric models for the X-ray emission and to lend support to coronal models. However, UV observations yielded no evidence for a corona (Bohm-Vitense, Dettmann, and Kapranidis 1979) and Martin et al. (1982) have recently demonstrated that soft X-ray data from HEAO-1, together with the optical, UV, and extreme UV data, are consistent with photospheric emission at $\sim$ 28,000 K, as shown in Figure 14. For more detailed, but earlier, reviews of extreme UV and soft X-ray emission from isolated degenerate dwarfs, see Garmire (1979) and Bowyer (1979).

III. CONTINUUM SPECTRA

a) Qualitative Picture

In the remainder of this review, we shall focus on X-ray emission by accreting degenerate dwarfs.

i) Disk inflow near the star

Many of the cataclysmic variable X-ray sources show clear optical and UV evidence of accretion disks. If the disk extends all the way in to the stellar surface, viscous dissipation in the disk will release approximately half of the available

ORIGINAL PAGE IS
OF POOR QUALITY

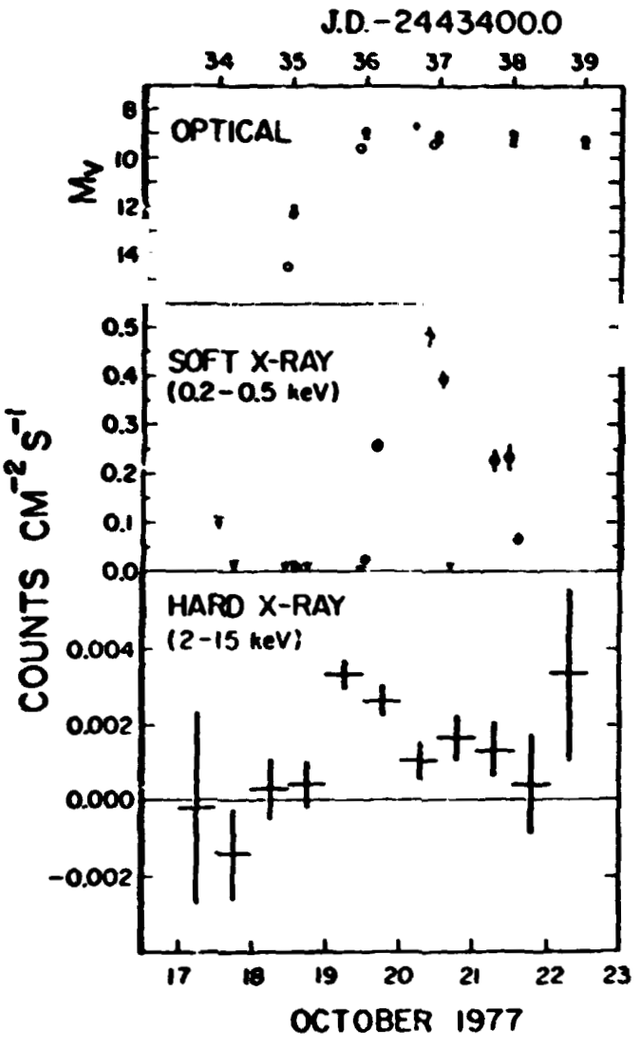

Fig. 12--Optical, soft X-ray, and hard X-ray light curves of U Gem through an outburst (from Mason, Cordova, and Swank 1979).

ORIGINAL PAGE IS
OF POOR QUALITY

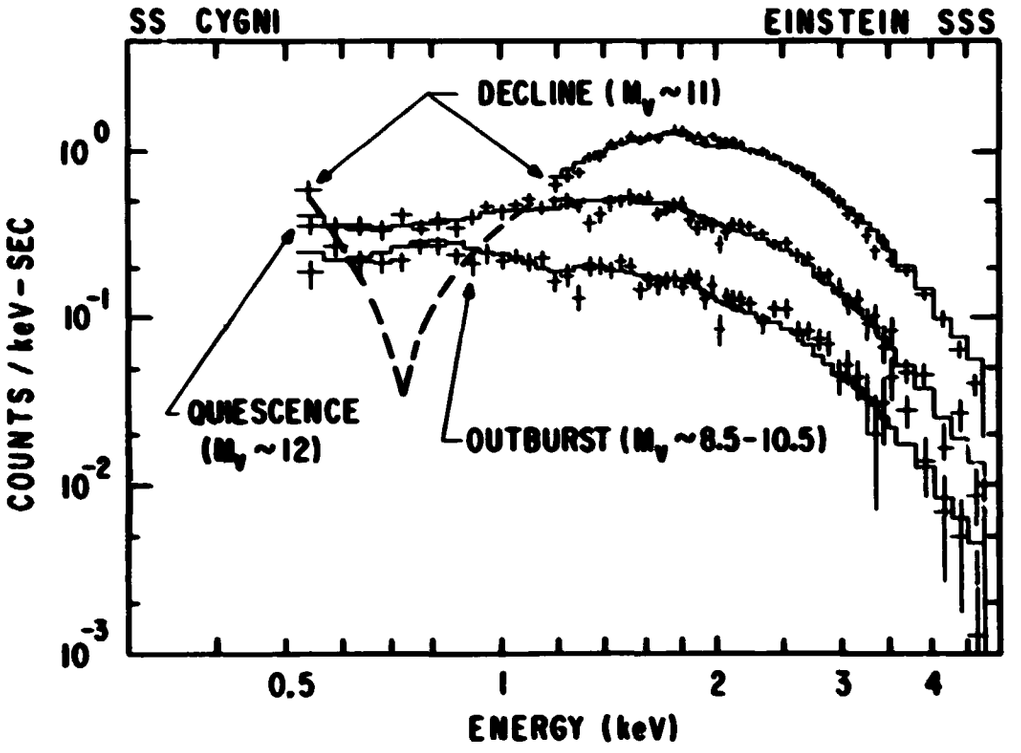

Fig. 13--Soft X-ray spectrum of SS Cyg showing the variation in the spectrum from outburst through decline to quiescence (from Swank and White 1981).

TABLE 4

ISOLATED STARS

STAR	d (pc)	L (10^{30} ergs s^{-1})	T_{eff} (k)	REFERENCES
Sirius B	2.7	0.06	≈ 28,000	4, 5, 6
HZ 43	65	40	≈ 60,000	2, 7
Feige 24	90	< 3	≈ 60,000	1, 3

(1) Bowyer (1979)

(2) Hearn et al. (1976)

(3) Margon et al. (1976)

(4) Martin et al. (1982)

(5) Mewe et al. (1975)

(6) Shipman (1976)

(7) Wesselius and Koester (1978)

ORIGINAL PAGE IS
OF POOR QUALITY

ORIGINAL PAGE IS
OF POOR QUALITY

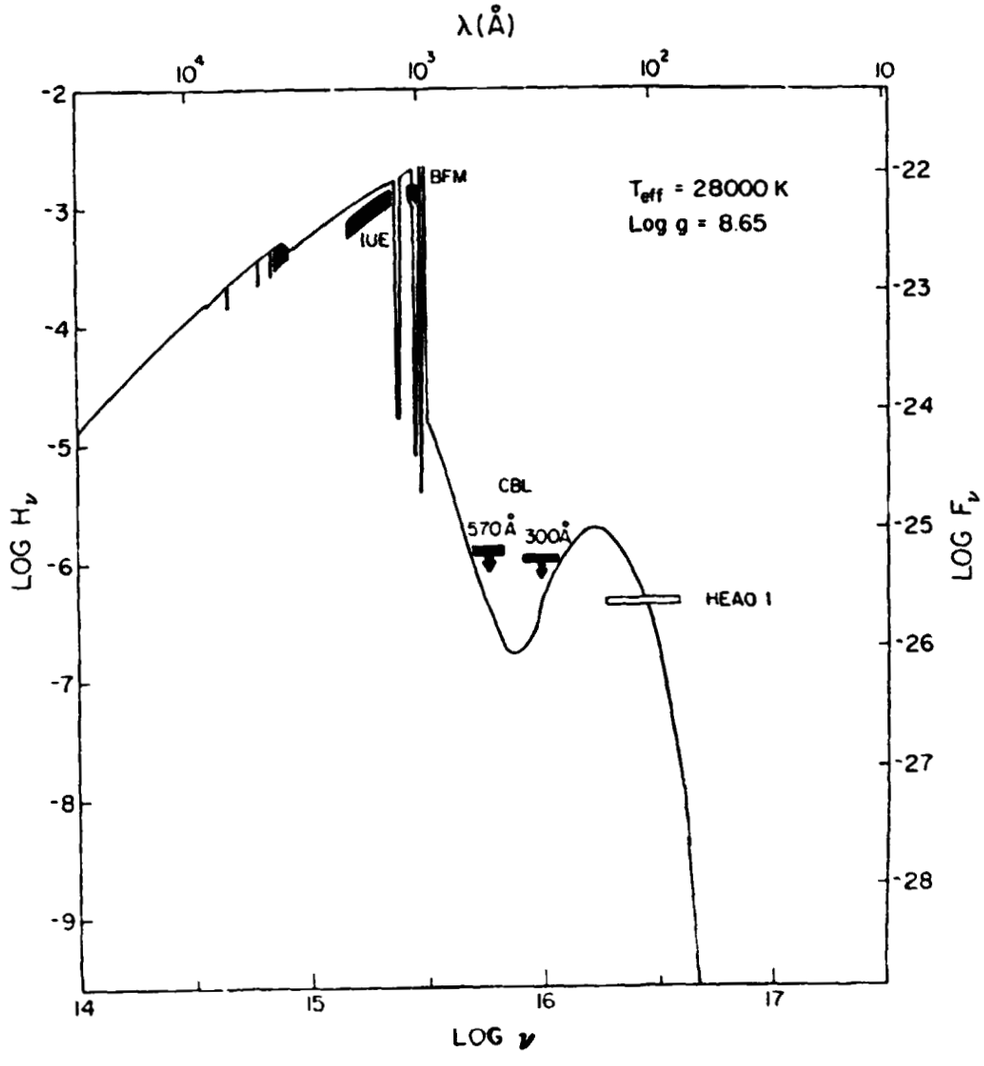

Fig. 14--Comparison of the flux from a 28,000 K hydrogen-rich model atmosphere with measurements and upper limits at UV, extreme UV, and soft X-ray wavelengths (from Martin et al. 1982).

gravitational energy, which will appear as blackbody radiation from the disk surfaces. The other half of the available gravitational energy will be released in a boundary layer at the inner edge of the disk where it encounters the surface of the star, unless the star is rotating near breakup. This luminosity is

$$L_{bdry} = \frac{1}{2}\frac{GM\dot{M}}{R} = 4 \times 10^{32} (M/M_\odot) (R/10^9 \text{ cm})^{-1} (\dot{M}/10^{-10} M_\odot \text{ yr}^{-1}) \text{ ergs s}^{-1}, \quad (1)$$

where M and R are the mass and radius of the star, and $\dot{M}$ is the mass accretion rate. At moderate or high accretion rates, the boundary layer is capable of producing soft X-rays by blackbody emission (Pringle 1977). After it was found that most cataclysmic variables emit hard, but not soft, X rays during quiescence, Pringle and Savonije (1979) proposed that the boundary layer might produce hard X-ray emission by optically thin bremsstrahlung if shocks occurred there. The maximum possible shock temperature is

$$T_s = \frac{3}{8} T_{ff} = 2 \times 10^8 (M/M_\odot (R/10^9 \text{ cm})^{-1} \text{ K}, \quad (2)$$

and thus the shocks must be strong ones. This is difficult to achieve in the strongly sheared flow of the inner disk whose geometry would tend to favor production of a large number of cooler, oblique shocks (in principle, the disk can join onto the star without the occurrence of any shocks). To attain the required strong shocks, Pringle and Savonije (1979) suggest a two-stage process in which gas that is initially mildly shocked in the boundary layer expands into the path of, and collides with, gas still circulating in the inner disk. Tylenda (1981), however, argues that turbulent viscosity will be a more efficient mechanism than shocks for dissipating energy in the boundary layer and that this mechanism can account for the observed high temperatures without resorting to complicated flow geometries.

Knowledge of whether the boundary layer can produce hard X-rays and, if so, how, is important for understanding the cataclysmic variable X-ray sources. But as yet, the ideas that have been proposed have not been worked out in any detail.

For up-to-date discussions of disks, see the review by Pringle (1981) and the paper by Tylenda (1981).

ii) Radial inflow near the star

If the degenerate dwarf has a magnetic field,

$$B \gtrsim 2 \times 10^3 (10^{-10} M_\odot \text{ yr}^{-1})^{1/2} (R/10^9 \text{ cm})^{-5/4} (M/M_\odot)^{1/4} \text{ gauss}, \quad (3)$$

the field will disrupt the disk and lead to approximately radial inflow near the star. This picture certainly applies to the AM Her and DQ Her stars, and may apply to other cataclysmic variables if magnetic fields are endemic in degenerate dwarfs as speculated earlier. Radial inflow may also occur if mass transfer takes place via a stellar wind rather than via Roche lobe overflow. Most theoretical work has assumed radial inflow because it is far more tractable; in the remainder of this review, we will concentrate on radial inflow.

A qualitative picture of X-ray emission by radially accreting degenerate dwarfs is shown in Figure 15. As accreting matter flows toward the star, a strong standoff shock forms far enough above the star for the hot, post-shock matter to cool and come to rest at the stellar surface (Hoshi 1973; Aizu 1973; Fabian, Pringle, and Rees 1976). The

ORIGINAL PAGE IS
OF POOR QUALITY

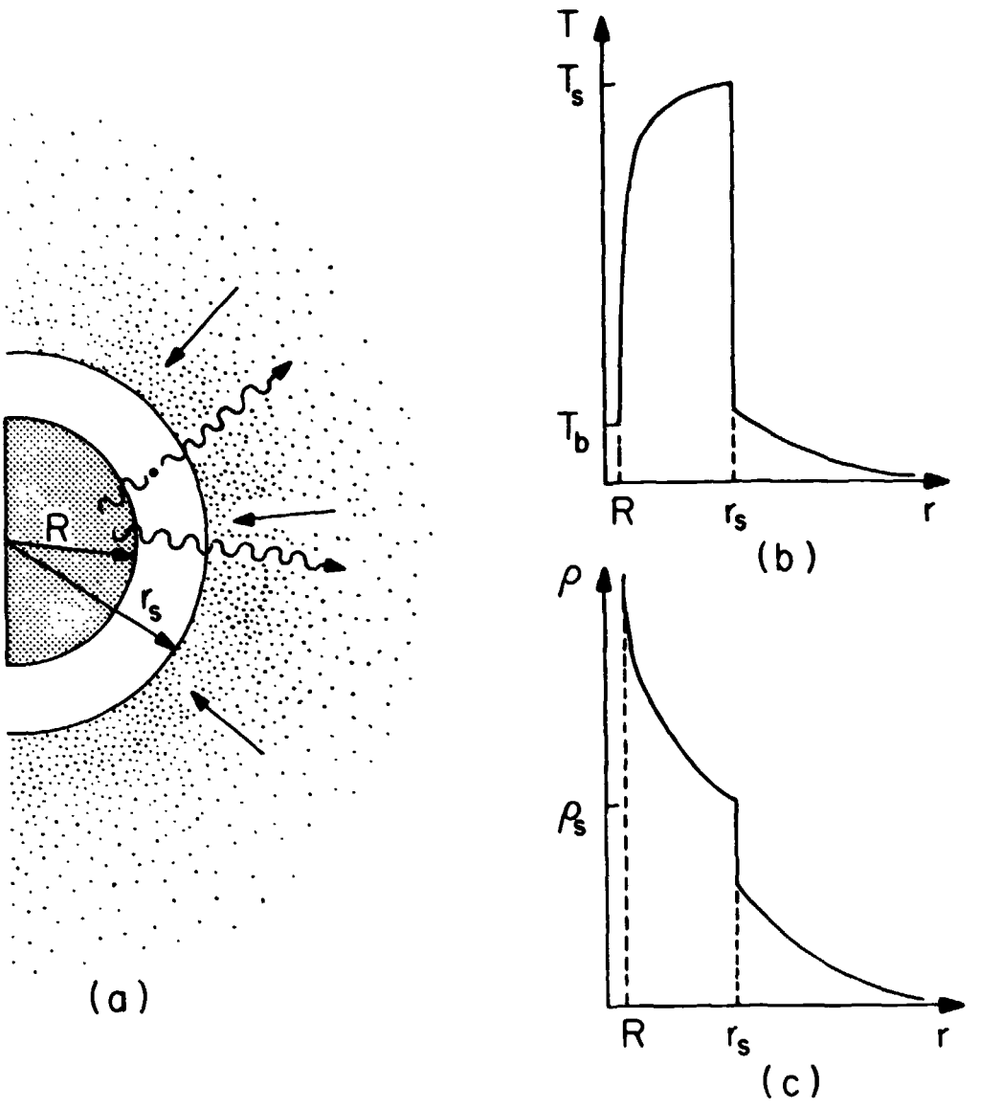

Fig. 15--Qualitative picture of X-ray emission from an accreting degenerate dwarf. a) Configuration of the star, the emission region, and the infalling matter. R is the stellar radius and r_s is the shock radius. The straight arrows indicate infalling matter, the wiggly arrows photons. b) Temperature profile of the infalling matter. T_s is the post-shock temperature and T_b is the stellar blackbody temperature. c) Density profile of the infalling matter; ρ_s is the post-shock density.

standoff distance

$$d \equiv r_s - R \approx 1/4\, v_{ff}(r_s)\, t_{cool}(r_s), \tag{4}$$

where r_s is the shock radius, R is the stellar radius, v_{ff} is the free-fall velocity, and t_{cool} is the time scale for cooling, due to bremsstrahlung and, if a magnetic field is present, cyclotron emission. Roughly half of the bremsstrahlung flux is emitted outward and forms a hard X-ray component. Roughly half of the cyclotron flux is emitted outward and forms a blackbody-limited component in the UV. The other halves of the bremsstrahlung and cyclotron fluxes are emitted inward and are reflected or absorbed by the stellar surface. The resulting blackbody flux forms a UV or soft X-ray component with

$$L_{bb} \approx L_{cyc} + L_{br}, \tag{5}$$

where L_{bb}, L_{cyc}, and L_{br} are the luminosities in the blackbody, cyclotron, and bremsstrahlung components. The total luminosity $L = GM\dot{M}/R$, or twice that given by equation (1).

If we allow for the possible presence of a magnetic field, the accreting matter may be channeled onto the magnetic poles and accretion may occur over only a fraction f of the stellar surface. The effective accretion rate of the accreting sector is $\dot{M}/f$, and the corresponding luminosity is L/f. X and UV radiation from magnetic degenerate dwarfs is thus a function of stellar mass M, magnetic field strength B, and effective luminosity L/f. The dependence on stellar mass is significant but is less than on the other two variables. If we specify the mass of the star, the parameter regimes encountered are conveniently displayed on a (B,L/f)-plane, as shown in Figure 16 for a 1 $M_\odot$. The upper left of the plane corresponds to low magnetic field strengths and high effective luminosities (and thus high densities in the emission region). In this portion of the plane, bremsstrahlung cooling dominates cyclotron cooling in the hot, post-shock emission region, and the character of the X-ray emission is essentially the same as that of a nonmagnetic degenerate dwarf. As one increases B or lowers L/f, moving toward the lower right in Figure 16, cyclotron cooling becomes more important until eventually it dominates (Masters et al. 1977). The solid line shows the location at which this occurs, as determined from detailed numerical calculations equating t_{cyc} and t_{br}, the cyclotron and bremsstrahlung cooling time scales. This line is approximately given by

$$B = 6 \times 10^6 \left(Lf^{-1}/10^{36} \text{ ergs s}^{-1}\right)^{2/5} \text{ gauss}. \tag{6}$$

To the lower right of this solid line, the magnetic field qualitatively alters the character of the X-ray emission.

b) Magnetic Stars

Fabian, Pringle, and Rees (1976), Masters et al. (1977), and King and Lasota (1979) have discussed the qualitative features of X-ray emission by magnetic degenerate dwarfs. Lamb and Masters (1979; see also Masters 1978) carried out detailed numerical calculations of high harmonic cyclotron emission from a hot plasma, and from them developed a self-consistent, quantitative model of the X-ray and UV emission. Wada et al. (1981) have carried out a few calculations for the regime im which bremsstrahlung,

ORIGINAL PAGE IS
OF POOR QUALITY

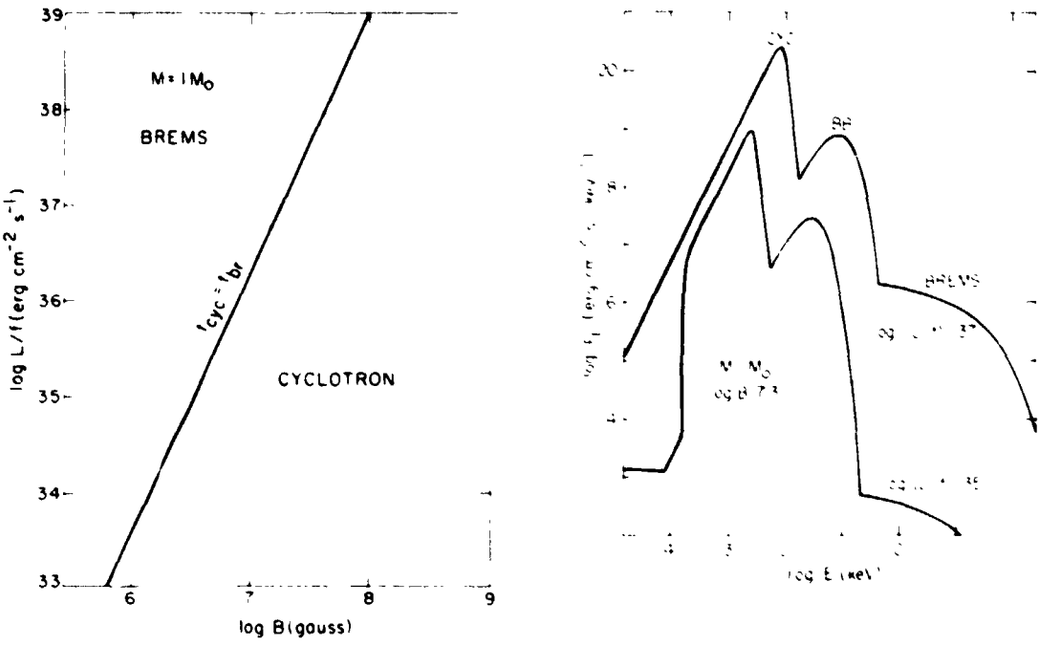

Fig. 16--Bremsstrahlung and cyclotron emission regimes in the (L/f,B)-plane for a 1 $M_\odot$ star (after Lamb and Masters 1979).

Fig. 17--X-ray and UV spectra produced by accretion onto a 1 $M_\odot$ star at two different accretion rates. The spectrum with $L/f = 10^{37}$ ergs s^{-1} is in the bremsstrahlung dominated regime, while the spectrum with $L/f = 10^{35}$ ergs s^{-1} is in the cyclotron dominated regime (from Lamb and Masters 1979).

not cyclotron emission, dominates (see Figure 16).

i) Spectra

The X and UV spectrum produced by accretion onto magnetic degenerate dwarfs generally has four components: 1) a blackbody-limited UV cyclotron component produced by the hot emission region, 2) a hard X-ray bremsstrahlung component also produced by the hot emission region, 3) a hard UV or soft X-ray blackbody component produced by cyclotron and bremsstrahlung photons that are absorbed by the stellar surface and re-emitted, and 4) secondary radiation from infalling matter above the shock or, possibly, from the stellar surface around the emission region. The first three components are clearly visible in Figure 17, which shows spectra produced by the hot, post-shock emission region alone. Since the secondary radiation is not included, the spectra do not accurately represent the observed spectrum below $\sim$5 eV. Figure 17 shows the X and UV spectra produced by accretion at two different rates, corresponding to $L/f = 10^{35}$ and 10^{37} erg s^{-1}, onto a 1.0 $M_\odot$ star having a magnetic field of 2×10^7 gauss.

The spectra illustrated in Figure 17 show two important features. First, strongly magnetic degenerate dwarfs should be intense UV sources with only a few percent of the total accretion luminosity ordinarily appearing as optical or soft and hard X-rays, and therefore easily accessible. Second, the position and relative strength of the spectral components change with variations in the accretion rate. For example, the change in accretion rate shown in Figure 17 moves the blackbody component from the UV into the soft X-ray region, and the luminosity of the bremsstrahlung hard X-ray component increases by nearly 4 orders of magnitude while the total accretion luminosity increases only by 2.

ii) Correlation between spectral temperature and luminosity

Variations in the shape and the strength of the spectral components are a function of both mass accretion rate and magnetic field strength. They can be conveniently displayed by plotting contours on a (B,L/f)-plane. Sets of such contours are shown in Figures 18 and 19 for a 1.0 $M_\odot$ star. Bremsstrahlung and cyclotron emission dominate in the same regions as in Figure 16. In Figure 18, contours of constant shock standoff distance $d = \delta R/R$ are shown as thick solid lines. The thin solid lines in the bremsstrahlung-dominated region show contours of constant $q = L_{cyc}/L_{br}$, while those in the cyclotron-dominated region show contours of constant T_e, the temperature of the bremsstrahlung hard X-ray component. In Figure 19, contours of constant E^*, the peak of the blackbody-limited cyclotron component, are shown as thick solid lines while contours of constant T_{bb}, the temperature of the blackbody component, are shown as dashed lines. The thin solid lines have their same meaning as in Figure 18. To the upper right of the curve labelled "soft excess" in Figure 19, the blackbody luminosity in soft X-rays exceeds the bremsstrahlung luminosity in hard X-rays.

Near and above $L/f = L_E = 1.4 \times 10^{38}$ erg s^{-1}, radiation pressure can be important and modify the results, but because photons can easily scatter out of the accretion column if $f \ll 1$, the Eddington luminosity does not represent the stringent upper limit to the luminosity that it does in the case of nonmagnetic degenerate dwarfs. Below and to the left of the curve $E^* = 2$ eV in Figure 19, the assumption $d < R$ breaks down, as can be seen from Figure 18.

If the geometry of the hot, post-shock emission region is such that most of the flux escapes through the face rather than through the edges of the emission region (i.e., $d \ll \sqrt{(2f)}R$), then Compton degradation of the bremsstrahlung hard X-ray component will occur if L/f exceeds $\sim 10^{37}$ erg s^{-1}. Such degradation is identical to that encountered

ORIGINAL PAGE IS
OF POOR QUALITY

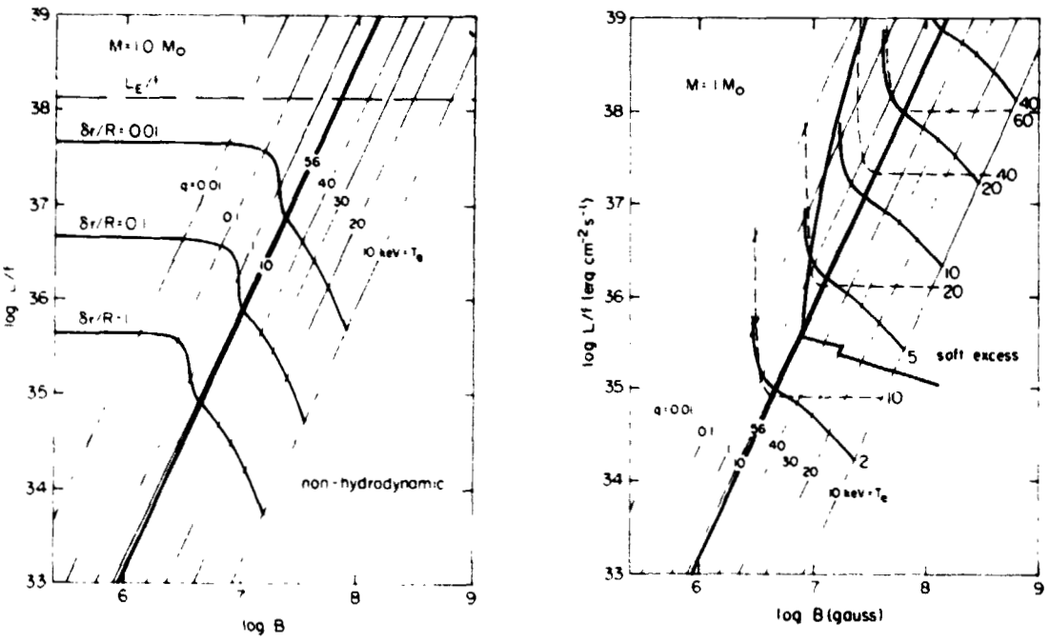

Fig. 18--Contours in the (L/f,B)-plane for a 1 $M_\odot$ star. For an explanation of the various lines, see the text.

Fig. 19--More contours in the (L/f,B)-plane for a 1 $M_\odot$ star (from Lamb and Masters 1979). For an explanation of the various lines, see the text.

in nonmagnetic degenerate dwarfs, and will be discussed below.

Figure 19 illustrates a third important feature of X-ray emission from magnetic degenerate dwarfs: observations of the qualitativr features of the X and UV spectrum can determine fairly accurately the physical conditions in the emission region, including the value of the magnetic field.

c) Nonmagnetic Stars

Studies of X-ray emission from accreting nonmagnetic degenerate dwarfs include those by Hoshi (1973), Aizu (1973), Hayakawa (1973), DeGregoria (1974), Hayakawa and Hoshi (1976), Fabian, Pringle, and Rees (1976), Katz (1977), and Kylafis and Lamb (1979, 1982a,b). These calculations are applicable, even if a magnetic field is present, as long as the accretion flow is approximately radial and bremsstrahlung cooling dominates cyclotron cooling in the X-ray emission region (recall Figure 16). Thus they are relevant to the AM Her stars, such as AM Her itself, which has a magnetic field $B \simeq 2 \times 10^7$ gauss (Lamb and Masters 1979; Schmidt, Stockman, and Margon 1981; Latham, Liebert, and Steiner 1981), and VV Pup, which has a magnetic field $B \simeq 3 \times 10^7$ gauss (Visvanathan and Wickramasinghe 1979; Stockman, Liebert, and Bond 1979), as well as to the DQ Her stars.

i) Spectra

The X and UV spectrum produced by accretion onto nonmagnetic degenerate dwarfs generally has three components: 1) a hard X-ray bremsstrahlung component produced by the hot, post-shock emission region, 2) a soft X-ray blackbody component produced by bremsstrahlung photons that are absorbed by the stellar surface and re-emitted, and 3) secondary radiation produced by Compton heating of infalling matter above the shock.

These components are clearly visible in Figure 20, which shows six spectra that span the entire range of accretion rates. Figure 21 shows for comparison three similar spectra when nuclear burning occurs at the accretion rate (see below). At low accretion rates, $\tau_{es} < 1$ and the observed hard X-ray spectrum is essentially the same as that produced in the emission region. As the accretion rate is increased, τ_{es} exceeds unity and Compton scattering begins to degrade the spectrum (Illarionov and Sunyaev 1972). The blackbody component then contains a contribution from bremsstrahlung photons which are backscattered by the accreting matter and absorbed by the stellar surface. The secondary radiation, which arises from accreting matter heated by the Compton scattering of the bremsstrahlung photons, is important only when degradation of the bremsstrahlung is substantial. As the accretion rate is increased further, this degradation becomes more severe. Finally, due to the combined effects of degradation and weakening of the shock by radiation pressure, the bremsstrahlung component disappears altogether. The star then ceases to be a hard (i.e., $T_{obs} > 2$ keV) X-ray source.

Figure 20 illustrates two important features of X-ray emission from nonmagnetic degenerate dwarfs. First, an intense blackbody soft X-ray component is always present. Second, at high accretion rates Compton degradation leads to low spectral temperatures even for high mass stars.

ii) Correlation between spectral temperature and luminosity

The resulting correlation between T_{obs} and L_h is shown in Figure 22 for stars of mass $M = 0.2\text{-}1.2\ M_\odot$. Note that the accretion rate increases as one moves from upper left to lower right along the curves. For sources found in the lower right of the figure,

ORIGINAL PAGE IS
OF POOR QUALITY

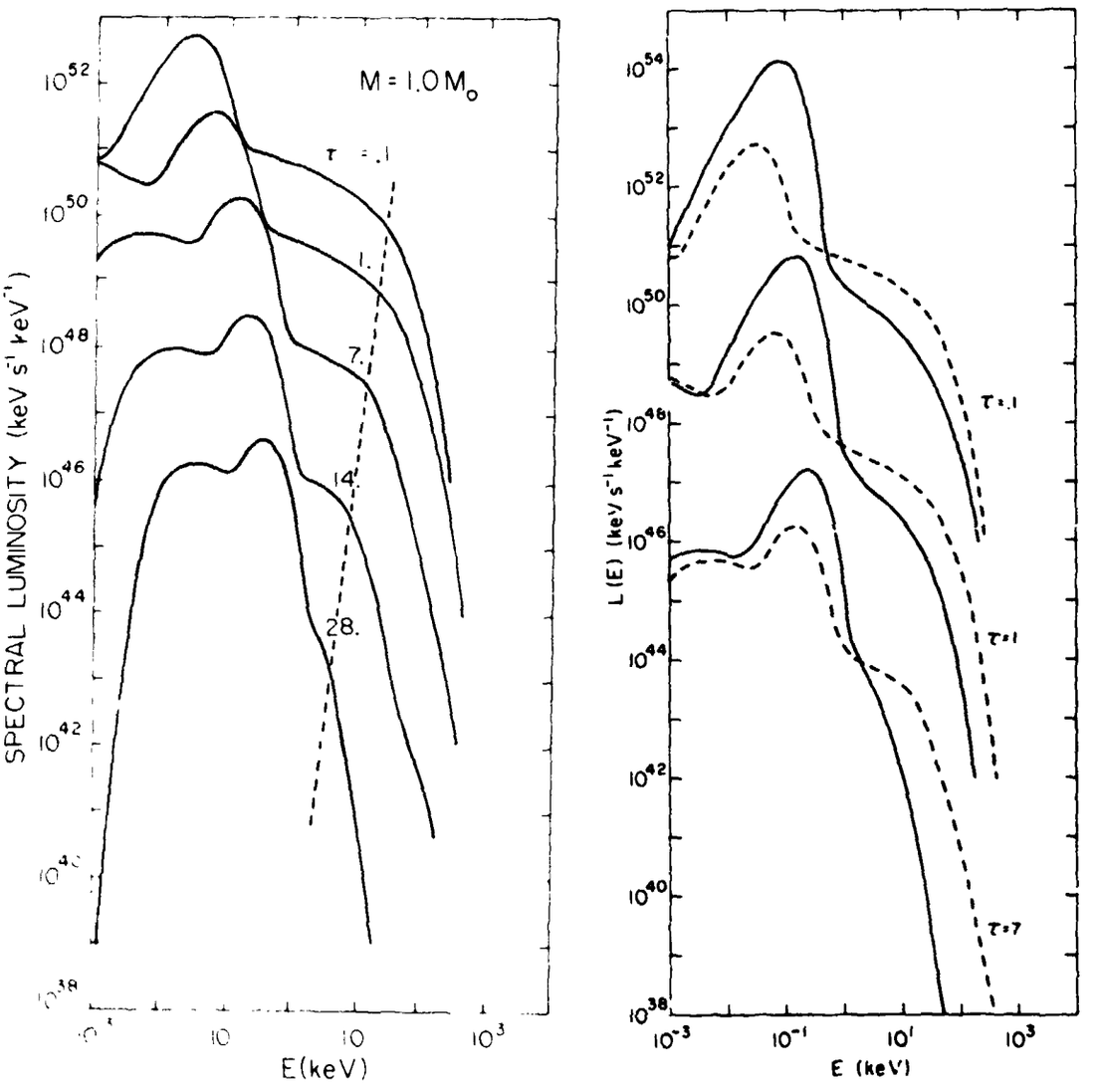

Fig. 20--X and UV spectra produced by accretion onto a 1 $M_\odot$ star for six different accretion rates (from Kylafis and Lamb 1982a). The dashed line shows the changing cutoff due to Compton degradation.

Fig. 21--Comparison of X and UV spectra produced by accretion onto a 1 $M_\odot$ star with nuclear burning at the accretion rate (solid curves) and without nuclear burning (dashed curves) (from Weast et al. 1982).

ORIGINAL PAGE IS
OF POOR QUALITY

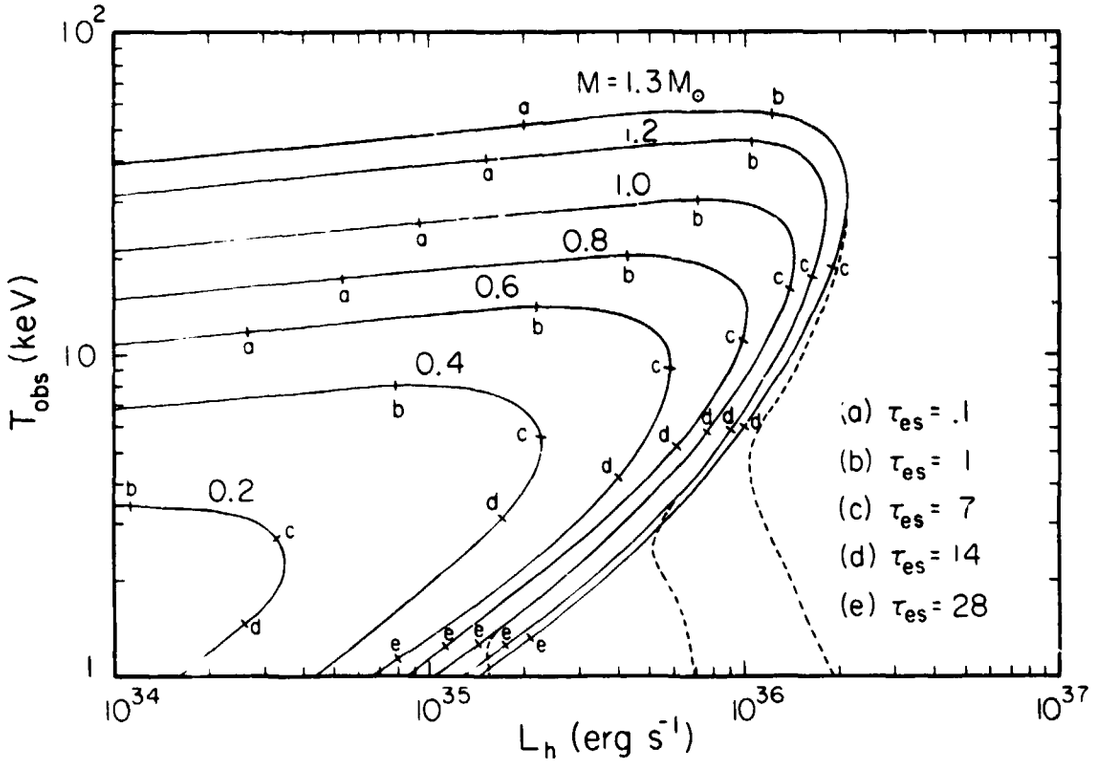

Fig. 22--Correlation between T_{obs} and L_h for stars with masses 0.2 - 1.2 $M_\odot$ (from Kylafis and Lamb 1982a). The dashed lines give the same correlation when the contribution of the blackbody component is included in L_h.

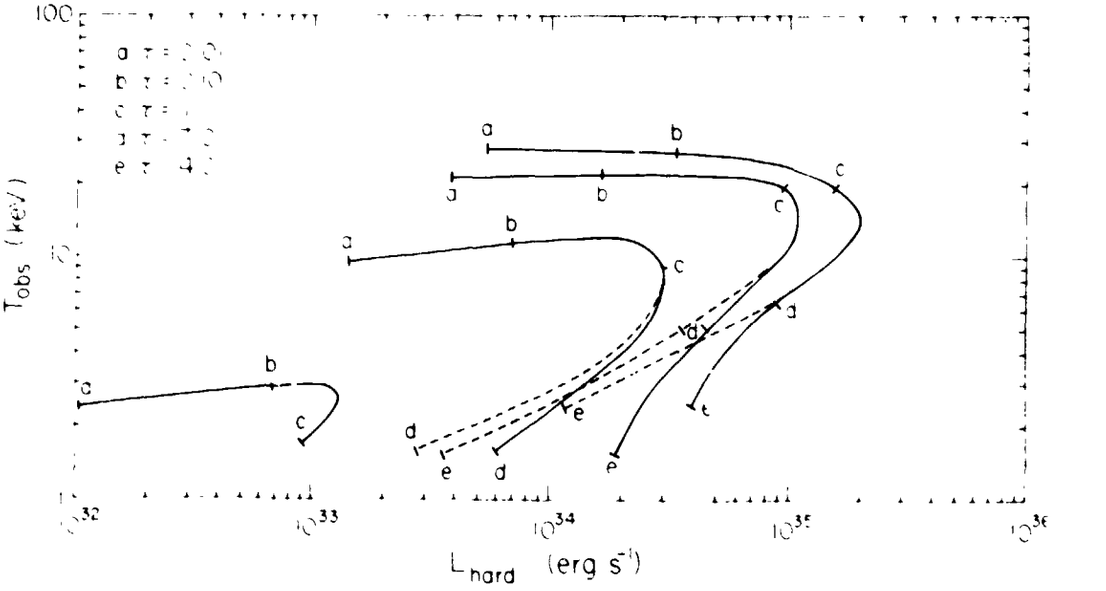

Fig. 23--Correlation between T_{obs} and L_h for stars with masses 0.2 - 1.2 $M_\odot$ (from Weast et al. 1982). The dashed lines give the same correlation when the contribution of the blackbody component is omitted.

an increase in T_{obs} and L_h therefore corresponds to a decrease in the accretion rate: t_{obs} and L_h increase since the smaller accretion rate lessens Compton degradation of the hard X-ray spectrum.

Figure 22 illustrates the dramatic variation in the spectral temperature at high accretion rates and the pronounced correlation between X-ray spectral temperature and luminosity.

d) Effects of Nuclear Burning

The energy liberated by nuclear burning of matter accreting onto degenerate dwarfs can be more than an order of magnitude greater than that available from the release of gravitational energy. If burning occurs quiescently, the resulting energy is transported to the stellar surface and produces an intense blackbody soft X-ray flux. Steady nuclear burning has therefore recently received a great deal of attention as a possible explanation of the intense blackbody soft X-ray components inferred in the AM Her stars (Raymond et al. 1979, Patterson et al. 1982) and in other cataclysmic variables, such as SS Cyg and U Gem, during outburst (Fabbiano et al. 1981).

i) Conditions for steady nuclear burning

Unfortunately, the conditions under which steady nuclear burning can occur are poorly understood. Detailed spherically symmetric calculations by Paczynski and Zytokow (1978), Sion, Acierno, and Tumshek (1978), and Sion, Acierno, and Tomczyk (1979) show that if the degenerate dwarf is initially cold and the accretion rate is not too high, the accreting matter becomes highly degenerate before it ignites. Electron conduction then rapidly transports energy away into the core, and it must be heated before ingition can occur. If the degenerate dwarf is hot, or if the accretion rate is high, the hydrogen in the accreting matter soon ignites due to compressional heating. In either case, eventually a violent nuclear outburst ensues. Such outbursts are believed to account for nc ae (cf. Starrfield, Sparks, and Truran 1974).

The outbursts are separated by quiescent periods, in which nuclear burning occurs steadily at only a small fraction of the accretion rate. The quiescent periods are shorter for higher accretion rates and can last from $\sim$ 20 years or less (Sion et al. 1979) to $> 10^7$ years (Paczynski and Zytkow 1978). For a narrow range of higher accretion rates, steady nuclear burning is possible at the rate of accretion (e. g. $1.0 - 2.7 \times 10^{-7}$ $M_\odot\ yr^{-1}$ for a 0.8 $M_\odot$ star; Paczynski and Zytkow 1978). Still higher accretion rates lead to envelope expansion and the formation of a red giant with a degenerate core.

Depletion of CNO nuclei in the accreting matter and the burning region by diffusion can lead to burning via the p-p chain rather than via the more temperature sensitive CNO-cycle (Starrfield, Truran, and Sparks 1981), and stabilize the burning at higher accretion rates. However, theoretical investigations show that such rapid depletion is unlikely (Fujimoto and Truran 1981; Papaloizou, Pringle, and MacDonald 1982).

Effects due to non-spherical geometries also warrant investigation. For example, in the AM Her and DQ Her stars a strong magnetic field channels the accreting matter onto the magnetic poles. If the matter is confined and burns over only a small fraction of the stellar surface, the burning might be stabilized by the rapid transpc of energy horizontally.

ii) Effects on X-ray emission

The effects of nuclear burning on X-ray emission by nonmagnetic degenerate dwarfs have been investigated in detail by Imamura et al. (1979, 1982) and Weast et al. (1979, 1982). The accreting matter does not burn in the hot X-ray emission region, but may do so deeper in the envelope of the star. The energy thus liberated is transported to the stellar surface and enhances the blackbody flux in soft X-rays. This flux of soft X-ray photons cools the X-ray emission region by inverse Compton scattering. As a result, the hard X-ray luminosity is often an order of magnitude less than it would be in the absence of nuclear burning, the hard X-ray spectrum is softer, and the soft X-ray luminosity can be 100 times the hard X-ray luminosity. Figure 21 compares the X-ray spectra of a 1 $M_\odot$ star in which nuclear burning occurs at the accretion rate to the spectra in the absence of burning. The three spectra shown span the entire range of accretion rates. Figure 23 shows the correlation between T_{obs} and L_h when nuclear burning occurs at the accretion rate for stars of mass 0.2 - 1.2 $M_\odot$. These curves should be compared with those in Figure 22, which assumes no nuclear burning.

The effects of nuclear burning on X-ray emission by magnetic degenerate dwarfs are not expected to be as dramatic. As long as cooling by cyclotron emission dominates cooling by inverse Compton scattering of the blackbody photons, the cyclotron UV and bremsstrahlung hard X-ray luminosities will be little changed. The spectral temperatures of these components will also be little affected. The blackbody soft X-ray luminosity will, however, be much larger.

IV. LINE SPECTRA

a) Ionization Structure

The circumstellar ionization structure of degenerate dwarf X-ray sources has been calculated analytically by Hayakawa (1973) and more recently by Kylafis and Lamb (1982b). These calculations assume spherical symmetry, and assume that the optical depth to absorption is small. The degenerate dwarf X-ray sources detected so far have low luminosities and low accretion rates. Therefore, the analytical calculations are valid, provided that the accretion flow is approximately radial.

The calculations by Kylafis and Lamb (1982b) show that the blackbody soft X-ray flux ionizes H, He, and C out to distances large compared with a typical binary separation. Furthermore, for high mass stars and low accretion rates, the bremsstrahlung hard X-ray flux ionizes heavy elements out to considerable distances. These features are illustrated in Figures 24 and 25, which show l_Z, the radius at which the element with charge Z is half ionized and half neutral, as a function of mass accretion rate for a 1.2 $M_\odot$ star. Figure 24 shows the effect of the blackbody soft X-ray flux, while Figure 25 shows the effect of the bremsstrahlung hard X-ray flux. In both figures, the solid lines correspond to no nuclear burning and the dashed lines to nuclear burning at the accretion rate.

The absorption optical depth τ^*_Z at the ionization edges of heavy elements remains small until the accretion rate exceeds about 3×10^{-3} $\dot{M}_E$ but thereafter increases rapidly, as shown in Figure 26. Compton scattering and the resulting degradation of the hard X-ray spectrum occurs primarily close to the star, while most of the absorption occurs relatively far from the star, as illustrated in Figure 27. Thus the amount of Compton degradation is less sensitive, and the amount of absorption more sensitive, to the distribution of accreting matter.

b) Absorption Features

Figure 28 shows the emergent hard X-ray spectrum from a 1.2 $M_\odot$ star for four different accretion rates as calculated analytically by Kylafis and Lamb (1982b), taking absorption into account. Ross and Fabian (1981) have carried out detailed numerical calculations of the emergent spectrum from a 1.0 $M_\odot$ star for three different accretion rates. The latter calculations treat the atomic physics carefully and are valid even for large absorption optical depths. The results are shown in Figures 29-31. Note both the absorption K-edges due to O VIII (0.87 keV), Si XIV (2.7 keV), and Fe XXI-XXVI (8.2 - 9.3 keV), and the emission lines, broadened by Compton scattering, due to the Kα lines of O VIII (0.65 keV), Si XIV (2.0 keV), and Fe XXV (6.7 keV).

c) Emission Lines

The temperatures in the X-ray emission regions of degenerate dwarf X-ray sources are high enough (> 10 keV) to produce thermal emission lines, including those of Fe at ∿ 7 keV, with significant equivalent widths. Emission lines can also be produced by fluorescence in the accreting matter above the X-ray emission region, as seen in Figures 29-31. Fluorescent emission lines may also be produced by X-rays striking the stellar surface surrounding the emission region, the disk, and even the companion star.

The emission lines may be broadened by 1) thermal Doppler broadening, 2) Compton scattering, and 3) Doppler broadening due to bulk streaming velocities. Thermal Doppler broadening produces a relative line width,

$$\Delta\nu/\nu \backsim (2kT/m_e c^2)^{1/2}. \tag{7}$$

The resulting width is ∿ 0.5 keV for the ∿ 7 keV Fe lines if they are formed in an X-ray emission region with temperature T_e ∿ 10 keV. Compton scattering produces a relative line width

$$\Delta\nu/\nu \backsim \tau^2 \frac{h\nu}{m_e c^2} \backsim 0.1\, \tau^2\, (h\nu\ /7\ \text{keV}). \tag{8}$$

Thus the ∿ 7 keV Fe emission lines will be relatively broad even if the electron scattering optical depth through accreting matter is only modest. Doppler broadening due to bulk motion produces a relative line width

$$\Delta\nu/\nu \backsim v/c \backsim 2 \times 10^{-2} \frac{v}{v_{ff}(R)}, \tag{9}$$

where in the last step we have scaled from the freefall velocity at the surface of a 1 $M_\odot$ star. Doppler broadening due to bulk motion is therefore generally less than thermal Doppler broadening and Compton scattering. These results imply that the X-ray emission lines produced by degenerate dwarfs are relatively broad. However, as noted above, emission lines can be produced by recombination and fluorescence in accreting matter far from the star. In this case, the temperatures may be low, and the electron scattering optical depth small. If so, narrow emission lines can be produced.

V. ISSUES

ORIGINAL PAGE IS
OF POOR QUALITY

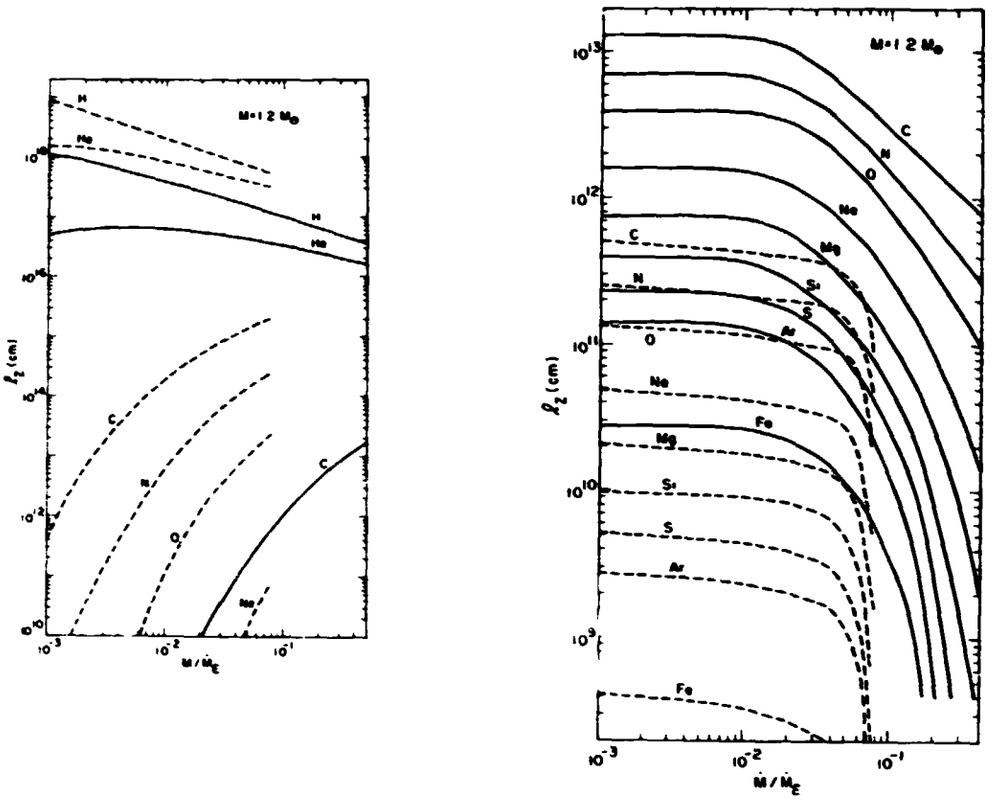

Fig. 24--Circumstellar ionization structure as a function of accretion rate produced by the blackbody soft X-ray flux of a 1.2 $M_\odot$ star (from Kylafis and Lamb 1982b). The quantity l_Z, the radius at which the element with charge Z is half ionized, is shown assuming no nuclear burning (solid lines) and nuclear burning at the accretion rate (dashed lines).

Fig. 25--Circumstellar ionization structure as a function of accretion rate produced by the bremsstrahlung hard X-ray flux of a 1.2 $M_\odot$ star (from Kylafis and Lamb 1982b). The curves have the same meaning as in Fig. 24.

ORIGINAL PAGE IS
OF POOR QUALITY

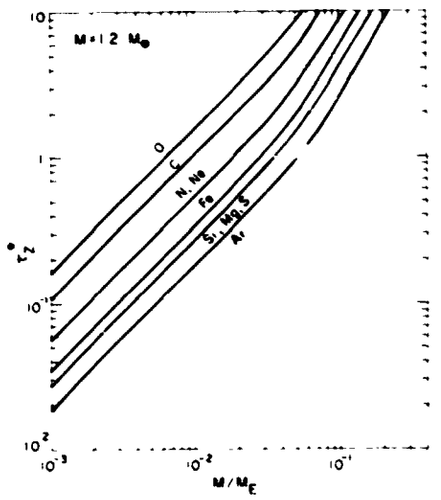

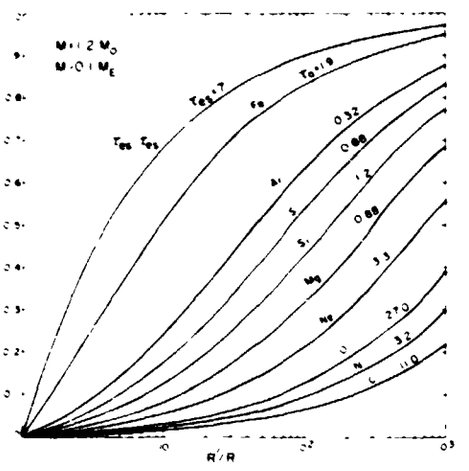

Fig. 26--Optical depth τ_Z^* at the absorption edge of a given element as a function of accretion rate for a 1.2 $M_\odot$ star without nuclear burning (from Kylafis and Lamb 1982b).

Fig. 27--Fractional electron scattering and absorption optical depths reached at a given radius for a 1 $M_\odot$ star accreting at a rate 0.1 $\dot{M}_E$ (from Kylafis and Lamb 1982b). Note that the electron scattering optical depth increases rapidly near the star, while the absorption optical depths remain small until larger radii.

ORIGINAL PAGE IS
OF POOR QUALITY

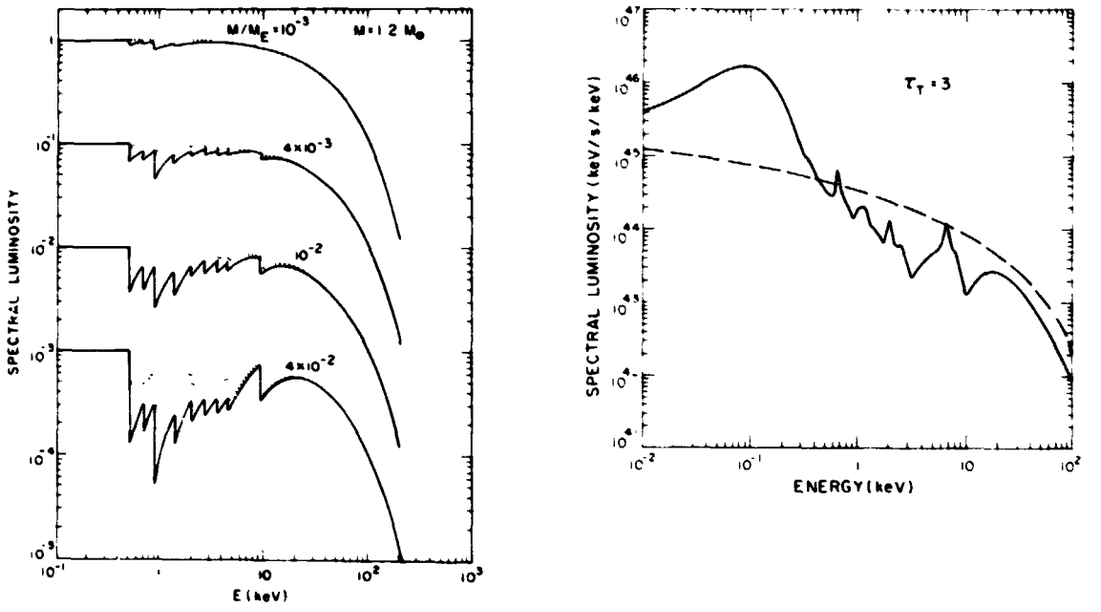

Fig. 28--Bremsstrahlung hard X-ray spectra produced by accretion onto a 1.2 $M_\odot$ star at 4 different accretion rates, taking into account the effects of absorption analytically (from Kylafis and Lamb 1982b).

Fig. 29--X and UV spectrum produced by a 1 $M_\odot$ star at an accretion rate 0.045 $\dot{M}_E$ (τ = 3) taking into account the effects of photoabsorption through detailed numerical calculations (from Ross and Fabian 1980).

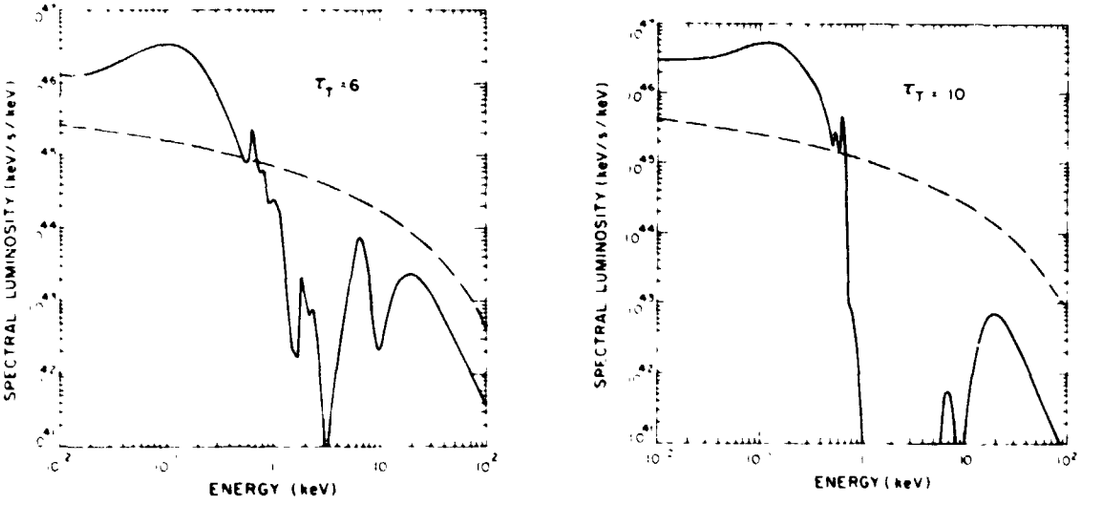

Fig. 30--Same as Fig. 29 for an accretion rate 0.090 $\dot{M}_E$ (τ = 6) (from Ross and Fabian 1980).

Fig. 31--Same as Fig. 29 for an accretion rate 0.15 $\dot{M}_E$ (τ = 10) (from Ross and Fabian 1980).

Among the important unresolved issues concerning degenerate dwarf X-ray sources are the following.

a) Magnetic Fields

Do only a few degenerate dwarfs have magnetic fields, and are the AM Her and DQ Her stars the only cataclysmic variables with magnetic fields? Or are magnetic fields endemic in degenerate dwarfs, and therefore in cataclysmic variables? If so, what are the field strengths? Are they large enough to affect the disk and the accretion flow near the stellar surface?

b) Origin of Hard X Rays

What is the origin of the hard X-rays emitted by cataclysmic variables? Are they produced by optically thin emission in the boundary layer between the disk and the star? If so, are the required high temperatures achieved by strong shocks, turbulence, or some other mechanism? Alternatively, are magnetic fields present in these sources sufficient to disrupt the disk near the star, producing quasi-radial inflow and a strong shock?

c) Origin of Soft X Rays

What is the origin of the intense blackbody soft X-ray emission inferred in the AM Her stars? How can it be so large compared to the optical and hard X-ray emission? Is its origin the same as the soft X-ray emission seen in SS Cyg and U Gem at outburst, or is it different?

d) Nuclear Burning

Under what conditions is steady nuclear burning possible? If it is generally not possible, as many calculations suggest, why are outbursts not more evident? Can steady burning occur more easily in non-spherical situations, as in the AM Her stars? If so, could it account for the intense blackbody soft X-ray emission in these stars? Could it account for the blackbody soft X-ray emission seen in cataclysmic variables like SS Cyg and U Gem?

e) Long Period Pulsing Sources

What is the nature of the long period pulsing sources? Are they actually degenerate dwarfs, or are they neutron stars? Why are they rotating so slowly; that is, why have they not been spun up more by their accretion torque? Does their rotation rate increase and then decrease with time, like the previously known pulsing neutron star X-ray sources with long periods?

f) Cyclotron-Dominated Sources

Although the AM Her stars are strongly magnetic, bremsstralung, not cyclotron emission, is the dominant cooling mechanism in the X-ray emission region (because the

accretion flow is channeled onto such a small fraction f $\sim 10^{-3}$ of the stellar surface that the density in the emission region is very high). Where are the sources in which cyclotron cooling dominates? Will they be found by a UV or extreme UV survey?

g) High Luminosity Sources

To date no high luminosity (L $\sim 10^{36}$ - 10^{38} ergs s^{-1}) X-ray source has been unequivocally identified with a degenerate dwarf, and the future does not look promising. Are there no high luminosity degenerate dwarf X-ray sources? If not, why not?

From these brief remarks, it should be evident that we have only begun to explore the nature of degenerate X-ray sources. We must rely on future X-ray astronomy missions to provide the data needed to understand them. In the following section, we outline the kind of instruments that would best advance our knowledge.

VI. OBSERVATIONAL NEEDS

a) High Throughput

Because degenerate dwarf X-ray sources are faint, the most important attribute of any instrument designed to study them effectively is high throughput. This requirement implies that the instrument should have a large area and a low background rate. A low background rate implies, almost inevitably, the necessity of a focusing instrument. A focusing instrument is also desirable from the standpoint of source confusion, which could be a problem at lower energies.

b) Pointing Capability and Flexibility

A central characteristic of degenerate dwarf X-ray sources, like other compact X-ray sources, is their time variability. They show quasi-periodicities on time scales ranging from several seconds to a thousand seconds, pulsing due to rotation periods ranging from 33 to as much as 4000 seconds, flaring behavior, variability correlated with the binary period, and, of course, the outbursts from which the cataclysmic variables derive their name. Pointing capability is essential for any instrument which is to study them successfully, and flexibility (so that one can move onto the source when it goes into outburst, for example) is desirable.

c) Hard and Soft X-Ray Spectral Sensitivity

As we have seen, many, and perhaps all, degenerate dwarf X-ray sources have two distinct components, one with $T_{br} > 10$ keV and another with $T_{bb} < 100$ eV. As a result, a soft X-ray capability is important and should extend down to at least 0.1 - 0.25 keV. Conversely, a number of sources have hard X-ray spectra with temperatures as high as 30 keV (e.g., AM Her). Therefore a hard X-ray capability extending up to at least $\sim$ 35

keV, and possibly beyond, would be highly desirable.

d) Broad-Band Spectral Measurements

Correlations between the shapes and intensities of both the hard and soft X-ray components have been seen, for example, as a source declines from outburst. Although many of these correlations are not yet understood, theoretical work indicates that they are potentially a powerful source of information about the physical conditions in the X-ray emission region, such as temperature, density, magnetic field strength, and mass accretion rate. Therefore broad band spectral measurements have been, and will continue to be, very useful.

e) Moderate Spectral Resolution

Further studies of the iron emission lines in these sources may yield information about the X-ray emission region, the accretion flow, and the geometry of the binary system. Other emission lines, if present, could provide similar information. All of them may be broadened, either thermally or by Compton scattering. Studies of such emission lines require instruments with moderate ($\Delta\lambda/\lambda \sim 10 - 50$) spectral resolution.

Table 5 summarizes the observational needs we have discussed above.

TABLE 5

FUTURE OBSERVATIONAL NEEDS

SOURCE FEATURE	INSTRUMENTAL REQUIREMENT
Faint	• Large area • Low background • Small field of view
Variable	• Pointing essential • Flexibility desirable
Distinct soft X-ray and hard X-ray components	• Soft X-ray capability important • Hard X-ray capability, extending up to ~40 keV desirable
Continuum spectral shape correlated with luminosity	• Low spectral resolution
Iron emission line seen, broad absorption lines expected	• Moderate spectral resolution

ORIGINAL PAGE IS
OF POOR QUALITY

REFERENCES

Agrawal, P. C., Rao, A. R., Riegler, G. R., Pickles, A. J., and Visvanathan, N. 1981, IAU Circ. No. 3649.

Aizu, K. 1973, Prog. Theor. Phys., 49, 1184.

Bailey, J. 1981, M.N.R.A.S., 197, 31.

Bath, G. T., Evans, W. D., and Pringle, J. E. 1974, M.N.R.A.S., 166, 113.

Becker, R. H. 1981, Ap. J., in press.

Becker, R. H., and Marshall, F. E. 1981, Ap. J. (Letters), 244, L93.

Berg, R., and Duthie, J. 1977, Ap. J., 211, 859.

Bohm-Vitense, E., Dettmann, T., and Kapranidis, S. 1979, Ap. J. (Letters), 232, L189.

Bowyer, S. 1979, in IAU Colloquium 53, White Dwarfs and Variable Degenerate Stars, ed. H. M. Van Horn and V. Weidemann (Rochester, N.Y.: University of Rochester), p. 66.

Cash, W, Bowyer, S. and Lampton, M. 1978, Ap. J. (Letters), 221, L87.

Chanmugam, G., and Wagner, R. L. 1977, Ap. J. (Letters), 213, L13.

Chanmugam, G., and Wagner, R. L. 1978, Ap. J., 222, 641.

Cordova, F. A., and Mason, K. O. 1982, in Accretion Driven Stellar X-Ray Sources, ed. W. H. G. Lewin and E. P. J. van den Heuvel (Cambridge, England: Cambridge University Press), in press.

Cordova, F. A., and Riegler, G. R. 1979, M.N.R.A.S., 188, 103.

Cordova, F. A., Chester, T. J., Mason, K. O., Kahn, S. M., Garmire, G. P., and Middleditch, J. 1981, submitted to Ap. J.

Cordova, F. A., Chester, T. J., Tuohy, I. R., and Garmire, G. P. 1980, Ap. J., 235, 163.

Cordova, F. A., Mason, K. O., and Nelson, J. E. 1981, Ap. J., 245, 609.

Cowley, A., and Crampton, D. 1977, Ap. J. (Letters), 212, L121.

DeGregoria, A. J. 1974, Ap. J., 189, 555.

Fabian, A. C., Pringle, J. E., and Rees, M. J. 1976, M.N.R.A.S., 173, 43.

Fabbiano, G., Hartmann, L., Raymond, J., Steiner, J., Branduardi-Raymont, G., and Matilsky, T. 1981, Ap. J., 243, 911.

Fujimoto, M. Y., and Truran, J. W. 1981, Ap. J., in press.

Garmire, G. 1979, in Compact Galactic X-Ray Sources, ed. F. K. Lamb and D. Pines (Urbana, Illinois: University of Illinois), p.62.

Gilliland, R. L. 1982, Ap. J., in press.

Griffiths, R., Lamb, D. Q., Ward, M. M., Wilson, A., Charles, P. A., Thorstensen, J., McHardy, I. M., and Lawrence, A. 1980, M.N.R.A.S., 193, 25P.

Haefner, R., Schoembs, R.,and Vogt, N. 1979, Astr. Ap., 77, 7.

Hayakawa, S. 1973, Prog. Theor. Phys., 50, 459.

Hayakawa, S., and Hoshi, R. 1976, Prog. Theor. Phys., 55, 1320.

Hearn, D. R., and Marshall, F. J. 1979, Ap. J. (Letters), 232, L21.

Hearn, D. R., and Richardson, J. A. 1977, Ap. J., 213, L115.

Hearn, D. R., Richardson, J. A., and Clark, G. W. 1976, Ap. J. (Letters), 210, L23.

Hearn, D., Richardson, J. A., Bradt, H. V. D., Clark, G. W., Lewin, W. H. G., Mayer, F., McClintock, J. E., Primini, F. A., and Rappaport, S. A. 1976, A. J. (Letters), 203, L21.

Heise, J., Mewe, R., Brinkman, A. C., Groenschild, E. H. B. M., den Boggende, A. J. F., Schrijver, J., and Grindlay, J. E. 1978, Astron. Ap., 63, L1.

Hildebrand, R. H., Spiller, F. J., and Stiening, R. F. 1981, Ap. J., 243, 223.

Horne, K., and Gomer, R. 1980, Ap. J., 237, 845.

Hoshi, R. 1973, Prog. Theor. Phys., 49, 776.
Illarionov, A. F., and Sunyaev, R. A. 1972, Astr. Zh., 49, 58 (English transl. in Soviet Astr.-AJ, 16, 45, 1972).
Imamura, J. N., Durisen, R. H., Lamb, D. Q., and Weast, G. J. 1979, in IAU Colloquium 53, White Dwarfs and Variable Degenerate Stars, ed. H. M. Van Horn and V. Weidemann (Rochester, N.Y.: University of Rochester), p. 406.
Imamura, J. N., Durisen, R. H., Lamb, D. Q., and Weast, G. J. 1982, submitted to Ap. J.
Joss, P. C., Katz, J. I., and Rappaport, S. 1979, Ap. J., 230, 176.
Katz, J. I. 1977, Ap J., 215, 265.
King, A. R., Ricketts, M. J., and Warwick, R. S. 1979, M.N.R.A.S., 187, 77P.
King, A. R., and Lasota, J. P. 1979, M.N.R.A.S., 188, 653.
Krzeminski, W., and Serkowski, K. 1977, Ap. J. (Letters), 216, L45.
Kylafis, N. D., and Lamb, D. Q. 1979, Ap. J. (Letters), 228, L105.
Kylafis, N. D., and Lamb, D. Q. 1982a, Ap. J. (Supp.), in press.
Kylafis, N. D., and Lamb, D. Q. 1982b, Ap. J., in press.
Kylafis, N. D., Lamb, D. Q., Masters, A. R., and Weast, G. J. 1980, Proc. Ninth Texas Symposium on Relativistic Astrophysics, Ann. N.Y. Acad. Sci., 336, 520.
Lamb, D. Q. 1974, Ap. J. (Letters), 192, L129.
Lamb. D. Q. 1979, in Compact Galactic X-Ray Sources, ed. F. K. Lamb and D. Pines (Urbana, Illinois: University of Illinois), p. 27.
Lamb, F. K. 1982, these proceedings.
Lamb, D. Q., and Masters, A. R. 1979, Ap. J. (Letters), in press.
Latham, D. W., Liebert, J., and Steiner, J. 1981, Ap. J., in press.
Linsky, J. 1982, these proceedings.
Margon, B., Lampton, M., Bowyer, S., Stern, R., and Paresce, F. 1976, Ap. J. (Letters), 210, L79.
Martin, C., Basri, G., Lampton, M., and Kahn, S. H. 1982, Ap. J., in press.
Mason, K. O., Lampton, M., Charles, P., and Bowyer, S. 1978, Ap. J. (Letters), 226, L129.
Mason, K., Cordova, F., and Swank, J. 1979, in (COSPAR) X-ray Astronomy, ed. W. A. Baity and L. E. Peterson (Oxford and New York: Pergamon Press), p. 121.
Mason, K. O., Middleditch, J., Cordova, F. A., Jensen, K. A., Reichert, G., Murdin, P. G., Clark, D., and Bowyer, S. 1982, Ap. J., in press.
Masters, A. R. 1978, Ph.D. Thesis, University of Illinois, unpublished.
Masters, A. R., Fabian, A. C., Pringle, J. E., and Rees, M. J. 1977, M.N.R.A.S., 178, 501.
Mewe, R., Heise, J., Gronenschild, E., Brinkman, A., Schrijver, J., and den Boggende, A. 1975, Ap. J. (Letters), 202, L67.
Nather, R. E., and Robinson, E. L. 1974, Ap. J., 244, 269.
Paczynski, B., and Zytkow, A. N. 1978, Ap. J., 222, 604.
Papaloizou, J. C. B., Pringle, J. E., and MacDonald, J. 1982, M.N.R.A.S., 198, 215.
Patterson, J. 1979a, Ap. J. (Letters), 233, L13.
Patterson, J. 1979b, Ap. J., 231, 789.
Patterson, J. 1979b, Ap. J., 234, 978.
Patterson, J. 1980, Ap. J. 241, 235.
Patterson, J. 1981, Ap. J. (Suppl.), in press.
Patterson, J. 1982a, Ap. J., in press.
Patterson, J. 1982b, Ap. J., in press.
Patterson, J., and Price, C. M. 1981, Ap. J. (Letters), 243, L83.
Patterson, J., and Steiner, J. E. 1982, Ap. J. (Letters), in press.
Patterson, J., Branch, D., Chincarini, G., and Robinson, E. L. 1980, Ap. J. (Letters), 240, L133.
Patterson, J., Fabbiano, G., Lamb, D. Q., Raymond, J., Horne, K., White, N., and Swank,

J. 1982, Ap. J., in press.
Patterson, J., Robinson, E. L., and Kiplinger, A. L. 1978, Ap. J., 226, L137.
Patterson, J., Robinson, E. L., and Nather, R. E. 1978, Ap. J., 224, 570.
Patterson, J., Robinson, E. L., and Nather, R. E. 1977, Ap. J., 214, 144.
Patterson, J., Williams, G., and Hiltner, W. A. 1981, Ap. J., 245, 618.
Patterson, J., Fabbiano, G., Lamb, D. Q., Raymond, J., Horne, K., White, N., and Swank, J. 1982, submitted to Ap. J.
Pringle, J. E. 1977, M.N.R.A.S., 178, 195.
Pringle, J. E., and Savonije, G. J. 1979, M.N.R.A.S., 187, 777.
Rappaport, S., Cash, W., Doxsey, R., McClintock, J., and Moore, G. 1974, Ap. J. (Letters), 187, L5.
Raymond, J. C., Black, J. H., Davis, R. J., Dupree, A. K., Gursky, H., Hartmann, L., and Matilsky, T. A. 1979, Ap. J. (Letters), 230, L95.
Robinson, E. L. 1973, Ap. J., 180, 121.
Robinson, E. L. 1976, Ann. Rev. Astron. Ap., 14, 119.
Robinson, E. L., and Nather, R. E. 1979, Ap. J. (Suppl)., 39, 461.
Robinson, E. L., Nather, R. E., and Patterson, J. 1978, Ap. J., 219, 168.
Ross, R. R., and Fabian, A. C. 1980, M.N.R.A.S., 193, 1P.
Rothschild, R. E., et al. 1981, Ap. J., 250, 723.
Schmidt, G. D., Stockman, H. S., and Margon, B. 1981, Ap. J. (Letters), 243, L157.
Shipman, H. 1976, Ap. J. (Letters), 206, L67.
Sion, E. M., Acierno, M. J., and Tomczyk, S. 1979, Ap. J., 230, 832.
Sion, E. M., Acierno, M. J., and Turnshek, D. A. 1978, Ap. J., 220, 636.
Starrfield, S., Sparks, W. M., and Truran, J. W. 1974, Ap. J. (Suppl.), 28, 247.
Starrfield, S., Truran, J. W., and Sparks, 1981, Ap. J. (Letters), 243, L27.
Steiner, J. E. 1981, private communication.
Steiner, J. E., Schwartz, D. A., Jablonski, F. J., Busko, I. C., Watson, M. G., Pye, J. P., and McHardy, I. M. 1981, Ap. J. (Letters), 249, L21.
Stockman, H. S., Schmidt, kG. D., Angel, J. R. P., Liebert, J., Tapia, S., and Beaver, E. A. 1977, Ap. J., 217, 815.
Stockman, H. S., Liebert, J., and Bond, H. E. 1979, in IAU Colloquium 53, White Dwarfs and Variable Degenerate Stars, ed. H. M. Van Horn and V. Weidemann (Rochester, N.Y.: University or Rochester), p. 334.
Stockman, H., Liebert, J., Tapia, S., Green, R., Williams, R., and Ferguson, D. 1981, IAU Circ. No. 3616.
Swank, J. H. 1979, IAU Colloq. No. 53, White Dwarfs and Variable Degenerate Stars, ed. H. M. Van Horn and V. Weidemann (Rochester, NY: Univ. of Rochester Press), p. 135.
Swank, J. H. 1980, private communication.
Swank, J. H. and White, N. 1981, private communication.
Swank, J. H., Boldt, E. A., Holt, S. S., Rothschild, R. E., and Serlemitsos, P. J. 1978, Ap. J. (Letters), 226, L133.
Swank, J., Lampton, M., Bolt, E. M., Holt, S., and Serlemitsos, P. 1977, Ap. J. (Letters), 216, L71.
Swedlund, J. B., Kemp, J. C., and Wolstencroft, R. D. 1974, Ap. J. (Letters), 193, L11.
Szkody, P., and Brownlee, D. E. 1977, Ap. J. (Letters), 212, L113.
Szkody, P., Schmidt, E., Crosa, L., and Schommer, R. 1981, Ap. J., 246, 233.
Tapia, S. 1977a, Ap. J. (Letters), 212, L125.
Tapia, S. 1977b, IAU Circ. No. 3054.
Tapia, S. 1979, IAU Circ. No. 3327.
Tuohy, I. R., Lamb, F. K., Garmire, G. P., and Mason, K. O. 1978, Ap. J. (Letters), 226, L17.

Tuohy, I. R., Mason, K. O., Garmire, G. P., and Lamb, F. K. 1981, Ap. J., 245, 183.
Tylenda, R. 1981, Acta. Astr., 31, 127.
Visvanathan, N., and Wickramasinghe, D. T. 1979, in IAU Colloquium 53, White Dwarfs and Variable Degenerate Stars, ed. H. M. Van Horn and V. Weidemann (Rochester, N.Y.: University of Rochester), p. 330.
Visvanathan, N., Hillier, J., and Pickles, A. 1982, IAU Circ. No. 3658.
Vogt, N., Krzeminski, W., and Sterkin, C. 1980, Astron. Ap., 85, 106.
Wada, T., Shimizu, A., Suzuki, M., Kato, M., and Hoshi, R. 1981, Prog. Theoret. Phys., in press.
Warner, B. 1974, M.N.R.A.S., 168, 235.
Warner, B. 1976, IAU Symposium 73, Structure and Evolution of Close Binary Systems, ed. P. Eggleton, S. Mitton, and J. Whelan (Dordrecht: Reidel), p. 85.
Warner, B., O'Donoghue, D., and Fairall, A. P. 1981, M.N.R.A.S., 196, 705.
Watson, M. G., Sherrington, M. R., and Jameson, R. F. 1978, M.N.R.A.S., 184, 79P.
Weast, G. J., Durisen, R. H., Imamura, J. N., Kylafis, N. D., and Lamb, D. Q. 1979, in IAU Colloquium 53, White Dwarfs and Variable Degenerate Stars, ed. H. M. Van Horn and V. Weidemann (Rochester, N.Y.: University of Rocheter), p. 330.
Weast, G. J., Durisen, R. H., Imamura, J. N., Kylafis, N. D., and Lamb, D. Q. 1982, submitted to Ap. J.
Wesselius, P., and Koester, D. 1978, Astron. Ap., 70, 745.
White, N. E. 1981, Ap. J. (Letters), 244, L85.
White, N. E., and Marshall, F. E. 1981, Ap. J. (Letters), 249, L25.
Young, P., and Schneider, D. P. 1979, Ap. J., 230, 502.

N82 26058

NEUTRON STAR BINARIES, PULSARS, AND BURST SOURCES[1]

F. K. Lamb

Departments of Physics and Astronomy
University of Illinois at Urbana-Champaign

ABSTRACT

Some important but as yet unresolved issues involving neutron star binaries, pulsars, and burst sources are described. Attention is drawn to the types of observations most likely to resolve them. Many of these observations are likely to be carried out during the next decade by one or more missions that have been approved or proposed. Missing so far is an opportunity to carry out sensitive flux measurements with an imaging detector and broad-band spectroscopic studies in the energy range 30-150 keV. There is also a need for soft X-ray and X-ray observations with an instrument which has arcminute angular resolution and an effective area substantially greater than that of ROSAT or EXOSAT.

I. INTRODUCTION

Many interesting and important questions about neutron star binaries, pulsars, and burst sources are still unanswered. As examples, twenty such questions are discussed in §II, together with the types of observations most likely to resolve them. Although plausible interpretations have been proposed for almost all interesting observations, and in many cases widely accepted, these interpretations are often based on very fragile evidence. Thus, our apparent understanding of such observations could be reversed very easily. Some of the questions considered are of this type. Key observations suggested by these questions are compared with the opportunities offered by approved and proposed missions in §III.

In discussing each question, I have referred to several of the most recent papers as well as one or two recent review articles. Where an appropriate review article is unavailable or unknown to me, I have provided more extensive references. Photons in the energy ranges 0.1-10, 2-60, and 30-150 keV are referred to as soft X-rays, X-rays, and hard X-rays, respectively. Spectroscopic studies are categorized as low-resolution ($E/\Delta E < 10$), moderate-resolution ($E/\Delta E \sim 10$-100), or high-resolution ($E/\Delta E > 100$).

[1]Supported in part by NSF grant PHY 80-25605 and NASA grant NSG 7653.

II. CURRENT ISSUES

a) Pulsing X-ray Sources

1. Are these sources disk-fed or wind-fed? -- By this I mean, does the neutron star accrete matter from a disk or from a more radial flow? In considering this question, one should not assume that a neutron star with a companion that is losing mass via a wind is necessarily wind-fed, since such a companion may transfer matter to the neutron star with sufficient angular momentum to form a disk. Furthermore, the initial phase of critical-lobe overflow of massive stars, which usually also have winds, is adequate to power the binary X-ray sources with orbital periods less than five days without smothering them, and leads to reasonable X-ray source lifetimes on the order of 10^4 - 10^6 yr (Paczyński 1976; Savonije 1978, 1979). The currently available evidence suggests that most pulsing X-ray sources are fed by accretion disks, although this conclusion is not yet secure (see Ghosh and Lamb 1979; Elsner, Ghosh, and Lamb 1980).

An answer to this question is important for understanding the mass transfer process in binaries, reprocessing of X-radiation within the accretion flow, the gross structure of the magnetosphere, and the behavior of the pulse frequency with time.

The types of observations most likely to furnish information that will help to provide the answer are high-resolution ultraviolet and soft X-ray spectroscopy, and X-ray timing studies. Ultraviolet and soft X-ray spectroscopy could sample the accretion flow at and outside the magnetospheric boundary, while timing studies could measure the specific angular momentum of the inflowing plasma. As an example of what may be possible with timing studies, Figure 1 shows the relationship between the pulse period, period derivative, and accretion luminosity predicted by the most detailed current theory of disk accretion. A sequence of measurements of these quantities which traced out a curve like those shown would confirm that the source in question was disk-fed and also determine its magnetic moment.

2. How do some sources reach long periods and why do such periods persist? -- The mechanisms by which the long-period pulsing X-ray sources were spun down initially is not yet clear, although several possibilities have been proposed (see Davies, Fabian, and Pringle 1979; Ghosh and Lamb 1979; Elsner, Ghosh, and Lamb 1980; and references therein). Long periods are most likely the result of alternating episodes of spin-up and spin-down. Further support for this hypothesis has recently been provided by the Hakucho observations of Vela X-1 shown in Figure 2, which reveal alternating episodes of spin-up and spin-down. In disk-fed sources, such behavior finds a natural explanation in the magnetic braking that occurs when the accretion rate falls (Ghosh and Lamb 1979; Elsner, Ghosh, and Lamb 1980). In wind-fed sources, such behavior might be explained by reversals in the circulation of the matter accreted by the neutron star.

Despite the profoundly different implications of these two explanations, it has so far not been possible to unambiguously identify the cause of alternating intervals of spin-up and spin-down in any long-period source. Thus, for example, the episodes seen in Vela X-1 may be due to accretion by the neutron star of vortices in the wind from its companion, but they are also

consistent with spin-up and spin-down due to accretion from a disk, assuming variations in the mass accretion rate of a few percent; such small variations in the accretion rate are not inconsistent with the constraints on X-ray flux variations reported to date.

Answers to these two questions are important for understanding the rate of formation of neutron star binaries, the typical lifetimes of X-ray binaries, and the properties of pulsars formed from massive X-ray binaries.

Among the more promising observations with which to explore these questions are X-ray timing of the low states of the long period sources and long-term monitoring of their luminosity behavior by, for example, a sky monitoring experiment. In connection with the latter, it is worth noting that the behavior on time scales longer than one or two months is known only for a handful of sources. As an example of what is expected, Figure 3 shows the different relationship between the luminosity and pulse frequency predicted for disk-fed sources which have small luminosity variations, like those reported in Her X-1, and sources which exhibit short, intense flares, like those reported in A0535+26.

3. What are the causes of pulse period fluctuations? -- The reasons for the pulse period fluctuations observed in Her X-1, Cen X-3, Vela X-1 and other sources could be due to fluctuations in the accretion torque acting on the crust, episodic unpinning of vortices in the neutron superfluid thought to interpenetrate the inner crust, repeated fracturing of the crust, or stochastic spin-up of the neutron superfluid expected in the core of the star (Lamb, Pines, and Shaham 1978; for a review, see Lamb 1979). At present it is not even known whether the observed period fluctuations are produced by processes outside or inside these stars.

Answers to this question could provide important information about fluctuations in the accretion flow or, alternatively, about the internal dynamics of neutron stars.

The most promising observational approach here is to look for correlations between the X-ray luminosity and the spin-up rate, since fluctuations in the accretion luminosity may accompany fluctuations in the accretion torque, whereas short-term fluctuations in the luminosity are not expected as a result of internal processes.

4. What are the respective roles of magnetospheric and surface plasmas in forming pulse shapes and spectra? -- There is some evidence that both play a role. Thus, for example, the complex waveforms seen in A0535+26 and Vela X-1 (see Fig. 4) have been interpreted as the result of cyclotron scattering by streams of accreting plasma above the stellar surface (Elsner and Lamb 1976), while spectral features reported in Her X-1 (see Fig. 5), 4U0115+63 (Wheaton et al. 1979), and 4U1626-67 (Pravdo et al. 1979) have been interpreted as the result of cyclotron scattering or emission (for reviews, see Lamb 1977; Stark et al. 1981; and Trumper 1982).

Theoretical work has so far focussed primarily on the role of plasma at the stellar surface (see, for example, Fig. 6 and Nagel 1981a,b; for a review, see Mészáros 1982), but plasma above the surface is also expected to play an important role (Lamb 1977), as is plasma near the magnetospheric boundary

(McCray and Lamb 1976; Basko and Sunyaev 1976; McCray et al. 1982).

Answers to this question are important for understanding the patterns of plasma flow within the magnetosphere, the characteristic flow velocities within the magnetosphere, magnetic field geometries, and the physical conditions in the emission regions. This is an extremely difficult theoretical problem, so observational guidance is especially important.

A key discriminant between magnetospheric and surface plasma is the time scale of fluctuations in the pulse waveform or spectral features. The dynamical time scale for plasma near the magnetospheric boundary is expected to be $\sim 0.1 - 1$ s, and anisotropies in the emission pattern or spectral features caused by plasma there are expected to show fluctuations on a similar time scale. In contrast, the dynamical time scale near the stellar surface is $\sim 0.1 - 1$ ms, and angular and spectral features produced by this plasma are expected to show fluctuations on this time scale. The magnetospheric plasma can probably be studied best by moderate resolution soft X-ray spectroscopy and high-resolution spectroscopy at the 7 keV iron lines, whereas the surface plasma can probably be studied best by phase-resolved spectroscopy at X-ray and hard X-ray energies.

5. What are the surface magnetic fields and dipole moments of these neutron stars? -- Theoretical interpretation of the observed spin-up rates, assuming disk accretion, yields dipole moments in the range $10^{29} - 10^{31}$ G cm^3, although the actual value for any given source is uncertain (Ghosh and Lamb 1979). Estimates based on reported spectral features give field strengths $\sim 4\text{-}6 \times 10^{12}$ G in Her X-1 and $\sim 2\text{-}3 \times 10^{12}$ G in 4U0115+63, while the variations of pulse shape with energy in A0535+26 and Vela X-1 have been interpreted as the result of cyclotron scattering by plasma streams channeled by small-scale magnetic loops of strength $\sim 1\text{-}2 \times 10^{12}$ G at distances $\sim 10^5\text{-}10^6$ cm above the stellar surface (for references, see question 4, above).

More information on this issue is important for understanding the evolution of magnetic fields in pulsars (see Lamb 1981a) and X- and gamma-ray burst sources (see below).

Measures of dipole field strengths can be obtained for stars which are disk-fed, if theoretical curves like those shown in Figure 1 are confirmed and a sufficient set of spin-up rates, pulse frequencies, and accretion luminosities are assembled for each source so that the particular curve followed by a given source can be determined. In some cases it may be possible to estimate surface magnetic field strengths using X-ray and hard X-ray observations of pulse waveforms and spectra, although the problem of interpreting these observations appears to be much more difficult than that of interpreting timing observations.

6. What is the equation of state of matter at very high densities? -- A substantial effort during the past decade has led to significant observational constraints on the equation of state of neutron star matter (for reviews, see Baym and Pethick 1979; Pines 1980; Lamb 1981b). Thus, for example, it has been possible to rule out several of the softer equations of state that have been proposed. However, large uncertainties still remain.

A precise knowledge of the equation of state is important for identifying black hole candidates, since the only presently known property of black holes that distinguishes them from nonmagnetic neutron stars is their mass, which may exceed the maximum stable mass of neutron stars. The equation of state is, of course, also of interest for the information it provides about the interactions of hadrons in dense matter.

Further progress will require refinements in our understanding of a variety of aspects of pulsing and bursting sources and is likely to be slower. New measurements of the orbits of neutron star binary systems can make a substantial contribution. In this connection, it is worth remembering that the orbits of only about half of the known systems of this type have been measured accurately. Measurements of the thermal fluxes from neutron stars, like those described below (question 11), could also make an important contribution, since the cooling rate of a hot neutron star is sensitive to the equation of state.

7. What are the internal dynamical properties of neutron stars? -- So far, there is no evidence for internal degrees of freedom in neutron star X-ray sources (see Boynton 1981; Lamb 1981). This is puzzling, given the evidence for a weakly coupled superfluid neutron component in pulsars and the variety of internal degrees of freedom expected theoretically (Lamb, Pines, and Shaham 1978).

X-ray timing observations are the most promising approach here (see Lamb 1979). Figure 7 shows the very different power transfer functions for pulse frequency fluctuations of a neutron star with and without an internal, finite-frequency normal mode.

b) "Galactic Bulge Sources"

8. How are they formed and how do they evolve? -- The bright galactic bulge sources are widely believed to be binary systems formed by capture processes (see Lewin and Clark 1980). However, there is evidence that the majority of bulge sources which are not currently surrounded by globular clusters may require a mechanism of formation other than capture of a general field star by a compact object (Lightman and Grindlay 1982). Moreover, the evolution of a white dwarf binary system into a neutron star binary does not produce a source with the high X-ray luminosities observed (Rappaport Joss, and Webbink 1982).

Why are globular cluster X-ray sources so much more common in M31 than in our own galaxy? Both in our galaxy and in M31, the globular cluster sources are grouped near the plane, suggesting that passage through the galactic plane plays an important role in forming or activating these sources.

The most promising approach to studying the formation and evolution of the "bulge" sources is to study their appearance in nearby galaxies using optical and X-ray instruments.

9. Why is there never more than one bright, compact X-ray source observed in a globular cluster? -- Lightman and Grindlay (1982) have shown that the data are not inconsistent with a probability of observing an X-ray source in a globular cluster which varies as the inverse of the time scale for two-body

binary formation, as would be expected if this is the formation process. Assuming that this is the formation process, they show further that only one X-ray source is to be expected in any one cluster. Direct evidence of the binary character of the globular cluster sources would help to secure this argument.

There are two promising approaches here: long-term monitoring of X-ray flux levels to discover the modulation with binary phase that must be present at some level, if these sources are indeed binaries, and optical and X-ray studies of nearby galaxies, such as M31.

10. How large are their surface magnetic fields? -- It has been widely argued that the reason no pulsations have been seen in these sources is that the magnetic fields of these neutron stars are extremely weak. Although this is a plausible hypothesis (see Lewin and Clark 1980), it becomes less comfortable when one notes that Her X-1, which is believed to be $\sim 10^8$ years old, apparently has a magnetic field that is still $\sim 5 \times 10^{12}$ G (see Lamb 1981a), that the most plausible explanation for the temporal "footprints" of the X-ray burst sources is channeling of fuel by magnetic fields, and that the two most promising models of gamma-ray bursters, episodic accretion and thermonuclear explosions on neutron stars which are presumably rather old, both require surface magnetic fields $\gtrsim 10^{12}$ G (see question 17). Thus, the answer to this question remains uncertain.

The question can be addressed by sensitive X-ray timing observations, to look harder for periodic flux variations, and sensitive X-ray and hard X-ray spectroscopy, to search for any evidence of magnetic fields manifested by spectral features.

c) Pulsars

11. What are the surface temperatures of pulsars? -- Pulsars are expected to have surface temperatures in the range $10^5 - 10^6$ K due to compressional heating when they were formed (see, for example, Van Riper and Arnett 1978; Bowers and Wilson 1980; Epstein and Pethick 1981; Richardson et al. 1982), bombardment of their surfaces by particles and gamma-rays (see, for example, Cheng 1981), heating of their interiors due to friction between the solid crust and the neutron liquid (see Greenstein 1981), and release of energy in crustal or core fracture events (see Pines, Shaham, and Ruderman 1972) or in episodes of vortex unpinning (see Alpar et al. 1981). Stimulated in part by the much more sensitive observations made possible by EINSTEIN, substantial improvements have recently been made in detailed calculations of neutron star cooling (Glen and Sutherland 1980; Van Riper and Lamb 1981; Gudmundsson, Pethick, and Epstein 1982; Richardson, et al. 1982) as well as in understanding which energy transport processes affect the results most strongly (Gudmundsson, Epstein, and Pethick 1982). Figure 8 shows a comparison of the theoretical cooling curves of Van Riper and Lamb with observations.

Important new results on neutron star surface emission have been obtained with the EINSTEIN observatory (for reviews, see Helfand, Chanan, and Novick 1980; Helfand 1981). Observations of about fifty supernova remnants, including seven remnants of historical supernovae, have placed stringent upper limits on the luminosities of any compact source in all but four. In the four

remnants where flux is detected above the nebular background, the identification of the flux with thermal emission from the surface of the pulsar is uncertain (see, for example, Tuohy and Garmire 1980). A different approach is the survey of a selected group of known pulsars within a distance of 300 pc. Of the eighteen pulsars observed, six were detected. Although a detailed analysis of these observations is still in progress, a preliminary analysis of data on PSR1055-52 indicates a luminosity in soft X-rays $\approx 4 \times 10^{33}$ erg s^{-1}, corresponding to ~ 0.1 of its rotational energy loss rate. The data is consistent with a blackbody of temperature $\sim 1 \times 10^{6}$ K.

Further progress in determining the surface temperatures of pulsars would give us information about the formation of neutron stars, ongoing processes at their surfaces and in their interiors, and the equation of state of neutron star matter. Thus, for example, neutron stars cool much more quickly if they contain condensed pions or quark matter.

The most promising observational approach here is soft X-ray imaging of additional nearby pulsars with high sensitivity and sufficient time resolution to test for pulsations.

12. What are the physical processes responsible for converting rotational energy into X-rays and gamma-rays? -- A variety of theoretical models predict the conversion of rotational energy to photons with energies up to and including gamma-rays (Elitzur 1979; Hardee 1979; Harding, Tademaru, and Esposito 1978; Ayasli and Ogelman 1980; Arons 1981; Cheng 1981; Ruderman 1981; for reviews, see Ruderman 1980; Michel 1982). Although longer period pulsars may be unable to produce a dense pair plasma above their polar caps, so that a larger fraction of their luminosity escapes as X- and gamma-rays, shorter period pulsars tend to have a much larger total luminosity. Thus, on balance short period pulsars are favored as X- and gamma-ray emitters. This conclusion is consistent with the fact that so far only the Crab and Vela pulsars are confirmed sources of X- and gamma-radiation (see Manchester and Taylor 1977; Bennett et al. 1977; Swanenberg et al. 1981). The reported detection of PSR1818-04 and PSR1747-46 above 35 MeV by SAS-2 (Ogelman et al. 1976) was not confirmed by COS-B (Mayer-Hasselwander et al. 1980), while Knight et al. (1982) using HEAO-1 were unable to confirm the detection of PSR1822-09 in hard X-rays reported by Mandrou, Vedrenne, and Masnou (1980). For a recent review of gamma-ray observations, see Buccheri (1981).

Answers to this question would shed important light on the magnetic field of the neutron star, the electrodynamics of the pulsar and the surrounding medium, the geometry of the emission region, and the properties of the emitting particles.

Broad-band spectroscopic observations of known nearby pulsars with greatly increased sensitivity at X-ray and hard X-ray energies appear the most likely to assist in answering this question. Of particular importance would be the discovery of one or more very nearby neutron stars with magnetic fields that are too weak or rotation periods that are too long to produce a dense pair plasma. According to some models, such stars would be expected to be "radio quiet," but might still emit an observable flux of hard X-rays or gamma-rays.

d) X-Ray Burst Sources

13. Are they binary systems? -- The X-ray burst sources are widely believed to be binaries (see the review by Lewin and Joss 1981), but direct evidence for binary membership has been discovered only recently. The transient X-ray burst sources Cen X-4 and Aql X-1 (Matsuoka et al. 1980; Koyama et al. 1981) have, in quiescence, optical counterparts which exhibit stellar spectra, a circumstance that has been taken as evidence for their binary nature (van Paradijs et al. 1980; Thorstensen, Charles, and Bowyer 1978). More recently, Walter et al. (1981) and White and Swank (1981) have reported the discovery of periodic absorption events in 4U1915-05 (= MXB1916-05) with a period of 50 minutes, which they interpret as the binary period of this system. This may be the first direct evidence for the binary nature of burst sources.

It is important to confirm the binary character of these sources and to determine their orbital parameters, both because their origin is at present still uncertain and because it is difficult to develop convincing models of their optical and X-ray emission without this information.

The most promising approach is likely to be further searches for evidence of X-ray variation with binary phase. Further optical and X-ray studies of burst sources in nearby galaxies would also make a valuable contribution.

14. To what extent does the thermonuclear flash model agree quantitatively with burst observations? -- Simple thermonuclear flash models (Joss 1978; Joss and Li 1980; Fujimoto, Hanawa, and Miyaji 1981) give reasonable qualitative agreement with the observed properties of so-called type I bursts, but a number of disturbing discrepancies remain (for reviews, see Lewin and Joss 1981; Lewin 1982). Thus, for example, more detailed calculations (Taam and Picklum 1979; Taam 1980, 1981, 1982; Ayasli and Joss 1982) give a wider variety of burst time scales and temperatures than have usually been associated with "standard" type I bursts. Some characteristic properties of burst profiles, such as the double-peaked bursts observed from some sources, have not yet been accounted for. Perhaps a more serious difficulty for current models is the observation of bursts separated by as little as 5-10 minutes (see Hayakawa 1981 and references therein). Such short intervals seem difficult to explain unless the nuclear fuel is burned incompletely (Lamb and Lamb 1978), contrary to the results of most current models.

The peak burst luminosities and temperatures given by current models (Taam 1982; Ayasli and Joss 1982), which assume blackbody emission, are significantly lower than those observed (see Fig. 9). In one calculation, Taam (1982) finds that the photosphere expands to a radius of at least 50 km, producing a very soft burst. Peak luminosities reportedly agree better with observation if the star is assumed to have a magnetic field of $\sim 3 \times 10^{12}$ G, which reduces the opacity of the surface material, but such models conflict with the idea that strongly magnetic stars don't burst. It is interesting to note, however, that most models of the Rapid Burster assume this star has an appreciable magnetic field in order to produce the rapidly repetitive type II bursts, yet the Rapid Burster also produces normal-looking type I bursts. Furthermore, strong magnetic fields are taken to be essential in most gamma-ray burst models. This raises the question of why the neutron

stars that produce X-ray and gamma-ray bursts should have different magnetic fields.

Some of these discrepancies may be resolved when models are developed which include factors, such as realistic initial temperature and composition profiles, propagation of detonation or deflagration fronts through the nuclear fuel, hydrodynamic motions, expansion of the photosphere and mass loss, and radiative transfer through the atmosphere and infalling matter, that are known to be important for at least some bursts.

A promising observational approach may be to study, at X-ray and hard X-ray energies, a much wider class of fast transients than the "standard" type I bursts.

15. How are individual burst sources to be interpreted? -- Still more challenging than acounting for the properties of the type I burst sources as a class is to account for the properties of an individual burst source. Among the quantities to be determined are the surface magnetic field, the thermal history of the star, and the history and current value of the mass accretion rate. So far no theoretical calculations have followed a succession of bursts. Given that time scales ~ 10^2-10^3 years are required for the cores of flashing neutron stars to reach a quasi-stationary thermal state (Lamb and Lamb 1978), while time scales much longer than the duration of single burst are required for the envelope to reach such a state, bursting neutron stars may always be evolving thermally.

Long-term monitoring of burst activity and inactivity, and accurate measurements of burst and persistent luminosities, may help to resolve these issues.

16. What is the gating mechanism for the Rapid Burster? -- The magnetospheric and thermal instability model, which assumes radial inflow, gives qualitative agreement with the behavior of the Rapid Burster (Lamb et al. 1977), but raises many questions (for a brief review of Rapid Burster models, see Lewin and Joss 1981). Indirect evidence for disk accretion in other bursters casts doubt on the assumption of approximately radial inflow made in this model, although the Rapid Burster clearly has unique properties. Perhaps a more serious difficulty for this model is the observation by Hakucho of flat-topped type II bursts lasting as long as 10 minutes with intervals between bursts of at least 20-30 minutes (see Fig. 10; Hayakawa 1981; Oda 1982; and references therein). Such large intervals between bursts would require a very large binary separation in radial flow models. More theoretical work is needed on those instabilities of accretion disks which may have the required very long time scales.

Another puzzle is the relatively small influence which the type I bursts, which are believed to be due to thermonuclear flashes, have on the type II bursts, which are believed to be due to instability in the accretion flow. The small size of the effect (see Fig. 11) favors models involving disk accretion, since disk flows are less affected by radiation from the surface of the star. It is interesting to note that most models of the Rapid Burster invoke an appreciable magnetic field, whereas models of type I bursters usually neglect magnetic fields (see below).

Optical and X-ray observations to constrain the parameters of the system, assuming that it is a binary, or to determine the mode of mass transfer, would be particularly important. One promising approach is X-ray timing and broad-band spectroscopic studies of the interaction between type I and type II bursts.

e) Gamma-Ray Burst Sources

17. What are they? -- An array of Earth-orbiting and interplanetary spacecraft have now provided confirmed positions of six gamma-ray bursts with arcminute accuracy (see Hurley 1982). Many other bursts have yielded positions which are either unconfirmed or less accurate than this. Although radio, X-ray, and optical candidates have been found in the error boxes, no clear association between gamma-ray bursts and other forms of emission has emerged. The event of 1979 March 5 was unique; its identification with the supernova remnant N49 in the Large Magellanic Cloud remains controversial (see Cline 1982). Arcminute positions will continue to be accumulated by multiple spacecraft timing during the next few years, but given the sizable number of positions of this accuracy already available, one cannot expect a major breakthrough in determining the nature of these sources.

Despite the absence of unambiguous identifications with known astrophysical objects, a consensus view that the bursts come from strongly magnetic neutron stars has emerged. The developments that have led to this consensus have recently been summarized by Lamb (1982). They include the properties of the 1979 March 5 event which, though unique, has had a major impact on thinking about gamma-ray bursts in general; theoretical arguments which suggest the presence of a magnetic field of $\sim 10^{12}$ G (Colgate and Petschek 1981); and the reports by Mazets and his colleagues of spectral features (see the review by Teegarden 1982).

The gamma-ray burst sources are one of the few major discoveries of the last decade whose natures remain a puzzle. Confirmation that they are strongly magnetic neutron stars would clear the way for a further advance in our understanding of them.

Arcminute positions based on multiple spacecraft timing may produce an identification, but it is clear that still smaller error boxes will generally be required. Another possibility is the serendipitous positioning of faint gamma-ray burst sources by sensitive hard X-ray imaging detectors, if the latter are flown for the purpose of studying bright, known X-ray sources.

18. What powers them? -- At present the most promising energy sources are accretion onto neutron stars (see, for example, Lamb, Lamb, and Pines 1973; Colgate and Petschek 1981) or nuclear outbursts on such stars (Woosely and Taam 1976; Woosely and Wallace 1982). It is interesting to contrast the latter models, which discuss strong surface magnetic fields, "pools" of fuel on the star, and propagating burning fronts, with the thermonuclear flash models of X-ray bursts, which do not mention such phenomena (for reviews, see Lamb 1982; Woosley 1982).

Hard X-ray spectroscopy may be the most promising method of addressing this question.

19. What is the origin of the continuum emission? -- The expression that has generally been used to characterize the continuum spectra of gamma-ray bursts (see Teegarden 1982) corresponds to the spectrum of optically-thin thermal bremsstrahlung, if the energy dependence of the Gaunt factor, relativistic corrections, and magnetic field effects are ignored. These are, however, substantial effects for the energies and magnetic field strengths of interest. Few attempts to fit an actual bremsstrahlung emission spectrum to the observations have been reported to date. Actually, for the source to be optically-thin would require an aspect ratio $\gtrsim 10^3$:1 (Bussard and Lamb 1982; Lamb 1982). Such a ratio could arise if the bursts are produced by thin sheets or filaments of plasma, but it is hard to see why such a distribution should always occur, as would be necessary to account for the apparent universality of the spectral shape.

Another possibility is that the bursts are made up of a sequence of brief flickers, each shorter than the 4s detector accumulation time, which emit Comptonized thermal spectra with falling temperatures. The average count-rate spectrum of such a source is quite similar to that of optically-thin bremsstrahlung, as pointed out by Bussard and Lamb (1982).

This issue can only be resolved by hard X-ray and gamma-ray spectroscopy with better spectral and temporal resolution.

20. What are the origins of observed spectral features? -- Reported spectral features are generally of two types: extinction in the energy range 10-50 keV, and excess emission in the energy range 300-650 keV (again see Teegarden 1982). The lower energy features could be due to cyclotron scattering, if the magnetic field in the source varies by at least a factor of two (Bussard and Lamb 1982), or a time-varying low energy cutoff (Lamb 1982). The extinction cannot be due to photoelectric absorption by iron or nickel unless the magnetic field is $\gtrsim 2 \times 10^{13}$ G.

The higher energy features are widely interpreted as redshifted electron-positron annihilation radiation. However, the shapes of these features are poorly determined at present, and hence their interpretation remains in doubt. If the lower energy features are due to cyclotron scattering, more accurate determinations of the 300-650 keV emission features could provide a cross-check on the inferred magnetic field strength, since magnetic broadening and one-photon annihilation become important for fields $\gtrsim 10^{13}$ G (see Fig. 12).

Again, the only observations with real promise of resolving these issues are hard X-ray and gamma-ray spectroscopic studies with better spectral and temporal resolution.

III. DEVELOPMENTS DURING THE NEXT DECADE

Table 1 lists the various types of observations that have been cited above as promising means to answer the questions that have been posed, together with approved or proposed missions that are capable of making the type of observation in question during the next decade. This accounting suggests that the most discovery space is available to an instrument capable of carrying out hard X-ray imaging and spectroscopy. There is also a need for

X-ray and soft X-ray observations with an instrument which has arcminute angular resolution and an effective area substantially larger than that of ROSAT or EXOSAT.

I thank Roger Bussard, Don Lamb, Christopher Pethick, and Gregory Zylstra for their help in the preparation of this review, and Larry Smarr for sharing EINSTEIN results on M31 in advance of publication.

TABLE 1

APPROVED OR PROPOSED MISSIONS

Suggested Observation	Missions[1]
Soft X-ray imaging	ROSAT, EXOSAT
Soft X-ray spectroscopy	ROSAT, EXOSAT
X-ray timing	XTE, EXOSAT, ASTRO-C
X-ray (2-60 keV) spectroscopy	XTE, EXOSAT, ASTRO-B
X-ray sky monitoring	XTE, ASTRO-B, ASTRO-C
Iron-line spectroscopy	(XTE, EXOSAT, ASTRO-B)
Hard X-ray imaging	------
Hard X-ray spectroscopy	------
Studies of nearby galaxies	ST, (AXAF)
Gamma-ray spectroscopy	GRO

[1]Missions whose primary objectives are other than the suggested observations listed here are shown in parenthesis.

REFERENCES

Alpar, M. A., Anderson, P. W., Pines, D., and Shaham, J. 1981, Ap. J., 249, L29.

Arnett, W. D. 1980, in Proc. 9th Texas Symp. on Relativistic Astrophysics, Ann. NY Acad Sci., 336, 336.

Arons, J. 1981, Ap. J., 248, 1099.

Ayasli, S. and Joss, P. C. 1982, Ap. J., in press.

Ayasli, S. and Ogelman, H. 1980, Ap. J., 237, 227.

'sko, M. and Sunyaev, R. A. 1976, Astron. Zh., 53, 950.

Baym, G. and Pethick, C. J. 1979, Ann. Rev. Astron. Astrophys., 17, 415.

Bennett, K., et al. 1977, Astr. Ap., 61, 279.

Lowers, R. L. and Wilson, J. R. 1980, Space Sci. Rev., 27, 537.

Boynton, P. E. 1981, in Pulsars, Proc. IAU Symp. No. 95, ed. W. Sieber and R. Wielebinski (Dordrecht: Reidel), p. 279.

Buccheri, R. 1981, in Pulsars, Proc. IAU Symp. No. 95, ed. W. Sieber and R. Wielebinski (Dordrecht: Reidel), p. 241.

Bussard, R. W. and Lamb, F. K. 1982, in Gamma-Ray Transients and Related Astrophysical Phenomena, AIP Conference Proceedings No. 77, ed. R. E. Lingenfelter, H. S. Hudson, and D. M. Worrall (NY: AIP), p. 189.

Cheng, A. F. 1981, in Pulsars, Proc. IAU Symp. No. 95, ed. W. Sieber and R. Wielebinski (Dordrecht: Reidel), p. 99.

Cline, T. L. 1982, in Gamma-Ray Transients and Related Astrophysical Phenomena, AIP Conference Proceedings No. 77, ed. R. E. Lingenfelter, H. S. Hudson, and D. M. Worrall (NY: AIP), p. 17.

Colgate, S. A. and Petschek, A. G. 1981, Ap. J., 248, 771.

Davies, R. E., Fabian, A. C., and Pringle, J. E. 1979, M.N.R.A.S., 186, 779.

Elitzur, M. 1979, Ap. J., 229, 742.

Elsner, R. F., Ghosh, P., and Lamb, F. K. 1980, Ap. J., 241, L155.

Elsner, R. F. and Lamb, F. K. 1976, Nature, 262, 356.

Epstein, R. I. and Pethick, C. J. 1981, Ap. J., 243, 1003.

Fujimoto, M. Y., Hanawa, T., and Miyaji, S. 1981, Ap. J., 247, 267.

Ghosh, P. and Lamb, F. K. 1979, Ap. J., 234, 296.

Ghosh, P., Lamb, F. K., and Zylstra, G. 1982, in preparation.

Glen, G. and Sutherland, P. G. 1980, Ap. J., 239, 671.

Greenstein, G. 1981, in Pulsars, Proc. IAU Symp. No. 95, ed. W. Sieber and R. Wielebinski (Dordrecht: Reidel), p. 291.

Gudmundsson, E. H., Epstein, R. I., and Pethick, C. J. 1982, preprint.

Gudmundsson, E. H., Pethick, C. J., and Epstein, R. I. 1982, submitted to Ap. J. (Letters).

Hardee, P. E. 1979, Ap. J., 227, 958.

Harding, A. K., Tademaru, E., and Esposito, L. 1978, Ap. J., 225, 226.

Hayakawa, S. 1981, Space Sci. Rev., 29, 221.

Helfand, D. J. 1981, in Pulsars, Proc. IAU Symp. No. 95, ed. W. Sieber and R. Wielebinski (Dordrecht: Reidel), p. 343.

Helfand, D. J., Chanan, G. A., and Novick, R. 1980, Nature, 283, 337.

Hurley, K. 1982, in Gamma-Ray Transients and Related Astrophysical Phenomena, AIP Conference Proceedings No. 77, ed. R. E. Lingenfelter, H. S. Hudson, and D. M. Worrall (NY: AIP), p. 85.

Joss, P. C. 1978, Ap. J., 225, L123.

Joss, P. C. and Li, F. K. 1980, Ap. J., 238, 287.

Knight, F. K., Matteson, J. L., Peterson, L. E., and Rothschild, R. E. 1982, submitted to Ap. J.

Koyama, K. et al. 1981, Ap. J., 247, L27.

C-2

Lamb, D. Q. 1982, in Gamma-Ray Transients and Related Astrophysical Phenomena, AIP Conference Proceedings No. 77, ed. R. E. Lingenfelter, H. S. Hudson, and D. M. Worrall (NY: AIP), p. 249.
Lamb, D. Q. and Lamb, F. K. 1978, Ap. J., 220, 291.
Lamb, D. Q., Lamb, F. K., and Pines, D. 1973, Nature Phys. Sci., 246, 52.
Lamb, F. K. 1977, Proc. 8th Texas Symp. Relativistic Astrophysics, Ann. NY Acad. Sci., 302, 482.
_____. 1979, in Compact Galactic X-Ray Sources, Proc. of the Washington Workshop, ed. F. K. Lamb and D. Pines (Urbana: UIUC Physics Dept.), p. 143.
_____. 1981a, in Pulsars, Proc. IAU Symp. No. 95, ed. W. Sieber and R. Wielebinski (Dordrecht: Reidel), p.357.
_____. 1981b, in Pulsars, Proc. IAU Symp. No. 95, ed. W. Sieber and R. Wielebinski (Dordrecht: Reidel), p. 303.
Lamb, F. K., Fabian, A. C., Pringle, J. E., and Lamb, D. Q. 1977, Ap. J., 217, 197.
Lamb, F. K., Pines D., and Shaham, J. 1978, Ap. J., 224, 969.
Lewin, W. H. G. 1982, in Proc. Symp. on Neutron Stars, 5th General Conference of the European Physical Society, Istanbul, Turkey, in press.
Lewin, W. H. G. and Clark, G. W. 1980, in Proc. 9th Texas Symp. Relativistic Astrophysics, Ann. NY Acad. Sci., 336, 451.
Lewin, W. H. G. and Joss, P. C. 1981, Space Sci. Rev., 28, 3.
Lightman, A. P. and Grindlay, J. E. 1982, Ap. J., in press.
Manchester, R. N. and Taylor, J. H. 1977, Pulsars (San Francisco: W. H. Freeman and Co.).
Mandrou, P., Vedrenne, G., and Masnou, J. L. 1980, Nature, 287, 124.
Matsuoka, M. et al. 1980, Ap. J., 240, L137.
Mayer-Hasselwander, K., et al. 1980, in 9th Texas Symp. Relativistic Astrophysics, Ann. NY Acad. Sci., 336, 211.
McCray, R. and Lamb, F. K. 1976, Ap. J., 204, L115.
McCray, R. A., Shull, J. M., Boynton, P. E., Deeter, J. E., Holt, S. S., and White, N. E. 1982, preprint.
Meszáros, P. 1982, in Proc. Symp. on Neutron Stars, 5th General Conference of the European Physical Society, Istanbul, Turkey, in press.
Meszáros, P. and Bonazzola, S. 1981, Ap. J., 251, 695.
Michel, F. C. 1982, Rev. Mod. Phys., 54, 1.
Nagel, W. 1981, Ap. J., 251, 278.
_____. 1981, Ap. J., 251, 288.
Oda, M. 1982, in Gamma-Ray Transients and Related Astrophysical Phenomena, AIP Conference Proceedings No. 77, ed. R. E. Lingenfelter, H. S. Hudson, and D. M. Worrall (NY: AIP), p. 319.
Ogelman, H., Fichtel, C. E., Kniffen, D. A., and Thompson, D. J. 1976, Ap. J., 209, 584.
Paczynski, B. 1976, in Structure and Evolution of Close Binary Systems, Proc. IAU Symposium No. 73, ed. P. Eggleton, S. Mitton, and J. Whelan (Dordrecht: Reidel), p. 61.
Pines, D. 1980, J. Physique, C2, 111.
Pines, D., Shaham, J., and Ruderman, M. 1972, Nature Phys. Sci., 237, 83.
Pravdo, S. H., White, N. E., Boldt, E. A., Holt, S. S., Serlemitsos, P. J., Swank, J. H., Szymkowiak, A. E., Tuohy, I., and Garmire, G. 1979, Ap. J., 231, 912.
Rappaport, S. and Joss, P. C. 1981, in X-ray Astronomy, ed. R. Giacconi (Dordrecht: Reidel), p. 123.
Rappaport, S., Joss, P. C., and Webbink, R. 1982, submitted to Ap. J.

Richardson, M. B., Van Horn, H. M., Ratcliff, K. F., and Malone, R. C. 1982, Ap. J. Suppl., in press.
Ruderman, M. 1980, in 9th Texas Symp. Relativistic Astrophysics, Ann. NY Acad. Sci., 336, 409.
Ruderman, M. 1981, in Pulsars, Proc. IAU Symp. No. 95, ed. W. Sieber and R. Wielebinski (Dordrecht: Reidel), p. 87.
Savonije, G. J. 1978, Astr. Ap., 62, 317.
_____. 1979, Astr. Ap., 71, 352.
Staubert, R., Kendziorra, E., Pietsch, W., Proctor, R. J., Reppin, C., Steinle, H., Trümper, J., and Voges, W. 1981, Space Sci. Rev., 30, 311.
Swanenberg, B. N., et al. 1981, Ap. J., 243, L69.
Taam, R. E. 1980, Ap. J., 241, 358.
_____. 1981, Ap. J., 247, 257.
_____. 1982, submitted to Ap. J.
Taam, R. E. and Picklum, R. E. 1979, Ap. J., 233, 327.
Teegarden, B. J. 1982, in Gamma-Ray Transients and Related Astrophysical Phenomena, AIP Conference Proceedings No. 77, ed. R. E. Lingenfelter, H. S. Hudson, and D. M. Worrall (NY: AIP), p. 123.
Thorstensen, J., Charles, P., and Bowyer, S. 1978, Ap. J., 220, L131.
Trümper, J. 1982, in Gamma-Ray Transients and Related Astrophysical Phenomena, AIP Conference Proceeedings No. 77, ed. R. E. Lingenfelter, H. S. Hudson, and D. M. Worrall (NY: AIP), p. 179.
Trümper, J., Pietsch, W., Reppin, C., Voges, W., Staubert, R., and Kendziorra, E. 1978, Ap. J., 219, L105.
Tuohy, I. R. and Garmire, G. 1980, Ap. J., 239, L107.
van Paradijs, J., Verbunt, F., van der Linden, T., Pederson, H., and Wamsteker, W. 1980, Ap. J., 241, L161.
Van Riper, K. A. and Arnett, W. D. 1978, Ap. J., 225, L129.
Van Riper, K. A. and Lamb, D. Q. 1981, Ap. J., 244, L13.
Walter, F. M., Bowyer, S., Mason, K. O., Clarke, J. T., Henry, J. P., Halpern, J., and Grindlay, J. 1981, preprint.
Wheaton, W. A., Doty, J. P., Primini, F. A., Cooke, B. A., Dobson, C. A., Goldman, A., Hecht, ., Hoffman, J. A., Howe, S. K., Scheepmaker, A., Rothschild, R., Knight, F. K., Nolan, P., and Peterson, L. E. 1979, Nature, 282, 240.
White, N. E. and Swank, J. H. 1981, preprint.
Woosley, S. E. 1982, in Gamma-Ray Transients and Related Astrophysical Phenomena, AIP Conference Proceedings No. 77, ed. R. E. Lingenfelter, H. S. Hudson, and D. M. Worrall (NY: AIP), p. 273.
Woosley, S. E. and Taam, R. E. 1976, Nature, 263, 101.
Woosley, S. E. and Wallace, R. K. 1982, Ap. J., in press.

FIGURE CAPTIONS

Fig. 1. Data from nine pulsing X-ray sources plotted against theoretical spin-up curves for disk accretion (from Ghosh, Lamb, and Zylstra 1982). Here P and $\dot{P}$ are the pulse period and period derivative, respectively, and L is the accretion luminosity. Each curve is labeled with the assumed stellar magnetic moment in units of 10^{30} G cm^3.

Fig. 2. The variation of the pulse period of Vela X-1 (from Hayakawa 1981). The straight line represents a constant spin-down rate $\dot{P}/P = -1.5 \times 10^{-4}$ yr^{-1}.

Fig. 3. Two examples of luminosity variations and the resulting pulse frequency behavior, illustrating the effects of different magnetic moments and luminosity patterns (from Elsner, Ghosh, and Lamb 1980). Also shown is the observed behavior of A0535+26.

Fig. 4. Pulse waveforms of Vela X-1 observed at different energies (see Rappaport and Joss 1981).

Fig. 5. Deconvoluted Her X-1 spectrum from the 1976 MPI/AIT balloon observation (from Trumper et al. 1978).

Fig. 6. Left and right panels show pulse shapes obtained by convolving model beam shapes with the rotation of the neutron star for two different sets of inclination angles (from Mészáros and Bonazzola 1981).

Fig. 7. Theoretical power transfer functions for a two-component neutron star model (left) and a generalized two-component model with a finite-frequency internal mode (right). The power transfer function describes the amplitude of pulse frequency fluctuations excited by an internal or external fluctuating torque of fixed strength (from Lamb 1981b).

Fig. 8. Theoretical cooling curves compared with observations (from Van Riper and Lamb 1981). The results for each star are shown as regions bounded by the cooling curves for zero magnetic field and B = 4.4×10^{12} G. Dark shading: soft equation of state; medium shading: stiff equation of state; light shading: star with a pion condensate; no shading: star with free quarks. Also shown are detections (dots) and upper limits (arrows) obtained from EINSTEIN soft X-ray observations of pulsars and supernova remanants. The cross-hatched rectangle characterizes the upper limits that have been obtained for 7 nearby pulsars.

Fig. 9. Variation of the surface luminosity with time for a burst produced by a combined hydrogen-helium shell flash (from Taam 1982). The effective temperature is given at the peak of the burst, and after one e-folding time.

Fig. 10. Time profiles of a typical trapezoidal burst from the Rapid Burster as seen in two different energy channels (from Hayakawa 1981).

Fig. 11. Bursts from the Rapid Burster (from Lewin and Joss 1981). The type I bursts (marked as "special") occur independently of the sequence of the rapidly repetitive type II bursts (numbered separately).

Fig. 12. Rate coefficients for nonrelativistic electron-positron annihilation into one or two photons, as a function of magnetic field strength (from Bussard and Lamb 1982).

ORIGINAL PAGE IS
OF POOR QUALITY

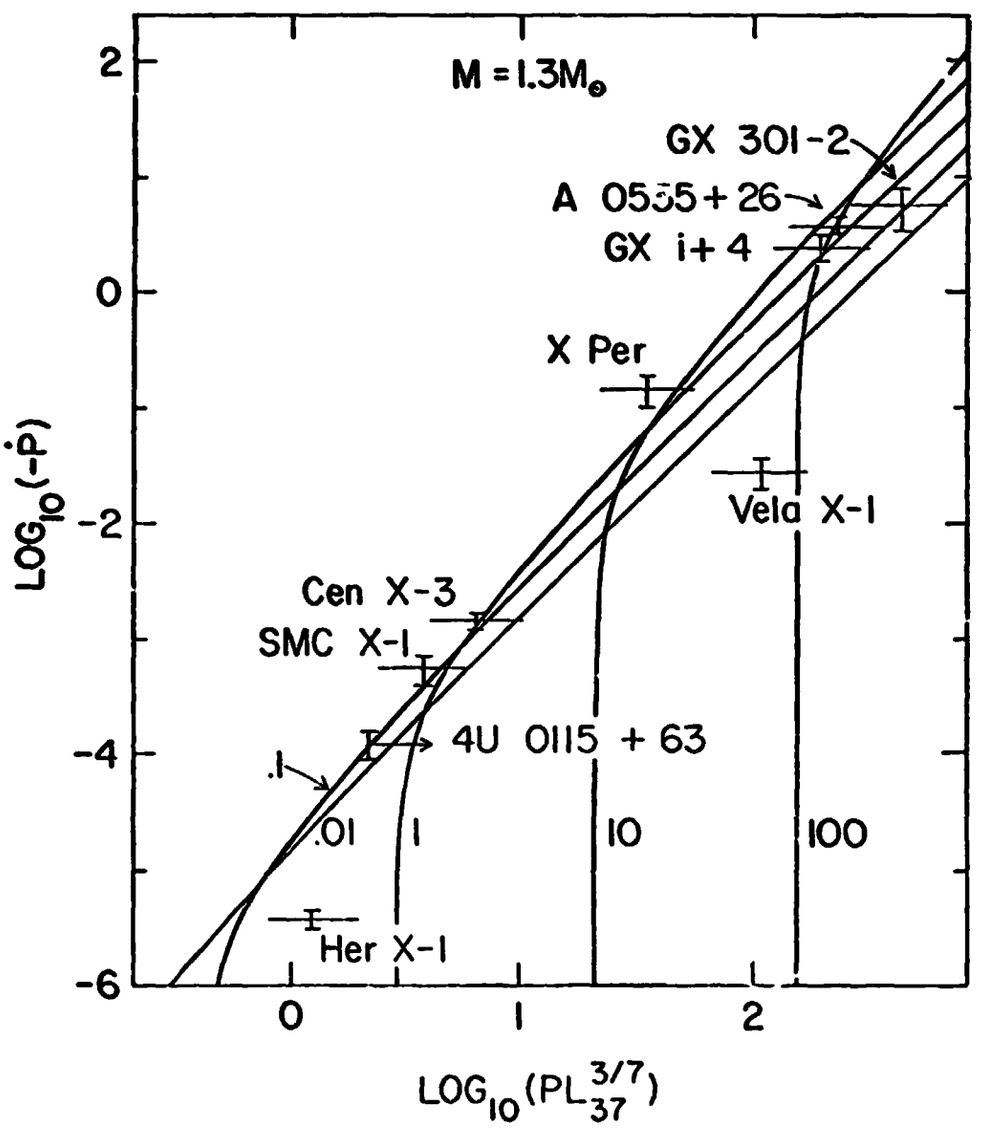

Figure 1

ORIGINAL PAGE IS
OF POOR QUALITY

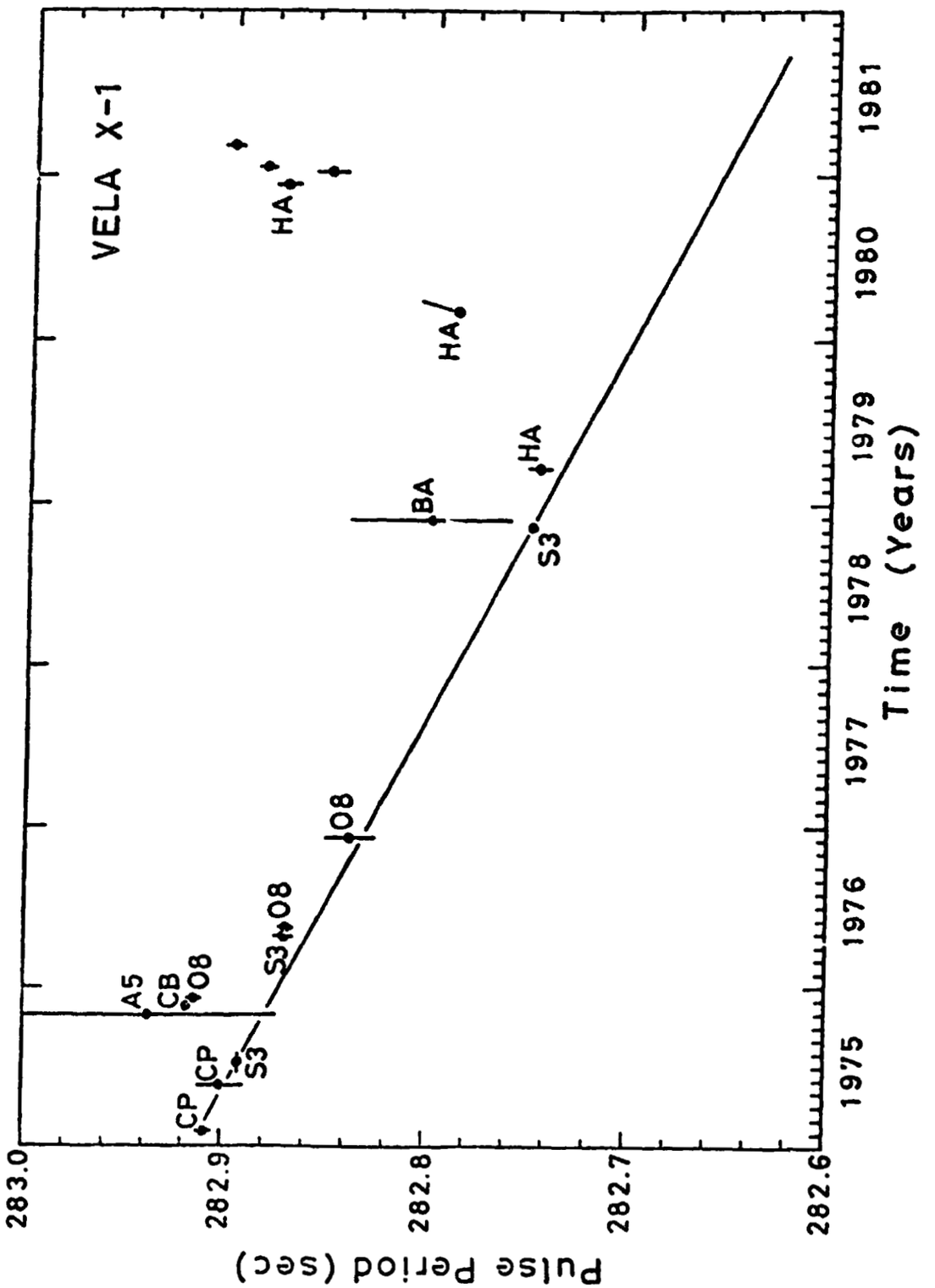

Figure 2

ORIGINAL PAGE IS
OF POOR QUALITY

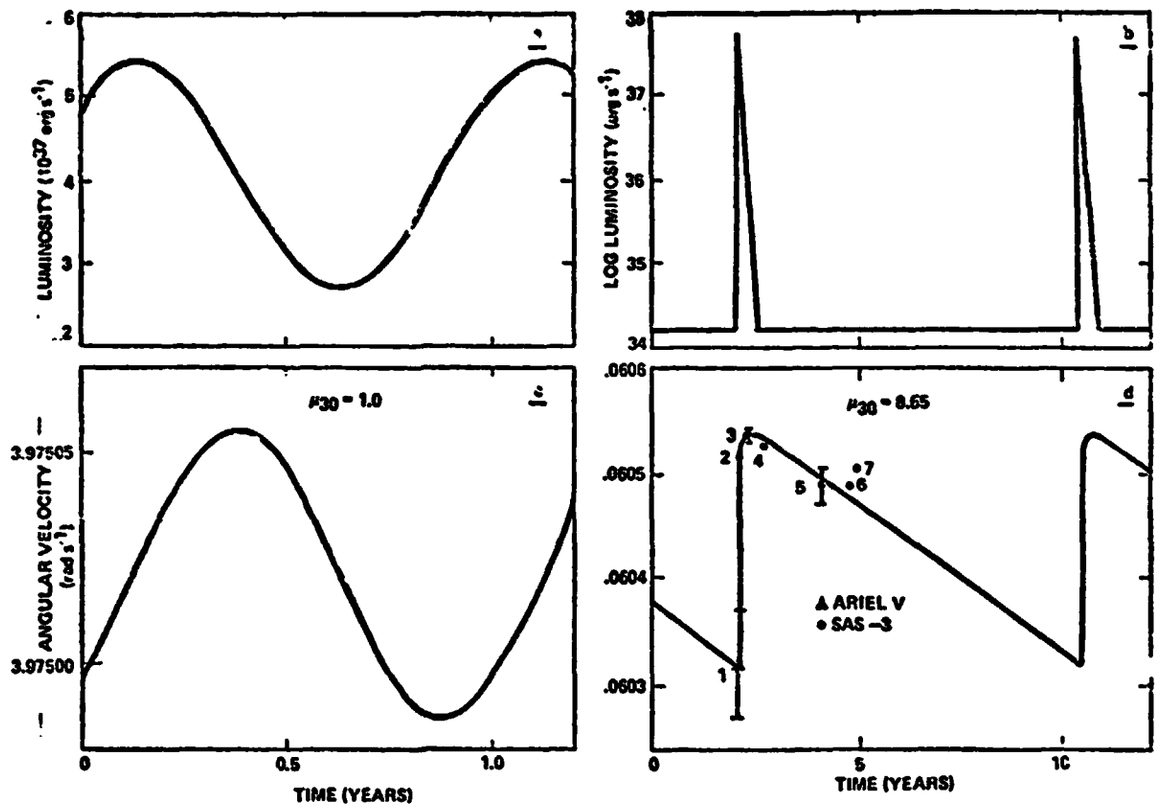

Figure 3

ORIGINAL PAGE IS
OF POOR QUALITY

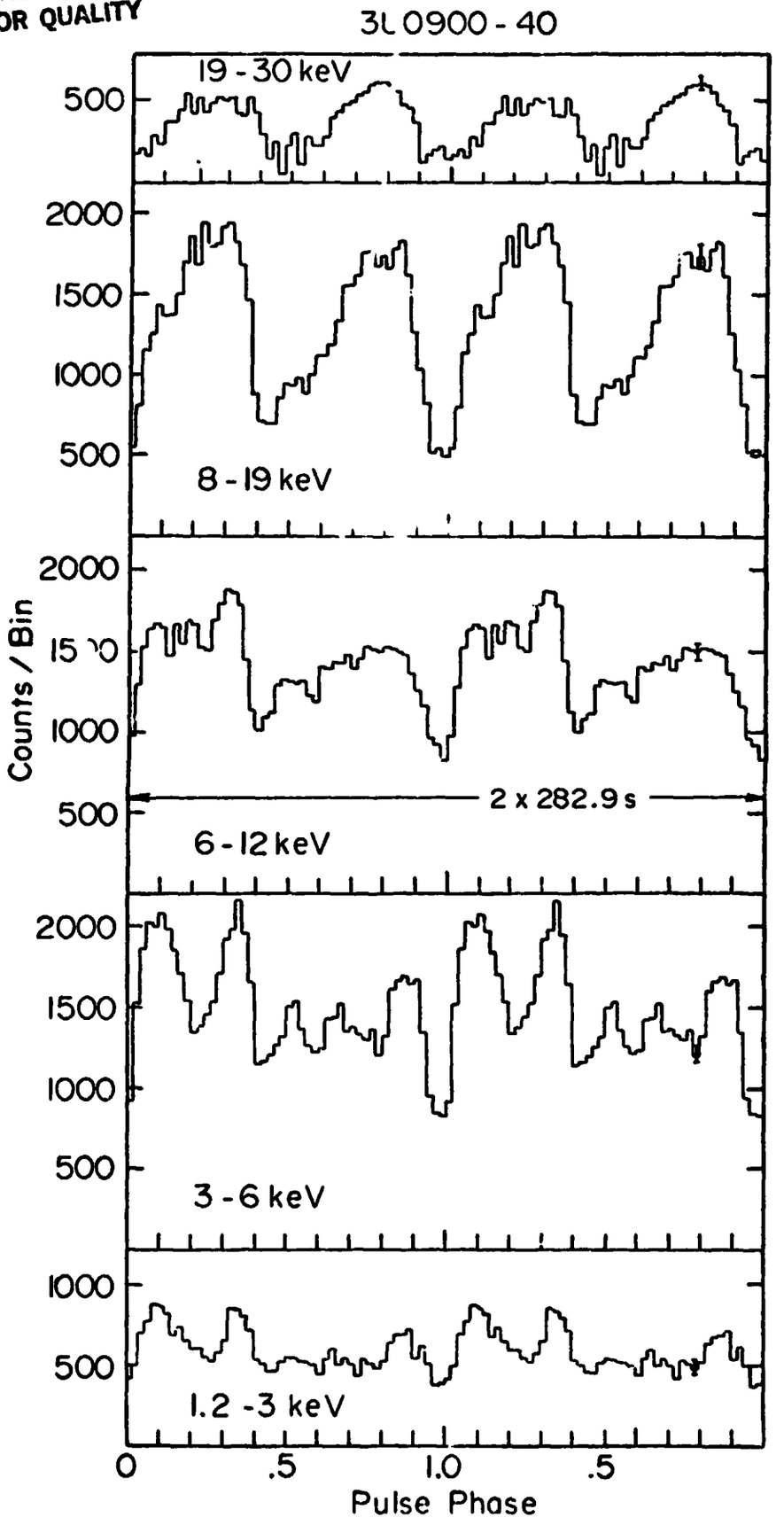

Figure 4

ORIGINAL PAGE IS
OF POOR QUALITY

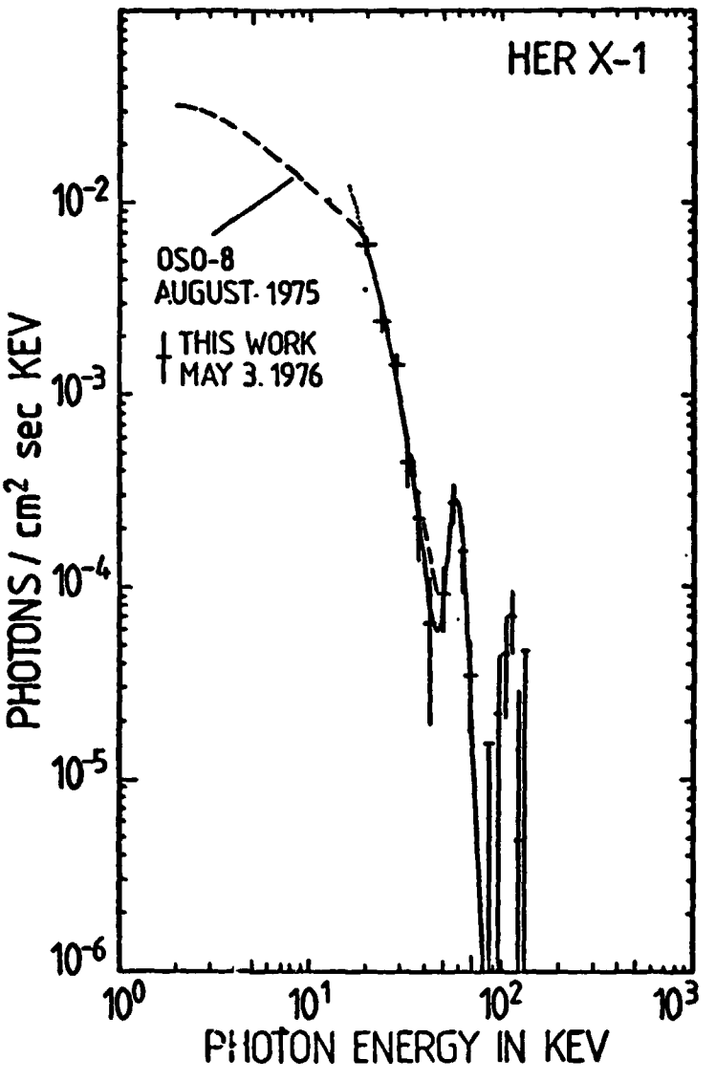

Figure 5

ORIGINAL PAGE IS
OF POOR QUALITY

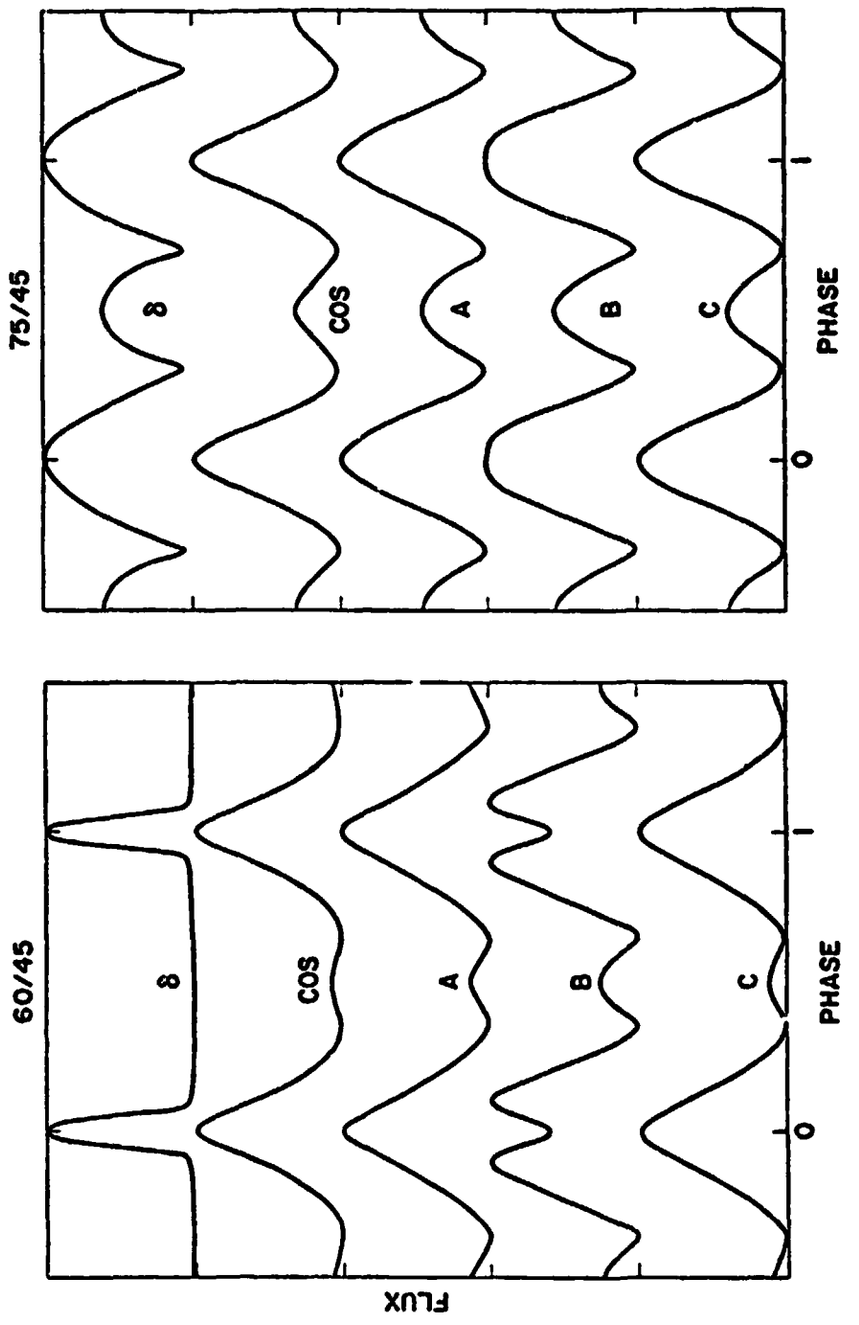

Figure 6

ORIGINAL PAGE IS
OF POOR QUALITY

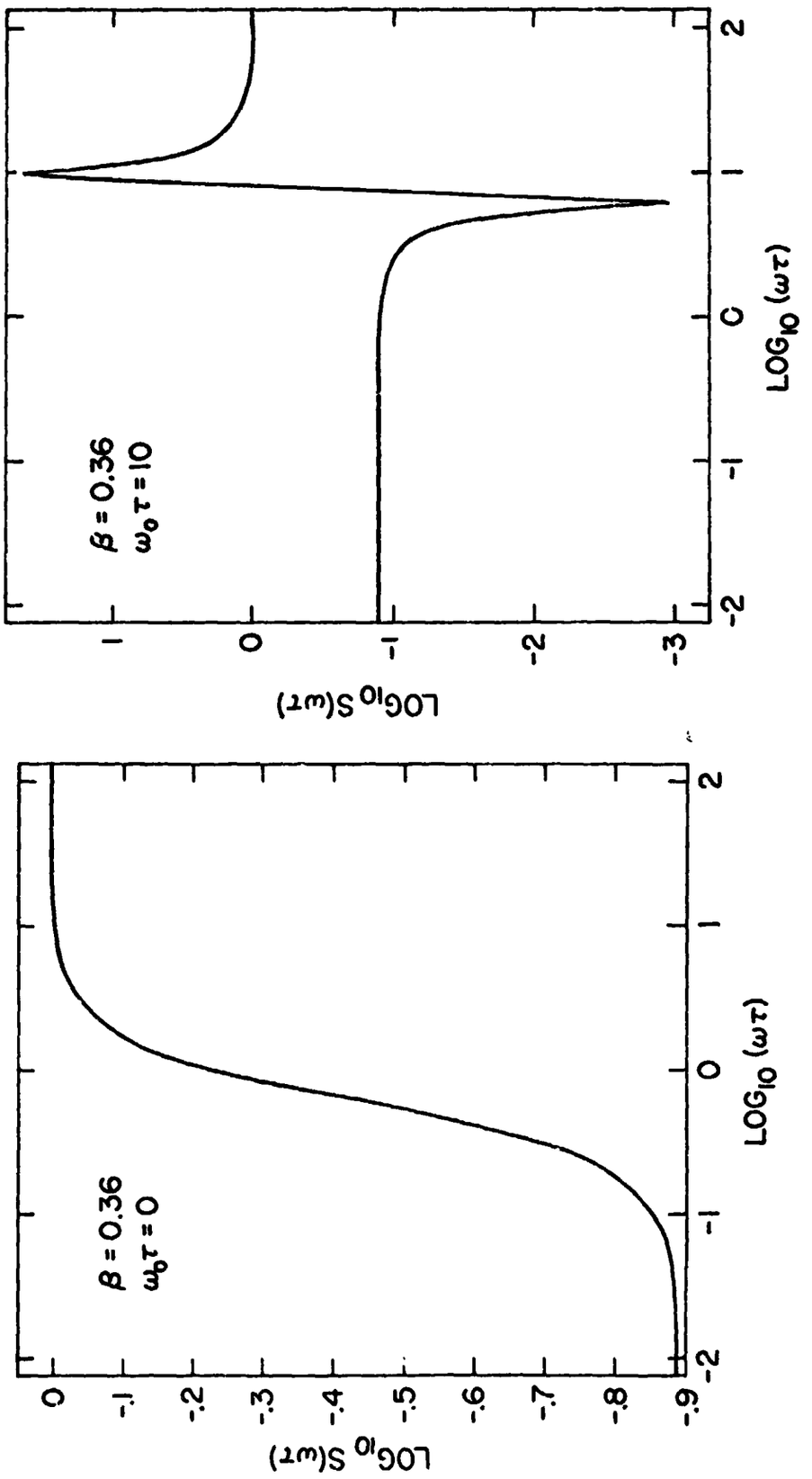

Figure 7

ORIGINAL PAGE IS
OF POOR QUALITY

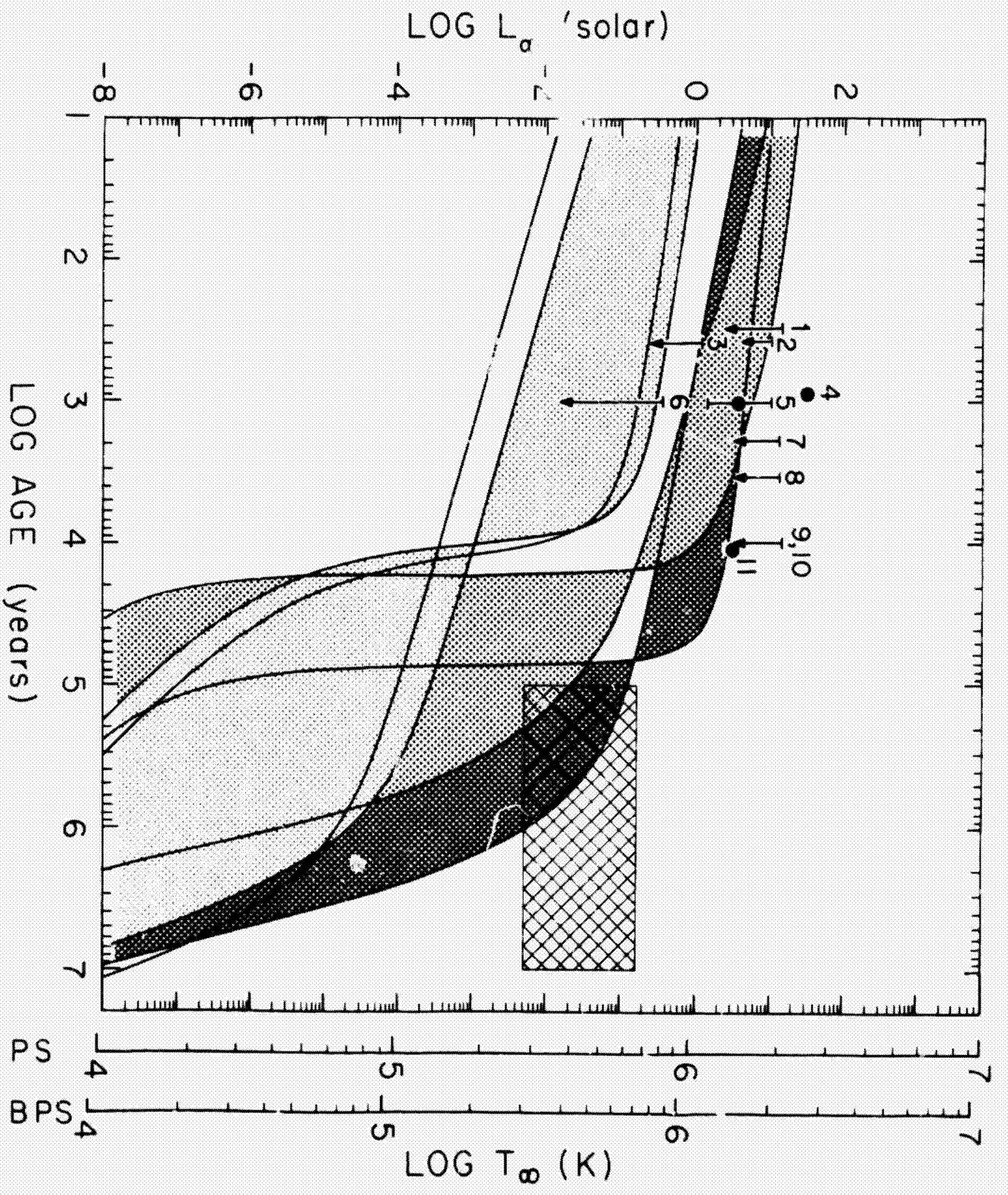

Figure 8

ORIGINAL PAGE IS
OF POOR QUALITY

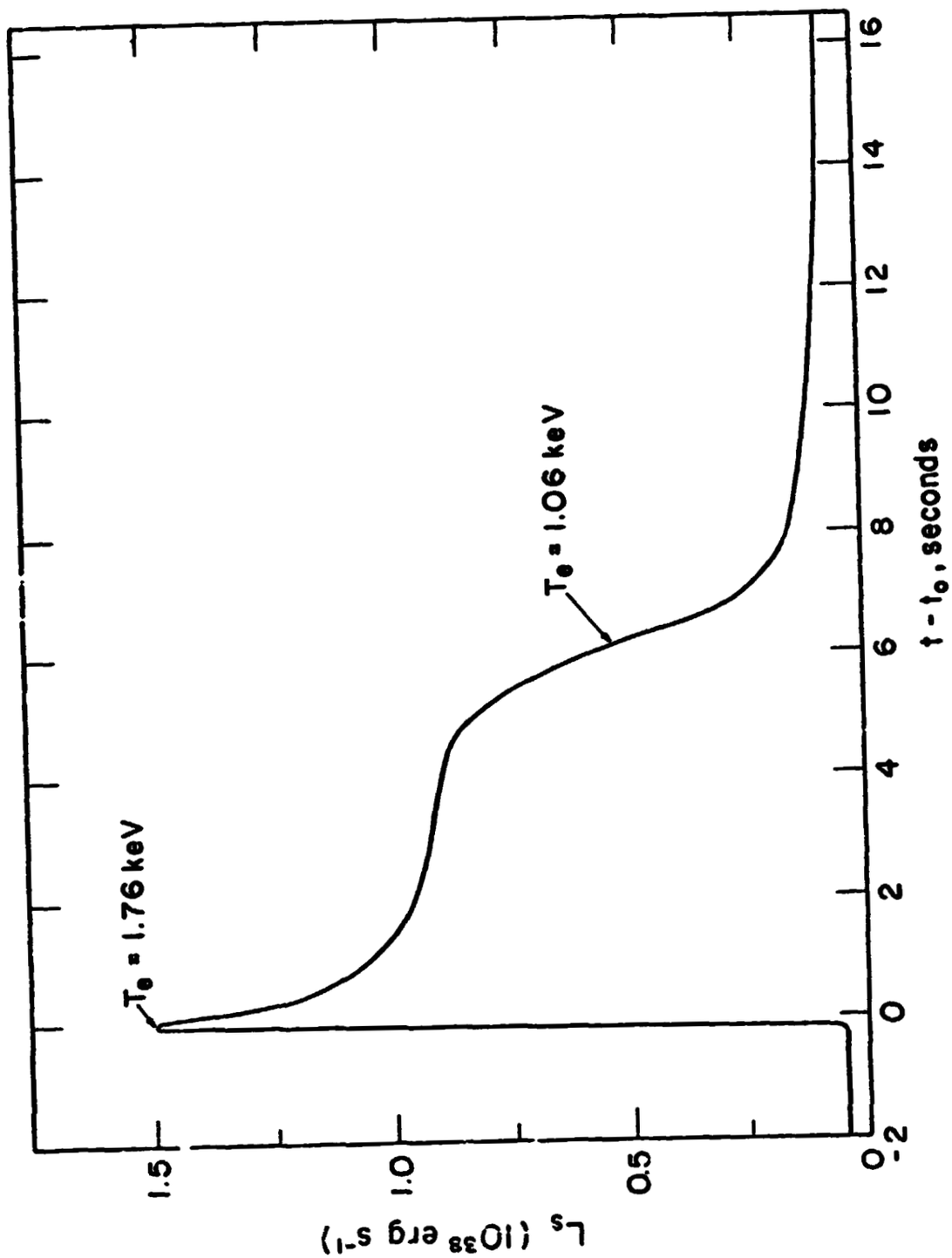

Figure 9

ORIGINAL PAGE IS
OF POOR QUALITY

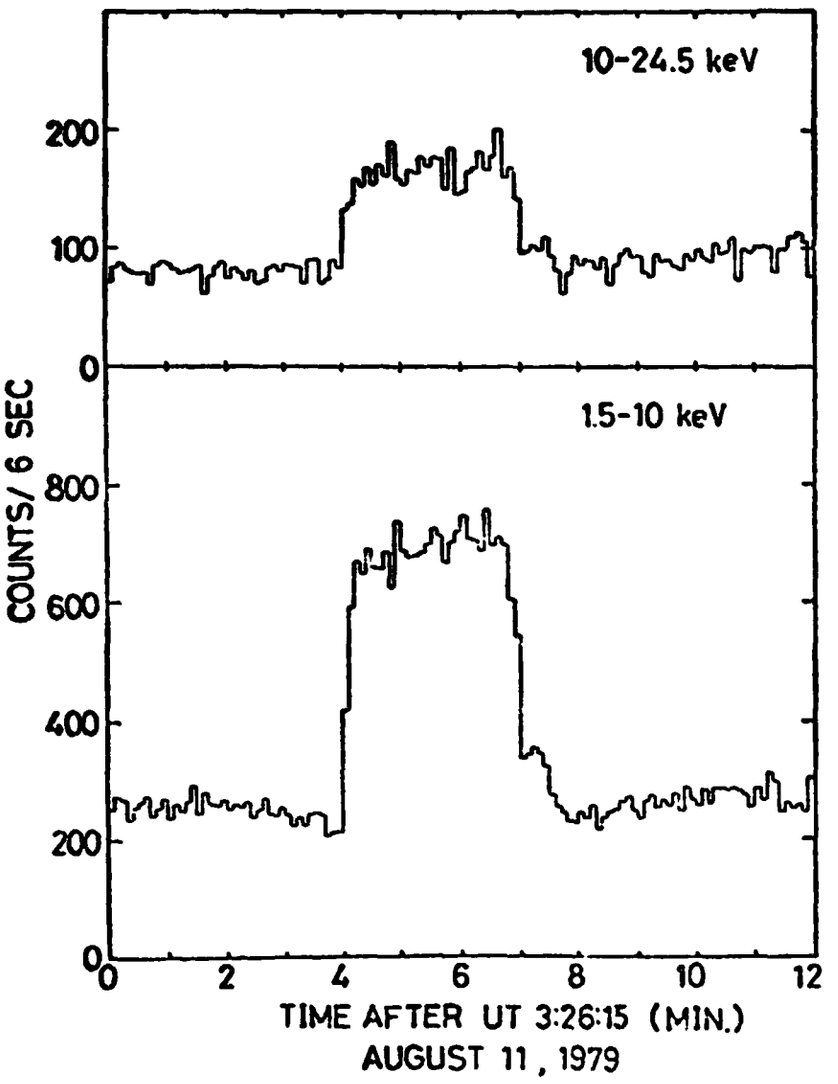

Figure 10

ORIGINAL PAGE IS
OF POOR QUALITY

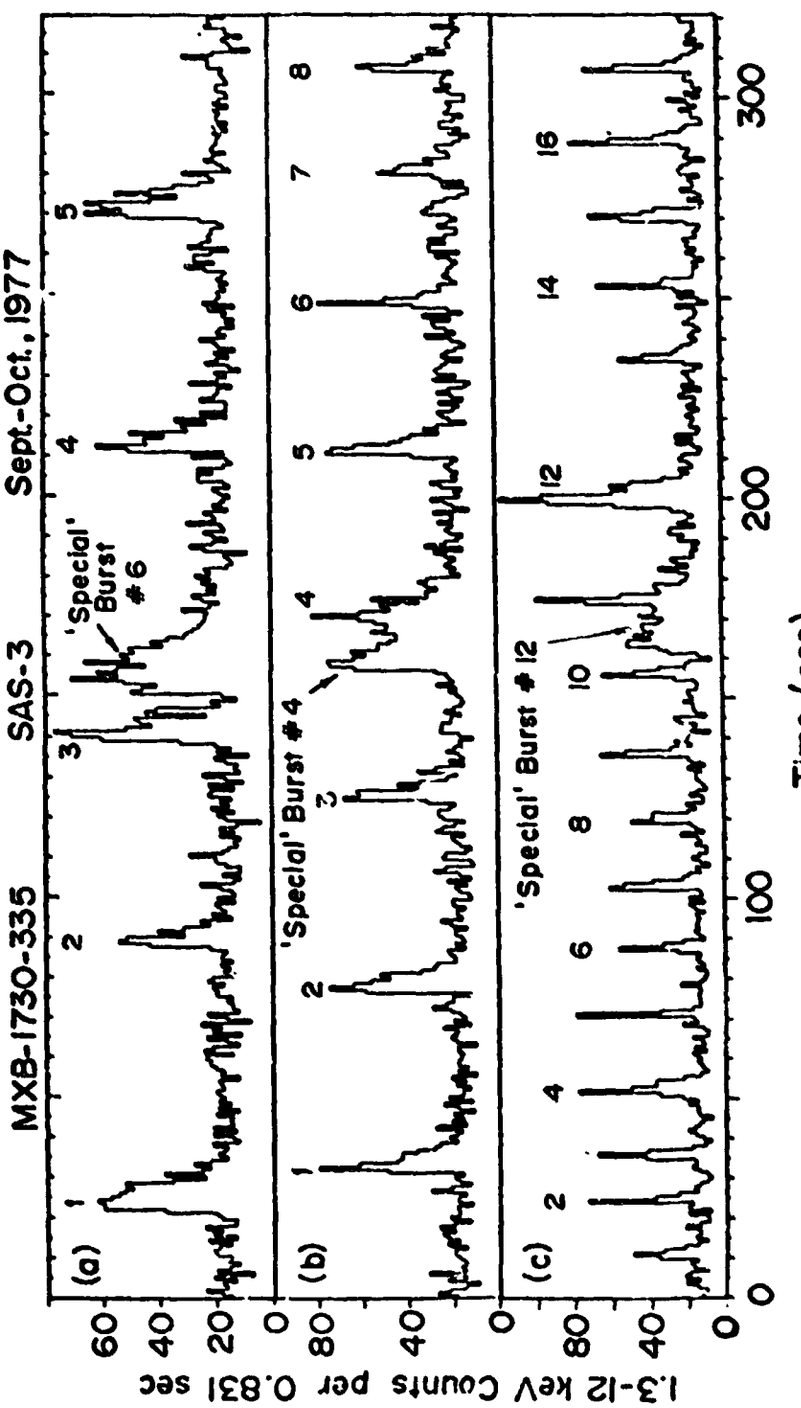

Figure 11

ORIGINAL PAGE IS
OF POOR QUALITY

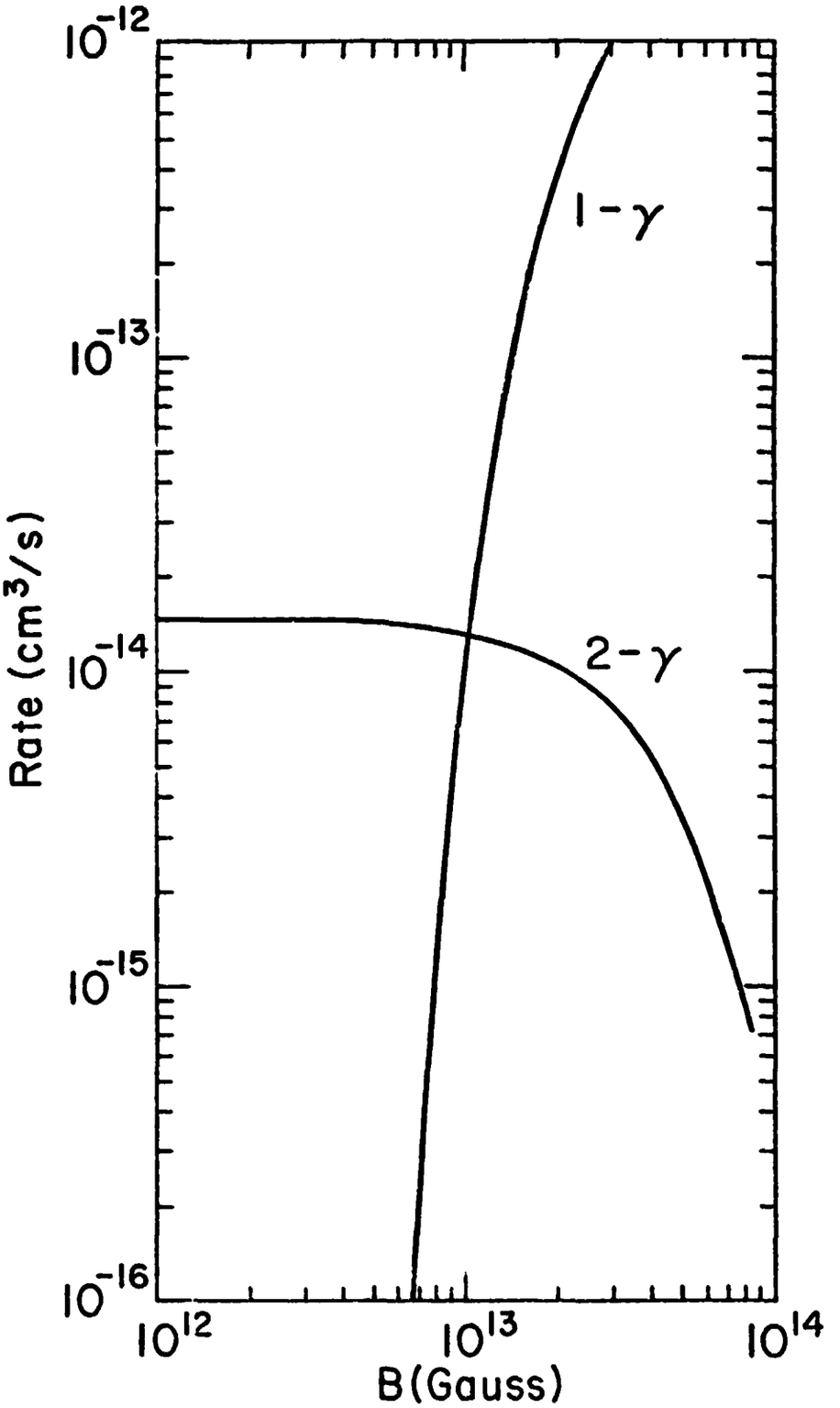

Figure 12

N82 26059

X-RAY SPECTROSCOPIC OBSERVATIONS AND MODELING OF SUPERNOVA REMNANTS

J. Michael Shull

University of Colorado
Laboratory for Atmospheric and Space Physics
and Joint Institute for Laboratory Astrophysics

ABSTRACT

X-ray spectroscopy can be a valuable tool in interpreting the temperatures, densities, and elemental abundances in young supernova remnants. Because of the large enrichment of the remnant ejecta in nucleosynthetic products of the stellar explosion, emission lines from He-like and H-like ionization stages of many heavy elements are prominent in HEAO-2 spectra. Precise abundance determinations, however, remain elusive because of the need for non-ionization equilibrium spectral modeling.

This review describes the recent x-ray observations of young remnants and their theoretical interpretation. A number of questions remain, concerning the nature of the blast wave interaction with the interstellar gas and grains and of atomic processes in these hot plasmas. Future x-ray spectrometers with high collecting area (10^3 cm^2), moderate spectral resolution ($E/\Delta E \sim 100$) and good spatial resolution (5-10") can make important contributions to our understanding of supernova remnants in the Milky Way and neighboring galaxies and of their role in the global chemical and dynamical evolution of the interstellar medium.

I. INTRODUCTION

If X-ray spectroscopy is to be used as a diagnostic tool for astrophysical plasmas outside the solar system, it will most likely prove itself in observations of young supernova remnants (SNRs). Heated to temperatures of 1-10 keV and enriched with the heavy element products of nucleosynthesis, the gas in these remnants emits prodigiously in X-ray lines (Holt 1980). Models of the emission from elements with atomic number $6 \leq Z \leq 28$ provide measures of plasma temperature, elemental abundances, and the degree of approach to ionization equilibrium. These observations yield valuable information on the type and structure of stellar explosion, the nucleosynthetic products, and the subsequent interaction of the blast wave with interstellar gas and grains.

Future X-ray spectrometers can make further contributions to our knowledge of SNRs in the Milky Way and neighboring galaxies. This review presents a brief summary of the past observations, the theoretical modeling, the primary unanswered questions, and the requirements for future instruments.

II. OBSERVATIONS

Most young remnants ($t < 1000$ years) have been observed by the HEAO-2 Imaging Proportional Counter (IPC) or by the High Resolution Imager (HRI). Shell-like emission was found in the remnants Tycho, Cas A, Kepler, and others; in a few cases such as the Crab Nebula and Vela, the remnant shells are filled. Although the spherical morphology is reassuring evidence for the blast wave model of SNRs, it is yet unclear whether the detailed emission structure is best described by the Sedov adiabatic similarity solution (Sedov 1959; Taylor 1950), or by reverse-shocked ejecta (McKee 1974; Gull 1975; Kirschner and Chevalier 1977).

ORIGINAL PAGE IS
OF POOR QUALITY

Two of the HEAO-2 spectrometers have resolved prominent emission lines from heavy elements in young SNRs. The Solid State Spectrometer (SSS), with effective area $\sim$100 cm^2, observed remnants in our galaxy and the Large Magellanic Cloud with an energy resolution $\Delta E \cong 160$ eV from 0.6 to 4.5 keV (Becker et al. 1980ab). The strongest lines (Figure 1) arise from He-like ionization stages of Ne, Mg, Si, S, Ar, and Ca, as well as from blended L-shell lines of Fe near 1 keV.

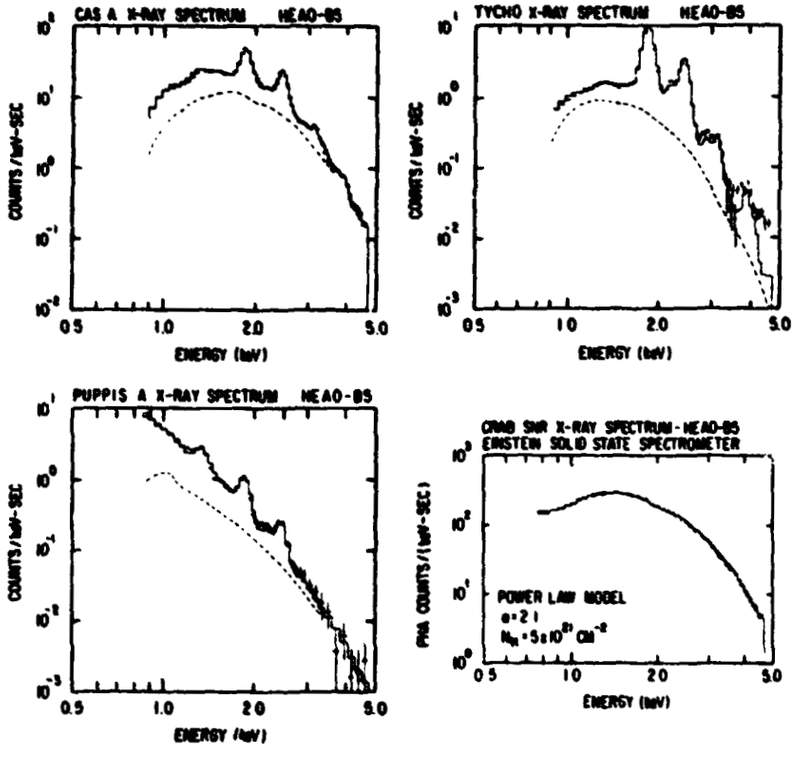

Figure 1. Einstein SSS experimental spectra from four young SNRs (Holt 1980).

The Focal Plane Crystal Spectrometer (FPCS), with effective area $\sim$2-3 cm^2, pushed X-ray spectroscopy even further, separating the He-like "triplet" lines (resonance, forbidden, and intercombination) of O VII and Ne IX in Puppis A

ORIGINAL PAGE IS
OF POOR QUALITY

(Winkler et al. 1981) and resolving the H-like Lα and Lβ lines of O VIII and Ne X and several lines of Fe XVII (Figure 2).

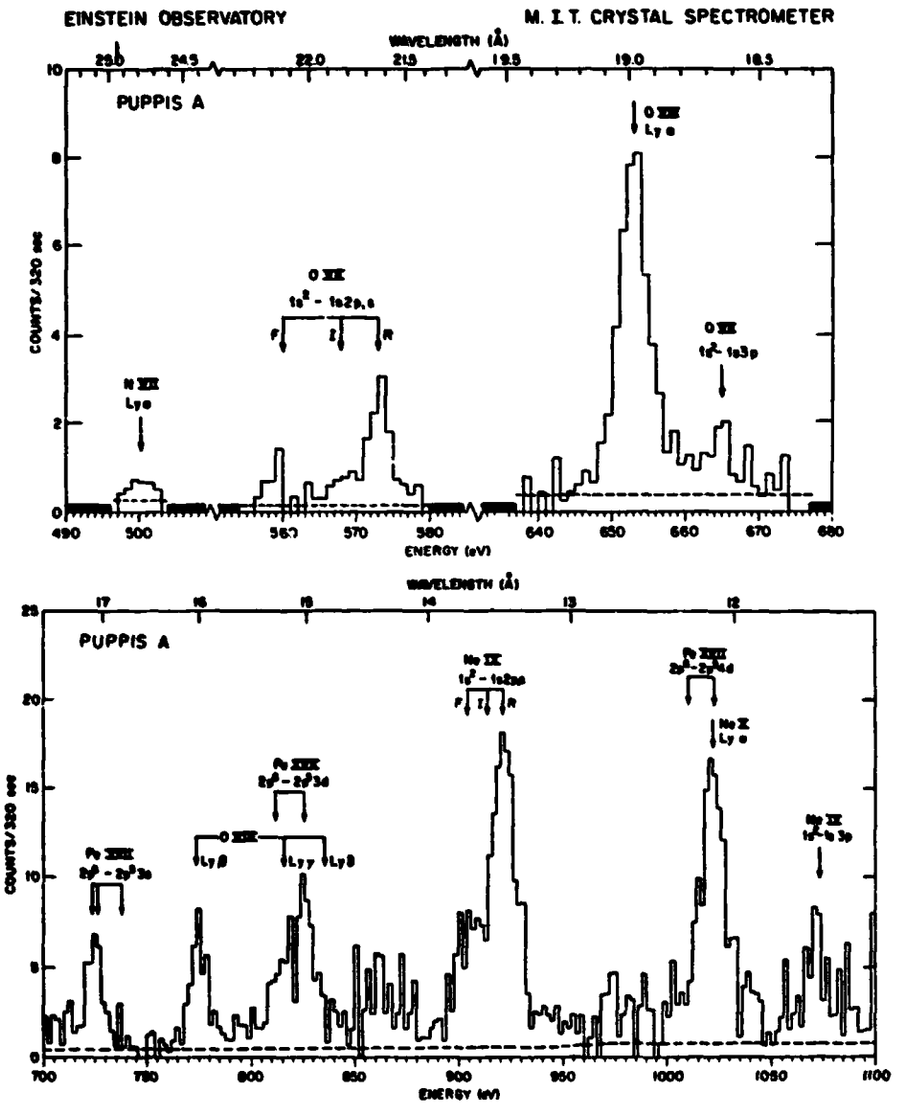

Figure 2. HEAO-2 (FPCS) spectra of the Puppis A SNR (Winkler et al. 1981), showing He-like "triplet" lines (marked F, I, R), H-like Lα and Lβ lines of O VIII and Ne X, and several L-shell lines of Fe XVII. Dashed lines indicate background.

Preliminary coronal equilibrium analyses of the SSS data (Becker et al 1980ab) required two temperature components to fit the spectra: a "hard" component with kT ∿ 5-10 keV to fit the continuum and a "soft" component with kT ∿ 0.5 keV to fit the H-like to He-like line ratios. These equilibrium models for Tycho suggested that Si and S were enhanced by factors ∿10 over their cosmic abundances, but that Fe was underabundant by a factor 0.15. Even stranger were the derived abundance enhancements of Ca (x 76) and Ar (x 35). All of these abundances are suspect, however, because of the possibility of substantial departures from ionization equilibrium.

III. THEORETICAL MODELING

Spectral emission models of hot, optically-thin, low-density plasmas (Shapiro and Moore 1976; Raymond and Smith 1977; Shull 1981a) are now a familiar tool in x-ray astronomy for deriving the temperatures, densities, and abundances in solar flares, stellar coronae, and intracluster gas. Using the most accurate available rates for collisional ionization and recombination to compute the equilibrium ionization fractions of the abundant elements, these models then generate the spectral emissivity of the hot plasma in the x-ray continuum and emission lines. Coupled with a χ-square fitting program, these spectral codes yield the plasma temperature and elemental abundances.

The application of ionization equilibrium (IE) models to young SNRs is questionable for three major reasons:

1. The SNR ages are often comparable to the characteristic collisional ionization time for He-like and H-like ions.
2. The dramatically different temperature components (∿5 keV and ∿0.5 keV) required to fit the continuum and lines, respectively, suggest an ionizing plasma in a transient stage.
3. The ratio of the resonance line to forbidden plus intercombination line of He-like O VII and Ne IX (Winkler et al. 1981) is too high for ionization equilibrium (Pradhan and Shull 1981).

ORIGINAL PAGE IS
OF POOR QUALITY

As shown by Itoh (1977), non-ionization-equilibrium (NIE) effects may have a significant effect on the emissivity of young remnants. If the shocked plasma has not had sufficient time to ionize Si or S to their equilibrium state at temperature kT ~ 5 keV, the He-like stages (and the resulting emission line strengths) may far exceed their values in equilibrium.

NIE models of X-ray emission from a hot plasma are far more complicated than IE models, because they involve the calculation of the time-dependent ionization history of every parcel of emitting plasma. For young SNRs, NIE modeling requires the coupling of gas hydrodynamics with a time-dependent ionization code and a spectral emission code (Shull 1981b). Recently computed NIE models of young remnants have been used (Shull and Szymkowiak 1981) to derive elemental abundances from the SSS data (Figure 3).

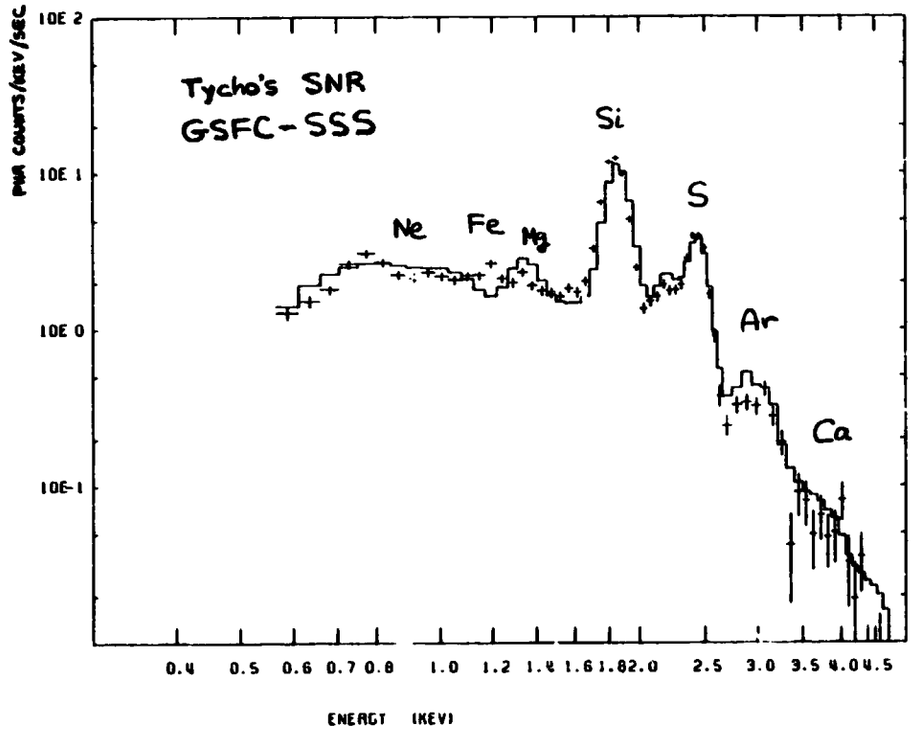

Figure 3. Einstein SSS data (crosses) and NIE model (solid lines) for Tycho's SNR (Shull and Szymkowiak 1981). Emitting elements are marked near their strongest lines.

Table 1 compares the abundances for Tycho derived from a single-velocity NIE blast wave model with those derived from a 2-temperature IE model. Although Si and S are still enhanced in the NIE model, Fe is no longer underabundant, and Ca and Ar have more realistic abundance enhancements. Although a great deal of further work remains in this area, it appears that NIE models with a single velocity can achieve nearly as good a fit to the Tycho spectrum as 2-temperature IE models. The Ca, Ar, and Fe abundances appear more realistic, and the single velocity parameter is physically simpler than the multi-component IE fit.

Several theoretical questions remain to be answered.

1. What is the ratio, T_i/T_e, of ion to electron temperatures behind the blast wave? (Pravdo and Smith 1979).
2. Do NIE effects fully explain the low ratio of He-like forbidden and intercombination lines to the resonance line?
3. What fractions of emission come from the blast wave and from reverse-shocked ejecta? What are the ejecta masses?
4. How sensitive are the derived NIE abundances to the assumed dynamical model (the range of densities and temperatures) of the remnant?

IV. FUTURE STUDIES

Further observational advances in answering the four questions posed in Section III will undoubtedly require x-ray instruments with higher sensitivity, greater spatial resolution, and better spectral resolution. However, in designing such instruments, one must decide which of these requirements are essential and which are only advantageous. Let us examine the four questions in order.

The degree of ion-electron temperature equilibration may be studied by measuring the hard x-ray (5 - 30 keV) continuum in SNRs (Pravdo and Smith 1979; McKee and Hollenbach 1980). At the low densities characteristic of remnants, the Coulomb equilibration time (Spitzer 1962) may be quite long. Plasma instabilities behind collisionless shock fronts may equilibrate T_i and T_e on a

faster scale (McKee 1974). To study these effects observationally, one requires high spatial resolution to identify the location of the hard continuum emission relative to the blast wave.

An observational study of He-like line ratios requires substantially greater spectral resolution than that afforded by the SSS. While the FPCS had the needed resolution, it was only capable of studying the brightest remnants. Therefore, these observations probably require a different type of spectrograph with both good energy resolution and high effective area. Table 1 presents the energies of the He-like resonance lines and the energy resolutions necessary to separate the forbidden and intercombination lines. Although O VII and Ne IX require the lowest resolution ($\sim$ 100), the Si XIII and S XV lines are far stronger in most remnants. A study of line ratios for a range of elements should show a progressive departure from equilibrium with increasing atomic number Z. However, it is probably most fruitful to study the O and Ne lines with a sensitive instrument having good spatial resolution in order to identify variations in ratios from specific regions in a large number of remnants.

The answer to the third question--that of the relative contribution of "blast wave" and "ejecta" x-ray emission--is the most dependent of the four on high spatial resolution. The ejecta appear to be unresolved on the HRI images (Seward 1981). Therefore, in order to measure the heavy element abundances in the true "blast wave" and distinguish them from the metal enriched ejecta, one must be able to obtain moderate energy resolution spectra of small regions of the remnant. The mass determinations of these ejecta require accurate abundances, since the emissivity of the plasma is greatly enhanced by metal enrichment and NIE effects. Because the x-ray intensity from these small regions will be less than that from the large-field SSS data, a high collecting area is required.

Question four may be the most important scientific issue concerning SNRs for the overall astrophysical community. If the x-ray spectra of young remnants are to be used as diagnostics of stellar evolution, stellar explosions, and nucleosynthesis, x-ray astronomers must increase the accuracy of the spectral data as well as refine the theoretical models. The HEAO-2 SSS provided remarkably good line determinations, considering its moderate energy resolution, $E/\Delta E \sim 10$-20. That this was possible was due primarily to its large effective area (~ 100 cm^2). Because the major uncertainties in the modeling of SNR x-ray spectra involve the effects of non-equilibrium ionization (i.e. time-dependent temperature and density history of the plasma), future observations can best help by providing high spectral resolution and a large collecting area. Resolving the Fe L-complex near 1 keV, as well as higher excitation lines of He-like and H-like ions of Ne, Mg, Si, and S, or determining the energy centroid of the Fe K-line complex near 7 keV can better constrain the model fits. Until this is done, further refinements in the theoretical modeling are probably unwarranted.

The conclusion drawn from the assessment of the four scientific questions appears to be that large collecting area ($\sim 10^3$ cm^2) and moderate spectral resolution ($E/\Delta E \sim 10^2$) are needed to make further progress in spectral studies of SNRs. Moderate spatial resolution, of order 5", would be advantageous for some specific problems in individual remnants. However, unless one achieves the high effective area and spectral resolution, SNR studies will be limited to only a few bright sources. While detailed studies of these sources at high spatial resolution will yield useful information on the masses and remnant structure, the scientific topic of greatest general interest--an abundance analysis of a large sample of remnants in our galaxy and the Magellanic Clouds--will almost certainly require the sacrifice of spatial resolution to achieve the required spectral resolution and sensitivity.

ORIGINAL PAGE IS
OF POOR QUALITY

TABLE 1. MODEL ELEMENTAL ABUNDANCES FOR TYCHO*

ELEMENT	EQUILIBRIUM[1]	NON-EQUILIBRIUM[2]
Ne	1	0.37
Mg	0.1	2.0
Si	6.0	7.6
S	13.5	6.5
Ar	34.6	3.2
Ca	76	2.6
Fe	0.15	2.1

*Abundances relative to Solar Values, determined from χ^2-fitting to HEAO-2 SSS data. H, He, and CNO are assumed to be in solar abundance.

[1]Becker et al. (1980a), 2-temperature component, ionization equilibrium model.

[2]Shull and Szymkowiak (1981), single-velocity, non-ionization-equilibrium model of SNR blast wave with immediate post-shock temperature, kT_s = 7.2 keV, explosion energy 10^{51}ergs, and ambient H-density $n_0 = 1\ cm^{-3}$.

TABLE 2. HE-LIKE LINES

ELEMENT	E_R*	ΔE(R-F)*	ΔE(R-I)*	RESOLUTION*
O	574 eV	13 eV	5.4 eV	110
Ne	922	17	6.8	140
Si	1865	25	11	170
S	2461	30	13	190
Fe	6702	64	26	260

*Energy E_R of the He-like resonance line (R); energy separations, ΔE(R-F) and ΔE(R-I), between R and the forbidden line (F) and intercombination line (I); and resolution, $E_R/\Delta E(R-I)$, required to analyze He-like line ratios.

REFERENCES

Becker, R.H., Holt, S.S., Smith, B.W., White, N.E., Boldt, E.A., Mushotzky, R.F., and Serlemitsos, P.J. 1980a. Ap. J. Letters, 235, L5.

Becker, R.H., Boldt, E.A., Holt, S.S., Serlemitsos, P.J., and White, N.E. 1980b. Ap. J. Letters, 237, L77.

Gull, S.F. 1975. M.N.R.A.S. 161, 47.

Holt, S. 1980. "X-Ray Spectra of Supernova Remnants," in X-Ray Astronomy, Proc. NATO Adv. Study Inst., Erice, Sicily (eds. R. Giacconi and G. Setti), p. 35.

Itoh, H. 1977. P.A.S.J. 29, 813.

Kirshner, R.P., and Chevalier, R.A. 1977. Ap. J. 218, 142.

McKee, C.F. 1974. Ap. J. 188, 335.

McKee, C.F., and Hollenbach, D.J. 1979. Ann. Rev. Astr. Ap. 18, 219.

Pradhan, A.K., and Shull, J.M. 1981. Ap. J. 249, in press.

Pravdo, S.H., and Smith, B.W. 1979. Ap. J. Letters 234, L195.

Raymond, J.C., and Smith, B.W. 1977. Ap. J. Suppl. 35, 419.

Sedov, L.I. 1959. Similarity and Dimensional Methods in Mechanics (New York: Academic Press).

Seward, F. 1981, private communication.

Shapiro, P.R., and Moore, R.T. 1976. Ap. J. 207, 460.

Shull, J.M. 1981a. Ap. J. Suppl. 46, 27.

Shull, J.M. 1981b. Ap. J., to be submitted.

Shull, J.M., and Szymkowiak, A. 1981, in preparation.

Spitzer, L. 1962. Physics of Fully Ionized Gases, 2nd Ed. (New York: Wiley-Interscience), p. 135.

Taylor, G.I. 1950, Proc. Roy. Soc. London, A201, 159.

Winkler, P.F., Canizares, C.R., Clark, G.W., Markert, T.H., Kalata, K., and Schnopper, H.W. 1981. Ap. J. 245, 574.

N82 26060

PRECEDING PAGE BLANK NOT FILMED

INTERSTELLAR, INTRACLUSTER AND SUPERCLUSTER GAS

Lennox L. Cowie

Physics Department, Center for Space Research, and
Center for Theoretical Physics
Massachusetts Institute of Technology
Cambridge, Massachusetts 02139

Talk Presented at:

Symposium on X-Ray Astronomy and Spectroscopy
Goddard Space Flight Center, October 1981

I. INTRODUCTION

The topics which this talk has to cover range in size from about 100 Pc to 100 MegaPc but in many respects are remarkably similar. In all cases we are considering hot tenuous plasmas with temperatures in the range $10^6 \rightarrow 3.10^8$ °K and densities of $10^{-6} \rightarrow 10^{-3}$ cm^{-3}. The dominant radiation processes are thermal bremstrahlung and collisional line excitation and all except the very hottest objects will have observable X-ray emission lines. However the most important unifying point is the angular scales involved. For the interstellar gas one may expect structure ranging in size from about 10' (shadowing by IS clouds; Fried *et al.* 1980) to tens of degrees (nearby evolved supernova remnants (Nousek *et al.* 1981). Nearby (distance ∿20 M Pc) irregular clusters will have structure on galaxy scalelengths of a few minutes, which is similar to the core sizes of distant more regular clusters (e.g. Forman and Jones 1982). The cores of very distant clusters at z=1 will be resolvable at 30'' → 1' [e.g. Henry *et al.* 1979]. Superclusters will have sizes of degrees [e.g. Murray *et al.* 1978].

Thus there are an enormously wide range of problems which an instrument with a spatial resolution of ½' → 1' and a field of view of degrees could tackle. Though there are problems in these areas which such an instrument could not cover,* I think it is fairly clear that what we need most is an instrument of this general type.

---

*Examples are the spatial mapping of cooling flows in clusters (Fabian *et al.* 1981) or the mapping of gas around galaxies in distant irregular clusters.

Of the three classes of problems listed in the title the only one on which we have really excellent X-ray data is the clusters [e.g. Forman and Jones 1982]. We have a good deal of information on X-ray emission from the interstellar gas both from rocket flights and the HEAO 1 and SAS C experiments [e.g. Fried *et al.* 1980]. Finally we have very little solid information of any sort on the superclusters. Despite this diversity in existing understanding, the way to the future in all three areas must be through larger collecting areas.* In the rest of the talk it will be seen that there are many problems where a highly *spectral* resolution [R $\sim$ 100-1000] would be useful or even essential. However, we could make a great deal of progress with an instrument of moderate resolution (R $\sim$ 10) provided we could obtain the necessary increase in sensitivity.

A rather incomplete list of important problems in these fields is as follows:

Interstellar Gas:

Mapping at moderate (1') spatial resolution:	Morphology of individual structures in the IS gas
	Separation of stellar and gaseous contributions to the soft X-ray background
	Interstellar cloud shadowing Structure of the galactic halo
(High Spectral Resolution Studies:)	Chemical composition of the galactic halo
	X-ray absorption line studies of the disk and halo
	Spectroscopy of individual structures

*The necessity for large area applies irrespective of the spectral resolution.

Clusters:	
Mapping at 1' resolution:	Samples of distant clusters/cluster evolution
	Outer halos of rich homogeneous clusters
	Interaction of galaxies and cluster gas in irregular clusters
	Morphology of gas in clusters
(High spectral resolution studies:)	Spectroscopy of the centers of radiatively cooling clusters
	Abundance gradients
	Primordial material in irregular clusters
Superclusters:	Detection and mapping of hot gas
	Interaction between clusters and superclusters
(High spectral resolution studies:)	Chemical enrichment in intercluster gas

I've split the list into experiments which could be performed without high spectral resolution and those in which it is essential. I think it's worth noting that roughly 50% of the experiments require high spectral resolution as well as the imaging capability. Clearly if both sensitivity and high spectral resolution could be obtained this would be ideal.

I now want to consider a few of these topics in more detail. The choice is somewhat arbitrary and I have avoided topics which are touched on elsewhere (in particular in the talks of Fabian and of Shull).

II. SUPERCLUSTER GAS

It seems increasingly probable that the general intergalactic gas lies at temperatures less than 10^6 °K and probably cannot be detected by its X-ray emission (e.g. Sargent *et al.* 1979). As

yet the arguments and observations of this point are in no way compelling but it seems worthwhile to focus our attempts to detect the IGM in the X-rays on those regions where the heat input is most likely to be concentrated.

The best location for this is probably in the intercluster regions of the superclusters. Bookbinder *et al.* (1980) have argued that galaxies of present visual luminosity $L_* = 10^{10.5}\ L_\odot$ release about $10^{61.7}$ ergs into the intergalactic gas at temperatures around $10^{9.0}$ K in their early stages of evolution. Such material will not be bound to any cluster of which the galaxy is a member. At this stage the cluster would then possess a hot outflowing wind.*

Assuming that the net visual luminosity of a typical supercluster is around $10^{14}\ L_\odot$, the total energy release would amount to about 2×10^{65} ergs. If this occurred at z=5, allowing for adiabatic expansion losses, it would heat a gas of density $n_e = 9.6\times10^{-6}\Omega h^2\ cm^{-3}$, ($h = H_o/100$ km s^{-1} Mpc^{-1}), filling a radius of 20 Mpc to a temperature of $\sim2\times10^6\Omega^{-1}h^{-2}$ °K.** The total mass of gas in the supercluster is $10^{16}\Omega h^2\ M_\odot$ while the galaxies will have released about $5\times10^{14}\ M_\odot$ of processed gas or about 10^{14}

---

*As was first pointed out by Ostriker (1979), this has two very attractive features. Firstly it drives out any primordial gas which would like to fall into the cluster. Secondly, by removing very metal enriched gas from the cluster it can solve various abundance problems of the type discussed by deYoung (1978).

**A complete self consistent calculation would follow the evolution of the blast wave generated by the overlapping cluster winds and calculate the temperature from this (Ostriker and Cowie 1981). The result is very close to the quick estimate given above and the present radius of the blast wave is around 20 Mpc for Ω=1.

$M_\odot$ of metals (Bookbinder *et al.* 1980). The metallicity may therefore be a substantial fraction of cosmic particularly if Ω is less than 1.

Assuming that the emissivity is around 10^{-23} n_e^2 ergs cm^3 s^{-1}, a temperature of about 200 ev-1 Kev, as is suggested by the above calculation, the total luminosity of the supercluster would be around 10^{45} $\Omega^2 h^4$ ergs s^{-1} and its surface brightness about 5×10^{-9} $\Omega^2 h^4$ ergs/cm^{-2} s^{-1} ster^{-1} or a fraction of the diffuse X-ray background at these energies.

In general terms and independent of this specific model it is clear that the most important requirement for a supercluster search is the ability to exclude member clusters and other X-ray objects from the field and to consider only the intercluster component. This requires an angular resolution of at least a fraction of a degree. The experiment must also be capable of imaging the whole supercluster which would generally mean a FOV of several degrees for relatively nearby superclusters.

For a supercluster of radius 3° at a distance of 500 Mpc we can estimate that a 3σ detection above fluctuations in the background would crudely require a source with 10% of the diffuse X-ray flux in the same region (Levine *et al.* 1977, Schwarz 1980). This would imply that a sensitive experiment could reach surface brightness limits of about 2×10^{-9} ergs cm^{-2} sec^{-1} ster^{-1} (Fried *et al.* 1980) and constrain $\Omega < 1$ or so for an individual supercluster. Clearly a survey of a large number of superclusters could provide very interesting constraints on the IGM density.

A spectroscopic instrument, measuring the relative line strengths, could also constrain the metallicities of the gas. This could be of crucial importance, if and when the superclusters were detected, in distinguishing between cluster heating of the intracluster gas as discussed above and alternative heating mechanisms such as gravitational in-fall. The history of cluster X-ray emission studies should remind us how important such information can be.

III. CLUSTER X-RAY SOURCES

I want to say relatively little about this topic, since the problems are so well known to everyone. Discussion can be found in the reviews of Cowie (1981) and Forman and Jones (1982). Briefly, a large area imaging instrument is needed to study distant clusters and to extend the Einstein results of Henry and coworkers (e.g. Henry *et al.* 1979). Realistically there is little hope of obtaining cosmological information from this type of measurement but a very large sample of distant clusters may allow us to obtain the evolution of the average X-ray luminosity and gas core radius for individual classes of cluster. Hopefully we may at least determine if there has been any evolution of the potential of the cluster over recent ($z \lesssim 1$) times. However, one should contrast the results of Cowie and Perrenod (1979) with those of Perrenod (1977) to see how small the expected differences are.

A second direct application of a large area imaging detector would be the study of gas lossage by galaxies in irregular

clusters (e.g. Fabian *et al.* 1980). Pushing existing results farther back in z would probably help us understand the nature of galaxy stripping in clusters, gas evolution in galaxies and cluster galaxy evolutionary effects such as the color changes described by Butcher and Oemler (1978). Models for the formation of cluster atmospheres such as those by Norman and Silk (1979) or Sarazin (1979) make detailed and testable predictions of the evolution of the gas distribution in clusters which could be checked.

There are a number of additional problems which a spectroscopic instrument could tackle. Perhaps the most interesting would be an extension of the fascinating Einstein SSS and FPCS results (e.g. Canizares *et al.* 1980, Mushotzky *et al.* 1981) on the cooling central cores of clusters out to more distant clusters. Refinement of the cluster metallicities which can be obtained in this way could be of primary importance in understanding galaxy evolution within the clusters and cluster gas evolution.

IV. INTERSTELLAR GAS

In this section I want to consider two very specific experiments, one of which illustrates what could be done with a large area imaging detector and one of which would additionally require high resolving power.

a. Cloud Shadowing of the Soft X-Ray Background

The great majority of the soft X-ray background appears to be truly diffuse, arising primarily from a local hot spot in the

galactic disk and from a hot gaseous galactic halo (Marshall and Clark 1981). About 20-30% at 1 Kev and substantially less at 200 eV arises from dM stars (Rossner *et al.* 1981) with about 10 stars in each square degree contributing most of the flux. The fractional contributions from Pop II stars to the halo emission may still constitute a problem. However if the soft X-ray background could be imaged on a scale of minutes, fluctuation analyses of the type given by Levine *et al.* (1977) at larger scales should allow us to obtain a stringent limit to the stellar contribution. Imaging of the X-ray background at such scales is a demanding problem however, since the high galactic latitude photon arrival rate in the 200 eV-1 Kev range is only around 5×10^{-6} ph cm^{-2} sec^{-1} $(\square')^{-1}$. Therefore both a large area detector with long exposure and a low background are necessary.

As Fried *et al.* (1980) have recently pointed out, typical diffuse interstellar clouds with column densities of 3×10^{20} cm^{-2} or more are opaque to radiation in the 200 eV energy range. The local hot gas behind such regions and, more importantly, the hot halo gas or halo star contribution will be substantially shielded by such regions. A typical line of sight at high latitudes is most likely to pass through exactly one cloud but has a finite possibility of passing through none or more than one (e.g. Spitzer 1977). Since the cloud sizes are large compared to arcmins (at 100 pc a 1 pc radius cloud has an angular radius of 30'), individual clouds will appear as large shadowed regions on the diffuse X-ray background at low energy. Since we may also estimate the distance from the amount of missing soft X-rays this type of

measurement could determine the size spectrum of interstellar clouds a quantity of crucial importance to theories of the ISM (McKee and Ostriker 1977). It is worth commenting that this quantity is remarkably difficult to determine by other methods.

b. X-Ray Absorption Lines from the Hot ISM

The possibility of making X-ray absorption line studies, analogous to the optical and UV absorption line studies which have been so important in studying the interstellar medium, has only recently begun to be considered. The reasons for this are clear – the instrument requirements are quite severe both as regards effective area and spectral resolution – but the potential for studying the intergalactic medium (Shapiro and Bahcall 1980) and the hot interstellar medium and the galactic halo (York and Cowie 1981) are enormous. The reason for this is that the absorption lines directly measure column densities of a given ionization stage and remain sensitive to low density gas in contrast to the emission lines.

In Table I, I have summarized from York and Cowie the strongest available lines together with the expected equivalent widths for a $10^{18.5}$ cm^{-2} column density of hot gas at the optimal temperature. This value is representative of the hot ISM (e.g. McKee and Ostriker 1977).

It can be seen from Table I that a resolution of at least $R \approx 100$ is required to discriminate neighboring strong lines. In addition, one may simply estimate on the basis of photon statistics the required instrument parameters. The necessary effective area

ORIGINAL PAGE IS
OF POOR QUALITY

Table 1 (adapted from York and Cowie 1981).

Species	Line Wavelength (Å)	Logarithmic Temp. at Which Species is Dominant Ionization Stage	f (Oscillator Strength)	$W_{E/E}$ ($N=10^{18.5}$)
C V	40.27,40.73,41.47	5.7	0.65	3×10^{-4}
C VI	33.7C	6.0	0.42	1.6×10^{-4}
O IV	22.86	5.4	0.45	1.6×10^{-4}
O V	22.52	5.4	0.62	3×10^{-4}
O VII	21.8,21.6	6.0	0.69	3×10^{-4}
O VIII	19.0	6.3	0.42	1.6×10^{-4}
Si VIII	61.0	6.0	1.2	10^{-}

A is given in terms of the source intensity I by

$$A(cm^2)Rt(hrs) = 3\times10^4 \; n^2 / \left[\left\{\frac{(W_E/E)}{10^{-4}}\right\}^2 J(kev/(cm^2 \; s \; kev))\right].$$

For a source with I = 5 kev cm^{-2} s^{-1} kev^{-1} at 500 eV, such as the Crab (Charles *et al.* 1979), a 3σ detection of a line with $W_E/E = 3\times10^{-4}$ in an hour's exposure would require $A(cm^2)R = 6000$. In rough terms this is a factor of 30 or so over the FPCS detectors aboard Einstein (Giacconi *et al.* 1979).

There are a number of problems with this technique, of course, not least that of finding sufficiently strong background sources with well defined continua in the neighborhood of the absorption lines. In some cases (e.g. ScoX1) there may be relatively narrow emission lines which will confuse the absorption line studies. Synchrotron sources such as the Crab are ideal, of course.

V. SUMMARY

Clearly this has been an idiosyncratic and personal view of a complex range of topics, but I think two points are very clear. Firstly, a large area imaging instrument could cover a great deal of ground with or without a spectroscopic capability. However, high resolution spectral capability is highly desirable and would greatly enhance the power of such an instrument. Either class of instrument would be highly flexible, capable of dealing with a wide range of problems and of great general utility.

ACKNOWLEDGEMENTS

I would like to thank J. Grindlay and A.C. Fabian, who pointed out omissions in the original presentation. This work was supported by NASA grants NAGW-208, NSG-7643 and NGL-22-009-638.

References

Bookbinder, J., Cowie, L.L., Krolik, J., Ostriker, J.P. and Rees, M. 1980. *Ap.J.* 237, 647.

Butcher, H. and Oemler, A. 1978. *Ap.J.* 226, 559.

Canizares, C. *et al.* 1980. In *Highlights of Astronomy* 5, 657, ed. P.A. Wayman (Dordrecht: Reidel).

Charles, P. *et al.* 1979. *Ap.J.* 230, L83.

Cowie, L.L. and Perrenod, S. 1978. *Ap.J.* 219, 354.

deYoung, D.S. 1978. *Ap.J.* 223, 47.

Fabian, A.C., Hu, E.M., Cowie, L.L. and Grindlay, J. 1981. *Ap.J.* 248, 47.

Fabian, A.C., Schwarz, J. and Forman, W. 1980. *MNRAS* 192, 135.

Forman, W. and Jones, C. 1982. *ARAA* 20, 000.

Fried, P.M., Nousek, J.A., Sanders, W.T. and Kraushaar, W.L. 1980. *Ap.J.* 242, 987.

Giacconi, R. *et al.* 1979. *Ap.J.* 230, 540.

Henry, J.P. *et al.* 1979. *Ap.J.* 234, L15.

Levine, A., Rappaport, S., Halpern, J. and Walter F. 1977. *Ap.J.* 211, 215.

Marshall, F. and Clark, G. 1981. Private communication.

McKee, C.F. and Ostriker, J.P. 1977. *Ap.J.* 218, 148.

Murray, S.S., Forman, W., Jones, C., and Giacconi, R. 1978. *Ap.J.* 219, L89.

Mushotzky, R., Holt, S.S., Smith, B.W., Boldt, E.A. and Serlemitsos, P.J. 1981. *Ap.J.* 244, L47.

Norman, C. and Silk, J.P. 1979. *Ap.J.* 233, L1.

Nousek, J.A., Cowie, L.L., Hu, E.M., Lindblad, C.J. and Garmire, G. 1981. *Ap.J.* 248, 152.

Ostriker, J.P. 1979. Private communication.

Perrenod, S. 1978. *Ap.J.* 224, 285.

Rossner, R. *et al.* 1981. *Ap.J.* 240, L5.

Sarazin, C. 1979. *Astrophysics Letters* 20, 93.

Sargent, W.L.W., Young, P.J., Boksenberg, A. and Tytler, D. 1980. *Ap.J. (Suppl.)* 42, 41.

Schwarz, D.A. 1980. *Physica Scripta* 21, 644.

Shapiro, P.R. and Bahcall, J.N. 1980. *Ap.J.* 241, 1.

York, D.G. and Cowie, L.L. 1981. *Ap.J.* In press.

N82 26061

X-ray Emission from Galaxies and the Universe

A.C. Fabian
Institute of Astronomy
Madingley Road
Cambridge CB3 OHA
U.K.

INTRODUCTION

The study of X-ray emission from normal galaxies began with the launch of the Einstein Observatory in 1978. Before that time only our own Galaxy and the Magellanic Clouds had been studied in any detail (see e.g. Markert et al. 1977). Now many galaxies of all Hubble types have been detected and $\sim$200 point sources have been resolved in the nearest ones. More sources are now known in other galaxies than were known in our own before 1978. It seems clear that statistical studies of bright Galactic sources, which relate to their evolution, are reliant upon the discovery of sources in many other galaxies. A substantial future increase (the Virgo cluster galaxies) requires a telescope system with better than arcminute resolution and a sensitivity better than 10 x that of Einstin.

Little is known of the diffuse X-ray emission from galaxies. The soft X-ray background in our Galaxy (Tanaka & Bleeker 1977, Fried et al. 1981) and evidence for a gaseous halo (Savage & de Boer 1980) suggest that a significant fraction of the gaseous matter in galaxies is at X-ray emitting temperatures. Unfortunately the potential wells of most galaxies are so shallow that the gas densities are then so low as to make detection difficult. Searches for diffuse sources of line emission are likely to be the most rewarding. We can study diffuse gas much better in the deeper wells provided by groups and clusters of galaxies. Here the evolution and cycling of gas is to be observed on a grand scale.

Finally, I would stress that the lumpiness of the Universe on large scales ($\gtrsim$ 10 Mpc) can best be determined from X-ray measurements. The investigation of the detailed patchiness of the X-ray background should be an important priority for the future.

NORMAL GALAXIES

The various components of X-ray emission in our own Galaxy are listed in Table 1. The emission is dominated by the bright Galactic "Bulge" sources and, below 0.25 keV, by the soft X-ray background. The most uncertain contribution is that due to stars (see e.g. Rosner et al. 1981), especially late-type low mass Population II stars that may constitute a large fraction of the stellar population. Unfortunately little has been reported on this issue, but if the indication of an inverse correlation between X-ray emission and age proves to be correct then they are likely to be only weak X-ray sources.

The point source population of a few nearby galaxies is given in Table 2 from the work of Long et al. 1980, 1981, Seward & Mitchell 1981, Van Speybroek et al. 1970, 1980 and Palumbo et al. 1981. The X-ray luminosity functions of M31 and our Galaxy are in marked contrast. Future work must decide why 20 globular cluster sources in M31 have an X-ray luminosity greater than any in our Galaxy and why M31 has so many more 'bulge' sources.

Long (1980) has pointed out that the X-ray emission of $\sim$40 galaxies of all Hubble type appears to be correlated with the optical brightness of the galaxy. $L_x \approx 10^{-3} - 10^{-4} L_{vis}$. Although the sample is small, this does suggest the presence of a common factor. Two possibilities are apparent. The first possibility is the prevalence of Population II ('bulge'-type) sources. One indication that this may be correct is to be found by noting that globular clusters with X-ray sources fall approximately on this correlation. Since the ration of L_x to the stellar X-ray emission in Population II sources

is $\sim 10^3$-10^4, only 1 'star' in $\sim 10^6$-10^8 is needed to be a 'bulge' type X-ray source, independent of Hubble type, in order to explain the correlation.

I cannot, however, see how the extended emission from M84 (Forman 1980) or from Cen A (Feigelson et al. 1981) can be easily explained by 'bulge' type sources, which should collect at the centres of galaxies. The second possibility is hot gas, from stellar mass loss heated by Supernova explosions. This cannot explain why globular clusters or the Magellanic Clouds fit the correlation, but could be a significant, or dominant, fraction of the emission from unresolved galaxies. Certainly the diffuse emission from our own galaxy rivals that of the point sources below $\sim$ 1 keV, and a contribution of this magnitude seems possible in M31 as well (Von Speybroeck et al. 1979).

Galactic coronae will be difficult to detect (see e.g. Bregman 1980). The gas temperature should be $\simeq \mu m_H \sigma^2/k$ where σ is the internal velocity dispersion. Thus a temperature of $\sim 10^6$-10^7K is to be expected. Hotter gas would be lost; cooler gas would cool further and collapse. If the IUE Galactic halo observations indicate that a 'galactic-fountain' is operating (Shapiro & Field 1976, Bregman 1980, Songaila 1981) then up to $\sim 1 M_\odot\ yr^{-1}$ of cooling must take place. This represents $\sim 10^{40}$erg s^{-1} in soft X-rays, much of which will emerge as lines below $\sim \frac{1}{4}$ keV. The routine detection of diffuse emission from galaxies will probably start when substantial high-galactic latitude exposures are made with detectors and spectrometers sensitive at 0.1 - 0.2 keV. This will have implications/or gas flows in galaxies, the stellar death and birth rates and for chemical enrichment.

Much of the gas lost in winds and by stripping in isolated galaxies must be trapped in the potential wells of clusters. The evolution of clusters, which appears to be continuing at the present time, and of the galaxies within them relies heavily on X-ray observations. A vigorous approach in the future should enable us to understand the evolution of these largest known entities.

The mass distribution in clusters can be determined from detailed observations of the surface brightness profile at two separate energies. Since we know that any gas motions are highly subsonic, that the gas is likely to be closely Maxwellian and that the emission is predominantly bremsstrahlung and line radiation then accurate solutions are possible. Later comparisons with the galaxy motions can unravel the expected anisotropies in their velocity distribution.

The formation of galaxies may be observed through their X-ray emission. Of interest now is the growth of central galaxies in clusters via a cooling flow of intracluster gas (Fabian & Nulsen 1977, Cowie & Binney 1977). Here the gas from other cluster galaxies settles and presumably forms stars around a central stationary galaxy. This process occurs around NGC 1275 in the Perseus cluster (Fabian et al. 1981) and is being observed in an increasing number of other clusters. Young (primeval) galaxies may be rich in X-ray phenomena if a large fraction of the energy produced with the metals is released as X-rays (Bookbinder et al. 1980; Sunyaev, Tinsley & Meier 1979). Perhaps also the non-thermal activity of galaxies is also inversely correlated with age, as for stars. The dissipation of chaotic motions may indirectly produce X-rays. Isolated extragalactic HII regions observed locally, in which bursts of star formation are taking place, may give a good picture of the emission from a primeval galaxy. We (Stewart et al. 1981) have detected one at $L_x \simeq 0.1\ L_{vis}$ with the Einstein Observatory.

The activity of galactic nuclei is discussed elsewhere, but does allow galaxies to be identified at large redshifts. E. Boldt has pointed out to me the possibility that X-ray spectral observations can test whether Seyferts and quasars are two separate classes or not. Basically, the energy spectral index of Seyferts is close to 0.7, at least from $\sim$ 3 - 100 keV, and an extrapolation of non-evolving Seyferts out to $Z \sim 1$ gives the MeV bump in the hard

X-ray background (see e.g. Boldt 1980). This suggests that the class of Seyferts does not evolve and predicts that many active galaxies with $L \lesssim 10^{44}$ erg s^{-1} should be observable with spectral indices of ~ 0.7 out to $Z \sim 1$. Quasars must have a much flatter spectrum if they compose the background, otherwise they must be relatively steep.

THE LUMPINESS OF THE X-RAY BACKGROUND

The usefulness of X-ray observations in constraining matter fluctuations on the scale of 100 - 1000 Mpc is discussed in Fabian, Warwick & Pye 1978, Rees 1979 and Fabian 1981. Limits on $\delta\rho/\rho$ of a few percent are obtained from the current limit of 1 percent on excess fluctuations on the scale of ~ 5 degrees (Fabian & Rees 1978, Schwartz 1979). Hopefully these will be improved when the HEAO-1 A2 analysis is complete (Shafer 1981). The observed P(D) fluctuations due to unresolved sources that are not clumped provide a basic limitation. An imaging detector (2 - 6 keV) that enables sources to be eliminated down to ~ 0.01 UFU and scale of $0^{\circ}.5$ would allow a residual fluctuation of $\frac{\delta I}{I} \gtrsim 30\ n^{-\frac{1}{4}}$ percent to be measurable where n is the number of regions surveyed. For ~ 100 fields, the clumping of galaxies (and of quasars) at the 20 Mpc end of the galaxy covariance function (Peebles 1974) should begin to be attainable if the source density is high enough.

Large-scale anisotropies in the X-ray background are expected due to the galactic background, our motion relative to and to shear and other effects on the X-ray background. The situation may be optimum at high energies (> 30 keV) where the galactic effects are hopefully small, and where the steepening of the background spectrum enhances $\frac{\delta I}{I}$ via the Compton Getting effect.

ACKNOWLEDGEMENTS

I thank E.A. Boldt and his colleagues at GSFC for support and hospitality.

REFERENCES

Boldt, E.A., Comm. on Astrophys., 9, 97.

Bookbinder, J., Cowie, L.L., Krolik, J.H., Ostriker, J.P. & Rees, M.J. 1980, Astrophys.J., 237, 647.

Bregman, J.N. 1980a, Astrophys.J., 237, 681.

Bregman, J.N. 1980b, Astrophys.J., 236, 577.

Cowie, L.L. & Binney, J. 1977, Astrophys.J., 215, 723.

Fabian, A.C., 1981, Ann.N.Y.Acad.Sci. in press.

Fabian, A.C. & Rees, M.J. 1978, M.N.R.A.S., 185, 69.

Fabian, A.C. & Nulsen, P.E.J. 1977, M.N.R.A.S. 180, 479.

Fabian, A.C., Warwick, R.S. & Pye, J.P. 1980, Phys.Scripta, 21, 650.

Fabian, A.C., Cowie, L.L., Hu, E. & Grindlay, J. 1981, Astrophys.J., 248, 47.

Feigelson, E. et al. preprint.

Forman, W. 1980. Proc . N.A.T.O. A.S.I. on X-ray Astronomy.

Fried, P.M., Nousek, J.A., Sanders, W.T. & Kraushaar, W.L. 1980, Astrophys.J., 242, 987.

Long, K.S. 1980, report of talk at 156th meeting of AAS.

Long, K.S., Helfand, D.J. & Grabelsky, D.A. 1981, Astrophys.J., 248, 925.

Long, K.S., d'Odorico, S., Charles, P.A. & Dopita, M.A., Astrophys.J., 246, L61.

Markert, T.H., Canizares, C.R., Clark, G.W., Hearn, D.R., Li, F.K., Sprott, G.F. & Winkler, P.F., 1977, Astrophys.J., 218, 801.

Palumbo, G.G.C., Maccacaro, T., Panagia, N., Vettolani, & Samorani, G. 1981, Astrophys.J., 247, 484.

Peebles, P.J.E. 1974, Astrophys.J., 32, 197.

Rees, M.J. 1980, IAU Symp. No. 92, ed. G.O. Abell & P.J.E. Peebles, Reidel (Dordrecht).

Rosner, R. et al. preprint

Savage, B.D. & de Boer, K.S. 1979, Astrophys.J., 230, L77.

Schwartz, D.A. 1980, Phys.Scripta, 21, 644.

Seward, F.D. & Mitchell, M. 1981, Astrophys.J., 243, 736.

Shafer, R. 1981, in preparation.

Shapiro, P.R. & Field, G.B. 1976, Astrophys.J., 205, 762.

Songaila, A. 1981, Astrophys.J., 248, 945.

Sunyaev, R.A., Tinsley, B. & Meier, D. 1978, Comm. on Astrophys., 7, 183.

Tanaka, Y. & Bleeker, J.A.M. 1977, S.S.R., 20, 815.

Van Speybroeck, L., Epstein, A., Forman, W., Giacconi, R., Jones, C., Liller, W. & Smarr, L. 1979, Astrophys.J., 234, L45.

Van Speybroeck, L. & Bechtold, J. 1980. Proc. A.A.S. Meeting on X-ray Astronomy, ed. R. Giacconi.

TABLE 1.

X-RAY EMITTING CONSTITUENTS OF OUR GALAXY

Source type	Number	$\langle L_x \rangle$ erg s^{-1}	η_x (local) erg $pc^{-3} s^{-1}$	L_{Tor}
Early type binaries $L_x > 5 \times 10^{36}$	~ 10	3×10^{37}		3×10^{38}
Pop II binaries(?)	~ 20	6×10^{37}		1.5×10^{39}
Low luminosity binaries	≥ 100	$< 10^{36}$		$< 10^{38}$?
Galactic nucleus		5×10^{35}		5×10^{35}
Cataclysmic variables	$\sim 10^5$?	$\leq 10^{32}$	$< 10^{26}$	$< 10^{37}$
O-stars	$\sim 5 \times 10^3$	10^{33}		5×10^{36}
Main sequence stars	$\sim 10^{10}$	2×10^{38}	$\sim 10^{27}$	2×10^{38}
Halo M-dwarfs	$< 10^{11}$??	$< 3 \times 10^{27}$?	$< 3 \times 10^{24}$	$< 3 \times 10^{38}$
Supernova remnants	$\sim 10^3$	10^{35}		10^{38}
Galactic (diffuse) background E < 0.25 keV			$\sim 2 \times 10^{28}$	10^{39}
E > 2 keV			10^{26}	10^{38}

ORIGINAL PAGE IS
OF POOR QUALITY

TABLE 2.

Galaxy	D	M	Binaries		SNR	?
			Pop I	Pop II		
LMC	55 kpc	10^{10} $M_\odot$	$\sim$ 8		$\sim$ 40	$\sim$ 20
SMC	65 kpc	$1.5.10^{9}$ $M_\odot$	1 + 2		$\sim$ 5	$\sim$ 15
M31	750 kpc	3.10^{11} $M_\odot$		20 Glob 19 Bulge	1	$\sim$ 47
M33	750 kpc	4.10^{10} $M_\odot$				$\sim$ 9
M101	6 Mpc	$\sim 10^{11}$ $M_\odot$				$\sim$ 5
M100	15 Mpc	$\sim 10^{11}$ $M_\odot$				$\sim$ 2

PRECEDING PAGE BLANK NOT FILMED

N82 26062

X-RAYS FROM QUASARS AND ACTIVE GALAXIES*

Alan P. Lightman
Harvard-Smithsonian Center for Astrophysics

I. INTRODUCTION

There is evidently a great deal of activity and commotion in deep space, unrevealed by the naked eye or the delicate twinkling of the stars. As far as we can tell, quasars (QSOs) and "active galactic nuclei" (AGN) have relatively enormous power outputs produced in very small volumes. A typical quasar can produce a hundred to a thousand times the luminosity of a normal galaxy from a region one hundred thousand times smaller in size. Roughly speaking, if the city of Boston were a galaxy in terms of its power output and size, then a quasar would have the power of the entire United States produced in a region the size of a baseball.

At various times, it has been suggested that new kinds of physical laws or phenomena must be required to explain these objects. But more and more evidence has accumulated that shows a continous range of energetic activity, starting with normal galaxies, going through Seyfert galaxies and other AGN, and joining with the less luminous quasars. Moreover, the hypothesized model of gas falling through a deep gravitational well, probably caused by a massive black hole, together with a net angular momentum in the bottom of the well, seems capable of explaining, at least qualitatively, the full range of observed phenomena, from the energetics to the striking, long-lived "jets" of matter observed to ema-

*Based on a lecture given at the Goddard Workshop on X-ray Astronomy (October 1981).

nate from the centers of these objects. In any case, there does seem to be good evidence for some universality in the mechanisms and physical conditions.

Among the most important issues in understanding QSOs and AGN are (1) the nature of the power source, (2) the radiation processes, and (3) the mechanism for formation and collimation of the jets. We will discuss these issues in turn, giving a brief, model-independent sketch of some of the important theoretical ideas and observations (with more emphasis on our own interests), and suggesting future work. It is possible that no new observations within the foreseeable future will satisfactorily pin down the above issues.

We will be particularly concerned with phenomena that produce X-rays. The clear association of strong X-rays with QSOs and AGN and the rapid time variability seen in X-rays indicate that this region of the spectrum may contain much information about the conditions near the central region of the objects. Of course, simultaneous observations of all regions of the spectrum may provide important clues to the mechanisms at work.

For some recent reviews of this subject, see e.g. Rees (1977,1978,1980), Fabian and Rees (1979), and Bradt (1980).

II. NATURE OF THE POWER SOURCE: ACCRETION ONTO A MASSIVE BLACK HOLE

A. General Considerations

We will tentatively adopt gas accretion onto a massive black hole as the "standard model" for the power source. The

ORIGINAL PAGE IS
OF POOR QUALITY

length scale is then set by the Schwarzschild radius of the black hole, $r_s = 2GM/c^2$, where M is the mass of the hole. We will use the notation $M_8 \equiv M/10^8 M_\odot$. Unless the hole is rotating near maximum angular velocity, we can expect the energy production to peak in the region $r \sim 10 r_s$. The luminosity, L, can be written as

$$L = \epsilon \dot{M} c^2, \tag{1}$$

where ϵ is the efficiency parameter and $\dot{M}$ is the mass accretion rate. The virial temperature, T_V, set by the proton rest mass energy, is

$$T_V = 10^{12} K \, (r/10 r_s)^{-1}. \tag{2}$$

The period of a circular orbit, P, also denoted by t_K, in the Newtonian approximation, is

$$P = t_K = 3 \times 10^5 s \; M_8 \, (r/10 r_s)^{3/2}. \tag{3a}$$

The light travel time across this region is

$$\Delta t_L \equiv r/c = 10^4 s \; M_8 \, (r/10 r_s). \tag{3b}$$

The total mass accreted, M_{acc}, in the active lifetime, t_{life}, is

$$M_{acc} \equiv \dot{M} t_{life} = 10^7 M_\odot \left(\frac{t_{life}}{10^8 yr}\right)\left(\frac{L}{10^{45} erg\, s^{-1}}\right)\left(\frac{\epsilon}{0.1}\right)^{-1}. \tag{4}$$

Both the combination of inferred active lifetimes and observed luminosities, and the sizes and velocity dispersions obtained from optical studies, indicate an M_{acc} and an M in the range $10^6 - 10^9 M_\odot$. We denote the ratio of radial velocity, V_r, to Kepler velocity, V_K, by

$$\beta \equiv V_r / V_K . \tag{5a}$$

The radial infall time, t_r, is then

$$t_r = t_K / \beta . \tag{5b}$$

Note that β is related to the viscosity parameter α of the

ORIGINAL PAGE IS
OF POOR QUALITY

"α-model" disks (Shakura and Sunyaev 1973) by

$$\beta = \alpha (h/r)^2 ; \qquad (5c)$$

where h is the disk thickness at radius r. In "thick accretion disks" we might expect $h \sim r$, so that $\beta \sim \alpha$. The continuity equation gives an ion number density, N,

$$N \simeq 10^{16} \mathrm{cm}^{-3} M_8^{-1} \left(\frac{\epsilon}{0.1}\right)^{-1} \beta^{-1} \left(L/L_{EDD}\right) \left(r/10 r_s\right)^{-3/2} , \qquad (6)$$

where we have normalized L in terms of the Eddington luminosity

$$L_{EDD} \equiv 4\pi G M c m_p / \sigma_T = 10^{46} \mathrm{erg\ s}^{-1} M_8 .$$

We will denote the mass of the proton and electron by m_p and m, respectively, and σ_T is the Thomson cross section. From equation (6) we obtain the "ion scattering depth"

$$\tau_N \equiv r N \sigma_T = 2 \left(\frac{L}{L_{EDD}}\right) \left(\frac{\epsilon}{0.1}\right)^{-1} \beta^{-1} \left(\frac{r}{10 r_s}\right)^{-1/2} \qquad (7)$$

The Thomson scattering depth is

$$\tau_{th} = r (n_+ + n_-) \sigma_T \gtrsim \tau_N \qquad (8)$$

where n_- and n_+ are the electron and positron number densities.

Although τ_N might be expected to approach unity in sources radiating at near the Eddington limit, equation (7), the large optical polarization seen in some QSOs and BL Lac objects (Stein, O'Dell, and Strittmatter 1976; Angel 1978), together with the as yet unobserved evidence of strong Comptonization, suggests $\tau_{th} < 1$. We then obtain an upper limit for the mass in the central, emitting region, M_{em} (Rees 1977)

$$M_{em} \equiv \frac{4}{3} \pi r^3 m_p n < 4 \times 10^{-4} M_\odot M_8^2 \left(\frac{r}{10 r_s}\right)^2 . \qquad (9)$$

Since $M_{em} << M$, most of the mass has already collapsed within the emitting region, arguing against some

non-black-hole models for the central power source. Of course, the majority of QSOs and AGN do not show strong optical polarization.

B. Gas flow models

The principal requirements for efficient conversion of gravitational energy into radiation, $\epsilon \gtrsim 0.1$, are that (a) the viscous dissipation time scale be comparable to or shorter than the radial infall time scale and that (b) the cooling time of the gas be shorter than the radial infall time scale. When angular momentum is present, an accretion disk forms; most accretion disk models proposed satisfy the above requirements. Even when the infalling gas does not have much net angular momentum, a disk may form out to a radius $r \sim 10^2 r_s$ due to the "dragging of inertial frames" by a rapidly rotating black hole (Bardeen and Petterson 1974). Spherical accretion models require rapid dissipation, since the infalling matter is not delayed by angular momentum.

For a review of the types of α-disk models, see Eardley et. al. (1978). These models differ in whether they are gas or radiation pressure dominated, optically thick or thin, equal or unequal temperatures for electrons and ions, and in the source of photons; they have in common the assumption of a spatially constant value for the viscosity parameter α and the assumption of a thin disk $h \ll r$. Recently, Lynden-Bell (1978) and Jaroszynski, Abramowicz, and Paczynski (1980) have considered geometricaly thick disks, but without including the effects of viscosity. These thick-disk models are characterized by an unspecified free function, $l(r)$, the

non-Keplerian angular momentum distribution along the disk. When more of the internal physics of the disk is included, this funtion may be determined. For some recent spherical accretion models, see Maraschi et. al. (1979) and Maraschi, Roasio and Treves (1981).

An alternative possibility, for both the matter surrounding the hole and the method of energy release, is a disk that anchors a large-scale magnetic field, torquing and spinning down a rapidly rotating black hole (e.g. Blandford and Znajek 1977). In this case the energy is supplied by the rotation of the hole. (At an earlier stage, this energy had to ultimately derive from energy made available in gravitational collapse.) Thermodynamically, this process can provide relatively low-entropy energy that is well suited for accelerating electrons to relativistic velocities.

C. Time Variability

Time variability in the X-rays of $\Delta t \sim 10^3 - 10^4 s$ has now been observed in a number of QSOs and AGN. Some of these results are shown in the Table below, where the observed luminosity L_x is typically in the range 2-10 kev.

ORIGINAL PAGE IS
OF POOR QUALITY

Table 1

Source	L_x (erg/s)	$\Delta L_x/L_x$	Δt (s)	$c\,\Delta t$ (cm)
Cen A	1×10^{43}	0.25	7×10^{3}	2×10^{14}
Mk 421	1×10^{44}	2.0	1×10^{5}	3×10^{15}
NGC 6814	1×10^{43}	1.5	2×10^{2}	6×10^{12}
OX 169	1×10^{44}	1.5	6×10^{3}	1.8×10^{14}
3C 273	1.7×10^{46}	0.1	6×10^{3}	1.8×10^{14}
NGC 4151	5×10^{42}	3.0	1×10^{3}	3×10^{13}

The observations for Cen A are from Delvaille et al. (1978), for Mk 421 from Ricketts, Cooke and Pounds (1976), for NGC 6814 from Tennant et. al. (1981), for OX 169 and 3C 273 from Tananbaum (1980), and for NGC 4151 from Tananbaum et. al. (1978). A typical observed fluctuation is shown in Figure 1 for Ox 169.

ORIGINAL PAGE IS
OF POOR QUALITY

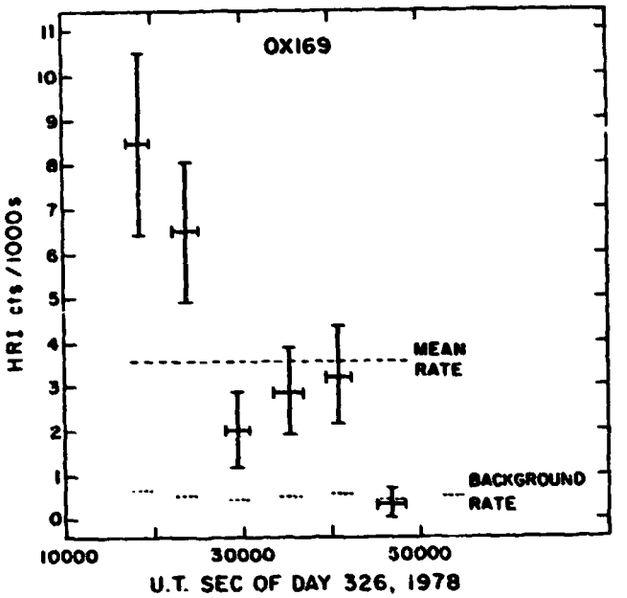

Figure 1: Einstein HRI observations of QSO OX 169, from Tananbaum (1980).

The condition that the size of the emitting region during a fluctuation, ℓ, be smaller than $c\Delta t$ can be written as

$$\left(\frac{\ell}{10 r_s}\right) < M_8^{-1}\left(\frac{\Delta t}{10^4 s}\right). \qquad (10)$$

Since many of the fluctuations in Table 1 have $\Delta L \sim L$, we can assume that a large fraction of the steady emission region is involved in the observed fluctuations, $\ell \sim r$. Note that, within the context of the black hole model, equation (10) and Table 1 are consistent for $M_8 \sim 0.1-10$. It is also important to note that if $M_8 \sim 1$, and the fluctuations are produced at a radius $r \sim 10 r_s$, the observed fluctuation timescales are shorter than an orbital period, cf.

ORIGINAL PAGE IS
OF POOR QUALITY

equation (3). Since gravitational energy cannot easily be released on a timescale $\lesssim t_K$, the energy in an outburst must have been stored.

Some very general arguments may be given concerning the relation between L, ΔL, and Δt. By assuming that the energy in an outburst is produced by material that is associated with opacity, thereby increasing the light travel time across the emission region, Cavallo and Rees (1978) and Fabian and Rees (1979) have obtained the inequality

$$\Delta L < m_p c^4 \epsilon \Delta t / \sigma_T = 2\times 10^{41} \text{erg s}^{-1} \left(\frac{\epsilon}{0.1}\right) \Delta t . \qquad (11)$$

By requiring that the steady luminosity be less than the Eddington limit and using equation (10), Lightman, Giacconi, and Tananbaum (1978) have pointed out the inequality

$$L < 10^{42} \text{erg s}^{-1} \left(\frac{\ell}{10 r_s}\right)^{-1} \Delta t . \qquad (12)$$

Fortunately (for theorists), none of the observations in Table 1 violate the above inequalities, although 3C 273 and NGC 6814 push them. That these inequalities seem to have something to do with the actual data suggest both high efficiencies, $\epsilon \gtrsim 0.1$, and an emission region of dimensions determined by the Schwarzschild radius of a black hole.

Clearly, long-term observations with large area detectors and high time resolution are desireable for further testing the above inequalities and related considerations. The proposed Large Area Modular Array of Reflectors (LAMAR) should be quite suitable for this task.

For time resolution sufficient to study a signal of magnitude $\Delta L/L \lesssim 0.1$, it may be possible to see large blobs of matter spiralling into the black hole. For a circular,

ORIGINAL PAGE IS
OF POOR QUALITY

non-spiralling orbit, we expect to see angular frequencies $\omega = (GM/r^3)^{1/2}$, in the Newtonian approximation, which can be written as

$$\omega = \omega_0 (r/r_0)^{-3/2} \tag{13a}$$

where $\omega_0 = 2\pi/P_0$ is the angular frequency at radius r_0 and P is given in equation (3). Now, for a radiating blob of matter that slowly spirals inward, the observed angular frequency will increase, seen as a low-Q quasi-periodicity, with decreasing period. To obtain an equation for this spiral, we may specify radius in terms of phase or azimuthal angle ϕ, and then integrate the relation $\omega = d\phi/dt$ along with equation (13a) to obtain $\phi(t)$. Signals would be modulated in proportion to $\cos\phi$.

The type of spiral depends on the local, nongravitational physics, particularly the viscous stresses. As a simple example, the "Archimedes spiral" is of the form

$$r = r_0 \left(1 - \frac{\phi}{2\pi n}\right)$$

where n is a free parameter, and yields

$$\phi(t) = 2\pi n \left[1 - \left(1 - \frac{5\omega_0 t}{4\pi n}\right)^{2/5}\right] \tag{13b}$$

Another spiral, which can be related to disk models in the literature, derives from equation (5a), $r^{-1}dr/d\phi = \beta$. If we assume that β is a constant (as given by a number of the α-disk models), then equation (5a) gives the logarithmic spiral

$$r = r_0 e^{-\beta\phi}$$

and yields

$$\phi(t) = \frac{2}{3\beta} \ln\left(1 - \frac{3\beta}{2}\omega_0 t\right)^{-1}. \tag{13c}$$

We mention that simple analytic solutions may also be obta-

ined when β is a general power law in radius, rather than a constant. The above forms for ϕ are only applicable several Schwarzschild radii away from the black hole; similar general-relativistic expressions could be obtained closer to the hole.

Further theoretical work needs to be done on the time variability to be expected by matter inhomogeneities near the black hole. Accretion instabilites (Pringle, Rees, Pacholczyk 1973; Lightman and Eardley 1974; Shakura and Sunyaev 1976) may contribute to the oberved variability. None of these possibilites has yet been modeled with sufficient detail, in the nonlinear regime, to make quantitative predictions.

D. Gas Supply

A clue to the environment of the power source might be gotten from study of the various sources of "fuel", the required conditions for these sources, and the different implications for luminosity evolution. Some of the models that have been proposed for the source of gas are (a) stellar collisions in a dense star system (e.g. Spitzer and Saslaw 1966), (b) tidal stripping of stars in a dense stellar system by a central massive black hole (Hills 1975), (c) infall of intergalactic gas (Gunn 1979), (d) galaxy mergers (e.g. Roos 1981), (e) intragalactic gas released by normal stellar evolutionary processes. One difficulty with models in which gas originates at large radii from the center is the necessity to dissipate a large amount of angular momentum. If the gas is provided by a dense stellar system, and if $M_8 \gg 1$ and

$L \gtrsim 10^{45}$ erg s^{-1}, then it can be shown that the dynamics of the stellar system must be dominated by physical stellar collisions (Shields and Wheeler 1978; McMillan, Lightman, and Cohn 1981).

It seems clear that substantial luminosity evolution occurs in QSOs (e.g. Turner 1979); AGN may be the late time phase of the same evolution. In principle, the gas supply mechanism should have something to do with luminosity evolution. The various mechanisms mentioned above, through their different dependences on the external environment of the QSO or AGN (in (c) and (d)), and on the internal parameters of the black hole and dense stellar system (in (a) and (b)), predict different functional forms for the evolving gas supply rate $\dot{M}(t)$, and hence for the evolving luminosity L(t). A comparison of theoretical models for the gas supply mechanism with a large data set of received fluxes and redshifts might be able to rule out or partly confirm some of the models and clarify the relevant physical conditions. For example, models (a) and (b), with evolution of the stellar-system parameters included, yield late-time asymptotic laws of the form (McMillan, Lightman and Cohn 1981)

$$\dot{M}(t) \propto t^{-p}, \qquad (14)$$

where p=2 for mechanism (a) and p=1 for mechanism (b).

The test of any theory of luminosity evolution is a statistical problem, requiring a value for the cosmological parameter q_0, some information about the distribution of initial conditions or luminosities (the luminosity function), and some information about the distribution of "turn-on

times" of the objects -- in addition to an evolutionary law of the form of equation (14) for a single object. If additional assumptions can be made about these distributions, they may not need to be completely specified a priori. For example, Turner (1979) assumes the luminosity function maintains its shape in time, which, in our context, would allow determination of a value for p for every assumed value of q_0. Unfortunately, Turner's assumption has little physical justification and seems to require some external clock that determines the physical conditions of each new quasar as it is born. In any case, a very dense X-ray Hubble diagram, with the fluxes and redshifts from many QSOs, will be necessary to solve the essentially statistical problem of luminosity evolution. X-rays seem particularly useful here, since QSOs may be readily identified by their X-ray emission, and this emission may constitute the majority of the total luminosity.

A good determination of the local luminosity function would be quite useful in the above project. Figure 2 below shows a luminosity function calculated for a number of nearby objects.

ORIGINAL PAGE IS
OF POOR QUALITY

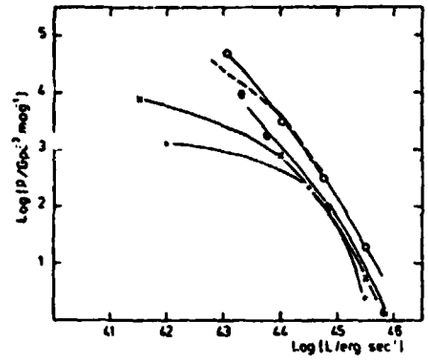

o *X-ray luminosity function of Seyfert galaxies.*
• *Local, optical luminosity function of QSO's.*
• *Space density of Seyfert nuclei (optical).*
× *Radio luminosity function of E+SO galaxies (1.4 GHz).*
+ *Radio luminosity function of E+SO cores (5 GHz).*

Figure 2: Luminosity function of QSOs and AGN. The dashed line is fit from model (d) and additional assumptions. From Roos (1981).

The universality of the forms in Figure 2, especially above about $L = 3 \times 10^{43}$, suggests some universal type of process that establishes the range of conditions for QSOs and AGN.

III. RADIATION PROCESSES

A. Types of Mechanisms

It should be stated at the beginning that, while much of the emission in the radio is easily diagnosed as synchrotron radiation, there is little agreement on how the X-rays and gamma rays are produced. It is almost certain that the conditions in the X-ray emitting region are far from simple. A good fraction of the particles, especially those that ultimately form the observed jets, may be relativistic; there are accretion instabilities; shock waves and magnetic fields

ORIGINAL PAGE IS
OF POOR QUALITY

abound; the emission may be part thermal and part nonthermal. The radiation mechanisms we discuss can be divided into two categories: 1. Power-law electron models and 2. Non-power-law electron models. The second category can be further subdivided into thermal (random motions of electrons dominate emission) and nonthermal (bulk motions of eletrons dominate emission) processes.

As will be shown below, the observed X-ray emission is well fit by a power law of the form

$$I_\nu \propto \nu^{-s} , \qquad (15)$$

where I_ν is proportional to the energy per unit frequency ν.

1. Power-law electron models

If the X-ray emission is synchrotron radiation (requiring electron Lorentz factors $\gamma \sim 10^4$ for equipartition magnetic fields of $B \sim 10^{-4} G$) or relativistic inverse Compton, then a spectrum of the form of equation (15) can be achieved by a power law distribution of electrons of form

$$dn_e/d\gamma \propto \gamma_e^{-r} \qquad (16a)$$

where

$$r = 2s+1 . \qquad (16b)$$

For the observed values of the power-law index, $s \sim 0.7$,see below, we require $r \sim 2.4$. A number of groups (Axford, Leer and Skadron 1977, Bell 1978, Blandford and Ostriker 1978) have investigated first order Fermi mechanisms, whereby particles are accelerated into a power law distribution by the converging flows across a shock front. These mechanisms yield values $r \sim 2$-3 , and have been applied to cosmic rays. It is also quite possible that such processes accelerate

ORIGINAL PAGE IS
OF POOR QUALITY

electrons in the central regions of AGN and QSOs, where strong shocks may be present, and evidently produce an electron index in the appropriate range for synchrotron or inverse Compton radiation. If this is the nature of much of the radiation produced, then high X-ray polarization might be expected. Future X-ray plarization experiments may be quite important in clarifying this possibility.

2. Non-power law electron models

A power law spectrum can also be produced by the scattering of soft photons transmitted through a finite medium of hot electrons, even when these electron do not themselves have a power-law distribution. In this case, a power law results from the absence of an energy scale over a large range of energy. When the electrons have a thermal, nonrelativistic distribution, then s may be related to the Thomson depth τ_{+h} and temperature T (Shapiro, Lightman and Eardley 1976, Katz 1976) $(\tau_{+h} > 1)$

$$s = -\frac{3}{2} + \left(\frac{9}{4} + \frac{4}{y}\right)^{1/2}, \qquad (17a)$$

where

$$y \equiv 4 T_* \tau_{+h}^2 \qquad (17b)$$

$$T_* \equiv kT/mc^2 \ . \qquad (18)$$

When the electrons have a thermal, relativistic distribution, then the corresponding result is (Pozdnyakov, Sobol and Sunyaev 1976) $(\tau_{+h} < 1)$

$$s = \ln \tau_{+h}^{-1} / \ln (16 T_*^2) \qquad (19)$$

We mention that power laws may also be produced by the above process for non-thermal electrons, as long as their distribution is sharply peaked at some "effective temperature." Takahara (1980), Takahara, Tsuruta and Ichimaru (1981) and Maras-

OF POOR PAGE IS
OF POOR QUALITY

chi, Roasio and Treves (1981) have recently considered models using the above radiation mechanism. The soft photons for this process could be generated by cyclotron radiation (Eardley and Lightman 1976; Takahara, Tsuruta and Ichimaru 1981), produced at perhaps 10^{10} Hz and absorbed up to about the 100th harmonic. Soft photons could also be produced by cold dense clouds in pressure equilibrium with the hot phase of the plasma.

A problem with the Comptonization mechanisms above is that the spectral index depends on the parameters τ_{th} and T, which might be expected to vary from one source to another, in contradiction with the narrow range of s actually observed (see D. below). For a scattering model to work in this context, a "characteristic" geometry or structure is required. For example, if the soft photons are externally incident on a region of hot, thermal electrons with a large scattering depth, then the reflected X-rays have a more universal spectrum. Lightman and Rybicki (1979a) have investigated this process and obtain the universal quasi-power law (for $\nu \gg \nu_0$)

$$s = \frac{3}{2} \left(\ln \frac{\nu}{\nu_0} \right)^{-1}, \qquad (20)$$

where ν_0 is the typical frequency of the soft photon input. This power law extends up to photon energies $h\nu \sim kT$ and into the relativistic domain if the electrons have relativistic random motions.

In the above scattering mechanisms, it is the <u>random</u> motion of the electrons that dominates the emission. A closely related mechanism that depends on the <u>bulk</u> electron motion is

ORIGINAL PAGE IS
OF POOR QUALITY

the scattering of intially soft photons by the converging flows across a shock front. This process has been investigated by Blandford and Payne (1981a, 1981b) and gives a high energy asymptotic result

$$s = (M^2 - 1/2)(M^2+6)(M^2-1)^{-2}, \qquad (21)$$

where M is the Mach number of the shock (not to be confused with a mass). This power law extends up to frequencies such that the photon momentum equals that of the electron. Thus, the bulk motions must be relativistic to produce photons of energies $h\nu \gtrsim mc^2$. Since characteristic bulk velocities are only of the order $v \sim 0.3c$ at $r \sim 10\, r_s$, this scattering process may have difficulty in producing relativistic photons. In any case, Equation (20) gives a value of s a little too small and equation (21), for a strong shock, $M \gg 1$, gives a value of s a little too large. It is possible that refinements of these models might be more satisfactory.

Some general statements may be made. Any thermal process must result in a characteristic thermal (exponential) turnover in the spectrum, and possibly a Wien hump, at $h\nu \sim kT$. A shock mechanism should have a cutoff in the spectrum at energies $h\nu \sim mc(\gamma v)_{shock}$ In almost all cases, no turnovers of any kind have yet been seen. <u>It is important to extend X-ray observations up to higher energies, in search of such a turnover</u>. In any case, it is clear that some turnover must occur, since the observed value of $s \sim 0.7$ indicates an infinite total energy if this power law continues to arbitrarily high frequencies.

Changes of the spectrum during luminosity fluctuations

may also provide some information about the emission mechanism. In any scattering model in which soft photon are scattered up to high energies, one expects the spectrum to harden during a fluctuation if the temperature remains constant. Rybicki and Lightman (1979b) and Payne (1980) have investigated the time-dependent versions of Comptonization by thermal electrons within this context. Some attempts have been made to model the observed (or absence of) spectral evolution in outbursts by such processes (e.g. Tennant et. al. 1981). If the Compton cooling time is much shorter than the energy input time, it may be the soft photon source rather than the temperature that remains constant during fluctuations. Guilbert, Ross and Fabian (1981) have investigated this possibility and find that the spectrum first hardens and then softens as the temperature decreases. Over a range of parameters with $y \gtrsim 1$, the time-averaged spectrum has a quasi power-law shape, with $0<s<1$, and a thermal cutoff (with no Wien hump) at the initial electron temperature. It is possible that in many cases, steady state spectra are not relevant and we should always be considering time averages of nonsteady processes. Better spectral resolution during luminosity fluctuations will be helpful here.

There are various pocesses that may be involved in producing the electron distribution, if it is not thermal. In addition to the shock acceleration already mentioned, large scale magnetic and electric fields may be present (Blandford 1976, Lovelace 1976, Blandford and Znajek 1977). Cavaliere and Morrison (1980) have pointed out that the electrons must

ORIGINAL PAGE IS
OF POOR QUALITY

be reaccelerated in crossing the emission region. Defining a parameter q by

$$q = \begin{pmatrix}\text{probability}\\ \text{of scattering}\end{pmatrix} \times \begin{pmatrix}\text{fractional energy loss}\\ \text{per scattering}\end{pmatrix} \qquad (22)$$

$$= (\sigma_T n_\gamma r) \times (\gamma^2 h\nu / \gamma mc^2) .$$

Here n_γ is the photon density

$$n_\gamma = L/(4\pi r^2 c h\nu), \qquad (23)$$

so that

$$q \sim 70\gamma \left(\frac{L}{L_{EDD}}\right)\left(\frac{r}{10r_s}\right)^{-1}. \qquad (24)$$

In any source where q exceeds unity, reacceleration is necessary. Note that q is about equal to the Kepler time divided by the Compton cooling time.

B. Thermalization Time Scales

A principal uncertainty is whether any of the observed X-ray emission from QSOs and AGN is thermal. Such emission requires that the electrons be able to thermalize, via two-body collisions or perhaps collective plasma motions, on a time scale shorter than energy is deposited or radiated and shorter than pair creation when the latter is important. We will consider two-body thermalization below, keeping in mind that collective effects may always be faster.

First we consider the ion thermalization time. The bulk of the released gravitational energy is probably intially deposited into the ions. Taking a value of 25 for the Coulomb logarithm, the ion thermalization time, t_{ii}, via ion-ion scattering is, cf. Spitzer (1962)

$$t_{ii} = (3kT)^{3/2} m_p^{1/2} (5.6\pi N e^4 \ell_n \Lambda)^{-1} = 5\times 10^{17}\,s\; N^{-1} \left(\frac{T}{10^{12}K}\right)^{3/2}. \qquad (25a)$$

Substituting equation (6) into equation (25a), and taking T=

ORIGINAL PAGE IS
OF POOR QUALITY

10^{12} K, we obtain

$$t_{ii} = 5\times10^{7}\,s\left(\frac{L}{L_{EDD}}\right)^{-1}\beta\left(\frac{\epsilon}{0.1}\right)M_8\,, \qquad (25b)$$

and using equations (3) and (5b), we obtain

$$t_{ii}/t_r = 1.6\times10^{2}\left(\frac{L}{L_{EDD}}\right)^{-1}\beta^2\left(\frac{\epsilon}{0.1}\right). \qquad (25c)$$

Here and elsewhere in this section, all quantities will be evaluated at $r=10r_s$ for simplicity, unless otherwise stated. Since energy is deposited into the ions on a timescale t_r, the last ratio must be less than unity for ion-ion collisions to thermalize the ions. Ions may also thermalize by scattering with the electrons. If we denote this timescale by t_{ie}, then

$$t_{ii}/t_{ie} \sim \left(\frac{m}{m_p}\right)^{1/2}\left(\frac{n_- + n_+}{N}\right)\left(\frac{m}{m_p}+\frac{T_e}{T_i}\right)^{-3/2}, \qquad (26)$$

where T_i and T_e denote the ion and electron temperature, respectively. (If the particles are not thermal, then temperatures should be replaced by mean energies.) For $T_i = 10^{12}K$ and $T_e = mc^2 = 6\times10^{9}K$, equation (26) gives $t_{ii}/t_{ie} \sim 50(n_- + n_+)/N$. Thus, a relatively low electron mean energy and the presence of many electron positron pairs may allow the ions to thermalize.

Next we consider electron thermalization via electron-electron scattering. For relativistic electrons, $T_* > 1$, this timescale, t_{ee}, is

$$t_{ee} = T_*^2\,(n_- + n_+)^{-1}(c\sigma_T \ln\Lambda)^{-1} \qquad (27)$$

$$= 2.4\times10^{2}\,s\;T_*^2\left(\frac{n_- + n_+}{N}\right)^{-1}\left(\frac{L}{L_{EDD}}\right)^{-1}\beta\left(\frac{\epsilon}{0.1}\right)M_8\,.$$

The electron cooling time, t_{cool}, may be evaluated in a model-independent way:

$$t_{cool} \equiv \frac{4}{3}\pi r^3 (n_- + n_+)(3kT)/L_- = T_* \left(\frac{n_- + n_+}{N}\right)\left(\frac{m}{m_p}\right)(\beta\epsilon)^{-1} t_K . \quad (28)$$

We then obtain the ratio

$$t_{ee}/t_{cool} \sim 0.1\, T_* \left(\frac{N}{n_- + n_+}\right)^2 \left(\frac{L}{L_{EDD}}\right)^{-1} \beta^2 \left(\frac{\epsilon}{0.1}\right)^2, \quad (29)$$

which must be less than unity for the electrons to thermalize. Equation (29) suggests that in some cases we might expect thermal electrons and in some cases not. As long as the electrons are only marginally relativistic, the electrons should be able to thermalize unless the luminosity is very much below the Eddington limit and there are few electron positron pairs. It seems likely, however, that a fraction of the electrons will be accelerated up to very relativistic energies by some of the processes mentioned above. In this case we would not expect the electrons to be able to sustain a thermal distribution. In any event, as is discussed below, the copious production of e^+e^- pairs prevents the temperature of an optically thin thermal medium from becoming very relativistic.

The time scale for electrons to receive energy from ions, t_{ei}, satisfies

$$t_{ei} = t_{ie} \left(\frac{T_e}{T_i}\right)\left(\frac{n_+ + n_-}{N}\right)$$

Since electrons can cool relatively efficiently, faster than they receive energy from the ions, we may expect the electron mean energy to be much lower than that of the ions, as suggested by Shapiro, Lightman and Eardley (1976).

The conclusion is that there may well be two populations of electrons: a marginally relativistic, thermal population and a highly relativistic, nonthermal population. Unfortunately, it is difficult to calculate the relative proportions of these two populations at the present time.

ORIGINAL PAGE IS
OF POOR QUALITY

ORIGINAL PAGE IS
OF POOR QUALITY

C. Pair Effects

With the high virial temperatures available, cf. equation (2), much exceeding the electron rest mass, it seems likely that some sizeable fraction of the electrons will be at least marginally relativistic, and most detailed models in the literature (e.g. Shapiro, Lightman and Eardley 1976; Maraschi, Roasio and Treves 1981; Takahara, Tsuruta and Ichimaru 1981) do indeed have this character. In such a situation, the effects of electron-positron pair production must be included. When pairs are present, the distributions of radiation and pairs must be solved for self consistently, since photons produce pairs, pairs produce photons, and all the cross sections are, in general, energy dependent. Some recent work in these processes has been done for steady plasmas by Stoeger (1977), Liang (1979), Lightman and Band (1981), Lightman (1981), and Svensson (1981), and in the context of a time-dependent cooling "fireball" by Cavallo and Rees (1978).

As an example, we consider production of pairs by the reaction

$$e^{\pm} + \gamma \longrightarrow e^{\pm} + e^{+} + e^{-},$$

which may dominate when a large photon density is present and the electrons are energetic. This reaction gives a positron production rate

$$\dot{n}_{+} \sim c \sigma_T \alpha_f n_\gamma (n_+ + n_-) \qquad (30)$$

(where α_f is the fine structure constant), only logarithmically sensitive to the particle and photon distributions, as long as the threshold condition

ORIGINAL PAGE IS
OF POOR QUALITY

$$\gamma h\nu > mc^2$$

is strongly satisfied. The pair production time scale for this process, $t_{pe\gamma}$, is

$$t_{pe\gamma} \equiv n_+/\dot{n}_+ = .06\, t_r\, \beta \left\langle \frac{h\nu}{mc^2} \right\rangle \left(\frac{L}{L_{EDD}}\right)^{-1} \left(\frac{r}{10 r_S}\right)^{1/2} \left(\frac{n_+}{n_+ + n_-}\right), \quad (31)$$

where we have used equations (23), (5b) and (3), and the L refers to the luminosity in those photons above threshold. In sources that are not too far below the Eddington limit, we therefore expect this process to have ample time to produce pairs. Since pairs produce more pairs, there may be a non-steady behavior in which, for a short period of time (and with n_γ varying rapidly perhaps), an overabundance of pairs is produced.

It is also of interest to compare the time scale, t_{ann} , for the pair annihilation process

$$e^+ + e^- \rightarrow 2\gamma$$

to the cooling time. (In a steady state the creation time would equal the annihilation time.) If pairs cool before they annihilate, then we might expect to see a feature in the spectrum at the electron rest mass energy, as has been seen (redshifted by 20%) in the March 1979 gamma ray burst event. For QSOs at redshift z, this feature would be at the energy 511 kev/(1+z). For electrons of Lorentz factor γ ,

$$t_{ann} = 16\gamma^2/(27\sigma_T c\, n_-). \quad (32)$$

In addition to comparing equation (32) to equation (28) we can assume a specific cooling mechanism. For example, the time scale for synchrotron cooling, t_{syn} , is

$$t_{syn} = 6\pi mc/(\gamma B^2 \sigma_T). \quad (33)$$

Then, using the expression for the gas and magnetic pres-

ORIGINAL PAGE IS
OF POOR QUALITY

sures, P_G , and P_B , respectively,

$$P_G = \frac{1}{3}\gamma mc^2 (n_- + n_+) \qquad (34)$$

$$P_B = B^2/8\pi , \qquad (35)$$

we can obtain the ratio

$$t_{syn}/t_{ann} = 3\gamma^{-4} (P_G/P_B) . \qquad (36)$$

For equipartition magnetic fields, $P_B \sim P_G$, pairs will evidently cool before they annihilate as long as $\gamma \gtrsim 2$. The absence of an observed annihilation line may indicate the magnetic fields are below their equipartion value. When relativistic pairs annihilate <u>before</u> substantial cooling, the photons produced will at most yield a broad feature at $h\nu \sim \gamma mc^2$, and even this may be dominated by Comptonized bremsstrahlung radiation (Lightman and Band 1981).

Recent work (Lightman 1981; Svensson 1981) has shown that there is a maximum temperature that can be achieved by a thermal, optically thin plasma in equilibrium, dependent on the value of the ion scattering depth, equation (7). A maximum temperature comes about because the pair annihilation rate decreases with increasing temperature and the pair production rate increases as the photon density increases (which increases with τ_N). This maximum (or, equivalently, the maximum τ_N possible for each value of T) is shown in Figure 3. Furthermore, there is generally an enormous range in luminosity over which the temperature remains in the narrow range $0.1 \lesssim T_* \lesssim 1$, with copious pair production at the high end and threshold effects at the low end serving as a thermostat.

ORIGINAL PAGE IS
OF POOR QUALITY

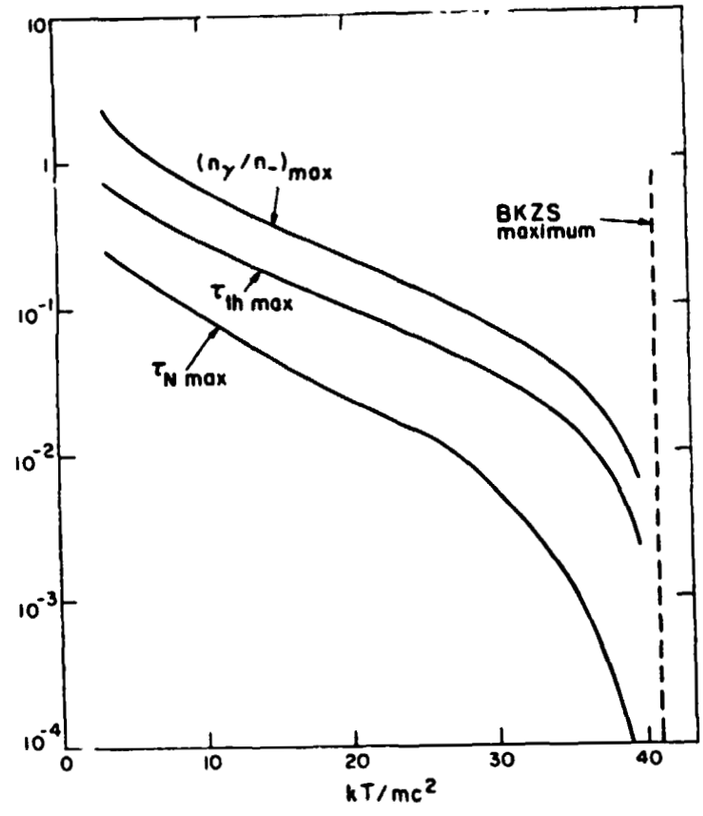

Figure 3: Maximum ion scattering depth, Thomson depth, and photon to electron ratio that can be achieved at each temperature in an optically thin, steady thermal plasma. From Lightman (1981).

Earlier work by Bisnovatyi-Kogan, Zeldovich, and Sunyaev (1971), which did not include finite size effects and neglected photon processes, obtained the maximum temperature $kT=4mc^2$. The magnitude of this maximum is set by the reciprocal of the fine structure constant. In the calculations resulting in Figure 3, only internal sources of photons were included (bremsstrahlung, double Compton, and annihilation). Any additional source of photons, e.g. a soft photon source, must lower the maximum T at each value of τ_N, since photons

ORIGINAL PAGE IS
OF POOR QUALITY

produce but do not destroy pairs in an optically thin plasma. Thus, the maxima shown in Figure 3 are upper limits. Observed spectra with power laws extending above $h\nu > kT_{max}$ indicate that either the plasma is nonthermal or nonsteady.

Another constraint on the mean energy and number density of the pairs arises from requiring that the total system of ions and pairs must be gravitationally confined. This leads to the inequality

$$\gamma \left(\frac{n_- + n_+}{N}\right) < \frac{1}{4}\left(\frac{m_e}{m}\right)\left(\frac{r}{r_s}\right)^{-1} . \qquad (37)$$

When equation (37) is violated, magnetic confinement requires magnetic fields above equipartition strength. Equation (37) must be satisfied on average, but could be violated for short times or over small regions.

We finally mention that photon-photon pair production

$$\gamma + \gamma \rightarrow e^+ + e^-$$

may limit the presence of nard gamma rays. If $h\nu_s$ is the energy of a soft photon and $h\nu_h$ is the energy of a hard photon, then the threshold condition for pair production is

$$\left(\frac{h\nu_s}{mc^2}\right)\left(\frac{h\nu_h}{mc^2}\right) \geq 2$$

The scattering depth to the above reaction is

$$\tau_{\gamma\gamma} = n_s \sigma_T r \qquad (38)$$

where n_s is the number density of "field" photons in a bandwidth $2\nu_s$ around ν_s. Some constraints may be placed on sources for which strong gamma emission is seen, by requiring that the number density n_s be sufficiently small to achieve $\tau_{\gamma\gamma} < 1$, (Herterich 1974). For example, Fabian and Rees (1979) have shown that the observed gamma and X-ray emission

from 3C 273 (see Figure 4) require that the gamma rays be emitted in a region $r > 10^{18}$ cm, much larger than the X-ray emitting region. We mention, however, that the above constraint may be violated if the produced pairs themselves produce more gamma rays that are not substantially downgraded in energy. Since the various reactions that would redistribute the spectrum, e.g. Compton scattering, are energy dependent, it is not clear how large $\tau_{\gamma\gamma}$ can be before the gamma rays would certainly be cut off. This is an area in which more research is needed.

D. Observed Spectra

The composite spectrum of the QSO 3C 273 is shown in Figure 4.

ORIGINAL PAGE IS
OF POOR QUALITY

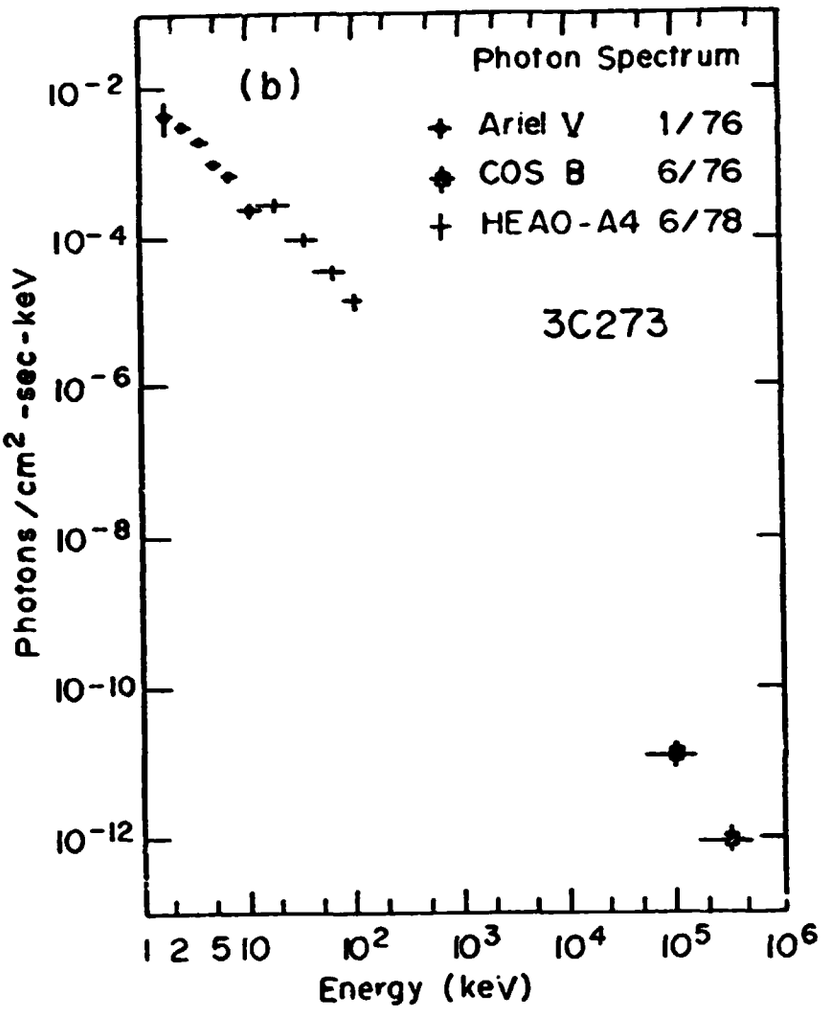

Figure 4: Spectrum of 3C 273. From Bradt (1980)

The portion of this spectrum from 13 to 120 kev is well fit by a power law with s=0.67. This spectrum is actually fairly characteristic of many AGN and QSOs. In Figure 5, we see a histogram of spectral indicies that describe power laws seen in Seyfert galaxies. (The index α in Figure 5 is the same as the s given in equation (15).)

ORIGINAL PAGE IS
OF POOR QUALITY

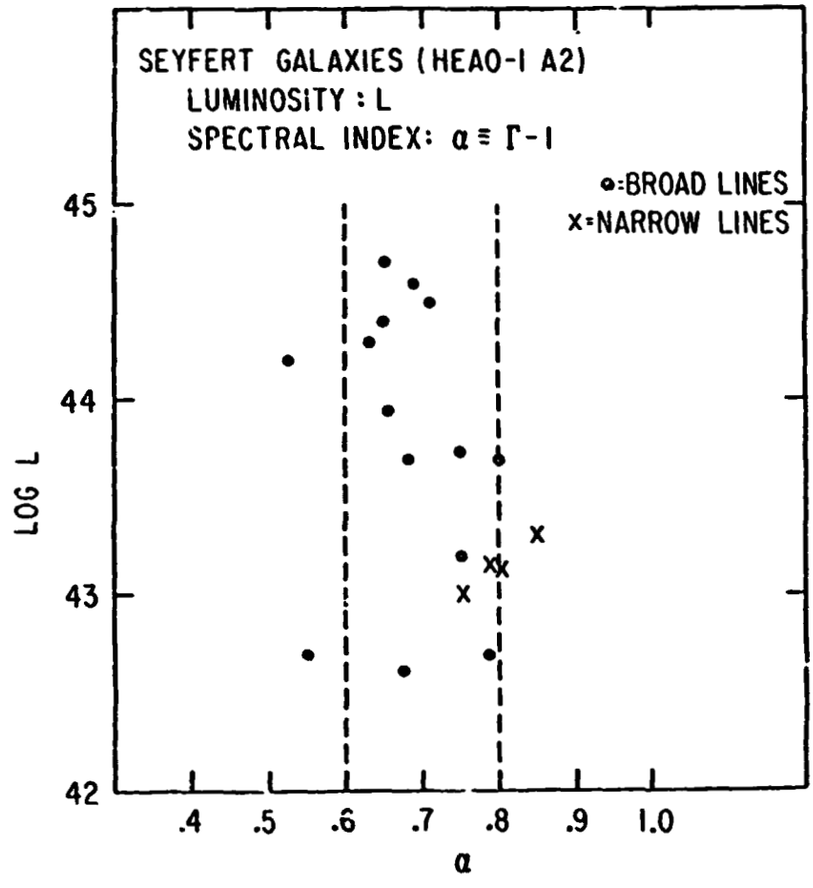

Figure 5: Histogram of spectral indicies observed for Seyfert galaxies. α is the energy index. From Mushotzky (1981).

The data, over an observed range 1-100 kev, are well fit with an $s \sim 0.69$, and a small scatter about this mean $\sigma \sim 0.15$. This result has been reported by Mushotzky (1981) and by Maccacaro, Perola and Elvis (1981). The universality of these spectra is striking and suggests a universal type of emission mechanism, as discussed above. Emission above 1 Mev has also been seen in a few other objects, e.g. NGC 4151 (Schonfelder 1978). It is crucial to obtain spectra of as many QSOs as possible, to confirm the similarity of their spectra to those

of AGN. For this purpose large area detectors like LAMAR should be useful.

From all the above considerations, there is a clear need for observations at higher energies, going into the gamma rays. There may be a wonderland of interesting physics waiting to be learned at $h\nu \gtrsim mc^2$. The proposed satellite GRO should have such a capability. To summarize the needs for such observations:

(1) With a spectral index of s=0.7, most of the total luminosity has yet to be observed! Look back at all the go-or-no-go formulae that contain an L. Until the observations are pushed to sufficiently high energies to see a turnover in the spectrum, we only have lower limits on that L.

(2) When a break, or turnover, in the spectrum is seen at high energies, we will have a much better idea of whether the emission is thermal or nonthermal.

(3) As suggested by the discussion in C. above, a number of interesting effects associated with electron-positron pairs may be seen at energies $h\nu \gtrsim mc^2$. These features and the physical effects they represent may be completely hidden at lower energies.

Observations of the spectra at low energies, especially near the soft X-ray absorption cutoff, $h\nu \lesssim 1$ kev, are also important. Lawrence and Elvis (1981) have recently found good evidence for a correlation between total X-ray luminosity and the ratio of hard ($h\nu$= 2-10 kev) to soft ($h\nu$= 0.5-4.5 kev) components. They interpret this result to indicate that the covering factor of the broad line emission

region over the continuum X-ray source is a monotonically decreasing function of X-ray luminosity. Two possible explanations are that brighter sources, either through radiation pressure or hydrodynamic effects, are able to "blow away" the surrounding absorbing gas, or that the accumulation of absorbing gas is associated with ageing (e.g. through stellar evolutionary processes) and older objects are in the declining phase of their activity (see luminosity evolution in II D. above).

IV. BEAMS AND JETS

It is impossible to consider the subject of QSOs and AGN without mentioning the dramatic, well collimated streams of matter seen emanating from the centers of these objects. These "jets" have been detected in a variety of different objects and in several different wavelengths. Recently, they have been seen in the X-ray band also (e.g. Schreier et. al. 1979, Feigelson et. al. 1981). The opening angle of a jet is typically $\theta \lesssim 10^{\circ}$, the velocity of the matter $300 km s^{-1} < v < c$, and the jet lifetime $t_{life} \gtrsim 10^{6} yr$. See Rees (1980) and Begelman, Blandford and Rees (1981) for recent reveiws of the physics of jets.

Since jets are ubiquitous in QSOs and AGN, whatever produces a jet should be a commonly occuring phenomenon, not requiring special conditions. Furthermore, the jet "remembers" its directionality for a million years or more, so the fundamental beaming mechanim must be associated with a longlived and stable axis of symmetry. Most researchers feel that net

ORIGINAL PAGE IS
OF POOR QUALITY

angular momentum is a key ingredient in defining the required axis, but the detailed mechanism for accelerating matter along this axis is not yet understood.

One of the earliest suggestions was the "twin-exhaust" hydrodynamic model of Blandford and Rees (1974), in which a heat source at the center of a rotating gas cloud, in an external gravitating potential, creates a low density channel of gas that burrows a tunnel along the path of least resistance, the rotation axis. The first detailed hydrodynamical calculations to test the validity of this suggestion have recently been completed by Norman et. al. (1981), and some of their results are shown in Figure 6.

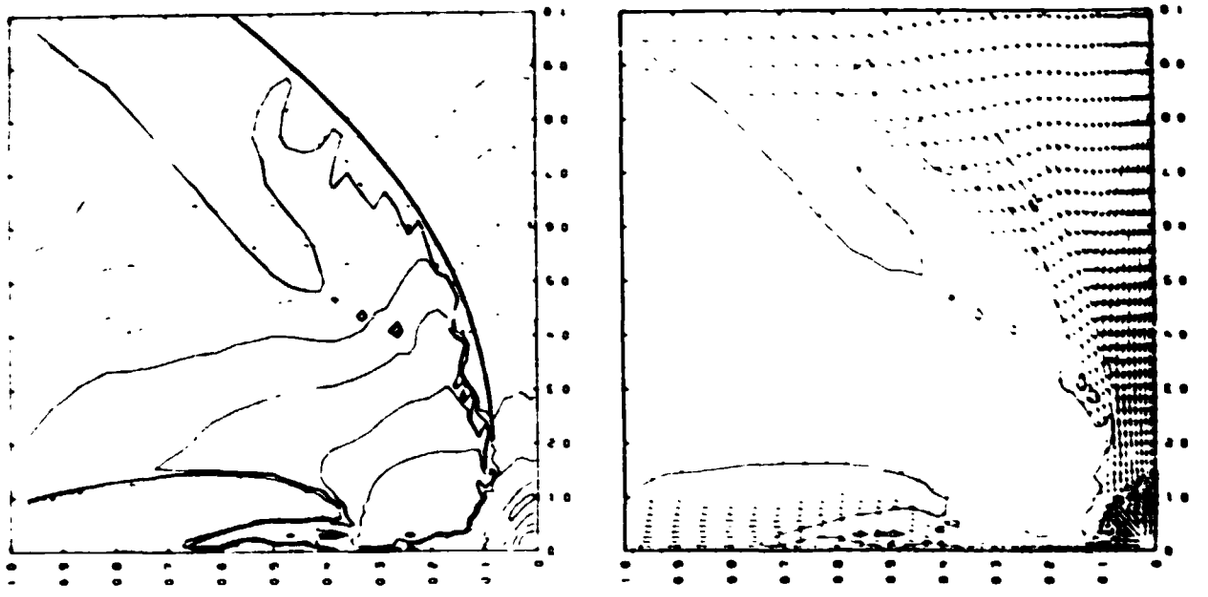

Figure 6a: Density contours of the cloud jet structure at t= 1.6. The solid line is the jet wall. The rotation axis is vertical. Units given in the text. From Norman et. al. (1981).

Figure 6b: The velocity vector field for the jet in 6a. Note the central shock. From Norman et. al. (1981).

The unit of length here is GM/e, where M is the mass of the confining cloud and e is the internal energy per unit mass of the hot, light gas introduced at the center. The unit of time is $GM/e^{3/2}$. The central cavity is at a radius R=0.15. The gas accelerates smoothly to supersonic velocity, terminating in a shock front at R=0.1, at which point collimation begins. These results indicate a cavity-nozzle structure more compact than that suggested by Blandford and Rees (1974). The calculations of Norman et. al. (1981) assume a flat bottomed gravitational potential, rather than a point source potential that would be generated by a central black hole. Future such calculations, perhaps more applicable to the AGN and QSO context, will yield one of the first reliable estimates for the amount of collimation that may be achieved by this mechanism.

Another idea, suggested by Lynden-Bell (1978), is that radiation pressure may accelerate matter along the interior funnel formed by a thick accretion disk (e.g. Jaroszynski, Abramowicz and Paczynski 1980). Some recent kinematical studies by Abramowicz and Piran (1980) suggest that the disk funnel must be extremely narrow for this method to yield adequate collimation, with a ratio of outer to inner disk radii of at least 10^4. No calculations have yet been done to self consistently determine the parameters of the funnel, or to test whether such a narrow funnel is stable in the presence of radiation and matter.

It is quite possible that none of the above mechanisms are able to achieve the observed collimation, and that much

of the collimation is actually achieved far from the black hole, perhaps by large scale magnetic fields. Blandford and Payne (1981c) have recently investigated such a model, in which angular momentum is removed from an accretion disk by magnetic fields that extend to large radii. An outflow of matter along the rotation axis is then possible. At large distances from the disk, the toroidal component of the magnetic field may collimate the matter.

V. CONCLUSIONS

We conclude by recapping some of the important future observations that may clarify the physics of QSOs and AGN.

1. Temporal Resolution. (a) The various theoretical constraints on L, Δ L, and Δ t, when pushed to their limits, may provide our best handles on the efficiencies and emission-region sizes. (b) Spectral changes during fluctuations may help specify the radiation mechanism. (c) Signatures of spiralling matter or accretion instabilities may be revealed by high time resoltuion.

2. Large Sample of QSO Spectra, Intensities, and Redshifts. (a) It is important to learn whether a single universal spectrum describes QSOs as well as AGN. (b) With a large X-ray Hubble diagram for QSOs, we can begin to test luminosity evolution against theoretical models of the gas supply mechanism.

3. X-ray Polarization. Synchrotron radiation typically produces large polarization. Most other mechanisms produce a small polarization.

4. High Energy Measurements $h\nu \sim 1\text{-}10$ MeV. (a) With an observed spectral index $S \sim 0.7$ for AGN, we now have only a lower bound on the total luminosity of most of these objects. (b) The shape of the turnover in the spectrum, at high energies, should tell us about the emission mechanism. (c) A good deal of physics associated with pair production (maximum temperatures of thermal, steady plasmas; annihilation features) can only be observed at energies $h\nu \gtrsim .5$ MeV.

To end with a note of caution: Most of the ideas have been presented as if there were one universal framework for all QSOs and AGN, one basic scenario of gas accretion onto a massive black hole, one dominant radiation process, one mechanism for producing and collimating the jets. I think sometimes, especially in astronomy, we tend to use Occam's razor too much. We should be receptive to the possibility that a number of different processes and mechanisms may be operating in different objects, or perhaps going on simultaneously in the same object -- even though the net results of luminosities, spectra, and variabilities can be squeezed into a common framework.

Acknowledgments

We thank D. Eardley, M. Elvis, P. Gorenstein, J. Grindlay, D. Payne, G. Rybicki, and H. Tananbaum at the Harvard-Smithsonian Center for Astrophysics for useful comments. This work was supported in part by NASA grant NAGW 246.

REFERENCES

Abramowicz, M.A. and Piran, T. 1980, Ap. J. Lett., 241, 17.

Angel, R. 1978, in Proc. Pittsburg Conference on BL Lac Objects, ed. A.M. Wolfe

Axford, W.I., Leer, E., and Skadron, G. 1977, Proc. 15th Int. Cosmic Ray Conference (Plovdiv, Bulgaria).

Bardeen, J. and Petterson, J.A. 1974, Ap. J. Lett., 195, L65.

Begelman, M.C., Blandford, R.D. and Rees, M.J. 1981, Ann. N.Y. Acad. Sci., in press.

Bell, A.R. 1978, M.N.R.A.S., 182, 147.

Bisnovatyi-Kogan, G.S., Zeldovich, Ya.B., and Sunyaev, R.A. 1971, Sov. Astr.-AJ, 15, 17.

Blandford, R.D. 1976, M.N.R.A.S., 176, 465.

Blandford, R.D. and Ostriker, J.P. 1978, Ap. J. Lett., 221, L29.

Blandford, R.D. and Payne, D.G. 1981a, M.N.R.A.S., 194, 1033.

Blandford, R.D. and Payne, D.G. 1981b, M.N.R.A.S., 194, 1041.

Blandford, R.D. and Payne, D.G. 1981c, preprint.

Blandford, R.D. and Rees, M.J. 1974, M.N.R.A.S., 169, 395.

Blandford, R.D. and Znajek, P.L. 1977, M.N.R.A.S., 179, 433.

Bradt, H.V. 1980, Ann. N.Y. Acad. Sci., 336, 59.

Cavaliere, A. and Morrison, P. 1980, Ap. J. Lett., 238, L63.

Cavallo, G. and Rees, M.J. 1978, M.N.R.A.S. 183, 359.

Delvaille, J.P., Epstein, A. and Schnopper, H.W. 1978, Ap. J. Lett., 219, L81.

Eardley, D.M. and Lightman, A.P. 1976, Nature, 262, 196.

Eardley, D.M., Lightman, A.P., Payne, D.G. and Shapiro, S.L. 1978, Ap. J., 224, 53.

Fabian, A.C. and Rees, M.J. 1979, in X-ray Astronomy, ed. W.A. Baity and L.E. Peterson (Pergamon).

Feigelson, E.D., Schreier, E.J., Delvaille, J.P., Giacconi, R., Grindlay, J.E. and Lightman, A.P. 1981, Ap J., in press.

Guilbert, P.W., Ross, R.R. and Fabian, A.C. 1981, M.N.R.A.S. in press.

Gunn, J.E. 1979, in Active Galactic Nuclei, ed. C. Hazard and S. Mitton (Cambridge University Press).

Heterich, K. 1974, Nature, 250, 311.

Hills, J.G. 1975, Nature, 254, 295.

Jaroszynski, M., Abramowicz, M.A. and Paczynski, B. 1980, Acta Astr., 30,

Katz, J.I. 1976, Ap J., 206, 910.

Lawrence, A. and Elvis, M. 1981, Ap. J., in press.

Liang, E.P.T. 1979, Ap. J., 234, 1105.

Lightman, A.P. 1981, Ap. J., in press.

Lightman, A.P. and Band, D. 1981, Ap. J., in press.

Lightman, A.P. and Eardley, D.M. 1974, Ap. J. Lett., 187, L1.

Lightman, A. P., Giacconi, R. and Tananbaum, H., 1978, Ap. J., 224, 375.

Lightman, A.P. and Rybicki, G.B. 1979a, Ap J. Lett. 229, L15.

Lightman, A.P. and Rybicki, G.B. 1979b, Ap. J., 232, 882.

Lovelace, R.V.E. 1976, Nature, 262, 649.

Lynden-Bell, D. 1978, Phys. Scripta, 17, 185.

Maccacaro, T., Perola, G.C., and Elvis, M. 1981, Ap. J., in press.

Maraschi, L., Perola, G.C., Reina, C. and Treves, A. 1979, Ap. J., 230, 243.

Maraschi, L., Roasio, R. and Treves, A. 1981, Ap. J., 1981, in press.

McMillan, S.L.W., Lightman, A.P. and Cohn, H. 1981, Ap. J., in press.

Mushotzky, R.F. 1981, Ap. J., in press.

Mushotzky, R.F., Holt, S.S. and Serlemitsos, P.J. 1978, Ap. J. Lett., 225, L115.

Norman, M.L., Smarr, L. Wilson, J.R. and Smith, M.D. 1981, Ap. J., 247, 52.

Payne, D.G. 1980, Ap. J., 237, 951.

Pozdnyakov, L.A., Sobol, I.M. and Sunyaev, R.A. 1976, Sov. Astron. Lett., 2, 55.

Pringle, J.E., Rees, M.J. and Pacholczyk, A.G. 1973, Astr. Ap., 29, 179.

Rees, M.J. 1977, Ann. N.Y. Acad. Sci., 302, 613.

Rees, M.J. 1978, Phys. Scripta, 17, 193.

Rees, M.J. 1980, in Origin of Cosmic Rays, ed. G. Setti, and A. Wolfendale (Reidel).

Ricketts, M.J., Cooke, B.A. and Pounds, K.A. 1976, Nature, 259, 546.

Roos, N. 1981, PhD thesis, Uinversity of Leiden.

Schonfelder, V. 1978, Nature, 274, 344.

Schreier, E. et al. 1979, Ap. J. Lett., 23:, L30.

Shakura, N.I. and Sunyaev, R.A. 1973, Astr. and Ap., 24, 337.

Shakura, N.I. and Sunyaev, R.A. 1976, M.N.R.A.S., 175, 613.

Shapiro, S.L., Lightman, A. P. and Eardley, D.M. 1976, Ap. J., 204, 187.

Shields, G.A. and Wheeler, J.C. 1978, Ap. J., 222, 667.

Spitzer, L. 1962, Physics of Fully Ionized Gases, (John Wiley and Sons: new York)

Spitzer, L. and Saslaw, W.C. 1966, Ap. J. 143, 400.

Stein, W.A., O'Dell, S.L. and Strittmatter, P.A. 1976, Ann. Rev. Astr. Ap., 14, 173.

Stoeger, W.R. 1977, Astr. Ap., 61, 659.

Svensson, R. 1981, preprint.

Takahara, F. 1980, Prog. Theo. Phys., 63, 1551.

Takahara, F., Tsuruta, S. and Ichimaru, S. 1981, Ap. J., in press.

Tananbaum, H. 1980, ir X-ray Astronomy, ed. R. Giacconi and G. Setti (Reidel).

Tananbaum, H., Peters, G., Forman, W., Giaconni, R. and Jones, C. 1978, Ap. J., 223, 74.

Tennant, A.F., Mushotzky, R.F., Boldt, E.A. and Swank, J.H. 1981, Ap. J., in press.

Turner, E. 1979, Ap.J., 231, 231.

Winkler, P.F. and White, A.E. 1975, Ap. J. Lett., 199, L139.

N82 26063

A European X-ray Astrophysics Mission

J.L. Culhane

Mullard Space Science Laboratory

Department of Physics and Astronomy

University College London

ABSTRACT

An X-ray Spectroscopy, Timing and Variability mission studied by the Eurpoean Space Agency is described. Five instruments (Bragg Spectrometer, Large Area Proportional and Scintillation Counter Detectors, Wide Field X-ray Cameras and a Gamma-Ray Burst Monitor) are discussed and estimates of their performance are given. Their scientific aims are summarised and sample observing programmes are discussed.

ORIGINAL PAGE IS
OF POOR QUALITY

II. THE PAYLOAD, THE SPACECRAFT AND THE MISSION.[1]

A possible payload for the X-80 mission is indicated in table I.

Table I. Scientific Payload for the X-80 Mission

Instrument	Photon Energy Range (keV)	Aims
Large area proportional counter (LAPC) (sensitive area 2500 cm^2)	1.2 - 20	Source variability (< 1 ms to days). Moderate resolution spectroscopy. Monitor for crystal spectrometers
Wide field (WFC) cameras (4 units, FOV ~ 1.4 ster)	2.0 - 20 (imaging) 2.0 - 50 (timing)	Source variability (seconds to years). All sky monitor (days to years). Localisation and study of transients, X-ray and weak gamma-ray bursts
Crystal spectrometer (projected area 6 panels typically 1000 cm^2 each)	4 intervals in the 0.5 - 10 keV energy range (O, Si, S, Fe)	High resolution spectroscopy. Spectral variability. Spectral mapping of extended sources.
Phoswich detector system (sensitive area 650 cm^2)	15 - 200	Source variability and moderate resolution spectroscopy. Cyclotron line spectroscopy.
Gamma-ray burst detector	40 - 130	Localisation of intense gamma-ray bursts and hard X-ray transients

1. Further details may be found in the ESA assessment study document No. SCI(80)5 Paris, June 1980. Science team members were R. Berthelsdorf, A. Brinkman, N. Lund, C. Reppin, R. Rocchia, A. Scheepmaker, H. Schnopper, G. Spada, R. Staubert, M. Turner. ESA staff involved were R. Laine, H. Olthof, B. G. Taylor.

While the payload has the ability to study source variability over a wide energy range by means of the large area proportional counters (LPAC) and the phoswich, it can also monitor instantaneously a field of 1.4 steradian with the aid of the wide field cameras (WFC). The free standing Bragg crystal spectrometers allow high resolution studies of source spectra over selected wavelength ranges. In addition the two broad band systems (LAPC and Phoswich) compliment the Bragg instrument by covering a larger photon energy range, albeit at lower resolution, and by permitting the slope and intensity of the continuous spectrum to be determined.

While missions like the Einstein observatory and the proposed Advanced X-ray Astronomy Facility (AXAF) are general purpose analogues of the Palomar 200" optical telescope, it is clear that the huge cost of such systems means that their number will inevitably be restricted. However some enormously exciting physics can be undertaken by the study of the 300-400 brightest sources with a mission of the kind described here. This possibilitiy has been recognized by several different nations and space agencies. Thus, in a time of fiscal stringency, it would seem appropriate that the possibilities of joint action in this area be examined carefully.

Following the Uhuru, Ariel V and HEAO-1 survey missions and the outstanding results that have been obtained with the Einstein obsrvatory, it has become apparent that observations at X-ray wavelengths are of fundamental importance in astronomy. X-rays are generated in high temperature ($T > 10^6$ K) plasmas or by the interactions of energetic charged particles with magnetic fields or lower energy photons. In order to understand the physics involved, it is necessary to proceed with the detailed study of the brighter X-ray sources. This work should include a complete investigation of source variability over a wide spectral range together with high resolution spectroscopic observations of

the high temperature plasmas that give rise to X-ray emission in many galactic and extra-galactic sources. Furthermore, it is the combination of spectroscopic and photometric observations in a single mission that can lead to major advances in our understanding of the physics of these sources. We will return to a discussion of the individual instruments later after a description of the spacecraft and some preliminary ideas on mission operations have been presented.

The principal parameters of the mission are given in table II. The spacecraft is compatible with half of the Ariane launcher capacity. Thus launching costs can be reduced if a suitable partner can be found. At a height of 600 km, the mission lifetime will be at least 3.5 years. The solar array is designed for an "end of life" capability of 385 watts. Since the most demanding angular

Table II Details of the X-80 Mission

ORBIT:	Circular, 600 km, 0° inclination
LAUNCHER:	ESA Ariane
MASS:	Instruments 500 Kg Spacecraft 400 Kg
DIMENSIONS:	Height ~ 3.2 m Diam. ~ 2.3 m max.
ATTITUDE CONTROL:	3 Axis inertia wheel Target acquisition to ± 5' Attitude determination i) Star sensors to ± 0.5' ii) Coarse + fine sun sensors iii) Gyros Orientation - anywhere within ± 30° of plane perpindicular to solar vector.
POWER REQUIREMENT:	~ 200 watts total
DATA SYSTEM:	Mean rate - 44 K bits/s Peak rate - 250 K bits/s Downlink rate - 700 K bits/s Mass memory - 250 M bit Data dump - 1 per orbit at Kourou Ground link - 8 K bits/s to ESOC, Darmstadt

resolution requirement is about 5' as set by the Bragg spectrometer and the WFC, the attitude control and measurement system parameters indicated in the table are more than adequate. Inertia wheel angular momentum is unloaded by a cold Nitrogen gas system. Use of a large bubble memory can allow peak data rates of 250 K bits/s to be sustained from individual instruments for periods of up to 20 minutes.

The proposed 600 km equatorial orbit will provide an environment of low and stable particle background. The spacecraft will not pass through the radiation belts or the South Atlantic magnetic anomaly. Since the spacecraft is in near-earth orbit, significant regions of the sky are obscured from view at any given time. However the large slew capability will allow the pointing axis to be moved rapidly between sources. Ground stations within 10° of the equator can be used. While both Malindi in Kenya and Kourou in French Guyana are available, the mission has been planned on the basis of 6 minute contacts with Kourou occurring once per orbit.

Although the solar array is a fixed structure, the sun-pointing face can be tilted by up to ± 30° off the sun-line, and still provide adequate power. With a 3-axis stabilised spacecraft, which is free to roll about the solar vector, the narrow field instruments can view anywhere within a band on the sky, which is 60° wide by 360°. The viewing band rotates around the sky with the Earth's motion and the whole celestial sphere is accessible within a six month season. Thus, any source can be observed for up to 2 months at a time, every half year, and observing is then only interrupted for a period in the orbit when the earth obscures the instrument field of view.

The optical axes of the narrow field instruments are perpendicular to the plane containing the WFC and the sun. The optical axes of the cameras are 60

degrees wide. The fields of the 4 cameras are adjacent to one another. The ± 30° solar off-set in the plane of the cameras allows us with the proposed lay-out to view the whole sky except for ± 30° around the sun. This cone can in principle be reduced further, by shifting the cameras nearer to the sun but in view of thermal problems, related to the solar illumination of the mask, the present design is constrained to ± 30°. The full width zero response (FWZR) of the WFC is four times 34 degrees squared i.e. 11% of the celestial sphere. With one attitude change per orbit, 9 orbits are needed to scan the whole sky.

As the satellite is in a low earth orbit, large regions of the celestial sphere are obscured by the earth at any instant. When a narrow field instrument target is occulted by the earth, it would be useful to switch to another one to maximise observation time. However such manoeuvres, typically 1-2 radians, should be accomplished in a few minutes. It should be noted however that the proposed lay-out of four wide field cameras has the advantage that in no situation are all the cameras obscured by the earth.

The organization of the ground operations is illustrated in Figure 1. During spacecraft contacts with Kourou, data from the on-board bubble memory are recorded at the station while commands for spacecraft and instrument reconfiguration and attitude manoeuvring are uplinked. After each pass, data are transmitted to the ESA control centre (ESOC) at Darmstadt by means of a permanent 44 k bit/s link. However this link has yet to be implemented. The present 8 k bit/s link would in fact be entirely adequate. At ESOC, after quick look analysis, data from the individual instruments will be sent to the appropriate institutes by telephone lines.

ORIGINAL PAGE IS
OF POOR QUALITY

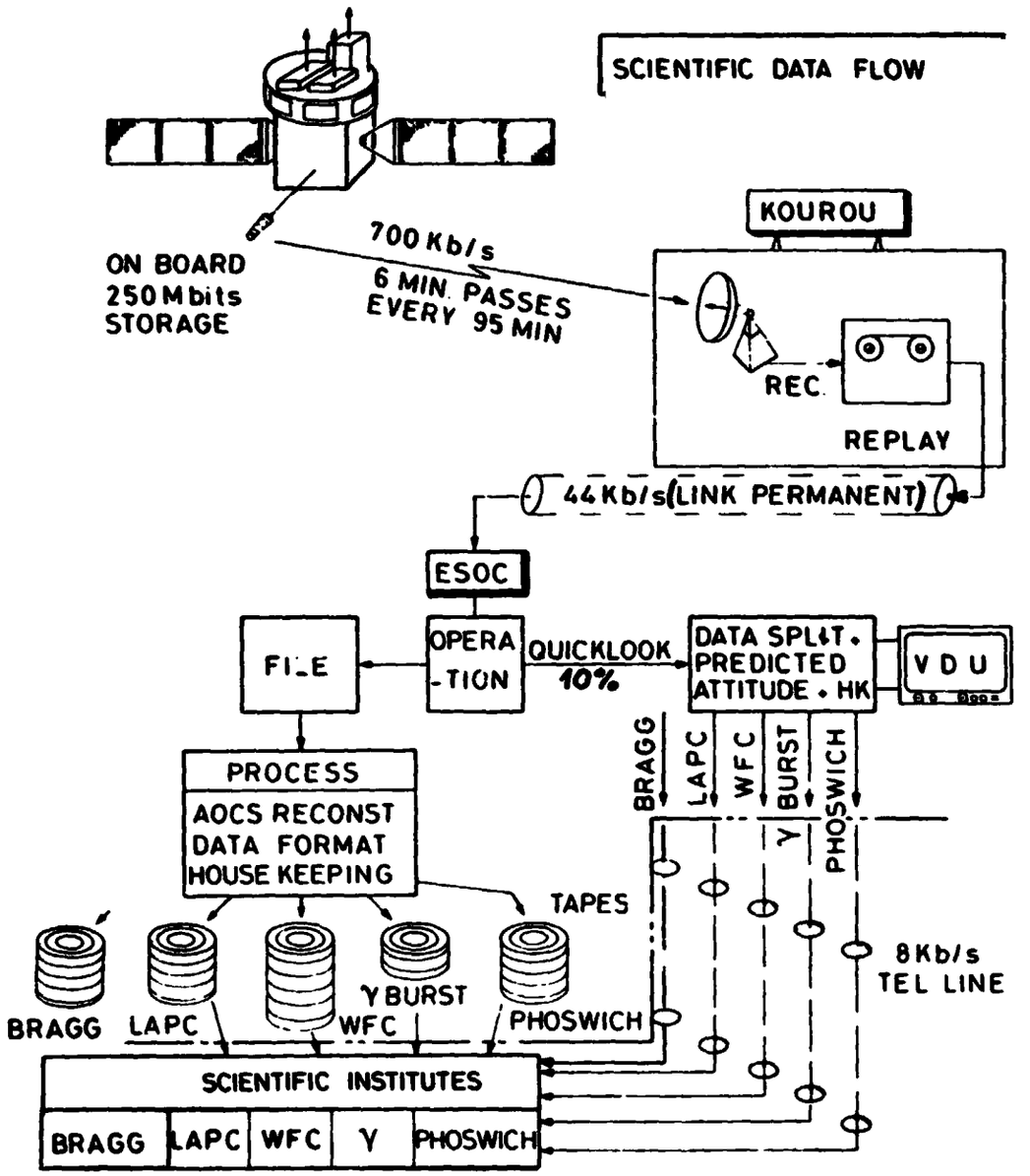

Figure 1.

Data flow on the ground after its reception from the Spacecraft.

ORIGINAL PAGE IS
OF POOR QUALITY

III. THE BRAGG SPECTROMETERS

High resolution spectroscopy permits us to study the physics of energetic coronal and photoionised plasmas which are known to be present in many sources both inside and outside the galaxy. Measurements of emission line intensities in these plasmas will allow estimates of gas temperature density and ionisation state, element abundance and gas velocity to be made for a variety of objects. The detection of absorption features can provide similar information in cases where intense compact X-ray sources are imbedded in extended gas clouds.

The proposed instrument includes four separate crystal spectrometers sensitive in the energy range 0.5 to 10.0 keV to spectral features arising from cosmically abundant elements that are ionised in 10^6 K to 10^8 K plasmas. The range of temperatures covered by the spectrometers is shown in Figure 2. The role of the broad band detectors is also indicated. It is clear that these detectors complement the spectrometer by their sensitivity to high temperature plasma over a wide range of temperatures.

Figure 2.
Line intensity plotted against electron temperature for the strong transitions in a number of important ions.

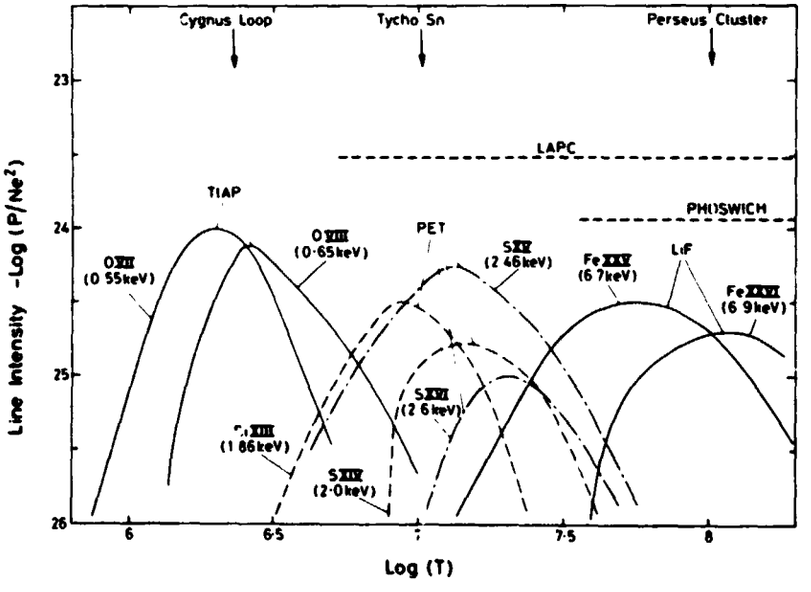

ORIGINAL PAGE IS
OF POOR QUALITY

The crystal panels are spherically curved and focus onto two dimensional position sensitive detectors. Curvature in the plane of dispersion establishes a wavelength scale on one dimension of the detector. Curvature in the other plane permits the mapping of extended sources and minimises the detector active volume for each wavelength resolution element. Focussing spectrometers have been discussed by Dasgupta (1961) in the neutron diffraction context and by Schnopper (1966). A detailed description of the conical focussing geometry was presented by Woodgate (1973). The advent of position sensitive detectors allowed the development of parallel entry systems (Rapley et al., 1977) which eliminate the need for scanning in wavelength. This provides for much more reliable data analysis and interpretation, particularly for rapidly varying sources.

The design of spherically curved spectrometers is discussed by Griffiths elsewhere in these proceedings. We will therefore simply list, in table III the parameters of the system chosen for the X-80 mission. The wavelength

Table III Spectrometer Parameters

Line System	Crystal	2d (Å)	Wavelength Range	Resolution	Projected Area
Iron	LiF (220)	2.85	1.7-2.0 Å	2.3 mÅ	1440 cm^2
Sulphur	PET 1	8.73	4.8-5.5 Å	4.0 mÅ	930 cm^2
Silicon	PET 2	8.73	6.1-6.8 Å	6.1 mÅ	695 cm^2
Oxygen	TlAP	25.76	18.-22. Å	92 mÅ	1470 cm^2

resolution is set by crystal properties on the assumption that a spatial resolution of better than 1 mm can be achieved in the detectors. A number of important transitions are listed in table IV. A spectrometer of this kind can be

ORIGINAL PAGE IS
OF POOR QUALITY

Table IV Important Transitions

Crystal	Transitions and Wavelengths			
	$1s^2$-$1s2p\,^1P$	$1s^2$-$1s2p\,^3P$	$1s^2$-$1s2s\,^3S$	$1s$-$2p\,^2P$
LiF	Fe XXV (1.852Å)	Fe XXV (1.857Å)	Fe XXV (1.867Å)	Fe XXVI (1.790Å)
PET 1	S XV (5.039Å)	S XV (5.067Å)	S XV (5.099Å)	S XVI (4.729Å)
PET 2	Si XIII (6.650Å)	Si XIII (6.690Å)	Si XIII (6.737Å)	Si XIV (6.182Å)
TIAP	O VII (21.602Å)	O VII (21.804Å)	O VII (22.100 Å)	O VIII (18.969Å)

Figure 3.
An Fe absorption edge in the spectrum of 4U 0900-40. Data from the GSFC OSO-8 spectrometer (Becker et al., 1978).

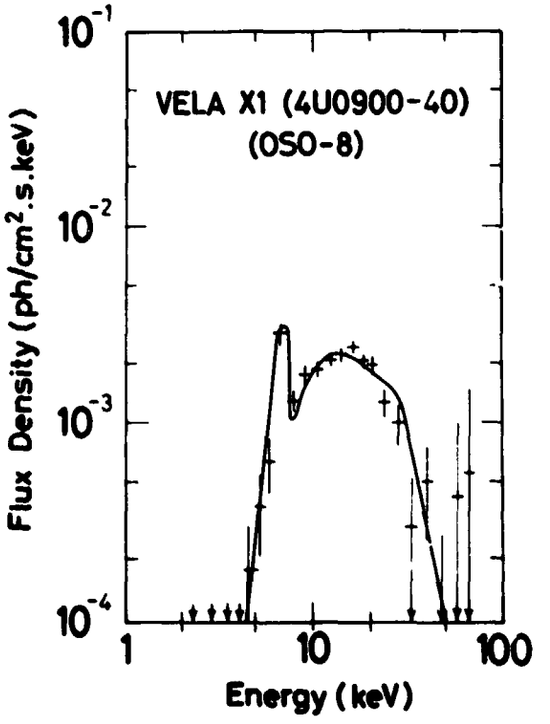

used for a large number of astrophysically important observations. Figure 3 shows a spectrum of the source 4U 0900-40 (Vela XI) obtained with the OSO-8 proportional counter spectrometer (Becker et al., 1978). A deep iron absorption edge is apparent. However the proportional counter ($\frac{E}{\Delta E} < 10$) can not establish the energy of the feature with sufficient precision to allow the Fe ionisation stage to be deduced. Alternatively photoionisation interactions by X-rays from the compact source with the surrounding gas may give rise to a range of ionisation stages the dynamic behaviour of which could supply important clues to the geometry and distribution of the accreting gas. It is clear also that precise determination of fluorescent emission line wavelengths can provide information of similar value though in this case, broadening due to Compton scattering or mass motions could render the observation more difficult for the crystal spectrometers to undertake.

A similarly exciting possibility may exist for the study of the gas distributed around the nuclei of Seyferts and other active galaxies. Evidence for the presence of variable iron emission features in the spectra of two active galaxies (Hayes et al., 1980, Hall et al, 1981) has been obtained with proportional counter detectors. Models for the production of this emission involve fluorescence emission from the gas in the broad line region (Hayes et al.) or recombination radiation from a hypothetical shell of fully ionised gas that exists very close to the nucleus (Fabian and Ross, 1981). In the former case, an increase in the luminosity of the nucleus (Lx) leads to an increase of the fluorescent line intensity. For the latter model, a reduction in Lx is required to permit the iron nuclei to recombine with electrons. In either case identification of the appropriate model and understanding the interaction of the active nucleus with its surroundings requires that individual lines be resolved and the wavelengths identified.

The role of X-ray emission line observations in the spectra of extended cluster sources is too well known to require much discussion here. However there is a tendancy to dismiss observations of the intra-cluster medium because difficulties with understanding the evolution of the clusters and their media render the use of these objects for cosmological testing much less simple than was once supposed. While this is undoubtedly true, it merely emphasises the tendancy of all cosmological testing techiques to become more complicated as they become better understood. Meanwhile a wealth of information on the formation and evolution of clusters and galaxies would be available from the study of density and temperature variations in intra-cluster media if the X-ray observations of adequate wavelength resolution and sensitivity could be carried out.

Finally it is obvious that the X-ray line emission from supernova remnants can provide a wealth of diagnostic information on the temperature, density, ionisation state and element abundances of the hot plasma. In particular there has been much discussion of the latter two points. Given the presently available low resolution Fe emission data from proportional counters, it is not possible to establish unambiguously the relative intensities Fe XXV and Fe XXVI features which, together with temperature information, would allow departures from ionisation balance to be recognised. Work at longer wavelengths with the Einstein FPCS clearly indicates the possibilities (Winkler et al., 1981) but emphasises the need for good wavelength resolution.

The potential of the spectrometers can be judged from the data presented in Figures 4a and b where minimum detectable line fluxes (at 5 σ) are plotted against continuum flux with observation time as a parameter. In Figure 4a, cluster sources are treated as both compact (i.e. 5' by 5') and extended targets. The broad line case for Cas A assumes expansion at the current shock velocity.

ORIGINAL PAGE IS
OF POOR QUALITY

The sensitivities of all four systems are more than sufficient to achieve the aims outlined in previous paragraphs. In particular the Oxygen line spectrometer (Figure 4b) is 100 times more sensitive than the Einstein FPCS.

The scientific role of the Bragg Spectrometers may be summarised in the following manner.

Study: High temperature (10^6 - 10^8K) and photo-ionised plasmas in emission and absorption (estimate temperature, density, ionisation state, abundance, gas velocities, redshifts).

Deduce: Intra-cluster gas origin, gas motion around active nuclei, binary system gas dynamics, ISM density and composition, SN element production, stellar corona and active star gas dynamics, extra galactic distances.

Observe: QSO's and other active galaxies, Clusters of galaxies, X-ray binaries, Supernova remnants, Active stars and stellar coronae, X-ray bursters and transients

Figure 4.

Minimum detectable line strength plotted against continuum flux for two of the four spectrometers

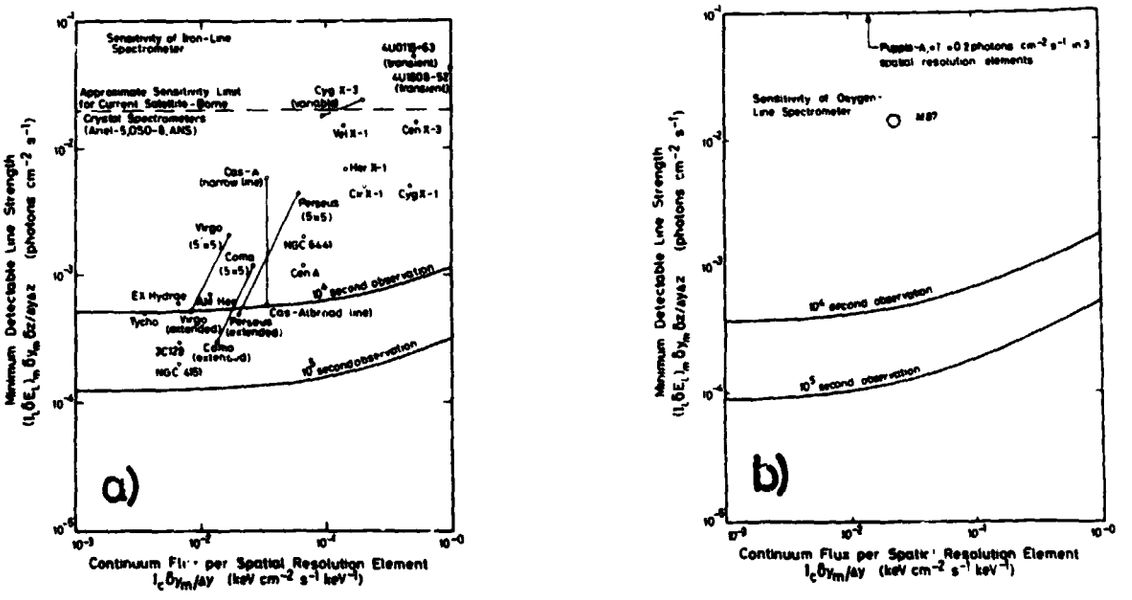

a) Iron line instrument.

b) Oxygen line instrument

IV. THE WIDE FIELD CAMERAS (WFC)

The Wide Field Camera is a Dicke or transform camera (Dicke, 1968) comprising a mask with a random array of holes located above a position sensitive detector. X-ray sources will cast shadows of the mask onto the detector. Correlation or deconvolution analysis is used to reconstruct an image of the sky field. An ideal mask pattern will have a flat spatial frequency response out to the frequency represented by the 'unit' hole in the mask. Deconvolution of the image will then reconstruct the sky brightness distribution. The Wide Field Camera is therefore able to provide high sensitivity over a wide field of view due to the large 'open' area of the mask, combined with good angular resolution.

Four cameras are arranged so as to allow maximum sky access. Rotation of the spacecraft around the Sun axis, combined with the $\pm$ 30° allowable off-set, makes nearly the whole sky available to the WFC array at any one time, except for a cone of 30° radius around the Sun. The field of view of the WFC system is 1.4 ster. The characteristics of the camera are given in Table V. The mask is 60 cm x 60 cm and contains a pattern of 0.5 mm square holes based on a Pseudo-Random-Noise sequence, repeated once in each dimension. It is mounted a distance of 48.6 cm from the position sensitive detector which has a FWHM position resolution of 0.5 mm in both dimensions over an active area 30 cm x 30 cm. For a perfect position sensitive detector the angular resolution would be set by the mask hole size and the detector-mask separation, yielding an angular resolution of 3.4 arc minutes. In the present case the resolution of mask and detector are equal giving an optimised angular resolution of $\sim$ 5 arc minutes.

The resolution degrades slightly off axis due mainly to the deeper penetration of energetic photons. Due to the predominance of low energy photons in the spectra of most sources the effect is slightly (resolution - 5 arc minutes).

The above configuration, with a repeated mask pattern and a collimator gives in principle perfect coding of the image, even for sources at the edge of

Table V. Characteristics of Wide Field Cameras

Configuration	4 wide field cameras
Field of view	34° x 34° FWZR per camera
Solid angle	0.35 ster per camera
Angular resolution	5 arc min
Error box area	1(arc min)^2 limited by camera internal alignment
Energy range: imaging	2.0 - 10 keV full field 2.0 - 20 keV centre of field
timing	2.0 - 50 keV
Energy resolution	20% at 6 keV
Sensitive area	320 cm^2 per camera (mask transmission, 50%)
Background (diffuse)	150 cts/sec per camera
Mask area	60 cm x 60 cm
Detector area	30 cm x 30 cm
Gas filling	Xe/CH_4 at 2 atm.
Window material	125 micron beryllium
Camera alignment	60° ± 1° between cameras
Total mass	126 kg

the field of view (Proctor, 1978). The mask can be constructed by etching the pattern into a stainless steel foil, or by electro-deposition of nickel. The position sensitive detector measures 40 cm x 40 cm 7.5 cm and is sealed with a 125 micron Be window. The Xe/CH_4 filling gas limits penetration of high energy photons. The detection efficiency exceeds 10% over the range 2 to 50 keV and spectra can be obtained throughout. Positioning is limited to the ranges 2 to 10 keV due to photon penetration problems at the edge of the field of view; in the center of these fields of view however a position resolution of a few arc minutes can be achived over the energy range 2 to 20 keV.

ORIGINAL PAGE IS
OF POOR QUALITY

The sensitivity of instruments of this type has been discussed by many authors (Dicke 1968, Palmieri 1974, Gunson 1976). It depends on area, background and observing time. Because of the large field of view the background is dominated by the diffuse X-ray emission at high galactic latitude and by the contribution of strong sources in the galactic plane. The charged particle component can be reduced to an insignificant level. The minimum detectable source strength at a 5 sigma confidence level is shown in Figure 5 as a function of the observation time for a high galactic latitude and the galactic center region. The instruments ability to observe intensity changes in the source is shown in Figure 6a.

Figure 5.

Wide Field Camera Sensitivity plotted against integration time

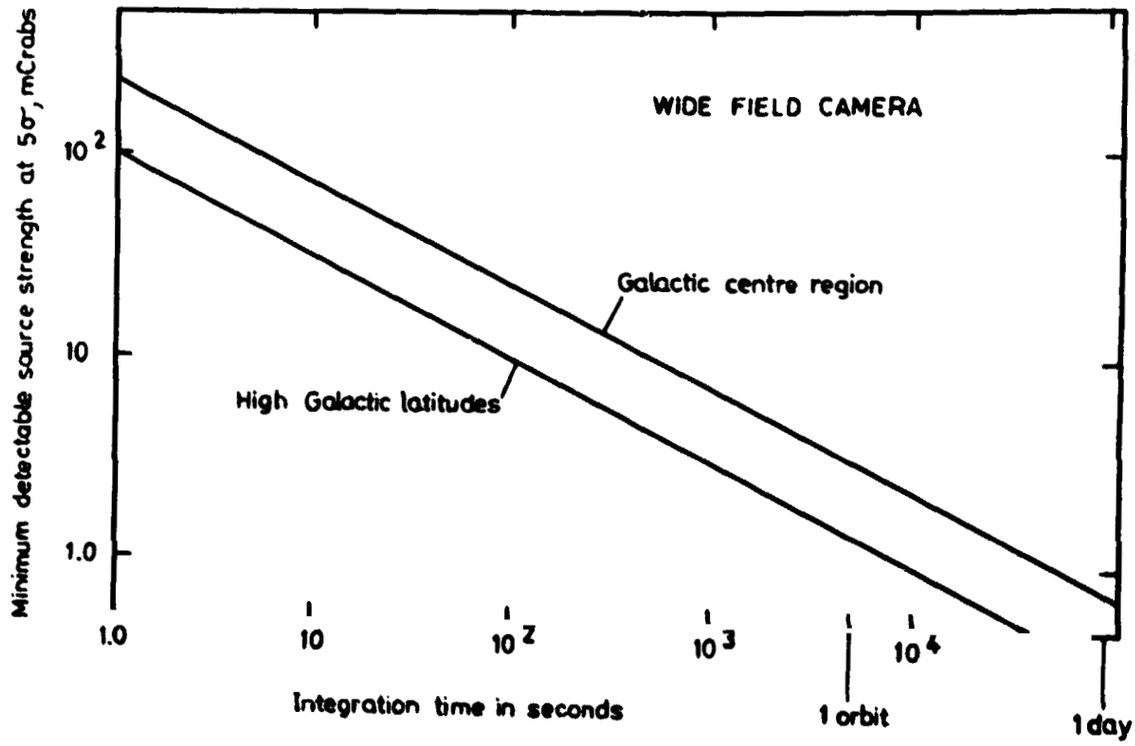

ORIGINAL PAGE IS
OF POOR QUALITY

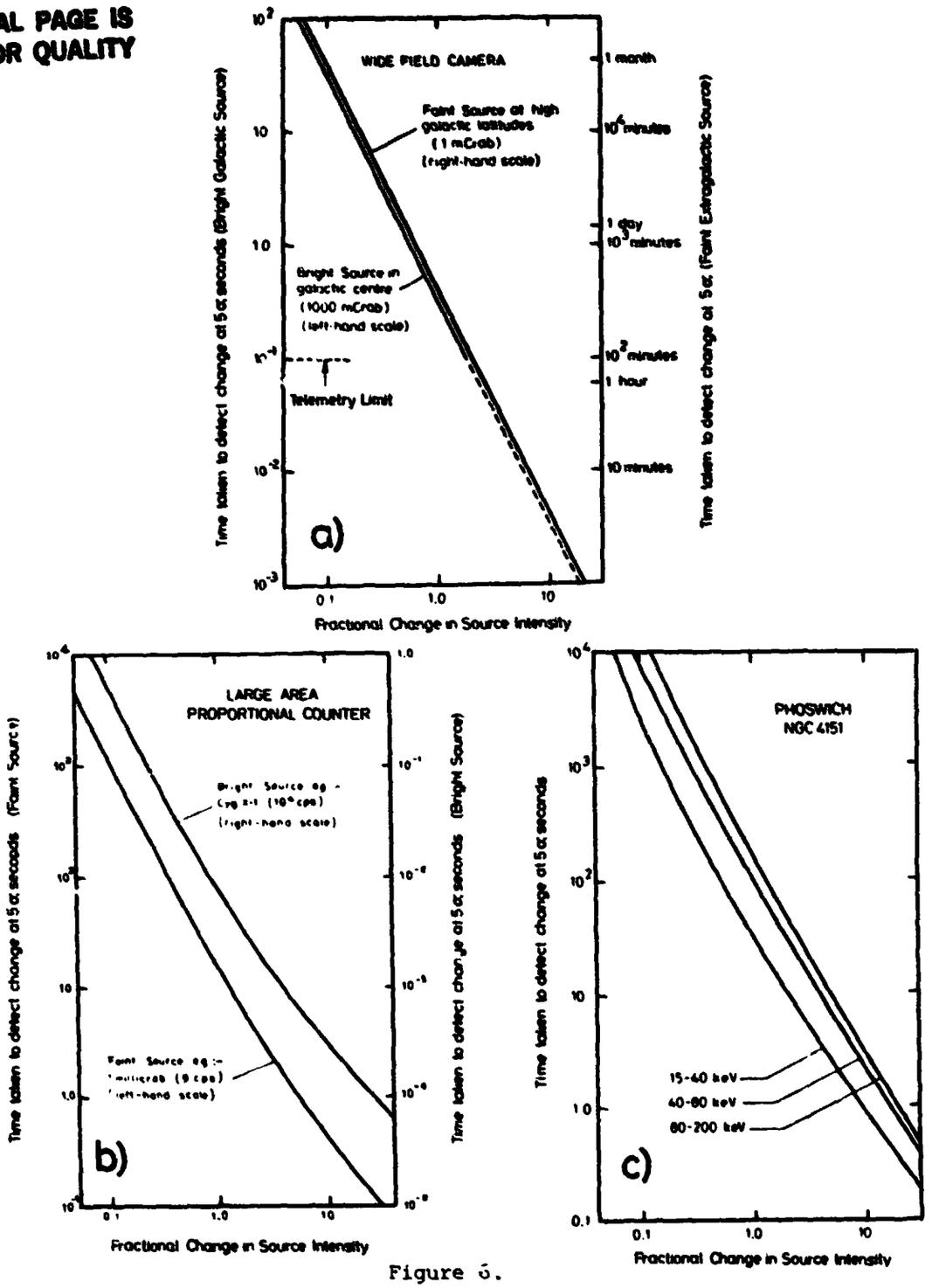

Figure 6.

Time taken to detect a specific fractional change in source intensity a) Wide Field Camera, b) Large area proportional counter and c) Phoswich.

ORIGINAL PAGE IS
OF POOR QUALITY

However the performance of the instrument is best illustrated by simulation. Deconvolved images of the galactic centre region and a reigon of high galactic latitude (Coma) are shown in Figure 7.

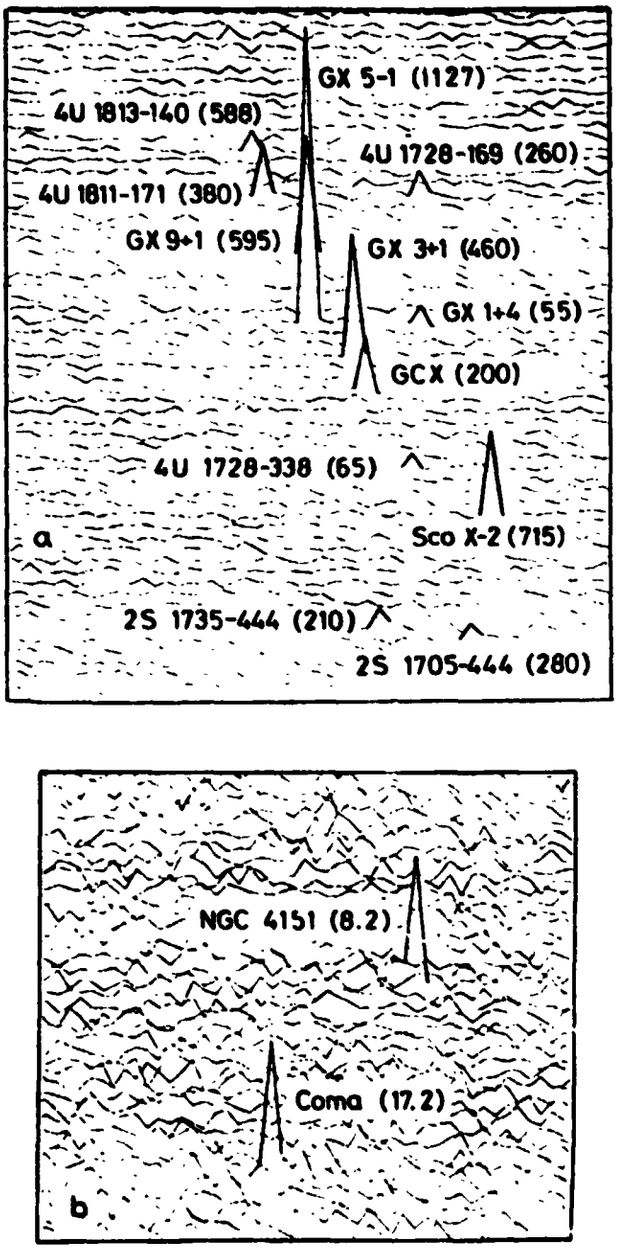

Figure 7.
Simulated performance of the WFC(for a) a 100s observation of the galactic centre region and b) 5000s observation of the Coma region. Source intensities (MiliCrab) are shown in brackets.

Since the scientific role of a wide field camera system is rather easy to understand we will simply sumarise the appropriate scientific aims.

Study: Galactic and extragalactic X-ray variability, long term behaviour of X-ray binaries, X-ray transient and burst activity.

Deduce: Properties of active galactic nuclei (size, energy release), X-ray masses, neutron star, white dwarf, or black hole presence, accretion disk properties, transient and burst source mechanisms.

Observe: QSO's and other active galaxies, X-ray binaries, X-ray transients, X-ray bursters, Galactic bulge sources, Active stars.

V. THE LARGE AREA PROPORTIONAL COUNTER (LAPC)

The instrument that covers the energy range 1.2 to 20 keV is a large area array (0.25 m^2) of sealed proportional counters. The energy resolution of proportional counters is moderate (19% at 6 keV) compared with other medium energy detectors (gas scintillator 10% at 6 keV, solid state detectors 3% at 6 keV) however, they have a lower ultimate background noise, can be produced with thin windows, are simpler and cheaper to build, and have by far the lowest mass per unit sensitive area. In addition their energy resolution has been demonstrated to be adequate for broad band spectroscopy.

The characteristics of the LAPC are given in Table VI. The modules are mounted, via two pivots and a tilt mechanism, to the spacecraft. This enables a ± 2° offset from the source for background determination. The detectors have a gas depth of 4 cm. The 37 micron beryllium window is supported against the internal pressure of 2 atmospheres by a collimator formed from Hexcell material giving a circular field of view of 45' diameter (FWHM). The gas used will be mainly Argon for efficient background rejection but will contain sufficient Xenon to give 10% efficiency out to 20 keV. Two anode layers will be used,

ORIGINAL PAGE IS
OF POOR QUALITY

these will incorporate guard wires, end guard cathodes (Bailey 1978) and when used in anticoincidence will give 5 sided protection to the upper layer for low background observations. In addition risetime discrimination will be employed for efficient background rejection. For bright sources the layers will operate in series to give a wider energy range.

Table IV. Characteristics of the Large Area Proportional Counter Array

Configuration	3 modules, 2 made up of 2 detectors and 1 made up of 4 detectors
Sensitive area	0.25 m^2
Field of view	45' x 45' FWHM
Energy range	1.2 - 20 keV at > 10% efficiency
Rate from Cyg X-1	~ 10^4 counts per second
Background	< 10 counts per second
Detector dimensions	40 cm x 20 cm x 35 cm
Window	37 micron beryllium
Gas filling	Argon/Xenon/quench at 2 atm.
Total mass	79 kg

The counter bodies will be of stainless steel and sufficient mass and volume has been allowed to permit inexpensive construction methods for detectors and collimators. This is particularly important with an instrument of this size.

Preamplifiers will be mounted on the back of each detector, together with high voltage generators. The pulses from each anode layer will be digitised with a 128 channel ADC and associated with a counter identification code, and time bits sufficient to time the photon arrival to ± 8 microseconds. Depending

on the total count rate, selections from this information will be presented to the spacecraft data handling system for storage and subsequent transmission.

To accomodate the occasional very high data rate (~ 250 kbps) experienced during observations of the brightest sources, the experiment will contain a high capacity buffer memory. This will feed the data, collected over short periods to the spacecraft data handling system at a compatible rate. For most observations the data rates will vary between 1 and 20 kbps.

The time resolution and sensitivity of the LAPC are shown in Figure 6b and 8 respectively.

VI. THE PHOSWICH DETECTOR SYSTEM

For the energy range 15 - 200 keV, an inorganic scintillation detector system is employed. The total sensitive area (~ 0.8 x geometric area due to collimator efficiency) will be ≥60 cm^2. Two different 'sandwiched' scintillation crystals, called a Phoswich, provide 2π protection against background events in a relatively low cost per unit area detector. X-ray induced scintillations in the 'front' crystal (NaI (Tl)) are distinguished from background induced scintillaitons in the 'rear' crystal (CsI (Na)) by means of the different fluorescent decay times of the two scintillators. A CsI (Na) scintillator shield surrounds the Phoswich and collimator so as to increase discrimination against charged particles and gamma rays. The bottom part of the detector is covered by a passive graded shield (Pb-Sn-Cu) to reduce the background counting rate in the CsI (Na) element of the Phoswich.

A Phoswich in combination with an inexpensive plastic scintillator shield gave background rates of a few x 10^{-4} counts $cm^{-2}sec^{-1}keV^{-1}$ (independent of detector area) in balloon flights (Scheepmaker 1976, Kendziorra 1977). The

ORIGINAL PAGE IS
OF POOR QUALITY

high energy experiment on the HEAO-a satellite (A-4) consisting of Phoswich detectors with an active CsI shield gave similar background rates (Primini 1979). The background rate in the proposed instrument will be lower than the A-4 experiment due to the equatorial orbit. Table VII gives the main characteristics of the instrument and Figures 6c and 9 show the time resolution and sensitivity, respectively.

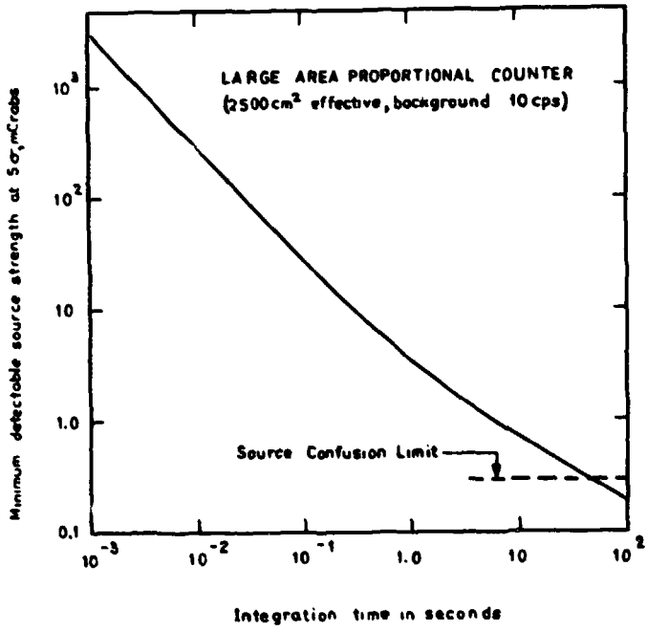

Figure 8.

LAPC sensitivity plotted against observing time.

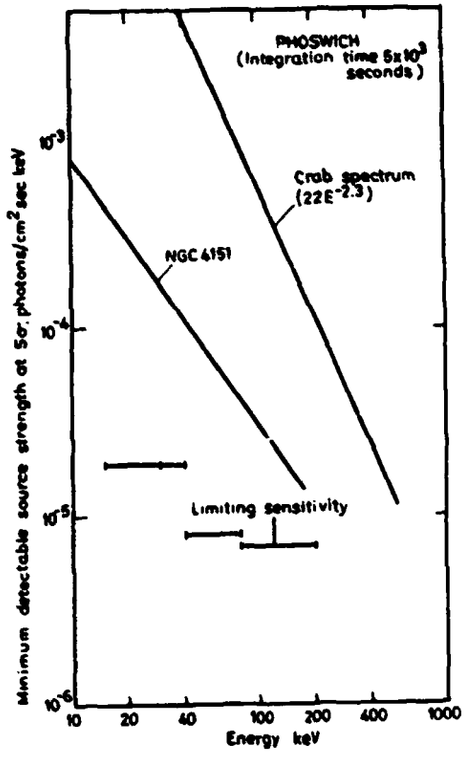

Figure 9.

PHOSWICH sensitivity plotted against observing time.

Table VII. Characteristics of Phoswich Detector System

Configuration	One unit comprising 4 Phoswich detectors
Field of view	1.9° x 1.9° FWHM
Energy range	15 - 200 keV
Energy resolution	30% at 20 keV, 19% at 50 keV, 12% at 200 keV
Geometric area	800 cm^2
Envelope	100 cm x 65 cm x 65 cm
Total mass	125 kg
Background	15-30 keV 3.1 x 10^{-4} cts/cm^2 sec keV 30-40 keV 2.3 x 10^{-4} cts/cm^2 sec keV 40-80 keV 1.7 x 10^{-4} cts/cm^2 sec keV 80-200 keV 1.1 x 10^{-4} cts/cm^2 sec keV

Each Phoswich detector consists of a 14 cm x 14 cm x 0.3 cm thick NaI (Tl) crystal, viewed by a 5 inch photomulitiplier through a CsI (Na) crystal 5 cm thick. The Phoswich is hermetically sealed in an enclosure, with a 1 mm Be X-ray entrance window and a quartz exit window. Four of these detectors, each with a geometric crystal area of ~ 200 cm^2 will make up the instrument.

To distinguish X-ray events in the NaI (Tl) crystal (~ 25 μs decay time), information from both a pulse shape discriminator (PSD) and a pulse height analyser (PHA) is used. To ensure that the distinction between NsI (Tl) and CsI (Na) events is maintained, the temperatures of the Phoswiches have to be maintained at 20 ± 10°C. This precaution is important in view of the strong temperature dependence of the fluorescent decay time of NaI (Tl).

To detect a weak X-ray source and determine its spectrum it is necessary to observe the source and background for equal periods of time. This is achieved by rocking the collimator some degrees from the centre position every few minutes.

The roles of the two broad band detectors may be sumarised as follows.

Study: Continuous plasma and non-thermal spectra, hard X-ray spectra, galactic and extragalactic source variability (millisec to years), source periods, cyclotron features.

Deduce: Properties of active nuclei (size, energetics), non-thermal cluster properties, nature of X-ray binaries (Black holes, neutron stars, white dwarfs), accretion disc properties, transient and burst mechanisms, neutron star magnetic fields, supernova and ISM properties, nature of X-ray background.

Observe: QSO's and other active galaxies, Clusters of galaxies, X-ray binaries, Supernova remnants, X-ray bursters and transients, Galactic bulge sources, Active stars and stellar coronae.

VII. THE GAMMA BURST MONITOR

The detector is based on a modification of the rotation modulation collimator (RMC) principle. The X-ray photons are detected in a scintillator mosaic consisting of alternating strips of CsI (Na) and NaI (Tl). The strips are 5 mm wide and 2mm thick. The mosaic is 80 mm in diameter and is viewed by a single 75 mm phototube. A large circular shadow mask consising of 5 mm wide tungsten strips 0.5 mm thick separated by 5 mm gaps is placed above the scintillator mosaic.

By means of a small motor the scintillator mosaic and the shadow mask are kept revolving around the symmetry axis at a spin rate of 60 revolutions per minute. During the spin, the tungsten strips will alternatively obscure the NaI - and the CsI - strips as seen from a source position in the sky. The obscuration (modulation) sequence is characteristic for each possible source position within the 120° field of view.

The important difference between the present design with the scintillator mosaic, and the conventional RMC design employing a single scintillator and two parallel shadow grids is that time fluctuations in the source flux, which is a well established characteristic of the gamma-burst sources, are not confused with the instrument modulation of the flux.

The signals from the two kinds of scintillator crystals can be separated at the output of the photomultiplier tube due to the different decay time characteristics of the light emission of the crystals.

Computer simulations of the detector performance have indicated that the burst sources can be located to better than 20 arc minutes for bursts with ~ 500 detected photons in the 30-130 keV interval (see Figure 10). This assumes that the burst duration is not much less than half the spin period.

The number of Vela-type bursts of this magnitude is roughly 25 per year within the field of view of the detector. The characteristics of the Gamma Burst Monitor are given in Table VIII.

Transient X-ray sources with hard spectra can also be positioned with this instrument. The expected background counting rate in the equatorial orbit is rougly 5 cps. A source of the same strength as the Crab can be localised within one orbit of observation.

The instrument will include a microprocessor with memory in which data can be stored at high rates during a burst. The microprocessor will also perform a deconvolution of the RMC patterns and determine source positions on line. Any decision to reorient the satellite for the purpose of studying a transient source with the narrow field instrument is thus facilitated and such a decision could be taken as early as the next ground station pass.

ORIGINAL PAGE IS
OF POOR QUALITY

Table VIII. Characteristics of the Gamma Burst Monitor

Field of view	120° (FWHP) 132° (FWZR)
Solid angle	3.1 sterad
Angular resolution	.20 arc minutes
Energy range	30 - 130 keV
Geometric area	50 cm^2
Detector size	25 cm x 25 cm x 25 cm
Total mass	6 kg

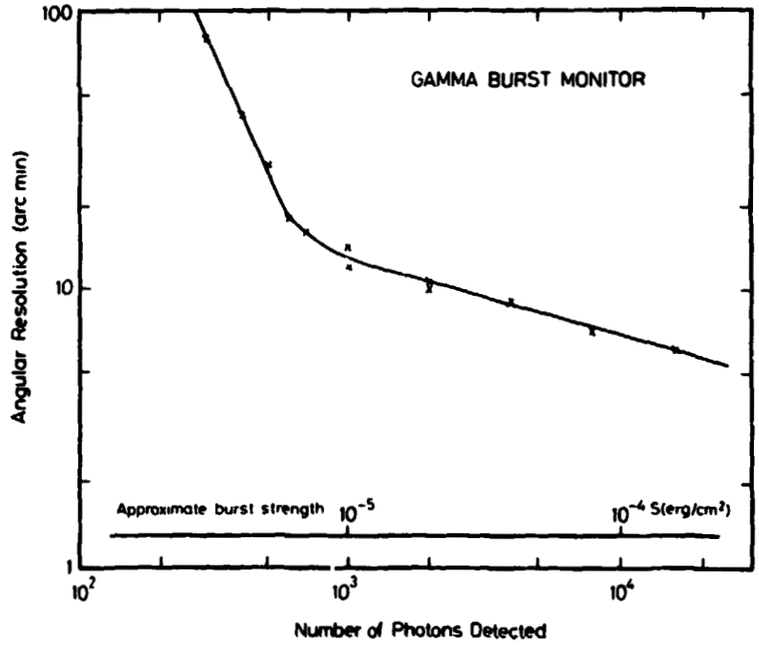

Figure 10.

Angular resolution of the Gamma Burst Monitor as a function of burst strength.

The role of the gamma burst monitor may be outlined in the following way.

Study: Hard X-ray transients and gamma ray bursts.

Deduce: Sky distribution of gamma ray burst sources.

Positions of X-ray transients allowing in-depth studies by the narrow field instruments.

Observe: All sky monitoring. As the purpose of the gamma burst monitor is to detect new, unknown sources over a very wide field of view, it does not constrain the pointing strategy of the spacecraft.

VIII INSTRUMENT DATA HANDLING

In a mission such as X80 where the need to acquire data at high rates and with good timing is dictated by the scientific requirements, it is necessary to permit some flexibility in assigning telemetry to the various instruments.

Bit allocations and the expected counting rates from the five instruments are given in Table IX. Time resolution to 0.1 seconds is available from spacecraft timing and telemetry synchronisation. Higher time resolution is derived from within the instrument.

The total mean bit rate available is 44 kbits/second with peak rates up to ~ 220 kbits/second. The LAPC and WFC can individually exceed this mean rate, for example when the LAPC observes Cyg X-1, or the WFC monitors the galactic centre. However these observations will occur infrequently and never simultaneously. For such an observation one instrument will have exclusive use of the data handling system and will fill the bubble memory in less than one orbit, the observation then being halted till data are telemetered to ground. Since the longest observation allowed by earth occultation will rarely exceed 60 minutes the available data capacity will in general be sufficient. For a few very bright sources, the LAPC will only observe for about 20 minutes, which is adequate to realise the scientific objectives. In all other cases the instruments will operate together and the total data capacity will not be exceeded.

ORIGINAL PAGE IS
OF POOR QUALITY

Table. IX Instrument Data Rates

		Source	Counting Rate (c/s)	Data Rate (kb/s)
Bragg Spectrometer				
Detector ID	2 bits	Maximum		
X-Y position	18 bits	envisaged	80	2.5
Detector energy	6 bits	flux on all		
Rise time	6 bits	spectrometers		
TOTAL	32 bits/ event			
LAPC				
Energy	7 bits	Cyg X-1	10^4	240
Detector ID	4 bits	NGC 4151	200	4.8
Timing	12 bits	Background	10	0.3
Spare	1 bit			
Total	24 bits/ event			
Phoswich				
Energy	7 bits	Crab	290	7
Detector ID	2 bits	NGC 4154	8	0.2
Pulse shape	7 bits	Background[x]	30	0.7
Time	7 bits			
Veto	1 bit			
TOTAL	24 bits/ event			
WFC				
Position	20 bits	Crab (1 camera)	590	16.5
Energy	4 bits	Galactic centre	1750	49
Camera Ident.	2 bits	(1 camera)		
Spare	2 bits	Diffuse back-		
		ground (4 cameras)	600	16.8
TOTAL	28 bits/ event	Particle background (4 cameras)	60	1.7
Gamma Burst Mon.				0.1

[x]based on a wide pulse shape window; further optimisation of signal to noise ratio can be done on the ground.

IX. SAMPLE OBSERVATIONS AND A POSSIBLE MISSION PLAN

In order to demonstrate the capabilities of the various instruments, it is instructive to list the observing times required to achieve a number of aims in the study of three sources. The first of these is NGC 4151, a Seyfert galaxy of typical intensity 3 Uhuru flux units (UFU). The instrument capabilities are listed for an overall observing time of 5 days.

A. LAPC

(i)	Detect NGC 4151	~ 10s
(ii)	Register 10% flux change	~ 300s
(iii)	Detect Fe feature	~ 3000s

B. Phoswich

(i)	Detect NGC 4151	~ 3000s
(ii)	Register 10% flux change	~ 10^4s

C. Bragg Spectrometer

(i)	Detect Fe lines	~ 3.10^4s
(ii)	Measure λ's to ~ 3mÅ	~ 3.10^4s
(iii)	Search for Fe edge	~ 3.10^5s

D. WFC

(i)	Detect NGC 4151	~ 3000s
(ii)	Register 100% flux change	~ 6000s

In the case of the Perseus Cluster which is an extended source of intensity 18 UFU, a one day observation would permit the following to be achieved.

A. Bragg Spectrometer

(i)	Detect Fe lines from the Persus Cluster	~ 1000s
(ii)	Map (5' x 5') in lines	~ 3.10^4s
(iii)	Detect S, Si, O lines (NGC 1275)	~ 1000s

B. Phoswich

(i)	Detect the Perseus Cluster	~ 4000s
(ii)	Establish hard spectrum	~ 9×10^4s

C. LPAC

(i)	Detect the Perseus Cluster	~ 1s
(ii)	Establish medium spectrum	~ 30s
(iii)	Detect Fe line	~ 10s

D. WFC

(i)	Monitor NGC1275 for variability, 100% change	~ 6000s
(ii)	Monitor other cluster galaxies (IC310, NGC1265)	~ 9×10^4s

Finally for the X-ray binary 4U 0900 - 40 (Vela XI), a source of typical intensity 250 UFU, the following observations are possible in a 10 day observing period.

A. LAPC

(i)	Detect 10% flux change in 4U 0900-40	~ 1000s
(ii)	Register Fe emission/absorption features	~ 100/1000s

B. Phoswich

(i)	Detect 100% flux change in 4U 0900-40	~ 1000s
(ii)	Search for cyclotron features	~ 3×10^5s

C. Bragg Spectrometer

(i)	Detect Fe Lines/edges	~ $10^3/10^5$s
(ii)	Measure λ's to 3mÅ	~ $10^3/10^5$s

Pointed instruments monitor for binary phase, related events and for pulse phase features.

D. WFC

(i)	Detect 4U 0900-40	~ 1s
(ii)	Register 100% flux change	~ 3s

It is also instructive to outline an observing programme for a three year mission in order to demonstrate how the instruments can work together. Table X shows such a programme.

Table X. Three Year Mission Observing Programme

1.	50 QSO's and active galaxies	400 days
2.	50 clusters of galaxies	200 days
3.	50 X-ray binaries	200 days
4.	50 active stars and coronae	100 days
5.	20 supernova reemnants	50 days
6.	Sky-survey with WFC (3 days every 10 days)	300 days
7.	Galactic centre region with WFC	50 days

It should be noted that many wide field camera aims can be satisfied by rotating ± 30° around the pointing direction determined by the narrow field instruments. Furthermore, it will be possible to conduct short observations of some sources with narrow field instruments during the wide field camera all sky surveys. The WFC and the Gamma Burst Monitor will continuously monitor a large fraction of the sky for the occurrence of bursts and transients.

X. CONCLUSIONS

The X-ray sky survey missions undertaken by spacecraft such as Uhuru, Ariel V and HEAO-1 and the high resolution observations carried out with the Einstein Observatory (HEAO-2) at longer wavelengths have established X-ray astronomy as one of the most exciting and productive branches of astrophysics. The European mission, EXOSAT, to be undertaken in 1981 through 1983 is expected to make an extensive contribution in enlarging the scope of the subject.

Appropriately instrumented follow-on missions must now be prepared for detailed studies of energy spectra and time variability, to develop our understanding of the sources which include such diverse and physically interesting objects as clusters of galaxies, quasars, neutron stars and black holes. Although other missions (e.g. ASTRO-C, XTE) have been studied, the mission

proposed here is unique in combining spectroscopic, timing and variability observations. It is designed to perform an integrated, systematic and comprehensive study of X-ray sources from a single free-flying satellite with the goal of obtaining:

- a determination of mass, dimensions, magnetic fields, and other basic information on matter under extreme conditions as found, for example, in neutron stars and degenerate white dwarfs.
- characteristic signatures of black holes and confirmation of their existence.
- an understanding of accretion processes on compact objects.
- detailed information on the conditions prevailing in high temperature plasmas, e.g. in stellar coronae, supernova remnants, galactic nuclei and clusters of galaxies, thereby gaining insight on evolutionary processes.
- a description of the photoionised gas that exists in binary systems and in the broad line regions around active galactic nuclei.
- an understanding of the innermost regions of active galaxies.

Five instruments, consistent with these goals are described, namely Bragg Crystal Spectrometers, Large Area Proportional Counters, Crystal Scintillators (Phoswich), Wide Field Cameras and a Gamma Burst Monitor.

The case for high resolution observations with crystal spectrometers is now overwhelming in view of the strong iron emission and absorption features detected by the proportional counters on Ariel V, OSO-8 and HEAO-1 and of oxygen, iron silicon and sulphur emission by the SSS and FPCS instruments on the Einstein Observatory. The Bragg Spectrometer has sufficient sensitivity to study the detailed structure of these features for a large number of X-ray sources with observation times of typically 10^4 seconds. The Large Area Proportional Counter will have sufficient sensitivity to perform sub-millisecond timing on bright sources and to study time and spectral variability in faint sources. It also has the broad spectral range to provide a monitor function for the crystal

spectrometers. The Phoswich detector will extend the spectral and variability measurements from a few keV to some 200 keV and will permit the detailed study of the recently discovered cyclotron features. The Wide Field Cameras will image the sky to detect, locate and meausre X-ray transient events, as well as X- and gamma-ray bursts. Furthermore it provides an efficient means of monitoring all X-ray sources on timesclaes of days to years A gamma ray burst monitor is included to provide wide field observations at higher energies.

The mission can be readily undertaken on a free-flying satellite with modest performance requirements on attitude control ($\sim \pm$ 5 arc min), and measurement (0.5') power ($\sim$ 350 watts) and mass ($\sim$ 900 kg). A low altitude (600 km) circular orbit at low inclination (approx. 0 deg.) is optimum and can easily be achieved with the Ariane vehicle launched from Kourou.

The Spectroscopy, Timing and Variability mission must be seen as a logical follow-on in X-ray astronomy for the mid-1980's, to capitalise on the non inconsiderable financial and manpower resources already invested and to consolidate the expertise and experience which have been firmly established in Europe. However in times of financial stringency on both sides of the Atlantic, the possibilities for collaboration should be examined carefully by both ESA and NASA.

ACKNOWLEDGEMENTS

I am grateful for the considerable effort put into the mission phase A study by the members of the X-80 study team. I have used their report extensively in preparing this presentation. The efforts of R. A. Laine (ESTEC, Future Projects Office), H. Olthof (ESA HQ, AWG Secretary), A. Peacock and B.G. Taylor (ESTEC, SSD) in bringing the study to a successful conclusion are also acknowledged with gratitude.

REFERENCES

Bailey, T.A., 1978, Nuclear Instr. Meth., 155, 177.

Becker, R.H., Rotschild, R.E., Boldt, E.A., Holt, S.S., Pravdo, S.H., Serlemitsos, P.J., Swank, J.H., 1978, Astrophys. J., 221, 912.

Das Gupta, K., 1961, Rev. Sci. Inst., 32, 602.

Fabian, A.C., Ross, R., 198 , Mon. Not. R. astr. Soc.,

Gunson, J., Polychronopulous, B., 1976, Mon. Not. R. astr. Soc., 177, 485.

Hall, R., Ricketts, M.J., Page, C.G., Pounds, K.A., 1981, In press, Space Science Reviews.

Hayes, M., Culhane, J.L., Blissett, R.J., Barr, P., Bell Burnell, S.J., 1980, Mon. Not. R. astro. Soc., 193, 15P.

Kendziorra, E., et al., 1977, Astrophys. J., 217, L93.

Palmieri, T.M., 1974, Astr. Sp. Sc., 20, 431.

Primini, F.A., et al., 1979, Nature, 278, 234.

Proctor, J., et al., 1978, Mon. Not. R. astr. Soc., 185, 745.

Rapley, C.G., Culhane, J.L., Acton, L.W., Catura, R.C., Joki, E.G., Bakke, J.C., 1977, Rev. Sci. Inst., 48, 1123.

Schnopper, H., et al., 1966, Paper presented to 133rd AAS meeting, Washington, DC.

Scheepmaker, A., et al., 1976, Astrophys. J., 205, L65.

Winkler, P.F., Canizares, C.R., Clark, G.W., Markert, T.H., Petre, R., 1981, Astrophys. J., 245, 574.

PRECEDING PAGE BLANK NOT FILMED

N82 26064

X-Ray Astronomy Program in Japan

Yasuo Tanaka

Institute of Space and Astronautical Science,
Komaba, Meguro, Tokyo 153
Japan

1. Introduction

One of the great achievements in the short history of X-ray astronomy is to have established the real existence of neutron star rather than just a theoretical conception. Pursuing this extreme astronomical body and its environment will undoubtedly continue to produce important science through this decade and beyond.

We have been operating the Hakucho satellite for over two years. It is amusing as well as amazing to find that this 96 kg satellite with limited capabilities gives us plenty of interesting results and significant questions concerning neutron stars. These questions in fact constitute the basis for our planning of the future program. I would, therefore, like to illustrate some of the problems that emerged from the Hakucho observations and are to be understood by future investigations.

2. X-ray pulsars

Among many X-ray pulsars, we have conducted so far most extended observation of Vela X-1. Vela X-1 is a slow pulsator with the approximate pulsation period of 283 sec and the binary period of 8.97 days. Fig. 1 shows the history of the pulsation period variation. It is clear that the neutron star had been spinning up until 1979, consistent with the picture of acceleration by the accretion torque (e.g. Rappaport and Joss 1981). Hakucho observations revealed two remarkable features. i) The spin period started to slow down since 1979 and this trend continues (Nagase et al. 1981). The average $\dot{P} / P \simeq 3.5 \times 10^{-4}$ yr^{-1} for the period 1979 - 1981. ii) An up-down fluctuation of the spin period with a time scale of the order of the orbital period is significantly resolved for the first time (Nagase 1981). $\dot{P} / P$ of this fluctuation ranges over $(-3 \sim +4) \times 10^{-3}$ yr^{-1}, an order of magnitude larger than that for the long-term variation. The observed long-term slowing down is not readily explained. There has been no significant

ORIGINAL PAGE IS
OF POOR QUALITY

change in the average X-ray luminosity through past several years. Would this be due to the change of the direction of accretion flow with respect to the spin vector of the neutron star? Ar entirely different idea suggested by Makishima is that the secular variation of the pulsation period might due to the Doppler effect by the orbital motion of the Vela X-1 binary around an unseen third body with a period of the order 10 years. If it were so, the mass of the third body would then be roughly 100 $M_\odot$, hence implying a giant black hole. It is worth noting that a similar slowing down of the neutron star revolution is also observed for GX 301-2 (Kelley, Rappaport and Petre, 1980).

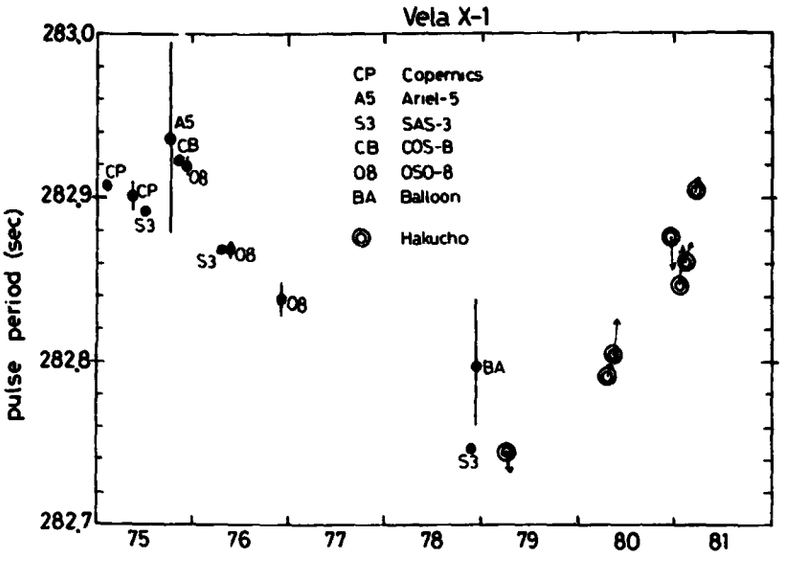

Fig.1 Histroy of the pulsation period of Vela X-1

The short-term up-down fluctuation of the pulsation period poses an intriguing question. If the fluctuation is of an external origin, the direction of the accretion flow may change rather quickly. If it is of an internal origin, this may be due to the coupling and decoupling between the crust and the superfluid interior such as proposed by Lamb, Pines and Shaham (1978).

The example of Vela X-1 demonstrates that we can learn a lot about inside and outside neutron stars by accurately monitoring the behavior of X-ray pulsars.

3. X-ray bursters

X-ray burst is another outstanding phenomenon that neutron star exhibits. As a matter of fact, one of the main emphasis of Hakucho was placed on the observations of X-ray bursts. Distribution of burst sources including those we found in the general direction of the galactic center is shown in Fig. 2. A distinct clustering towards the galactic center is evident. This distribution by itself suggests the Pop. II nature of burst sources, which is strongly enhanced by the fact that nearly half as many burst sources are associated with globular clusters.

Of particular importance of bursts is that one can in principle measure the radius of the neutron star. Owing much to the SAS-3 group (Lewin and Joss 1981), it is by now established that the "black-body" radius is conserved during the burst decay and of the order 10 km. We estimated the "black-body" radii for several

ORIGINAL PAGE IS
OF POOR QUALITY

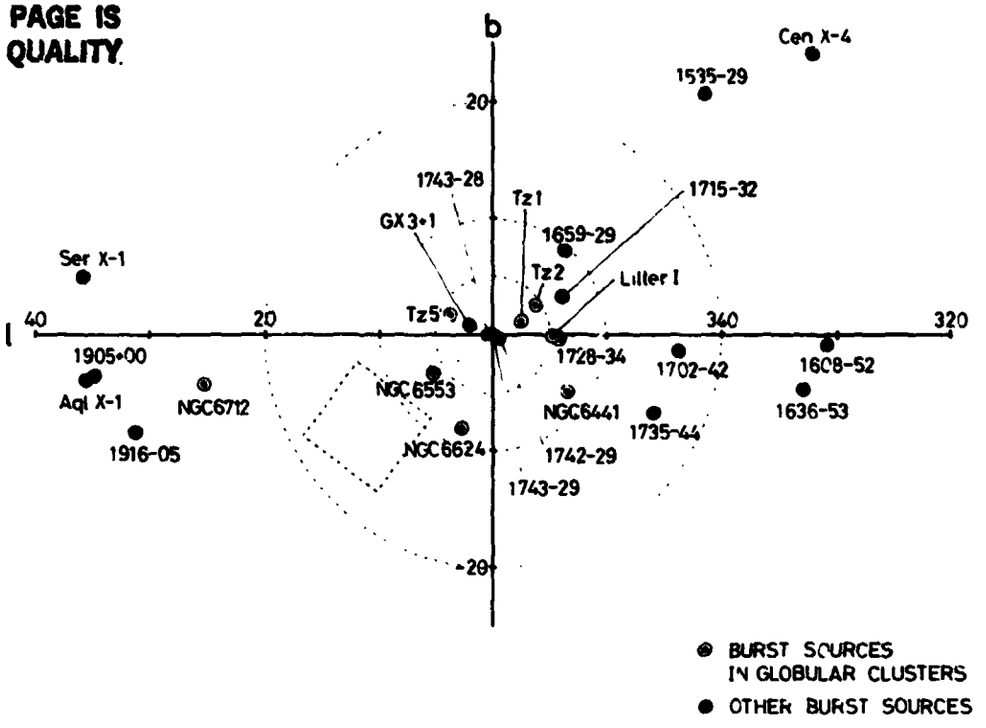

Fig.2 Distribution of burst sources around the galactic center

burst sources, including three globular cluster sources, that are most probably near the galactic center. They all come close to 10 km within 20%, implying that they are about the same size. I must caution, however, that it is too early to take this number as the actual neutron star radius for this requires correct interpretation of the burst spectrum which is yet the theme of further investigations. Nevertheless, it is very important that we have means to measure the neutron star radius in our hands. While, X-ray pulsars enable us to measure the mass of neutron stars.

We have sofar learned that every individual burst source can produce a variety of bursts in the time profile, peak luminosity and total energy. The thermonuclear flash model provided a persuasive picture of the burst phenomenon. There are, however, several observational facts that challenge theoretical interpretations.

i) Successive bursts at a very short interval

We observed three such events; 10 min. for 1608-52 (Murakami et al. 1980), 8 min. for Terzan 5 source (see Fig. 3), and 8 min. for MXB 1636-53. The SAS-3 group observed three bursts in such short succession from a galactic-center source (Lewin et al. 1976). Such an interval is definitely too short to replenish the required nuclear fuel by the mass accretion. The nuclear fuel ought to be hidden somewhere on the neutron star surface, but where? and how? are the big questions.

ORIGINAL PAGE IS
OF POOR QUALITY

ii) Possible supercritical luminosity

A puzzling result was obtained from examination of the burst peak luminosities (Inoue et al. 1981). The peak luminosity distributions for five burst sources near the galactic center are shown in Fig. 4. If the distance to the galactic center is taken to be 10 kpc, the largest peak luminosity observed for each source largely exceeds the Eddington limit for a 1.4 $M_\odot$ neutron star. This conclusion remains valid unless the galactic center distance is much smaller than 7 kpc.

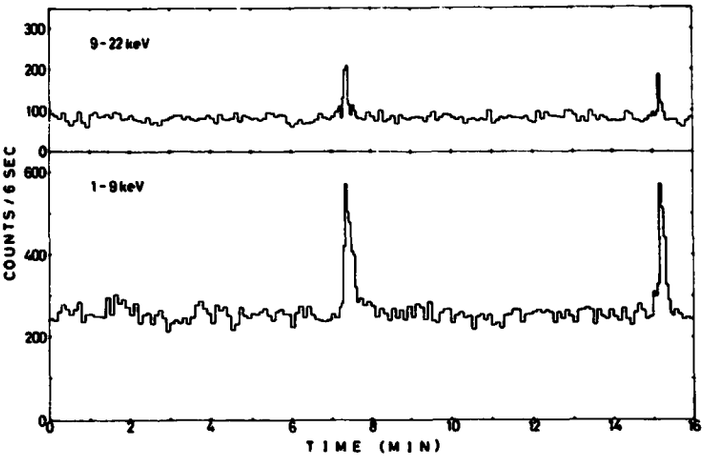

Fig.3 X-ray bursts at 8 min. interval from Terzan 5.

The same can be concluded for a Terzan 2 burst (Grindlay et al. 1980) and for the bursts from NGC 6624 (Clark et al. 1976), the distance to the latter being pretty well estimated.

One might think that the critical luminosity can be exceeded by blowing off the neutron star atmosphere. However, the observational result indicates that the "black-body" radius remains constant from the burst peak through the decay, excluding the expanding photosphere. Strong magnetic field can reduce the Thomson cross section, thereby increase the critical luminosity. This effect is significant only if the field is of the order or greater than 10^{12} Gauss. Why then does the distinct difference in the behavior and the spectral hardness between X-ray pulsars and X-ray bursters exist?

We assess a great significance upon this problem of possible supercritical luminosity. There may very well be physics intrinsic to the superdense photons.

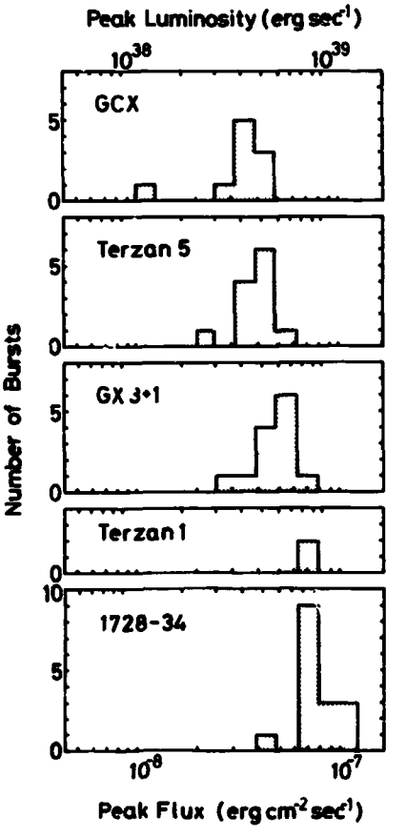

Fig.4 Distributions of burst peak luminosities for five sources near the galactic center.

ORIGINAL PAGE IS
OF POOR QUALITY

iii) The rapid burster

The rapid bursts from MXB 1730-335 are interpreted by Lewin et al. (1976) as due to the chopped accretion flow caused by a certain instability. Fortunately, we met its remarkable benavior in August 1979 (Inoue et al. 1980). By then, the rapid burster produced a long train of bursts with trapezoidal shape. The length of the flat top of these trapezoidal bursts ranged from half a minutes to over 10 minutes. The famous linear relation between the burst size and the time to the next burst still holds for these bursts, implying a reservoir of the capacity in excess of 10^{21} g of matter.

As can be seen in Fig. 5, an important result is that, during th flat top of a trapezoidal burst, the luminosity as well as temperature are kept constant. Hence, the emitting area is also constant. This seems to indicate that the trapezoidat burst itself represents a stationary state. Another stationary state exists, which corresponds to the low level ($\sim$ 1/10 the burst peak) persistent emission that appears between two bursts. We, therefore, revise the picture of the rapid burster that it undergoes rapid switchings between the high and low states rather than a single shot of matter onto the neutron star. However, the mechanisms of the reservoir, switching and controlling the mass flow are key questions to be answered by future study.

In two of the trapezoidal bursts, clear oscillations were discovered. As shown in Fig. 6, the power spectrum for each exhibits a prominent spike at about 0.5 sec. The oscillation does not appear as due to the neutron star revolution, since the observed spikes show a structure and are slightly but significantly different from each other. The origin of this oscillation is unknown.

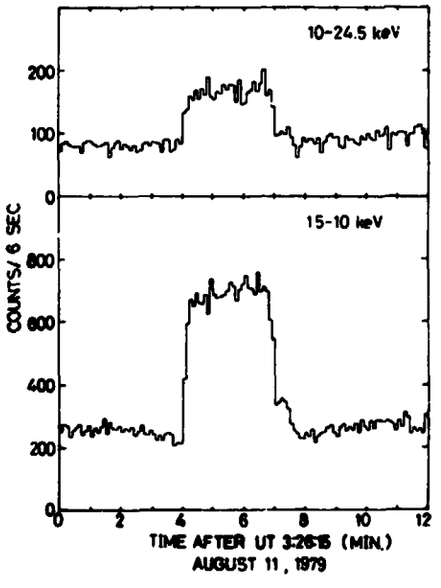

Fig.5 Example of the trapezoidal burst from the rapid burster.

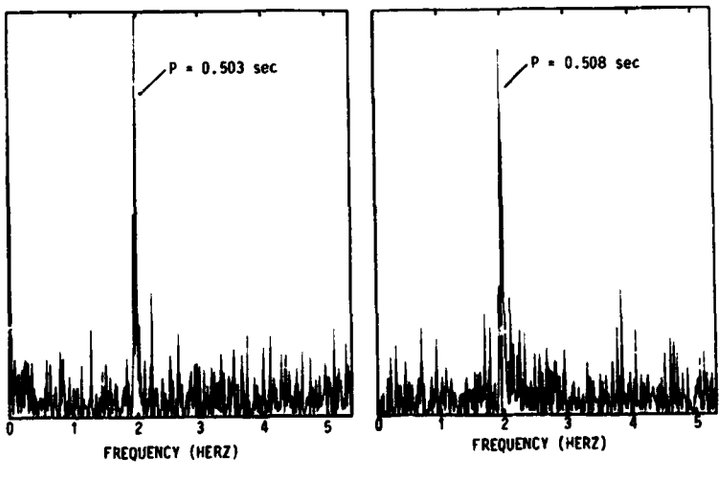

Fig.6 Power spectra for two trapezoidal bursts, for which a prominent spike is seen.

ORIGINAL PAGE IS
OF POOR QUALITY

4. Future satellite program

So far, I have briefly covered the crucial problems that the Hakucho observations have put forward concerning neutron star and its system. Following Hakucho, we have two more approved X-ray astronomy missions, ASTRO-B and ASTRO-C. The task of these missions is to better understand the above-described problems and to explore further.

Since the time of the Hakucho launch, the capability of the satellite launch vehicle at ISAS has been steadily increasing. The present ISAS launcher, M-3S, is capable of launching a $\sim$ 250 kg satellite into a 500 km altitude circular orbit. New development effort has started to upgrade the launch power. The first step is M-3S II which can carry a payload over 400 kg for a 500 km orbit. The second step, M-3S III, would achieve substantial increase of the launch capability over that of M-3S II.

Fig. 7 illustrates the current mission plan at ISAS. Those with solid circles are approved missions to date, whereas those with dashed circles are yet to be approved. Main features of ASTRO-B and ASTRO-C are listed in Table I, in comparison with those of Hakucho.

ASTRO-B weighing 220 kg is due for launch in early 1983, and the flight hardware is presently under fabrication. The main instrument of ASTRO-B is gas scintillation proportional counters with the total area of about 1000 cm^2. Major increase

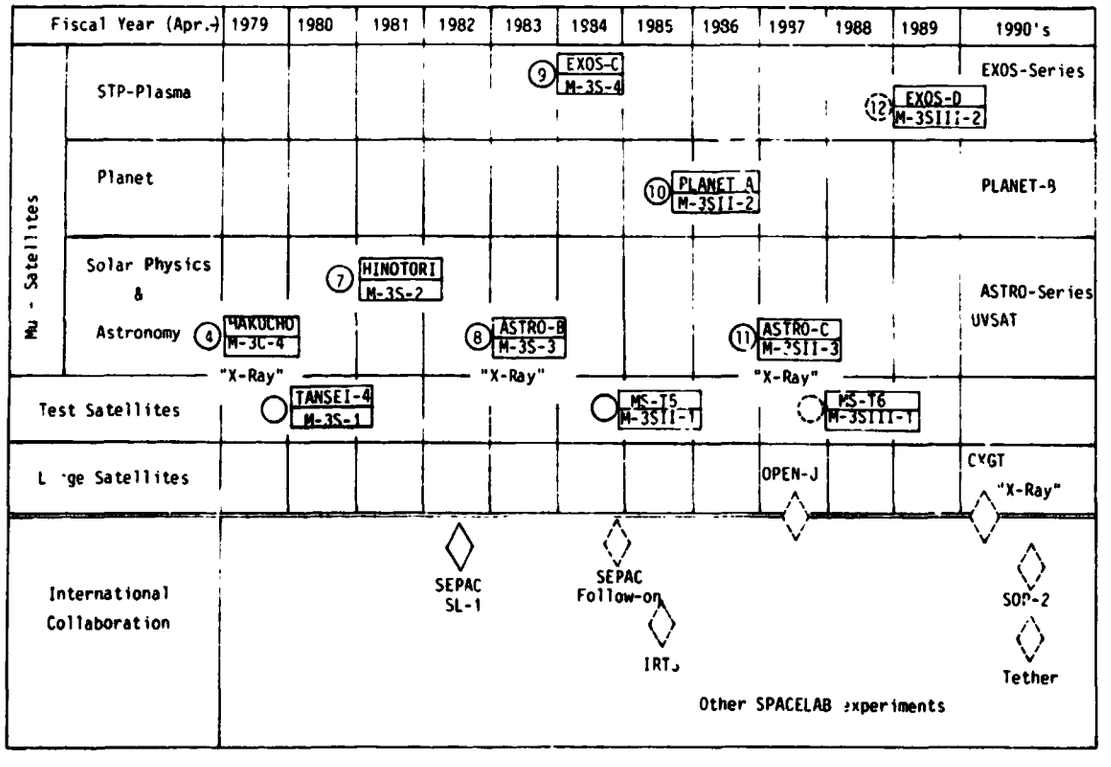

Fig.7 Current mission plan at ISAS for 10 years. The serial number of scientific satellite, mission name and launch vehicle are indicated for each.

ORIGINAL PAGE IS
OF POOR QUALITY

as compared to Hakucho is made in the sensitivity as well as in the spectral resolution. ASTRO-B will consequently provide us with much better temporal and spectroscopic information about the galactic sources than we are having from Hakucho. As a significant feature, the energy resolution of the gas scintillation proportional counter which is twice that of the conventional proportional counter would enable us to study the spectral detail and in particular emission lines or absorption features.

ASTRO-C is the follow-on X-ray astronomy satellite scheduled for launch in 1986-87. The spacecraft will be approximately 400 kg in weight and 3-axis stabilized. At present, we are in the biginning of the prototype design phase. The main instrument will be low-background proportional counters with the total area of about 5000 cm^2. Gas scintillation proportional counters may well be a part of it. An all-sky monitor will also be included.

The primary mission objective of ASTRO-C is the study of the time variability. Main emphasis here is not only accurate timing analysis of the galactic sources but the scrutiny of the time variability of active galactic nuclei. Exoticism of active galactic nuclei is immense but yet little is explored. We consider that study of the time variability is of crucial importance of the physics involved in the power house problem.

We hope that the ASTRO-series missions with the improved M-launcher will

Table I. Main features of Hakucho, ASTRO-B and ASTRO-C.

	HAKUCHO	ASTRO-B	ASTRO-C
LAUNCH YEAR	1979	1983	1986-7
WEIGHT (kg)	96	220	$\sim$ 400
MAIN INSTRU.	PROP. COUNTER	G.S.P.C.	P.C. (MULTI-CELL)
EFFECTIVE AREA	6° x 6° 80 cm^2 17° x 17° 70 cm^2	3° x 3° 1000 cm^2	$\sim$ 1° x 3° $\sim$ 5000 cm^2
SCIENTIFIC OBJECTIVES	◦ WIDE F.O.V. RMC BURST SURVEY ◦ MONITORING SEVERAL SOURCES AT A TIME ◦ SOURCE LOCATION CMC 0.5° FMC 0.05°	◦ SPECTRAL AND TEMPORAL VARIATION OF GALACTIC SOURCES ◦ $\Delta E/E$ = 10 % AT 6 keV POWERFUL FOR IRON LINES CYCLOTRON LINES ◦ 1-50 keV IN 128 CH / 0.5 S 32 CH / 0.125 S	◦ TIME VARIATION OF EXTRAGALACTIC & GALACTIC SOURCES ◦ 0.5 μJy SOURCES IN 10 MIN. $\gtrsim$ 300 GALAXIES ◦ SIZE OF ACTIVE GALACTIC NUCLEI ◦ STRUCTURE OF DEGENERATE STARS
AUXILIARY INSTRUMENTS	◦ SCANNING P.C. 35 cm^2 x 2 1.7° x 37° ◦ SUB-keV X-RAY MONITOR 80 cm^2 x 2 P 80 cm^2 x 2 S	◦ 1-DIM. HADAMARD TEL. 70 cm^2 x 2 20° x 20° ◦ SCANNING P.C. 100 cm^2 x 2 ◦ 1-DIM. REFLECTOR 20 cm^2 x 2	◦ ALL SKY MONITOR $\gtrsim$ 100 μJy $\gtrsim$ π STERADIAN

continue through 1990's. Besides this stream, we also envisage to carry out a larger X-ray astronomy mission than the planned capability of the M-launcher. This mission was originally named the Cosmic X-ray and Gamma-ray Telescope (CXGT). Over past years, the concept of CXGT has evolved. As X-ray astrophysics advances, more and more sensitivity and spectroscopic resolution are inevitably needed. It is therefore logical to consider a focusing optics for CXGT.

Finally, I would like to mention that the government level agreement on the U.S.-Japan collaboration programs in space science including X-ray astronomy was made. We very much hope to enhance the tie through possible collaborations in this field.

References

Clark, G.W., Jernigan, G., Bradt, H., Canizares, C., Lewin, W.H.G., Li, F.K., Mayer, W. and McClintock, J.E. 1976, Ap.J. (Letters), 207, L105.

Grindlay, J.E., Marshall, H.L., Hertz, P., Soltan, A., Weisskopf, M.C., Elsner, R.F., Ghosh, P., Darbro, W. and Sutherland, P.G. 1980, Ap.J. (Letters), 240, L121.

Inoue, H., Koyama, K., Makishima, K. et al. 1980, Nature, 283, 358.

Inoue, H., Koyama, K., Makishima, K. et al. 1981, Ap.J. (Letters), in press.

Kelley, R., Rappaport, S. and Petre, R. 1980, Ap.J., 238, 699.

Lamb, F.K., Pines, D. and Shaham, J. 1978, Ap.J., 224, 969.

Lewin, W.H.G., Hoffman, J.A. and Doty, J. et al. 1976, M.N.R.A.S., 177, 83.

Lewin, W.H.G. and Joss, P.C. 1981, Space Science Rev., 28, 3.

Murakami, T., Inoue, H., Koyama, K. et al. 1980, Publ. Astron. Soc. Japan, 32, 543.

Nagase, F., Hayakawa, S., Kunieda, H. et al. 1981, Nature, 290, 572.

Nagase, F. 1981, talk presented at 15th ESLAB Symposium on X-Ray Astronomy, June 1981, Amsterdam.

Rappaport, S. and Joss, P.C. 1981, "X-Ray Astronomy", ed. R. Giacconi, Proceedings of the HEAD-AAS Meeting, January 1980, Cambridge.

N82 26065

THE LAMAR:
A HIGH THROUGHPUT X-RAY ASTRONOMY FACILITY
FOR A MODERATE COST MISSION

Paul Gorenstein and Daniel Schwartz
Harvard/Smithsonian Center for Astrophysics
Cambridge, MA 02138

Presented at the Workshop on X-ray Astronomy
Goddard Space Flight Center
5-7 October 1981

1.0 INTRODUCTION

Large collecting power is essential for many of the objectives of future programs of X-ray astronomy. In order to carry out astrophysical investigations directly in X-rays, a minimum number of photons must be obtained. It is evident that good angular resolution is needed to recognize and image diffuse sources, obtain precise positions, reduce background, and avoid confusion. The specific role of the high throughput instrument is to collect a sufficient number of photons from sources, both point-like and extended, to permit an in-depth study of individual objects and group properties to be accomplished within a reasonable time without the limitations of background, confusion, and shot noise. The studies include: measurements of fluxes and luminosity functions, studies of morphlogy and imaging of low surface brightness features, temporal variations, and spectral properties. To achieve a good measurement of these parameters, e.g. to characterize a temporal variation in quantitative terms or measure a temperature gradient with precision, the measurements must of necessity be made at a high level of significance, typically tens of σ, which is well beyond that merely required to establish the existence of a source.

A value for effective area that represents a reasonable goal for future high throughput imaging instruments is about 10^4 cm^2. This is approximately 50 times that of the Einstein Observatory and 10 times AXAF. A reasonable goal for the angular resolution is about a minute of arc (diameter of circle containing 50% of the power). With this combination of large area and angular resolution, this instrument would be unique in

capability when compared to all other mission concepts under study. The Large Area Modular Array of Reflectors (LAMAR) is a practical approach for achieving this desired combination of large effective area and good angular resolution. For imaging purposes, the sensitivity of an array of identical modules (imaging telescopes and detectors) is equivalent in every respect to that of a single long telescope with the same total aperture and angular resolution. Given the appropriate manufacturing technology for mass production, the array of modules are much easier and less costly to fabricate than a monolithic telescope. There is no need for precise co-alignment of the modules. Furthermore, the modular approach results in more efficient use of the available volume on any spacecraft because the viewing aperture can be the large area side of the spacecraft.

In the discussion of scientific objectives and estimated performance, the name LAMAR is used in a generic sense. It covers a number of technical approaches for both the mirrors and detectors, including several described at this workshop, that are capable of being made into an array of 10^4 cm^2. Different choices for the mirror and detector technology provide varying degrees of effective area, angular resolution, field of view, short wavelength response and energy resolution No one mirror-detector system is optimum in all respects. The key to low cost, namely remaining within the limits of a moderate cost Explorer mission, is adopting a single set of technologies for the mirrors, detectors, and dispersive elements, in particular technologies which are amenable to mass production methods at low unit cost. Also, the technique should not require so specialized

skills or tools that there would be difficulty, irrespective of cost, of producing the required number of modules in a reasonable interval of time. A moderate cost approach is discussed in Sect. 4. In the discussion that appears in Sect. 2, a high throughput X-ray imaging instrument with energy resolution is shown to be an important tool for studying key problems in galactic and extragalactic astronomy. In so doing, the basic parameters assumed for the system are:

effective area (mirror): 10^4 cm^2 at 2 keV (50X Einstein / 10X AXAF)
2×10^3 cm^2 at 5 keV

resolution (50% flux diameter): 1 arcminute or better on axis

field of view: 1 degree

For objectives involving moderate resolution X-ray line spectroscopy ($E/\Delta E \approx 100$) the use of objective gratings is assumed, in particular, reflection gratings forward of the mirrors as discussed in Sect. 3.

LAMAR is unique with respect to any other mission under discussion. Its combination of large collecting area and good angular resolution is not paralleled by any past mission nor any future facility that is being planned. It collecting power represents an improvement over that of the Einstein Observatory, as well as that of EXOSAT and ROSAT, the next two telescope missions in X-ray astronomy, by about two orders of magnitude. With respect to future missions, it has an order of magnitude larger collecting power than AXAF, as well as facilities that are being discussed by the European Space Agency and Japan. LAMAR

can address scientific objectives in many areas of both galactic and extragalactic astronomy. It is not restricted to the study of one aspect of X-ray sources nor to a single class of objects. It can obtain results on many objects in a time that is short compared to any other facility. Being able to obtain results in a reasonably short time is essential because many studies are simply impractical if the observer requires more than about two years to carry out his/her program. Thus, LAMAR can serve the scientific community in a very general way and can accommodate the needs of a very large number of users.

2.0 EXPECTED PERFORMANCE OF LAMAR

We consider the performance of a LAMAR in several hypothetical observations relevant to the fundamental problem areas of astronomy and astrophysics that were described in the theoretical presentations during the first day of this workshop. These areas are:

(1) Cosmology, the X-ray Background, and Large Scale Structure of the Universe

(2) Clusters of Galaxies and Their Evolution

(3) Quasars and Other Active Galactic Nuclei

(4) Compact Objects in Our Galaxy

(5) Stellar Coronae

(6) Energy Input to the Interstellar Medium

Examples are considered in each of these subject areas.

2.1 Cosmology

LAMAR can study the overall isotropy of the sky in the redshift range $z \approx 1$ to 3 by measuring the 2-4 keV background. By studying apparent volume density vs. z for several classes of extragalactic X-ray source, LAMAR may allow an independent estimate of q_o. Studies of evolution can be carried out by obtaining complete X-ray selected samples (with detailed X-ray information) of Seyferts, quasars, BL Lac objects and clusters of galaxies to redshifts $z \approx 0.5$ to 3. Features in the X-ray background may reveal large scale structures, and events associated with the initial formation of clusters or of galaxies in clusters.

The X-ray background above a few keV is free of galactic effects and offers the best chance to measure the isotropy of the universe over the entire sky on scales between 1 deg^2 and 12 hours, and in the redshift interval of $z \sim 1$ to 3 from which the bulk of the X-ray background probably originates. As pointed out by Fabian at this Workshop, the X-ray background is sensitive to the structure of the universe on a scale of 10-100 Mpc. The fundamental limit to measuring the isotropy arises from source confusion noise due to the X-ray source counts $N(>S) = 2.7 \times 10^{-16} \; S^{-3/2} \; ster^{-1}$, where S = ergs/$cm^2$ s 0.3 to 3.5 keV. Focusing instruments are essential in order to eliminate individual discrete sources to as low a level as possible while integrating the diffuse background flux in the remainder of the field of view. In an observation of 2000 seconds, LAMAR can eliminate sources down to a level of 10^{-14} erg/cm^2 s. Scaling from measured background rates in the

Einstein Observatory, we estimate that in this time, about 6000 counts from diffuse X-ray background (2-4 keV) and 4×10^4 counts at most of non-X-ray background accumulate in 1 deg^2. Source confusion noise over the 1 deg^2 is expected to be 350 counts. Therefore, the total uncertainty due to statistical fluctuation is 7%. Systematic errors in the non-X-ray background can probably be reduced to 1%, therefore, the practical limit is about 10% for a single 1 deg^2 field. For those objectives requiring smaller uncertainty, the observation of many fields will reduce this uncertainty considerably. Measurement of $\sim 10^4$ independent fields would bring it down to 0.1%. This would be feasible in several years of LAMAR operation, and would occur naturally in the course of normal observing. Such precision is essentially unobtainable with an instrument having less area.

Based upon LAMAR's high throughput and its ability to study many sources, it is possible to define various cosmological tests. For example, it has been pointed out that the apparent volume density vs. redshift depends on q_o more strongly than the classical tests of apparent optical magnitude or apparent size vs. redshift.[1] At that time only clusters of galaxies were known to be ubiquitous extragalactic sources. Now, we might apply the test independently to Seyferts or BL Lac objects. All of these classes have luminosity functions of roughly 10^{-7} Mpc^{-3} for $L > 10^{44}$ erg/s. Although redshifts would have to be obtained by optical means, the power of LAMAR is that the samples can probably be defined completely based purely on X-ray properties, e.g., finite spatial extent for clusters of galaxies, a power law spectrum of index 0.5 to 0.6 for Seyferts (cf.

Mushotzky et al. 1980),[2] and a soft X-ray excess and time variability for BL Lac objects. To detect ~100 objects in a range of $\Delta z = 0.1$ at $z = 1$ requires 1000 fields of 1 deg^2 observed for 2000 sec each. The LAMAR sensitivity will be to 10^{-14} erg/cm^2 s, or $L = 10^{44}$ erg/s, in this time. Of course, any such measurement of cosmological parameters must simultaneously address the possibility of source evolution. Use of the classical $\langle V/V_m \rangle$ test will prevent us from being fooled, even if the test were inconclusive. However, in X-rays we have a unique possibility of deconvolving the evolution because of the rigorous constraint of not exceeding the X-ray background.

2.2 Clusters of Galaxies and Their Evolution

The results of the Einstein Observatory have confirmed our expectations based upon previous results that X-ray observations are an important source of new information concerning clusters of galaxies. Clusters of galaxies are easily identified in X-rays as a diffuse source with kT above 2 keV. The X-ray picture of clusters may exhibit considerable structure. In fact, the X-ray signature of a cluster of galaxies is so characteristic that new clusters of galaxies will probably be found much more easily in the future by X-ray measurements than by optical.

The Einstein Observatory was able to study relatively nearby clusters. It established that there exists a diversity of morphological types (cf., Forman and Jones, A.R.A.A. 1982).[3] A surprising preponderance of clusters with complex structure and asymmetry was found in comparison to clusters with more smoothly distributed gas, such as the Coma Cluster. Subsequent optical

measurements have tended to show that the distribution of galaxies is indeed correlated with the increases in X-ray surface brightness as in Abell 2069.[4] As explained below, X-ray measurements are potentially a good method for mapping the distribution of mass within a cluster, as well as for determining the total mass of clusters. However, the Einstein Observatory did not have the throughput required to map the temperature and temperature gradient of the cluster gas. Thus, it could not provide much direct information pertaining to the measurement of cluster masses and their distribution inside the cluster. While the Einstein Observatory produced important results on the morphology of several dozen individual clusters, its sample of distant clusters was too small for results on cluster formation and evolution to be conclusive.

The Einstein morphological studies reveal clusters of different ages, at the current epoch (cf. Forman and Jones 1982).[3] We would like to study clusters of different age at a variety of cosmological epochs back to $z = 1$. It is not obvious a priori what is required to perform the morphological study. From an examination of the Einstein X-ray images, it seems that clusters with 5 x 5 pixels above the 3σ contour and with a peak contour of at least 10σ significance can be qualitatively classified. With an estimated 3/4 to 1 arcmin resolution, a 10^4 second LAMAR observation will give a morphological picture of a cluster to redshifts of $z = 0.2$ ($L_X \geq 3 \times 10^{43}$ erg/s), $z = 0.5$ ($L_X \geq 10^{44}$ erg/s) and $z = 1.0$ ($L_X \geq 3 \times 10^{44}$ erg/s.

LAMAR is the key instrument in this regard because clusters

of galaxies are extended X-ray sources and moderate angular resolution is adequate for carrying out many of the objectives. Figure 1 is an X-ray contour plot of Abell 2069 as observed by the Imaging Proportional Counter of the Einstein Observatory.[4] In addition to the three principal condensations, LAMAR would see gas of much lower surface brightness. Superimposed upon this diagram is a 1' x 1' grid representing cells in which temperature could be measured. Simulations indicate that in 10^4 seconds of observing time the temperature could be measured in each of those cells to an accuracy of better than 10%. A2069 is at $z = 0.12$. At 2 or 3 times this distance, according to certain models of cluster evolution, we should be able to detect systematic differences in luminosity, morphology and temperature distribution between those objects and the relatively nearby clusters, and thus detect the manifestations of cluster evolution.

Mass of Galaxies and Clusters of Galaxies

Under conditions of hydrostatic equilibrium hot gas will be distributed in a gravitation potential according to the expression:

$$-kT_{gas}/G\mu M_H \frac{d\ \mathrm{Log}\ \rho_{gas}}{d\ \mathrm{Log}\ r} + \frac{d\ \log T_{gas}}{d\ \log r}\ r = M\ (r)$$

Thus, measurements of local temperature, the temperature gradient, and the density gradient will provide a good determination of M(r), the total mass interior to r. The result is rather unambiguous if the condition of isothermal equilibrium can be established. Galaxies in clusters, particularly if they

ORIGINAL PAGE IS
OF POOR QUALITY

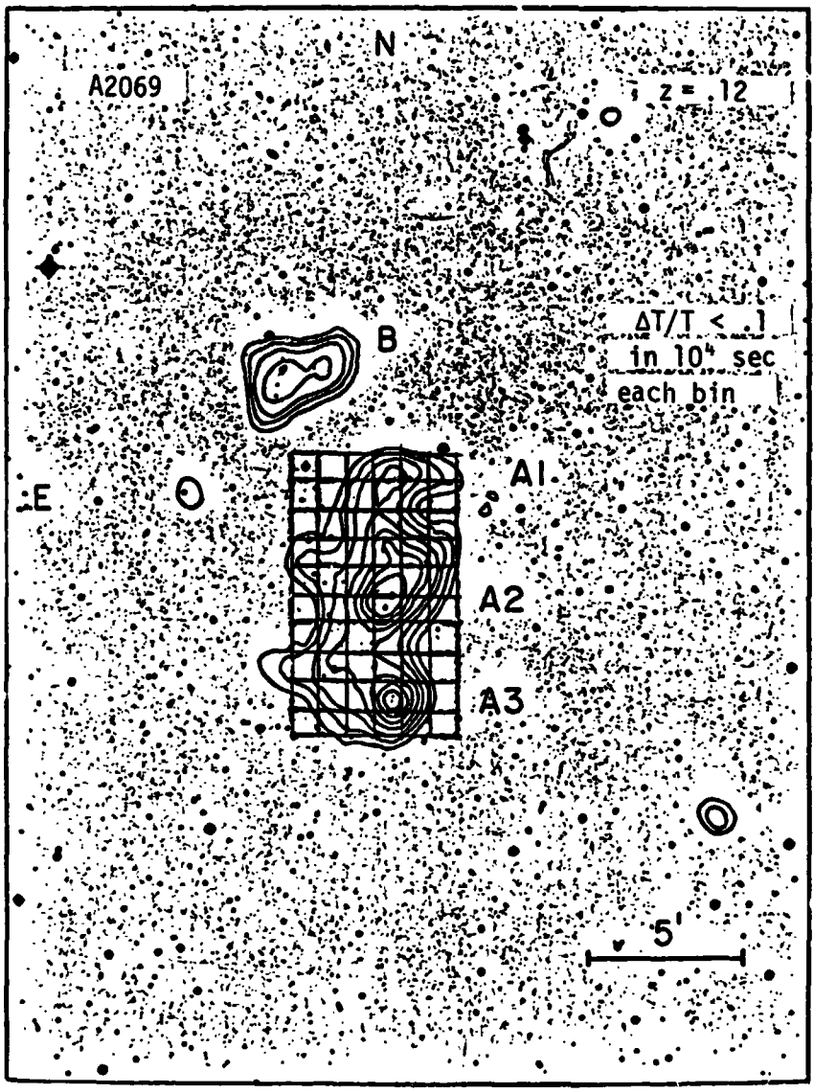

Figure 1

are relatively stationary such as M87 in Virgo, are in a position to have gaseous halos and can be expected to be in a condition of hydrostatic equilibrium. With the Einstein Observatory, it was possible to measure a mass of M87.[5] A LAMAR would have 50X the effective area of the Einstein Observatory (even more above 3 keV) and thus much better capability for measuring temperature and temperature gradients. Consequently, it will be able to determine masses for many more galaxies. With these results, we can study the relations between dark and luminous matter for galaxies of various types and in various environments.

By the same method, the total masses of clusters of galaxies and groups of galaxies can be studied with LAMAR. This is beyond the capability of the Einstein Observatory because of the rapid fall of its effective area above 3 keV. As kT of many clusters are typically 5-8 keV, good response in that energy range is needed to measure temperature gradients and consequently to derive their masses.

Large Scale Structure of the Universe

One of the important objectives in astronomy is to study the structure of the universe on various size scales and to search for other clustering hierarchies. There is reason to believe that X-ray measurements will prove to be very useful for this study. A. Fabian has pointed out at this workshop that diffuse X-rays may be the best probe of the universe in the range 10-100 Mpc. The factor of 50 larger throughput of LAMAR compared to the Einstein Observatory and even more above 3 keV will enable it to examine regions of much lower surface brightness which extend further from the cluster center. In principle, this will permit the search for structure on a larger scale than clusters.

As X-ray measurements (> 2 keV) are so specific to extragalactic objects, LAMAR is expected to find a large number of new extragalactic objects. The distribution of some category or sub-category may exhibit a structure or clustering hierarchy that is not apparent in visible light against the optical background of stars and normal galaxies. For example, the tendency to form superclusters may be more apparent in the correlation or lack thereof between regions of diffuse X-ray emitting gas than in galaxies.

Structural features of large scale may be evident in studies of the X-ray background. Recent papers suggest two possible mechanisms that may indeed result in larger scale structure. A 100 Mpc void has been reported in Bootes (Kirschner et al. 1981).[6] If the X-ray background is linearly proportional to total mass along the line of sight out to the Hubble distance of

say 4000 Mpc (i.e. the sum of all active galactic nuclei and possible hot gas), then a 100 Mpc void would be detectable as a diminution in the X-ray background over the entire 1^{o} field.

$$\frac{100 \text{ Mpc}}{4000 \text{ Mpc}} = 0.025$$

Source confusion noise may make it impossible to detect an effect of this amount in any one field but the observation of many fields should be revealing of structure of this magnitude. Another possible source of variations in the X-ray background has been suggested by Ostriker and Cowie.[7] In their picture, the agent of galaxy formation is multiple supernova explosions in the ambient gas occurring at the epoch $z = 5$. The process of galaxy formation in the intergalactic medium is analogous to that of star formation in our own galaxy. A consequence of this process is the creation of hot cavities; $T = 10^{8}K$, with a diameter of 15 Mpc. Their surface brightness is about 2×10^{-8} ergs/cm^{2}-sec-ster (i.e., equal to the isotropic background) and angular size about 15' to 30'. This should lead to significant variations in the X-ray background within the LAMAR $1^{o} \times 1^{o}$ field of view that are easily detectable. The Einstein Observatory, as well as EXOSAT and ROSAT, do not have sufficient throughput above 2 keV to detect variation in the extragalactic X-ray background.

2.3 Quasars and Other Galaxies with Active Nuclei

One of the significant features of X-ray measurements is their specificity for extragalactic objects for data above 2 keV

in energy and above 20^{o} in galactic latitudes. In that regime, X-ray images are dominated by point-like active galactic nuclei and the diffuse emission of clusters of galaxies. In particular, measurements by LAMAR would result in finding a large number of new quasars. Optical observations would still be needed to determine redshifts, but the selection process based upon X-ray characteristics would make that a relatively straightforward and routine procedure as the sample should be relatively free of galactic objects. The key point about LAMAR is that it would allow studies and classification of quasars according to their X-ray characteristics, such as luminosity, spectral index, and possible X-ray emission or absorption lines, and temporal benavior. Large throughput is needed to obtain a level of significance much beyond that required to merely establish existence.

Temporal Behavior

The study of temporal variations promises to be a very important diagnostic tool for active galactic nuclei as described by A. Lightman at this symposium. There are theoretical reasons to believe and considerable observational evidence to indicate that active galactic nuclei will exhibit fast time variations in their X-ray flux. LAMAR is essential for observing temporal variations in all but the few very brightest and nearest objects. Imaging is necessary for removing background and avoiding source confusion. Figure 2 is a simulation of a type of temporal variation expected to occur often in a QSO[2] (c.f. Lightman) if the energy source is accretion onto a black hole. A QSO of

ORIGINAL PAGE IS
OF POOR QUALITY

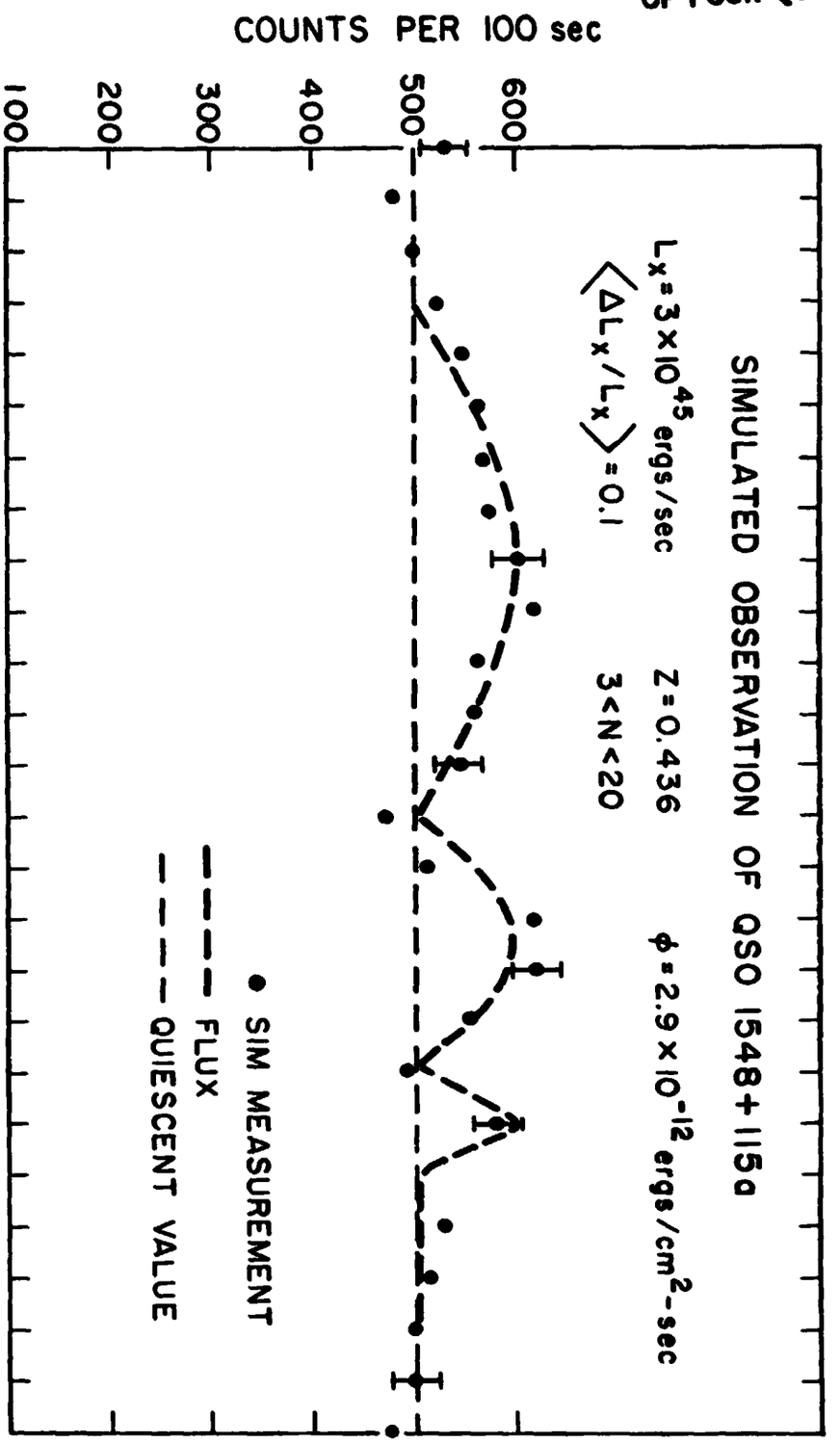

Figure 2

ORIGINAL PAGE IS
OF POOR QUALITY

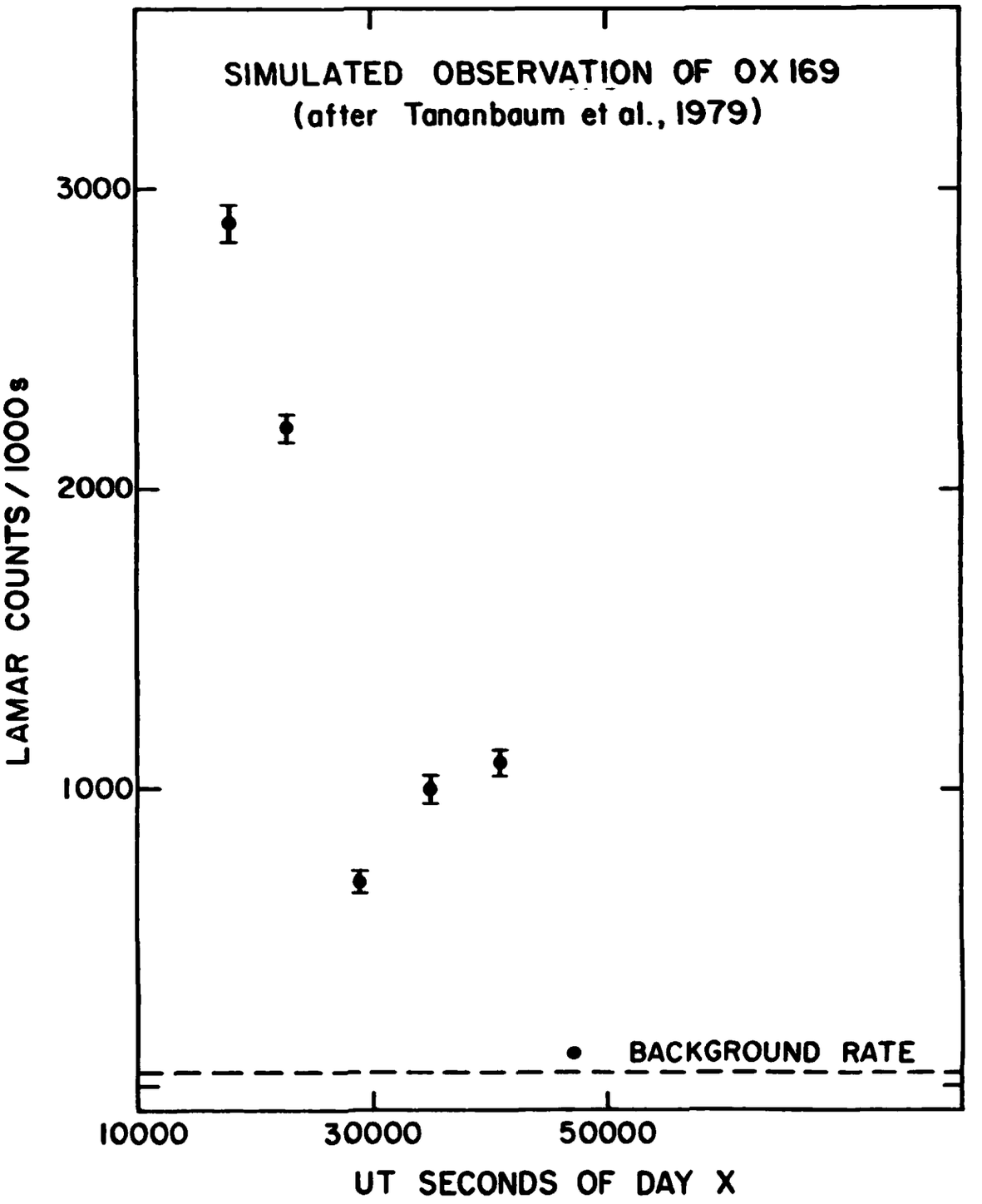

Figure 3

moderate X-ray intensity has been selected for simulation. Sinusoidal periods of decreasing length correspond to a series of three final orbits around the nucleus. A more spectacular temporal variation is simulated in Figure 3. This is based on an actual Einstein Observatory measurement of a faint quasar in which only 47 counts were obtained. There is an indication of large variability in a short time.[8]

The coupling of spectral measurements to temporal will provide even more diagnostic information about the environment surrounding an active galactic nucleus. There is evidence from a combination of Ariel 5 and Einstein Observatory data for systematic correlations between the total X-ray emission from Seyfert galaxies and the ratio in flux between a soft (0.5-1 keV) and a harder component (2-10 keV) (Elvis and Lawrence 1981).[9] Variable intrinsic absorption of soft X-rays plays a role in the correlation. LAMAR will be able to carry out spectral/temporal studies in detail for many objects.

2.4 Compact Objects in the Galaxy

One of the great contributions of X-ray astronomy to astrophysics is the discovery of close binary systems containing compact objects that exhibit a remarkable range of time variations of intensity. These systems present an opportunity to study the behavior of neutron stars and other compact objects in an environment where they are accreting substantial streams of matter. The X-ray Timing Explorer (XTE) will be undertaken as a dedicated low cost mission to study these systems using large area non-imaging detectors. While XTE is expected to produce

significant results based upon observations of the hundred or so most intense galactic objects, we can already anticipate the need for follow-on investigations with a more sophisticated instrument that can deal with fainter objects. With its imaging capability and large area, LAMAR will be able to observe much fainter objects because background effects and source confusion are eliminated. Thus, it can address a variety of new systems such as neutron stars in other environments, as well as cataclysmic variables containing degenerate dwarfs.

Neutron Stars

The greater sensitivity of the LAMAR extends the scope of neutron star investigations considerably by increasing the number of channels of observation. They are described below.

(1) Compact Objects in Supernova Remnants

A number of supernova remnants have been shown by the Einstein Observatory to contain compact X-ray emitting objects. These include W50 (SS433), G109-1, RCW103, the Vela SNR, and others. Although this collection of objects represents a mixture of X-rays from accreting binary systems, synchrotron acceleration of particles and hot neutron star surfaces, they are as a group rather young neutron stars. They may present aspects of neutron star behavior that are different than compact binaries which are generally much older objects.

(2) Radio Pulsars

The Columbia University group has detected X-ray emission from several radio pulsars with the Imaging Proportional Counter of the Einstein Observatory (Helfand 1981).[10] The

objects seem to be spatially extended indicating that X-rays are produced as a result of active particle acceleration as in the Crab Nebula and Vela. Pulsars are isolated neutron stars and represent objects intermediate in age between those found in supernova remnants and those in compact binary systems. With 50 times the throughput of the Einstein Observatry, LAMAR shoould be able to study many pulsars.

(3) Possible Persistent X-ray Sources at Gamma Ray Burst Positions

Several models for gamma ray bursts (e.g. Woosley and Wallace)[11] predict that there will be persistent X-ray emission. There is marginal evidence for such a correspondence in an Einstein Observatory observation. If the fluxes are within an order or two of magnitude of predicted, then the catalog of precise gamma ray burst positions can be examined with LAMAR for a study of highly magnetized neutron stars.

(4) Faint Compact Binary Systems (Neighbor Galaxies)

The discovery of individual systems exhibiting a new type of behavior, such as Cyg X-1, Her X-1, and AM Her, has had a profound effect upon our perception and understanding of the physics of compact objects. Thus, the detection of additional objects with unique temporal behavior could have a great significance that is difficult to predetermine. The imaging capability of LAMAR will allow it to study much fainter compact binary systems whether they are within our own galaxy and of relatively low intrinsic luminosity or in neighbor galaxies where they are faint because of distance. Thus, LAMAR would make a considerably larger number of neutron star compact binaries

accessible to study. While there is no reason to believe a priori that this larger group will contain phenomena or features that are not seen among the more intense group, the previous history of compact objects indicates that even a single object can have an impact that is revolutionary.

Cataclysmic Variables

In addition to compact binary systems containing neutron stars, there exists fainter objects containing degenerate dwarfs which includes cataclysmic variables (CV). Their time scales of temporal change are not likely to be as rapid but not necessarily less interesting. This means that with an imaging detector faint objects can be studied because we can integrate for longer periods of time without background or confusion becoming a factor. The recently discovered X-ray CV's (AM Her, 2A0311-227, V1223 Sag, 2237-035) show both optical and X-ray periodicities and quasi-periodicities which allow diagnosis of the structure and mass transfer in these systems.

As an example of how LAMAR will perform in the study of the temporal behavior of cataclysmic variables, we consider the faintest object that is likely to be of interest. As described by D. Lamb at this workshop, it is one that emits at 10^{31} ergs/sec at a distance of 1000 pc. There are hundreds of objects more intense than this. (More distant objects are difficult to study optically.) In LAMAR this source will count at a 0.5 cts/sec with essentially no background. We can easily study temporal behavior of individual flares on a time scale of 50 seconds or more. Search for periodicities and spectral changes

will be accomplished quite easily. The spectral resolution of LAMAR will permit a study of correlated changes of soft and hard components.

2.5 Stellar Coronae

One of the major contributions of the HEAO program and the Einstein Observatory (HEAO-2), in particular. has been to establish X-ray measurements as a major diagnostic tool for stellar coronae. X-rays have been detected from stars of virtually every spectral type and flare activity has been found. Some moderate resolution line spectroscopy was obtained for the few most intense objects. As impressive as the Einstein Observatory results may be, they represent only the beginning phases of what could be a major new means of fundamental investigations of stellar coronae. The effective area of the Einstein Observatory telescope was only 200 cm^2. Because its effective area will be 50 times that of the Einstein Obervatory and 10 times that of AXAF, the LAMAR is a much more powerful tool for stellar photometry. With the use of more efficient dispersive techniques, LAMAR's increase of throughput over Einstein for moderate resolution spectroscopy ($E/\Delta E \simeq 100$) is potentially even much larger than that for imaging and photometry.

It should be possible to make a grating that is at least 10 times as efficient as the objective transmission grating of Einstein. Reflection gratings, as discussed by W. Cash at this symposium, will allow much higher line densities and, consequently, much higher dispersions. The key point is that the

dispersion would be large enough to make an Imaging Proportional Counter feasible as the detector of the dispersed spectrum. The IPC's efficiency is about four times higher than that of the high resolution imager of the Einstein Observatory. Hence, even if only a fourth of the full area of the LAMAR were devoted to spectroscopy, the increase in throughput relative to Einstein would be larger by a factor of:

$$50/4 \times 10 \times 4 \approx 500.$$

This would be a large enough increase to make moderate resolution spectroscopy applicable to many stellar objects. Assuming that 1/4 of the LAMAR's total area is devoted to reflection gratings and assuming that the grating efficiency is [illegible], the estimated count rate in the dispersed spectrum of a star emitting 10^{29} ergs/s at a distance of 25 pc is 0.5 counts/s in the 0.5 to 1.5 keV band. Thus, an observation of 2×10^4 seconds will provide some 10^4 counts, and a comparable number of background counts. For a resolution of 100, the average energy bin will contain 100 counts, and many of these will be in the form of lines so that many bins will contain several hundred counts. This is sufficient to provide meaningful measurements of temperature and ionization equilibria.

Photometry in conjunction with low resolution spectroscopy ($E/\Delta E \approx 2$) at 1 keV can be applied to many stars. This is useful for monitoring flare activity and detecting changes in temperature that are correlated with increases in intensity. Figure 4 is an illustration of the spectrum of a star at a

distance of 40 pc emitting 10^{28} ergs/s as observed in LAMAR for a time of 10^4 sec. Spectra are shown for a pure thermal spectrum (Raymond & Smith) of kT = 0.17 keV, as well as for various amounts of an additional component flux with kT = 1.0 keV. There is no difficulty in detecting a small percentage of the higher temperature component. In the example taken, the star could be in the Hyades cluster. When the LAMAR is pointed to that region, we would expect that several stars would be observed simultaneously within the 1^o field of view of LAMAR.

The features of stellar coronae that could be studied with X-ray measurements have been discussed by Linsky at this symposium. They are:

Temperatures, range and dependence upon luminosity
Densities
Flow velocities
Total energy input and heating mechanism
Energy balance
Geometry, fraction of the volume filled by loops
Wind acceleration mechanisms
Interaction of winds with interstellar medium
Flares on stars of various types

The types of measurements needed to carry out these studies are:

(a) Imaging for measurement of flux with some spectral resolution (low resolution spectroscopy) to distinguish between soft and harder bands.

(b) Identification of new stellar sources with high

ORIGINAL PAGE IS
OF POOR QUALITY

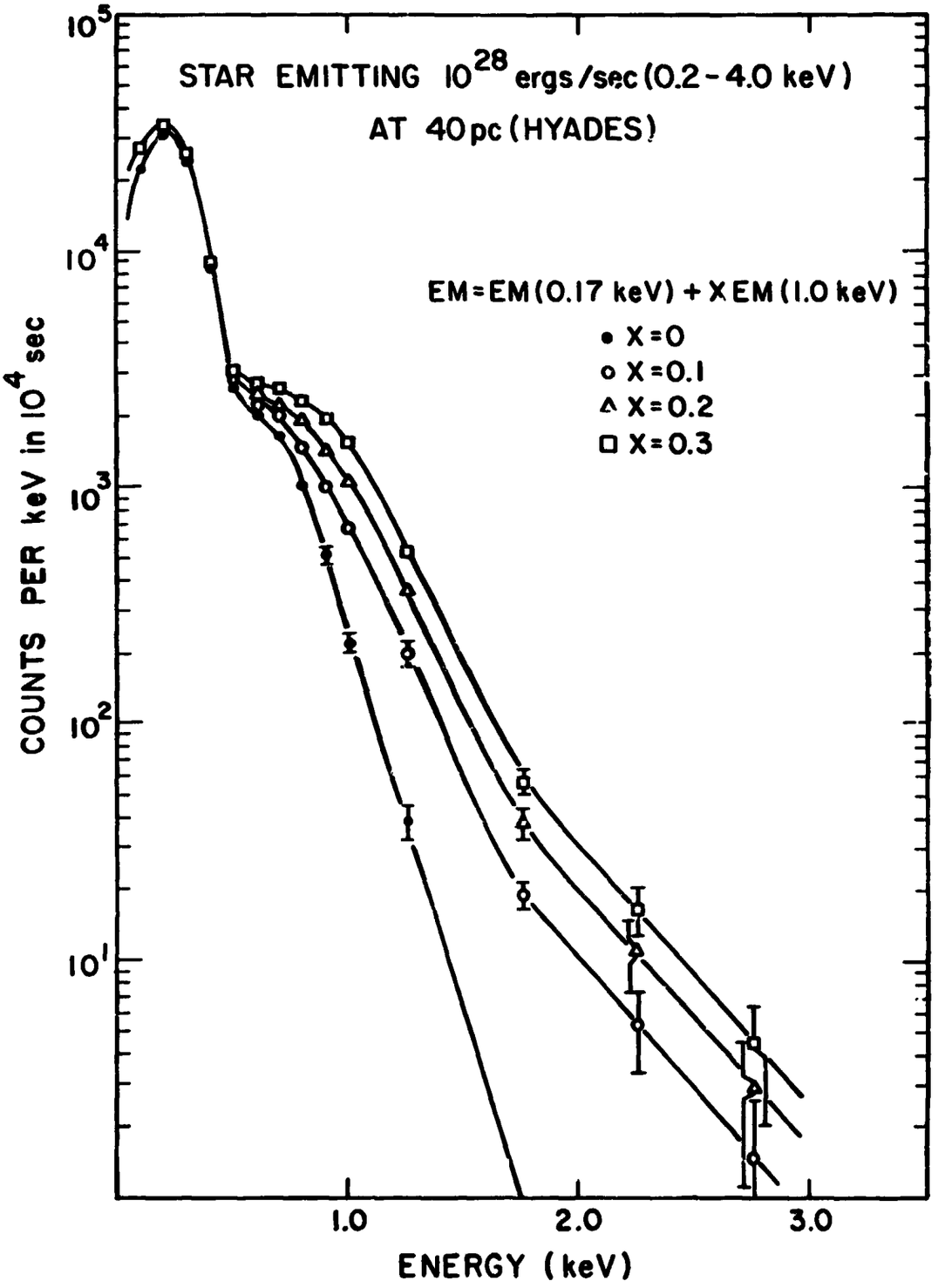

Figure 4

sensitivity providing the capability to obtain X-ray luminosity functions of various categories of stars.

(c) Temporal studies of flares and other activity, simultaneous temperature-flux measurements.

(d) Moderate resolution spectroscopy ($E/\Delta E \approx 100$).

(e) High resolution spectroscopy ($E/\Delta E \approx 1000$).

LAMAR will be able to provide measurement capabilities (a), (b), and (c) for many stars when used in its imaging mode. With the use of reflection gratings forward of the mirror assemblies over at least some of the mirrors (e.g. at 25% of the total area) it can provide (d), a moderate resolution spectroscopy capability. High resolution spectroscopy measurements will be out by AXAF. Thus, LAMAR will be able to address many of the areas of principal concern in stellar coronae.

2.6 Interstellar Medium

It has been established that a large fraction of the volume of the interstellar medium (ISM) contains a hot gaseous component of low density. The signature of this component is the soft X-ray background which is the predominant source of diffuse X-rays in the 0.1-0.3 keV band. Several years of sounding rocket measurements by the University of Wisconsin group have produced a soft X-ray map of the entire sky in $6^{o} \times 6^{o}$ bins. This map shows a highly structural gas that is perhaps within a hundred parsecs or so of the Sun. With the high throughput imaging ($\sim 10^{4}$ cm^{2} effective area, 1' angular resolution, 1^{o} field) and its spectral ability which consists of low resolution

($E/\Delta E \approx 2$) spectroscopy for diffuse regions and moderate resolution spectroscopy ($E/\Delta E \approx 100$) for point sources, it is possible to carry out additional studies of the ISM that are relevant to the topics discussed by Cowie and Shull at this symposium.

(1) Imaging of the Galactic Component of the X-ray Background in Several Spectral Bands, 0.1-0.3 keV, 0.5-1 keV, and 1-2 keV.

Because of absorption within the plane of our galaxy, we detect higher energy X-rays out to larger distances. The 0.1-0.3 keV band is primarily local, up to 200 pc, the 0.5-1 keV band can reach out to 1000 pc, while the 1-2 keV band extends the reach almost to the galactic center. With the LAMAR, we have sufficient throughput to image the background on the scale of a fraction of a degree. The count rate in a 1^{o} field would be 20 counts/s in the 0.1-0.3 keV band, on the average perhaps a factor of 3 lower in the 0.5-1 keV band, and another factor of 3 lower at 1-2 keV. (Above 2 keV the extragalactic component is dominant.) With integration times of 10^{3} seconds or more for each 1^{o} field, we would be able to construct surface brightness maps with considerable significance in each of the three energy bands on a scale of a fraction of a degree. We would detect the surface brightness variations that result from old supernova shells that are no longer identifiable as discrete radio sources. We would also detect diffuse regions that are heated as a result of stellar particle emission.

(2) Resolution of Discrete Sources Which Contribute to Heating of the ISM.

Resolving discrete sources is essential for identifying the residual diffuse component that represents the interstellar gas. Furthermore, it will lead to the identification of discrete objects that are significant sources of energy input to the ISM. Probable examples of the latter are the X-ray emitting OB stars and associations detected by the Einstein Observatory. In the η Carinae region and in Orion, there is circumstantial evidence for this process by the proximity of diffuse emission to a high density of discrete X-ray sources.

(3) X-ray Absorption Spectra as a Probe of the ISM.

Absorption features in the continuum spectra of discrete sources can be studied with the moderate resolution spectroscopy capability of the LAMAR. The LAMAR's high throughput will make these studies feasible for many objects by providing a probe of the galaxy along the many directions to fairly intense sources. We would detect the O and Ne edges of cold material and perhaps that of matter in a higher ionization state.

(4) Imaging of Old SNR's and Giant Bubbles.

Although these objects are of large diameter, good angular resolution is still required for imaging because of the need to resolve and remove numerous discrete sources. The hot component of the ISM is undoubtedly related to shock heating by old SNR's as described by Cox and Smith, McKee, Cowie, and Ostriker, among others. We should see the diffuse shells of old SNR's plus

"giant bubbles" like the one found in the Cygnus region that may have originated from the interaction of multiple SNR's.[12]

(5) Studies of the ISM Neighbor Galaxies.

Our understanding of the ISM of our own galaxy will be greatly aided by images of neighbor galaxies, such as the LMC, SMC and M31. For the LMC and SMC, we will obtain a complete picture of the hot component of their ISM and the relation of the major spatial features to SNR's and other sources of heating.

(6) Coronae of Normal Galaxies Within 3 Mpc.

The production of hot gas by supernova explosions and active stellar objects will lead to the establishment of a steady hot corona around normal galaxies. The corona is an integral effect of the heating processes. The features of the corona, such as its density, scale height, and relation to the plane, can be measured. There are theoretical calculations by Bregman,[13] which suggest that LAMAR should be able to measure the coronae of nearby edge on galaxies within a few Mpc. Figure 5 indicates the signal expected at various heights above the plane in an observation of 10^4 seconds.

3.0 HIGH THROUGHPUT SPECTROSCOPY WITH LAMAR

Requirements for high throughput are even greater for spectroscopy than for imaging. The existence of an X-ray source and even its position can be determined from relatively few photons. When background is negligible, 10 photons in the image are sufficient. However, to carry out spectroscopy studies, many

X-ray Coronae Around Galaxies
J.N. Bregman, Ap.J., 237, 681 (1980)
Model D
Edge On Galaxy at 3.3 Mpc 1' ~ 1 kpc

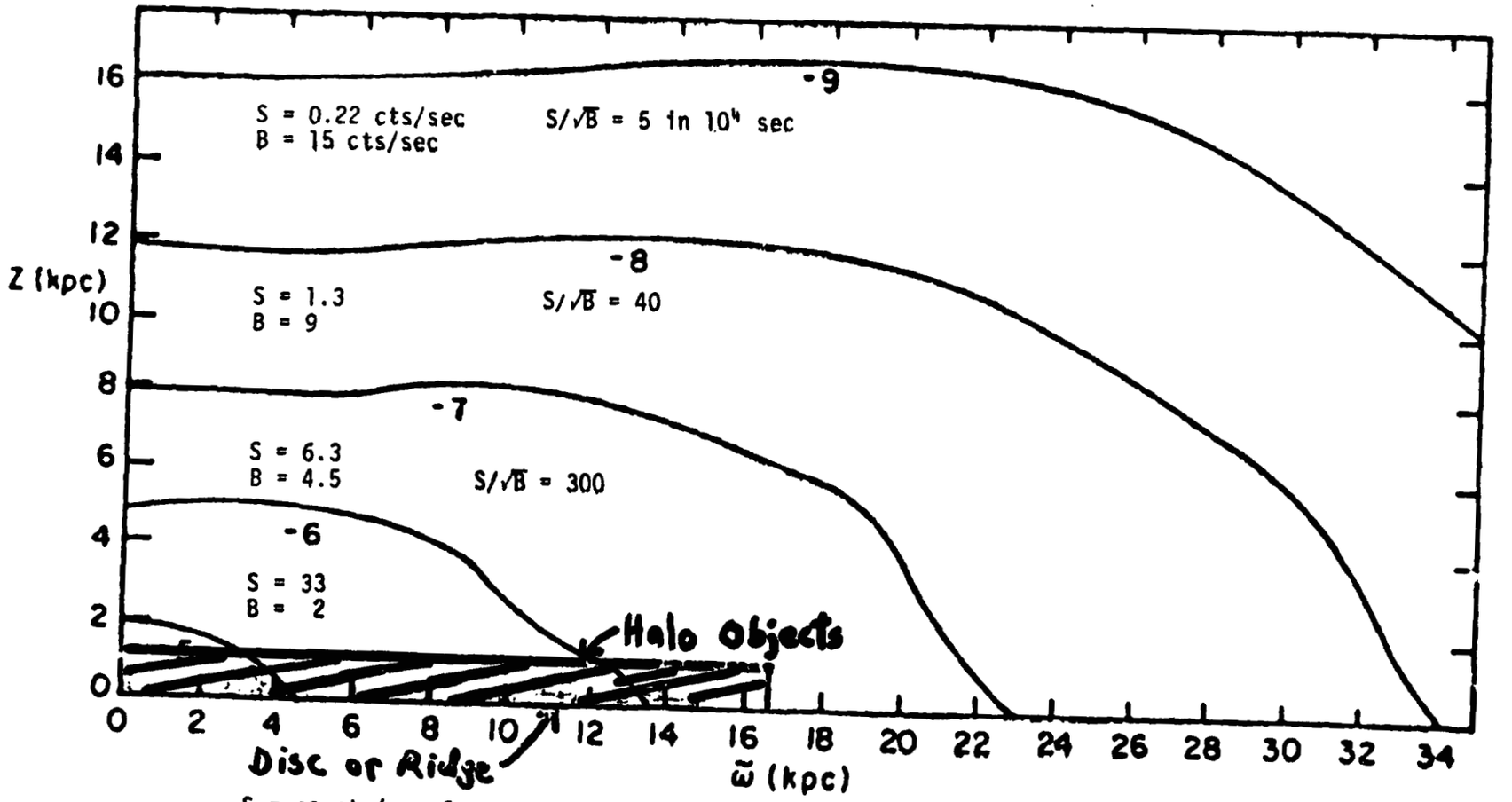

S = counts/sec from corona integrated over area between contours.
B = counts/sec from background integrated over area between contours.

Figure 5

ORIGINAL PAGE IS
OF POOR QUALITY

more photons are needed. For example, if kT = 4 keV, simulations show that 4000 photons are required in order to determine a value for the temperature with ±10% precision by fitting model spectra to continuum data obtained with a telescope system having good response at higher energy, such as LAMAR or AXAF. (Without good response at 4 keV, the measurement takes much longer or cannot be done.) If the spectrum is a power law with -1.5 as the number-energy spectral index, in order to obtain ±10% accuracy in the spectral index, 500 counts are required if the spectrum is not self-absorbed ($N_H = 2 \times 10^2$), but the number of photons needed climbs rapidly as intrinsic absorption increases. At $N_H \approx 10^{22}$, which is not unlike several Seyfert galaxies studied, 10^4 counts are needed for a 10% precision in the spectral index measurement. Thus, for broad band spectral measurements, we require from a factor of 50 to 1000 more photons than for merely establishing existence. For dispersive line spectroscopy, the details of the discussion are different, but the general conclusion is the same; a large number of photons is needed to arrive at a quantitative result. For example, to measure temperature, we may need to determine the ratio of two lines to better than 10% precision. At least 200 photons are needed in each line. The counts in lines are generally only a fraction of the total number of incident photons. Taking the finite efficiency of the dispersive element into account, we conclude that the collecting area of the system must take in several hundred to several thousand total photons for line spectroscopy to provide a quantitatively meaningful result.

We consider two forms of spectroscopy that could be carried

out by LAMAR. One is non-dispersive spectroscopy for gross spectral characteristics of sources dominated by continuum, temperature and temperature gradients in diffuse sources, such as clusters of galaxies, and spectrophotometry for faint and variable sources. These are carried out in conjunction with imaging. The other form of spectroscopy is a dispersive option that requires additional hardware.

3.1 Non-Dispersive Spectroscopy

For many faint and diffuse sources, there is no alternative to non-dispersive spectroscopy. In cases where lines are weak, such as quasars, non-dispersive spectroscopy may be the only form of spectroscopy that is feasible. As an example of non-dispersive spectroscopy in a diffuse source, we consider a measurement of the temperature distribution of the cluster A2069 in cells of 1' x 1' (Fig. 1). Simulations show that $>10^4$ sec are required for a measurement resulting in $\Delta T/T < .1$. The temperature gradient in combination with the surface brightness map could then be used to create a map of the mass distribution.

The detector for non-dispersive spectroscopy could be the imaging proportional counter. Recent devices provide as good an energy resolution as conventional proportional counters, $E/\Delta E \approx 5$ at 6 keV. With this level of energy resolution, it was possible for proportional counters aboard Ariel 5, OSO-8 and HEAO-1 to detect Fe lines in clusters of galaxies and spectral features in supernova remnants. Use of a scintillating imaging proportional counter as described by W. Ku[14] at this meeting and elsewhere and Anderson[15] could provide about twice as good energy

resolution. This type of detector is still in the development stage, so it is not yet known what loss of spatial resolution is involved compared to an ordinary IPC or how reliable these detectors would be in long term operation.

3.2 Dispersive Spectroscopy

A paper presented by W. Cash at this meeting describes a method for dispersive spectroscopy by use of reflection gratings in the extreme off-axis configuration, forward of the mirror. The rulings are nearly parallel to the incident direction of the radiation. The reflection efficiency of the gratings are high, below 1.5 keV. Because the ruling density is high, 10^4 lines/mm, dispersions are large enough for an imaging proportional counter to be used as the detectors. A system with 1' of angular resolution would provide an energy resolution, $E/\Delta E$ of about 100 at 1 keV. As a LAMAR imaging system is compatible with the requirements of the reflection gratings, it is worthwhile to consider a combined imaging-spectroscopy LAMAR system. There are two possibilities. In one, every module has a dual function. Gratings would be placed before each mirror for spectroscopy measurements. When the gratings are removed, each module operates in an imaging mode. The second possibility is to have two types of modules, one for imaging, the other optimized for spectroscopy. The advantage of removable gratings is higher throughput as the full power of the LAMAR is available in any given observation whether the objective is imaging or spectroscopy. The advantage of the second configuration is simplicity, compactness, and no moving parts. Study is needed to

determine which configuration is preferred.

Assigning reasonable values to the various efficiencies and obscurations, one can estimate that in the dispersive spectroscopy mode the LAMAR would have an effective area of about 10^3 cm^2. This is substantial and would permit dispersive spectroscopy to be carried out on many objects.

4.0 MODERATE COST APPROACH FOR LAMAR

Although the LAMAR is a large area facility, it can be developed with the cost constraints of a moderate mission. There are two considerations which mitigate the cost. One is the fact that the resolution goal is only about a minute of arc which allows a number of telescope manufacturing techniques to be feasible that would fail at the arc second level. For example, high cost figuring and polishing techniques are not required. The other factor is the modular construction of LAMAR. The problem of developing an array of large area reduces to one of finding a manufacturing technique that is efficient at making many copies of a module. Numerically controlled machines and computer assistance are two techniques that are useful in this regard. The module itself can be of optimum size with respect to problems of construction, testing, and integration. Furthermore, the modular approach has another cost advantage over a monolithic device in that it allows the essential elements of the system to be fully tested and understood from studies of one or a few sample modules. No "scale-up" problems, changes in technique, or other uncertainties arise when embarking upon the major phase of construction. One key to controlling costs is to use a single

technology for each of the three items, mirror assemblies, detectors, and gratings.

At present, there are several technologies for the development of mirror assemblies that seem promising for LAMAR. To provide some credibility to the idea that LAMAR can be developed at moderate cost, we consider the particular techniques under study at the Center for Astrophysics for mirrors and detectors as an example. Our approach is based upon the construction of mirror assemblies consisting of nested plates of float glass with imaging proportional counters as detectors. The elements of this method are listed in Table 4-1. It is based upon the use of commercial materials and the avoidance of polishing for the reflecting surface. Numerically controlled machining and computer assistance are used for the formation of the figure.

4.1 The Mirror Assembly

The mirror assembly can be constructed of commercially available float glass with a gold coating. X-ray reflectivity is good at short wavelengths. Glass plates are constrained mechanically to form a figure that is almost parabolic. A nested system equivalent in size to one LAMAR module has been used successfully on a series of rocket flights.[16] The theoretical angular resolution of such a system is limited by elastic deformations in the bent plates. Several measures can be taken to improve the resolution as summarized in Table 4-2. Mechanical tolerances are expected to be important long before reaching the ultimate resolution of a pre-figured or "slumped" plate.

Table 4-1
MODERATE COST APPROACH FOR 10^2 MODULES
FOR LAMAR

Nested Plate Mirrors	
Reflecting Surfaces:	Commercial float glass (Au coated) No polishing required
Figure Formation:	Automated interactive microprocessor control of positicn adjustments based upon sensing of visible light image by reticon diode arrays
Mirror Assembly Structures:	Mass production using numerically controlled machines to fabricate top, bottom, and side plates, .001" accuracy easily achieved
	Mass production of screw machine products relatively inexpensive in quantity
Imaging Proportional Counters	
Electronics:	No critical elements, extensive use of integrated circuits
Bodies:	Numerically controlled machines
	No critical tolerances
Wire Planes:	Special precision tooling facilitates wire winding
Reflection Gratings	
Surfaces:	Replication

ORIGINAL PAGE IS
OF POOR QUALITY

TABLE 4-2

LAMAR MIRROR SYSTEM PERFORMANCE

(ENCIRCLED ENERGY vs. SYSTEM TYPE)

ADJUSTED BENT PLATE
(ON-AXIS OPTIMIZED)
50% ≈ 0.63 arc minutes diameter

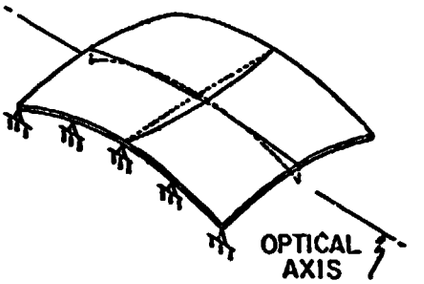

MASKED ADJUSTED BENT PLATE
(OPTIMIZED MASKED)
50% ≈ 0.59 arc minutes diameter
AREA LOST ≈ 18%

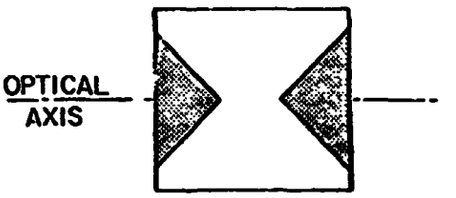

STIFFENED FLAT BENT PLATE
50% ≈ < 0.45 arc minutes diameter

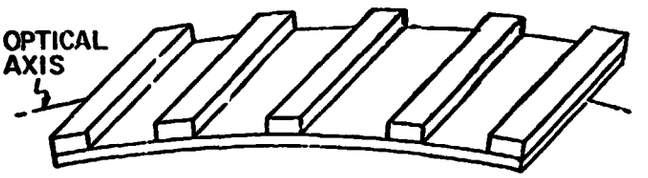

ADJUSTED PRESLUMPED PLATE
50% ≈ 0.16 arc minutes diameter

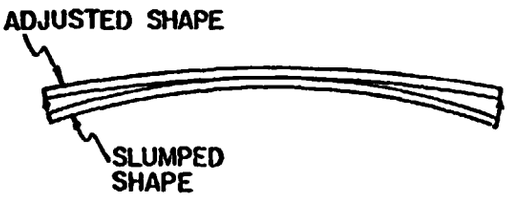

PERFECT NESTED SYSTEM
50% ≈ 0.12 arc minutes diameter

NOTES:

- ALL NUMBERS APPROX.
- UNIT REFLECTANCE ASSUMED
- FOCAL LENGTH ≅ 213 cm
- 30.5 cm SQUARE PLATES ASSUMED
- NO INITIAL SURFACE RIPPLES ASSUMED

SAO 9-25-81

Computer assistance would be useful for bending of the plates to the desired shape. Figure 6 illustrates the method that we plan to study. A microprocessor controls the position of a slit that can be driven alcng a precise linear encoder. A portion of a plate is illuminated by visible light through the slit. The line image is read at three points by diode arrays. The centroidal position of the three images are determined by the microprocessor. This information is used to drive stepper motors which apply bending moments to plate until the images are acceptable. The slit is moved to another part of the plate and the process is repeated. As experience is gained in this procedure the microprocessor program will be updated to incorporate refinements in the plate adjustment procedure.

4.2 Reflection Gratings

Although more definition of the reflection gratings is needed at the present time, it is expected that mass production methods are applicable. A nested array of identical grating plates would seem to be a good match to the optics of the nested plate telescope. Replication seems extremely promising as a method for producing a large number of identical gratings.

4.3 The Detectors

Imaging proportional counters (IPC's) in their various forms can be manufactured by well established and straightforward methods. The techniques include circuit board manufacturing, extensive use of integrated circuits as components, and numerically controlled machining. Little difficulty is

ORIGINAL PAGE IS
OF POOR QUALITY

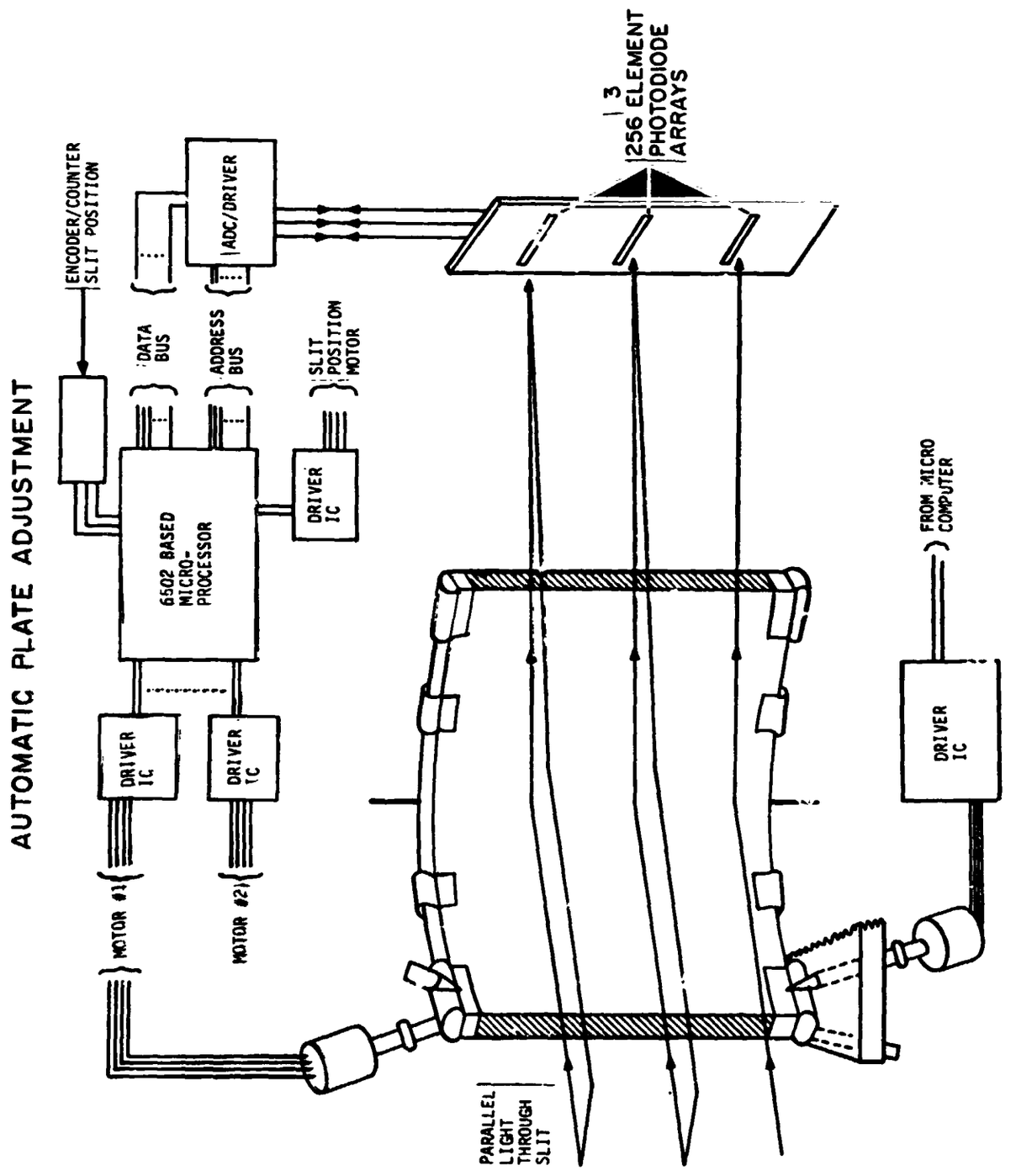

Figure 6

anticipated in assigning these tasks to conventional manufacturing shops.

5.0 SUMMARY AND CONCLUSIONS

The high throughput capabilities of LAMAR will satisfy many of the requirements of future programs in X-ray astronomy. It will excell in measurements requiring:

moderate resolution imaging for flux measurements and positions

detection of low surface brightness features

timing for temporal variability

spectral measurements

The high throughput of LAMAR is unique and will greatly surpass that of all other telescope instruments, including the Einstein Observatory and all other facilities being planned for the future both in the U.S. and abroad. LAMAR is applicable to a wide range of scientific objectives and will serve many investigators.

The general utility of the LAMAR may be appreciated from an analysis of the guest observer usage by instrument of the Einstein Observatory. This is summarized in Table 5-1. Guest observer usage is a good indicator of how the astronomical community in general perceives the various instruments in terms of being relevant to their interests. The table shows that the Imaging Proportional Counter was the overwhelming choice both in terms of the number of observations and the total time in the focal plane. The essential characteristic of the IPC that

TABLE 5-1
EINSTEIN OBSERVATORY
GUEST OBSERVER STATISTICS BY INSTRUMENT

Total Time Done

IPC	-	6518.68 ksec	78.2%
HRI	-	1550.99	18.6%
SSS	-	229.10	2.7%
FPCS	-	39.60	.5%
TOTAL	-	8338.37 ksec	

Total Number of Observations

IPC	-	1571	90.7%
HRI	-	138	8.0%
SSS	-	20	1.2%
FPCS	-	2	.1%
TOTAL	-	1731	

resulted in its being selected so frequently was its high throughput. LAMAR will exceed the IPC of the Einstein Observatory by a factor of 50 in that capability which was found in practice to be most useful to the astronomical community as a whole.

Despite its large collecting area, the modular approach intrinsic to LAMAR will greatly simplify its development and will allow it to be compatible with a moderate cost Explorer mission.

ACKNOWLEDGEMENTS

We would like to thank Wallace Tucker and Daniel Fabricant for informative discussions and aid in the estimation of performance of the LAMAR. We would also like to thank Lester Cohen and Paul Brown for their contribution to the discussion of the nested plate mirror system.

REFERENCES

1. Schwartz, D.A. (1976), Ap.J. (Letters), 206, L95.
2. Mushotzky, R.F., Marshall, F.E., Boldt, E.A., Holt, S.S., and Serlemitsos, P.J. (1980), Ap.J., 235, 361.
3. Forman, W. and Jones, C. (1982), to be published in Annual Reviews of Astronomy and Astrophysics, Vol. 20.
4. Gioia, I.M., Geller, M.J., Huchra, J., Maccacaro, T., and Stocke, J. (1981), submitted to Ap.J.
5. Fabricant, D., Lecar, M., and Gorenstein, P. (1980), Ap.J., 241, 552.
6. Kirschner, R., Oemler, A., Jr., Schecter, P.L., and Shectman, S. (1981), Ap.J. (Letters), 248, L57.
7. Ostriker, J. and Cowie, L. (1981), Ap.J. (Letters), 243, L127.
8. Tananbaum, H., Avni, Y., Branduardi, G., Elvis, M., Fabbiano, G., Feigelson, E., Giacconi, R., Henry, J.P., Pye, J.P., Soltan, A., and Zamorani, G. (1979), Ap.J. (Letters), 234, L9.
9. Elvis, M. and Lawrence, A. (1981), submitted to Ap.J.
10. Helfand, D., Becker, R.H., and Novick, R. (1981), Bull. A.P.S., 26, 570.
11. Woosley, S.E. and Wallace, R.K. (1981), Lick Observatory preprint.
12. Cash, W., Charles, P., Bowyer, S., Walter, F., Garmire, G., and Riegler, G. (1980), Ap.J. (Letters), 238, L71.
13. Bregman, J.N. (1980), Ap.J., 237, 681.
14. Ku, W. and Hailey, C.J. (1981), I.E.E.E. Trans. on Nuc.

Sci., Vol. NS-28, 830.

15. Anderson, D.F. (1981), I.E.E.E. Trans. on Nuc. Sci., Vol. NS-28, 842.

16. Gorenstein, P., Gursky, H., Harnden, F.R., Jr., De Caprio, A., and Bjorkholm, P. (1975), I.E.E.E. Trans. on Nuc. Sci., Vol. NS-22, 616.

PRECEDING PAGE BLANK NOT FILMED

N82 26066

A Wolter Type I LAMAR

K.C. Catura, W.A. Brown and E.G. Joki

Lockheed Palo Alto Research Laboratory
Dept. 52-12, Bldg. 255
3251 Hanover Street
Palo Alto, California 94304

1 November 1981

This paper presented at the

Goddard Workshop on X-Ray Astronomy and Spectroscopy

5-7 October 1981

A Wolter Type I LAMAR

R.C. Catura, W.A. Brown and E.G. Joki
Lockheed Palo Alto Research Laboratory

Abstract

Observational objectives for the LAMAR and their influence on the instrument design are discussed. It is concluded that the most important design parameter is the angular resolution of the LAMAR modules since it so strongly influences sensitivity, optical identifications, source confusion, spectral resolution for objective gratings and the ability to resolve small extended sources. A high resolution Wolter Type I LAMAR module is described, its hardware status discussed and the performance of a LAMAR observatory presented. A promising technique for enhancing the reflectivity of Wolter Type I X-ray optics in a selected bandpass at high energy has been investigated and the performance of the LAMAR module, utilizing this method, has been calculated.

I. Introduction

There are a number of important objectives in X-ray astronomy which require large collecting area to achieve high sensitivity in timing measurements, spectroscopy and the study of faint sources. Because of detector background noise and source confusion problems, the only practical way of achieving such large area instruments is to utilize X-ray imaging with good angular resolution. Due to the properties of X-ray reflection, however, large effective areas cannot be achieved at X-ray wavelengths with a single telescope and thus the concept of an array of co-aligned telescopes, in modular units, has arisen. This concept has become commonly known as the Large Area Modular Array of Reflectors and is identified by the acronym, LAMAR. The purpose of this paper is to discuss, in general terms, the objectives of LAMAR observations and to show how achieving these objectives very strongly influences design of the instrumentation. Also, the current status of a hardware program to develop Wolter-I X-ray optics for the LAMAR will be described and the design of a LAMAR module utilizing these optics will be discussed. Capabilities and performance of a 24 module LAMAR have been calculated and compared with those of the Einstein Observatory and AXAF. Finally, a promising technique for improving the high energy response of Wolter I optics by deposition of multilayered diffraction coatings on their reflecting surfaces will be discussed.

II. Important LAMAR Characteristics

Many specific objectives in X-ray astronomy which can be addressed by LAMAR observations were presented during the first day of this workshop. Several general observational objectives for the LAMAR and how their achievement very strongly influences the LAMAR design are discussed below.

1. Surface Brightness Measurements of Faint Diffuse Emission.

This objective includes study of emission from intracluster gas in galaxy clusters, galactic halo emission, shadowing of the diffuse component of the extragalactic X-ray background by absorption in nearby galaxies and

investigation of soft diffuse emission within the Galaxy.

Since higher angular resolution will not concentrate the diffuse X-rays onto a smaller detector area, sensitivity to extended emission depends primarily on maximizing the LAMAR effective area and minimizing detector background rates. However, good angular resolution is also very important in providing increased sensitivity for detecting and subtracting the contribution from discrete sources. Since the temperature of cluster sources is 5 keV it is important that the LAMAR sensitivity extend to as high an energy as possible. Also, since the detector in each module adds noise, it is important to achieve the large effective area with the fewest number of modules.

2. High Sensitivity Timing Measurements

Studying the size of the emitting volume and the efficiency of energy conversion in active galactic nuclei are important objectives of these measurements. Also, such measurements allow the investigation of evolution in binary, pulsating and burst sources during periods of low mass transfer, the study of stellar flares, cyclic variability in stars and the identification of time variable sources in nearby galaxies.

For brighter sources, where background is negligible, statistical uncertainties in timing measurements depend only on LAMAR effective area. However, for faint point sources, where sensitivity to time variability is statistically limited by background, it is critical to minimize the counting rates from detector background. Also, the importance of assigning observed variability to a particular source requires minimizing source confusion by achieving good angular resolution. Since sensitivity to the largest possible region of the sky maximizes observational efficiency by allowing concurrent study of many sources, it is important for the LAMAR modules to have as large a telescope field as possible.

3) Survey Observations

Such observations may take the form of limited surveys of particularly interesting regions of the sky or an all-sky survey. These surveys will provide the resource for extending luminosity functions of various classes of objects to much lower luminosities and for various statistical studies in correlating X-ray characteristics with properties measured at other wavelengths. An all sky survey would provide a source of reference data for many studies, identifications, archival data for tests of models and theories without requiring further observations. Perhaps most important, a deep survey would discover interesting new objects of low population which answer or raise important questions in astronomy or provide an immediate test of theory.

The sensitivity of a survey, of course, depends on maximizing signal from the sources, minimizing detector noise and being able to survey as large a field as possible in a single observation. Thus, survey observations require not only large effective area but also good angular resolution to minimize noise, reduce source confusion and improve chances for optical identifications. In addition, the LAMAR telescopes must provide uniform response over their fields to allow a survey of uniform sensi-

tivity.

4) Spectroscopic Measurements

The importance of spectroscopy at optical wavelengths is well known and it will provide the same advantages to X-ray astronomy. Study of temperatures, electron densities, chemical abundances, emission mechanisms and red shifts all become possible with the capability for highly sensitive medium resolution ($E/\Delta E \sim 150$) spectroscopy.

Broad band spectroscopy with non dispersive detectors again requires maximizing effective area and minimizing background noise. However, the resolving power of objective grating spectroscopy depends linearly on the telescope resolution and its uniformity over the telescope field. In addition, the spectral range covered by the instrument is dependent on the size of telescope field.

Obviously all of the above discussion can be summarized by saying we need a LAMAR with largest effective area over the widest energy range, lowest background noise, best angular resolution with uniform response over the broadest possible field. However, assuming comparable effective area, angular resolution of the telescopes has the most important impact on LAMAR performance.

The image sensors in a LAMAR will experience an appreciable counting rate from both the diffuse X-ray flux, B_d, and charged particle background, B_p, that will degrade the instrument's sensitivity to point sources. These background counting rates, summed for all modules of the LAMAR, are given by:

$$B_d = FR^2A \text{ counts sec}^{-1} \quad (1)$$

$$B_p = K(Rf)^2 N \text{ counts sec}^{-1} \quad (2)$$

where F is the intensity of diffuse X-rays, A, R and f are the LAMAR effective area, angular resolution and focal length respectively, K is the charged particle counting rate per unit detector area, and N is the total number of detectors (modules) in the LAMAR. The product Rf is the pixel size on the detector. The total background counting rate, B_t, is then:

$$B_t = B_d + B_p = R^2(FA+Kf^2N) \quad (3)$$

The extragalactic component of the diffuse X-ray background, with no interstellar absorption ($\sim 1 E^{-1.4}$ ph cm^{-2} s^{-1} keV^{-1} sr^{-1}), is a reasonable lower limit to the flux from most places in the sky at energies above 0.5 keV. In the range 0.5 - 6 keV this provides an intensity, $F = 2 \times 10^{-6}$ photons cm^{-2} sec^{-1} (arc min)$^{-2}$. For imaging proportional counters in the range .5 - 6 keV, K is approximately 5×10^{-4} counts sec^{-1} per mm^2 of detector area. For a LAMAR with 10^4 cm^2 effective area, and a focal length of 2m the total background counting rate, B_t, is:

$$B_t = R^2 (.02 + 1.5 \times 10^{-4} N) \text{ counts sec}^{-1} \quad (4)$$

where R is measured in arc minutes. It is evident that the diffuse X-ray background is the principal source of noise in a LAMAR. However, if the number of modules grows to of order 100 the particle background is no longer negligible.

ORIGINAL PAGE IS
OF POOR QUALITY

Also, if an appreciable fraction of the diffuse X-ray background may be resolved into discrete sources, as it now appears from Einstein observations, particle background rates will become dominant for a LAMAR with many modules.

When background is negligible, the faintest detectable source strength varies as $(AT)^{-1}$, where T is the observing time. When the X-ray source must be detected above random fluctuations in the background counting rate the faintest detectable source intensity, I, varies as:

$$I \propto \frac{(B_t\, T)^{1/2}}{AT} \simeq \frac{(R^2 FAT)^{1/2}}{AT} = R\left(\frac{F}{AT}\right)^{1/2} \qquad (5)$$

where the particle background in eq. 3 has been neglected. A telescope's sensitivity, therefore, varies linearly with its resolution, but only as the square root of other parameters. This effect is shown in Figure 1 where the faintest detectable source (5 counts detected with zero background or sufficient detected counts to be 5 standard deviations above the background) is plotted as a function of observing time, for three values of angular resolution in a LAMAR with 10^4 cm^2 effective area. These calculations utilize the background rate in equation (4), neglecting B_p. The limiting sensitivity of a telescope with perfect resolution varies as T^{-1} and is indicated by the solid line. Telescopes with finite angular resolution depart from this line as they begin to acquire background counts and thereafter their sensitivity varies as $T^{-1/2}$, indicated by the dashed lines. A LAMAR having an angular resolution of 1 arc min or larger becomes background limited in less than 100 sec of observing time. Figure 1 indicates that if X-ray optics of 20" resolution instead of 3' resolution are utilized it is possible to improve the LAMAR sensitivity by a factor of 10. Thus, sources down to 10^{35} ergs sec^{-1} (.01 Her X-1) can be detected in M31 in 10^4 sec observing time and with a spatial resolution of ~ 70 pc, if 20 arc sec optics are employed for LAMAR.

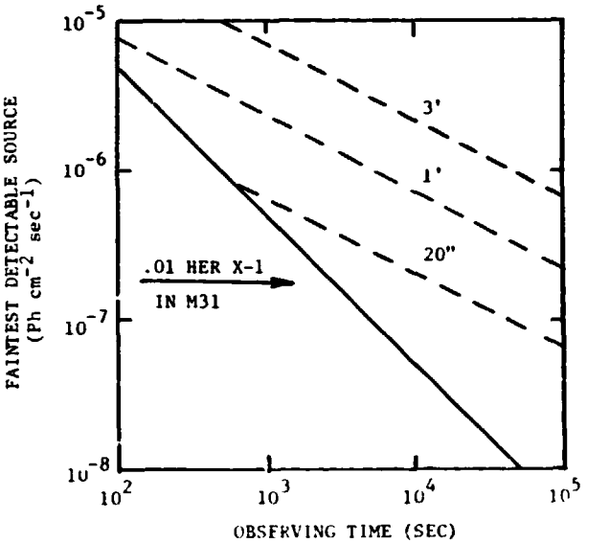

Figure 1. Sensitivity of a 10^4 cm^2 LAMAR as a function of observing time for various values of its angular resolution.

Figure 2 shows the effect of LAMAR angular resolution on the ability to detect time variability of faint sources. A step function change of intensity, δI_4 is assumed to occur in the intensity, I, of a source at the center of the 10^4s observation (eg. a partial X-ray eclipse). Detection of this change with a significance of 5 standard deviations above background noise is assumed for these calculations. Figure 2 indicates nearly a factor of 10 improvement in

ORIGINAL PAGE IS
OF POOR QUALITY

ability to detect faint eclipsing binaries (δI/I=1) if the LAMAR angular resolution is improved from 3' to 20".

Other advantages of the higher angular resolution, not related to sensitivity are:

1. Improved ability to optically identify newly discovered sources.

2. Higher spectral resolution in using objective gratings. For a telescope with 20" resolution and a 6000 1/mm grating one can obtain $\lambda/\Delta\lambda \sim 200$ while 3' resolution allows $\lambda/\Delta\lambda$ of only 20.

3. Ability to distinguish extended sources from point sources on a much finer scale. This is important in distinguishing emission of distant extended clusters from that of compact galactic nuclei and in separating discrete low luminosity galactic sources from diffuse emission. Studies of the angular diameter-redshift relation in distant cluster X-ray sources provide an even more important application for a telescope of improved angular resolution, since the distant clusters are expected to be smaller than a few arc minutes in angular diameter.

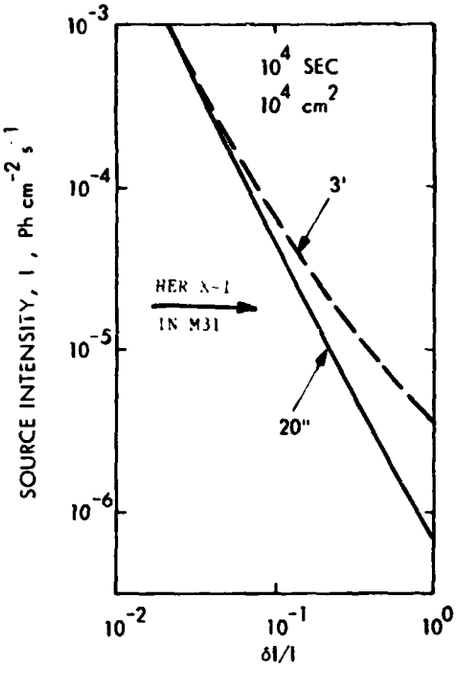

Figure 2. Ability to detect time variability in faint sources as a function of LAMAR telescope angular resolution.

4. Less source confusion. The limit that there should be no more than one source per 40 pixels becomes an important factor in studies of faint sources. This will be discussed in more detail later.

III. Hardware Status

A large Wolter-I X-ray telescope has recently been fabricated in a joint program involving the Mullard Space Science Laboratory and the National Physical Laboratory in the U.K. and our own laboratory here in the U.S. The Wolter-I telescope is the same optical design that was used on the Einstein Observatory and involves

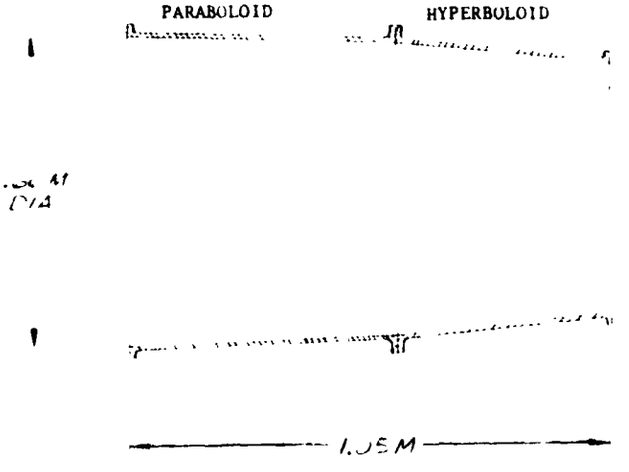

Figure 3. The Aries rocket telescope shown in cross section.

ORIGINAL PAGE IS
OF POOR QUALITY

successive X-ray reflections from paraboloidal and hyperboloidal mirror elements. The telescope, which was flown on a NASA-Aries sounding rocket, has a focal length of 2.3 m, a grazing angle of 1.9°, an entrance aperture 66 cm in diameter and a geometrical collecting area of 380 cm^2. The telescope mirrors, shown schematically in Figure 3, were made from rolled ring forgings of 5083 aluminum alloy. These mirror blanks were figured by the process of diamond turning, which utilizes a precision air-bearing lathe and a diamond cutting tool to machine the required curves to within 1 micron. These figured surfaces were then plated with a thin coating of electroless nickel and polished to obtain the final X-ray reflecting surfaces.

Prior to flight, the telescope performance was measured in the 1000 ft. X-ray calibration facility at the Marshall Space Flight Center. Measurements were made at X-ray energies of .277, .572, .705, .933, 1.5 and 2.05 keV. Preliminary results of the measured effective area which the mirrors present to a distant point source are shown in Figure 4. The solid disks indicate the effective area calculated from the X-ray optical constants (Ershov, Brytov and Lukirskii, 1964) of the nickel surface, while the crosses show the measured values. The statistical uncertainty in the measurements is negligible, however, there are systematic uncertainties in these data due to imprecise knowledge of the imaging proportional counter efficiency, which is now being determined. The data points at .277 keV disagree appreciably because some X-ray events at this energy fall below the lower level pulse amplitude discriminator on the imaging proportional counter (IPC) output and therefore fail to be counted. Corrections for this effect are also being determined. The measured effective area at .933 keV falls well above the calculated value because this is in the vicinity of the L-shell X-ray absorption edges in the nickel reflecting surfaces where the optical constants are very poorly known. At .572 and .705 keV, where the systematic uncertainties are smallest, the measured values are approximately 60% of those calculated. Since there are two reflections in the telescope, these data indicate the polishing process has achieved ~ 75% of the theoretical reflection efficiency.

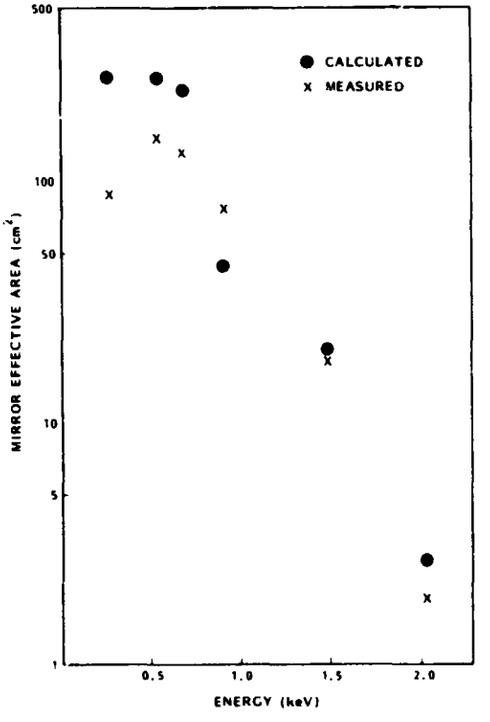

Figure 4. Comparison of measured and calculated effective area for mirrors in the Aries rocket telescope.

The Point Spread Function (PSF) of the telescope (mirrors plus IPC) measured at 1.5 keV is shown in Figure 5. The PSF is obtained by determining the centroid of the X-ray source image and summing the counts in IPC pixels which lie within successive annuli of increasing radius. The total counts within each annulus is then divided by the number of pixels contributing to the sum to obtain the normalized PSF. The PSF is shown on a semi-log plot where the hori-

ORIGINAL PAGE IS
OF POOR QUALITY

zontal coordinate, which is given in IPC pixels, corresponds to off-axis angle in the telescope field. Since each pixel is 15 arc sec in size, the entire plot covers the central .4° radius of the field. This point spread function shows the typical response of an X-ray telescope in having a very intense central core followed by a low intensity tail (down by a factor of 10^4). When the image broadening due to the IPC is removed from the telescope PSF we obtain a value of 30 arc sec FWHM for the PSF from the mirrors alone. This is very encouraging since the design goal for figuring the mirrors was a blur circle diameter of 40 arc sec. This result, along with having achieved 75% of theoretical X-ray reflectivity from the mirror surfaces, on our first attempt at fabricating a telescope, is very encouraging and gives us confidence in using this technique of mirror fabrication for LAMAR applications. Figure 6 shows an image of Cyg X-1 obtained during the Aries rocket flight. This object was observed as a point source calibration late in the flight and for spectral observation by a companion experiment.

Our laboratory, in collaboration with our U.K. colleagues, is currently in the process of fabricating two additional mirror pairs utilizing refinements in production technique gained from experience with the present telescope. Diamond turning of the mirrors will be carried out in the U.K. on their newly commissioned diamond turning facility. These mirrors will be nested within the existing set to form a three-element telescope which will be used with objective reflection gratings for spectroscopic observations. This spectroscopic application is undertaken in collaboration with Webster Cash at the University of Colorado, who will discuss objective reflection

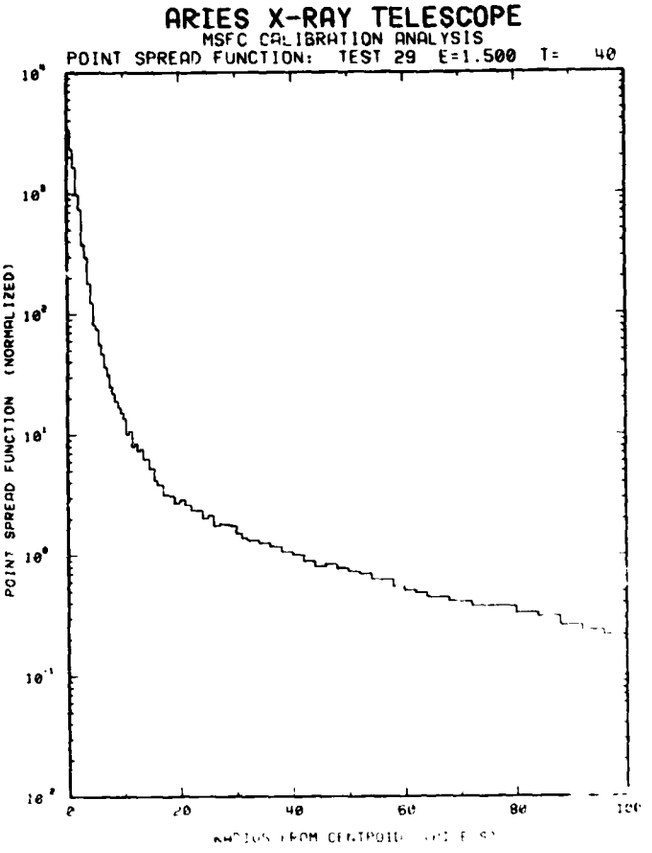

Figure 5. Point spread function for the Aries telescope, including IPC, at an energy of 1.5 keV.

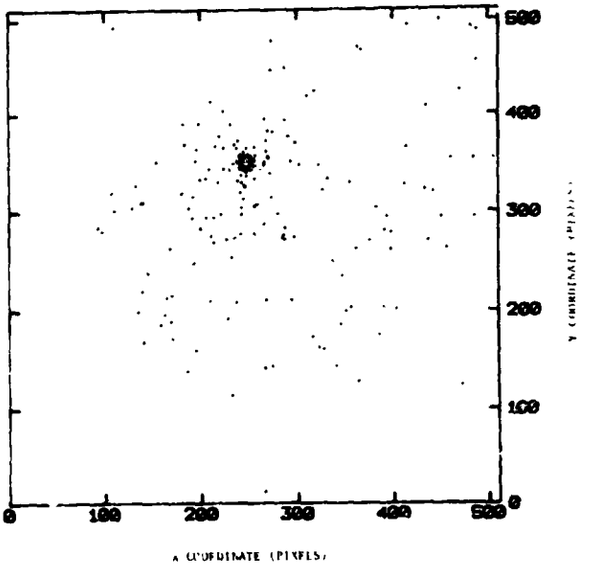

Figure 6. An image of Cyg X-1 obtained during the Aries rocket flight.

ORIGINAL PAGE IS
OF POOR QUALITY

grating spectroscopy later in this workshop.

Another telescope fabrication effort, also utilizing diamond turning to figure Wolter I mirrors, is being carried out in parallel by Gordon Garmire at Penn. State University. This effort differs from that described here in the preparation of the X-ray reflecting surfaces. The diamond-turned mirrors are coated with an acrylic lacquer which provides a very high quality surface finish. This thin ($\sim$ 10 μm) lacquer coating is then overcoated with a metal deposit to provide the final X-ray reflecting surface. Peter Serlemitsos, here at GSFC, has pioneered this technique of fabricating X-ray reflectors and will describe it in more detail later in this workshop.

IV. A Wolter Type I LAMAR

The definition phase of a NASA funded Spacelab investigation has recently been completed, in which a single Wolter-I LAMAR module was designed. This definition study was carried out by a consortium of seven institutions including Penn. State University, University of Washington, Mullard Space Science Laboratory, University of Leicester, The U.K. National Physical Laboratory, University of Cambridge and Lockheed Palo Alto Research Laboratory. The design goals for the telescope were to maximize the effective area of the module and provide the best possible angular resolution over the broadest telescope field within the cost constraints. The resulting High Resolution LAMAR (HRL) module is shown in Figure 7 and consists of a ten element nested array of Wolter-I mirrors. The HRL focal length is 3.6 m and the mirror diameters range from 90

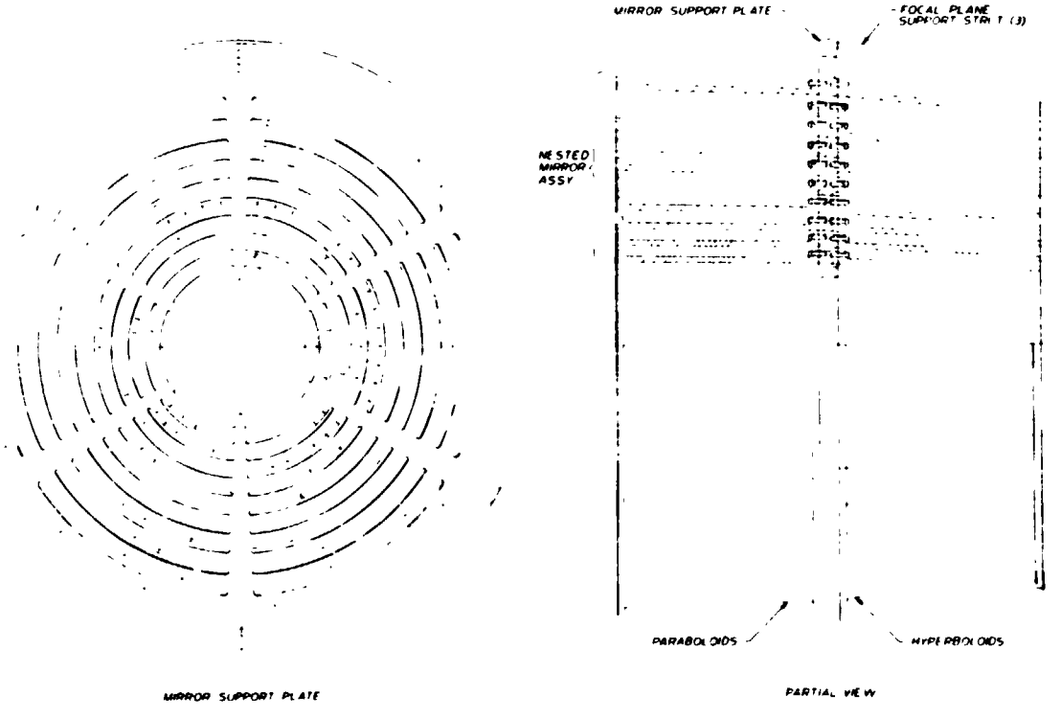

Figure 7. The High Resolution LAMAR (HRL) mirror assembly utilizing Wolter-I X-ray optics.

ORIGINAL PAGE IS
OF POOR QUALITY

cm to 30 cm with grazing angles between 1.7° and .56°. The mirrors are 36 cm long in their axial dimensions, the telescope has a geometrical area of 1350 cm^2 and the design goal was to achieve an on-axis image blur of 20 arc sec radius or less. It is anticipated that these mirrors would be fabricated in the same manner as described earlier for the Aries rocket telescope. However, if the technique of coating the diamond turned surfaces with acrylic lacquer proves effective in preserving the 20 arc sec figure, it would be utilized to reduce costs. As shown in Figure 7, the mirrors are attached to a cental support plate, which also serves as an alignment fixture for the nested array. This alignment is obtained by utilizing the precision machining capability of the diamond turning facility to machine the mating surfaces of the paraboloids, hyperboloids and the support plate. The mating flange surfaces of each mirror are machined at the same time as its interior surface is figured and thus the flange provides a true reference for the mirror axis. Surfaces of the support plate are diamond turned to be flat and parallel, for axial alignment, and the inner surfaces of raised lugs, present on the six radial webs are also diamond turned to provide mirror alignment in a direction normal to the telescope axis. This alignment technnique utilizes the precision of the diamond turning machine to greatly reduce, what otherwise would be a time consuming and expensive effort in the telescope production. This method is being utilized in fabricating the three mirror nested array for the Aries rocket program.

Figure 8 is a schematic of the HRL telescope showing the mirror assembly on the left and the focal plane on the right. The focal plane assembly, which includes a rotary interchange mechanism to position either of two IPC detectors at the HRL focus, is attached to the mirror support plate by a tripod structure. A shutter door, which seals the telescope entrance aperture, also serves as a sun shade when observations are being conducted. This payload, which is 1.1 m in diameter and slightly over 4 m long, is designed for flight on the Space Shuttle utilizing a pointing control system. Further details of the HRL Payload have been discussed by Catura et al. (1981).

The calculated response of the HRL mirror assembly is shown in Figures 9 and 10, assuming the outer 3 mirrors are Ni coated and the inner 7 mirrors have Au reflecting surfaces. The effective area as a function of energy, which the

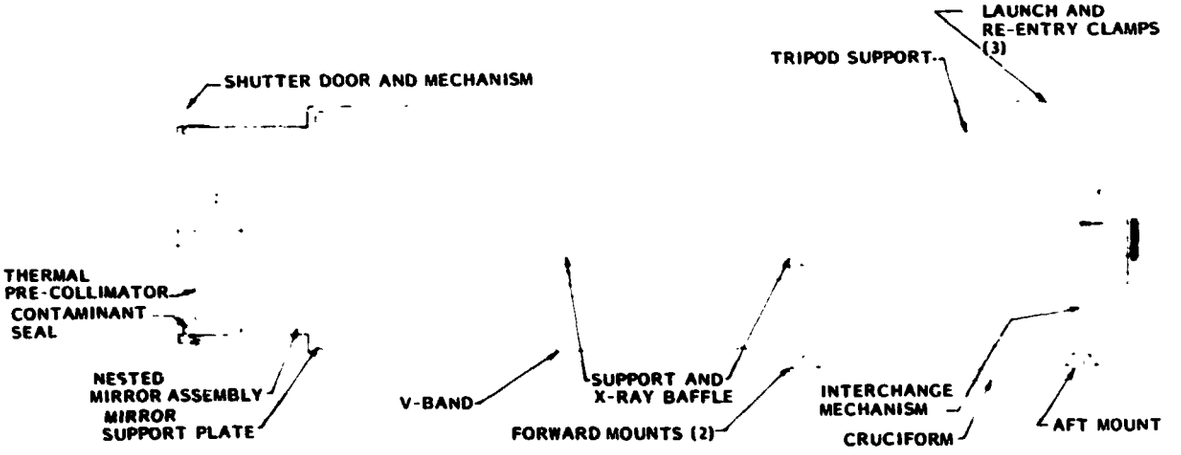

Figure 8. A drawing of the HRl payload designed for Spacelab observations.

ORIGINAL PAGE IS
OF POOR QUALITY

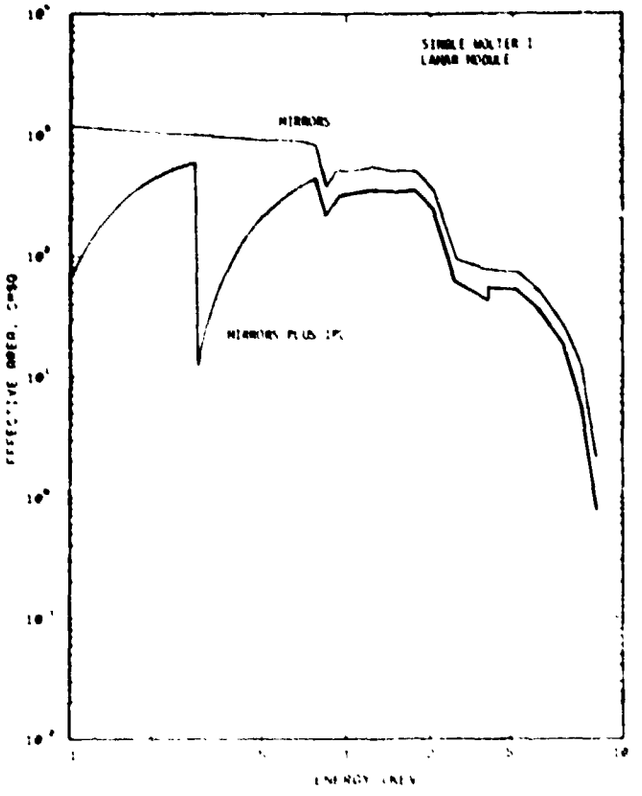

Figure 9. Effective area of a single HRL module as a function of energy.

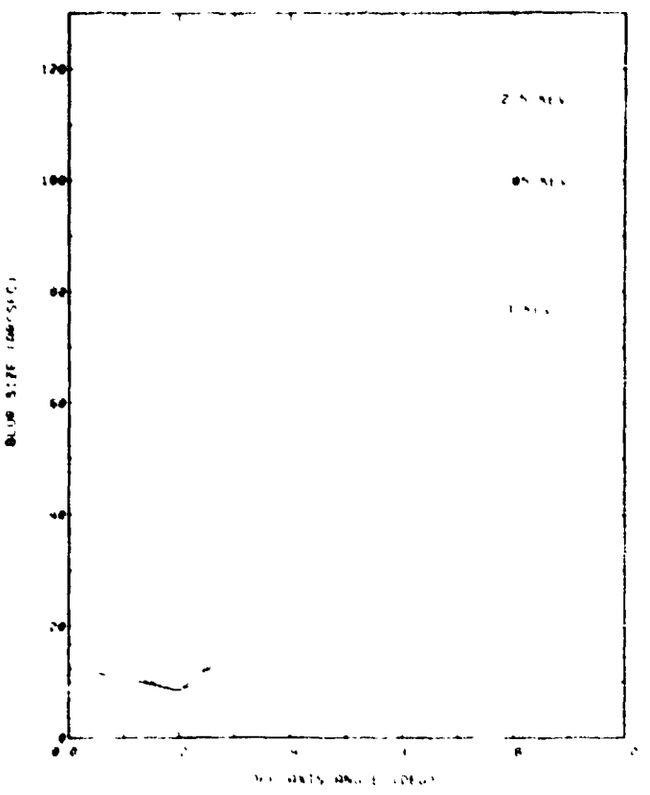

Figure 10. Image blur as a function of field angle in the HRL focal plane.

mirrors present to a focal plane instrument, is shown in the top curve of Figure 9 along with the response of the HRL telescope when a Xenon filled IPC is utilized as an image sensor. The mirror assembly has ~ 1000 cm^2 effective area below the Ni L-shell absorption edges at .85 keV and provides nearly 20 cm^2 at the Fe line energy of 6.7 keV. Figure 10 shows the radius of the image blur as a function of field angle in the focal plane. It is somewhat energy dependent but, by defocusing the detector slightly (trading on-axis resolution for a larger telescope field), it is possible to maintain an image blur of < 20 arc sec out to a field angle of nearly 0.4° in radius.

Figure 11 shows how HRL telescopes could be conceptually arranged in a 4 module subassembly of the LAMAR. Such a subassembly could be flown as a Spacelab facility instrument or assembled into a full scale LAMAR. Figure 12 schematically illustrates a 24 module LAMAR, shown here as a free flying satellite. The Wolter-I LAMAR illustrated in Figure 12 could be placed in orbit by a single shuttle launch. However, it would be possible to establish the array with a smaller number, for example, on the Space Platform and add further modules as budgets and shuttle availability permitted. In this way the overall array performance could be progressively enhanced and the specific capability of array members could be altered to reflect changing scientific priorities and developments in the instrumentation field.

ORIGINAL PAGE IS
OF POOR QUALITY

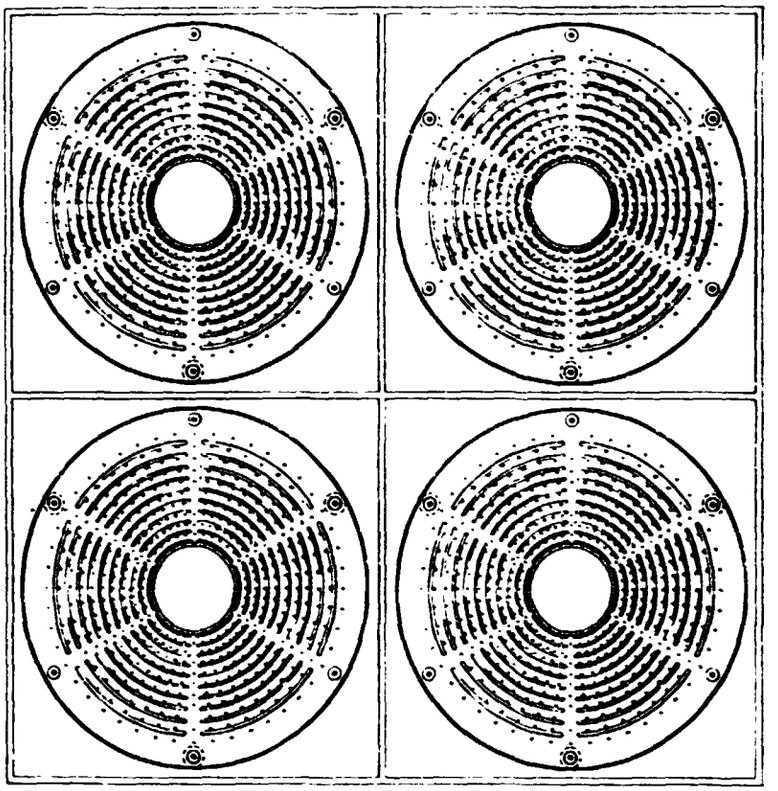

Figure 11. 4 Module LAMAR Subassembly.

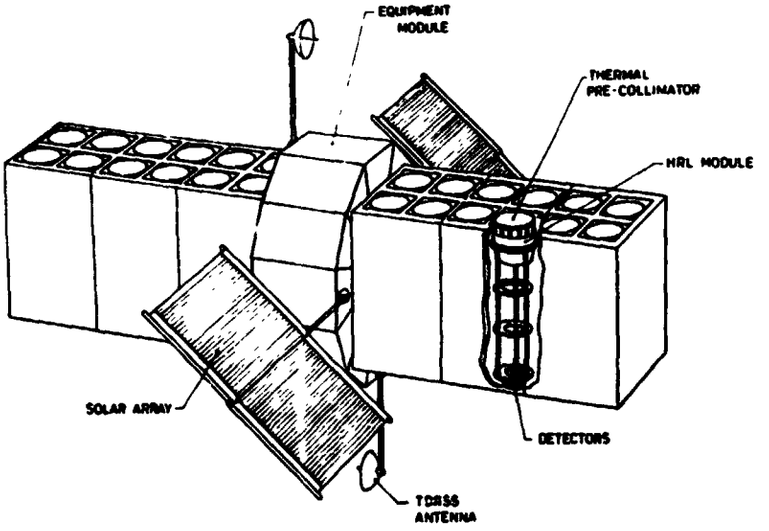

Figure 12. Schematic of a 24 module free flying Wolter-I LAMAR.

ORIGINAL PAGE IS
OF POOR QUALITY

The effective area of a 24 module LAMAR as a function of X-ray energy is compared in Figure 13 with the effective areas of the Einstein Observatory and the future Advanced X-Ray Astrophysics Facility (AXAF). The areas shown are for the mirrors alone, as presented to a focal plane instrument. The data of Figure 13 has been used to compare sensitivities of these three observatories as a function of observing time. For purposes of this comparison, unit detector efficiency is assumed. Charged particle counting rates were taken to be 5×10^{-5} counts s^{-1} mm^{-2} and the extragalactic diffuse X-ray intensity (the largest background for the LAMAR) was represented as $11E^{-1.4}$ ph cm^{-2} s^{-1} keV^{-1} sr^{-1}. A Crab-like energy spectrum was assumed for the source and was folded through the telescope responses given in Figure 13. The relative sensitivities for detecting faint point sources with the three observatories, under the above assumptions, are indicated in Figure 14. The dashed curve indicated for the LAMAR would result if the entire extra-galactic diffuse X-ray back-ground could be resolved into discrete sources and only the detector noise from charged particles remained. The three horizontal lines indicate the source confusion limits for three different values of pixel sizes determined by the telescope angular resolution. These limits are independent of the observatory and use only the number-flux relationship:

$$N(>S) = 2.7 \times 10^{-16} S^{-1.53} \quad \text{sources sr}^{-1} \qquad (6)$$

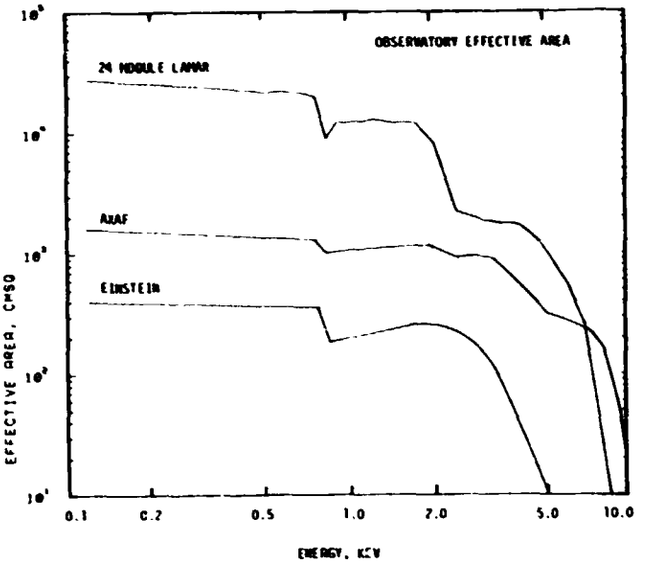

Figure 13. Effective collecting area of three observatories as a function of energy.

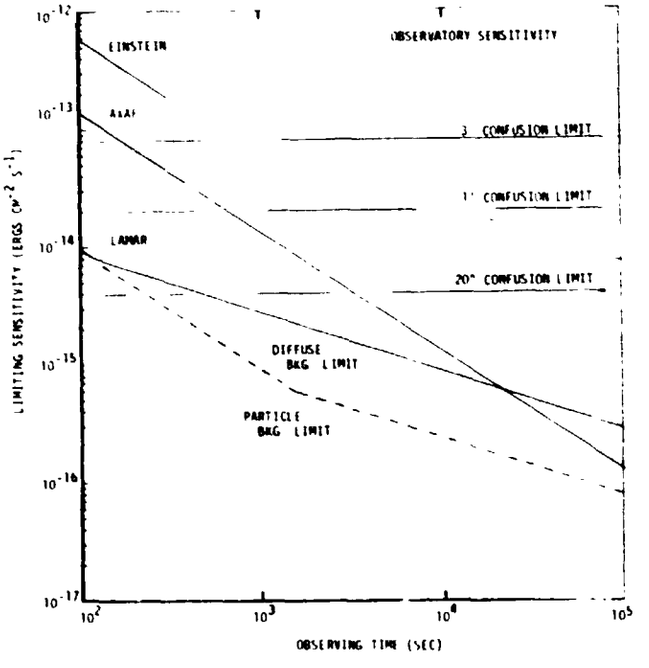

Figure 14. Sensitivity for detecting point X-ray sources as a function of observing time for three observatories.

determined by Maccacaro et. al. (1981) and the confusion limit defined as 1 source per 40 pixels. It is apparent that confusion becomes a problem for an observatory with $3\frac{1}{3}$ angular resolution at the sensitivity which Einstein achieved in a 10^3 sec observation. Results of the Einstein deep survey (Giacconi, et al. 1979) show no apparent turnover in the

ORIGINAL PAGE IS
OF POOR QUALITY

number-flux relation for extragalactic sources down to $\sim 2 \times 10^{-14}$ ergs cm^{-1} sec^{-1}, so that the confusion limit for 1' resolution is observationally verified. Even with 20" pixels, the 24 module Wolter I LAMAR will be at its confusion limit in a 600 sec observation, unless there is a turn over in the number counts between 2×10^{-14} and 4×10^{-15} ergs cm^{-2} sec^{-1}. One must conclude that angular resolution is a critical factor for extragalactic studies in a highly sensitive observatory such as the LAMAR.

V. X-Ray Reflectivity Enhancement with Multilayers

The technology for depositing extremely thin alternating layers of high and low density materials, which act as Bragg diffractors, is now becoming well established (Underwood, Barbee and Keith, 1979; Spiller and Segmuller, 1980 and Barbee, 1981). These coatings are applied by vacuum deposition with highly uniform layer thicknesses down to 10A, essentially replicating the surface finish of the underlying substrate. Deposition of these multilayer diffraction coatings on the reflecting surfaces of a Wolter-I telescope offers the potential of increaasing its effective area in a selected bandpass at high energy. If the underlying mirror finish is preserved by the multilayers, the low energy specular reflection of the telescope will not be diminished. However, it is necessary to arrange the high energy band pass well above the energy at which the normal mirror reflectivity cuts off, since interference effects will otherwise degrade the specular reflection. Since the outer mirrors of the HRL module reflect efficiently only below about 2.5 keV, they will in principal allow reflectivity enhancement for Fe-line emission at 6.7 keV by multilayer deposition without disturbing their low energy response.

The Bragg reflectivity of gold-carbon multilayers of various thicknesses and number of layer-pairs has been calculated with the aid of a computer code which predicts their response as a function of wavelength. A result of these calculations is shown in Figure 15 for 15 layer pairs of gold and carbon optimized for 1.85A X-rays at a grazing angle of 1.7° (appropriate for the outer mirror of the HRL module). The peak reflectivity of this rocking curve is 42% and its FWHM is .14A, which has an angular equivalent of .13° from the Bragg equation. Since the grazing angle varies slightly along the length of a Wolter I mirror, the width of the rocking curve should be broad enough to encompass this variation

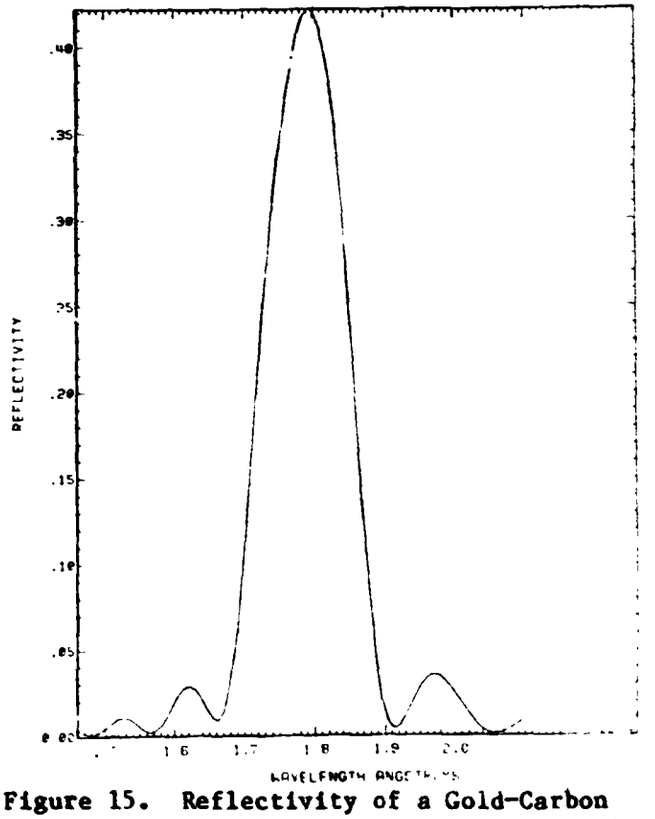

Figure 15. Reflectivity of a Gold-Carbon multilayer with 15 layer-pairs as a function of wavelength. The layer thickness is 16Å.

ORIGINAL PAGE IS
OF POOR QUALITY

Also, because two reflections are involved, the telescope efficiency depends on the square of the multilayer reflectivity. However, peak reflectivity and rocking curve width are competing parameters in the multilayer design and so they must be optimized. Figure 15 is the optimum in this case and represents a structure having 15 layer pairs where each layer is 16A thick. This provides a peak efficiency for double reflection of ~ 16% and has a rocking curve wider than all but the largest mirror.

For purposes of calculation, the outer 4 mirror pairs were assumed to be coated with multilayers of appropriate layer spacing such that the rocking curve peaked for the grazing angle at the center of each mirror. The computer ray tracing program used for the calculations of Figure 9 was modified to include the angular dependence of the Bragg reflectivity of the multilayers, assuming no degradation of the low energy specular reflection. Figure 16 indicates the HRL response when the multilayers on all four outer mirrors are appropriate to reflect 1.85A X-rays. The multilayers increase the response at 6.7 keV over that from specular reflection on the inner mirrors by a factor of 7, providing a peak effective area of 125 cm^2 in a band pass which is .5 keV FWHM. For a 24 module LAMAR, one would obtain ~ 3000 cm^2 at this energy. The off-axis response of the telescope is also shown in Figure 16 at angles of 0.1^o and 0.3^o and indicates that the multilayer response degrades approximately the same as that for specular reflection at this energy.

It is possible to broaden the band pass of the telescope at the expense of peak response by tuning each mirror pair to reflect a slightly different energy. Figures 17 and 18 show results of these calculations where the peak wavelengths for each of the four mirror pairs are separated by .04A and .08A respectively.

While the results of these calculations are encouraging, a number of practical matters need to be addressed. These include the practicality of depositing uniform multilayers on such large surfaces and whether the low energy specular response can be maintained after multilayer deposition.

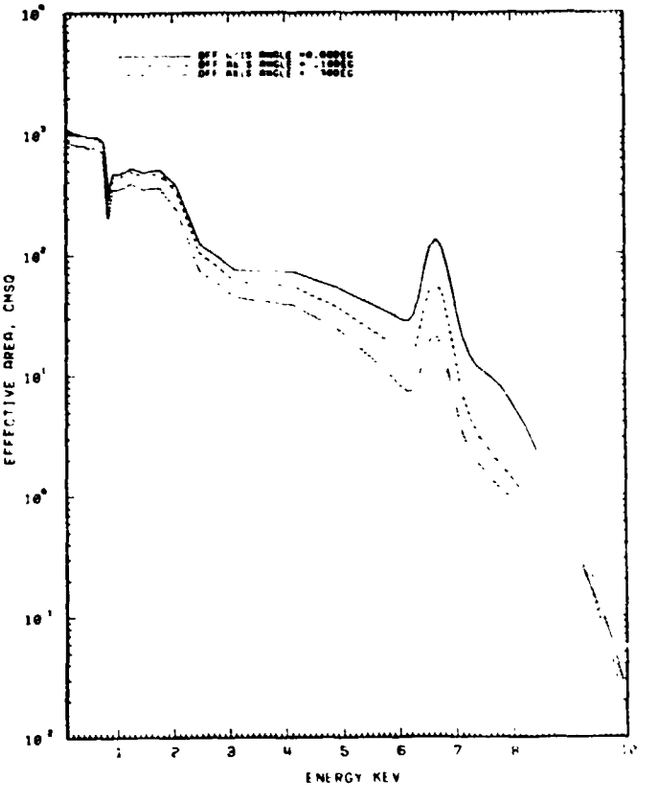

Figure 16. Effective area of an HRL module with the outer 4 mirror pairs coated by multilayers and optimized for 1.85A X-rays. Three off-axis angles in the telescope field are shown

VI. Conclusions

Angular resolution of the X-ray optics in a LAMAR most strongly influences its performance. A LAMAR with 20" resolution has a factor of 10 better sensitivity than one of the same effective area but with 3' angu-

ORIGINAL PAGE IS
OF POOR QUALITY

lar resolution. Also, a LAMAR with 10^4 cm^2 effective area and 3' angular resolution will be source confusion limited in about two minutes of observing time at the sensitivity level reached by Einstein in about 800 sec. The comparable confusion limit for a LAMAR of 20" resolution is 20 times better, at a sensitivity 3 times below the level of the Einstein deep surveys. The spectral resolution achievable with objective gratings is linearly related to angular resolution of the X-ray optics. Consequently, it is critically important to the LAMAR Observatory's performance to utilize the highest angular resolution possible within the mission cost constraints. The technology for producing Wolter Type I X-ray optics with 20" angular resolution is rapidly reaching maturity and a detailed design and a development plan now exists for a high resolution LAMAR module which utilizes these optics. Deposition of multilayered diffraction coatings on the outer mirrors of this telescope module appears to be a promising way of enhancing the high energy performance in a selected bandpass.

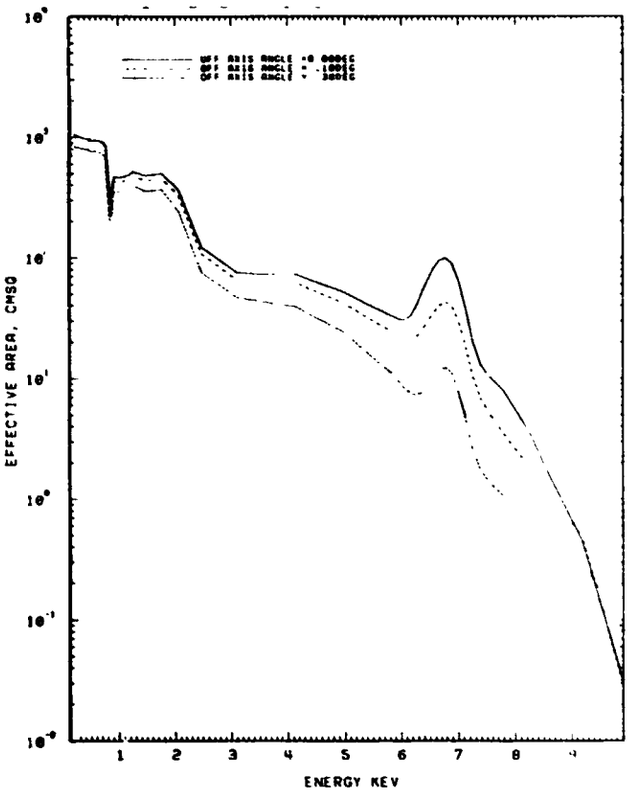

Figure 17. Response of the HRL module when the peak wavelengths for multilayers on the outer 4 mirrors differ by .04Å.

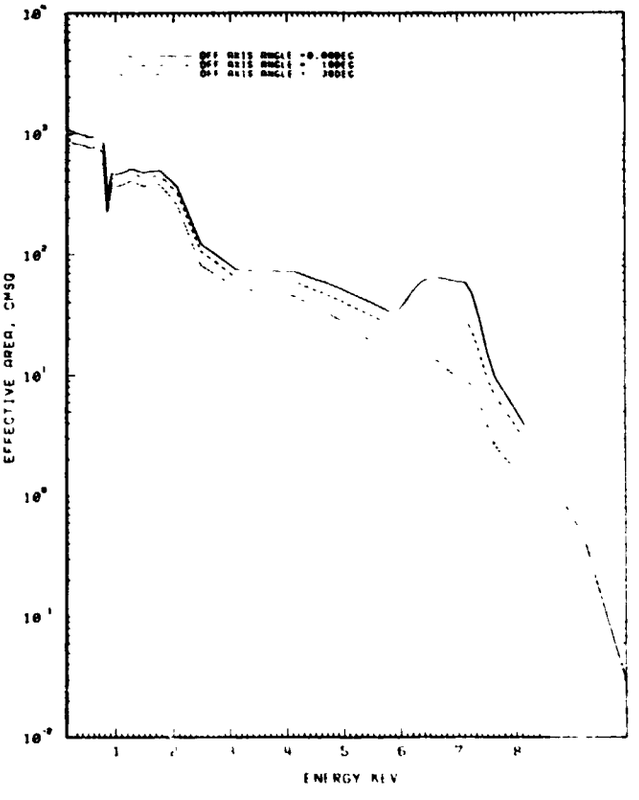

Figure 18. Response of the HRL module when the peak wavelengths for multilayers on the outer 4 mirrors differ by .08Å.

Acknowledgements

Portions of this research have been supported by NASA Contracts NAS5-23563 and NAS5-26090 and by the Lockheed Independent Research Program. We are grateful to Dr. J.L. Culhane for very useful discussions and for providing the drawing of the 24 module LAMAR. We also acknowledge indispensable help by the members of the HRL consortium on portions of the design of that instrument which have been reported here.

References

Barbee, T.W. 1981, Proceedings of AIP Topical Conference on Low Energy X-Ray Diagnostics, Monterey, CA., to be published.

Catura, R.C., et al. 1981, S.P.I.E. Proceedings, 284, to be published

Ershov, O.A., Brytov, I.A. and Lukirskii, A.P. 1964, Optics and Spectroscopy, 22, 66.

Giacconi, R. et al. 1979, Ap. J. (Letters), 234, L1.

Maccacaro, T., et al., 1981, CFA preprint No. 1519, submitted to Ap. J. March 1981.

Spiller, E. and Segmuller, A. 1980, Appl. Phys. Lett., 37, 1048.

Underwood, J.H., Barbee, T.W. and Keith, D.C. 1979, S.P.I.E. Proceedings, 184, 123.

N82 26067

PRECEDING PAGE BLANK NOT FILMED

PERFORMANCE OF SINGLE PHOTON-COUNTING X-RAY CHARGE COUPLED DEVICES

G. R. Riegler

R. A. Stern

K. Liewer

F. Vescelus

Jet Propulsion Laboratory

California Institute of Technology

Pasadena, CA 91109

J. A. Nousek and G. P. Garmire

Department of Astronomy

Pennsylvania State University

State College, Pennsylvania

PERFORMANCE OF SINGLE PHOTON-COUNTING X-RAY CHARGE COUPLED DEVICES

G. R. Riegler, R. A. Stern, K. Liewer, and F. Vescelus
Jet Propulsion Laboratory, California Institute of Technology
Pasadena, CA 91109

and

J. A. Nousek and G. P. Garmire
Department of Astronomy, Pennsylvania State University
State College, Pennsylvania

ABSTRACT

Results of initial performance tests on x-ray sensing properties of charge-coupled devices (CCDs) are presented. CCDs have demonstrated excellent spatial resolution and good spectral resolution, superior to that of non-imaging proportional counters.

I. INTRODUCTION

A charged coupled device (CCD) can be expected to combine the best properties of high-resolution imaging detectors and solid-state spectrometers, namely high spatial resolution and moderate spectral resolution, at high efficiency. Because of the importance of such a device for x-ray astronomy, a number of researchers have begun laboratory studies of x-ray CCDs (Griffiths et. al. 1981 and reference therein). This paper describes the status of x-ray CCD studies at the Jet Propulsion Laboratory.

Elsewhere within this conference, reviews of the known properties and open questions for a wide range of galactic and extra-galactic sources have been presented. These reviews have called for moderate resolution, e.g., $E/\Delta E \sim 40$ at $E \sim 6$ keV, which CCDs are expected to provide. The ability to produce a spectrum for each image element (pixel) is important for the studies of supernova remnants, clusters of galaxies, and wherever source confusion would be a problem for non-imaging solid state spectrometers.

II. DESCRIPTION OF THE TEST CAMERA

Several CCD cameras have been built at JPL for the study of CCDs and for the testing of CCDs to be used by the Galileo Jupiter orbiter and the Wide Field Planetary Camera of the Space Telescope. Two cameras were used in these tests, one for the virtual phase devices (Janesick et al., 1981) and the other for the three phase devices (Blauke et al., 1981). The timing and amplitude of the clock pulses required to shift the data out of the two types of CCDs differ, but all the amplifiers and signal processing circuits are identical.

The signal processing circuitry uses a double correlated sampler where output is digitized to 16 bits. The pixels are clocked out at a rate of 5×10^4 pixels per second which minimizes the noise associated with sampler. These items plus very careful camera layout allow us to achieve a noise figure of 4.5 electrons RMS for the camera system and an amplifier noise of 7 electrons for the virtual phase CCD or 13 electrons for the three phase CCD. The difference in read noise is due to differences in the on chip amplifiers.

The CCDs are contained in a vacuum chamber which is evacuated to a pressure of a few Torr. Cooling is accomplished by a regulated flow of liquid nitrogen. The temperature can be varied from room temp to -190°C with a stability of 0.1°C. A shutter in the vacuum chamber controls the exposure for all the sources used.

The removable front face of the vacuum chamber can hold an optical window, a beryllium foil window, or the window can be replaced by a flourescent X-ray source with interchangeable targets which is activated by a 1mCu source of alpha particles.

The CCDs used in these tests were all manufactured by Texas Instruments Co. Both the three phase and virtual phase devices have 15.2 micron square pixels in 800 x 800 arrays. The three phase devices were thinned to approximately 10μ and operated with the radiation incident from the non-circuit side (backside). The virtual phase CCD is a thick device and the radiation is incident on the circuit side. Because the virtual phase CCDs have only a single gate structure, the circuit layer is thin (0.6 micron). There is an additional 0.5 micron protective overcoat. While the absorbtion in these layers would require that the CCD be thinned and run in the back illuminated mode for energies below one kilovolt, thinning was not required for these tests (80% transmission at 1.5 keV).

Although the virtual phase device is 250 microns thick it is a layered structure with only a 10 micron thick layer adjacent to the gate structure that acts as an active detector region for x-rays.

For the tests described here the CCDs were cooled to about -100°C. At this temperature the dark current is near $10^{-2}e^-$/pixel/sec for the 3-phase device and $10^{-3}e^-$/pixel/sec for the virtual phase. Our exposure times vary from 1 to 30 seconds depending on which source is used and so dark current is completely negligible. The virtual phase devices have an additional noise source which comes from currents generated within the device when it is clocked. This noise source amounted to 40 electrons RMS for the device used in these tests.

A more complete description of the 3-phase device was given by Blauke et al. (1981). The virtual phase device was described by Janesick et al. (1981).

III. X-RAY PERFORMANCE

Both three-phase and virtual-phase CCDs were illuminated with 5.9 keV x-rays from a Fe 55 source. Figure 1 shows a portion of a pseudo-image which displays relative amount of charge for each pixel. With the array orientation shown in Figure 1, events are transferred out (charge-coupled) in a downward direction in each column. Some "smearing" along the vertical direction is apparently due to incomplete charge transfer and is frequently referred to as "deferred charge". The gray scale of the image is highly "stretched" to reveal this low-level incomplete charge transfer.

The distribution of individual pixel event sizes is shown in Figure 2. The "background" curve is off scale below relative event size 7200. The response to Fe 55 x-rays is shown by the peak near event size 7720.

To account for charge smearing along the read-out direction and the finite probability of charge deposition in two adjacent pixels, various data summation techniques have been used. Figure 3 shows the histogram of the number of events as a function of relative event size for pixels when the deferred charge is included with the main event charge. Starting with the main event, the computer algorithm for this approach adds the charge for successive pixels in a vertical column below the initial event until the pixel charge is less than two standard deviations above an average background level. Figure 4 shows the same set of data as in Figure 3, except that those events have been excluded for which the main charge deposition was observed in two adjacent pixels. It is apparent that, compared to the histogram in Figure 3, the background events below the energy peak have been significantly reduced.

Figure 4 represents the best performance obtained so far in an x-ray CCD. The full width at half maximum response (FWHM) is ~ 12%, corresponding to an energy resolution of 700 eV FWHM. In order to obtain the equivalent RMS noise figure, which is frequently used to characterize CCDs, we use a conversion factor of 8.5 (3.6 eV/electron-hole pair x 2.35, the number of standard deviations per FWHM). The noise performance in Figure 4 corresponds to 74 electrons equivalent RMS noise. Figure 5 was derived from the same set of data as in Figure 2 through 4 except that a 3 x 3 mask was used for the array of pixels to be included for each event. A somewhat better performance is obtained in Figure 6 where a rectangular mask of 2 x 6 pixels was used; the mask was aligned along the charge readout direction. In the latter two cases, no additional correction for incomplete charge transfer was made.

The performance for virtual-phase CCDs is comparable to that of 3-phase CCDs except that a poorer noise performance was obtained. From tests at optical wave lengths it was observed that additional charge is created in the serial register under the clocked well. This amount of charge, which appears to be a function of the clock pulse shape, contributed to poor noise performance at optical and x-ray wavelengths. Figure 7 shows the response of a virtual-phase CCD to Fe 55 x-rays. Comparable graphs for sulfur x-rays (2.3 keV) and aluminum x-rays (1.49 keV) are shown in Figures 8 and 9.

IV. PRESENT AND EXPECTED PERFORMANCE

The best noise performance achieved to date with visible light was 8.8 electrons rms for a three-phase device and 22 electrons rms for a virtual-phase CCD. The average widths observed in visible-light tests are 22 electrons and 44 electrons, respectively. Compared to these values, the results for mono-energetic x-rays of 5.9 keV are still significantly poorer.

The most recent analysis of x-ray calibrations shows that the depth of the active regions deduced from optical tests is in fact consistent with the detection efficiency as determined from x-ray absorption measurements and the manufacturer's specifications, i.e., 10 microns.

Spatial resolution obtained is comparable to the size of a pixel, i.e., 15 microns x 15 microns. This pixel size corresponds to an angular resolution of 1/3 arc second for a telescope of 10 meter focal length, for example, for an AXAF.

V. SUMMARY

The preceding data show conclusively that CCDs have excellent spatial resolution and good spectral resolution, superior to non-imaging proportional counter resolution. However, further research is required to understand the difference between the noise performance at optical and x-ray wavelengths. Various techniques to optimize CCD performance for x-ray applications need to be explored, but these preliminary results are clear evidence that CCDs will become an important tool for x-ray astronomy.

REFERENCES

Blauke, M., Janesick, J., Hall, J., and Cowens, M. 1981, Proc. S.P.I.E., 290.

Griffiths, R. E., Polucci, G., Mak, A., Murray, S. S., and Schwartz, D. A. 1981, Proc. S.P.I.E., 290 (in press).

Janesick, J., Hynecek, J., Blouke, M. 1981, Proc. S.P.I.E., 290.

ORIGINAL PAGE
BLACK AND WHITE PHOTOGRAPH

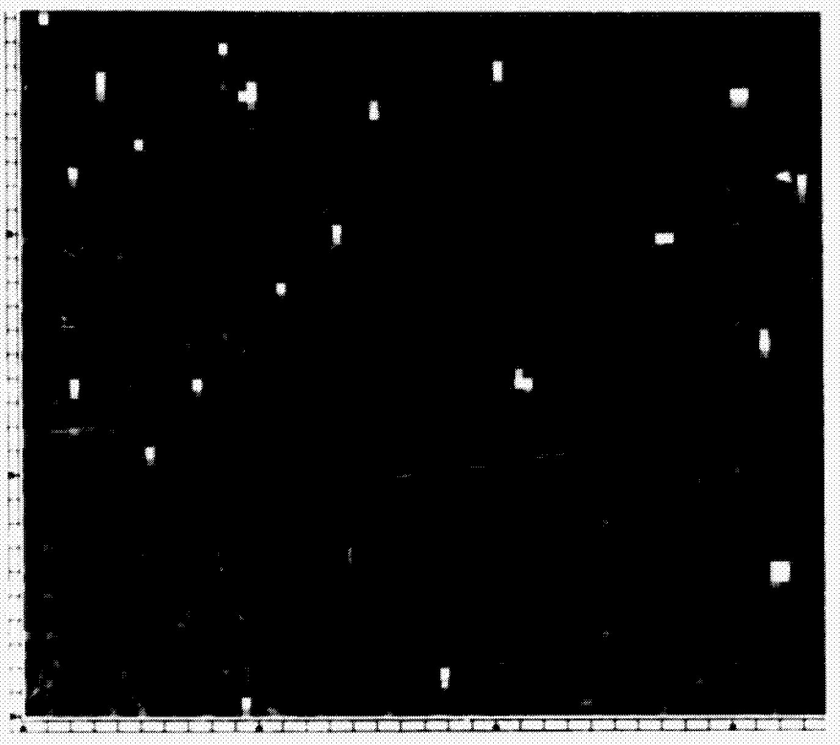

FIGURE 1

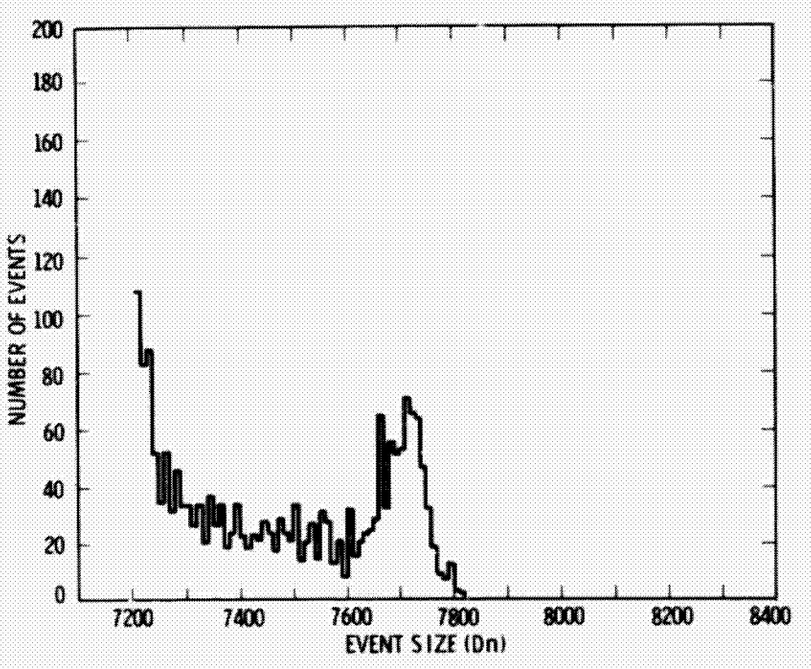

FIGURE 2

ORIGINAL PAGE IS
OF POOR QUALITY

3-PHASE CCD: Fe55, ADJACENT EVENTS INCLUDED

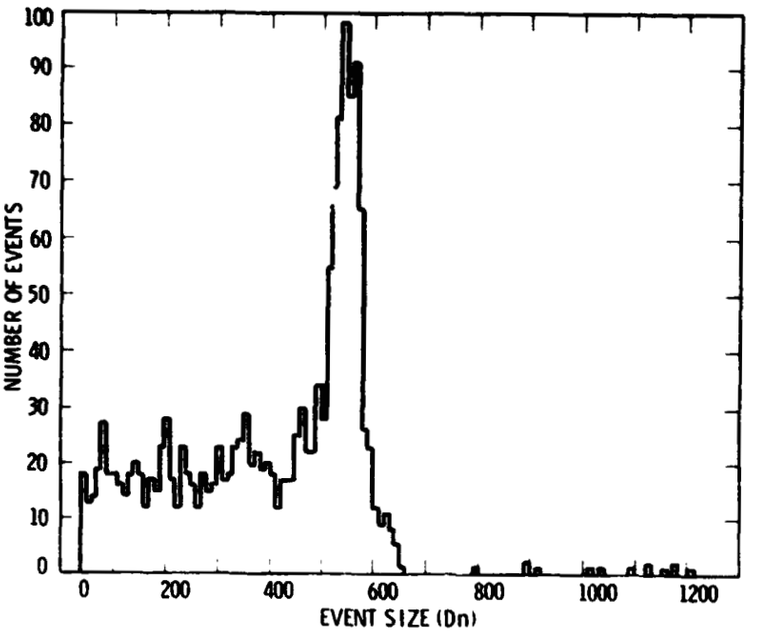

FIGURE 3

3-PHASE CCD: Fe55, ADJACENT EVENTS EXCLUDED

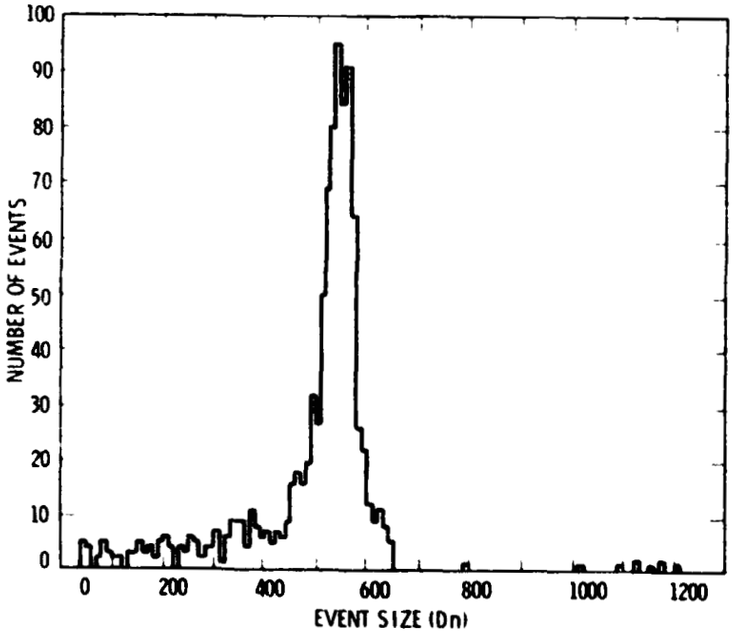

FIGURE 4

ORIGINAL PAGE IS
OF POOR QUALITY

3-PHASE CCD: Fe55, 3 × 3 MASK

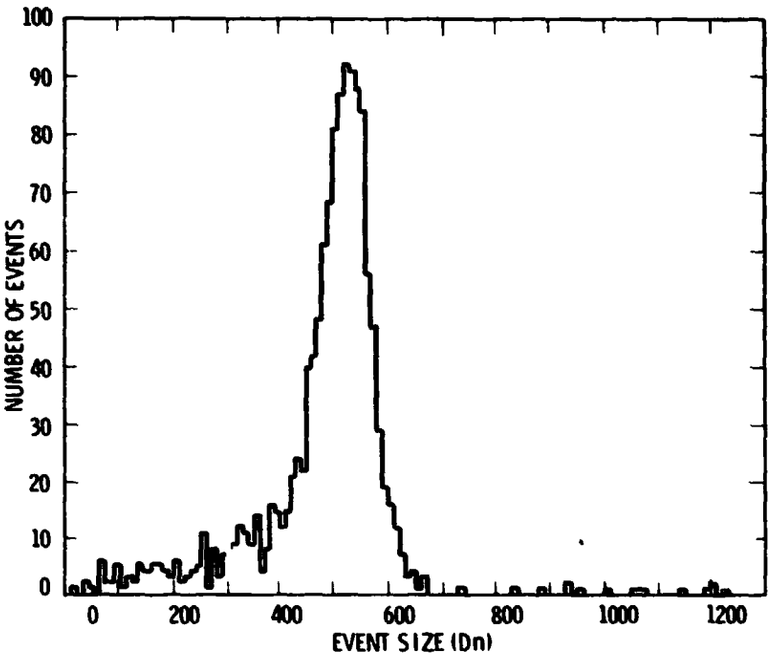

FIGURE 5

3-PHASE CCD: Fe55, 2 × 6 MASK

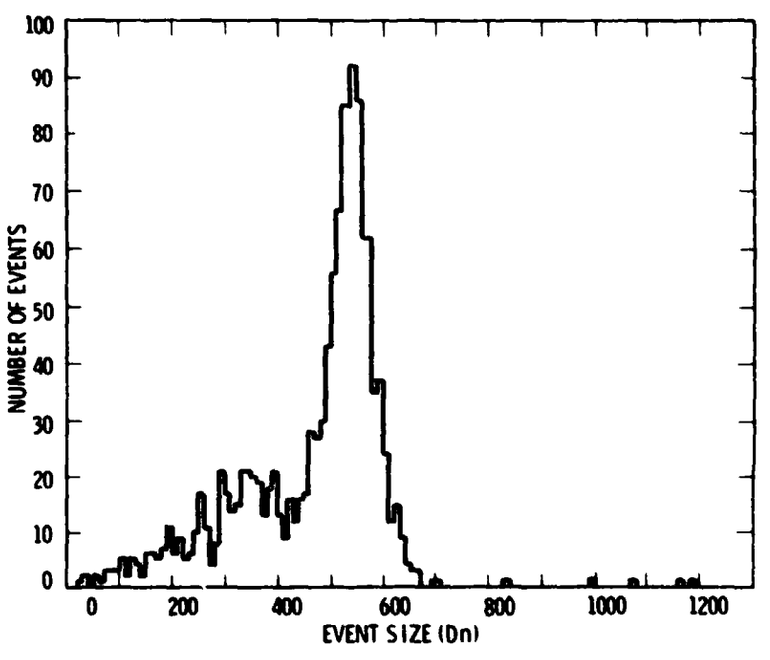

FIGURE 6

ORIGINAL PAGE IS
OF POOR QUALITY

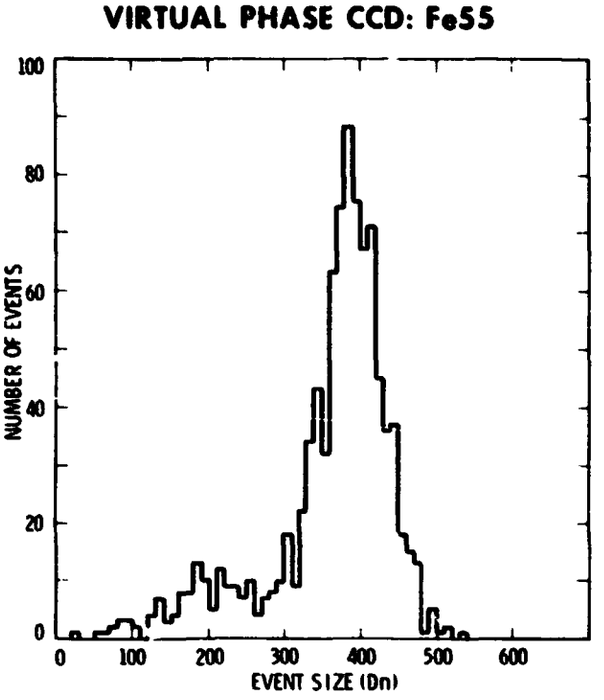

FIGURE 7

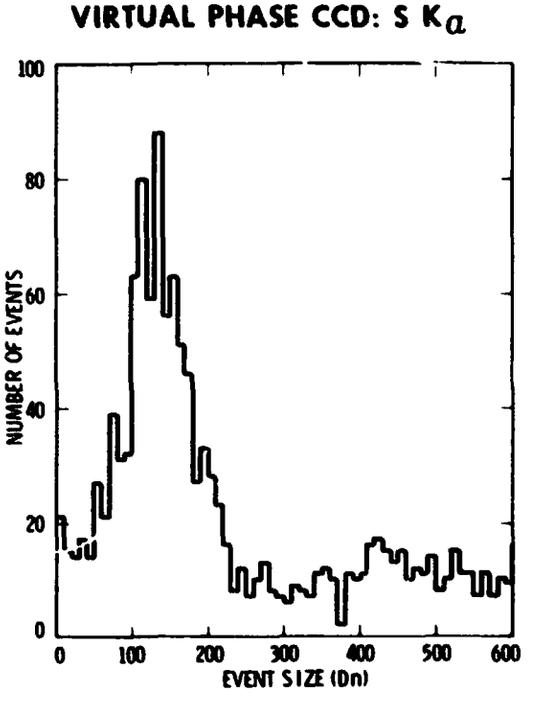

FIGURE 8

ORIGINAL PAGE IS
OF POOR QUALITY

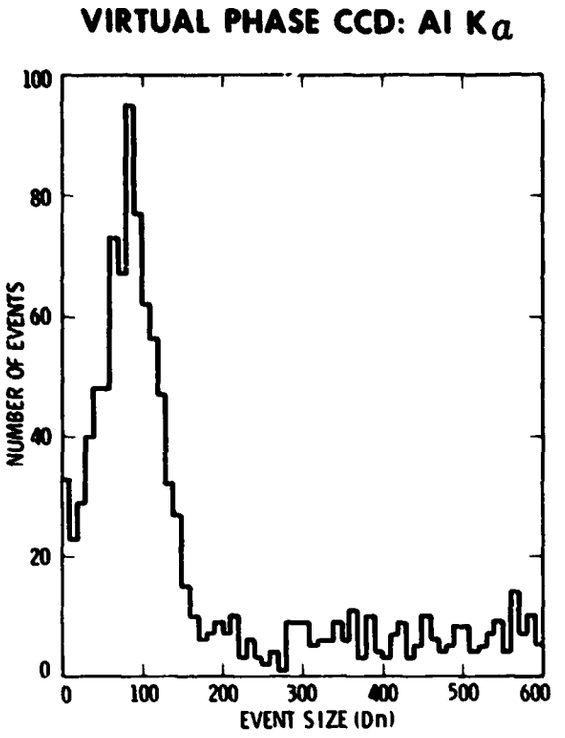

FIGURE 9

N82 26068

AN IMAGING GAS SCINTILLATION PROPORTIONAL COUNTER FOR THE DETECTION OF SUBKILOELECTRON-VOLT X-RAYS

Charles J. Hailey, William H.-M. Ku, and Michael H. Vartanian

Columbia Astrophysics Laboratory, Columbia University

ABSTRACT

A large area imaging gas scintillation proportional counter (IGSPC) has been constructed for use in X-ray astronomy. The IGSPC consists of a gas scintillation proportional counter (GSPC) with a 1 μm polypropylene window coupled to a multiwire proportional counter (MWPC) via a calcium fluoride window. The MWPC, filled with a mixture of argon, methane, and tetrakis (dimethylamino) ethylene, detects the UV photons emitted by the xenon gas in the GSPC. Over a sensitive area of 21 cm^2 the instrument has a measured energy resolution of 17.5% (FWHM) and 1.9 mm (FWHM) spatial resolution at 1.5 keV.

PRECEDING PAGE BLANK NOT FILMED

I. INTRODUCTION

Recent research into gas scintillation proportional counters by ourselves (Anderson et al. 1978; Ku et al. 1979; Hamilton et al. 1980) and others (Charpak, Policarpo, and Sauli 1980; Andresen et al 1978; Hoan et al. 1980; Peacock et al. 1980; Manzo et al. 1980), has demonstrated the enormous versatility of this device for X-ray detection. These counters offer a factor of 2 improvement in energy resolution over conventional proportional counters in the energy range 0.1 to 60 keV (Ku et al. 1979; Hamilton et al. 1980]. The use of a photomultiplier tube array to collect the UV light from the GSPC has demonstrated the feasibility of achieving millimeter resolution imaging capabilities (Hamilton et al. 1980; Charpak, Policarpo, and Sauli 1980; Andresen et al. 1978; Hoan et al. 1980]. Finally, the well defined pulse shape corresponding to X-ray capture in the GSPC allows rise-time discrimination, enhancing the usefulness of this instrument in high background environments such as outer space (Ku et al. 1979, Manzo et al. 1980).

Three years ago, Policarpo (1978) suggested using a photoionization chamber in place of a photomultiplier tube to detect the UV radiation. TEA was found to be a suitable gas for krypton scintillation (Policarpo 1978; Charpak, Policarpo, and Sauli 1980) but a more versatile gas (TMAE) was suggested by Anderson (1981). We extended the usefulness of the GSPC by combining the good energy resolution capabilities of the GSPC with the good spatial resolution capabilities of the MWPC (Ku and Hailey 1981). That instrument, with its 100 μm aluminum foil window, was useful above several kilovolts. We have extended the spectral range of our instrument to the subkiloelectron-volt

X-ray region. We discuss the design and operation of the IGSPC and present data acquired with our counter.

II. INSTRUMENT

The instrument we have designed is shown in Figure 1. The GSPC is a pillbox-shaped chamber of 150-mm diameter. It is made of a machineable ceramic material (Macor). X-rays enter the counter through a polypropylene window. The polypropylene is coated with approximately 100 Å of aluminum to ensure that the window is an electrical ground. The GSPC is designed with an O-ring seal so that the X-ray window may be replaced. The X-ray photons are absorbed by xenon atoms in the drift region. Photoelectrons ejected from the xenon atoms drift to a light producing region defined by two stainless steel meshes held at high voltage. The electrons are accelerated, producing UV photons by excimer deexcitation. The UV photons escape through the calcium fluoride window into the 30 cm × 30 cm × 5 cm MWPC. The MWPC is filled with TMAE and P-20. TMAE moleculres absorb a large fraction of the UV photons. Photoelectrons ejected from the TMAE molecules drift down through a low field region defined by a stainless steel mesh located on the lower surface of the calcium fluoride window and a cathode wire plane located below the window. The photoelectrons are accelerated through the cathode plane toward a high voltage anode plane. A lower cathode plane with wires set orthogonal to the wires on the upper cathode plane defines the total active region. The avalanching electrons are collected on the anode while ions collect on the cathode wires. The charge signals induced on the two cathode planes set perpendicularly to one another are processed digitally to yield the centroid of the

charge distribution in orthogonal directions (Reid et al. 1979). Energy information is obtained by collecting the electrons in a charge-sensitive preamplifier attached to the anode plane. Important parameters of the IGSPC are summarized in Table 1.

III. DESIGN

The goal was to build a soft X-ray IGSPC with 18% (FWHM) energy resolution and 1.0 mm (FWHM) spatial resolution at 1 keV. Good energy resolution requires maximizing UV light output from the GSPC and detection by the MWPC. Good UV light production is obtained by using as high a differential voltage as possible on the GSPC without allowing charge multiplication. The UV photons produced are proportional to the thickness of the light producing region so this must be large (Conde, Ferreira, and Ferreira 1977). Good UV collection requires transparent UV window and grids and a large solid angle of interception. The calcium fluoride disk is made as thin as mechanical constraints allow and provides approximately 80% transmission. Optimal position resolution sets additional constraints on design (Ku and Hailey 1981). A flashless getter in a separate chamber connected by two tubes to the main counter chamber maintains the purity of the xenon gas. The upper O-ring seal in the GSPC allows easy replacement of thin windows which are mounted on aluminum carrier plates. The entire GSPC assembly is attached to the MWPC via an O-ring and may be removed to provide access to the MWPC chamber.

IV. MEASURED PERFORMANCE OF THE IGSPC

a. Gain and Energy Resolution

The GSPC was filled with 760 torr of high purity (99.995%) xenon gas. The MWPC was filled with 620 torr of P-20 and 0.3 torr of TMAE. Results similar to those described below were also obtained with an MWPC fill of 608 torr of argon, 152 torr of isobutane, and 0.3 torr of TMAE. A small ^{55}Fe source (5.9 keV Mn-K) was epoxied to a window support rib to allow continual monitoring of gain while measurements were taken at lower energies with a variety of fluorescence X-ray sources. GSPC settings of 0.5 kV and 3.8 kV on the upper and lower grids, respectively, and 0.5 kV on the MWPC cathode were chosen as nominal. Figure 2 shows a typical energy resolution versus anode high voltage curve at 0.94 keV (Cu-L). The curve exhibits a minimum at about 2.2 kV, which was chosen as the nominal anode operating voltage. Figure 2 also shows the total cathode plane output as a function of MWPC anode HV. The system gain tends to run away above about 2.3 kV. Figure 3 summarizes the best energy resolution performance of the IGSPC at the energies measured: 0.28 keV (C-K), 0.68 keV (F-K), 0.94 keV (Cu-L), 1.5 keV (Al-K), 2.3 keV (S-K), 5.9 keV (Mn-K). The results agree well with the expected $E^{-1/2}$ scaling. The 8.5% (FWHM) resolution obtained at 5.9 keV is consistent with energy resolution measurements taken on a photomultiplier tube using the same polypropylene window. The gain of the counter was measured as a function of position. The gain is uniform to better than 10% across the entire 51-mm diameter of the X-ray entrance window. The good gain uniformity is a result of the small X-ray window diameter with respect to the total GSPC diameter (ensuring minimal field fringing at the window edge) as well as the large area of the MWPC which

ensures efficient UV collection even for events near the edge of the window. Figure 4 shows the energy resolution as a function of position in the direction parallel to the anode wire direction. The energy resolution is uniform across the entire window as expected from the good gain uniformity. Similar results are obtained in the orthogonal direction.

b. Position Resolution and Sensitivity

We have mapped the counter response over the entire 51-mm polypropylene window. Figure 5 shows a plot of the weighted average position versus the source position parallel to the anode wire direction. Again, similar results were obtained for the direction perpendicular to the anode wire direction. The measurements were taken at 0.94 keV (Cu-L) with a copper anode Henke tube mounted approximately 300 cm from the window plane of the counter and connected via a vacuum vessel to the test chamber. Movable slits defined a 150 μm × 150 μm beam size. The counter response is linear over almost the entire range, slowly flattening towards the window edges. This flattening is due to the loss of light intercepted by the 130 mm x 130 mm MWPC as the X-ray source is displaced from the center. The effect is quite small, in marked contrast to results we had previously obtained with a 75 mm x 75 mm MWPC (Ku and Hailey 1981). The desire to improve our position sensitivity was a prime motivation in going to a larger sized MWPC. Figure 6 shows position-resolution data obtained at different X-ray energies. Various collimation schemes allowed us to obtain measurements at 5.9 keV (Mn-K), 1.5 keV (Al-K), and 0.29 keV (C-K), in addition to our measurement at 0.94 keV (Cu-L). The data have been corrected for the effects of finite source size. The data scales roughly as $E^{-1/2}$. Figure 4 shows the position resolution versus source position parallel

to the anode wires. As with the energy resolution, good uniformity is obtained (in both directions).

c. Rise-Time and Background-Rejection Efficiency:

Pulse-shape discrimination has been applied with good success in GSPCs to reject non-X-ray background events (Andresen et al. 1977). The time between initiation of secondary light multiplication and the complete collection of all the light is a function of the electron cloud size, the drift velocity in the absorption region, the size of the scintillation region, and the drift velocity in the scintillation region. For our counter geometry and xenon, this rise time is 2.1 microseconds for X-rays captured near the window. The spread in the rise time is a function of the variance on the size of the electron cloud as it enters the scintillation region, variations in drift velocities arising from distortions in the electric fields, and variations in the depth at which the X-rays are absorbed. These variations can be minimized by maximizing the drift velocity and minimizing the field distortions. The parallel grid geometry of our present counter is ideal for the formation of X-ray pulses. The spread in rise times is less than 0.06 microseconds (1 σ). The rise time is essentially the same for all X-rays in the energy range 0.1 to 6 keV within the central 51-mm active area of the counter, although the spread in rise times increases for lower energy X-rays due to the stronger effect of poor fields near the polypropylene window. The pulse formation times for minimum ionizing particles and γ-rays is much less well-defined and ranges from very short times for those events absorbed in the scintillation region to very long times for those events which track through the whole counter. The narrowness of the rise-time distribution for X-rays then, allows us to set a very narrow rise-time window for acceptance and reject a large

percentage of the non-X-ray background events. Background rejection rates of 95% have been achieved while maintaining 90% X-ray acceptance rates. Moreover, more than half of the cosmic ray induced background events occur near the edge of the GSPC and can be rejected by virtue of their location outside the central 5!-mm field of view.

V. CONCLUSION

The preliminary results from our soft X-ray IGSPC demonstrate the potential usefulness of this instrument. However, there are several steps we will take to improve the energy and position resolution. Improvement of our gettering system should lead to purer xenon gas and thus larger UV light output. Reducing the calcium fluoride thickness through the use of double pumping and reducing the distance from the lower GSPC grid to the calcium fluoride window should allow better UV collection efficiency and also lessen the intrinsic light cloud spread. Finally, a systematic program to examine various fill gases for our IGSPC will be undertaken. These steps should help us attain our goal of 18% (FWHM) energy resolution and 1.0 mm (FWHM) spatial resolution at 1 keV.

The authors wish to acknowledge helpful discussions with R. Novick. This work was supported by the National Aeronautics and Space Administration under grant NGR 33-008-102. This is Columbia Astrophysics Laboratory Contribution No. 214.

ORIGINAL PAGE IS
OF POOR QUALITY

TABLE 1

Parameters of IGSPC's Design

Parameter	IGSPC
GSPC	
- Gas mixture*	xenon
- Gas pressure (torr)*	760
- Absorption depth (mm)	10
- Light multiplication depth (mm)	11
- Bottom grid to UV window (mm)	4
- UV window material	CaF_2
- UV window dimensions (mm)	7.0 x 150
- X-ray window material (μm)	1 polypropylene
- X-ray window dimension (mm)	51 dia.
- Grid transparency	90%
- Nominal HV (kV)* V_3, V_1, V_2	0, 0.5, 4.0
IPC	
- Gas mixture*	TMAE + P-20
- Gas pressure (torr)*	0.3 + 620
- Absorption depth (mm)*	12
- Anode-cathode distance (mm)	4.5
- Anode wire dimension (mm)	0.02 x 130
- Cathode wire dimension (mm)	0.063 x 130
- Cathode group size	6.0
- Anode wire spacing (mm)	2.0
- Cathode wire spacing	0.55
- Grid transparency (ground)	90%
- Nominal HV (kV)*	
V_a, V_c, V_G	2.2, 0.5, 0

*Adjustable

REFERENCES

Anderson, D. F. 1981, Nucl. Instr. Methods, submitted.

Anderson, D. F., Ku, W. H.-M., Novick, R., and Scheckman, M. 1978, IEEE Trans. Nucl. Sci., NS-15, 813.

Andresen, R. D., Leimann, E. A., Peacock, A., and Taylor, B. G. 1977, Nucl. Instr. Methods, 146.

Andresen, R. D., Leimann, E. A., Peacock, A., and Taylor, B. G. 1978, IEEE Trans. Nucl. Sci., NS-25, 800.

Charpak, G., Policarpo, A., and Sauli, F. 1980, IEEE Trans. Nucl. Sci., NS-28.

Conde, C. A. N., Ferreira, L. R., and Ferreira, F. A. 1977, IEEE Trans. Nucl. Sci., NS-24, 221.

Hamilton, T. T., Hailey, C. J., Ku, W. H.-M., and Novick, R. 1980, IEEE Trans. Nucl. Sci., NS-27, 190.

Hoan, N. N., Jeanjean, J., Itoh, H., and Charpak, G. 1980, Nucl.Instr. Methods, 172, 603.

Ku, W. H.-M., and Hailey, C. J., 1981, IEEE Trans. Nucl. Sci., NS-28.

Ku, W. H.-M., Anderson, D. F., Hamilton, T. T., and Novick, R. 1979, IEEE Trans. Nucl. Sci., NS-26, 490.

Manzo, G., Peacock, A., Andresen, R. D., and Taylor, B. G. 1980, Nucl. Instr. Methods, 173, 301.

Peacock, A., Andresen, R. D., Leimann, E. A., Long, A., Manzo, G., and Taylor, B. G. 1980, Nucl. Instr. Methods, 169, 613.

Policarpo, A. J. P. L. 1978, Nucl. Instr. Methods, 153, 389.

Reid, P. B., Ku, W. H.-M., Long, K. S., Novick, R., and Pisarski, R. L. 1979, IEEE Trans. Nucl. Sci., NS-26, 46.

FIGURE CAPTIONS

FIG. 1 - Schematic diagram of the imaging gas scintillation proportional counter (IGSPC).

FIG. 2 - Total pulse height from the cathode planes plotted as a function of anode high voltage (x); energy resolution plotted as a function anode high voltage (*). The data are for Cu-L with V_c = 0.5 kV and the GSPC at (3.8 - 0.5) kV.

FIG. 3 - The energy resolution vs.X-ray photon energy of the IGSPC. The solid line is proportinal to $E^{-1/2}$.

FIG. 4 - The energy (o) and position (·) resolution for Cu-L as a function of source position parallel to the anode wire direction.

FIG. 5- Position sensitivity and linearity in the direction parallel to the anode wires in the MWPC. The divider output is plotted vs. the source positon.

FIG. 6 - The IGSPC position resolution vs. X-ray photon energy. The solid line in proportional to $E^{-1/2}$.

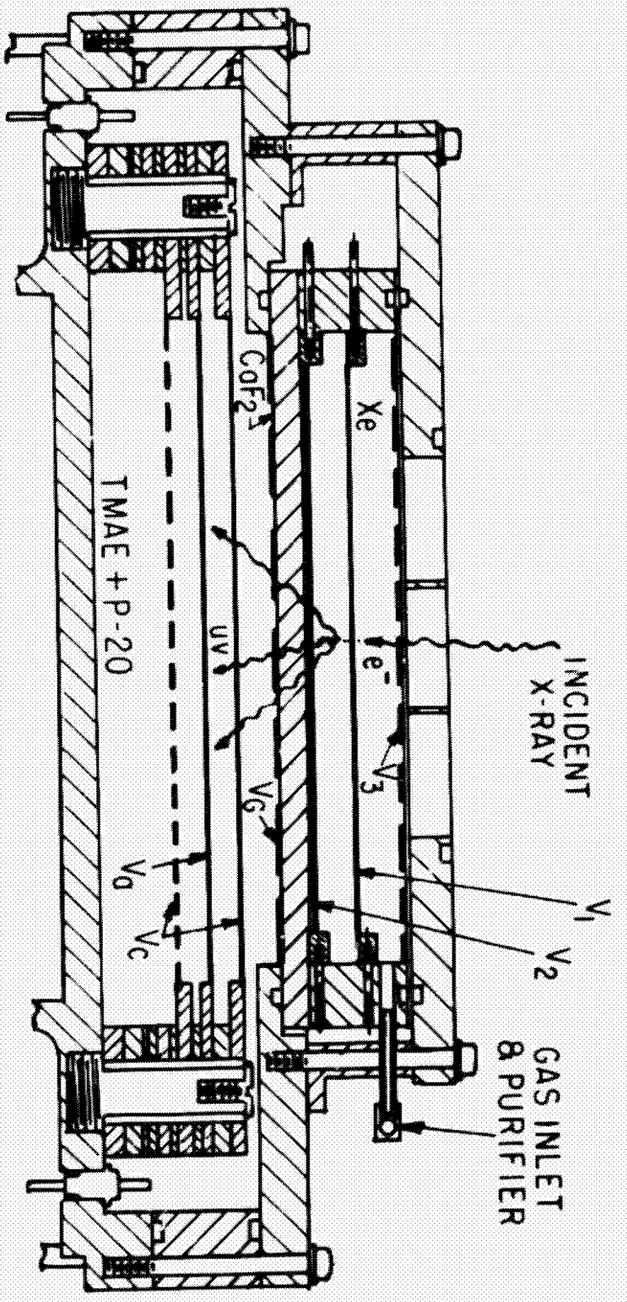

FIGURE 1

ORIGINAL PAGE IS
OF POOR QUALITY

ORIGINAL PAGE IS
OF POOR QUALITY

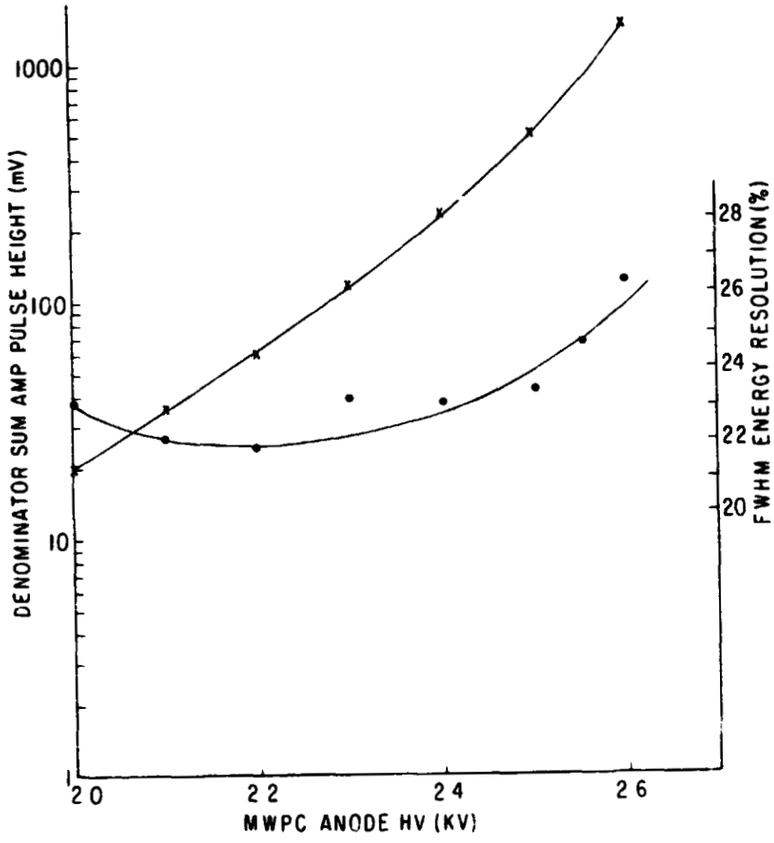

FIGURE 2

ORIGINAL PAGE IS
OF POOR QUALITY

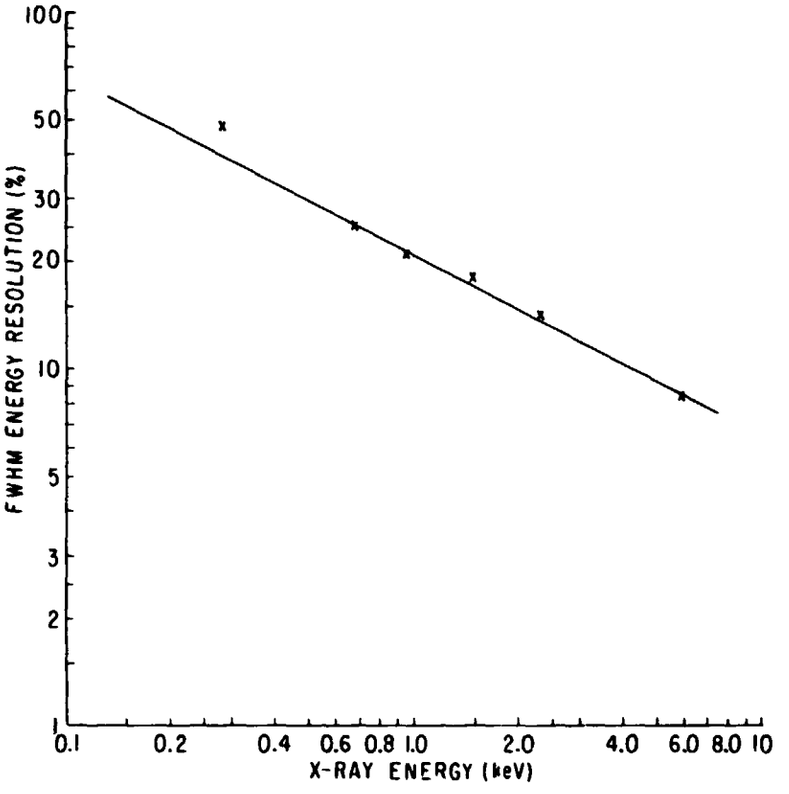

FIGURE 3

ORIGINAL PAGE IS
OF POOR QUALITY

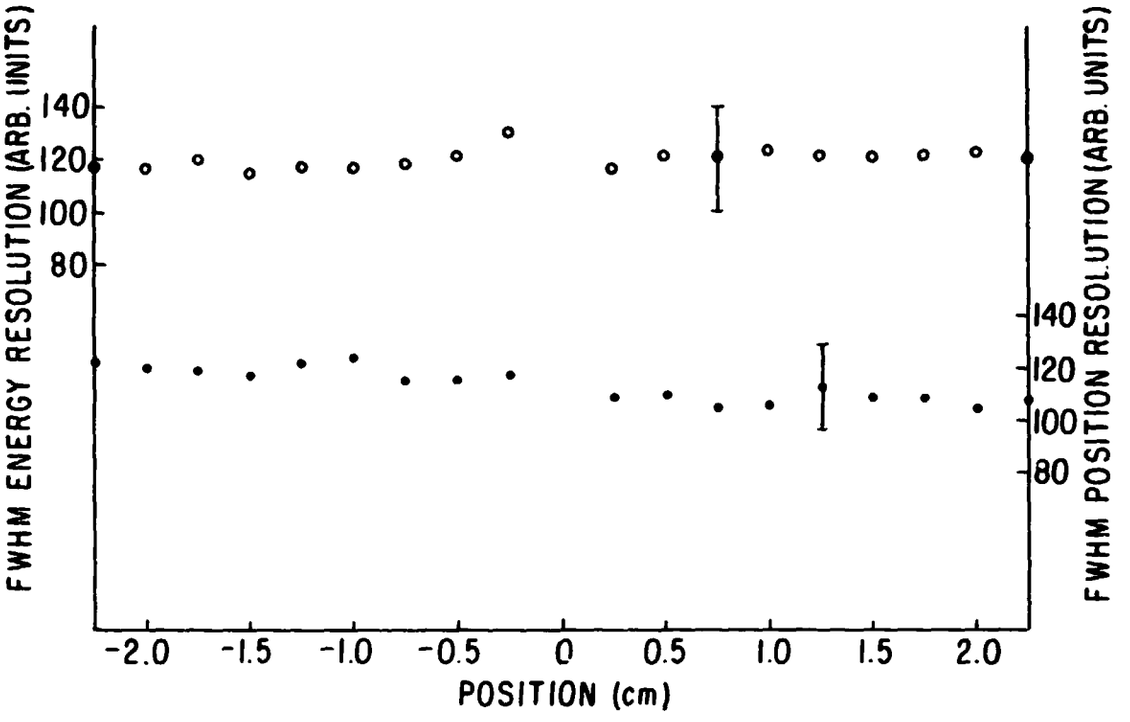

FIGURE 4

ORIGINAL PAGE IS
OF POOR QUALITY

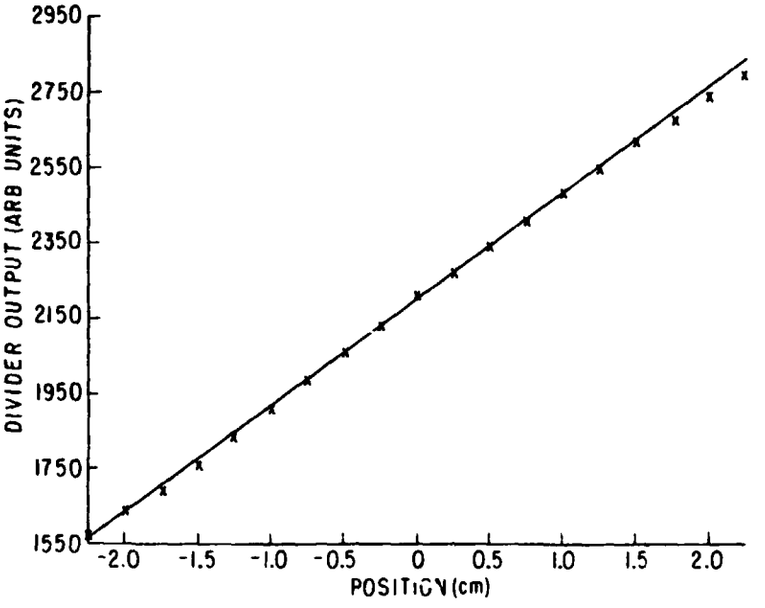

FIGURE 5

ORIGINAL PAGE IS
OF POOR QUALITY

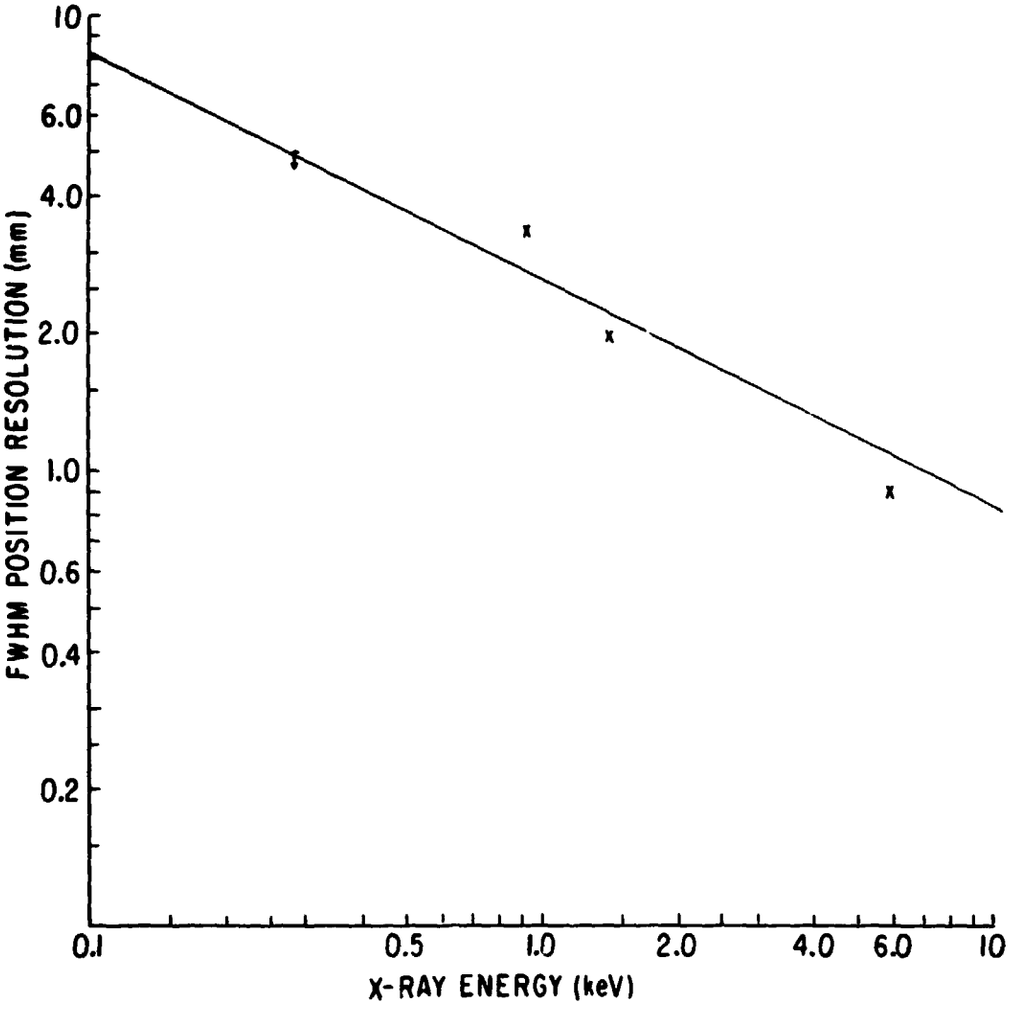

FIGURE 6

N82 26069 D14

PRECEDING PAGE BLANK NOT FILMED

A WIDE-FIELD SOFT X-RAY CAMERA

Robert Petre

Massachusetts Institute of Technology
Cambridge, MA

ABSTRACT

We describe a Wide-Field Soft X-ray Camera (WFSXC) sensitive in the 50 - 250 eV band. which is presently under development by MIT and Leicester University. The camera features Wolter-Schwarzschild optics with an 8 degree field of view and 300 cm^2 collecting area. The focal plane instrument is a microchannel plate detector. Broad-band energy discrimination is provided by thin-film filters mounted immediately in front of the focal plane. The WFSXC is capable of detecting sources with intensities > 5 per cent of HZ 43 during typical sounding rocket exposures, and it would approach the same sensitivity range as EUVE during a typical exposure from the Shuttle.

The X-ray Astronomy sounding rocket group at MIT, along with collaborators from Leicester University, have developed a Wide Field Soft X-ray Camera (WFSXC). The instrument features Wolter-Schwarzschild optics (Wolter 1952a,b) with an 8 degree diameter field of view and a microchannel plate detector at the focal plane. The WFSXC was designed to carry out an all-sky survey in the ultrasoft X-ray band (50 - 250 eV; 50 - 250 A), with moderate sensitivity and arc-minute angular resolution.

The primary attractions of using WFSXC as part of an explorer mission or Shuttle payload are its wide field and its operation in an energy band that is complementary to the traditional soft X-ray band (e.g.,the 0.1-4 keV band of Einstein). Although this camera by itself would not warrant an explorer mission, especially in light of the pending EUV Explorer, WFSXC would be an ideal complement on an explorer mission to a more conventional soft X-ray telescope or other soft X-ray spectrometer. Perhaps the most appropriate application of the WFSXC would be as a Shuttle payload. Since it is a survey instrument, it could simply be mounted in the Shuttle bay without any independent pointing mechanism, observing in whatever direction the Shuttle points. Alternatively, its short focal length makes it easily adaptable into an Experiment of Opportunity (EOP) package.

A schematic of the WFSXC appears in Fig. 1. A photo of the payload (prior to final wiring for a sounding rocket experiment) is shown in Fig. 2. Briefly, the experiment consists of three nested Wolter-Schwarzschild type I mirrors. with a microchannel plate detector in the focal plane. Broad-band energy discrimination is provided by thin-film filters mounted immediately above the focal plane.

The mirrors have an 8 degree field of view and a geometrical area of ~300 cm^2. In order to obtain a reasonable angular resolution over such a wide field, it was necessary to machine the mirrors in a Wolter-Schwarzschild type I configuration, rather than the more

commonly used Wolter type I paraboloid-hyperboloid. The Wolter-Schwarzschild optics are similar to those of the Wolter type I (Wolter 1952a), except that the surfaces exactly fulfill the Abbe sine condition (Wolter 1952b). The optimum focal surface is therefore free of those aberrations which grow linearly with off-axis angle (i.e., coma). Hence the Wolter-Schwarzschild is the superior design for wide-field grazing-incidence optics (Chase and VanSpeybroeck 1973).

The design of such a wide-field mirror also necessitated a small focal ratio and the associated large grazing angles. The mirrors therefore have little response above ~250 eV. This is indicated in Fig. 3a, which shows the effective area of the optics as a function of off-axis angle for various wavelengths. Approximately two-thirds of the effective area is preserved out to 4 degrees off axis. The mirrors essentially comprise an f:1 optical system, with a 55 cm focal length and a 38 cm entrance aperture.

The resolution of the mirrors (rms blur circle radius) as a function of off-axis angle is illustrated in Fig. 3b. The dotted curve shows the focal plane characteristics for a flat detector located at the on-axis focus. Since a major aberration is curvature of field, it is possible to significantly improve the off-axis point response by curving the front microchannel plate to match the optimum focal surface. The optimum focal characteristics of the mirrors are represented by the solid line in Fig. 3b. The Leicester University group is developing such a curved-plate microchannel plate detector for future use with the WFSXC. At the present time, a flat microchannel plate detector has been repositioned 1.25 mm in front of the on-axis focal position to provide the best average imaging properties over the inner 5 degree diameter of the focal plane, as represented by the dashed line in Fig. 3b.

The mirrors were machined out of 18 cm aluminum plate stock. Since each of the two reflecting surfaces is so short, it was possible to machine both surfaces from a single piece of aluminum. The mirrors were machined on an ordinary numerically-controlled lathe and plated with 250 microns of electroless nickel. The final surfaces were then cut on the single-point diamond-turning lathe at the Y-12 plant at Oak Ridge, Tennessee. The reflecting surfaces were polished to a low-scatter finish and electroplated with 1000 A of gold to enhance their reflectivity below 250 eV (Malina and Cash 1978).

In order to attain even a modest (~1 arc minute) angular resolution (the scale of an image on the focal plane is 10 arc minutes / mm), as well as detect X-rays with energies less than ~100 eV, it was necessary to use a microchannel plate detector as the focal plane instrument. The detector consists of two microchannel plates in the chevron configuration with a resistive anode readout (Lampton and Paresce 1974). The detector was designed and constructed by the Leicester University group using plates supplied by Mullard, Ltd. and a resistive anode fabricated by EMI, Ltd.. Since the reflected X-rays are incident on the microchannel plate at large angles (~30 degrees) and microchannel plates are relatively inefficient at these angles, a top plate with a 0 degree bias was chosen. thus preventing asymmetries in the camera efficiency across the focal plane. The microchannel plate efficiency was enhanced in the soft X-ray region by coating the top plate with magnesium fluoride (Lapson and Timothy 1976). The resistive sheet readout provides positional information accurate to ~0.1 mm (1 arc minute).

Broad-band filters are placed in front of the focal plane to provide crude spectral information as well as to filter out unwanted geocoronal background radiation (304 A and 584 A). The transmissions of three such filters as a function of wavelength are shown in Fig. 4a. We have chosen the parylene N and the Beryllium/parylene N filters for our first sounding rocket flight. For the sounding rocket experiment we have simply mounted the two filters side by side, each covering half the focal plane. (A filter wheel would be used on a Shuttle or explorer mission.) The camera will perform its observations scanning at a constant rate in the direction that allows a source passing across the focal plane to be observed through both filters. In addition to the two transmitting filters, an opaque filter covers a small portion of the detector surface so that the counting rate from non-imaged events may be monitored during flight. Fig. 4b shows the on-axis effective area of the entire camera (filter, telescope and detector) for the various filters as a function of wavelength.

The sensitivity of WFSXC as a function of time is shown in Fig. 5. In sounding rocket exposures (~10 sec) we can detect sources down to ~1/20 the intensity of HZ 43, the brightest known ultrasoft X-ray / EUV source (Lampton et al. 1975). In a typical exposure available during a Shuttle flight (100-1000 sec), the experiment will be 10-100 times more sensitive, placing it in the same sensitivity range as EUVE. Of course, the primary advantage of this instrument is its wide field of view, which makes it particularly suitable for survey application. The entire celestial sphere can be imaged in ~1000 exposures. An example of such an application is on the German satellite ROSAT. The WFSXC complements the energy band of the main ROSAT telescope, and is ideally suited for the survey mission ROSAT is to undertake. In fact, a scaled-up version of WFSXC has been proposed by a consortium of British groups as an ancillary experiment on ROSAT, and has been tentatively incorporated into the satellite design.

The rocket-borne version of the WFSXC was launched from White Sands Missile Range on October 16, 1981. Its flight plan consisted of a series of scans across ~100 degrees of sky in which several potential ultrasoft X-ray / EUV sources are located. The data from the flight are presently being processed, and the instrument is being refurbished for a spring, 1982 launch.

REFERENCES

Chase, R.C., and VanSpeybroeck, L.P. 1973, Ap. Opt., 12, 1042.

Lampton, M., Margon, B., Paresce, F., Stern, R., and Bowyer, S. 1976 Ap. J. (Letters), 203, L71.

Lampton, M., and Paresce, F. 1974, Rev. Sci Instrum., 45, 1098.

Lapson, L.B., and Timothy, J.G. 1976, Ap. Opt., 15, 1218.

Malina, R.F., and Cash, W. 1978, Ap. Opt., 17, 3309.

Wolter, H. 1952a, Ann. Phys., 10. 94.

Wolter, H. 1952b, Ann. Phys., 10, 286.

ORIGINAL PAGE IS
OF POOR QUALITY

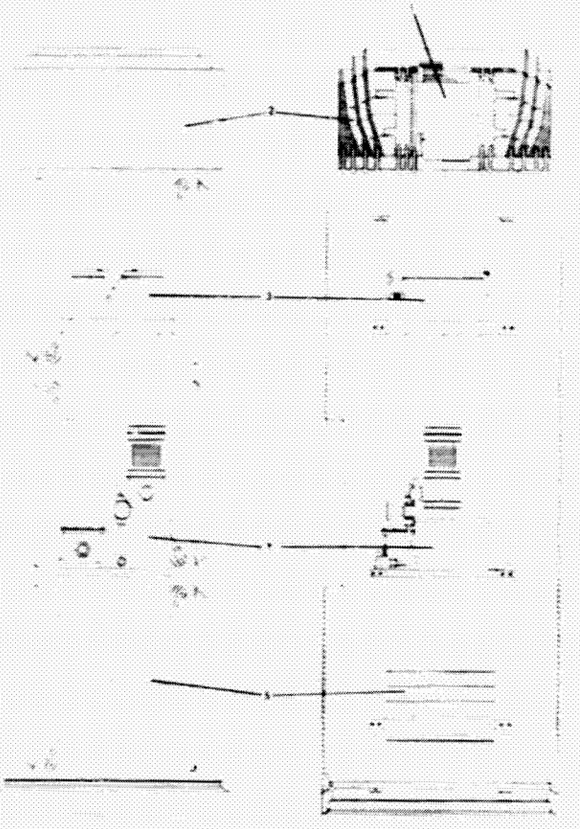

Figure 1: Schematic of the Wide-Field Soft X-ray Camera payload. Key components include: (1) aspect camera, (2) nested telescopes, (3) detector vacuum housing, (4) ion pump, (5) electronics boards.

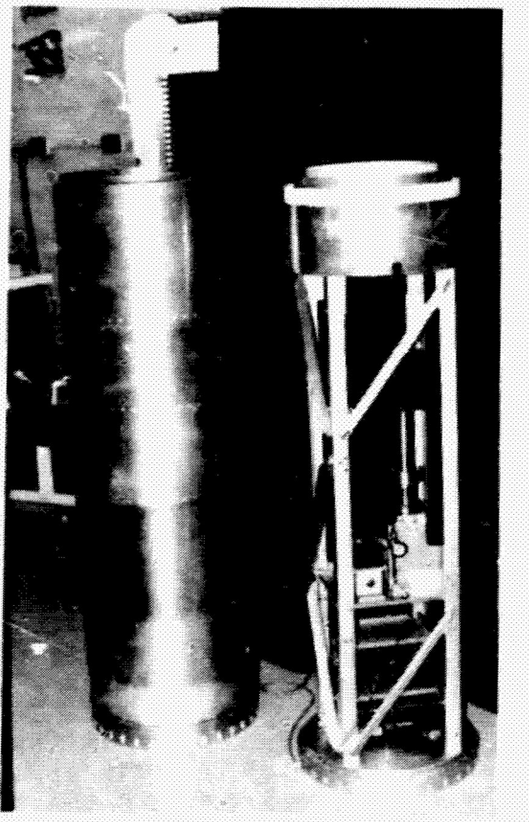

Figure 2: The rocket-borne version of the WFSXC, prior to final wiring.

Figure 3: Imaging properties of the WFSXC mirrors. (a) Effective area at various wavelengths vs. off-axis angle. (b) RMS blur circle radius vs. off-axis angle for various focal plane configurations.

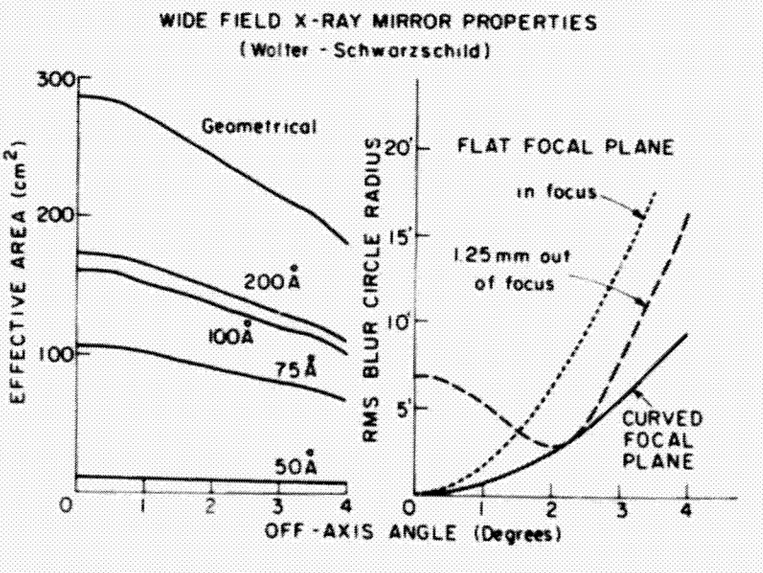

ORIGINAL PAGE IS
OF POOR QUALITY

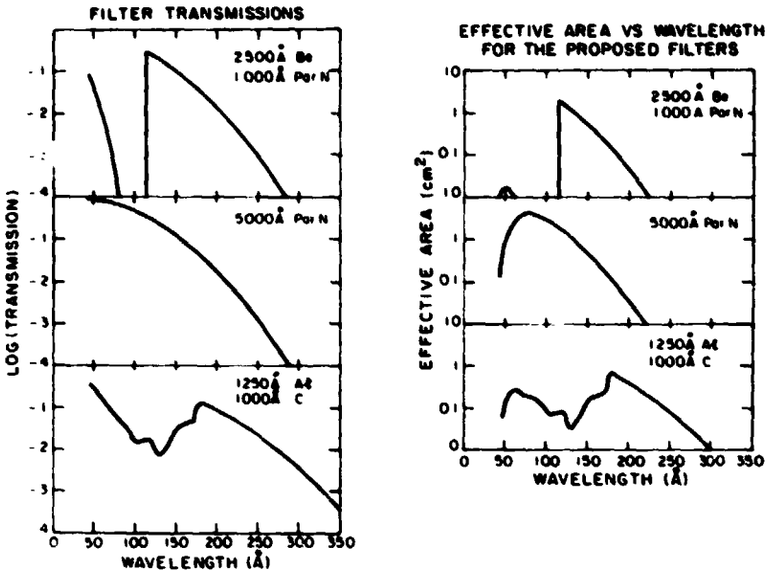

Figure 4: (a) Transmission of the thin-film filters vs wavelength. (b) Effective area of the Wide-Field Soft X-ray Camera vs. wavelength for each of the three filters. These areas include the reflectivities of the X-ray mirrors, transmission of the filters, and efficiency of the microchannel plate detector.

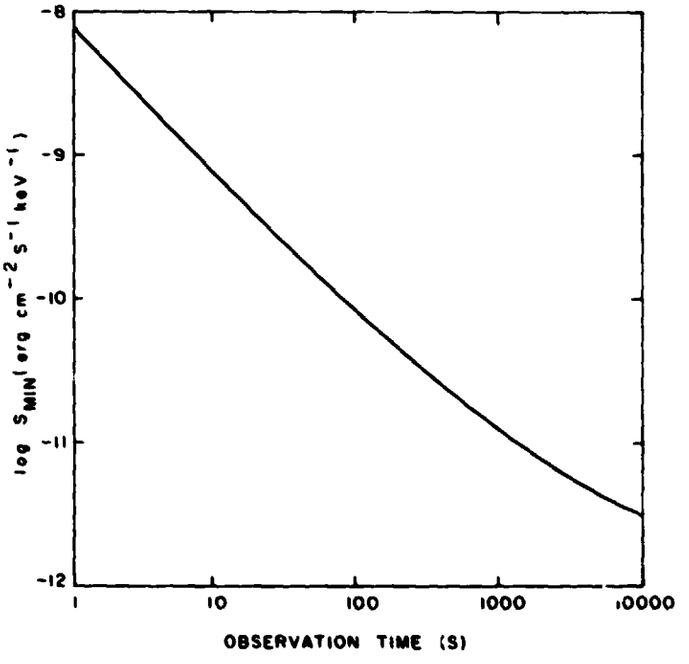

Figure 5: Sensitivity of the WFSXC vs. observation time. Sensitivity represents the minimum source flux observable with 5 sigma significance over imaged background for the Parylene N filter. Imaged background rate is approximately 300 photons s^{-1} sr^{-1}.

PRECEDING PAGE BLANK NOT FILMED

N82 26070

X-RAY IMAGING ABOVE 3 keV

by

Melville P. Ulmer
Department of Physics and Astronomy
Northwestern Univeristy
Evanston, Illinois 60201

I. INTRODUCTION

My original motivation for the designs presented here was to produce energy dependent x-ray maps of clusters of galaxies. Of course, these designs can also be used to study supernova remnants, galactic nuclei, etc.

II. PENCIL BEAM DESIGN

The first design is that for a stacked, etched grid collimator, shown in Figure 1. This could, in principle, be put on the XTE. This would allow the XTE satellite to be used for diffuse object study as well as for point sources in confused regions of the galaxy. Admittedly, AXAF will study diffuse emission. The AXAF's large focal plane scale is not optimal for 10' to 1° extents, however. Furthermore, the stacked, etched grid design can be used out to 15 or 20 keV quite easily, and AXAF only has a token effective area above ~7 keV.

The particular design and experiment parameters that we present below are based on a Space Lab proposal done in collaboration with G. Fritz and R. Cruddace. It demonstrates the power of this relatively simple experiment. The collimator design has more than one solution; the one presented here was done by the Bendix Corporation. Note, the only drawback to usage of this design on the XTE is that the pointing requirements are higher than those of the XTE saltellite. Also, note that the 8×10^{-3} UFU sensitivity is quite good, and is achievable because of the small field of view.

Experiment Summary Table 1

Objective To study clusters of galaxies, galactic nuclei and other extended and point x-ray sources with high sensitivity and large dynamic energy range.

Technique Passive collimators and gas filled proportional counters.

Field of View 4' x 4' and 12' x 12'.

Collimators 9 units of stacked electroformed invar gold coated mesh.

Detectors Low background wire wall proportional counters.

Energy Range .25 - 15 keV.

Effective Area 3000 cm^2 at 2-10 keV, 1000 cm^2 at 0.1-0.25 keV and 10-15 keV.

Sensitivity (5σ) Point source 8×10^{-3} UFU in 10^5 seconds, 2-6 keV.

Required Pointing Stability and accuracy 1' of arc, measurement to better 20" of arc.

Accomodation 1 meter square by 0.6 meter in height.

Mass 215 kg power 100 watts.

Table 2: Collimator Properties

Field of View	4 x 4 arc min and 12 x 12 arc min
Transmission (Over active area of proportional counter)	50 per cent
Effective Area (each)	320 cm^2
Size (each collimator)	230 mm x 280 mm x 360 mm high
Weight	13.1 Kg
Thermal Heat Leak (each)	7W @ °C (10 watts @ 30° C)
Total Weight (9 collimators, optical bench, thermal cover)	135 Kg
Total Heat Leak (9 collimators and thermal cover)	81W

III. MIRROR ARRAY DESIGN

The second design we present overlaps with the capabilities of AXAF, but the design is optimized to work at 7 keV. Below, we show below that at 7 keV, the present design is quite good for sources that are to be studied on scales >1'

The basic design was used for a Space Lab proposal which I submitted in collaboration with the University of Birmingham group (A. P. Willmore, P.I.). A single mirror module consists of 4 nested Wolter Type I mirrors (Figure 2). Then 80 of these modules would be combined as shown in Figure 3. The 80 separate images would be formed, and combined later by software. The design and sensitivities are summarized below.

Experiment Summary: Table 3

*80 mirror units, each comprising 4 nested sections, focal length 200 cm, maximum mirror ~12 cm diameter, ~40 cm long (Figure 2)

*Grazing angle 25' allowing operation to at least 8 keV

*Resolution 2'; Field of view ~20' diameter

*Large effective area from one position sensitive proportional counter for detecting the images from 20 mirror units. Background consequently minimized by large guard region surrounding each image region and manufacturing problems reduced.

*Cost minimized by:

(1) Aiming for moderate resolution, as above

(2) 'Mass' producing mirrors by electro forming replicas from a superpolished master

Table 4: Sensitivity in 4×10^4 seconds (5σ)

Energy	Point Source	20' Diameter Source
2-7 keV	2×10^{-3} UFU	2×10^{-2} UFU
7-9 keV	6×10^{-3} UFU	6×10^{-2} UFU
at 6.7 keV, iron line	5×10^{-6} photons/cm^2 sec	5×10^{-5} photons/cm^2 sec

Table 5

Source Detected	Time Required
10^{35} ergs/sec at the Galactic Nucleus	200 seconds
10^{36} ergs/sec in M31 Nucleus+	4×10^5 seconds
NGC4151-like object at Z = .13	4×10^4 seconds
Iron line from Coma-like Cluster at Z = .3	4×10^4 seconds
Cluster 1/3 as bright as Coma with 10' isothermal sphere 80 resolution elements > 5σ	4×10^4 seconds
Cluster 1/30 as bright as Coma--simple detection if 10' radius	4×10^3 seconds

+2' resolution allows a region of .2kpc radius to be isolated.

We calculated the effective area of the entire system, and this is shown in Figure 4. Note, this area is only ~30% of the geometrical area, because of estimated losses due to scattering, shadowing, and proportional counter response. This area of ~300 cm^2 compares quite well with the AXAF area at 7 keV of ~200 cm^2. The AXAF quoted area does not take into account losses due to scattering or the proportional counter. We estimate that the true effective area could be as low as 100 cm^2, and hence the design we present here has 1.5 to 3 times the area of AXAF at 7 keV. The focal plane scale of AXAF is ~5 times that of our design, and therefore, for diffuse sources, with scales >1', the signal to noise ratio will be similar for AXAF and the design presented here.

IV. MIRROR REPLICATION

Is it possible to make many mirrors cheaply? We have been re-evaluating and old technique--electro-forming. We found that optical flats that have a "low scatter" or "super polished" finish can be quite easily reproduced. Total integrated scattering (Bennett, 1978) tests were performed on both the mandrel (prior to use) and the 14th electro-formed nickel pieces. For both pieces, the r.m.s. surface roughness was 15 ± 2 Å (Bennett, private communication). The 7 keV x-ray scattering results we performed are being analyzed. The present preliminary analysis showed that the reflected x-ray beams from the flats had < 1.4' half power radii, and the total reflectivity of the flats was > 60 %. Electro-forming optical flats is actually more difficult than electro-forming cylindrical pieces. Thus, we are optimistic about this technique, and we are proceeding ahead with plans to reproduce super-polished cylindrical pieces.

V. CONCLUDING REMARKS

In conclusion, designs of modest projects that are not covered by XTE and AXAF are difficult to find. The designs presented here would make available more observing time for projects that would not require the high spatial resolution capabilities of AXAF. Given the funding situation, and the high interest in ~7 keV astronomy, modest instruments with capabilities that overlap XTE and AXAF should be given consideration.

REFERENCES

Bennett, H. E. 1978, Optical Engineering, 17, 480.

ORIGINAL PAGE IS
OF POOR QUALITY

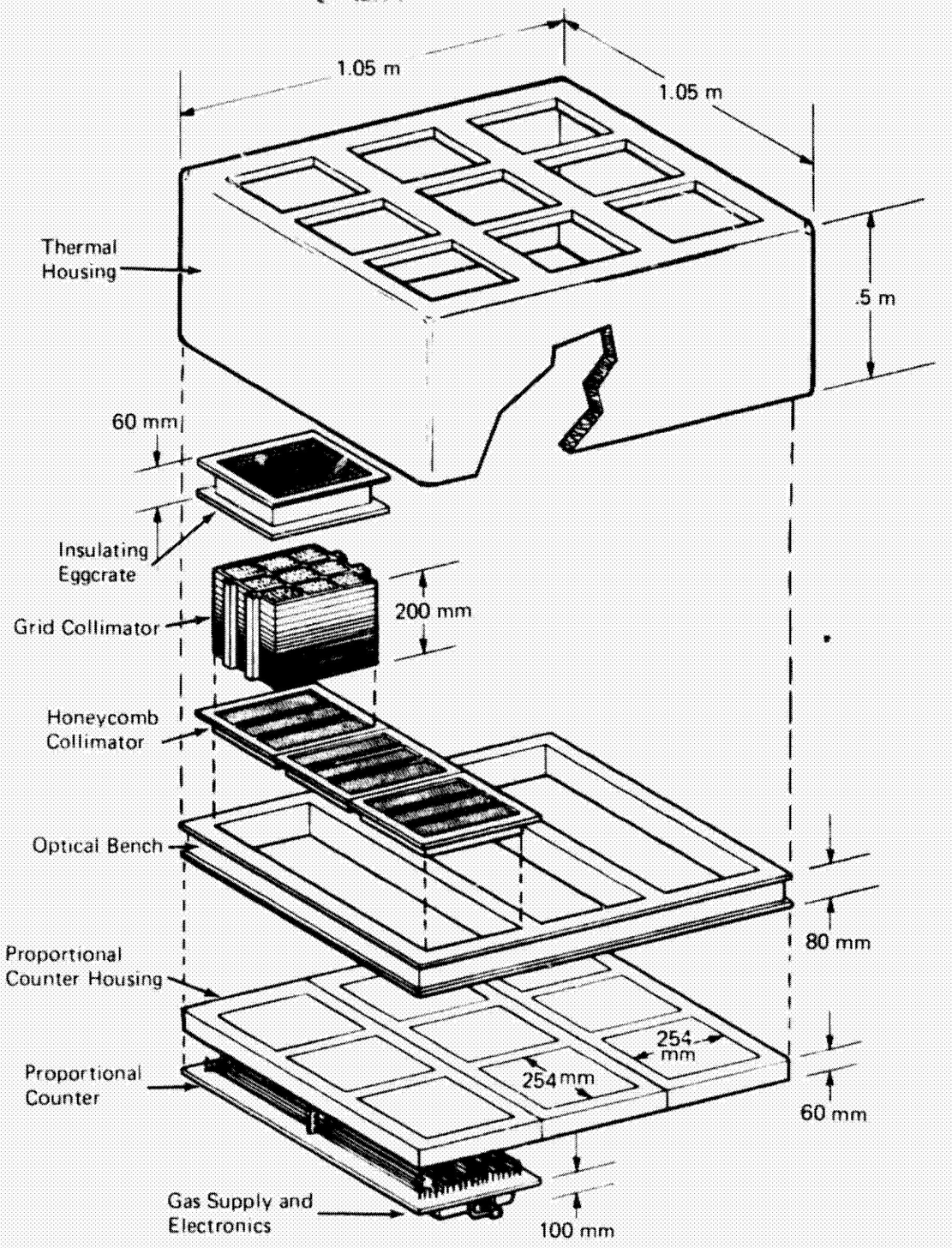

Figure 1 X-Ray Collimator (Exploded View)

ORIGINAL PAGE IS
OF POOR QUALITY

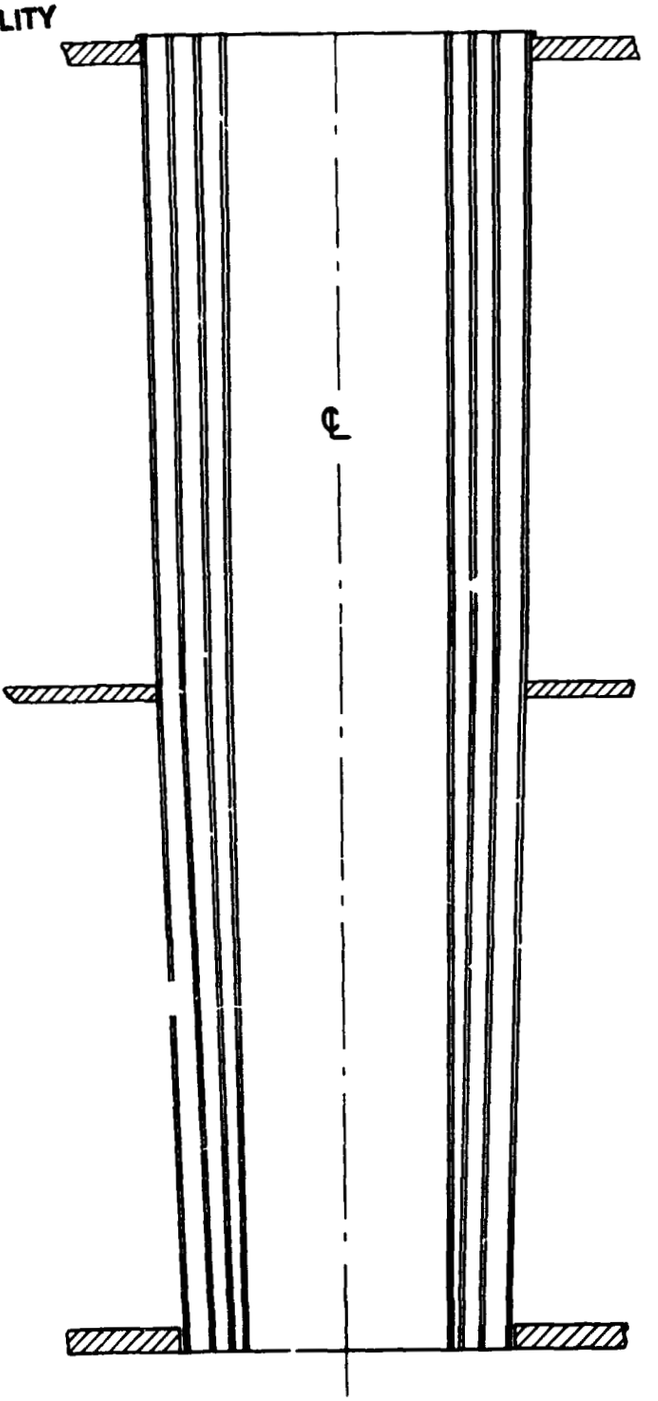

Figure 2 Four nested Wolter Type I mirrors. One of 80 modules

ORIGINAL PAGE IS
OF POOR QUALITY

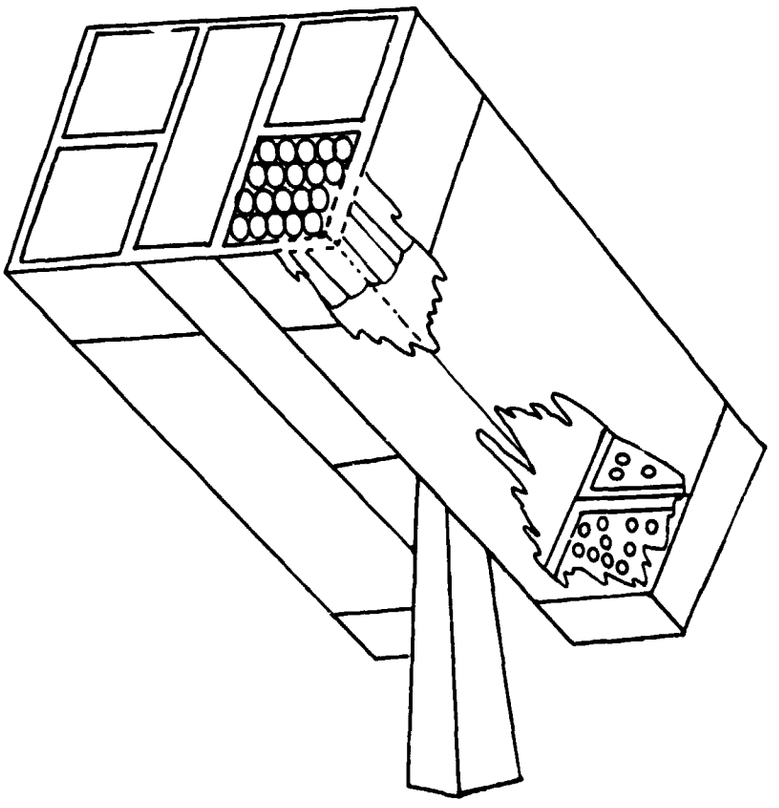

Figure 3 Four units, each comprised of 20 nests of 4 mirrors and approximately .64x.64x2.5m are mounted ? on each side of the Birmingham SL2 pointing system. The startracker, gyros, etc., are situated in the central space.

ORIGINAL PAGE IS
OF POOR QUALITY

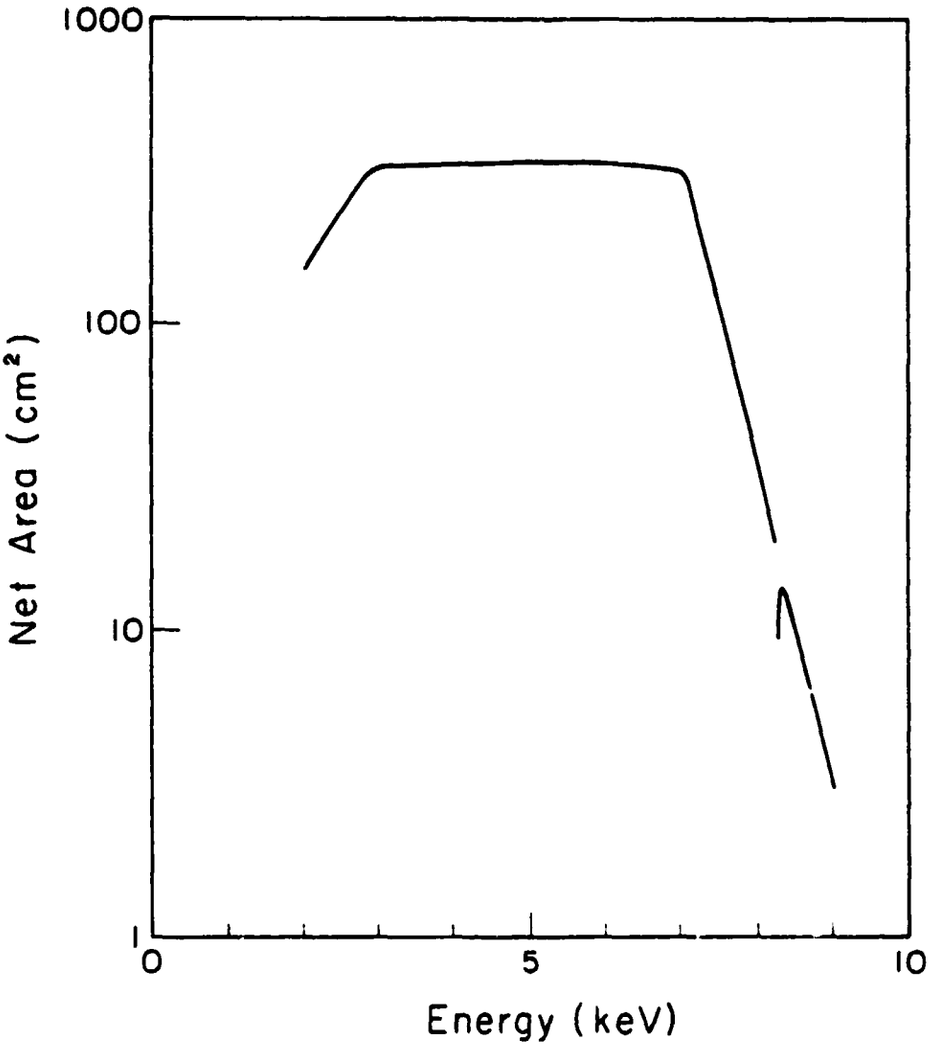

Figure 4 The effective area versus energy for the full 80 mirror/ proportional counter system

ORIGINAL PAGE IS
OF POOR QUALITY

TEMPORAL APERTURE MODULATION

N82 26071

Raymond J. Proctor

Center for Astrophysics and Space Sciences
UCSD, San Diego, 92093

ABSTRACT

The two types of aperture modulation techniques useful to X-ray imaging are reviewed. The use of optimum coded temporal aperture modulation is shown, in certain cases, to offer an advantage over a spatial aperture modulator. Example applications of a diffuse anisotropic X-ray background experiment and a wide field of view hard X-ray imager are discussed.

1. INTRODUCTION

In all fields of astronomy imaging satisfies the prime need for source locations and structure. In X-ray astronomy imaging also provides a freedom from source confusion and an answer to the question of "which part of the detected flux is source and which part is detector background?". The latter requirement is particularly relevant at photon energies greater than 10 Kev, the regime of "hard X-ray" astronomy. Unfortunately at energies above 10 KeV it is not efficient to use reflecting optics for imaging and some other method is necessary. The means to produce images at energies greater than 10 KeV appear to be limited to aperture modulation or scanning methods. Aperture modulation is the encoding of the photons incident on a detector such that their angular dependence can be recovered. This method has a multiplex advantage over more classical scanning methods (Fellget 1958) and is thus to be preferred.

2. TYPES OF APERTURE MODULATION

There are two basic types of aperture modulation, spatial and temporal aperture modulation. Spatial aperture modulation is a static method providing time independent imaging and is epitomized by Dicke's random pinhole camera (Dicke 1968), whilst temporal aperture modulation is a dynamic method and is epitomized by Mertz's mock interferometer (Mertz 1965) which is more generally known as the rotation modulation collimator of X-ray astronomy (Oda,1965; Schnopper,1968). The basic principles of the two methods are illustrated in Fig 1. The spatial aperture modulator casts an X-ray shadowgram onto the position sensitive detector and hence requires N detector elements to detect N mask elements whilst each element of the temporal aperture modulator detects the full N elements of the modulator, albeit in a finite time. This basic time to produce an image is the image cycle time defined as the time it takes the *complete* N aperture elements to traverse the detector element. For both methods the reconstruction of the source direction can be achieved by back-projection of the count rate modulation through the mask onto the sky. Both methods have been improved by the use of optimum coded apertures based on Cyclic Difference Sets (Gunson and Polychronopulos,1976) or one of their less generalized subsets such as PN codes, Hadamard codes or Uniform redundant arrays (Harwit & Sloane,1979; Fenimore & Cannon,1978). The optimum encoding allows the *unique* decoding of complicated point and extended source fields. Optimum coded spatial aperture modulation has been used in X-ray astronomy to image the galactic center between 2 and 10 KeV (Proctor,Skinner and Willmore,1978) whilst optimum temporal aperture modulation has been used in numerous infra-red spectroscopy and imaging applications (Harwit and Sloane,1979)

The future of spatial aperture modulation with its time independent imaging has been recognized by many people. An optimum coded telescope to image clusters of galaxies to 3' in the energy range 2 to 25 KeV has been built by the University of Birmingham and is scheduled to fly on Spacelab 2 (Skinner,1980). Wide field of view spatial aperture modulation cameras have been proposed for the European X80 and Japanese ASTRO B missions to monitor large fractions of the sky for transient sources. At extreme separations between the coded aperture and the detector, the spatial aperture modulation technique allows the possibility of very good angular

ORIGINAL PAGE IS
OF POOR QUALITY

resolution (Hudson and Lin,1978) The Pinhole/Occulter Facility Science Working group has incorporated this feature into a strawman model for a spatially coded aperture modulation telescope for providing 20 arc second images of the sun combined with a Fourier Transform telescope to provide ≈arc second images over a smaller field of view (Hudson et al.,1980). The concept is shown in Fig 2.

3. TEMPORAL APERTURE MODULATORS

When constant or slowly varying X-ray sources are of interest then the technique of temporal aperture modulation can be used. It offers the unique feature that one detector element can produce an image of many elements of sky Thus a high resolution, wide field of view camera can be built. A spatial aperture modulation system cannot provide this option because it is constrained to have N detector elements to image N sky elements, thus it only provides options of high resolution,narrow field of view or poor resolution, wide field of view A high resolution camera normally involves the difficult problem of attitude solution but a high resolution wide field of view camera can see the brighter X-ray sources and generate its own internally consistent attitude solutions. One potential disadvantage appears to be that variable background and source components create image background fluctuations. Provided the time to complete one image cycle of the dynamic mask is less than one minute a temporal modulator will experience no difficulty from normal cosmic ray background variations in near earth orbit. A variable source in the field of view adds a component to the image only of amplitude $\delta I/\sqrt{2}/N$ where δI is the amplitude change and N is the number of mask elements. Additionally variable sources will have a period uncorrelated with the image cycle period hence over M image cycle periods the residual image fluctuations will be uncorrelated and introduce a further $1/\sqrt{M}$ reduction in their relative amplitude. Two example instruments, DAXBE and FOXI, will be discussed to illustrate that the features of temporal aperture modulation can be applied to X-ray astronomy.

4. THE DIFFUSE ANISOTROPIC X-RAY BACKGROUND EXPERIMENT (DAXBE).

Most cosmic radiations are thought to have "diffuse" background components. The microwave 2.7^{o}K background and neutrino background are believed to be truly diffuse and date from the "Big Bang" of current cosmology whilst the X-ray background is believed to originate from discrete sources since the epoch of galaxy formation i.e. at redshifts of $z \lesssim 3$. Very little is as yet known about a gravitational radiation background. There may be a difference in the anisotropies of the microwave and neutrino backgrounds which are effectively at redshifts of $z \approx 1000$ as compared to the locally produced X-ray background at $z \lesssim 3$ (Wolfe,1970; Fabian & Warwick,1979; Rees,1980). Unfortunately the neutrino background has not as yet been observed but microwave observations from balloons have determined a 24 hour anisotropy in the approximate direction of our local supercluster (Conklin,1969; Smoot et al.,1977; Cheng et al.,1979) Assuming the dipole effect is totally due to the motion of the sun and not intrinsic to the 2.7^{o}K background then the effect is equivalent to an infall of our galaxy towards the local supercluster at a velocity of 401±19 kms/sec (Cheng et al.,1980). Recent studies on the redshifts of 300 spiral galaxies give a net solar motion with respect to nearby galaxies ($\lesssim$30 Mpc) of comparable velocity but of widely different direction from the motion with respect to the 2.7^{o}K background (Rubin et al.,1976; de Vaucouleurs et al ,1981). The 24 hour diffuse anisotropy has been measured in the range 2-10 KeV by the HEAO-1 A2 experiment to be 0.005±0.0009 of the diffuse flux (Boldt,1981). The pole of the distribution lies at the same position as the microwave, at approximately the position of the local supercluster. However Boldt also shows that this anisotropy may not be inconsistent with a reasonable luminosity of X-ray sources in the local supercluster. It may be possible to test this hypothesis if the anisotropy can be detected without using the data from the local supercluster. The situation is made more interesting by the discovery of an inhomogeneity in the universe which is larger than the local supercluster. An apparent deficit in the number of optical galaxies exists in the constellation of Bootes. It is interpreted as a void of size 10^{6} Mpc^{3} at a distance of ≈200 Mpc with $\delta M/M \approx 1$ (Kirshner,Oemler,Schecter and Shectman,1981). It is calculated by Kirshner et al. that such an inhomogeneity will give an approximately 150 Km/sec perturbation to our galaxy's velocity relative to distant galaxies ($z \approx 1$).

In the near future the Cosmic Background Explorer will make very detailed microwave & far infrared observations of the cosmological background radiation to provide the large scale picture of our galaxy's peculiar

ORIGINAL PAGE IS
OF POOR QUALITY

velocity whilst surveys of the redshifts of nearby galaxies will provide the local picture of our galaxy's peculiar velocity. Better X-ray data are needed to complement and complete these studies by providing the intermediate picture and allow the local and cosmological effects to be separated.

HOW WELL CAN WE MEASURE THE X-RAY ANISOTROPY?

The basic 2.7°K 24 hour effect has an amplitude of 0.0013 of the diffuse background. In X-rays the Compton-Getting effect (Compton & Getting,1935), magnifies the amplitude to 0.005 of the diffuse background. Hence our detection sensitivity must be at least 0.001 in order to obtain a 5 sigma detection. The measurement of the anisotropy to an accuracy of at least 0.001 requires an approach free of systematic problems. The requirement is effectively to map the sky with sufficient accuracy to exclude known X-ray sources. The conventional method involves the scanning of an asymmetric detector in the local anisotropic radiation field which especially at energies > 20 KeV produces a variable background problem. The use of wide field, optimum coded temporal aperture modulation allows the use of a symmetrical detector *and* gives a much greater signal to noise ratio such that the local background becomes negligible The problem of experimental systematic effects should be greatly reduced and because only a single detector element is needed for imaging the experiment is very simple to build and operate.

An example of how such an instrument could be operated is shown in Fig 3 The figure shows no superstructure but only the spinning detectors and coded mask. The detectors are simple detectors of either gas counter or scintillating type optimised for a symmetric response. No position sensitivity is required. The detectors are constrained by the superstructure to see the diffuse background only through the coded aperture. Low level leakage through the superstructure is not critical as only photons coded by the mask are "imaged". The spinning subsatellite receives an optimally modulated count rate from which an image of the fluctuations in a strip of the sky is made Taking the dimensions of Table 1, the statistical sensitivity of DAXBE in one month is given in Fig 4 in terms of a one sigma sensitivity as a fraction of the diffuse background flux. The sensitivity is per image element If the sensitivity to a 24 hour component of the background is required then this may be considered as the comparison between two hemispheres of sky. Thus the sensitivity is obtained by dividing by $\sqrt{Q}/4$ where Q is the number of source free image elements used in the analysis. The fundamental limitation on the precision that can be obtained for the anisotropy is from the fluctuation in the individual image element intensities due to sources just below the detection threshold. For the example instrument outlined here (e.g with 43 elements) the limit is $\delta I/I \approx 0.004$ per image element (Warwick,Pye & Fabian,1980). This translates into a 24 hour anisotropy detection of 0.005 ± 0.0006 of the diffuse background. This is much worse than the 5-80 KeV statistical limits from one month of observation, e.g. for 5-15 KeV its ± 0.00015 (± 12 kms/sec) The statistical limit can be reached if external information on the number of bright extragalactic sources per image element is known because it is mainly the sources just below the detection threshold (≈ 1 UFU for DAXBE) which cause the fluctuations. This information should be forthcoming from optical surveys and ROSAT (the German X-ray sky survey satellite) The presence of high latitude galactic components (≥ 10 times the 2-10 KeV anisotropy) complicates the analysis still further but these components fall more rapidly with energy than the diffuse X-ray flux (Iwan et al.,1981) Hence more reliable measurements will be obtained if energies greater than 20 KeV are used where the galactic components are smaller. It is noted that any incomplete galactic component subtraction leaves a 12 hour component and hence the minimisation of the galactic component gives more confidence in any detected 12 hour component. Such components are expected from the shear on the X-ray background produced by large mass inhomogeneities (Fabian & Warwick,1979).

5. FERRIS-WHEEL ORBITING X-RAY IMAGER (FOXI)

The study of the energy generation mechanisms in active galactic nuclei (AGN's) is complicated by the need to monitor the variability of their total energy output with time (Lightman, these proceedings). Previous observations have shown that the majority of the power emitted by many Seyfert galaxies, some QSO's and Centaurus A lies in the high energy X-ray range The typical variability observed for AGN's is of order 1 day with the record for the fastest time of variation of $T \approx 100$ seconds held by NGC 6814 (Tennant et al.,1981). The problem then is to monitor as many AGN's as possible for variability on time scales of minutes to years over

as wide a photon energy range as possible. A possible method uses a Ferris-wheel Orbiting X-ray Imager (FOXI) imaging a strip of the sky every 3-4 secs (an eighth of the rotation period). The concept is shown in Fig 5. FOXI is similar to DAXBE in principle but the dimensions are enormously inflated to 50 meters diameter. The use of a flexible jointed mask which unfurls in orbit, after a Space Shuttle launch, allows such a rotating configuration to be attained. The rotating mask modulates a large solid angle of sky in its rotation thus providing the large field of view neccessary for a survey instrument. To obtain good angular resolution the central detector must be one dimensionally position sensitive in its azimuthal direction and be fixed with respect to the stars i.e. non co-rotating. The parameters of a system composed of 100 cm long, 1cm wide strip detectors imaging 4% of the sky to 3' x 140' over a photon energy range of 3-500 KeV are given in Table 2. The instrument would be constrained to image perpendicular to the ecliptic in order to limit differential heating of the mask. This constraint means a complete sky survey would occur every 6 months. The time spent on any one source in this time would be 4 days. The minimum detectable source fluxes are given in Table 3. These minimum fluxes combined with the linear relationship between X-ray and M_B optical luminosity (Zamorani et al.,1981) suggest that the sensitivity is such that QSO's of the mean or greater L_x/L_{opt} ratio will be detected down to M_B=+15 at 80-120 KeV and down to M_B=+17 between 3 and 20 KeV. It is noted that the large scatter in the ratio of L_x/L_{opt} means that some QSO's of $M_B > +15$ or $> +17$ will be detected. The Log N versus M_B curve of Bracessi et al.(1980) shows that we would expect $\geq$ 50 QSO's to be detected in the 80-120 KeV energy band and $\geq$1000 to be detected 3-20 KeV. All Seyferts within 100 Mpc (≈500) would be detected if brighter than 10^{-12} ergs.sec^{-1} and those above 2×10^{-13} ergs.sec^{-1} would be detected at 80-120 KeV.

FOXI was concieved as a free flying satellite but with the advent of long duration manned space stations the working environment should include spin induced "gravity". Such large spinning structures could easily include a coded mask and central detector to perform FOXI type X-ray imaging. Similarly in a future which included O'Neill space colonies a FOXI type imager could be added to the very large ≈1km diameter structures !

ORIGINAL PAGE IS
OF POOR QUALITY

ORIGINAL PAGE IS
OF POOR QUALITY

TABLE 1

Parameters for DAXBE

ITEM	*VALUE*	*COMMENTS*
General System		
Mode	2-4 weeks free flyer	-Recoverable ?
Spin period	≈5 seconds	
Image cycle time	Same as spin period.	
Sky coverage	40% per rotation	-Precession quickly results in 100%
Data rate	300-2000 bits/s	-Function of mask & spin period.
Attitude Solutions	Internal from bright sources.	
Mask		
Dimensions	0.2cmx50cmx300cm diameter	
Material	Graded Z Tungsten	
Pattern	15-43 element optimum coding	-Tradeoff
Angular-Resolution	24^{o}-8^{o} x18^{o}	
Detectors:		
Dimensions	50cmx20cm diameter	-3 detectors
Material	Xenon and/or Phoswich	
Energy range	5-10 KeV to 200 KeV.	
Solid angle	1x2.0 Steradians 2x1.5 Steradians	
Area to a point source	3x500cm^2	-Allows a factor 0.5 for the mask
Options:		
Non-rotating segmented detector	Allows detection of the whole diffuse BG and not just the fluctuations in it.	-Tradeoff Study.

ORIGINAL PAGE IS
OF POOR QUALITY

TABLE 2

Parameters for FOXI

ITEM	*VALUE*	*COMMENTS*
General System		
Spin period	20-30 seconds	
Image cycle time	[spin period]/8= 3-4 secs.	
Sky coverage	4% per rotation	-100% every 6 months
Data rate	≤30 Kbits/s	
Attitude Solutions	Sun pointed and X-ray sources.	-Sources ≥5 UFU seen in one spin.
Mask		
Dimensions	0.3cmx100cmx5000cm diameter	
Material	Graded Z Tungsten	
Pattern	8 times a 1023 element code	
Mask element dimensions	0.3cm x 2cm x100 cm	
Angular-Resolution	3' x 140'	
Detectors		
Dimensions	100cm x 100cm diameter	-3 cylindrical detector blocks.
Material	Xenon gas counter plus Phoswich	-Xenon on the outside Phoswich inside
Element size of a detector "strip"	1cm wide x 5 cm x 100cm	-Xenon and Phoswich systems are independent.
# of detector elements/block	≠300	-On the circumference of a cylinder.
Energy range	Xenon 3-20 KeV Phoswich 20-500 KeV	
Solid angle	3 x 0.25 steradians	
Area to a point source	3x3500cm^2	-Allows a factor 0.5 for the mask

ORIGINAL PAGE IS
OF POOR QUALITY

TABLE 3

FOXI MINIMUM DETECTABLE SOURCE FLUXES (5 SIGMA)

In units of photons.cm^{-2}sec^{-1}KeV^{-1}

	1 minute	1 hour	4 days
5 - 15 KeV	7×10^{-4} *(2 UFU)*	1.5×10^{-4} *(0.4 UFU)*	1.5×10^{-5} *(0.04 UFU)*
80 - 120 KeV	7×10^{-5}	1.5×10^{-5}	1.5×10^{-6}
200 - 300 KeV	4×10^{-5}	8×10^{-6}	8×10^{-7}

ORIGINAL PAGE IS
OF POOR QUALITY

REFERENCES

Boldt,E.,Comments on Astrophysics,1981,9,97.
Bracessi,A.,Zitelli,V.,Bonoli,F. and Formiggini,L.,1980,Astron Astroph.,89,80
Cheng,E.S.,Saulson,P.,Wilkinson,D.T. and Corey,B.,1979,Ap.J.,232,L139
Cheng,E.S.,Boughn,S. and Wilkinson,D.T.,1980,Bulletin AAs 12,Vol 2,489.
Compton,A.H. and Getting,I.A.,1935,Phys.Rev.47,817.
Conklin,E.A.,1969,Nature,222,971.
de Vaucouleurs,G.,Peters,W.L.,Bottinelli,L.,Gouguenheim,L and
Dicke,R.H.,1968,Ap.J.,153,L101.
Fabian,A.C. and Warwick,R.S.,1979,Nature,280,39
Felget,P.B.,1958,J.Phys.,Radium,19,187
Fenimore,E.E. and Cannon,T.M.,1978,Applied Optics,17,337.
Gunson,J. and Polychronopulos,B.,1976,Mon.Not.R.Astr.Soc.,177,485.
Harwit,M. and Sloane,N.J.A.,1979,"Hadamard Transform Optics',Acad Pr
Hudson,H.S. and Lin,R.P.,1978,Space Sci. Instr.,4,101.
Hudson,H.S.,Kohl,J.L.,Lin,R.P.,MacQueen,R.M.,Tandberg-Hanssen,E. and
Dabbs,J.R.,"The Pinhole/Occulter Facility",1981,NASA TM-82413.
Iwan,D.,Boldt,E.A.,Marshall,F.E.,Mushotzky,R.F.,Shafer,R.A.and
Stottlemyer,A.,1981,Ap.J.,in press
Kirshner,R.P.,Oemler,A.,Schechter,P.L. and Schectman,S.A.,1981,Ap.J.,
248,L57
Mertz,L.,1965,"Transformations in Optics",(New York-Wiley).
Oda,M.,1965,Appl.Opt.,4,143
Proctor,R.J.,Skinner,G.K. and Willmore,A.P.,1978,Mon.Not.R.Astr.Soc.,
185,745
Rees,M.J.,"X-ray Astronomy",1980,Giacconi,R and Setti,G.,(Eds),p377.
Rubin,V.C.,Thonnard,N.,Ford,W.K.,Jr and Roberts,M.S.,1976,Ap.J.,81,687
Schnopper,H.W.,Thompson,R.I and Watt S.,1968,Space Sci.Rev.,8,534
Skinner,G.K.,1980,Journal of the British Interplanetary Society 33,3??
Paturel,G.,1981,Ap.J.,248,408.
Smoot,G.F.,Gorenstein,M.V. and Muller,R.A.,1977,Phys.Rev.Letters,39,898
Tennant,A.F.,Mushotzky,R.F.,Boldt,E.A. and Swank,J.H.,1981,NASA TM-82143.
Warwick,R.S.,Pye,J.P. and Fabian,A.C.,1980,Mon.Not.R.Astr.Soc,190,243
Wolfe,A.M.,1970,Ap.J.,159,L61
Zamorani,G.,Henry,J.P.,Maccacaro,T.,Tananbaum,H.,Soltan,A.,Avni,Y.,
Liebert,J.,Stocke,J.,Strittmatter,P.A.,Weymann,R.J.,Smith,M.G. and
Condon,J.J.,1981,Submitted to Ap.J.

FIGURE CAPTIONS

FIGURE 1

The basic principles of the two methods are shown. The spatial aperture modulator casts an X-ray shadowgram onto the position sensitive detector and hence requires N detector elements to detect N mask elements whilst each element of the temporal aperture modulator detects the full N elements of the modulator. Both methods provide an N element image of the sky.

FIGURE 2

The layout of a "Pinhole/Occulter Facility" to be deployed from the Space Shuttle. The 50 meter boom supports a spatially encoded aperture mask to give ≤ 1 arc second spatial resolution for hard X-rays. For solar observations an occulter will also be used to provide a shadow for coronagraphic observations.

FIGURE 3

A conceptual Diffuse Anisotropy X-ray Background Experiment (DAXBE) is shown. The concept is for a free-flying internally powered experiment The spinning sub-satellite causes the individual detectors to see an optimum modulated count rate from separate strips of sky. The total active field of view is $\approx$40% of the sky per rotation. With precession a 100 % coverage can be obtained in a short time. The energy range is detector dependent but 5-200 KeV seems easily achievable.

FIGURE 4

The one sigma statistical sensitivity *per sky bin* of DAXBE in one month (2×10^6 seconds) is shown. It is thought that the effect of source fluctuations and the galactic diffuse component will not significantly degrade the sensitivity (see Text).

FIGURE 5

A conceptual Ferris-wheel Orbiting X-ray Imager (FOXI) is shown. The concept is of a free-flying satellite which unfurls in orbit after a Shuttle launch. It is envisaged that the mask would rotate every 20-30 seconds whilst the detector remained fixed relative to the stars The mask would consist of a basic 1023 element optimum code repeated 8 times to give an image cycle time of one eighth of the spin period. The detector consists of 3 units of 1 meter diameter made up of 1 cm wide gas counter and scintillator strip elements FOXI will image 4% of the sky every 3-4 seconds with a resolution of 3' x 140' over the photon energy range 3-500 KeV 100% sky coverage is obtained every 6 months. Over 2000 Active Galactic nuclei should be detected (see Text).

ONE DIMENSIONAL REPRESENTATION OF APERTURE MODULATION

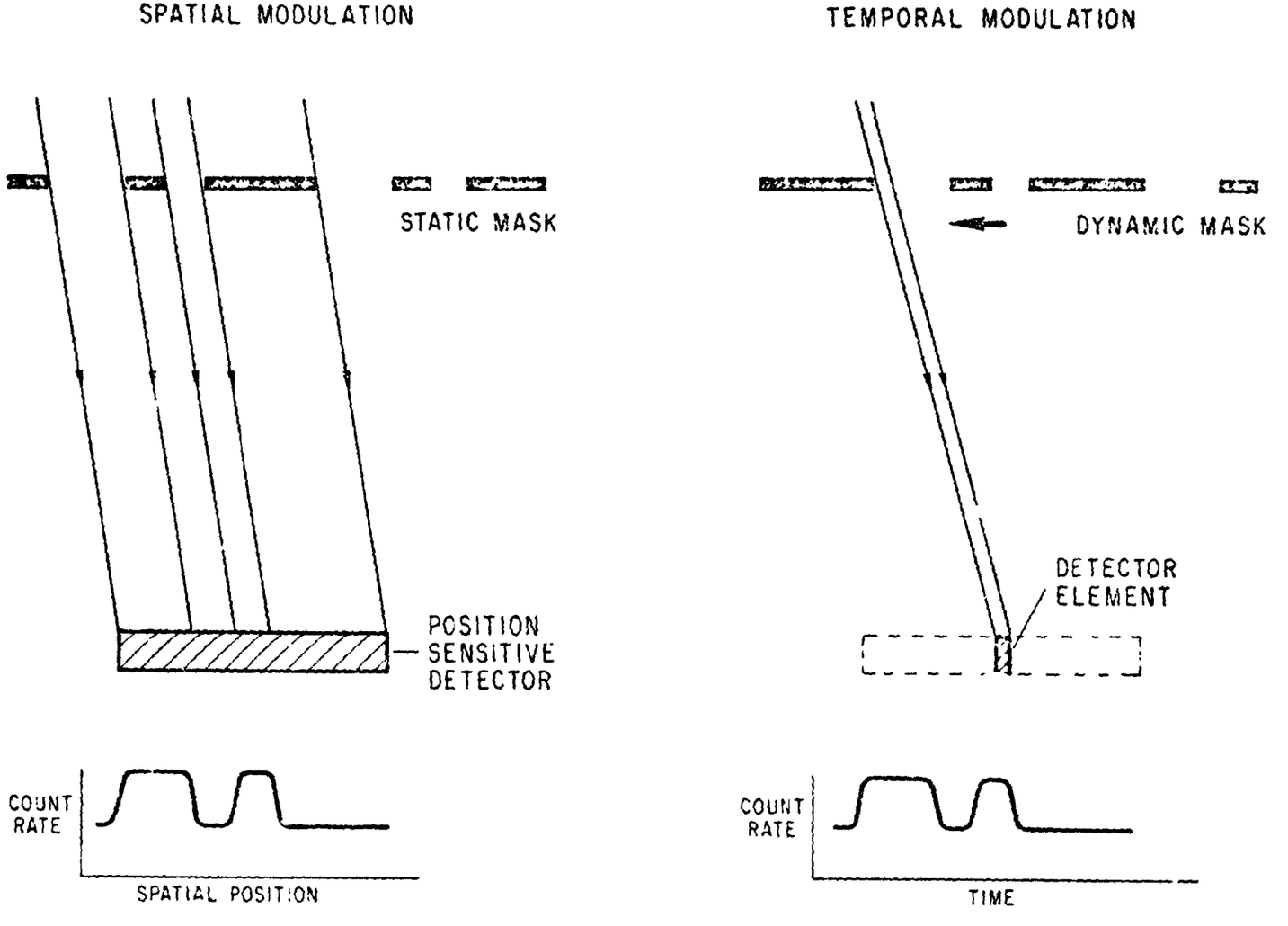

ORIGINAL PAGE IS
OF POOR QUALITY

ORIGINAL PAGE IS
OF POOR QUALITY

SPACELAB
PINHOLE / OCCULTER
FACILITY

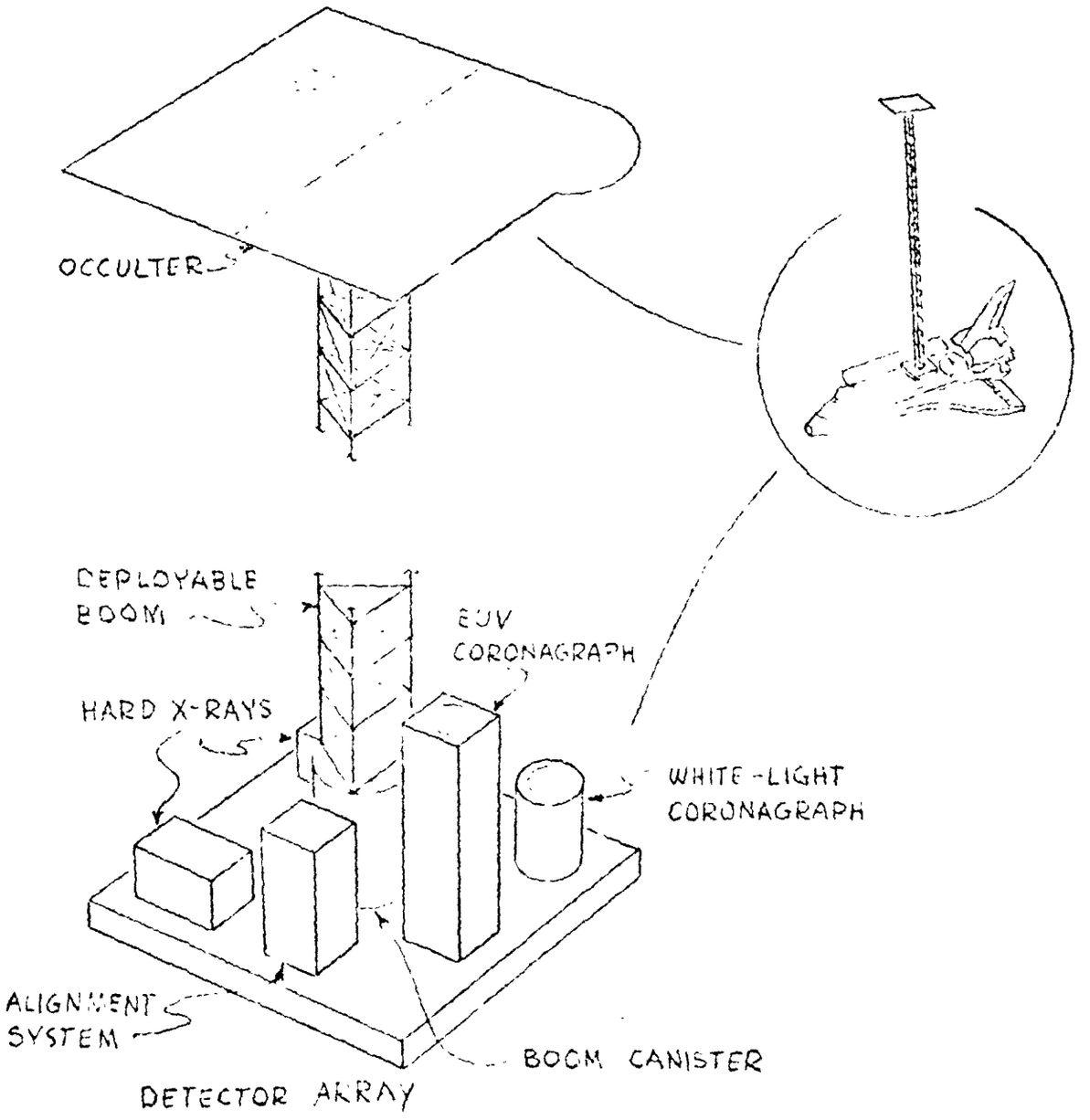

ORIGINAL PAGE IS
OF POOR QUALITY

DIFFUSE ANISOTROPIC X-RAY BACKGROUND EXPERIMENT

ORIGINAL PAGE IS
OF POOR QUALITY

SENSITIVITY OF DAXBE FOR A ONE MONTH MISSION

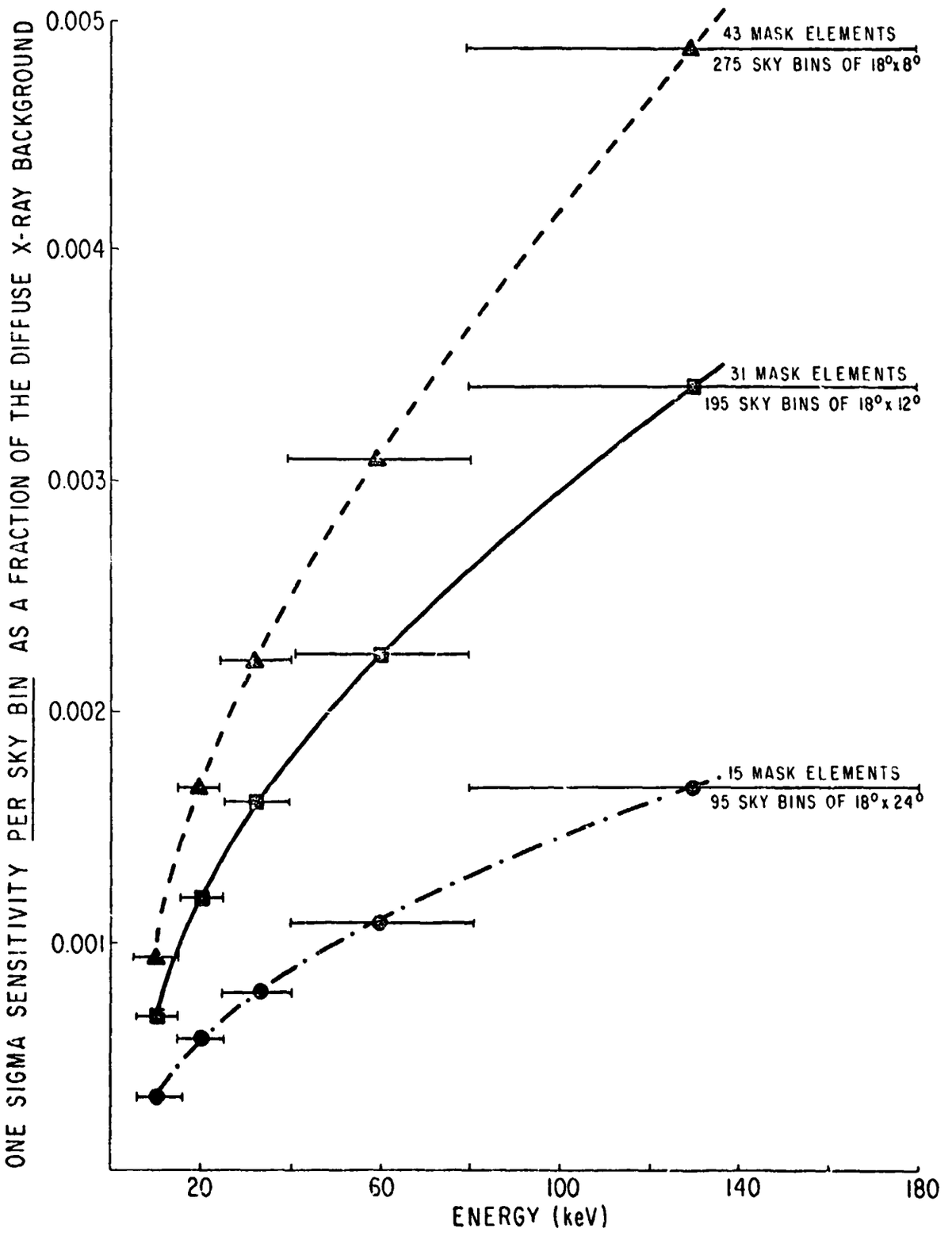

FERRIS-WHEEL ORBITING X-RAY IMAGER

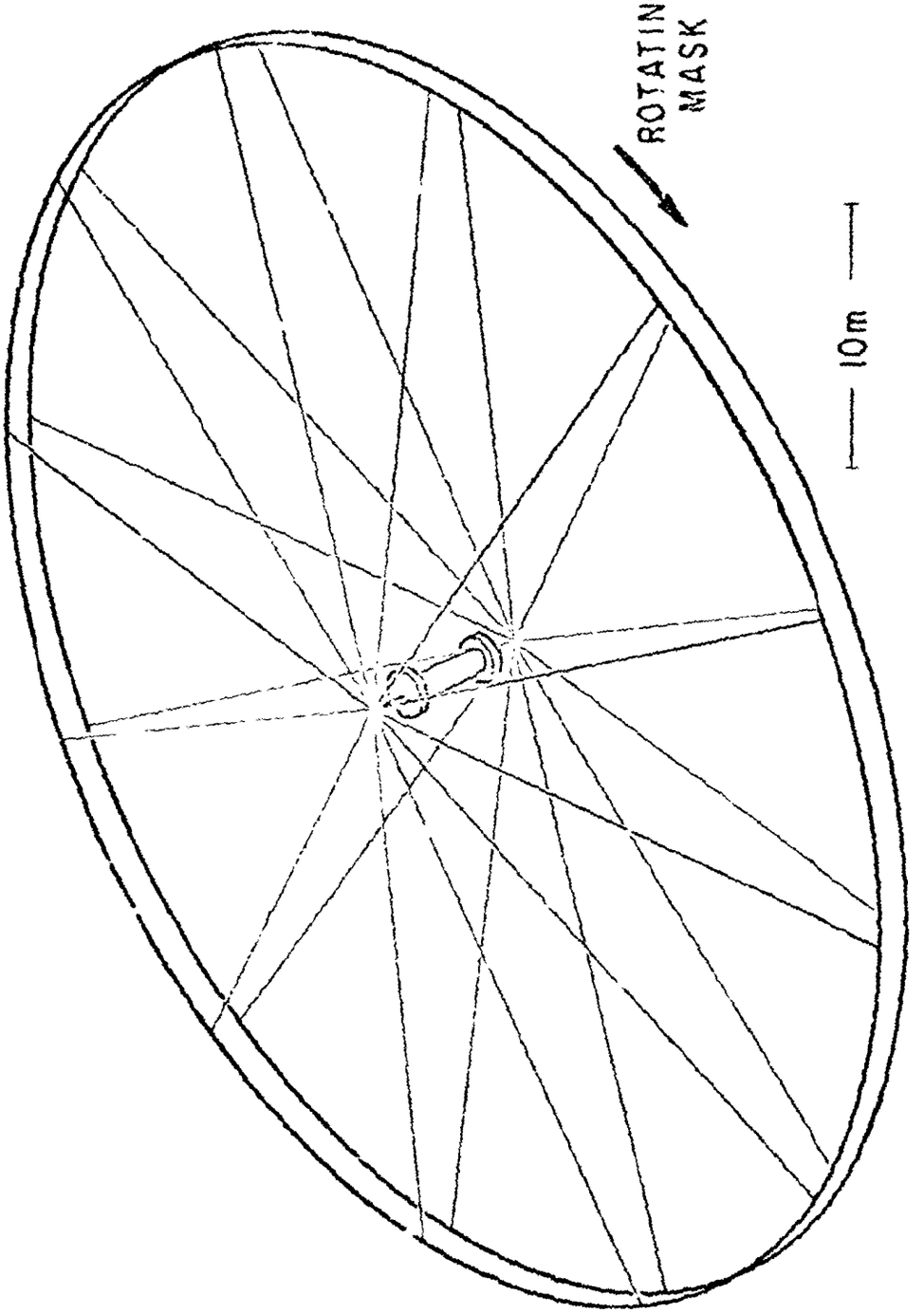

N82 26072

HARD X-RAY IMAGING FROM EXPLORER

J. E. Grindlay and S. S. Murray
Harvard-Smithsonian Center for Astrophysics

ABSTRACT

Hard X-ray Astronomy (at energies $\gtrsim$10 keV) has not yet enjoyed the high sensitivity and high resolution that imaging techniques and the Einstein Observatory have allowed for the soft X-ray band. Many fundamental problems in high energy astrophysics require greatly increased sensitivity and observing time at hard X-ray energies. It is possible to obtain such large increases in sensitivity as well as angular resolution with coded aperture imaging X-ray detectors. A new hard X-ray coded aperture detector concept is described which would enable very high sensitivity studies of persistent hard X-ray (~15-300 KeV) sources and gamma ray bursts (~50-550 KeV). Coded aperture imaging is employed so that ~2′ source locations can be derived within a 3° field of view. Gamma bursts could be located initially to within ~2° and X-ray/hard X-ray spectra and timing, as well as precise locations (~2′), derived for possible burst afterglow emission. Hard X-ray imaging should be conducted from an Explorer mission where long exposure times are possible.

1. INTRODUCTION

With the Einstein Observatory, soft X-ray astronomy has become fully competitive with optical and radio astronomy in that virtually all major classes of astronomical object have proven to be detectable in this energy band. Such spectacular growth has not yet occurred in hard X-ray astronomy. However, the results which are available suggest a rich variety of astrophysical problems. For example, although Einstein observations have revealed that quasars and active galactic nuclei (AGN) are almost always detectable in (soft) X-rays, their spectra and hence source radiation mechanisms are still largely unknown. In the few brightest quasars, and in a somewhat larger number of still brighter Seyfert galaxies, hard X-ray emission extending out to at least several hundred keV is detected. Most of the radiation and luminosity from quasars and AGNs may be in the hard X-ray band, and thus realistic models will not be possible until many high quality X-ray observations at energies up through the probable high energy spectral break (at ~200-300 keV) are available.

In addition to the quasars, a number of other fundamental problems in high energy astrophysics may also be studied, and in some cases understood, best in the hard X-ray band. The scientific need for high sensitivity and high angular resolution at hard X-ray energies (~10-500 keV), as discussed in the next section, could be met with a coded-aperture imaging detector. An Explorer-class hard X-ray imaging experiment would be the ideal compliment to future direct imaging X-ray telescopes (e.g., EXOSAT, ROSAT, AXAF, and eventually, LAMAR) which will, of course, be sensitive only below ~5-8 keV.

2. SCIENTIFIC NEED FOR HARD X-RAY OBSERVATIONS

A wide range of fundamental problems in astrophysics can best be attacked with sensitive new observations at hard X-ray energies. It is possible to summarize these in the form of a table of particular problems and the approximate ranges of photon energies required for their solution. Table 1 contains such a summary, in which each entry is an area of study which requires observations in the photon energy range shown. Arrow tips mean that the energy limit (high or low) is not well determined, whereas vertical ticks at the energy range ends mean that the range is more or less fixed.

In the general study of compact objects hard X-ray spectra can provide a key test for the nature of the object. White dwarfs would not be expected to have thermal spectra with temperatures above the free full temperatures of ~200 keV whereas neutron stars could have thermal components extending to MeV energies. X-ray bursts have shown that neutron star radii can be measured from the blackbody spectra at low energies whereas recent gamma ray burst studies by the Soviets at ~30-500 keV suggest that the 511 keV annihilation line has been detected at a gravitational redshift of ~0.2-0.3, or approximately that expected for a neutron star. Cyclotron lines have been detected at hard X-ray energies (~60 keV) and neutron star magnetospheres might be studied at either hard (~100-200 ') energies corresponding to local free full temperatures at the Alfven radius or soft (~0.3 keV) energies if there is optically thick re-emission.

Accretion flows and the distribution of cool gas and hot electrons in accreting systems require hard X-ray observations. In particular, the study of Comptonization of a soft spectral component by energetic electrons can lead to hard Compton-tails out to several hundred keV. The resulting power law - type spectra and thermal cutoffs might be expected in many more objects than just Cyg X-1 where they have been observed. Studies of the simultaneous variations in the soft vs. hard X-ray spectra as a function of binary phase might allow the spatial temperature and density structure of the accretion flow to be studied.

Determination of the radiation mechanisms involved in given X-ray sources obviously requires broad band spectra extending to hard energies. Thermal cutoffs at high energies can distinguish Comptonization of thermal spectra from non-thermal processes. Sources with predominantly ~10 keV thermal bremsstrahlung spectra (e.g., most galactic bulge sources) may be expected to have underlying hard components from thermal processes (free fall, Comptonization, etc.) or non-thermal particle acceleration as in SS433.

Finally, and perhaps most important, the basic understanding of any object requires knowing its luminosity and overall energetics. For quasars and active galactic nuclei (AGN) in general, this requires hard X-ray observations since the spectra already observed from the few brightest sources indicate that the hard band (>100 keV) contains a large fraction of the total energy radiated. It is not possible to

Table 1

QUESTIONS IN X-RAY ASTRONOMY vs. ENERGY

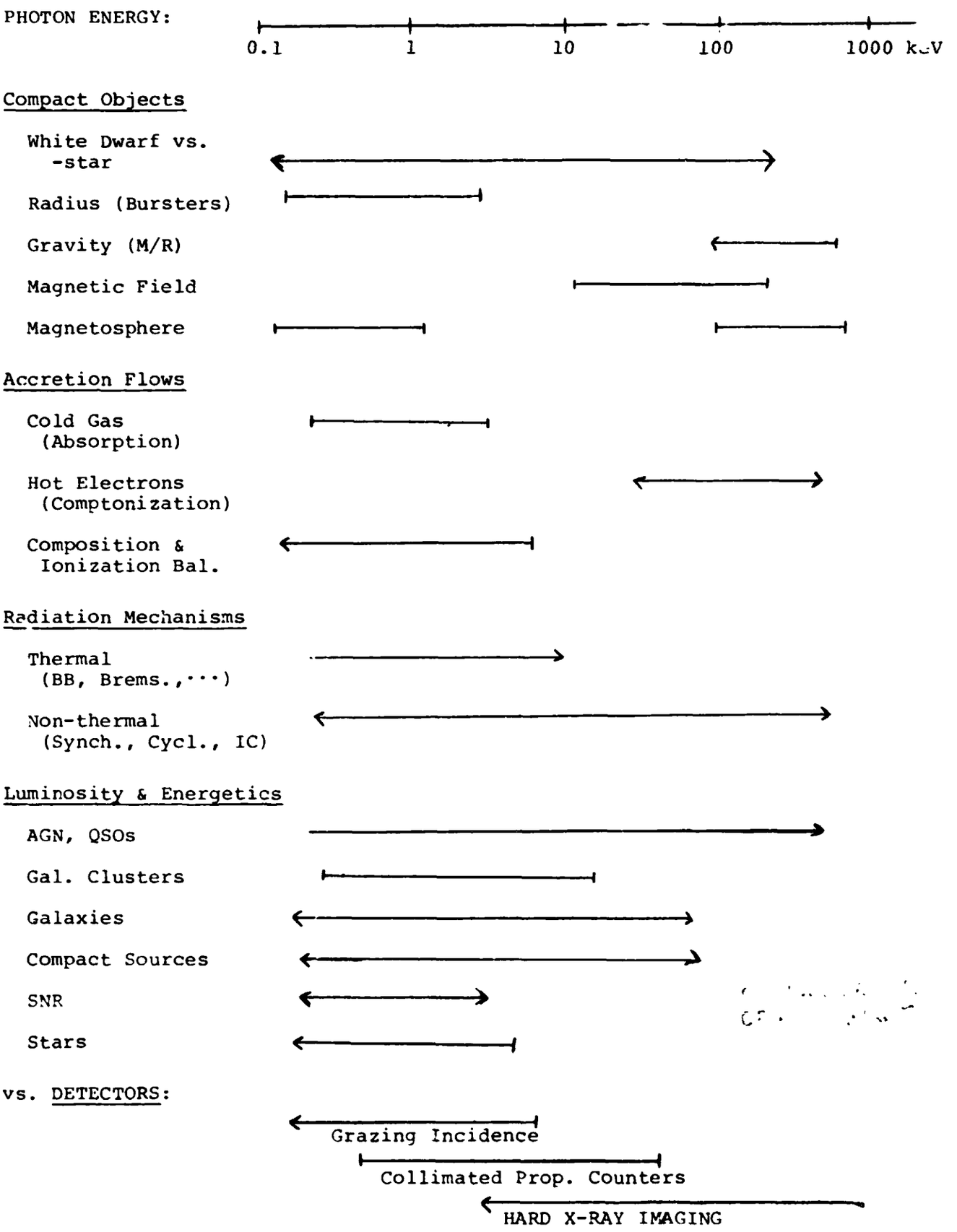

construct meaningful models for quasars without knowing where (and why) their spectra finally cutoff at high energies. Galaxy clusters must emit some level of inverse Compton radiation from synchrotron radio electrons scattering on the microwave background. This should extend to hard energies and its detection would constrain the energetics of relativistic gas in galaxy clusters. At somewhat lower luminosities, emission from normal galaxies and compact objects have hard X-ray components which are almost certainly significant whereas SNR and stars probably have negligible luminosity at hard X-ray energies.

At the bottom of Table 1, we give the approximate energy ranges of the principal detector systems used to attack the problems discussed above. It is clear that grazing incidence imaging, as used on Einstein, cannot deal with a significant number of these major problem areas, nor can collimated proportional counters of the sort employed in all X-ray astronomy missions thus far. Hard X-ray imaging, however, could attack all of the major problems.

3. CODED APERTURE SYSTEMS FOR HARD X-RAY IMAGING

At energies above the grazing incidence limit of ~10 keV, X-ray imaging can be accomplished by at least two techniques. Bragg diffraction flux concentrators can be employed to achieve large effective detector areas with small detecting elements (and thus detector backgrounds). Such a system is described by Ricker (1981) but it is limited to energies $\lesssim$100 keV. For the broad-band studies described above, where good sensitivity and angular resolution up to ~500 keV is desired, it appears that coded aperture imaging is the optimum technique. This scheme employs an aperture, with an array of transmitting holes, followed by a position-sensitive detector. It is thus just the multiple pinhole camera proposed by Dicke (1968). Images are reconstructed (uniquely) by, essentially, re-projecting each detected photon back through each open mask hole. All counts from a given source are detected in the true image pixel although (in contrast to true imaging) the total background (including sources) is also necessarily re-projected into each image pixel. For imaging hard X-rays, the requirement that the detector and mask planes be parallel and the detector be thin (for minimum detected position ambiguity and thus image smearing) means that crystal scintillators are preferred for the detector. Position-sensitive detection of the optical light produced by a hard x-ray in a crystal scintillator is then the technical requirement for a coded aperture hard X-ray imaging detector. We shall describe in the next sections a proposed detector in some detail.

First, we summarize the main advantages of a coded aperture system for hard X-rays. The angular resolution can be high, and is just the angular spacing of mask holes (which become image elements) as seen from the detector. Thus source confusion in crowded fields (e.g., the galactic center region) can be eliminated. The field of view can be large although the diffuse background is then also large,

ORIGINAL PAGE IS
OF POOR QUALITY

but must be commensurate with the number of image elements and their angular size as governed by the mask. Finally, and most important, the detected background can be measured simultaneously with a source by simply comparing the rates in the reconstructed image in and out of the pixel(s) of interest containing the source(s). This means, of course, that continuous pointings of long exposure can be carried out for very large increases in sensitivity over previous scanning detectors such as HEAO-A4. This is also an improvement over detectors which chop on and off source (e.g., the NRL experiment on GRO) since chop times must always be shorter than the (uncertain) timescales for background variations if these are to be removed.

In Figure 1 we compare the approximate sensitivity that a plausible coded aperture hard X-ray imaging detector system might give relative to the sensitivities achieved with HEAO-1 and HEAO-2. The hard X-ray imaging experiments will, in general, not be designed to operate below ~10 keV (the domain of normal imaging X-ray telescopes) and will not perform as well above ~500 keV-1 MeV, where Compton scattering and pair production in the mask become significant. Sensitivities could be achieved (from an Explorer mission) in the ~10-500 keV range which are at least a factor of 10-30 greater than available previously above 10 keV even for the modest-sized hard X-ray imaging experiment described next.

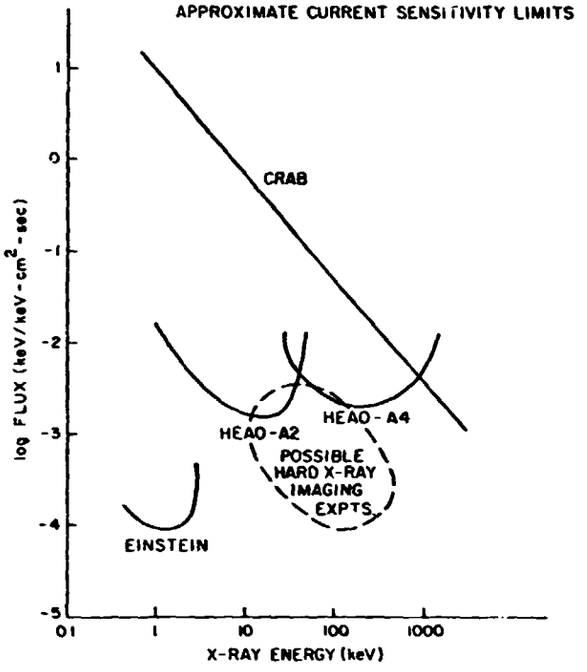

Figure 1: Approximate relative sensitivity of X-ray experiments and the Crab spectrum for comparison.

4. PROPOSED HARD X-RAY IMAGING EXPERIMENT

We now describe a particular experiment configuration for hard X-ray imaging from an Explorer. This is the Energetic X-ray Imaging and Timing Experiment (EXITE) which was proposed as a second experiment to XTE. Either this experiment as proposed, or an enlarged version (EXITE is modular) for an entire Explorer mission, would enable the major astrophysical problems discussed above (cf. Table 1) to be studied in detail.

The scientific objectives (in abbreviated form) of EXITE are: (1) to measure Comptonization tails and cyclotron features in source

ORIGINAL PAGE IS
OF POOR QUALITY

spectra to determine physical conditions at the source; (2) to measure spectral-temporal variability at high energies and study accretion flows; (3) to locate and identify hard X-ray sources in complex fields; (4) to measure high energy spectra of quasars and locate serendipitous sources; and (5) to measure the size spectrum (log N - log S), broad energy spectrum (including line emission) and source locations for gamma ray bursts.

General Description of EXITE

EXITE represents a fundamentally new concept in hard X-ray astronomy. It applies coded aperture imaging to the hard X-ray band (~15-300 KeV) and at once realizes several key advantages mentioned above which were previously only possible at low X-ray energies: (1) background is measured simultaneously with the object flux; there is no need to scan or off-set point; (2) a source can be resolved in complex fields; and (3) precise (~2-5 arcmin) positions can be derived for the first time at hard X-ray energies (~100 KeV) by centroiding between resolution elements of the reconstructed image.

Coded aperture imaging systems are based on the multiple pinhole camera (Dicke 1968) where N overlapping images of a source distribution are formed on a detector viewing the source through N pinholes in an aperture mask. Although Dicke suggested using a random hole pattern, images reconstructed using a "random" pattern (never truly random) contain an additional source of systematic noise. To overcome this we suggested (in a 1976 Spacelab 2 proposal) using a "pseudo-noise" (PN) array since these have the optimum property (Calabro and Wolf 1968) that their autocorrelation function (ACF) is identically constant off axis and a δ-function on axis. PN arrays were independently pointed out by Gunsen and Polychronopulos (1976) and have been discussed extensively by Fenimore (1980, and references therein) who call them uniformly redundant arrays (URA). The (systematic) noise-free imaging possible with a URA mask is not compromised by a physical realization of such a pattern where the hole size is smaller than the hole spacing. Furthermore, the URA is cyclic and has the very desirable "window property" that a complete pattern is available to surround every element of an extended mask.

The EXITE detector makes optimum use of these desirable properties of the URA in that each single detector (a 15 cm diameter CsI scintillator crystal) views the sky through a URA mask composed of a number (~50) of contiguous cycles of a basic URA pattern (each of dimension 13 x 11; see Figure 2). A single detector, which is read out as one device, then effectively (in the analysis) produces ~50 independent and parallel 13 x 11 pixel images which are then co-added. This allows a very much

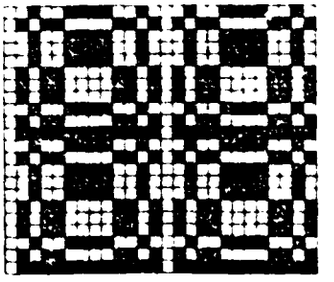

Figure 2: A 2 x 2 Cycle Portion of the Extended URA Coded Aperture Collimator.

ORIGINAL PAGE IS
OF POOR QUALITY

faster analysis (by a factor of 50) of the total image than if the entire detector area viewed the entire URA mask as in a "conventional" coded aperture camera. The mosaicing of the detector and mask also allows the optimum packing of the rectangular URA pattern into the round detector elements required (because of the need for a diode image intensifier tube to amplify the scintillator optical output). Finally, the URA mask is made self-supporting by placing the (1.5 mm square) holes on a 1.7 mm grid. This is turned to additional advantage by using the 1.5 mm holes as the detector collimator. Collimation (2.9° FWHM) is achieved by making the mask effectively very thick (3 cm) using spaced tungsten laminates (see Figure 3).

Design Principles and Operation of EXITE

The principles of operation of the EXITE detector are illustrated in Figure 4. The URA mask projects a collimated image of the sky onto a CsI scintillator. The light produced in the CsI scintillator by an incident X-ray is amplified by the intensifier while preserving the spatial distribution of brightness. The intensified image is decreased in scale to match the input of the MAMA detector through a reducing fiber-optic (12:1). The light losses in this reduction are compensated by the gain of the intensifier so that the total number of photons incident on the photon-counting imaging detector is the same as initially collected from the scintillator. This preserves the energy resolution capability of the system which is basically limited by the counting statistics of the light from the CsI. The imaging optical detector required could be a resistive anode (Martin et al. 1981) crossed grid (Kellogg, Murray, and Bardas 1979) or multi-anode (Timothy, Mount, and Bybee 1979) type system. The Multi-Anode-Microchannel-Array (MAMA) detector (Timothy, Mount, and Bybee 1979) is especially well suited for EXITE and, therefore, included in the design here.

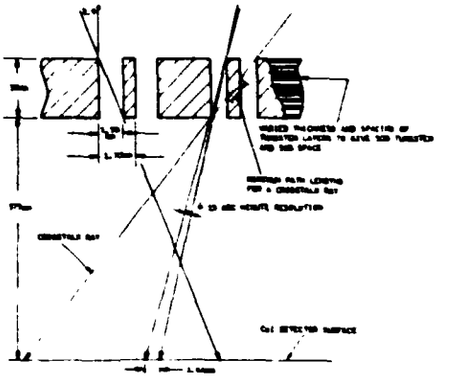

Figure 3: Laminated Tungsten Coded Aperture Collimator.

The anodes of the MAMA detector are 140 μm x 140 μm which corresponds to the hole spacing in the URA mask (1.7 mm) when the reduction factor of 12:1 is considered. Light reaching the MAMA from a single X-ray results in the production of a few tens to several hundreds of photoelectrons depending on incident energy. These will be spread out over several of the 140 μm pixels due to the thickness of the CsI crystal and the front window of the image intensifier. Thus, several of the anode lines along each axis will detect the event. A centroid estimate of the event position is then determined for each axis by the processing electronics. Since the photoelectrons are spread out on a large scale relative to the MCP channel size

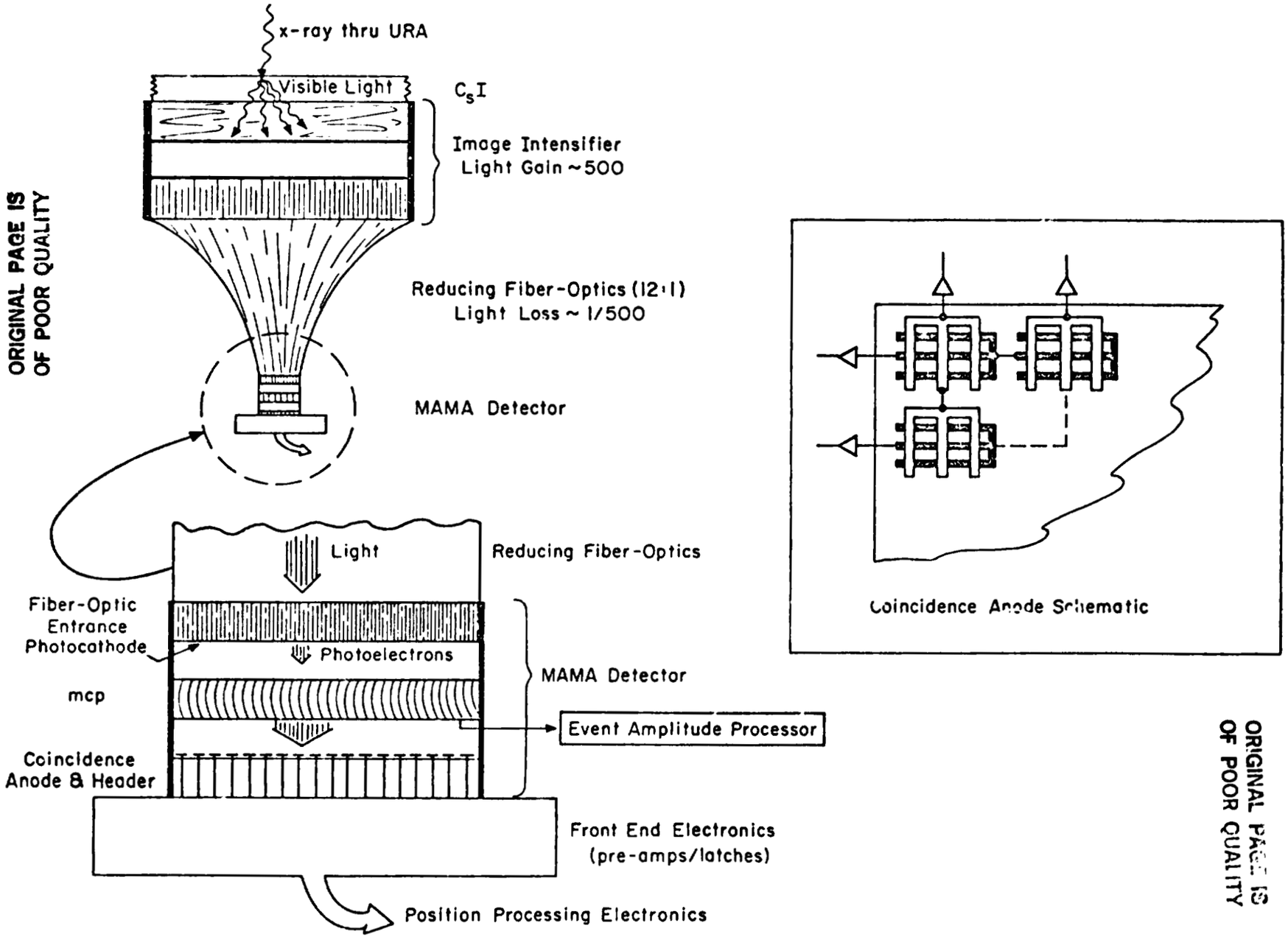

Figure 4: Schematic of Position-Sensitive Scintillation Detection with Optical Imaging Readout.

ORIGINAL PAGE IS
OF POOR QUALITY

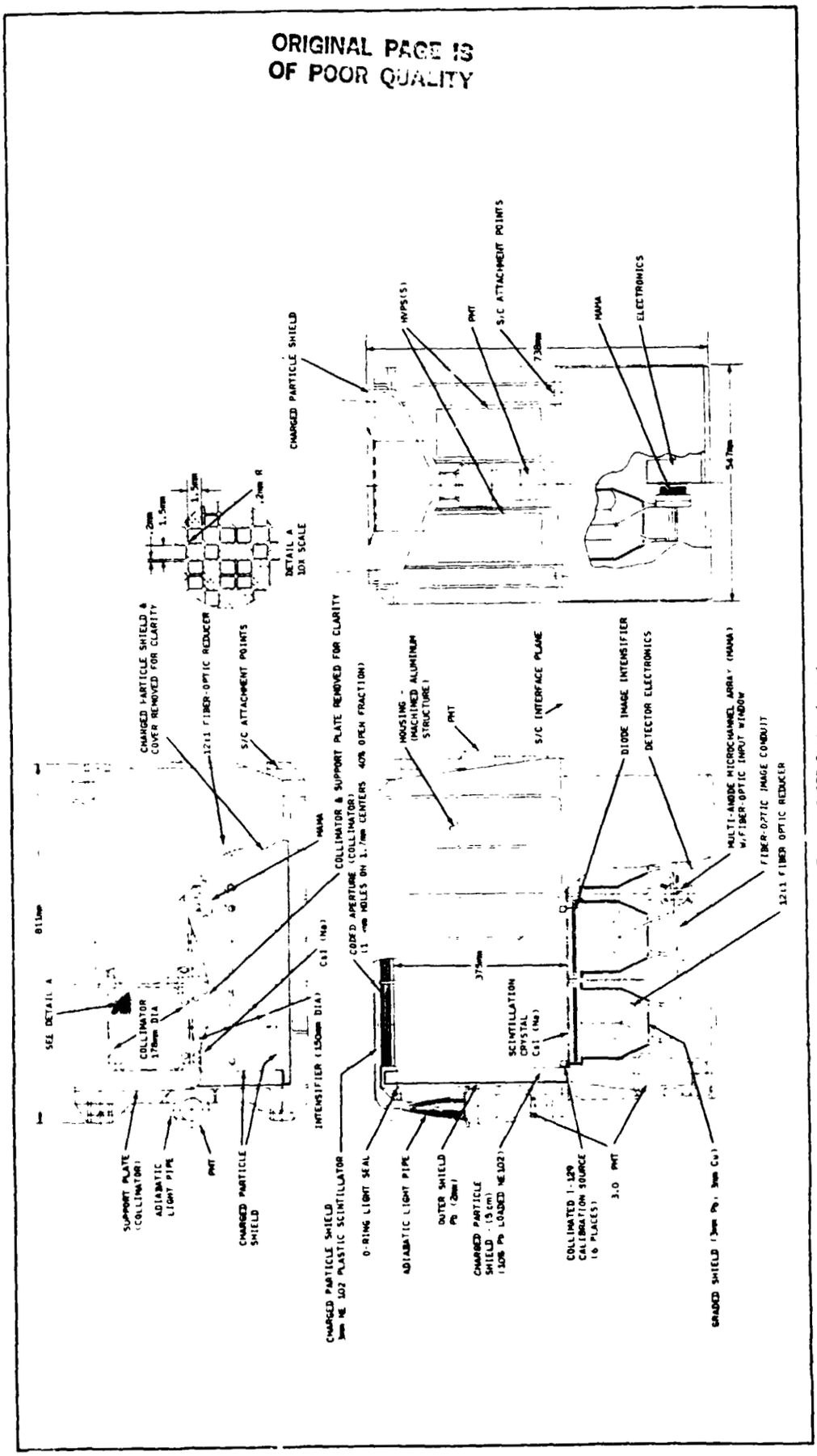

Figure 5: EXITE System Layout

(~15 μm), each electron will be independently amplified in the microchannel plate (MCP) array (with gain ~10^7) and the total charge coming out of the plate will be proportional to the incident number of photoelectrons and thus the primary X-ray energy. This will be measured using a separate amplifier at the output of the MCP to provide energy information (64 channel PHA). Single electron events due to thermal generation either in the MAMA or the image intensifier can easily be discriminated against using the total charge output from the MCP since a 20 KeV X-ray is expected to produce at least 20 photoelectrons.

EXITE is a modular detector concept. As proposed for XTE, two independent MAMA detectors (each viewing three 15 cm diameter scintillator X-ray detectors) are included for maximum area and the desired redundancy against single point failures. Each detector, however, is actually composed of three independent and parallel scintillators (for maximum usage of the 25 mm circular photocathode area of the MAMAs), and each single 15 cm diameter scintillator operates (in the coded aperture imaging) as a mosaic of adjacent but independent image-forming subdetector elements. All detector subelements (each is 2.2 cm x 1.9 cm) view the same 2.9° (FWHM) field of view on the sky. Thus, each of the two MAMA detector systems is itself actually multiredundant while at the same time easy to test, calibrate, and read out as a single device.

The EXITE design for XTE has a total active detection area of A_{eff} = 438 cm^2 (= geometric area times 0.4 transmission of the collimating coded aperture mask). The detector employs both active and passive shielding to reject and reduce background. The system is shown in Figure 5 above and occupies an area of 81 cm x 54 cm and height (above the spacecraft interface) of 40 cm. It weighs 237.9 kg and requires 3.3 Kbps (max.) of telemetry and 39 watts of power.

Anticipated EXITE Performance

A full simulation of the EXITE detector and optical imaging characteristics has been carried out. Comparison of the EXITE detector system with that (Matteson 1978) flown on HEAO-A4 indicates the total background count rate in the ~15-300 KeV band should be ~35 counts sec^{-1} outside the SAA. Model source spectra were allowed to be incident (on axis) on the full system for a given integration time and were "detected" with the complete system efficiencies and a gaussian blurring (σ = 0.5 pixel) in the centroid determination.

Images of Cyg X-1 for a short (10 sec) and long (500 sec) exposure and of 3C273 for a long (5 x 10^4 sec) exposure are shown in Figure 6 as they should appear from EXITE. These images contain the full 15-300 KeV bandwith of the instrument; similar images could be shown for any band. The full 13 x 11 pixel (2.9°) image is shown; each pixel is 15 arcmin. The sources are detectable in a ~1 pixel radius about the center due to blurring in the MAMA detector readout;

ORIGINAL PAGE IS
OF POOR QUALITY

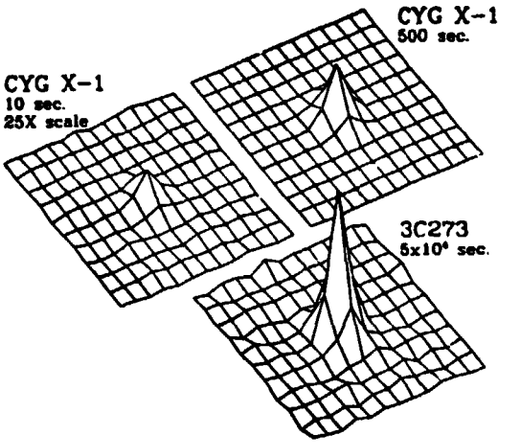

Figure 6: Images (15-300 keV) from Simulated EXITE Data

centroiding is then possible and (for the long exposures) would yield positions with 2 arcmin accuracy. Additional sources in the field which were up to 86 times fainter than Cyg X-1 and ~42 times fainter than 3C273 would be detectable (and located to ~5 arcmin) in the two "long" exposure images, respectively. The total detected count rate of Cyg X-1 by EXITE is 110 counts sec^{-1} while 3C273 is 2.8 counts sec^{-1}. Since Cyg X-1 is the brightest known (steady) source in the ~20-300 KeV energy band, the 100 counts sec^{-1} allowed for in the telemetry has been selected.

The spectra of counts detected in both long exposures are shown in Figure 7 as the plotted points (with actually "observed" 1σ error bars). Also plotted as lines are the assumed input (power law) spectra for both sources. The spectral indices could be derived from the data for either source with uncertainties $\Delta\alpha/\alpha$ of only a few percent.

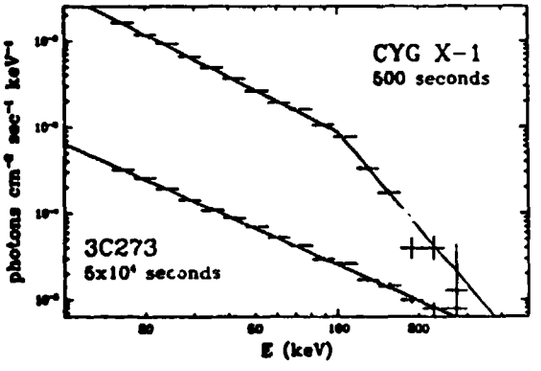

Figure 7: Spectra Derived from Simulated Images.

ORIGINAL PAGE IS
OF POOR QUALITY

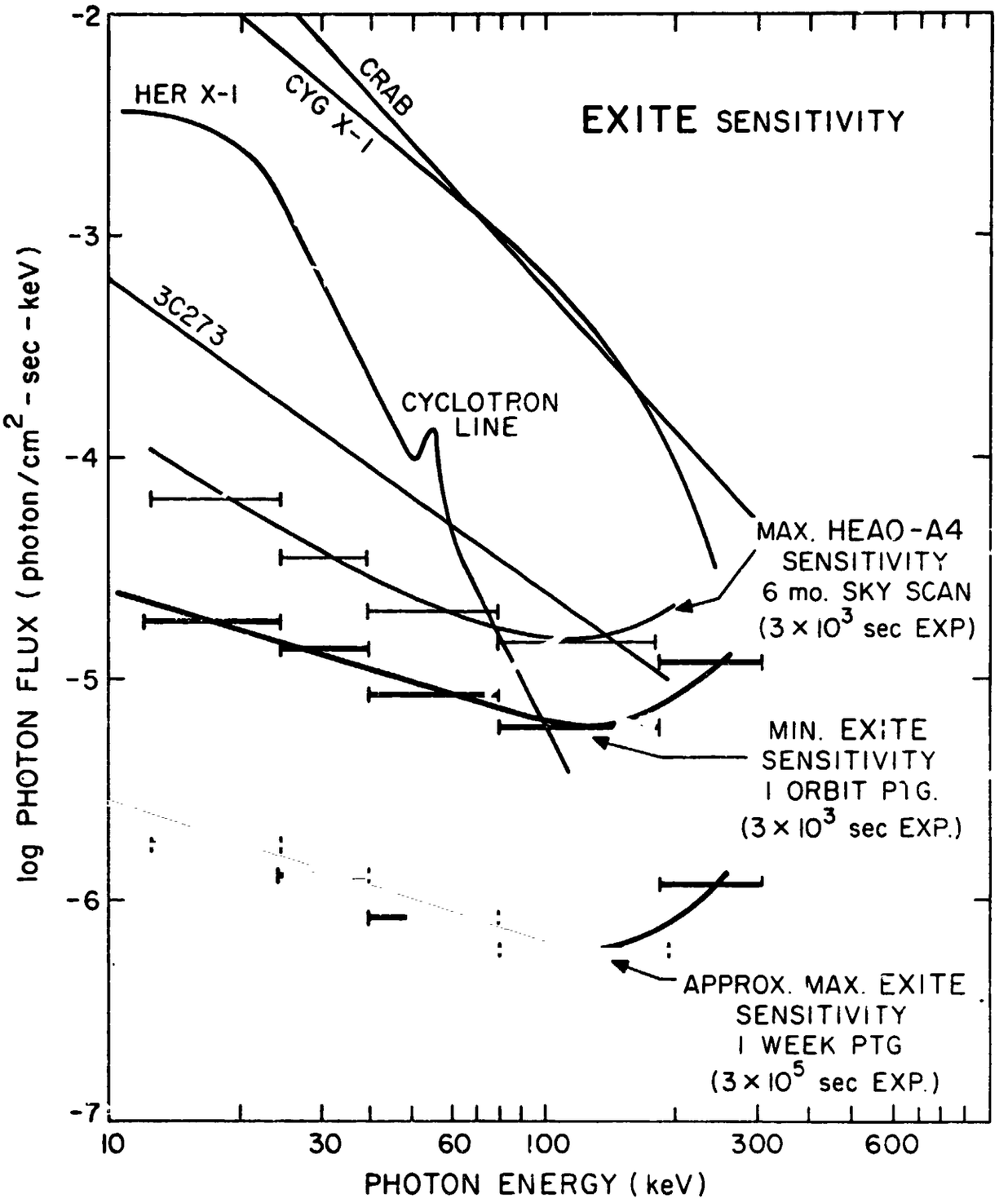

Figure 8: EXITE Sensitivities for 5σ Detection.

The overall sensitivity which EXITE should achieve is shown in Figure 8 for both single orbit (~3000 sec) and ~ 1 week (~3 x 10^5 sec) exposure times. The sensitivity is about a factor of 3-30 times greater than HEAO-A4, also plotted, and is sufficient to meet the science objectives. Approximately 50 new quasars could be detected as serendipitous sources in XTE pointings and located to $\lesssim$5 arcmin. Spectra could thus be measured on a large number of AGNs.

5. GAMMA RAY BURST STUDIES WITH EXITE ON XTE

The proposed EXITE detector on XTE would also enable detailed studies of gamma ray bursts to be made. For the first time, both high sensitivity X-ray (~1-30 KeV) as well as hard X-ray (~15-500 KeV) spectra and timing of gamma bursts could be obtained by the large area proportional counter (LAPC) assumed present on XTE and EXITE instruments, respectively. Since recent (Soviet) experimental evidence (Mazets et al. 1979) for cyclotron and positron annihilation lines from bursts as well as the ~8 sec pulsations from the spectacular March 5, 1979, burst (Cline et al. 1980) point toward a neutron star origin, gamma bursts are more than ever appropriate for study from XTE. Nuclear flash models for gamma bursts can account for many of the essential features (Woosley et al. 1981) of bursts and- because of the requirement for strong magnetic fields--would predict an X-ray (~20 KeV) afterglow for perhaps ~10^3 sec. This afterglow emission may have already been detected by the Vela satellite X-ray detectors (Terrell 1980) but more sensitive X-ray and hard X-ray observations are very much needed. This could be conducted on XTE with the EXITE detector, which would both initially detect gamma bursts and measure their spectrum (~50-500 KeV) and approximate source location (~2°) as well as precisely locate (~2′) and study the afterglow emission. No other gamma burst detector systems now being considered could accomplish such broad band (X-ray through gamma ray) studies (spectra and single-station burst location capability) of gamma bursts.

Burst Detector System

The burst system consists of six identical CsI(Na) scintillation detectors (see Figure 9) mounted externally to the EXITE instrument (or even elsewhere on the spacecraft) in such a way as to provide a constant complete sky survey of X-ray/gamma-ray radiation in the ~50-550 KeV energy range. Each detector assembly is composed of a 15.2 cm square by 0.64 cm thick CsI(Na) scintillator, an adiabatic twisted light pipe, a short 38 mm diameter photomultiplier tube (PMT), and associated electronics. Approximately half of the sky is visible to groups of three adjacent detectors. Burst arrival direction cosines may be computed from the relative rates in these various groups of three detectors. Moderately intense bursts ($\gtrsim 1 \times 10^{-5}$ erg cm^{-2}) can thus be located to within ~2° and a real-time spacecraft slew performed (for events sufficiently close to the XTE pointing direction) to obtain a precise (~2 arcmin) location

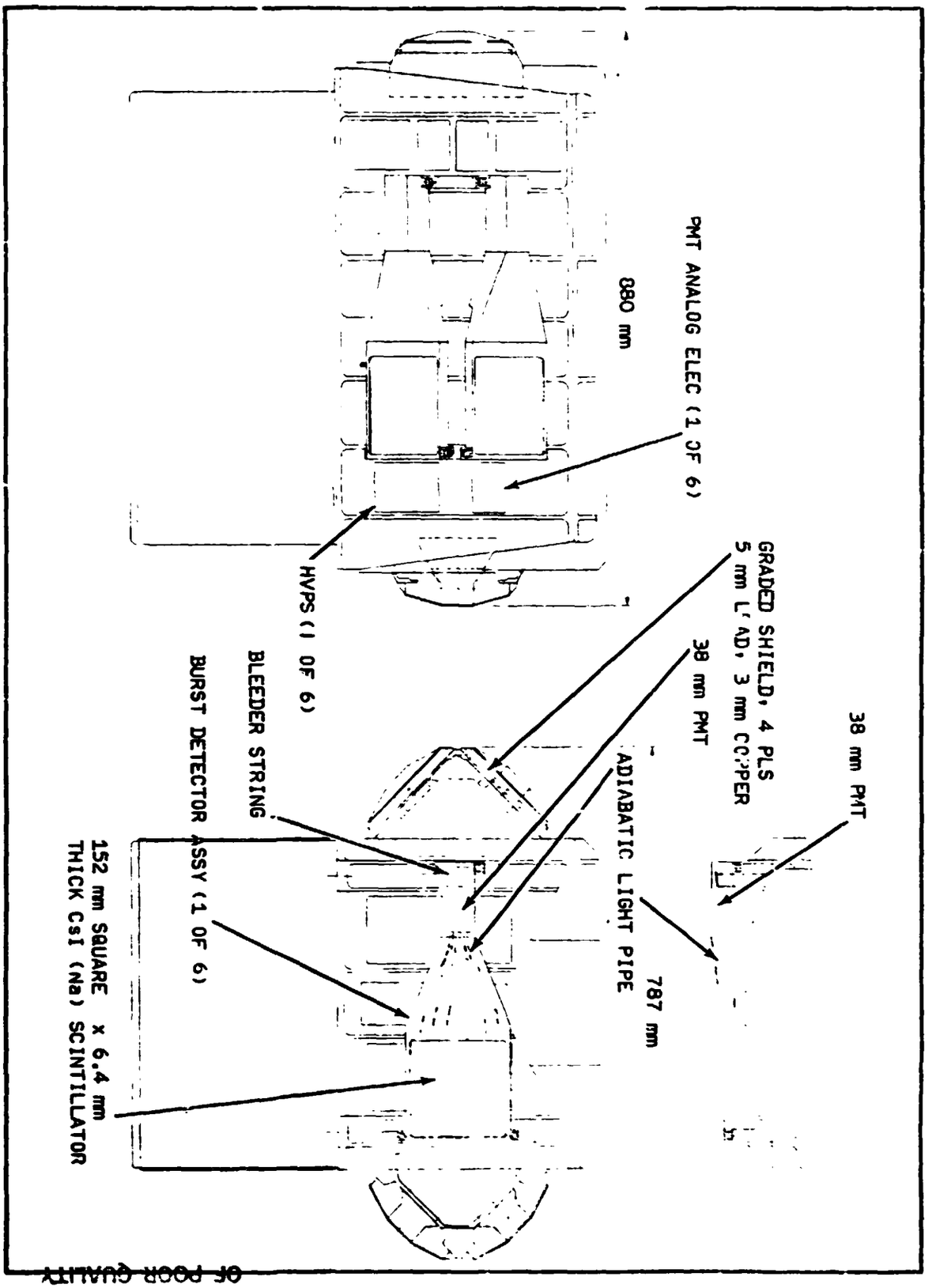

Figure 9: Burst Detector Add On Option.

with the primary EXITE imaging detector system.

For the detectors mounted at 45° to the EXITE shields, a graded shield of lead/copper has been placed on the back side of each scintillator to limit the scintillators to forward viewing only in the gamma-ray energy range below 500 KeV. The window over the front side of all six scintillators is about 1.6 mm thick aluminum. This thickness provides electron shielding to 900 KeV but at the same time only attenuates the X-ray/gamma-ray intensity at 50 KeV by 15 percent (but the high background from lower energy discrete sources and diffuse background is attenuated). Alternatively, a plastic scintillator (~1 cm NE-102) could be mounted on top of the CsI crystals and viewed by the same light pipe and PMT. Particle events could be easily discriminated against by a pulse decay-time discriminator circuit on each detector. Particle-induced burst events are otherwise rejected (in the analysis) by the large area anti-coincidence shields (lead-doped plastic scintillator) on which the burst detector scintillators are mounted (see Figure 8). Rate data from these shields during a burst should also allow the burst radiation scattered from the spacecraft and Earth's atmosphere (thus producing incident particles) to be isolated and the systematic errors in gamma burst arrival directions to be corrected.

Burst Detector Data Handling System

The burst data consists of both high time resolution (0.1 sec) count rates in a fixed band (nominally ~50-300 KeV, but commandable and with a veto for phosphorescence events) and lower time resolution (2 sec) energy spectra (32 channel PHA--~50-550 KeV and 16 bits per channel, or sufficient for even a $\sim 10^{-3}$ erg cm^{-2} burst) for each detector. Each detector event rate contained in the 50 to 300 KeV window is counted into 16 bit counters once every 0.1 seconds. Each counter's content is stored sequentially in memory which has the capability (~0.5 Mbit) to hold three minutes worth of data. The counter data are also routed to a µp subsystem where they are reformatted into 0.3-second samples for the continuous on-going normal telemetry data stream. In addition, the µp continually monitors these six rates via a burst mode algorithm to detect bursts (required in 2 detectors). If a burst is detected, a burst flag is set. The flag has 0.1 second time resolution. A sixteen level command buffer is provided for inflight control of the burst level criterion. As an option, the µp can also use the rate data to calculate the direction cosines of the burst location. These direction cosine values are routed through a special spacecraft interface port for possible use in automatically slewing the spacecraft to point at the burst source.

When a burst is detected, the burst flag is set but the memory continues to accept/spill data for an additional two minutes. At the end of this 2-minute period, the memory contents are frozen and remain frozen until the burst flag is cleared by command. Thus, three minutes of time/energy spectrum burst data, one minute before the flag and two minutes after the flag, are preserved. At the end of the

2-minute period, these memory data are automatically sent to the data stream by usurping the telemetry space normally taken by the prime science (imaging) data and housekeeping data. Approximately 164 seconds are required to transfer all the data to the ground. After the initial dump, additional memory data dumps can be made as desired (by command) until the burst flag is reset.

The total EXITE telemetry is organized in two formats. The normal format contains 0.3 second rate data, coded aperture prime science data, and housekeeping data. In the event of a burst (or if the burst flag is set by command) a burst mode format is set. In this format, the rate data continues as before with 0.3 second samples of the six burst detectors and five CPDs, but the memory dump usurps the 3.298 Kb/sec prime data plus housekeeping data rate long enough to be automatically transmitted at the end of flag plus two minutes, or upon command. When no memory dump is needed, the system reverts back to sending prime imaging data and housekeeping data as in the normal mode.

The weight addition for the Burst Detection System (including added electronics and HVPSs) is estimated at 33.4 kg. The power estimate for the burst detector system electronics is 12 watts.

Burst Detector Sensitivity and Performance

The background detected by the burst system is due to Earth albedo gamma rays and neutrons, spacecraft albedo, activation of the scintillators, diffuse and discrete source background and phosphorescence from charged particle interactions in the scintillators. Above the ~50 KeV threshold, phosphorescence is negligible and the largest background contribution for these wide-angle detectors is from atmospheric and spacecraft albedo. Using results from Ling (1975) and Trombka et al. (1973) for these components, respectively, and allowing for a factor of ~2 uncertainty, we estimate a total background spectrum $dN/dE \simeq 2.6\ E^{-0.9}$ cts/cm^2 sec KeV in the ~50-300 KeV band. This gives a total average background count rate $B \simeq 1700$ cts/sec in each of the six detectors. For orbits transiting the SAA (approximately one-third of the orbits), this average rate will increase substantially (factor of ~2-3) due to long-lived (~0.5 hour) activation decays. An increased effective background rate, incorporating the SAA duty cycle, has been used in deriving the sensitivities below.

Using the typical gamma burst spectra derived by Cline and Desai (1975) the total signal count rate expected in each detector is $S \simeq 3.7 \times 10^4$ cts/sec for a burst with total energy 10^{-4} erg cm^{-2} and assumed ~1 sec (peak) duration. Thus, the threshold for (5σ) burst detection (in three detectors) should be for energies $>4 \times 10^{-7}$ erg cm^{-2}. This is the approximate threshold for coarse ~20° positions and log N - log S studies. To achieve ~2° burst positions (and high S/N spectra to search for line features), a signal-to-noise ratio of >30 is required in each of three detectors.

This should occur for bursts larger than ~1.0 x 10^{-5} erg cm^{-2}, which are expected (from present log N-log S results) at a rate of ~40 per year within the ~2π steradians for which accurate locations can be derived. (Note that although bursts are detectable with approximately all-sky coverage, accurate locations are possible for about half the sky.) Thus, even if XTE slews could only be carried out within a ~1000 sec afterglow period for burst directions within ~45° of the pointing position, ~10 bursts per year would be accurately located by EXITE and observed with high sensitivity by EXITE and the LAPC. We note that estimates by Woosley et al. (1981) for the afterglow spectrum ($L_x \simeq 10^{35}$ erg s^{-1}, $kT \simeq 20$ KeV) would predict EXITE sensitivities of ~25σ per second for a typical burst source at ~500 pc distance. Thus, high signal-to-noise spectra and timing observations should be possible.

Finally, the EXITE burst detection system could detect (5σ) persistent hard X-ray sources with strengths ~1/3 Crab and a Crab-like spectrum in ~300 sec. Thus, hard sources can be monitored continuously and an all-sky monitor capability provided for XTE.

REFERENCES

Calabro, D. and Wolf, J. 1968, Inform Control, 11, 537.

Cline, T. and Desai, U. 1975, Ap. J. (Letters), 196, L43.

Cline, T.L., et al. 1980, Ap. J. (Letters), 237, L1.

Dicke, R. 1968, Ap. J. (Letters), 153, L101.

Fenimore, E. 1980, Applied Optics, 19, 2465.

Gunsen, J. and Polychronopulos, B. 1976, MNRAS, 177, 485.

Kellogg, E., Murray, S.S., and Bardas, D. 1979, IEEE Trans. Nuc. Sci., NS-26, 403.

Ling, J.C. 1975, J Geophys. Res., 80, 3241.

Martin, C., Jelinsky, J., Lampton, M., Malina, R., and Anger, H. 1981, Rev. Sci. Instr., in press

Matteson, J. 1978, AIAA 16th Aerospace Sc. Meeting.

Mazets, E.P., et al. 1979, FTI (Leningrad), Preprint No. 599, 618.

Rocker, G. 1981, these proceedings.

Terrell, J. 1980, Talk at Texas Symposium, Baltimore, MD.

Timothy, J., Mount, G., and Bybee, R. 1979, SPIE-Optics, 183, 169.

Trombka, J., et al. 1973, Ap. J., 181, 737.

Woosley, S., et al. 1981, Preprint.

PRECEDING PAGE BLANK NOT FILMED
367-370

N82 26073

D,8

The Stellar Coronal X-ray Explorer: STCOEX

G. S. Vaiana
Harvard-Smithsonian Center for Astrophysics

A. Introduction.

With the end of the observational phase of the *Einstein Observatory* mission, it behooves us to consider the status of the newly-born field of stellar x-ray astronomy. Although *Einstein* clearly allowed a quantum leap over previous observations of x-ray emission from stars (Vaiana *et al.* 1981), its relatively short lifespan allowed only a fraction of the variety of projects, developed in response to this instrument's capabilities, to be completed. In response to the consequent perceived need for further observational capability, we have conducted a overview of the available *Einstein* data for the purpose of deciding which projects will *both* in all probability not be completed by future analysis of the *Einstein* data *and*, in addition, seem to us to be of particular importance for the study of stellar surface "activity"; a natural outgrowth of this analysis was the development of design criteria for a follow-up mission to *Einstein*, one whose primary emphasis would be on stellar observations, and whose general capabilities lay within the scope of the NASA Explorer program. In the following, I will attempt to briefly review the criteria which lead us to the desired instrumental capabilities (§ B); and provide an overview of the proposed instrument and some of its capabilities, as indicated by our simulations (§ C).

B. Scientific Goals and Design Criteria.

One of the remarkable aspects of the stellar observations made possible by the *Einstein Observatory* was their serendipity: the instrumentation and the observing plans were not optimized for stellar observation, but rather for primarily extragalactic studies. In spite of this lack of optimization, well in excess of a third of all guest observer programs focussed on stars; and the stellar survey constituted one of the major research areas of the Consortium groups. What are some of the principal scientific problems, and to what extent have they been resolved? In the following, I will briefly recap some of the major issues, and attempt to define the work which remains to be done.

1. Dependence of Coronal Plasma Parameters on the Characteristics of the "Underlying" Star. The *Einstein* observations have enabled us to sketch in broad outline the x-ray emission properties of stars throughout the H-R diagram; however, in many portions of the H-R diagram, the data is relatively sparse (because of severe restrictions on the allowable observing times). In particular, it has not been possible to assemble uniform, unbiased (viz. volume-limited) samples for every spectral types and luminosity classes. In consequence, phenomenological studies of the variation of x-ray luminosity with stellar parameters such as rotation and mass loss rate may remain biased by selection criteria for several stellar categories because (at least in the beginning of the mission) emphasis was largely placed on targets most likely to be x-ray sources. More severe difficulties beset the plasma diagnostics (such as temperature analysis). the strong constraints on observing time allowed only a very limited sample of stars to be examined by the higher-resolution spectrometers on *Einstein*, such as the OGS and the SSS. Thus, questions regarding possible changes in spectral characteristics along the 'dividing line' separating low and high mass loss late-type evolved stars (cf. Ayres *et al.* 1981); soft x-ray absorption and possible multiple temperature component structure in OB stars; and flare spectroscopy, may all be only partially resolved. Furthermore, the quite limited sensitivity of relatively high resolution spectroscopy ($\lambda/\Delta\lambda > 100$) on *Einstein* prevented any study of line broadening or doppler shift effects; the latter is particularly of interest in the case of OB

stars, since some models predict rapid outflow of the hot plasma (which may be observable with $\lambda/\Delta\lambda$ ~ 300-1000). The observational requirements thus call for pointings with point source sensitivities of several times 10^{-15} erg/sec/cm^2, in conjunction with spectroscopic instruments capable of resolution in excess of 100, and with line sensitivities of order 10^{-14} erg/sec/cm^2.

2. Temporal Variability. Again because of observing time constraints, virtually all temporal variability data for *Einstein* stellar targets are restricted to the few thousand seconds of contiguous observing time; in only a few select cases (for example, for some flare stars and OB associations) are data spanning substantially longer intervals available – and virtually without exception, the longer data base showed evidence for substantial variability. It is evident that 'coronal' emission from stars is highly variable on a wide range of time scales, from seconds or less (flares), to days and weeks (viz. rotational modulation), to months and possibly longer time scales (cycles?). Such variability in stellar 'activity' is seen by ground-based observers (e.g., in Ca II), but only in a very restricted portion of the H-R diagram: in contrast, x-rays allow us to look for activity modulation (via rotation and/or cycles) in stars independent of spectral type or luminosity class, including stars in the spectral range O - A. These observations therefore call for the ability to carry out extended observations (> 10^5 sec) which can be repeated on time scales ranging from 10^6 sec to 10^8 sec.

3. Galactic Effects of Stellar Activity. In addition to being a major research area in its own right, stellar x-ray astronomy forms a new bridge between the stellar astronomers and the galactic and extragalactic astronomers: the radiative and particulate emission of active stars may well contribute significantly to the radiation field and matter content of the galaxy. For example, Rosner *et al.* (1981) have shown that late-type dwarf stars contribute a not insignificant amount of radiation to the galactic component of the diffuse soft x-ray background between ~ 0.28-1.0 keV. Because of *Einstein*'s spectral coverage, the stellar contribution at lower energies is not well established (as it depends sensitively on the assumed 'coronal' temperature). Furthermore, the limited effective spectral resolution did not permit relative elemental abundance analysis; such analysis is of great interest for studies of the elemental composition of stellar mass input to the ISM (as it is known from solar observations that the photospheric and coronal/wind abundances are not identical). The necessary observational capability to conduct such studies corresponds to that of § B.1 above.

4. Desired Instrument Characteristics. In order to place the instrument discussion on concrete grounds, we shall adopt the following desirata.

(i) *Energy Range:* ~ 10-200 A; this range encompasses virtually all of the significant spectral lines of interest to coronal observations.

(ii) *Optics:* Imaging, with spatial resolution better than ~ 1'; such resolution is required both for accurate target identification and for optimal signal-to-noise.

(iii) *Detectors:* Photon-counting (i.e., IPC or HRI-like); this requirement follows from the necessity of observing flares on sub-second time scales (so that, for example, read-out noise of integrating detectors becomes a significant liability). Note, however, that CCD detectors may be preferable for extremely-high sensitivity observations for which high temporal resolution is not required.

(iv) *Spectroscopy:* High throughput, with resolution in excess of 100 (300 for OB star wind diagnostics), calls for transmission or reflection gratings.

(v) *Sensitivity:* Assuming that of order 1000 pointings (with spectroscopy) are to be carried out on a time scale of 2 years, with sufficient sensitivity to probe stars down to a level of 10^{-27} erg/sec at distances of order 50 pc (these numbers will yield a sufficiently large sample to carry out statistical analysis of luminosity functions throughout the H-R diagram), one requires a point source sensitivity @ 10^5 sec approximately 3-4 times that of *Einstein*.

C. Instrument Characteristics.

Following the above considerations, we have recently developed two versions of a trial payload (the STellar COronal EXplorer) which meets in essentially all respects the observational desirata. Perhaps the most crucial aspect of the design is that the instrument is *dedicated* to stellar observations. This point is not to be slighted: the character of stellar observing programs (i.e., large numbers of very extended pointings, with substantial degree of repetition) is such that it severely conflicts with the requirements of, for example, extragalactic observations; in this circumstance, combined missions may well be false economy as the principal scientific goals (which presumably underly such ventures) may not be realized. This emphasis on *dedication*, however, does not exclude the possibility of including non-stellar programs whose observing strategies do not overtly conflict with stellar observations (such as observations of galactic high-luminosity x-ray sources).

Figure 1 shows a schematic of the 'simpler' instrument; the optics consist of a nested pair of classical paraboloid-hyperboloid mirror assemblies, together with a movable objective transmission grating and an HRI and imaging proportional counter (PSPC) in the focal plane (mounted on a stage so that the entire dispersed spectrum may be explored); the more 'complex' design simply calls for two additional nested mirror assemblies, which results in a rough doubling of the instrument effective area. The physical characteristics of the instruments and the relevant sensitivities in both the imaging and spectroscopic modes are given in Tables 1 and 2; and graphs of the total effective area of the instrument in the high resolution mode and of the resolving power are shown in Figures 2 and 3. It is to be noted that these results are not speculations, but rather reflect the current state-of-the-art in detector and transmission grating technology: no development is required to obtain such capabilities.

In order to appreciate the power of such an instrument, we show first the range of spectral lines (and source temperatures) accessible to observation (Table 3): the STCOEX can observe coronal line emission from plasma in the temperature range $5.6 < \log T < 7.5$; the lines chosen take advantage of the spectral sensitivity of the instrument, and so are not just marginally detectable. A more revealing analysis is to fully simulate a typical observation. Consider an observation of an RS CVn star at ~50 pc, whose volume emission measure is $\sim 10^{53.4}$ cm^{-3}; the source spectrum is shown in Figure 4 (using recent Raymond 1980 calculations with solar abundances). We have simulated a STCOEX observation by folding this source spectrum through the instrument response (unless otherwise stated, for the 2-mirror system), including the mirror reflectivities, the grating transmission, the detector sensitivities, and the instrument resolution (including mirror pfr and abberations for a coma-corrected grating). If detector noise is *not* taken into account (but photon statistics are), one obtains the spectrum shown in Figure 5 in 10^4 sec; adding detector noise (we assume a background of 1 ct/sec over the entire HRI) then leads to the spectrum shown in Figure 6. Comparing Figs. 4 and 6, we see that a 10^4 sec exposure is sufficient to allow one to resolve most of the strong lines in the source spectrum; however, the limited count statistics would not permit sensible line ratios to be calculated. If one goes to longer exposure times, this restriction is completely eliminated: Figure 7 shows what can be accomplished in 10^5 sec, using the 4-mirror system; again, both photon statistics and detector noise have been taken into account in the simulation. Spectroscopy of such resolution and sensitivity, in combination with the capability for dedicated observations, will clearly allow the observational goals outlined above to be met.

Support of the above studies by NASA grant NSG 7176 is acknowledged.

Bibliography.

Ayres, T. R., Linsky, J. L., Vaiana, G. S., Golub, L., and Rosner, R. 1981, *Ap. J.* (in press).
Pallavicini, R., Golub, L., Rosner, R., Vaiana, G. S., Ayres, T. R., and Linsky, J. L. 1981, *Ap. J.*, **248**, 279.

Rosner, R. *et al.* 1981, *Ap. J. (Letters)*, **249**, L5.
Vaiana, G. S. *et al.* 1981, *Ap. J.*, **245**, 163.

ORIGINAL PAGE IS
OF POOR QUALITY

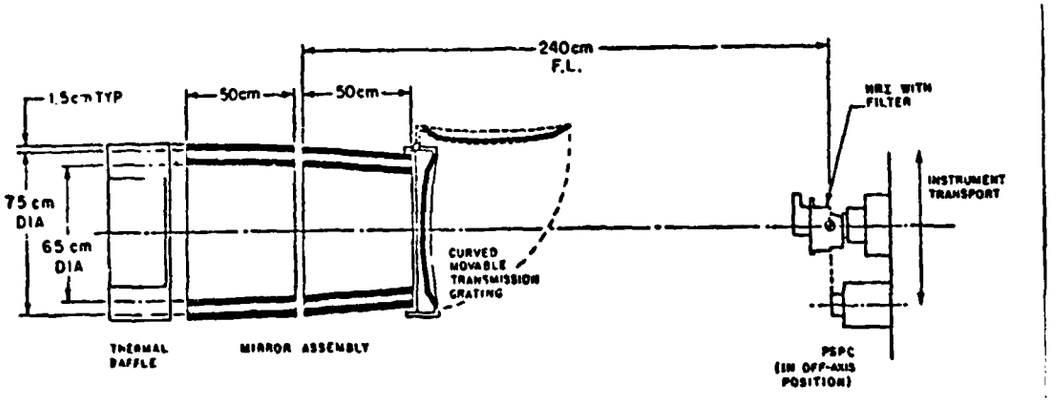

Figure 1: Schematic of the STOBEX, showing the principal instrumentation. Only the 2-mirror system is shown; an alternative design calls for 2 additional concentric mirror assemblies.

ORIGINAL PAGE IS
OF POOR QUALITY

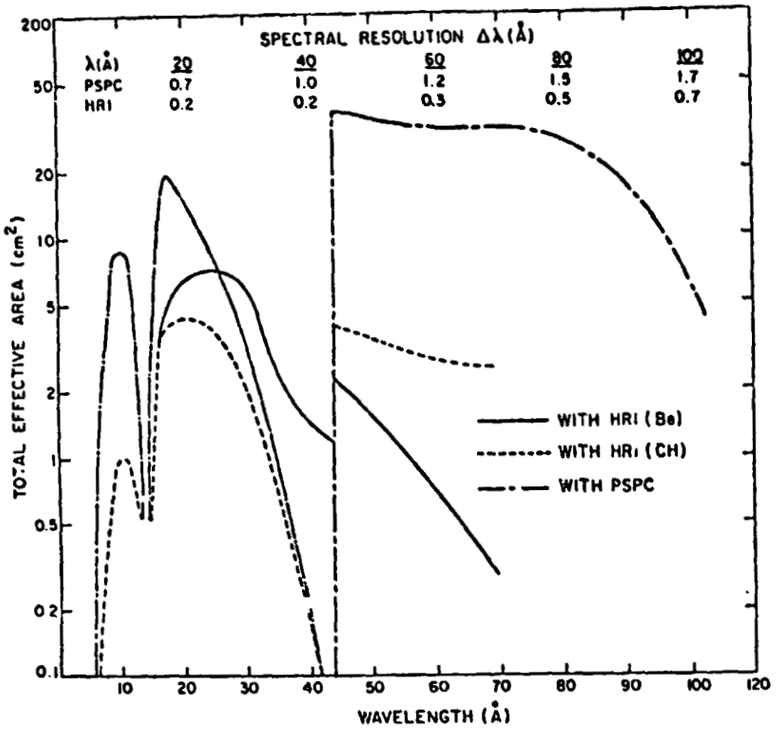

Figure 2: Total effective area of the 2-mirror STCOEX design, including mirror reflectivities, transmission grating performance, and detector sensitivity. We show results for the HRI with either a Beryllium (solid) or organic (dashed) filter, and for the imaging proportional counter (PSPC; solid/dashed). Note that the grating spectral resolution with the high-sensitivity PSPC would be comparable to or somewhat better than that of the *Einstein* SSS.

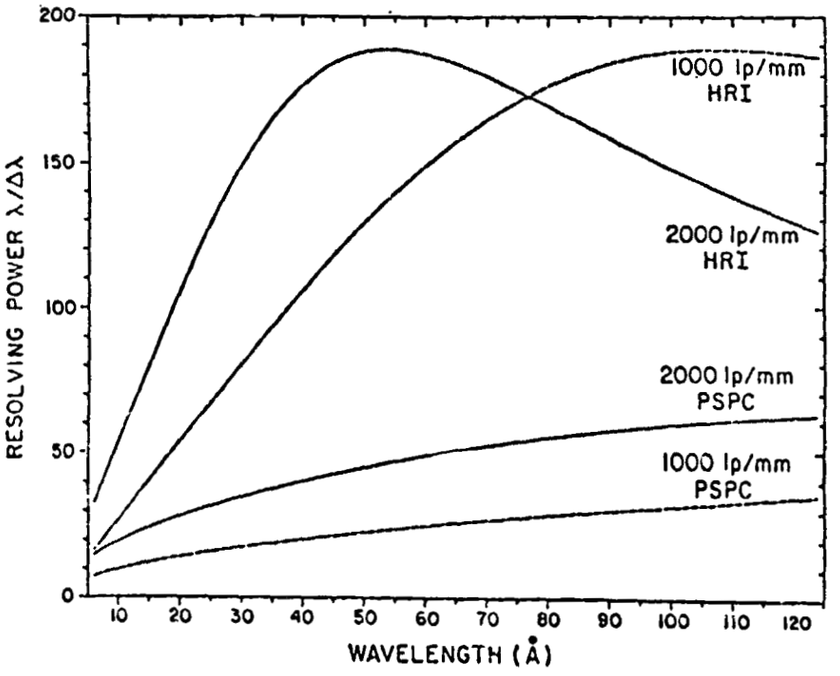

Figure 3: Detailed spectral resolution of the transmission grating for two different grating periods and the two possible focal plane detectors.

ORIGINAL PAGE IS
OF POOR QUALITY

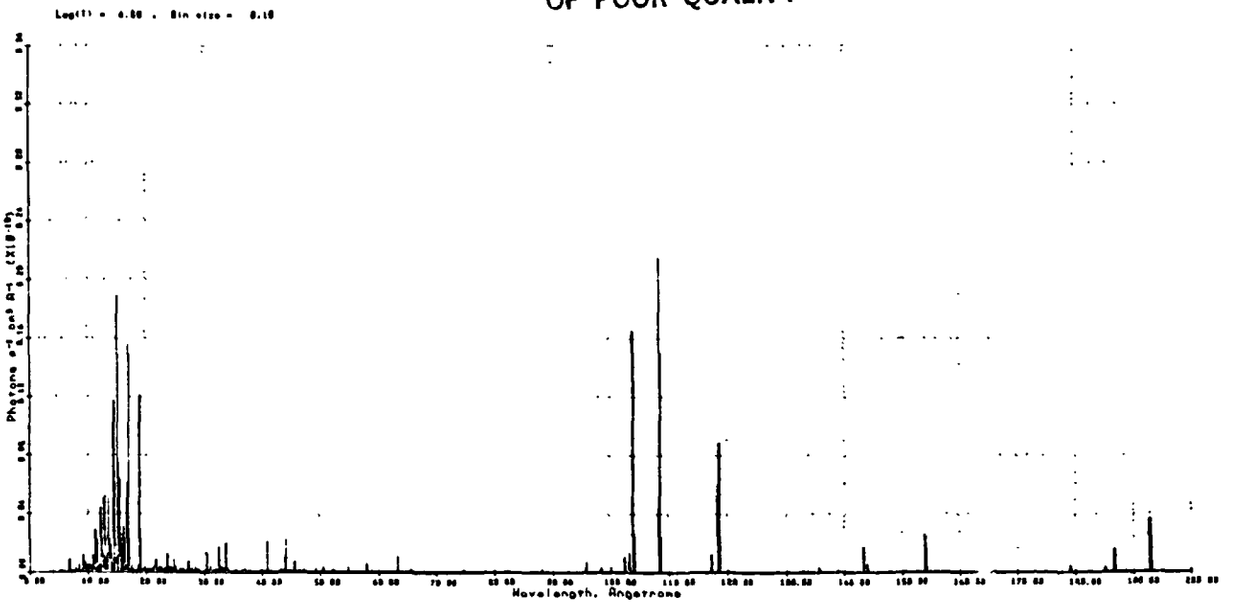

Figure 4: Source spectrum for an 'active' late-type star, with T = $10^{6.8}$ K; the model is that of Raymond (1980).

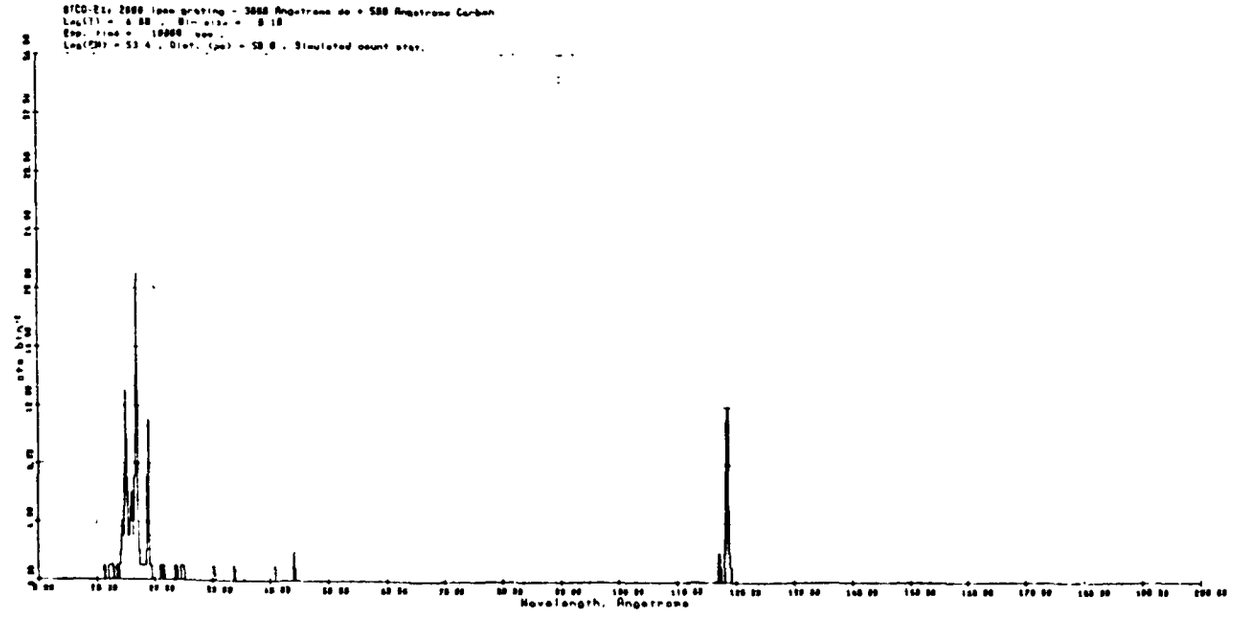

Figure 5: Convolution of the source spectrum of Fig. 4 with the total instrumental response of the 2-mirror design, assuming a source volume emission measure of $10^{53.4}$ cm^{-3} at a distance of 50 pc; we assumed the Beryllium filter, use of the 2000 lpmm grating, an exposure time of 10^4 sec, and *no detector noise* (photon statistics were taken into account).

ORIGINAL PAGE IS
OF POOR QUALITY

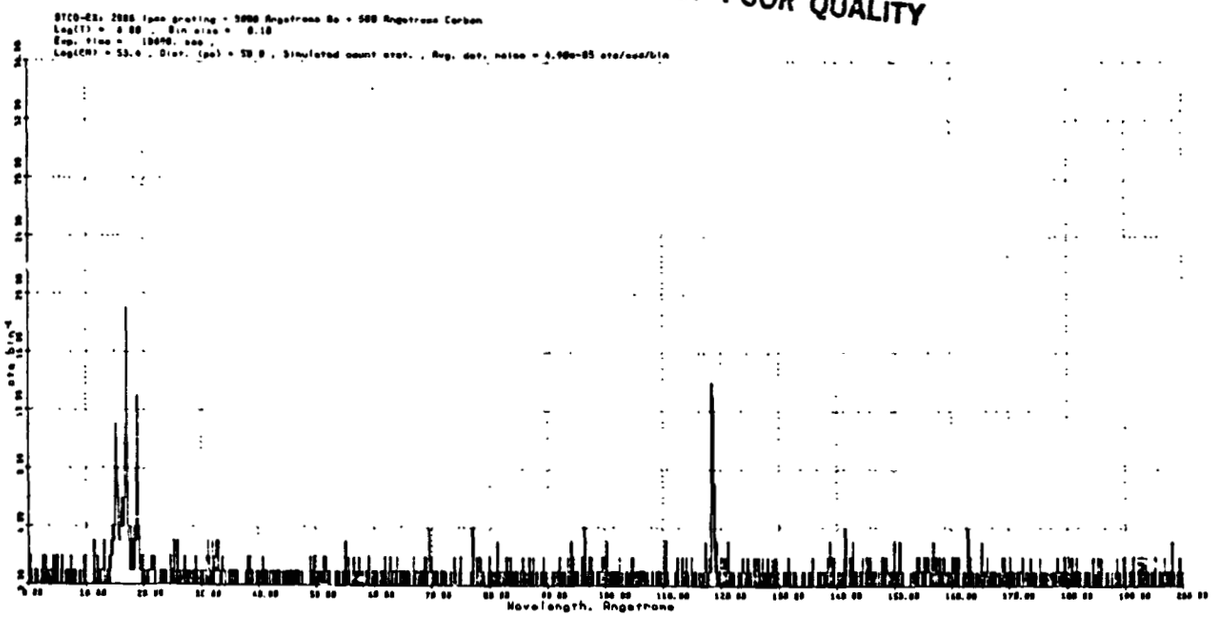

Figure 6: Same as Fig. 5, but now taking the detector noise into account; note that most of the strong lines in the parent source spectrum are detected, but that line intensity ratios cannot be reliably calculated.

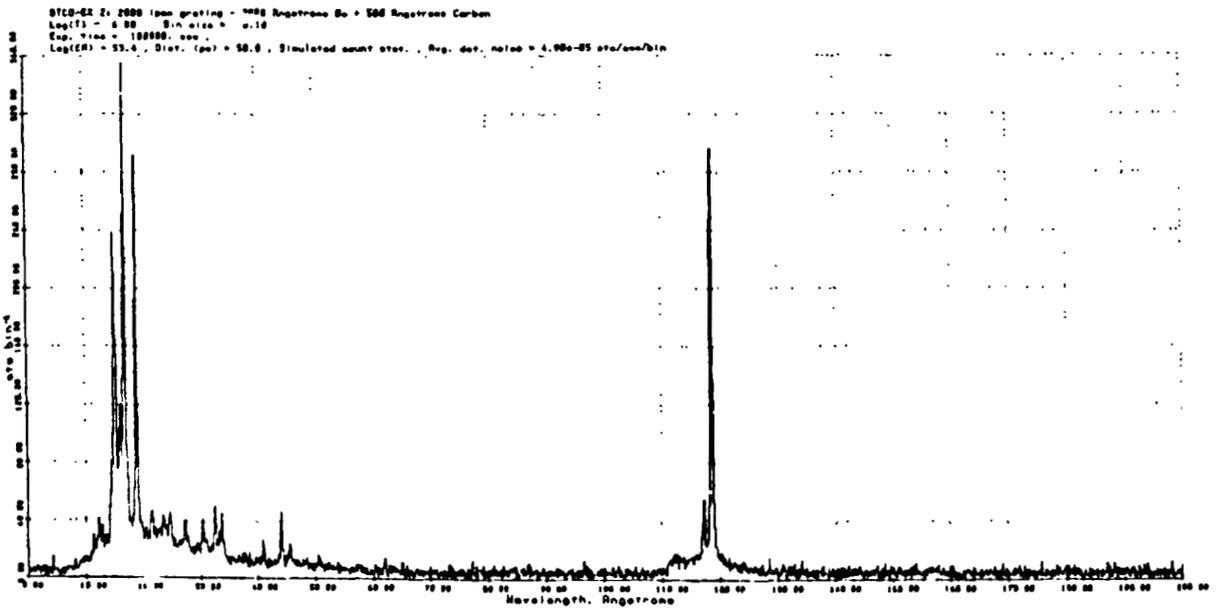

Figure 7: Same as Fig. 6, but for the 4-mirror design at an exposure of 10^5 sec. In this case, the spectroscopic goals discussed in the text are readily within reach; note that the 2-mirror design would lead to somewhat degraded signal-to-noise.

N82 26074

A DIFFUSE SOFT X-RAY SPECTROMETER

Dan McCammon

Department of Physics, University of Wisconsin, Madison

Abstract

A design for a diffuse X-ray spectrometer utilizing Bragg reflection is described. The geometry has a very high throughput for a given physical size and allows simultaneous observation at all wavelengths within its range. An implementation with overall dimensions about 33 x 66 x 66 cm uses 1800 cm^2 of lead stearate multilayer Bragg reflector to cover the wavelength range 42 to 84 Angstroms with a throughput of about 0.01 cm^2 sr, including detector efficiency. Spectral resolving power is about 35 to 50. A similar unit equipped with thallium acid pthallate crystals will cover the 11 - 24 A range with about half this throughput and twice the resolving power.

PRECEDING PAGE BLANK NOT FILMED

I. INTRODUCTION

There is now strong evidence indicating that most of the diffuse X-ray background at energies less than 1 keV is local to the Galaxy (Sanders et al. 1977). Discrete sources seem to account for at most a small fraction of this, at least below 0.3 keV (Vanderhill et al. 1975; Rosner et al. 1981). The lack of acceptable non-thermal diffuse emission mechanisms (Williamson et al. 1974) leads to the conclusion that most of this X-ray flux is due to thermal emission from a hot ($T \sim 10^6$ K), tenuous component of the interstellar medium. It has been argued on theoretical grounds that such material occupies a large fraction of the volume of the Galactic disk, with a filling factor perhaps as high as 0.5 - 0.9 (Cox and Smith 1974; Smith 1977; McKee and Ostriker 1977). If this is true (and the ubiquity of O VI absorption in the ultraviolet lends considerable credence to the idea: see review by Jenkins 1977), then the hot component must have a profound influence on the nature of the ISM, and any comprehensive understanding of Galactic structure and evolution will require much more detailed knowledge of this high temperature material than we currently possess (McCray and Snow 1979, and references therein).

Our picture of the ISM is getting so complicated that broad-band spectral measurements are no longer adequate for testing the more detailed and complex models now being proposed. Fortunately, radiation from gas around 10^6 K with any reasonable composition is almost entirely in characteristic lines of the heavier elements, and observations of these can in principle supply a wealth of information on physical conditions within this component, and even its past history. Interpretation

of spectra will admittedly be complicated considerably by multiple temperatures, abundance variations, and non-equilibrium conditions, but optical spectroscopy has had to deal with similar or even more severe complications and still managed to make significant contributions to astrophysical understanding.

II. OBSERVATIONAL APPROACHES

The following are possible avenues to observing interstellar gas at $\sim 10^6$ K:

1. Optical and U.V. forbidden lines: These have been observed in some high surface brightness supernova remnants, but seem hopelessly faint from the general ISM.
2. Resonance absorption lines: In this temperature range, only the O VI lines fall longward of the Lyman limit. The anomalously low local neutral hydrogen density might allow observation of other lines in the XUV out to a distance of 100 pc or so, and could provide much useful information about the solar neighborhood. Observation of absorption lines in the X-ray region could be done against bright Galactic X-ray sources with AXAF-class instrumentation and should give some very interesting results. However, suitable sources are few in number and almost all at large distances, so only a very limited amount of information can be obtained in this way.
3. Photoionization signatures: One could conceivably look for evidence of absorption of X-ray and XUV photons in surrounding cooler material. However, none of the accessible resulting states seems sufficiently unique to make this a practical approach.

4. X-ray emission lines: These represent the dominant cooling mechanism for the hot gas and have potentially the highest information content. One of the major observational difficulties is the low surface brightness. Since this is a true diffuse source, collecting or focussing optics can serve only to increase spatial resolution, which will be desirable someday, but in a first-generation instrument the additional inefficiency introduced by these elements would exacerbate the major problem of getting enough photons.

III. TYPES OF SPECTROSCOPIC INSTRUMENTS

Possible instrumental types for moderate-resolution spectroscopy below 1 keV include:

1. Solid state detectors: These have wide acceptance angles, but at the current state of the art give little improvement over proportional counters below 1 keV.

2. Reflection gratings: Allow observation of all wavelengths simultaneously, but must be used near grazing incidence, making acceptance angles and throughput extremely small for diffuse sources.

3. Transmission gratings: Small dispersions again require small acceptance angles. Efficiency is also lower than reflection gratings.

4. Bragg crystals and multi-layer analyzers: These have relatively high integrated reflectivities, can work at large angles, and thus can have relatively high throughput. Their major disadvantage is that a given crystal area can be used for only one wavelength at a time, if all incoming X-rays are arriving from the same direction.

For studying the diffuse background, we can get around the problem of one wavelength at a time when using Bragg reflection by looking at many wavelengths simultaneously, but from different parts of the sky. The spatial coverage can either be smeared out to get an average spectrum or sorted out by spatial bins as the instrument pointing is changed to eventually obtain a complete spectrum of each spatial element while retaining the spectral multiplex advantage. The following section describes one geometry which has been worked out to take advantage of this scheme.

IV. GEOMETRY FOR A DIFFUSE X-RAY BRAGG SPECTROMETER

To obtain a finite counting rate from a truly diffuse source, the detector must accept X-rays from a finite range of angles. To keep the Bragg reflection angle (and thus the observed wavelength) from changing as fast as the angle with respect to the detector, the crystal can be curved to compensate for the changing look direction, keeping the reflection angle constant. For a one-dimensional detector, the required curve is an exponential spiral. This allows the field of view to be made as large as desired without affecting the spectral resolution, but it works only for a single wavelength.

Our approach is to extend a position-sensitive detector along the x-axis, and to make the curvature of the crystal above each point on the counter appropriate to an exponential spiral about that point, subject to the constraints that the crystal be continuous and have a continuous slope. This allows the use of a plane detector with a simply constructed collimator directed perpendicular to the counter face at all

positions. The reflection angle for rays perpendicular to the detector will vary with position on the x-axis, but at any given position there will be no change in this angle to first order as the collimation angle departs from perpendicular. The shape thus determined for the crystal turns out to be a circular cylinder, with the detector located along a diameter, as shown in Figure 1. This makes it simple to calculate analytic expressions for parameters of interest, which are given in Table 1. These follow from the Bragg condition, $\lambda = 2d \sin \theta'$, the exact expression $\cos \theta' = \cos \theta \cos \Delta\phi$, and the approximation $\sin \theta' \approx \sin \theta \cos \Delta\psi$, where θ is the reflection angle for the ray perpendicular to the detector, and θ' is the reflection angle for a ray which is at an angle $\Delta\phi$ from perpendicular in the dispersion direction or $\Delta\psi$ from perpendicular in the cross direction. As can be seen from these expressions, going off-axis in the dispersion direction always increases the wavelength from the nominal value at that x-position, while going off-axis in the cross direction always decreases it. These effects partially cancel over most of the off-axis field of view, and the FWHM of the resulting profile is less than half the $\Delta\lambda$ calculated using the FWHM angle of the collimator.

Figure 2 shows a cross section of an instrument as it might be built using a lead stearate (PbSt) Bragg reflector to cover the 148-295 eV band. The inherent resolving power of PbSt varies from 40 to 60 over this range and the collimation angles on the detector can be opened up to 20° x 20° FWHM before this is degraded by a factor of $\sim \sqrt{2}$. A ray-tracing computer model has been written to predict the response of such an instrument to an arbitrary input spectrum. The program takes into account off-axis

rays, vignetting, collimator transmission, and detector efficiency for a practical proportional counter, as well as the full rocking curve and specular reflection of the Bragg crystals. The latter were measured for PbSt at the Tantalus synchrotron radiation facility of the University of Wisconsin's Physical Sciences Laboratory, using a grating double monochrometer. The high intensity, low scattered light, and steep-skirted 0.5 A bandpass of this source allowed measurements of the wings of the rocking curve down to three orders of magnitude below the peak, and specular reflectivity out to angles where it dropped below 10^{-5}. These parameters are important in determining the response of a Bragg spectrometer to such quasi-continuous sources as astrophysical plasmas.

Calculations for the geometry of Figure 2 with a detector 23 cm wide in the x-direction and both detector and crystal 53 cm long give a throughput as shown in Figure 3. Figure 4 shows the calculated response to a sky uniformly bright in boron and carbon K-alpha emission. The natural widths of these lines when they are excited from elemental solids as published by Holliday (1967) have been included; the response to a monochromatic line of the same nominal wavelength is shown by the dashed line. A spectrometer has been built to the above specifications and exposed to large alpha-particle excited targets of boron and carbon which entirely filled its field of view. The data points in Figure 4 show its response. (The horizontal scale, for which nominal wavelengths are given, is linear in x-position on the detector. The position resolution of the proportion counter is about 1 mm FWHM at 70 eV pulse height, and does not contribute significantly to the line profile widths.) We do not know why

the boron line appears significantly narrower than the published profile, but this has also been noticed when testing flat crystal samples in a monochrometer with an electron-excited boron source. The spreading of the profiles at low amplitudes (most noticeable on the long-wavelength wing of the carbon line) is probably due to imperfections in the cylindrical figure at the edges of the individual elements of the mosaic crystal panel. Absolute intensity calibrations of the sources agree with the calculated throughput to better than 15% for both lines.

Figure 5a shows the response to a two-temperature Raymond and Smith (1977) thermal spectrum which has been fit to three-band sky survey data for a typical region in the southern hemisphere. The brighter lines in the spectrum are also indicated as they appear before being folded through the instrumental response. The dashed line shows the contribution due to the cosmic-ray background level predicted by laboratory measurements (6×10^{-4} counts cm^{-2} s^{-1} keV^{-1}). It slopes because the pulse height limits used in integrating the signal have been varied with position on the counter to roughly optimize the signal to noise ratio. Figure 5b shows the same response integrated into position bins for an assumed 5000-second observation, with the resulting number of counts in each bin further subjected to a Poisson randomization. For this and the following figures showing the PbSt bandpass, the collimation angles have been reduced to 10° x 10° FWHM in order to preserve essentially the full inherent resolving power of the crystals.

A similar geometry can be used with other Bragg crystals. Thallium acid pthallate (TAP) shows the greatest promise for covering the interesting

M band region (.5 - 1.0 keV) where the number of important lines is not so large as at lower energies and the physics should be easier to disentangle. Unfortunately, the much higher inherent resolving power of TAP means that the integrated reflectivity is lower than for PbSt, and this, coupled with the much lower fluxes, means that long observing times will be necessary. Figure 6 shows the predicted results from an instrument the same size as the PbSt spectrometer, but using a TAP crystal to cover the 516 to 1032 eV range. The collimation angle has been opened up to 15° x 15° in order to increase the throughput, and as a result the observed line profile widths are almost entirely due to effects of the collimation angles. Even thermal equilibrium fits to the three-band sky survey data are not unique, and Figures 7 and 8 show the result of two different multicomponent spectral fits to another part of the sky. These are one- and three-temperature fits with equilibrium models, and while non-equilibrium models would certainly be different, they are unlikely to be significantly more complex.

V. OTHER BRAGG REFLECTORS

No natural crystals have 2d spacings long enough to cover the 150-300 eV region, and PbSt is the best material tested so far for a Langmuir-Blodgett multilayer analyzer. For the 500-1000 eV range, TAP has the highest integrated reflectivity of commercially available crystals.

However, recent successful work with artificial multilayers is very promising (Spiller et al. 1980; Barbee 1981; Underwood and Barbee 1981). The rocking-curve width of PbSt is actually rather well matched to the

resolving power which could be used on even a fairly lengthy shuttle-based observation. The materials are also nearly optimum and there is probably not more than a factor of two to be gained by going to an optimized artificial multilayer. TAP, on the other hand, has an inherent resolving power of about 10^3, which is much higher than can be used with expected observing times and instrumental backgrounds, and we calculate a factor of five potential improvement for artificial multilayers that seem feasible to fabricate.

VI. CONCLUSIONS

Spectroscopy of the Galactic component of the diffuse X-ray background is necessary for an adequate understanding of the coronal phase of the interstellar medium. This is especially important if this phase is as pervasive as has been predicted.

Whether this spectroscopy eventually is done with an instrument similar to the one described here, or with some more clever specialized design, or as a sideline by a much larger general-purpose instrument, two major characteristics must be kept in mind and designed in. The first of these is simply high throughput. It is probably impractical to attempt these observations with less than about 10% of the area-solid angle factor of the examples in this paper. For an imaging telescope with a small field of view, this implies very large areas. For example, an imaging instrument equipped with very high efficiency (50%) objective reflection gratings and having about the same physical size as the two instruments described above put together has about three orders of magnitude less throughput.

The second vital consideration is a low-background detector. The Bragg spectrometers whose responses are shown in Figures 5-8 have about aslarge a convergence angle at the detector and as high an optical efficiency as is practical to design into an instrument, particularly a general-purpose imager, and so we expect that these simulations represent an upper limit to the surface brightness of the spectrum at the detector. Even so, it can be seen that they are very nearly cosmic-ray background limited at an assumed background rate of 6×10^{-4} counts cm^{-2} s^{-1} keV^{-1} between 70 eV and 1000 eV. During a sounding-rocket flight, position-sensitive proportional counters showed a cosmic-ray background rate (door-closed or earth-looking) which was actually about one-third of this, but with the spectrometer field-of-view exposed to the sky an additional background due to electrons scattering off the crystal panel and penetrating the counter windows was observed. This can be reduced adequately with magnetic field screens, but there is also another sky-related background which may be due to a softer and much more intense component of the electron flux producing fluorescence and bremmsstrahlung X-rays as they strike the crystal panel.

This is brought up to emphasize the care that must be taken to minimize all extraneous sources of background at the detector, whether from cosmic rays, scattered electrons, or stray ultraviolet, if there is any intention of making these interesting and potentially important measurements.

TABLE 1. GEOMETRICAL CHARACTERISTICS

$$\lambda = 2d \sin \Theta = 2d \frac{y}{R} = 2d \sqrt{1-\left(\frac{x}{R}\right)^2}$$

x = distance from center of curvature, O.

If: I_λ = source brightness in photons cm^{-2} s^{-1} $sterad^{-1}$

and: $(A^*\Omega)_\lambda$ = spectrometer throughput in cm^2 sterad

Then counting rate = $I_\lambda (A^*\Omega)_\lambda$.

$$(A^*\Omega)_\lambda = \ell R \, R_I(\lambda) \Delta\phi \, \Delta\psi \sin \Theta_B(\lambda) \, \varepsilon_\lambda.$$

Where: ℓ = length of detector and crystal

R = crystal radius of curvature

$R_I(\lambda)$ = integrated reflectivity of crystal

$\Delta\phi$ = collimation HWB in dispersion direction

$\Delta\psi$ = collimation HWB in cross direction

$\Theta(\lambda)$ = Bragg angle

ε_λ = detector efficiency

Contributions to limited resolving power:

A) Collimation in dispersion direction:

$$\frac{\lambda}{\Delta\lambda} \approx \frac{-2 \tan^2 \Theta}{\Delta\phi^2}$$

B) Collimation in cross-dispersion direction:

$$\frac{\lambda}{\Delta\lambda} \approx \frac{2}{\Delta\psi^2}$$

C) Position resolution of detector:

$$\frac{\lambda}{\Delta\lambda} = \sin \Theta \tan \Theta \frac{R}{\Delta x}$$

D) Finite width of crystal Rocking curve:

$$\frac{\lambda}{\Delta\lambda} = \tan \Theta \frac{1}{\Delta\Theta}$$

REFERENCES

Barbee, Troy W. Jr. 1981, Proceedings of the Topical Conference on Low-Energy X-ray Diagnostics, A.I.P., Monterey, Calif. (Preprint).

Cox, D. P., and Smith, B. W. 1974, Ap. J., 189, L105.

Holliday, J. E. 1967, Norelco Reporter, XIV, 84.

Jenkins, E. B. 1977, in Topics in Interstellar Matter, H. van Woerden ed., Dordrecht, Reidel.

McCray, R., and Snow, T. P. Jr. 1979, Ann. Rev. Ast. and Ap., 17, 213.

McKee, C. F., and Ostriker, J. P. 1977, Ap. J., 218, 148.

Raymond, J. C., and Smith, B. W. 1977, Ap.J.(Suppl.), 35, 419.

Rosner, R., Avni, Y., Bookbinder, J., Giacconi, R., Golub, L., Harnden, F. R. Jr., Maxson, C. W., Topka, K., and Vaiana, G. S. 1981, preprint (to be published in Ap.J. (Letters)).

Sanders, W. T., Kraushaar, W. L., Nousek, J. A., and Fried, P. M. 1977, Ap.J., 217, L87.

Smith, B. W. 1977, Ap.J., 211, 404.

Spiller, Eberhard, and Segmüller, Armin 1980, Appl. Phys. Lett., 37, 1048.

Underwood, J. H., and Barbee, T. W. Jr. 1981, Proceedings of the Topical Conference on Low-Energy X-ray Diagnostics, A.I.P., Monterey, Calif. (Preprint).

Vanderhill, M. J., Borken, R. J., Bunner, A. N., Burstein, P. H., and Kraushaar, W. L. 1975, Ap.J. (Letters), 197, L19.

Williamson, F. O., Sanders, W. T., Kraushaar, W. L., McCammon, D., Borken, R., and Bunner, A. N. 1974, Ap.J., 193, L133.

FIGURE CAPTIONS

Figure 1: The Bragg reflector is on the inner surface of the circular cylinder of radius R. The detector occupies a portion of the x-axis below the reflector.

Figure 2: Cross section of an instrument to cover the energy range 148-195 eV, showing sample ray tracings.

Figure 3: Area-Solid Angle product vs. photon energy for a PbSt spectrometer with a 23 cm x 53 cm proportional counter detector and 20° x 20° collimation.

Figure 4: Predicted and actual responses of a PbSt spectrometer with 20° x 20° collimation to uniform diffuse illumination of the field of view with boron and carbon K-alpha radiation. The dashed curve shows the predicted response to a monochromatic line of the same nominal wavelength.

Figure 5a: Predicted response of a PbSt spectrometer with 10° x 10° collimation to a two-temperature equilibrium plasma model fit to observed broad-band counting rates at a typical region in the southern Galactic hemisphere. The brighter lines also are shown before folding through the spectrometer response. The right-hand scale gives the individual line intensities, the left-hand scale gives spectrum surface brightness on the detector.

FIGURE CAPTIONS, cont.

b: The above spectrum integrated into bins over an assumed 5000-second observation, with the counts in each bin subsequently modified by a Poisson-distributed Monte-Carlo procedure.

Figure 6a: The spectrum of figure 5 folded through a TAP spectrometer with 15° x 15° collimation which covers the 515 - 1030 eV range.

b: The above spectrum integrated for 5000 seconds, binned and randomized.

Figure 7a: PbSt spectrum of three-temperature fit to a part of the North Polar Spur.

b: TAP response to above spectrum.

Figure 8a: Single temperature plus power law fit suggested by Nagoya Univ. group for data from North Polar Spur. PbSt spectrometer.

b: As above, but TAP spectrometer response.

ORIGINAL PAGE IS
OF POOR QUALITY

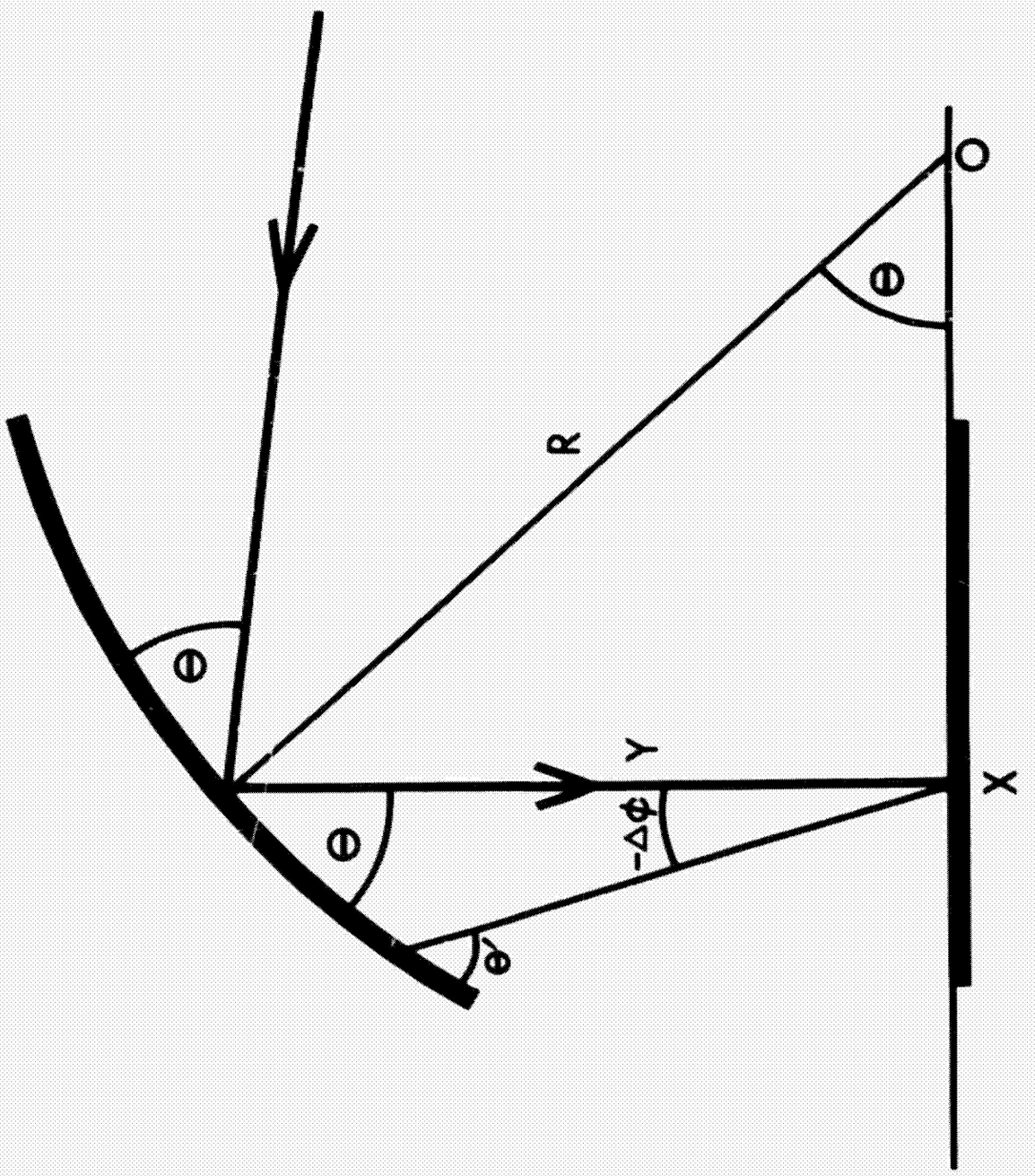

FIGURE 1

ORIGINAL PAGE IS
OF POOR QUALITY

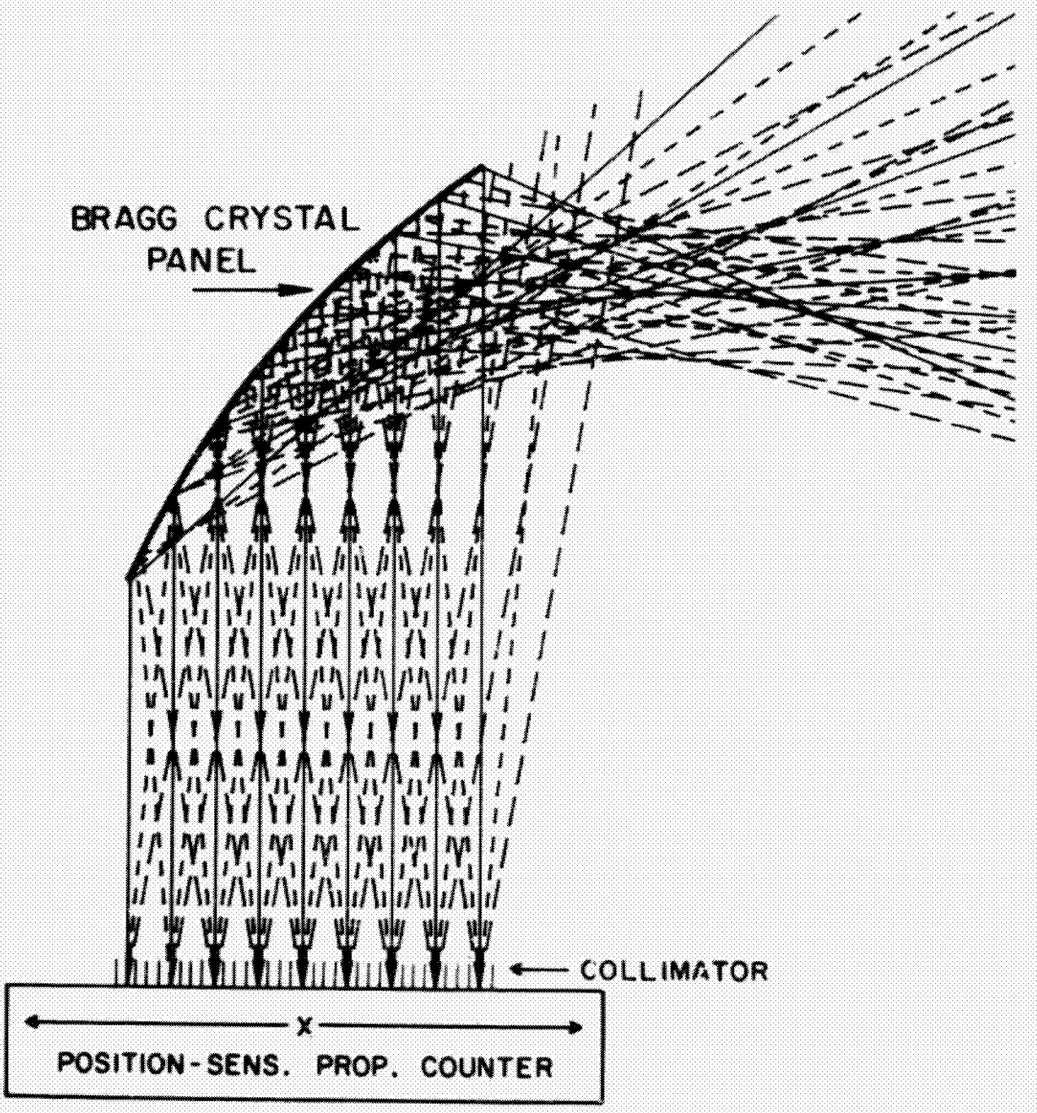

FIGURE 2

ORIGINAL PAGE IS
OF POOR QUALITY

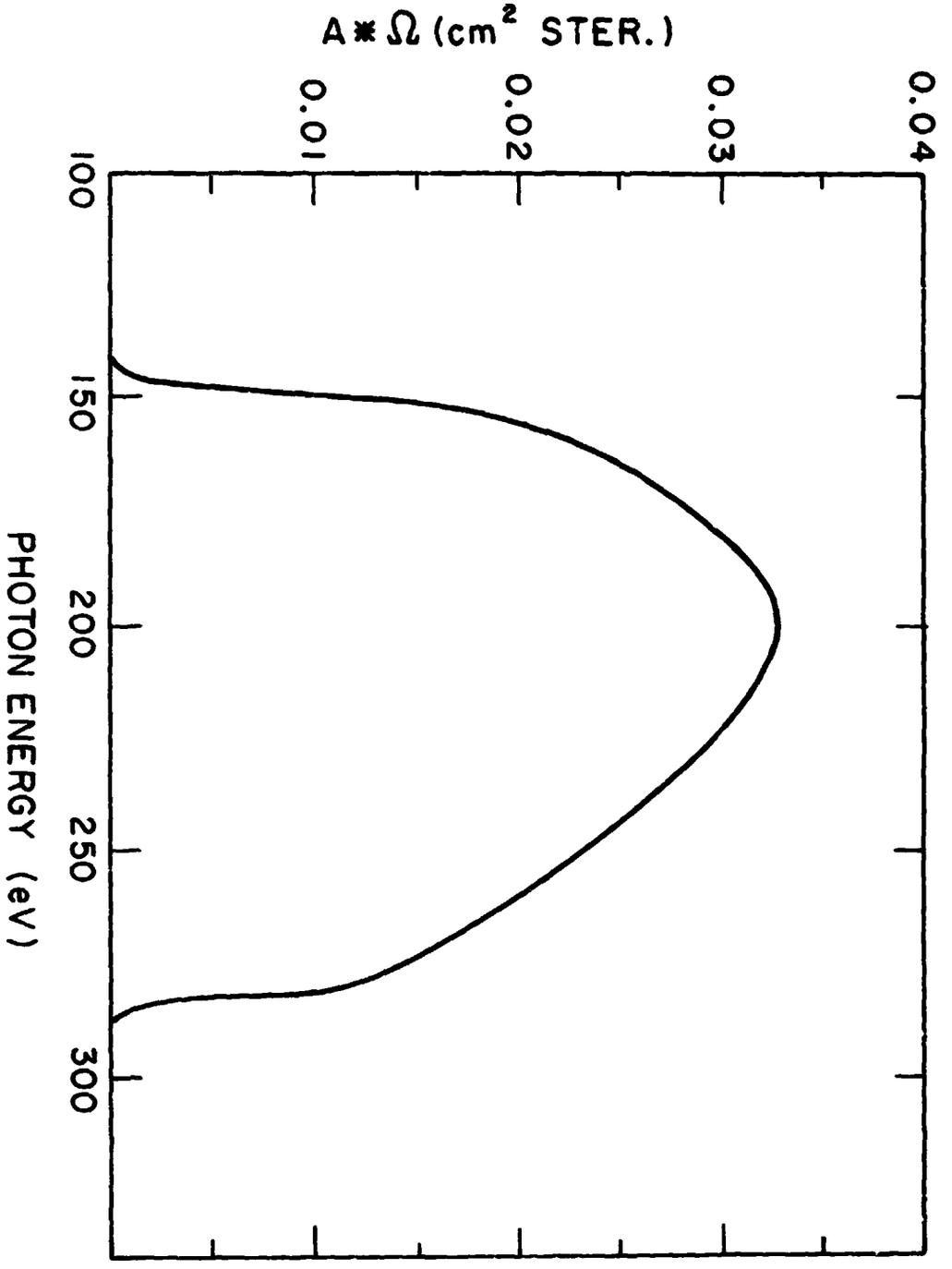

FIGURE 3

ORIGINAL PAGE IS
OF POOR QUALITY

ORIGINAL PAGE IS
OF POOR QUALITY

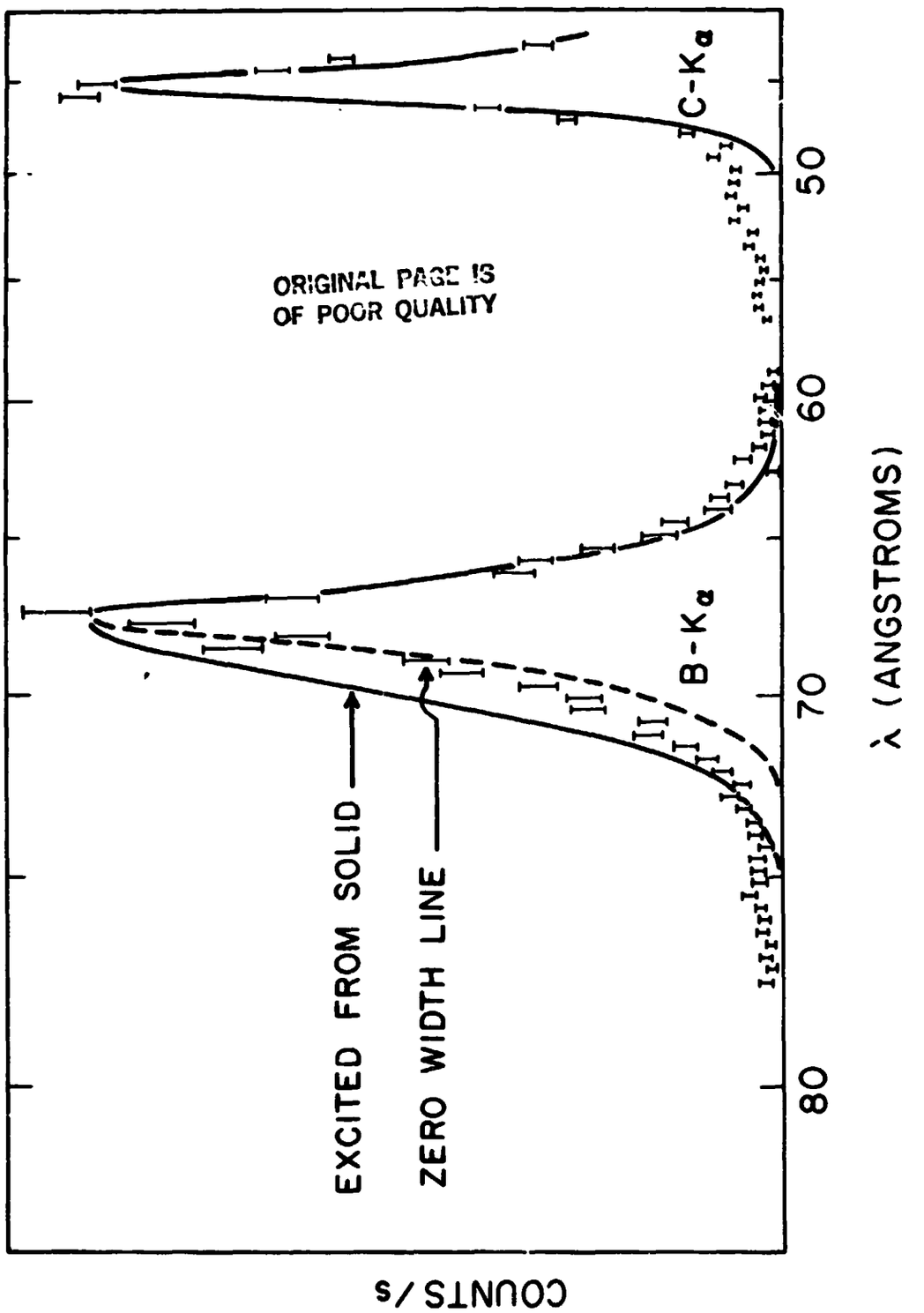

ORIGINAL PAGE IS
OF POOR QUALITY

FIGURE 4

ORIGINAL PAGE IS
OF POOR QUALITY

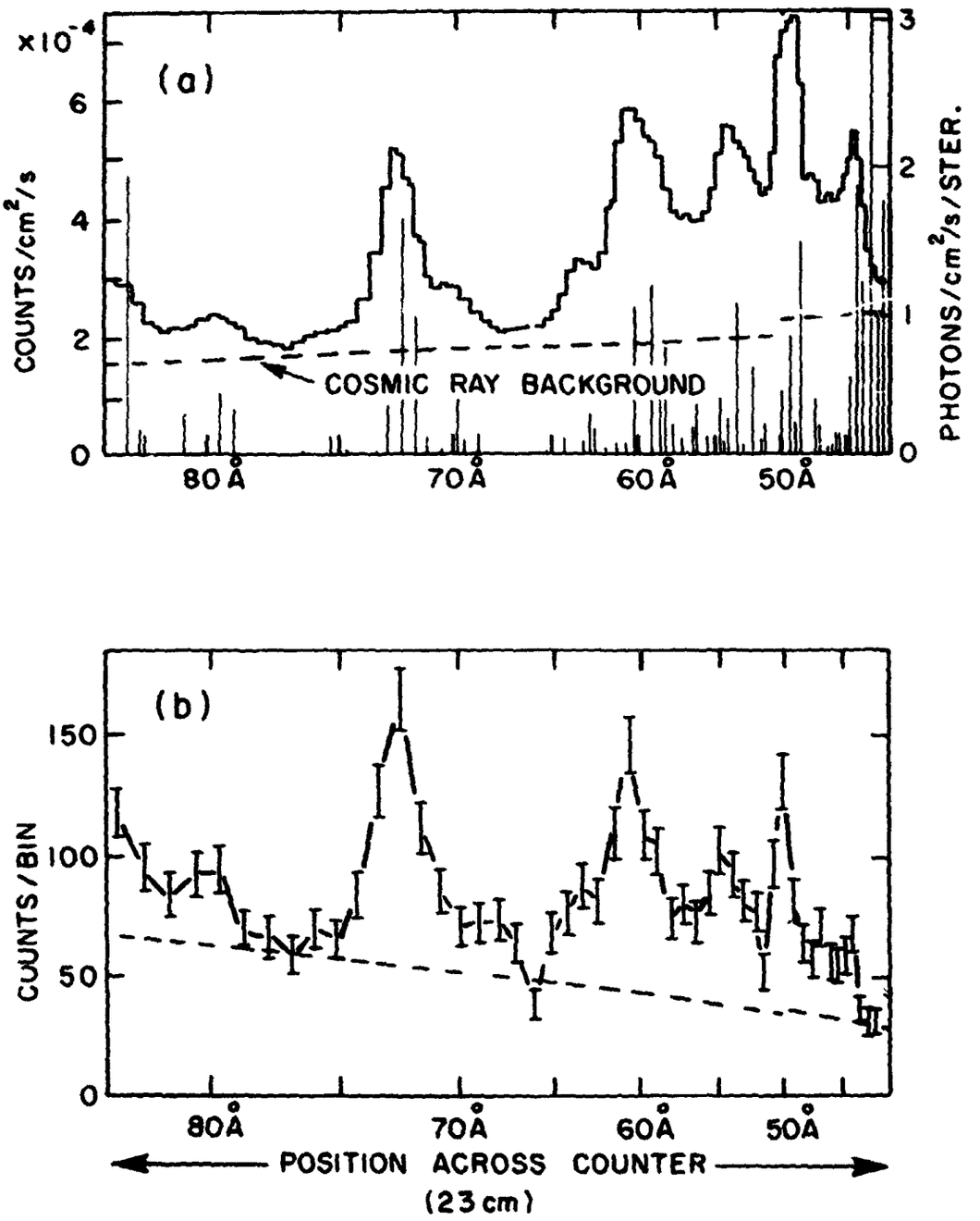

FIGURE 5

ORIGINAL PAGE IS
OF POOR QUALITY

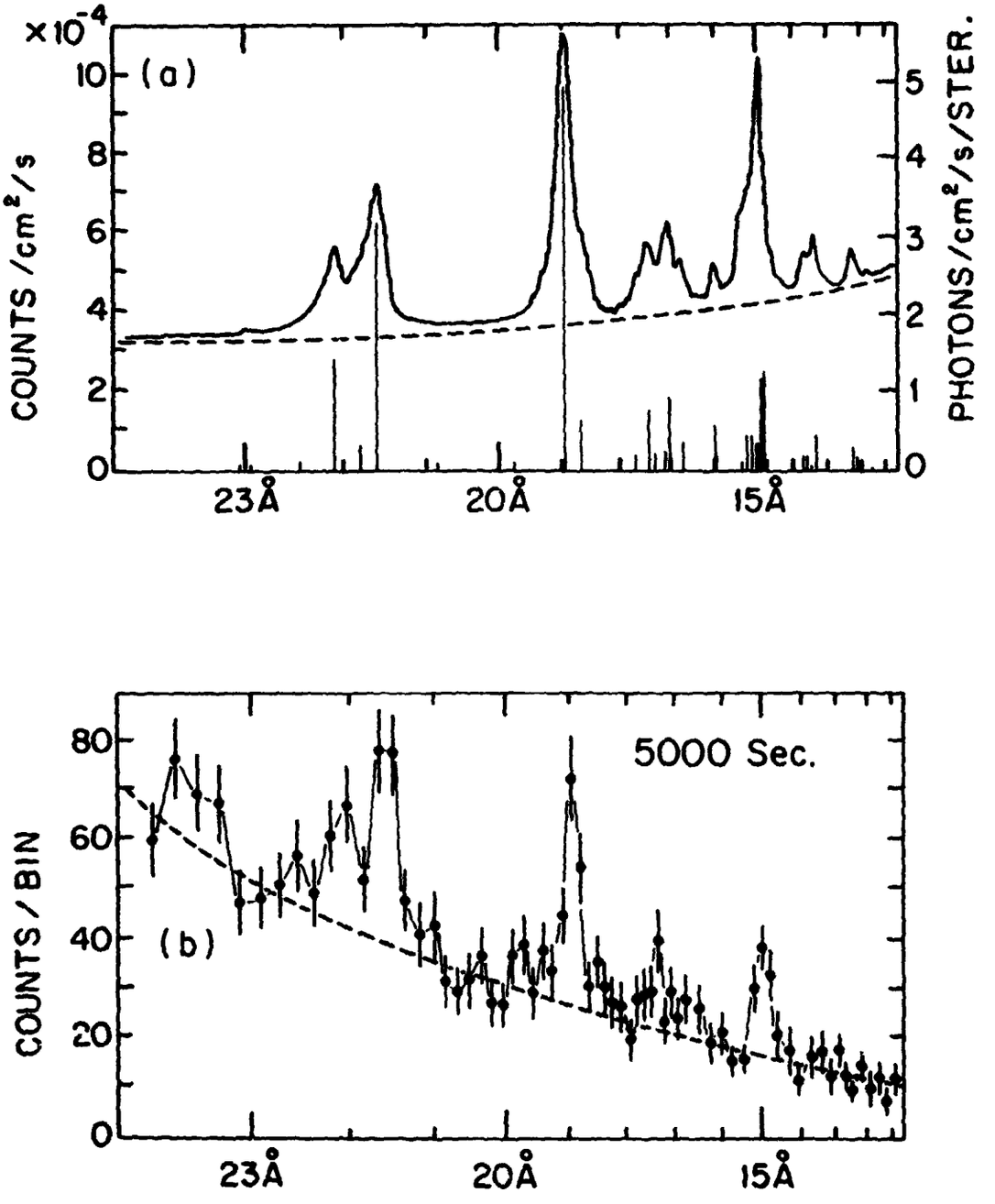

FIGURE 6

ORIGINAL PAGE IS
OF POOR QUALITY

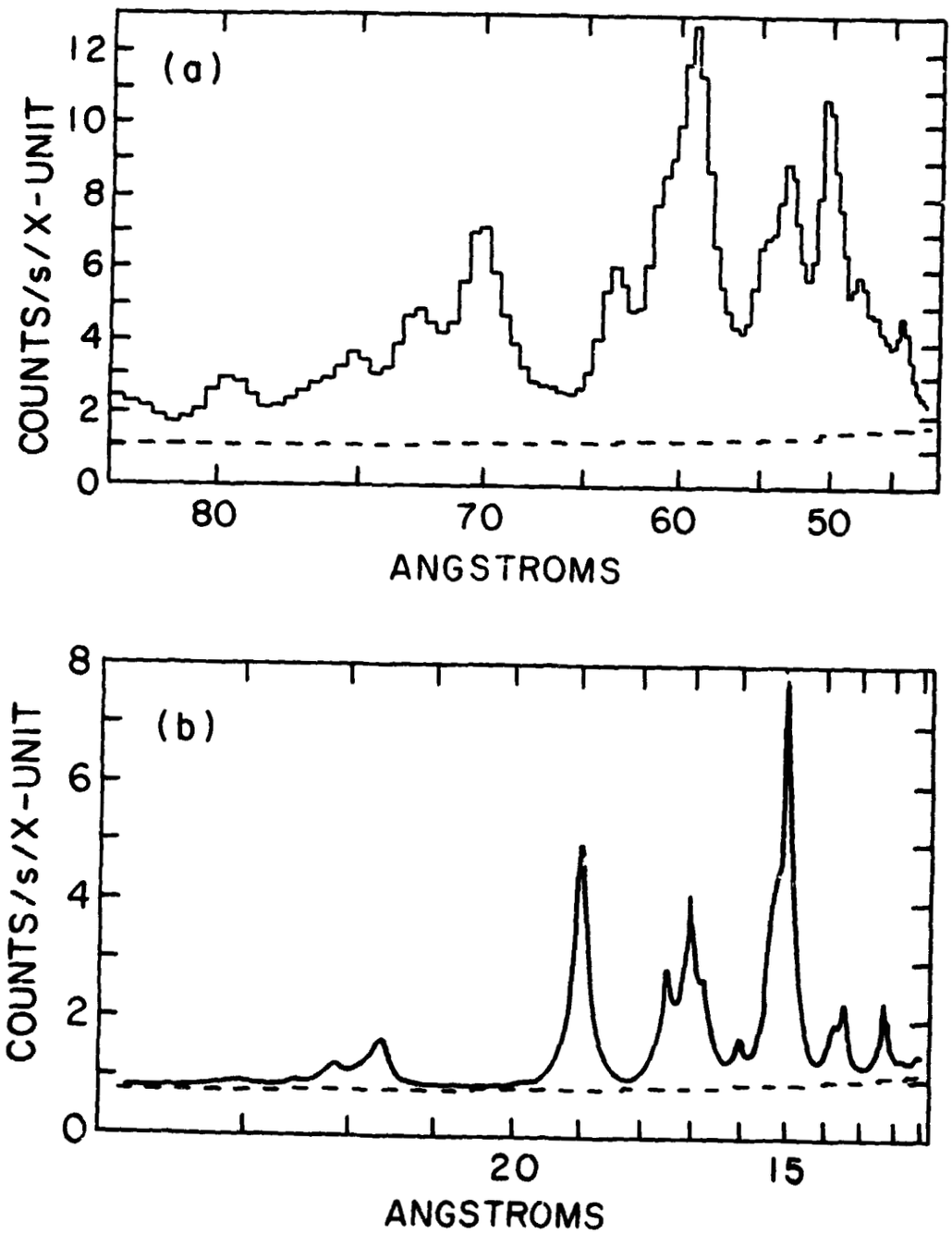

FIGURE 7

ORIGINAL PAGE IS
OF POOR QUALITY

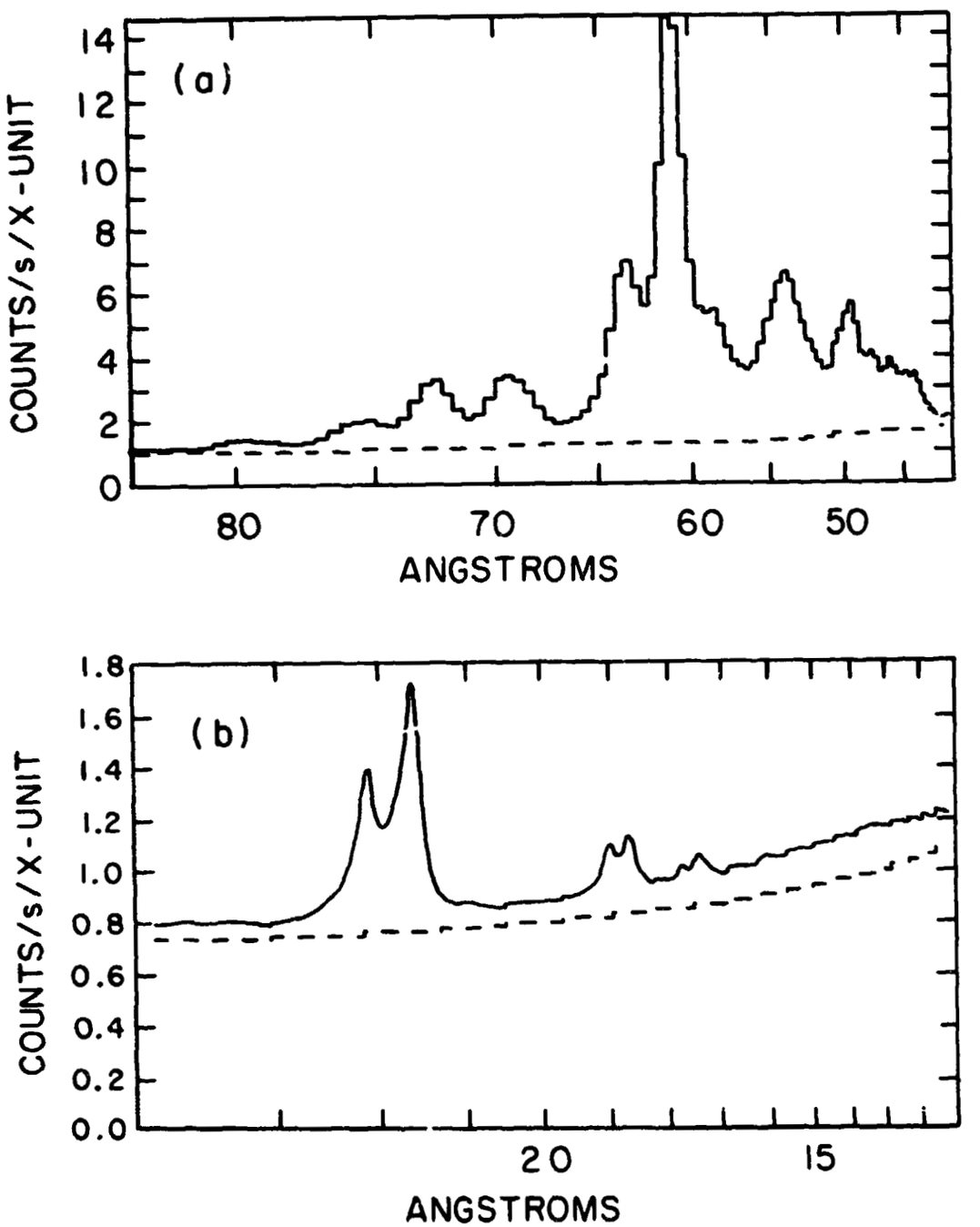

FIGURE 8

N82 26075

PRECEDING PAGE BLANK NOT FILMED

REQUIREMENTS FOR HIGH QUALITY X-RAY SPECTROSCOPY IN AN EXPLORER CLASS MISSION

Webster C. Cash, Jr.

Laboratory for Atmospheric and Space Physics
University of Colorado
Boulder, Colorado 80309

ABSTRACT

Through the use of simulated x-ray spectra we address the question of instrument requirements for a spectrograph that could significantly advance x-ray astronomy. We conclude that resolution ($\lambda/\Delta\lambda$) in the range of 200-500, and effective collecting area in excess of 200 cm^2 are required. We present one design, based on the objective reflection grating concept, which would meet these stringent requirements in an Explorer class mission.

I. INTRODUCTION

In the last meeting of this nature, the Workshop on Compact Galactic Sources, Rappaport (1979) gave a brief overview of x-ray astronomy in terms of the three major disciplines: imaging, spectroscopy and timing. At that time, with the Einstein Observatory starting operations, x-ray imaging had reached a level of maturity far beyond that of timing or spectroscopy. The workshop concluded that an X-ray Timing Explorer was the next logical step to balancing the advance of x-ray astronomy. But, the decision to pursue timing at the expense of spectroscopy was made on technological and budgetary grounds; we know how to build a timing experiment faster and cheaper than a spectroscopy experiment. Now, with XTE in the Explorer queue, our attention must turn to spectroscopy if new scientific domains are to be opened.

The history of astrophysics also supports the argument that spectroscopy must be next. Optical astronomy did not evolve into astrophysics until well into this century, when high quality photographic spectroscopy was developed and the results interpreted through modern physics. At the turn of the century, optical astronomy was in a situation very similar to the current status of x-ray astronomy. The first concave grating spectrograph of the sun, obtained by Rowland (1882), showed an amazing wealth of information. The Solar Maximum Mission is currently showing us a fabulous array of x-ray spectral features in the sun. Yet, following Rowlands solar spectrum, there was a delay of more than twenty years before observatories became sufficiently sensitive to study stars with high resolution. In that same period imaging became quite advanced: The first photographic surveys of the sky were completed, and extragalactic astronomy was born through the discovery of vast numbers of nebulae. Simultaneously, timing studies were advancing with the quantitative studies of eclipsing

variables and novae. The problem with spectroscopy was that the bright sources in the sky were, to first order, simple blackbodies, while the objects with exotic spectra were too faint to observe.

Today, we know from low resolution x-ray spectroscopy that the brightest sources in the sky have, to first order, featureless continua , while many of the fainter sources have quite exotic spectra. The pursuit of very high resolution spectroscopy of bright sources, and adequate resolution spectroscopy of faint sources, is still the primary concern of optical astronomers. Over ninety percent of all observing time on the world's major telescopes is dedicated to spectroscopy. I think in the future it will be the same for x-ray astronomy.

In this talk I will address primarily the question of what performance level is needed before x-ray spectroscopy will mature. I will finish with my suggestion of how the necessary performance level can be achieved.

II. A SIMULATED X-RAY SPECTRUM

The quality of a spectrum, and hence the quality of science derived from it, depends on a variety of factors in the spectrograph and in the source. The performance of a spectrograph is mainly determined by spectral resolution and collecting area, while bandpass and noise characteristics play lesser roles. Since the spectrograph must be able to clearly detect the targeted spectral features, so the brightness of the source, as well as the size and shape of its spectral features play a central role in determining the spectrograph design.

To investigate the interplay between spectrograph design and source characteristics I have performed a simple computer simulation. With the help of Mike Shull, I have created a synthetic spectrum containing many of the x-ray

spectral features we know should be present. Then, by smoothing the spectrum I could determine the resolution necessary to locate, separate, and identify typical features. By introducing varying amounts of Poisson noise, I could determine how many photons are needed to make the features statistically significant. Through this exercise I have reached some conclusions that I believe are convincing.

III. RESOLUTIONS

The initial spectrum entered in the computer was an array one thousand elements long, with each bin of 2eV width. Thus, the spectrum extended up to 2 keV. By doing a simple boxcar smooth, I was able to simulate lower resolution spectra.

The series of smoothings is shown in Figure 1. Part (a) shows the spectrum smoothed to 280eV, typical of a proportional counter. The spectrum is devoid of features. Pulse height spectra such as these were obtained with HEAO-1, and through a clever inversion technique found the O absorption edge in the Crab and Sco X-1 (Kahn and Blissett, Charles et al., Kahn et al).

Moving to Figure 1(b) we see a smooth spectrum with a ledge at the position of the oxygen edge. It has a resolution of 180eV, similar to that of the SSS on Einstein, although the SSS was not able to observe below about 600eV.

Tripling the resolution (to 64eV) in 1(c) produces a dramatic difference. The absorption dip at the O edge is clearly delineated, and an emission line has appeared at the position of the Fe L lines. Figure 1(d) doubles the resolution again, with the effect of sharpening the emission line and hinting at structure in the O edge.

In Figure 1(e), where the resolution is 16eV (comparable to the OGS on Einstein), the structure in the O edge has clearly become an absorption line

at the position of the O VIII Lyman α line. The iron line is starting to show structure.

The next doubling of resolution, to 8eV, brings with it the resolution of the iron line into a complex of closely spaced lines. Also visible for the first time is the fact that the intensity drop across the O edge is not a single step. Several ionized species of oxygen are contributing to the edge.

At a resolution of 4eV in Figure 1(g) the last hidden feature emerges. A weak absorption line at the position of the O VIII Lyman α line is visible.

The last part, Figure 1(h), shows the original spectrum with full 2eV resolution. It now shows the O VIII absorption line to be saturated; the Fe line complex is fully resolved.

With each improvement in resolution we discovered new features in the spectrum until, in the last two graphs, all of the original features were apparent. By pushing the resolution beyond 2eV one could study emission and absorption line profiles, but this would require resolution of nearly 0.2eV. Since we currently don't even know the gross spectral features of x-ray sources, talk of observing line profiles seems a little absurd - that should be left for the following generation of spectroscopy. In short, 2ev resolution will be enough to discover and classify features, but little extra will be gained until resolution is almost an order of magnitude higher.

Converting to the more conventional spectroscopy notation,

$$R = \frac{\lambda}{\delta\lambda} = \frac{E}{\delta E} = \frac{500eV}{2eV} = 250.$$

IV. POISSON NOISE

In spectroscopy as in imaging, Poisson noise is the great enemy of the x-ray astronomer. Our experiment must collect enough photons in each spectral

resolution bin to make the bin-to-bin variations (which carry the information) sufficiently small. To investigate this effect, I have taken the same synthetic spectrum at full resolution and run a Poisson randomizer over it with various scale factors. The results are displayed in Figure 2. Taking the figure part by part:

a. This is a minimal spectrum, typically two photons per bin, with a total of 1281 counts in the spectrum. Nothing is visible except the overall shape of the curve, an exponential with an interstellar cutoff.

b. With 10 c/bin we start to see the O edge.

c. At 30 c/bin the O edge is clear. The O VIII Ly α is becoming statistically significant.

d. With 100 c/bin the spectrum is looking fairly good. Most of the major features are visible. The biggest problem is that, while it is clear that the features are present, quantitative statements about their size will be inaccurate.

e. This is an excellent spectrum. With 1000 c/bin all the features are clear, and quantitative assessment is clearly possible.

f. At 10^4 c/bin there is virtually no difference between the original and the randomized spectra.

From Figure 2 we have learned that a spectrum with less than 100 c/bin is inadequate while in most cases 10^4 c/bin is more than is required. A good number to shoot for is 1000 c/bin, and a barely adequate spectrum is 100 c/bin. I recommend that the Explorer be able to obtain 100-1000 c/bin in a reasonable period of time on all prime sources.

The situation is different when emission line sources are considered. Take the case of the synthetic emission line spectrum shown in Figure 3(a). When these lines are Poisson randomized we find that far fewer photons are

required. Figure 3(b) is the same spectrum with a total of only 46 photons, rebinned into 80 bins to best show the data. It is a fair representation of the original spectrum. Figure 3(c) is a similar spectrum with 188 photons. In 3(d) we have 830 photons and in 3(e), 55,000 photons. It is clear that in order to retrieve the basic physics of a line source, only 100 photons per line are needed. A total of 10^4 photons should show all the major features in a line source. This compares to the 10^5 to 10^6 photons required for a good spectrum of a continuum source. It is particularly good news for the studies of stellar coronae and supernova remnants.

V. COLLECTING AREA

Starting with the level of statistics recommended in the previous section, we can derive the needed spectrograph collecting area. With an Explorer, a typical observation should be completed in 2×10^4 seconds of exposure. In real terms this requires an entire day. In this amount of time we require enough collecting area to observe a large number of sources from many classes. This diversity of application is necessary if the Explorer is to make a major contribution to astronomy.

In Table I we list the four most prominent classes of x-ray point sources: the x-ray binaries, stellar coronae, Seyfert galaxies, and quasars. We would like to be able to observe ten or more objects in each of these classes, so we have listed the approximate flux (in HEAO-2 IPC counts) of the tenth brightest member of each class in column 2. In column 3 this flux has been converted to ph $cm^{-2}s^{-1}bin^{-1}$, except in the case of stellar coronae where it is in units of ph $cm^{-2}s^{-1}line^{-1}$. Multiplying by the maximum observing time (2×10^4s) we obtain column 4 which shows the ph $cm^{-2}bin^{-1}$ collected. Then, it is an easy matter to calculate column 5, the collecting area needed to achieve the desired 1000 c/bin, or for coronae, the 100 c/line.

It is apparent that, at an absolute minimum, the spectrograph should have 50 cm^2 of collecting area. This would permit the collection of good data on stellar coronae and x-ray binaries, but barely reach the Seyferts. It would fail completely on the quasars. However, with 200 cm^2 the Seyferts could be well studied, and the brightest quasars would be within reach. This higher collecting area valuable on the x-ray binaries and coronae as well, since it is less likely that variability could change the spectrum before the observation is completed, and more targets could be observed.

I recommend that the spectrograph have no less than 200 cm^2 effective collecting area.

VI. SPECTROGRAPH DESIGN

We are now faced with a very large order: Design an Explorer class instrument with resolution of 250 and collecting area of 200 cm^2. I believe it can be done, and in this section I outline one possible design.

The first point to recognize is that we must use dispersive spectroscopy coupled with grazing incidence optics. All alternatives simply will not produce the required performance. Crystal spectrographs will not achieve the necessary collecting area in a reasonable size payload because crystals operate by absorbing the great bulk of the incident photons. Solid state spectroscopy has low resolution (180eV versus the 2eV required), and there is no foreseeable chance that it will achieve high resolution during this generation. The only other alternative is dispersive spectroscopy.

In the soft x-rays we have the choice of either transmission gratings or reflection gratings for the dispersive element. There are arguments in favor of each of these which I do not wish to pursue here. I will merely say that I

personally believe that in the future x-ray astronomers, like optical astronomers, will perform virtually all their spectroscopy with reflection gratings. Reflection gratings offer higher efficiency, greater stability and higher dispersion - all properties of central importance to achieving high spectral resolution.

I have been investigating in the laboratory the level of efficiency one can expect from reflection gratings. Figure 4 shows the result obtained on a gold coated grating at 13 Å (Cash and Kohnert, 1981). This grating, replicated from a 6000 ℓ/mn, 21^{o} blaze master, was ruled by Hyperfine, Inc. to make an optical element for the High Resolution Spectrograph on Space Telescope. It shows a peak efficiency of 40% in first order. With a nickel coating this would have been closer to 50%. Such very high efficiency is critical to achieving the 200 cm^2.

In addition, it is necessary to keep the number of elements in the optical train to an absolute minimum. With this is mind I have been working on the concept of the Objective Reflection Grating Spectrograph (ORGS), which, coincidentally, maximizes spectral resolution. It is quite simple, requiring only that an array of reflection gratings be mounted in front of an x-ray telescope such that the telescope views the surface of the gratings.

I have joined in a collaborative effort with Dr. Richard Catura of the Lockheed Palo Alto Research Laboratory and Dr. J.L. Culhane of the Mullard Space Sciences Laboratory to build an ORGS. We are modifying their existing telescope to hold an array of reflection gratings as shown in Figure 5. It is an Aries class telescope, and we hope to obtain our first spectrum from a rocket flight in one to two years.

It can be shown that the resolution ($\lambda/\Delta\lambda$) of an ORGS is given by

$$R = \frac{n\lambda}{d \cdot B}$$

where n is the order number, λ the wavelength, d the grating ruling spacing, and B the telescope resolution in radians. We take the best telescope resolution consistent with an Explorer mission and a proportional counter detector to be 20" ($B = 10^{-4}$). The highest ruling density currently available is about 10^4ℓ/mm or d = 1000 Å. Thus, if R = 250 we must have

$$n\lambda = 25 \text{ Å}.$$

At energies below 0.5keV we can achieve full resolution and collecting area, while above this energy we have the choice of either full collecting area and reduced resolution (1st order), or full resolution and reduced collecting area (higher orders). This is not an ideal situation, but it is adequate.

The telescope needed to support this concept is of reasonable size. To achieve a 200 cm^2 spectrograph, we need a telescope with an effective area of 400 cm^2. A telescope the same size as ROSAT will suffice, but the mirrors need only perform at the 20" level. A proportional counter with .125 mm resolution is adequate, although one might hope that some other efficient, imaging detector might become available.

We conclude by pointing out that objective gratings cannot perform well on extended sources. There is a possible solution. A 1 x 30 arcminute collimator mator could be mounted in front of the gratings, allowing study of extended objects with R = 80.

VII. SUMMARY

I have demonstrated that in order for x-ray spectroscopy to become a serious tool of astronomy, we need to build a spectrograph with resolution in excess 250 and collecting area in excess 200 cm^2. I have presented the ORGS concept, which I believe is the easiest way to achieve these stringent specifications.

I wish to thank R. Catura and M. Shull for help in preparing this talk. I acknowledge support from NASA grant NAG5-96.

TABLE 1: TARGET FLUXES

	FLUX 10th BRIGHTEST (IPC COUNTS)	ph $cm^{-2}s^{-1}bin^{-1}$ (R = 200)	in 2×10^4s ph $cm^{-2}bin^{-1}$	cm^2 needed for 1000 ph/bin or 100 ph/line
X-RAY BINARIES	30	1.5×10^{-3}	30	30
SEYFERTS	3	1.5×10^{-4}	3	300
QUASARS	0.2	1×10^{-5}	0.2	5000
STELLAR CORONAE	1	1×10^{-4} ph $cm^{-2}s^{-1}line^{-1}$	2 ph $cm^{-2}line$	50

REFERENCES

Cash, W. and Kohnert, R. 1981 Appl. Opt., in press.

Charles, P.A., et al., 1979, Ap. J. (Letters), 230, L83.

Kahn, S.M. and Blissett, R.J. 1980, Ap. J., 238, 417.

Kahn, S.M., Charles, P.A., Bowyer, S. and Blissett, R.J. 1981, Ap. J., in press.

Rappaport, S. 1979, in "Compact Galactic X-ray Sources," ed. F. Lamb and D. Pines, p. 181.

Rowland, H.A. 1882 Phil. Mag., 13, 469.

FIGURE CAPTIONS

FIGURE 1: A synthetic x-ray spectrum is shown smoothed to various resolutions: a) 280eV; b) 180; c) 64; d) 32; e) 16; f) 8; g) 4; h) 2eV. See text for discussion.

FIGURE 2: The synthetic spectrum with 2eV is shown randomized by poisson statistics with increasing number of photons.

FIGURE 3: The effect of Poisson statistics on a line spectrum is investigated.

FIGURE 4: 13A efficiency of a 6000 ℓ/mm reflection grating is shown as a function of graze angle.

FIGURE 5: Schematic of an Objective Reflection Grating Spectrograph

ORIGINAL PAGE IS
OF POOR QUALITY

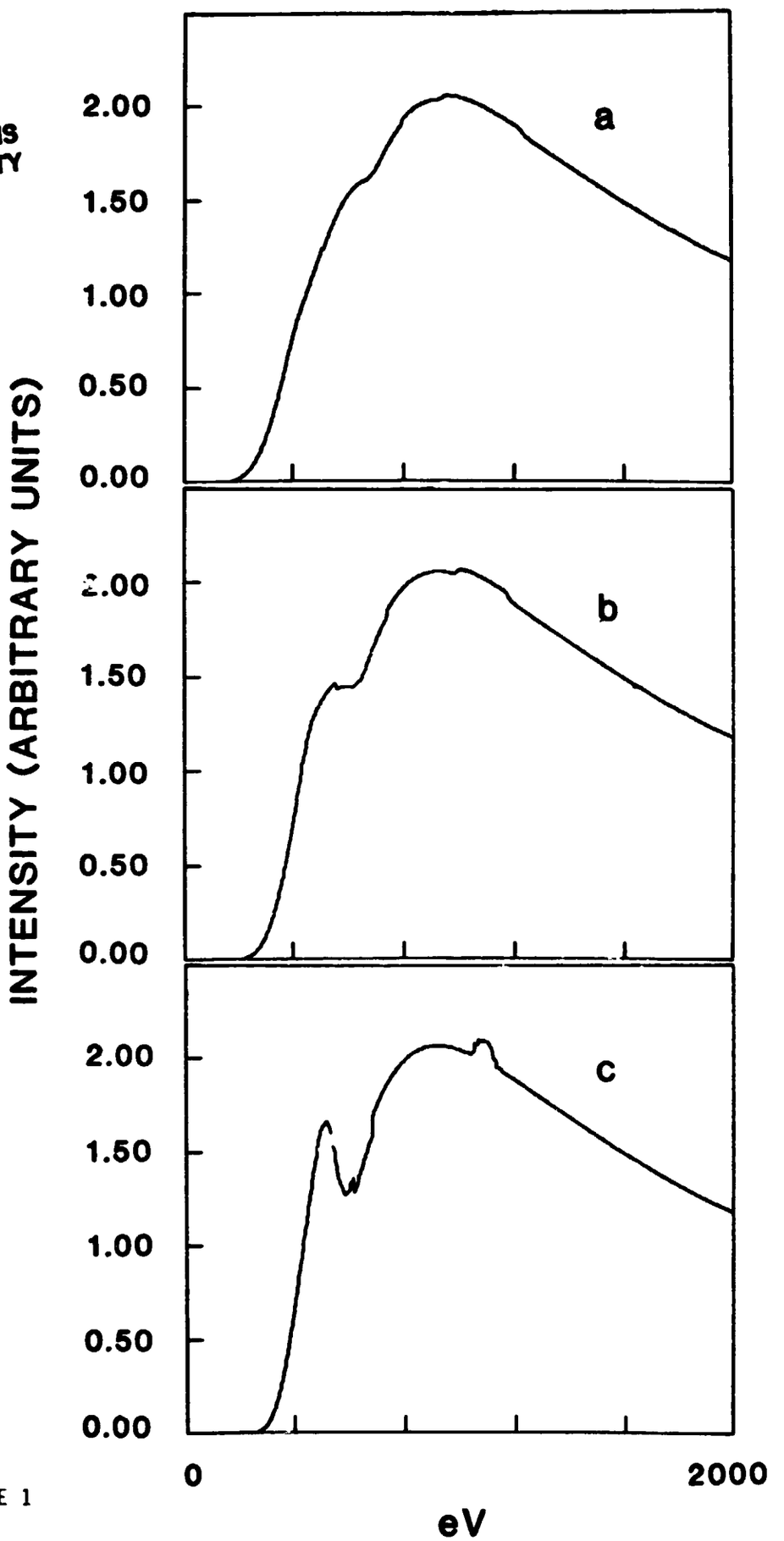

FIGURE 1

ORIGINAL PAGE IS
OF POOR QUALITY

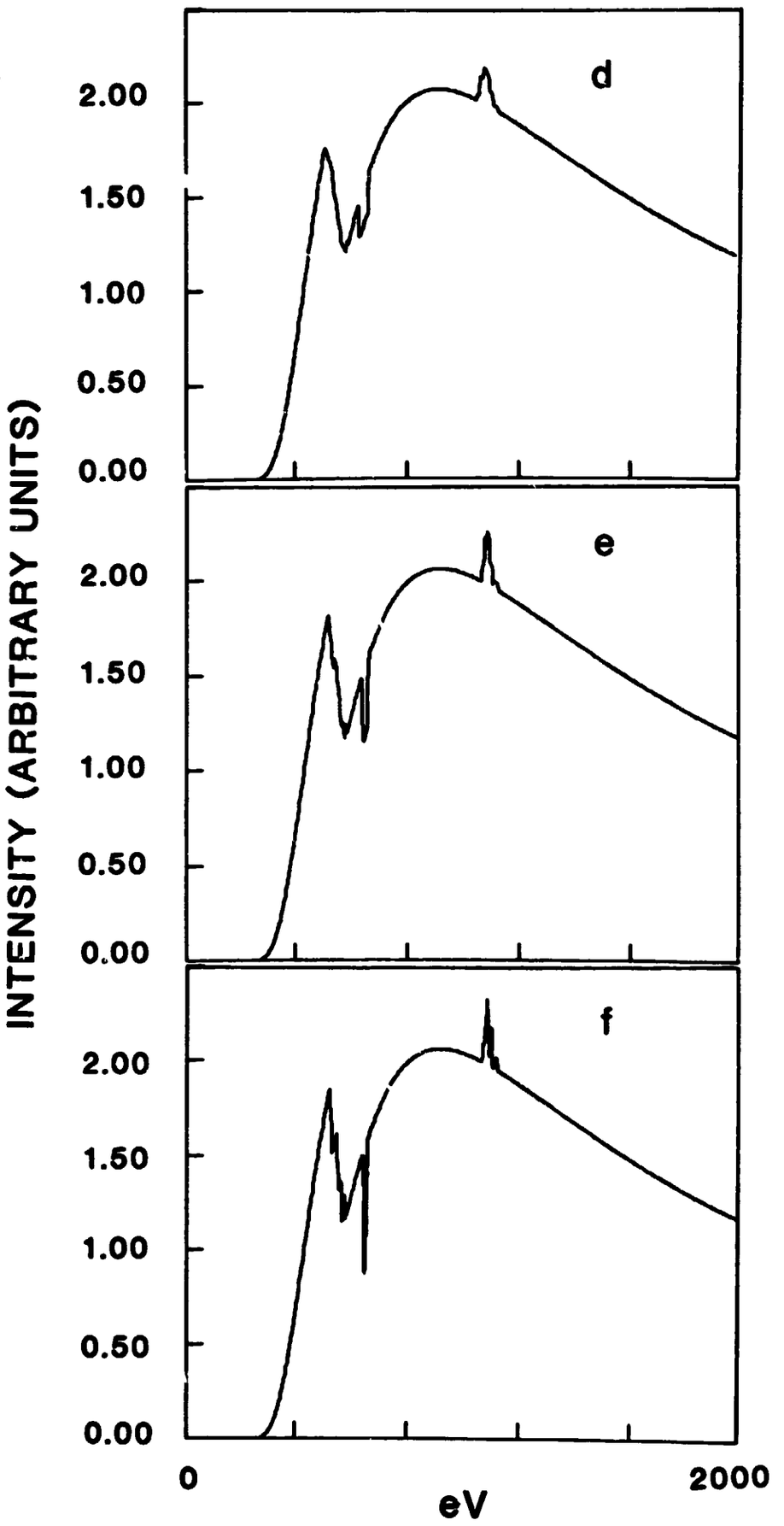

ORIGINAL PAGE IS
OF POOR QUALITY

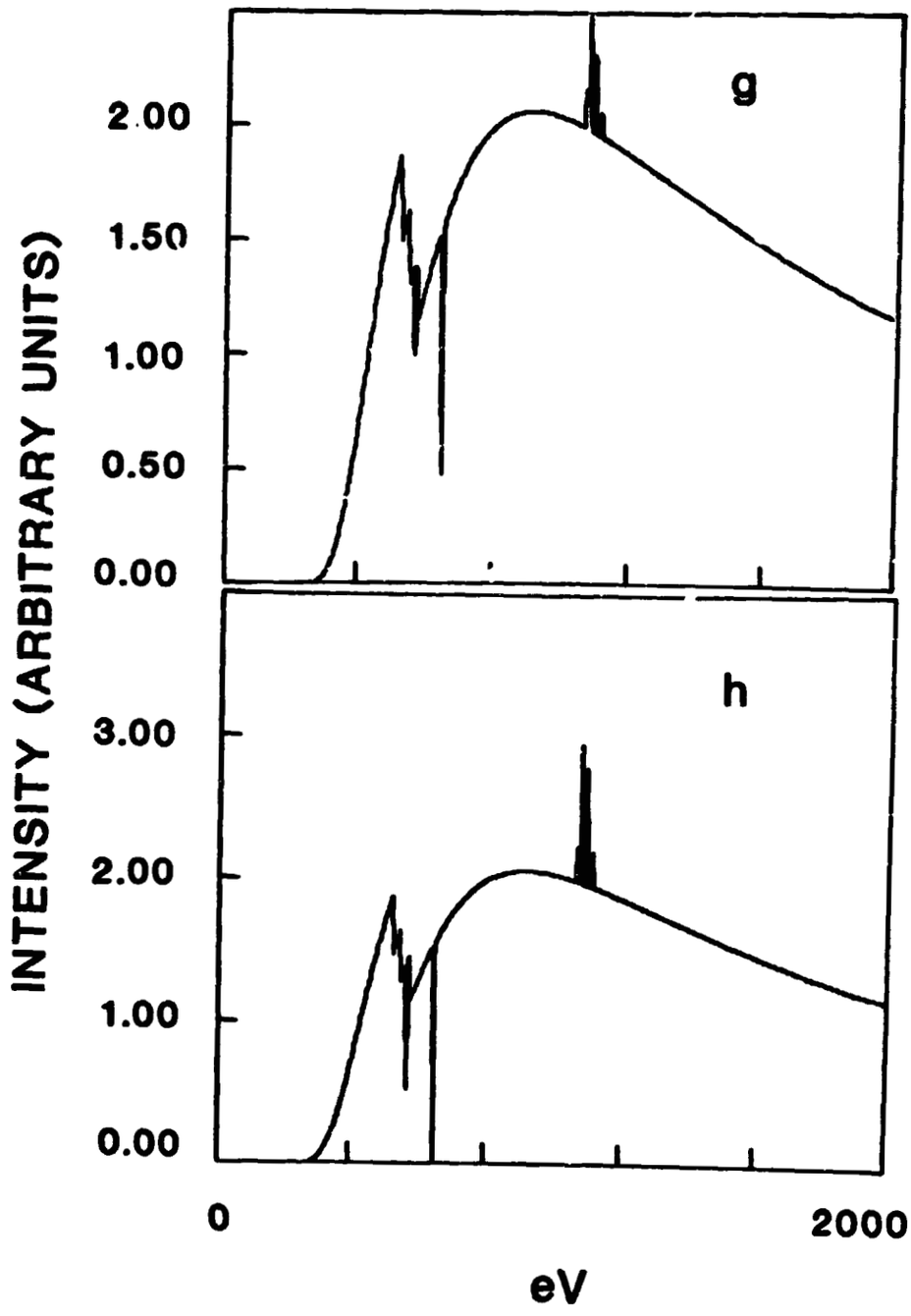

ORIGINAL PAGE IS
OF POOR QUALITY

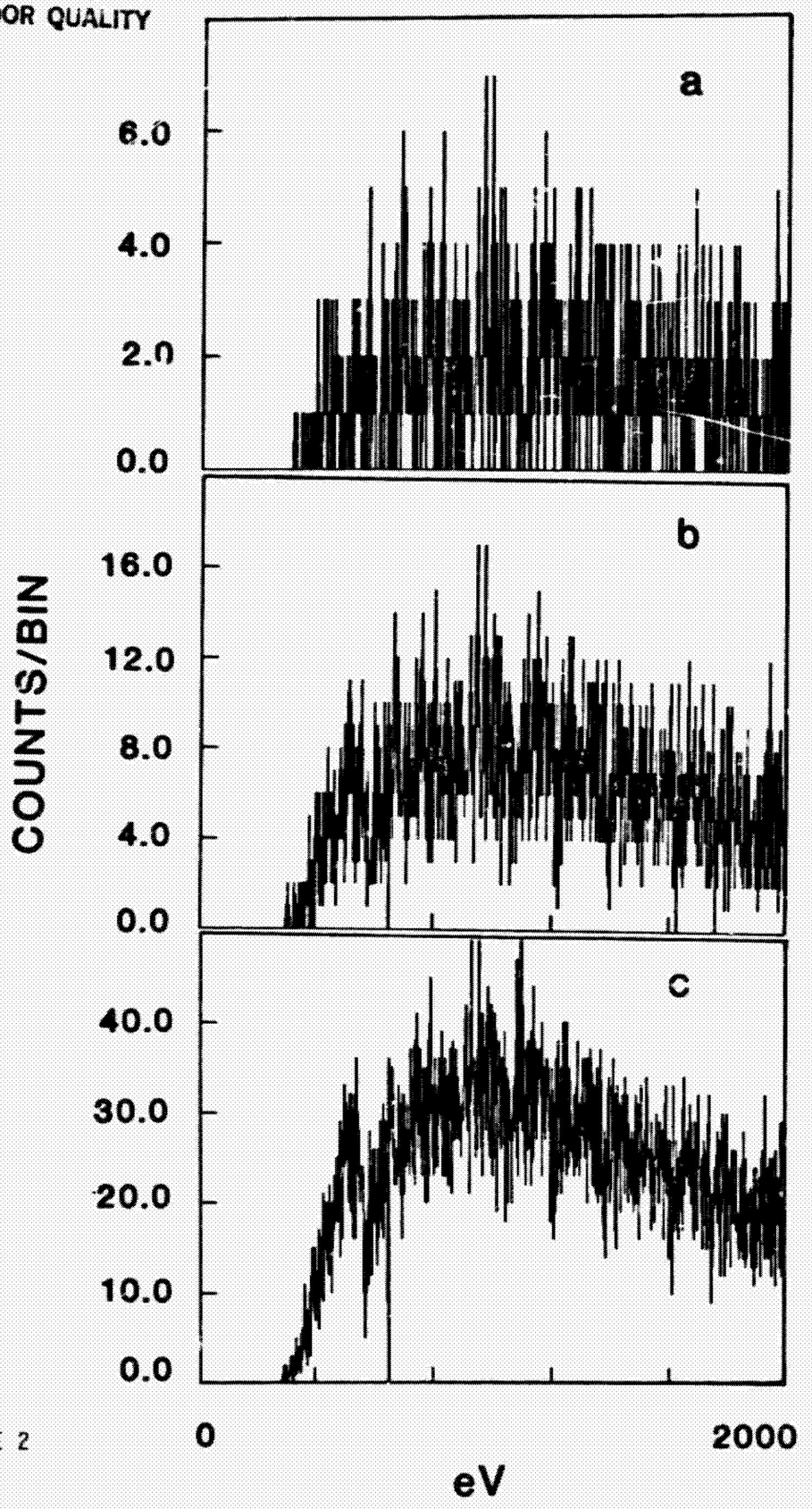

FIGURE 2

ORIGINAL PAGE IS
OF POOR QUALITY

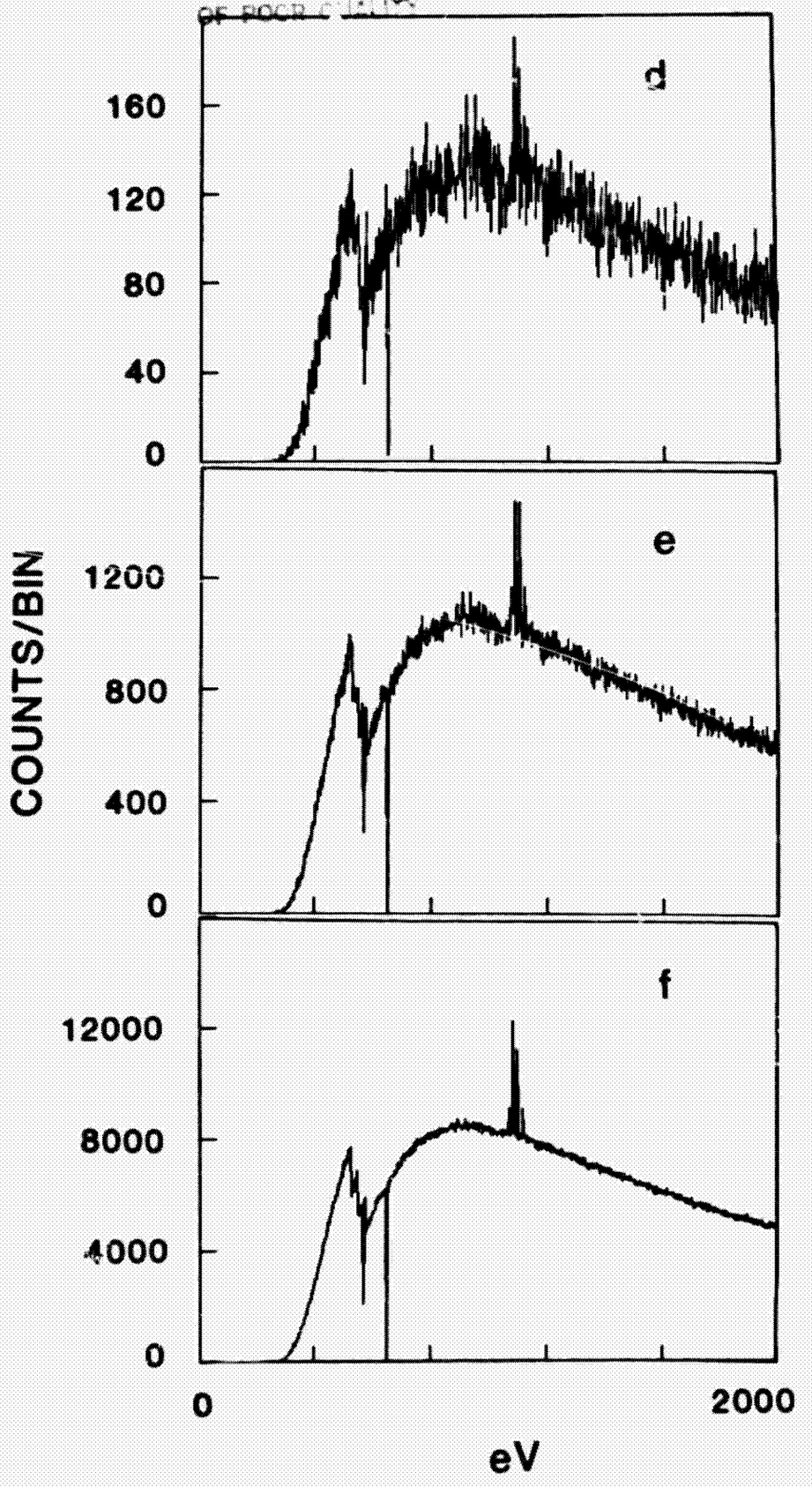

ORIGINAL PAGE IS
OF POOR QUALITY

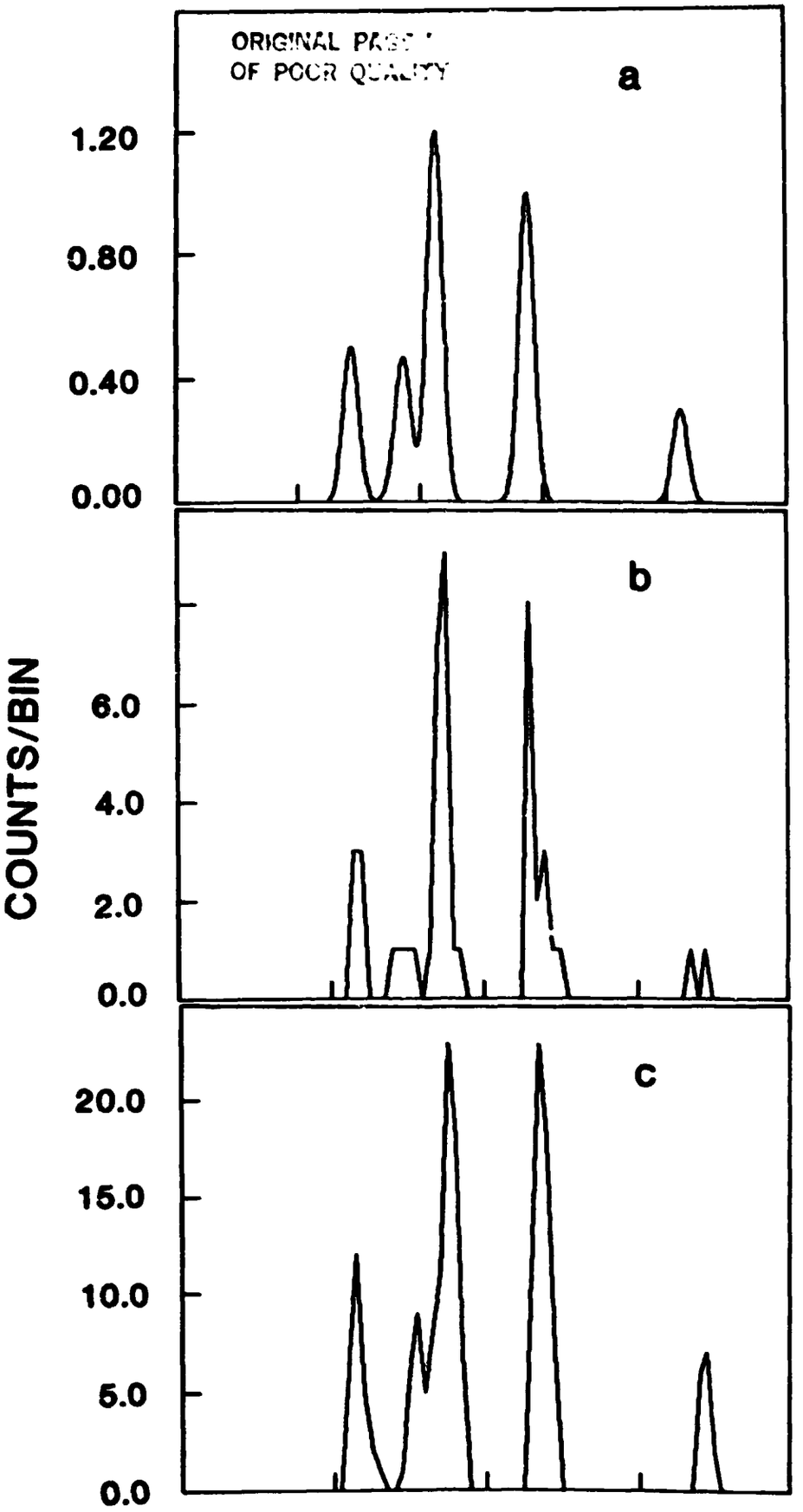

FIGURE 3

ORIGINAL PAGE IS
OF POOR QUALITY

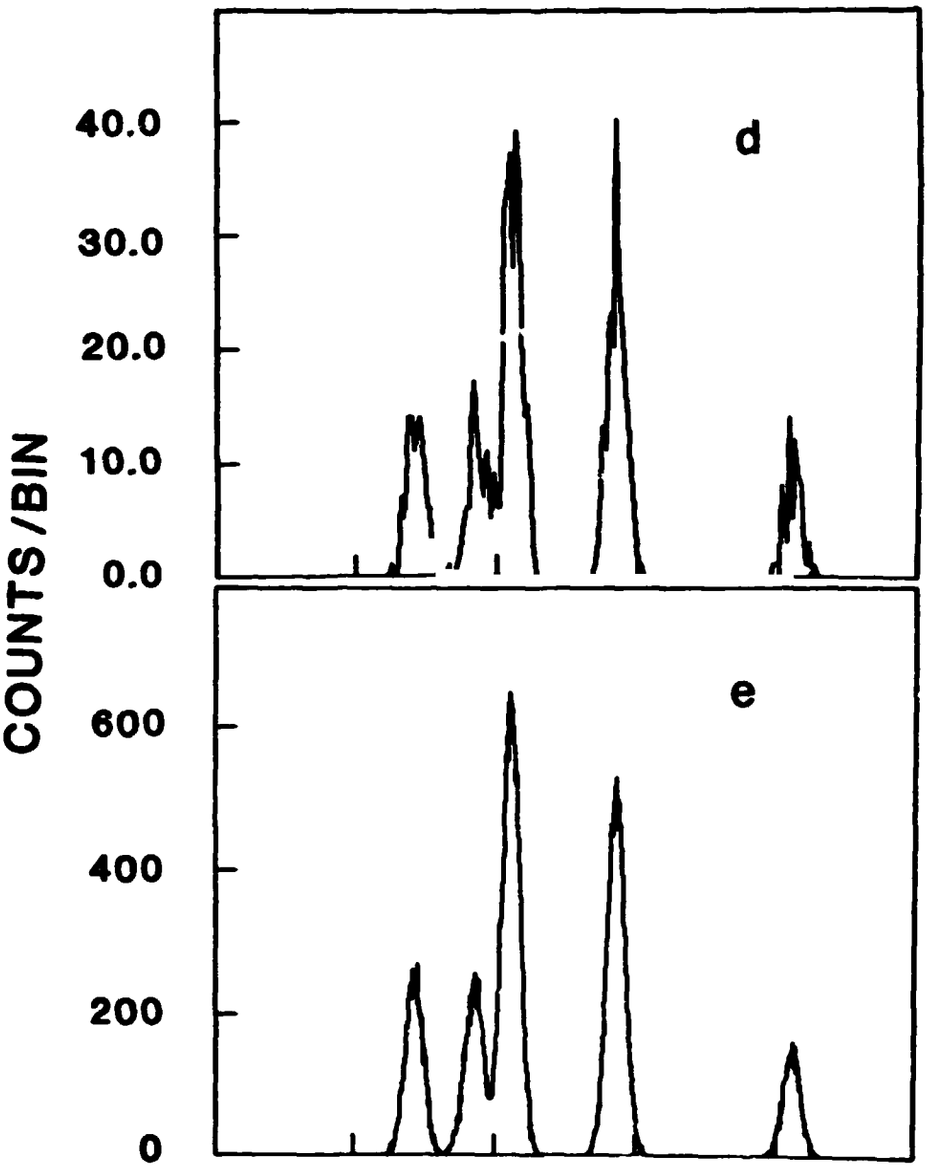

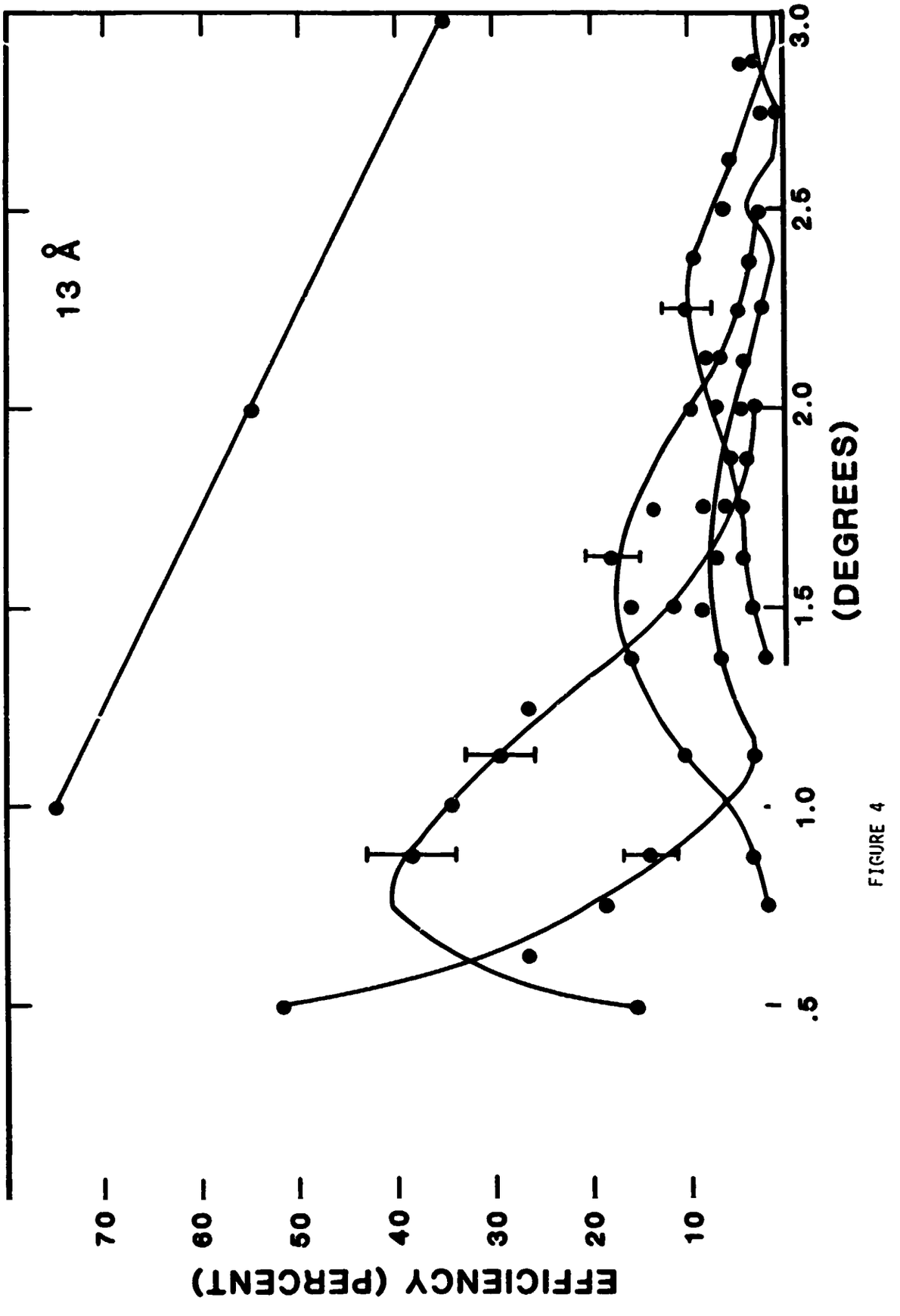
EFFICIENCY (PERCENT)
70
60
50
40
30
20
10
13 Å
.5
1.0
1.5
2.0
2.5
3.0
(DEGREES)

FIGURE 4

ORIGINAL PAGE IS
OF POOR QUALITY

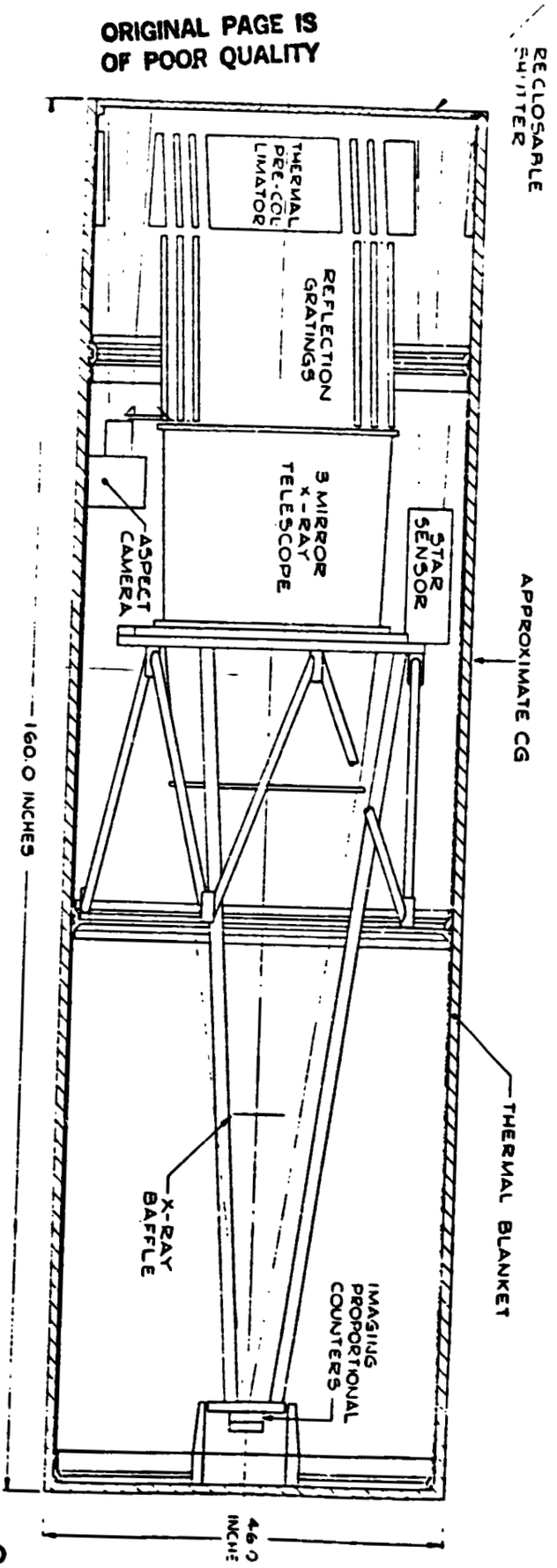

FIGURE 5

ORIGINAL PAGE IS
OF POOR QUALITY

N82 26076

FUTURE PROSPECTS FOR HIGH RESOLUTION X-RAY SPECTROMETERS

Claude R. Canizares

Center for Space Research, M.I.T.

and

Institute of Astronomy, University of Cambridge

I. INTRODUCTION

The task I set myself for this meeting was to review and compare the capabilities of the kinds of X-ray spectroscopy payloads I knew about, to compare those with some of my own estimates of the anticipated capabilities of AXAF, and to do this in the context of the science we want to achieve. Let me preface all this by echoing in general terms what many of yesterdays speakers said in detail; namely that Einstein has demonstrated the tremendous scientific power of spectroscopy to probe deeply the astrophysics of all types of celestial X-ray source. However, its limitations of sensitivity and resolution have in most cases permitted us only to whet our appetites. The next generation of spectroscopic instruments can and will provide the banquet.

II. PARAMETERS OF X-RAY SPECTROMETERS

The comparison of alternative types of X-ray spectrometer is extremely difficult because so many orthogonal parameters must be considered and weighed against one another. A probably incomplete list of these includes the energy range, the sensitivity or throughput (which is usually a strong function of energy, E), the degree of background rejection, the resolving power ($E/\Delta E$, also often a function

of E), the degree of spatial and spectral multiplex advantage (ability to observe multiple spatial/spectral elements simultaneously), the effectiveness on extended sources (often involving trade-offs of throughput and resolution with field-of-view), the technical difficulty of the instrument and, not least, the size and weight.

a) General Considerations

I will only consider instruments capable of moderate to high spectral resolution ($E/\Delta E > 100$) on discrete celestial sources (but see McCammon's contribution) as the Einstein results demonstrate that this is what is needed for the plasma diagnostics of a source (e.g. Winkler et al. 1981). The state-of-the art then limits us to dispersive instruments. Another clear requirement is that any instrument has some degree of signal concentration so that the detector area (A_D is << the effective collecting area (A_C). This is simply because the lines from all but the strongest sources have fluxes $\lesssim 10^{-3} cm^{-2} s^{-1}$, instruments generally have peak efficiencies $\lesssim$ 20% and a more or less irreducible particle induced background rate for low-background detectors (achieved in flight by the FPCS and IPC as well as the Wisconsin rocket payload, for example) is $\sim 1 \times 10^{-3} cm^{-2} s^{-1} keV^{-1}$. One needs a concentration factor A_C/A_D just to achieve a signal-to-noise ratio > 1. Of course, with sufficient concentration an instrument becomes signal limited.

Dispersive spectrometers divide into two distinct classes: (i) Bragg spectrometers that use crystal diffractors (like the Einstein FPCS; see Giacconi et al 1979, Canizares et al. 1979) and (ii) spectrometers that use gratings in either transmission (like the Einstein OGS, see Schnopper et al. 1977) or reflection.

The Bragg instruments are capable of high spectral resolution, but they suffer the tremendous shortcoming of having no inherent spectral

multiplex advantage. The latter point is crucial, since meaningful plasma diagnostics require at least 4 - 6 line strengths. For Bragg instruments X-rays from a given direction incident on a given cm^2 of Bragg crystal, are reflected only in a narrow passband near the Bragg energy - all others are absorbed. The effective area at a given energy of a Bragg spectrometer is $A_{EFF} = A_{PROJ}\ \eta\ R_C/\Delta\theta$ where A_{PROJ} is the projected area of the diffractor (or telescope in a focal plane instrument), η is the total efficiency of all elements other than the diffractor, R_C is the inherent "integrated reflectivity" of the crystal, and $\Delta\theta$ is the total "acceptance angle" of the crystal (the range of incident angles on the crystal if it is bent or the range through which it is rocked). I assume a uniform area or exposure across $\Delta\theta$. R_C is approximately $\tilde{\propto}$ WR_P, where W is the "rocking curve width" of the crystal and R_P is its "peak reflectivity", so a near-optimum efficiency (A_{EFF}^{MAX}) is obtained if $\Delta\theta \sim W$. In practice this may not be possible or desirable for various reasons; for example one may want $\Delta\theta$ to be large enough so the corresponding ΔE covers adjacent lines such as the He-like triplets. Selection of a particular $\Delta\theta$ may be one of the design trade-offs. But ultimately all Bragg spectrometers are limited by the limited availability of diffractor materials and so they share the same relevant inherent parameters such as R_C or R_P and $E/\Delta E$ for point sources. For reference the Einstein FPCS had $A_{EFF}^{MAX} \sim 2 - 3\ cm^2$ near 1 keV and up to 10 times less at some energies. The concentration required to reduce background is obtained either with a telescope, or by suitably curving the crystal so it acts as a concentrator/diffractor.

Grating instruments have the spectral multiplex advantage over at least a sizeable part of the energy spectrum. Here concentration is inevitably performed with a telescope. The only truly viable designs I am familiar with call for objective gratings in transmission or

reflection. The latter is a relatively new concept for X-ray astronomy (see W. Cash's paper at this meeting). Although focal plane reflection gratings have been discussed at various times in the past, there appears to be no good solution yet to the fundemental limitation of the mismatch between the f/numbers of the grazing incidence telescopes and reflection gratings; telescopes produce ray bundles with angular divergences of $\sim 10^{o}$, which is many times larger than the acceptance angle of standard X-ray reflection grating spectrometers.

b) Bragg Spectrometer Design

(i) AXAF Focal Plane Crystal Spectrometer (AXAF FPCS)

Here I assume a scaled up version of the Einstein FPCS. The telescope provides concentration by a factor of $\sim$ 1000 for a point source. The instrument operates in a scanning mode with selectable diffrators to cover the full energy range. It can handle extended sources by virtue of its astigmatic imaging properties, although an aperture should be used to limit the field of view, e.g., to 3 x 30 arc min for the Einstein FPCS. (I do want to note in passing that scanning generally does not limit the time resolution for studies of adjacent lines because the event rate is so low. For $A_{EFF} \sim 10 - 50$ cm^{-2} and line fluxes $\sim 10^{-3}$cm^{-2}s^{-1} there are 20 - 100s per event, and reasonable scan times have negligible effect on the achievable time resolution.)

(ii) Conical Crystal Spectrometer (CCS)

This design is associated largely with Bruce Woodgate and collaborators (Woodgate et al. 1973). A crystal panel is conically curved to give a concentration factor of $\sim$ 100 to a line focus. A given panel can be rocked to cover a moderate energy range ($\sim$ 50%). Larger ranges must be covered by independent instruments. Extended sources must be collimated

to $\sim 10'$ to give $E/\Delta\theta \sim 100$.

(iii) Spherical Crystal Spectrometer (SCS)

This design is due to Schnopper and colleagues (Schnopper and Taylor 1980) and is described fully by Griffiths at this meeting (see also Culhane's presentation). The main difference between this and the CCS is that the bent crystal concentrator (again $A_C/A_D \sim 100$) has a second bend which introduces a pseudo-multiplex advantage at the expense of peak offective area. (e.g. $\Delta\theta$ is >> W by design). Thus the SCS need not be scanned (saving mechanical complexity), and there is a further advantage in the imaging capability (a more subtle point is that the instrument can benefit from the high reflectivity of mosaic crystals without necessarily suffering fully the usually accompanying degradation of energy resolution.) The price one pays is in flexibility. A given fixed panel will cover a $\Delta E/E$ of $\sim 10 - 20\%$. One cannot bring all the area to bear on a single line nor avoid devoting area to what may be uninteresting portions of the spectrum for some sources. Again, multiple energy ranges require multiple instruments But the extended source capabilities are very good: resolving powers of ≥ 100 can be achieved over a full $\frac{1}{2}^{o}$ field.

(iv) Imaging X-ray Spectrometer

This is a "barn-door" objective crystal spectrometer such as the one described by Angel and Weisskopf (1970). I proposed such an instrument with Ken Pounds and collaborators for spacelab. A flat crystal panel is followed by a moderate resolution telescope, which gives a concentration factor of $\sim 10^5$ for a point source and full field imaging over nearly 1^{o}. Thus this instrument has a significant spatial/spectral multiplex advantage.

At a single setting one obtains a full image in a narrow band whose central energy varies along one dimension . The crystal must be rocked to build up a spatially resolved spectrum over the whole image. The flat crystal panel can yield higher resolutions than bent crystal spectrometers over its spectral range (like the SCS it can get high resolution with mosaic crystals), and unlike the other instruments its resolution is not degraded by source extent.

c) Grating Spectrometer Designs

(i) AXAF Transmission Gratings Spectrometer (AXAF TGS)

Although results from the Einstein OGS have been slow in coming, the instrument did acquire some remarkable spectra, and significant improvements have been made in grating fabrication since the HEAO program at Utrecht, MPI and MIT. EXOSAT has a grating system and gratings are under consideration for other missions (e.g. ROSAT reflight). I will concentrate on the parameters of a possible AXAF OGS, but any similar system would share many of the same properties. The concentration factor of such a system for a point source is 10^6 - 10^7 because of the small image size.

As a slight digression let me describe some of the improvements in grating fabrication being made at MIT. This is work of Prof. Henry Smith of our Electrical Engineering Department, with whom I and Mark Schattenburg are collaborating to perfect gratings of high spatial frequency. We have been particularly interested in making thick gratings for use around the 6 keV iron lines using the technique of soft X-ray lithography perfected by Smith and his co-workers at MIT and Lincoln Lab. Figure one shows the calculated, one-sided first order efficiency for an 0.9 μm thick grating. This acts as a phased grating in the region of interest giving ultimate peak two-sided efficiencies of 50%. That such gratings are feasible is shown in Figure 2, which is an electron micrograph of a

3000 lpmm gold grating of thickness 0.6 μm. The gratings are all mounted on polyimide substrates (taken into account in Fig. 1) that make them extremely rugged. Of course at lower energies the gratings should be free-standing. A 5000 lpmm grating has been made and we are presently pushing for increasing the thickness to the desired value.

Transmission gratings in coma-corrected mountings (Beuerman et al. 1978) could give very high throughput and resolution ($E/\Delta E \sim 100 - 600$) for point sources. They would even be useable on extended sources in which most of the flux is in a few emission lines. This is indeed the case for many supernova remnants. The remnants in the LMC are particularly well suited to this because of their small size, and cooling cores in galaxy clusters may be similarly accessible.

(ii) Objective Reflection Grating Spectrometer (ORGS)

This clever design is discussed in detail by Cash (this meeting). The concentration factor is $\sim 10^5$ for point sources. For extended sources one needs rather fine collimation (1' x 20') to avoid degradation of the resolution to below $E/\Delta E = 100$, and this will both add complexity and limit the signal on extended sources such as SNR's and clusters. The ORGS has great promise, but as the youngest of the instruments mentioned here it naturally has the highest degree of undemonstrated technology at this time.

III. COMPARATIVE ANALYSIS

A comparison of the performance of the various spectrometer designs is extremely difficult and fraught with pitfalls. Each design contains enough free parameters that it is nearly always possible to improve one characteristic at the expense of another (e.g., A_{EFF} at some energy at the expense of energy range). Thus only hard and fast designs can be compared in any detail. Nevertheless, it is instructive to analyze the

relative merits of several "strawman" instruments. I do so with apologies to the various proponents of each instrument and with the warning that the parameters listed below can change by factors of up to 10 as the designs are modified.

I have made various assumptions in computing Tables 1 and 2. The AXAF parameters are estimated from various AXAF working group papers. For the crystal instruments (CCS, SCS, IXS) I assume crystal projected areas of $10^3 cm^2$ and diffractor properties appropriate to TAP (1 keV) or LiF (6.7 keV). For the ORGS and IXS I take telescope effective areas of 500 cm^2 at 1 keV (and zero at 6.7 keV). I assume all detector efficiencies are 1.0. Collimator transmission is taken as 0.7 for the CCS and 0.5 for the ORGS. The SCS is assumed to have $\sim$ 150 spectral resolution elements that span the 5 lines in question (e.g. it has pseudo spectral multiplex advantage). I take the weak source limit in which the background is all of non-X-ray origin with flux $10^{-3} cm^{-2} s^{-1} keV^{-1}$. I assume that the CCS like the FPCS can measure this background simultaneously with the signal in unilliminated portions of the position sensitive detector (as we have done with the Einstein FPCS). The 20' source is assumed to have uniform surface brightness, so that apertures reduce the flux to the instrument.

The listed 3σ flux limits are for each of five lines (to allow some plasma diagnostics) and a total exposure of $5 \times 10^5 s$. Of course, the multiplexed instruments will get information about the entire spectrum simultaneously. This is of greater value near 1 keV than near 7 keV, as there are many more lines near the former energy. Except where indicated the instruments are signal limited and so the number of detected photons is very small.

IV. CONCLUSIONS

One immediate conclusion is that each of the straw-man instruments

has a sensitivity that is at least an order of magnitude better than that of the Einstein FPCS. This means that the next generation of instruments is sure to provide the spectral banquet I referred to in §1. For illustration I show in Table 3 some crude estimates of the typical line strengths for a given class of objects (i.e., not just the brightest one or two). With limiting fluxes of 10^{-5} to 10^{-6} $cm^{-2}s^{-1}$ one will have many hundreds of galactic and extragalactic objects to study.

A second conclusion is that each instrument involves trade-offs and compromises that must be weighed with great care. Even my crude analysis shows how strongly the relative merits of a given design depend on the details of the objective (e.g. extended vs. point sources). I have not even addressed important details such as how the resolution degrades with source extent or how sensitive the instrument may be to spacecraft pointing uncertainties.

A third conclusion is that AXAF promises to have a powerful spectral capability when it is eventually launched. Probably the greatest weakness of the two AXAF instruments considered here is the at least partial breakdown of the multiplexed TGS for sources > 20" in extent. It would seem that this leaves a major hole for some other future mission, especially around the Fe line where the effective area of the FPCS is severely limited by the telescope efficiency.

I am grateful to the Institute of Astronomy for their hospitality, to the Royal Society for their support through a Visiting Research Fellowship, and to NASA for partial support under contract NAS-8-30752. I thank Andy Hawrylick, Mark Schattenburg, and Henry Smith for Figures 1 and 2. I thank the Alfred P. Sloan Foundation for a Research Fellowship

REFERENCES

Angel, J.R.P. and Weisskopf, M.C. 1970, Astron.J., 75, 231.

Beuerman, K.P. et al. 1978, Applied Optics, 17, 2304.

Canizares, C.R. et al. 1979, Ap.J., 234, L33.

Giacconi, R. et al. 1979, Ap.J., 230, 540.

Schnopper, H.W. et al. 1977, Applied Optics, 16, 1088.

Schnopper, H.W. and Taylor, P.O. 1980, Applied Optics, 19, 3306.

Winkler, P.F. et al. 1981, Ap.J., 246, L27.

Woodgate, B.E. et al. 1973, Applied Optics, 12, 2759.

TABLE 1

WEAK SOURCE FLUX LIMIT FOR DETECTION OF 5 LINES AT 1 keV IN 5×10^4s.

INSTRUMENT	A_{EFF}^{MAX} (cm^2)	A_{DET}^{POINT} (cm^2)	FOV (arc min)	$I_{MIN}(cm^{-2}s^{-1})$ POINT	$I_{MIN}(cm^{-2}s^{-1})$ 20'
AXAF FPCS	340(a)	1	3' x 30'	3×10^{-6}	3×10^{-5}(b)
CCS	240(a)	10	10' x 5°	1×10^{-5}(b)	4×10^{-5}(b)
SCS	2	0.02	30' x 5°	1×10^{-4}	1×10^{-4}
IXS	170	0.005	1° x 1°	6×10^{-6}	4×10^{-5}
AXAF TGS	200	10^{-4}	-	1×10^{-6}	(C)
ORGS	75	0.005	1' x 20'	2×10^{-6}	2×10^{-4}

Notes:

a. No multiplex advantage; I_{MIN} assumes 10^4s each on 5 lines.

b. Sensitivity is background limited at 10^4s.

(C) Extended source capability for sources < 20" and strong emission line sources. Deconvolution possible on other sources.

TABLE 2

WEAK SOURCE FLUX LIMIT FOR DETECTION OF

5 LINES AT 7 keV IN 5×10^4s

INSTRUMENT	A_{EFF}^{MAX} (cm^2)	A_{DET}^{POINT} (cm^2)	FOV (arc min)	I_{MIN} ($cm^{-2}s^{-1}$) POINT	I_{MIN} ($cm^{-2}s^{-1}$) 20'
AXAF FPCS (a)	20	1	3' x 30'	5×10^{-5}	4×10^{-4}(b)
CCS (a)	140	10	10' x 5°	2×10^{-5}(b)	4×10^{-5}(b)
SCS	4	.02	30' x 5°	5×10^{-5}	5×10^{-5}
AXAF TGS	50	10^{-4}	1' x 20'	4×10^{-6}	(c)

Notes:

(a) No spectral multiplex advantage; I_{MIN} assumes 10^4s each on 5 lines.

(b) Sensitivity is background limited.

(c) Extended source capability for sources < 20" and strong emission line sources. Deconvolution possible on other sources.

TABLE 3

ESTIMATED LINE FLUXES FOR CLASSES OF ASTROPHYSICAL OBJECTS

LINE FLUX ($cm^{-2}s^{-1}$)	SIZE		
	< 10"	~ 1'	~ 20'
10^{-2}			
	• BINARIES (Fe LINES)		• SNR
10^{-3}		• LMC SNR	
		• COOLING CLUSTER CORES	• CLUSTER Fe LINES
	• STELLAR CORONAE		
10^{-4}	• AGN		
10^{-5}	• GAS IN GALAXIES (e.g. M86)		
10^{-6}	• CLUSTERS @ Z = 0.5		

FIGURE CAPTIONS

Figure 1: Calculated one-sided first-order efficiency for the illustrated gold transmission grating on a polyimide substrate.

Figure 2: Electron micrograph of a 3000 lpmm gold grating on a polyimide substrate. The grating thickness is 0.6 μm plus 1.0 μm of polyimide. This grating was fabricated by a multistep process involving both holographic exposure and soft X-ray lithography.

ORIGINAL PAGE IS
OF POOR QUALITY

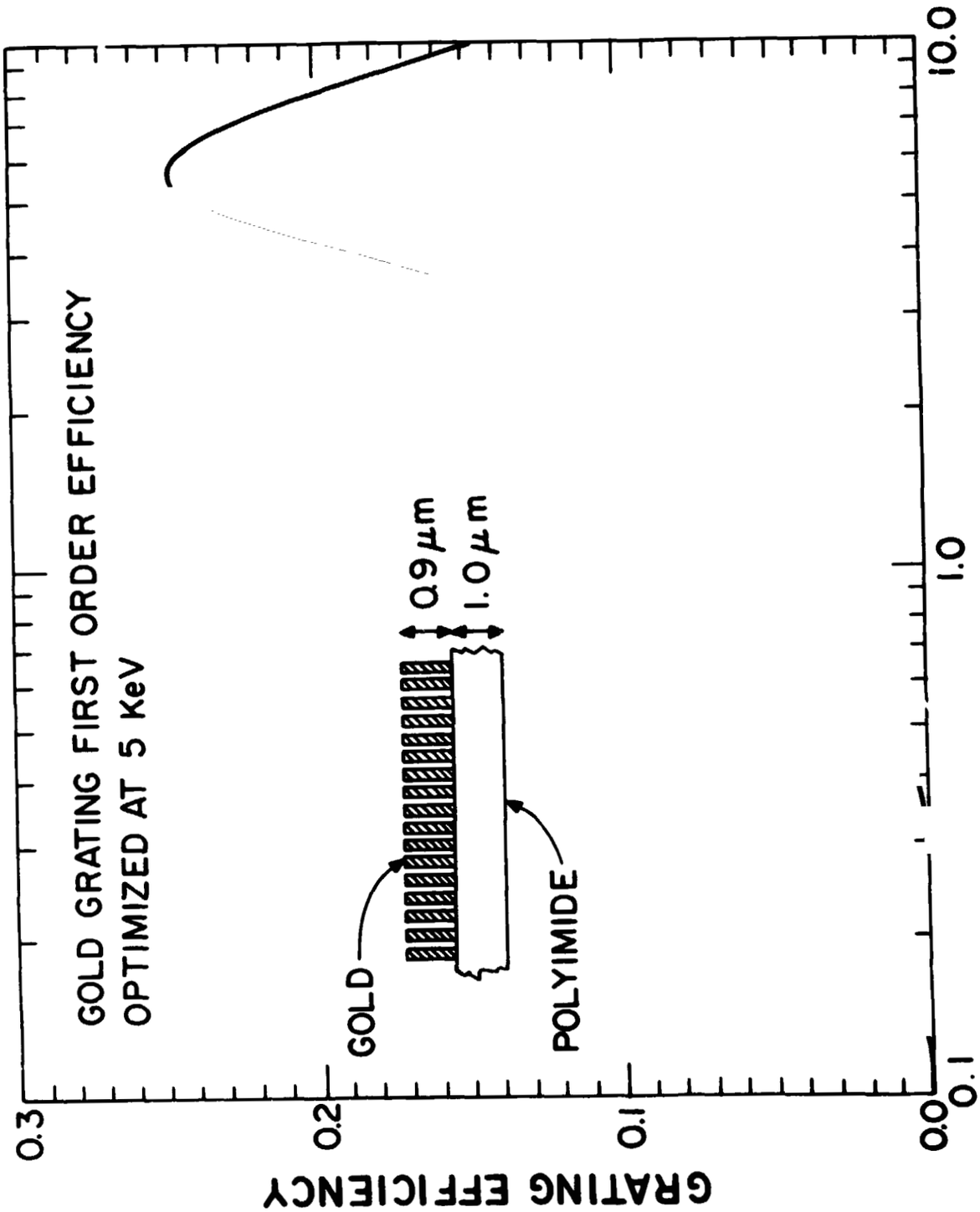

FIGURE 1

ORIGINAL PAGE
BLACK AND WHITE PHOTOGRAPH

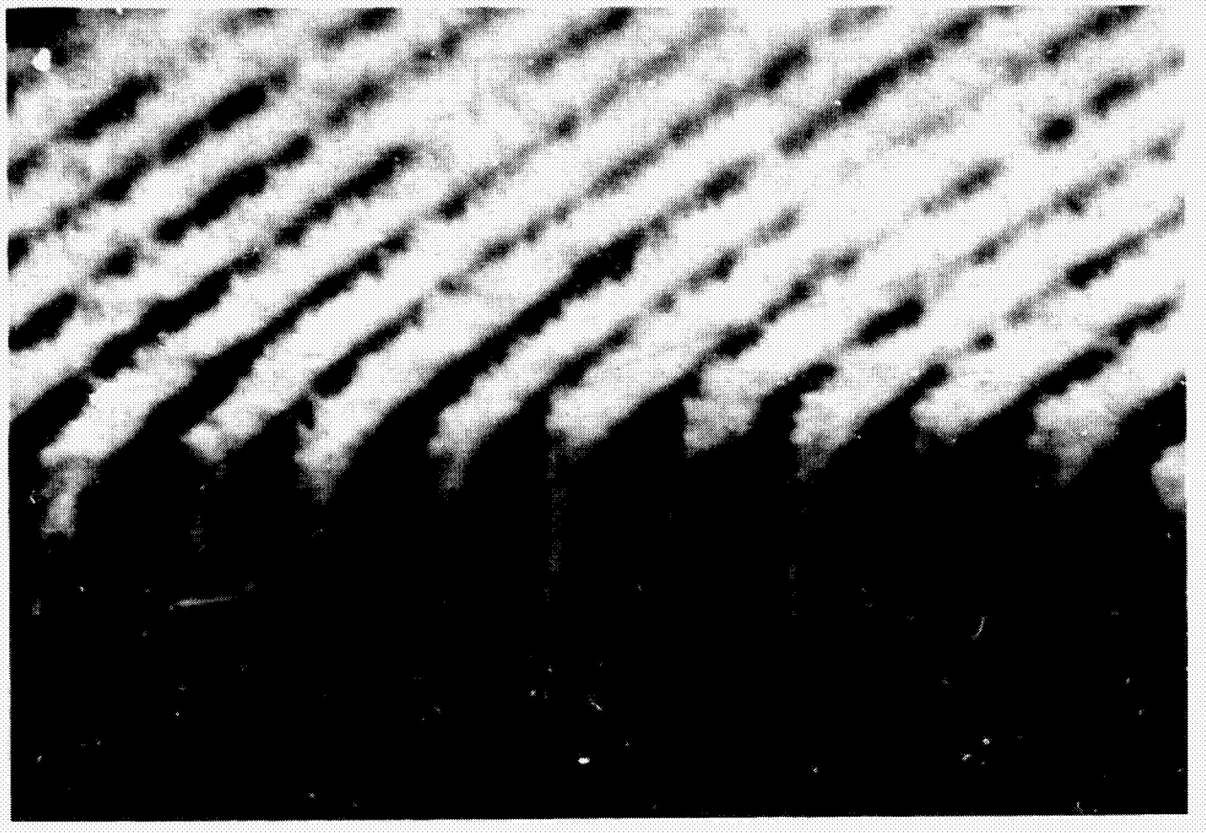

FIGURE 2.

N82 26077

BROAD BAND X-RAY TELESCOPE (BBXRT)

P.J. Serlemitsos
Laboratory for High Energy Astrophysics
NASA/Goddard Space Flight Center
Greenbelt, MD 20771

ABSTRACT

An approach is presented along with corroborating measurements for significantly enehancing the potential of Si(Li) spectrophotometry in X-ray astronomy. The key new element is an unconventional X-ray mirror that meets qualifications of low cost, light weight, and large throughput over a broad energy band ($\gtrsim$ 7 keV) at moderate angular resolution. The potential for other applications is also discussed.

I. INTRODUCTION

I will be reporting on a 0.5-10 keV non-dispersive spectroscopy experiment proposed by the Goddard X-ray group some three years ago in response to NASA's Spacelab AO. It consists of 2 co-aligned grazing incidence telescopes with cooled Si(Li) spectrometers at each focus. BBXRT is a follow-up experiment to the solid state spectrometer contributed by the Goddard group and flown aboard the Einstein Observatory (experiment B-5; Joyce et al. 1978). It represents a major effort to tap new research areas that were not accessible with the previous instrument. Assigned to NASA's OSS-2

mission, it has been funded for definition and some limited hardware development. OSS-2 is not as yet on NASA's approved flight program. Some preliminary test results involving prototype telescope and detector hardware will be presented and discussed. We will also consider some specific observations from a shuttle mission that link the instrument's potential to several of the items that have surfaced in this meeting from the theoretical reviews as well as to potential goals of an explorer mission.

II. OBJECTIVES AND IMPLEMENTATION

BBXRT was conceived and is presently under development to meet the following objectives:

1. Expand the energy band of Si(Li) spectrophotometry to adequately include iron K-shell transitions.
2. Recover some measure of the spatial information that telescopes provide but which is lost in single-pixel photometry.
3. Reduce detector background sufficiently to make possible the study of the many new sources identified in Einstein IPC and HRI fields.

In spite of obvious limitations with resolution, focal plane Si(Li) spectroscopy has a potential that we have only begun to exploit with the instrument aboard Einstein. One direction to go for a predictably large impact on future observations is to extend the response of grazing incidence optics to about 10 keV. This would make possible the study of iron K-shell transitions which are the dominant transitions whether collisionally excited in hot plasmas with kT > a few keV or due to the fluorescence process. Even when the spectrum is featureless, a broad band-pass will result in better determination of the shape of the continuum and of any detectable absorption

effects at the low end of the spectrum.

Efficient reflection at the higher (~ 7 keV) energies will only occur from surfaces at small ($\lesssim$ 0.5 degrees) angles to the incident beam. In a cylindrical telescope geometry, the instrument focal length determines the maximum mirror aperture that satisfies the above condition. The high energy throughput will depend on how effectively we utilize the area within this limiting aperture. When nesting confocal surfaces it is imperative that we maximize the ratio of the reflecting to dead areas, the latter made up of mirror walls, gaps and supports.

The BBXRT mirror design opts for maximum high energy response at the expense of high resolution imaging. The latter is compromized by a drastic reduction in mirror wall thickness and by the use of an approximate geometry: both the paraboloid and the hyperboloid in the Wolter type I geometry are replaced with tightly nested confocal thin foil cones. Note that the approximation improves for small grazing angles and short cone segments. We have chosen a cone length which results in an intrinsic spatial resolution < 0.5 arc minute half power radius (i.e. if we neglect mirror distorsions and assembly tolerances). The foil reflectors are formed from .005-inch, high quality but commercially available aluminum foil overcoated with ~ 10μ of acryllic lacquer on which ~ 500 $\mathring{A}$ of gold is vacuum deposited. This simple surface preparation replaces the customary polishing which, aside from cost, would be quite impratical in this case. As we shall show, it produces a surface smoothness comparable with that of highly polished surfaces.

The parameters for each of the 2 BBXRT mirrors are listed in Table 1. Note in particular that the efficiency for utilizing the telescope aperture is 0.7 (0.6 if the small central void is added to the dead area) which is not too different from the transmission efficiency of the collimation to a large area

gas proportional counter. In Figure 1 we have plotted the net geometric area for each mirror as a function of the angle for an off-axis incident beam. We wish to point out that as the effective area is reduced due to vignetting, the image quality is independent of off-axis position for this type of geometry.

We have used the 150 ft long X-ray calibration facility at Goddard to calibrate a telescope segment (quadrant) equipped with only the inner most 50 reflectors due to beam size limitations. This segment is shown in Figure 2. The beam divergence results in considerable vignetting which was taken into consideration when computing the reflection efficiency. Furthermore, it increases the grazing angles at the front mirror by about 30% which would tend to reduce the measured response at high energies. We have not corrected for this effect. Figure 3 shows the measured response for the 50 reflector complement of the BBXRT mirror (net geometric area 220 cm^2) using bremsstrahlung off a beryllium target intercepting a 20 keV electron beam as well as characteristic lines from the various other targets listed on the figure. We used at the focus a cooled Si(Li) detector ~ 6 arc minutes in radius. Our measurements did not extend below ~ 1.2 keV because of a beryllium detector cover. Reflection efficiencies inferred from these results are in good agreement with those compiled by Seward (1977) for gold-coated mechanically polished mirrors. Assuming that this agreement holds for the entire range of grazing angles of the full telescope complement we have estimated the combined effective area of the 2 BBXRT telescopes as shown in Figure 4. For a rough comparison, we have included in the figure the measured response of the Einstein solid state spectrometer.

We have not as yet been able to fully evaluate the imaging potential of this telescope. Ray tracing indicates that the approximate geometry yields images with < 0.5 arc minutes half power radius (HPR). Aside from the

geometry however, the image quality will depend on other factors as well such as distortions of the foil reflectors whether inherent in the foil or introduced in the assembly process and, possibly, surface roughness. Preliminary results from our calibration of the prototype telescope segment indicate an image with ~ 3 arc minutes HPR independent of energy. This energy independence rules out surface roughness as the major cause of image broadening. Other evidence seems to indicate that errors in the reflector assembly may be mostly responsible for the observed degraded image. A goal of ~ 2 arc minutes HPR, consistent with the size of the BBXRT detectors, should be achievable.

Coming next to our second objective of recovering some of the spatial information while still maintaining the Si(Li) energy resolution, we have developed a 5-element Si(Li) detector specifically for this application by segmenting a single silicon crystal as shown in Figure 5. At the focus of the BBXRT mirror, the central element extends to 3.7 arc minutes radius whereas the outer pixel perimeter is at 8.6 arc minutes. The partitioning grooves are 0.5 arc minutes wide. This type of detector allows the study of isolated weak point sources while simultaneously monitoring background in adjacent pixels. For diffuse sources with several arc minutes extent it increases the efficiency for generating rough spectral maps. In preliminary tests we find identical performance for all pixels with an energy resolution comparable to that of the Einstein instrument.

Our third objective stems from the fact that virtually nothing is known about the X-ray spectra of sources at flux levels $\lesssim 10^{-11}$ ergs $cm^{-2}s^{-1}$. The sample includes the majority of the new sources discovered with the imaging detectors aboard the Einstein observatory from stars to distant clusters of galaxies and quasars. What prevented the Si(Li) spectrometer aboard Einstein

from supplying some of this information was a high background rate totally unrelated to the telescope throughput.

Background reduction schemes relevant to this instrument must necessarily deal with the radiation environment and its effects as contrasted, for example, with reducing the size of pixels. Background events may result from direct interactions in the detector sensitive volume, intercations near the detector edges resulting in partial charge collection, electronic cross talk from large events in the outer unused detector perimeter, enhanced noise associated with electronic baseline distortions caused by large ionizing events, etc. The 5-pixel detector offers us the opportunity to apply pixel-to-pixel anticoincidence which is a proven technique for eliminating a large fraction of the above-mentioned background. In addition, we have incorporated a charged particle guard in the form of a CsI(Tℓ) cup placed around the detector and its cold finger assembly as shown in Figure 6. The size of this cup and, therefore, the cost and complexity associated with it have been kept to a minimum by the use of a cooled Si(Li) detector for detecting the light pulses from the CsI. The detector views the CsI without coupling through a port at the inner surface of the base of the crystal. The threshold for anticoincidence is set at ∿ 300 keV, well below the ionization losses of singly charged minimum ionizing particles. Although this relatively small crystal would not be very effective in actively guarding the detector from γ-rays as well, the 0.5 inch high-Z walls form an efficient passive shield up to γ-ray energies of ∿ 200 keV.

We have completed an initial evaluation of the BBXRT detector background using a prototype cryostat assembled in the manner shown in Figure 6. This was done in an enhanced radiation environment from a Co^{60} source as well as at ambient ground level (no source) conditions. We did confirm that, at ground

level, the dominant background reduction scheme is the pixel-to-pixel anticoincidence rather than the CsI guard. Figure 7 shows the background reduction effected when the Co^{60} source was in the proximity of the cryostat. Note the relatively small improvement obtained near the threshold energy of 0.5 keV as compared with the substantial gains at higher energies.

Ground level detector performance in the absence of sources is significant in that it is often a reliable measure of the performance to be expected in space: in the few keV range, gas proportional counters flown by our group displayed in space a background rate typically within a factor of ~ 2 of their ground level background. In Table 2 we have tabulated the observed BBXRT ground level background along with a measure of the gain realized in a direct comparison to solid state spectrometer aboard Einstein. Again we point out the relatively modest improvement at the lower energies in rough agreement with the Co^{60} results.

In summary, we have demonstrated that the background reduction techniques we have incorporated result in substantial gains especially at energies > 1 keV. It is apparent that some additional effects dominate the background rate at the very low energies and these have to be dealt separately.

III. OBSERVATIONS FROM THE SPACE SHUTTLE

BBXRT is well suited to carrying out observations with typical exposures of a few x 10^3 s as would be the case with a ~ 7 day shuttle mission. With regard to extragalactic objects we may single out quasars and clusters of galaxies as the two classes of sources where substantial gains could be made with this instrument. In Table 3 we indicate what could be a typical example involving a quasar with a spectrum as in 3C273 (Worrall et al. 1979) at a flux

level of 10^{-12} ergs cm^{-2} s^{-1}. For our field of view, source confusion would not generally come into play for at least one order of magnitude below this sensitivity. We have assumed a 2-fold increase in instrument background over what was measured at ground level. We note that such an observation would be essentially photon limited over most of the spectral range and that a 2000 s exposure would be quite adequate for deducing the shape of the spectrum for such an object.

Similar arguments apply to the sensitivity for measuring the spectral shape and, therefore, the temperature of distant clusters of galaxies. On the other hand, the possible detection of Fe lines from these sources from which other parameters such as the redshift may be inferred is considerably more demanding. BBXRT will have typically 200 eV FWHM resolution at 7 keV. In a 2000 s observation the prominant Fe line blend from a Perseus-like cluster at $Z \approx .2$ will be detected at the 3σ level. For the nearby clusters it will be possible to make accurate Fe abundance determinations and to search for possible temperature and Fe abundance grandients with distance from the cluster center. For the Virgo cluster we will be studying the emission associated with individual galaxies such as M86. An observational program will, of course, include other classes of extragalactic sources as well. The two-component spectra of BL Lac objects and the large column densities and iron absorption edges associated with some of the Seyferts are spectral characteristics that can best be studied with this broad-band instrument.

Potentially interesting observations of galactic sources will include the temperature classification of the various types of stars. Iron line equivalent widths should help us determine the nature of the high energy component associated with some systems such as the RS CVn binaries (Swank et al. 1981). Iron line emission and absorption features invariably appear in

the spectra of the more luminous binaries and X-ray pulsars (Pravdo 1978). The type of questions that could be answered with this instrument deal with line broadening, multiple components, Doppler shifts, fluorescence, phase dependence, etc. Spectra of supernova remnants obtained with the Einstein instrument are rich in line features (Becker et al. 1980). The addition of the higher energy lines and continuum should help separate non-equilibrium effects from bonafide abundance anomalies.

IV. FUTURE PROSPECTS

We believe that all aspects of the experiment we have described may well have a bearing on a future Explorer mission. We have demonstrated the feasibility of segmenting a large Si(Li) detector into smaller elements for focal plane use. We have also outlined techniques for suppressing the background for such an array in order to make it effective in the study of weak sources. However we view as the single most important contribution the radically new way of realizing a broad-band, large throughput instrument at moderate angular resolution. Key elements are a simple reflector surface preparation and an approximate telescope geometry which greatly simplifies reflector preparation and assembly. The fabrication of such a telescope is actually not too different from what is involved in the assembly of a large area gas proportional counter. To the extent that large throughput at low cost is a necessary ingredient of a future Explorer mission, we believe that our approach deserves serious consideration. For example we can achieve 10^4 cm^2 of effective area in 16 modules inside a 2 M envelope. The corresponding area at 7 keV would be $\bullet$ 1600 cm^2.

The BBXRT spatial resolution is probably inadequate for an Explorer

instrument although it suffices for the instrument we are developing. We wish to emphasize that the cause of the broader image does not lie in the approximate geometry. It is quite conceivable that even with the thin foil reflectors we are using we could eventually improve on our image quality through better reflector preparation and assembly. If not, it would be a matter of seeking a better balance between throughput and reflector thickness. The potential for 0.5 arc minute HPR image is simply there.

I wish to acknowledge major contributions to this project by C. Glasser, F. Birsa and D. Arbogast.

REFERENCES

Becker, R.H., Holt, S.S., Smith, B.W., White, N.E., Boldt, E.A., Mushotzky, R.F., and Serlemitsos, P.J. 1980, Ap. J. (Letters) 235, L5.

Joyce, R.M., Becker, R.H., Birsa, F.B., Holt, S.S., and Noordzy, M.P. 1978, IEEE Trans. Nuc. Sci 25, 453.

Pravdo, S.H. 1978, Proceedings of the XXI COSPAR/IAU Symposium in X-Ray Astronomy, Pergamon Press, Ltd., Oxford.

Seward, F.D. 1977, Lawrence Livermore Lab., UCID-17505.

Swank, J.H., White, N.E., Holt, S.S., and Becker, R.H. 1981, Ap. J. 246, 208.

Worrall, D.M., Mushotzky, R.F., Boldt, E.A., Holt, S.S., and Serlemimtsos, P.J. 1979, Ap. J. 232, 683.

TABLE 1

BBXRT TELESCOPE PARAMETERS

Max (Min) Dia.	43 (17.8) cm^2
Focal Length	3.8 M
Focal Plane Scale	0.91 arc min/mm
Spatial Resolution	
Intrinsic	< 0.5 arc min HPR
Goal	2 arc min HPR
Mirror Material	.005 inch Al foil (Gold)
Number of Nested Mirrors	101 (4-inch cones)
Grazing Angles	0.34 - 0.75 deg
Aperture Utilization	0.6
Weight	10 kg

TABLE 2

BBXRT PROTOTYPE GROUND LEVEL DETECTOR BACKGROUND

E(keV)	COUNTS s^{-1} keV^{-1}	GAIN OVER SSS
.5 - 1.0	2.3×10^{-2}	9
1.0 - 1.5	4.1×10^{-3}	20
1.5 - 2.0	1.8×10^{-3}	33
2.0 - 3.0	5.4×10^{-4}	89
3.0 - 11.0	2.4×10^{-4}	--

TABLE 3

QUASAR SPECTRA; 2000 s EXPOSURE
EXPECTED COUNTS

	ENERGY BINS (keV)		
	1-2(1000 cm^2)	3-4(450)	6-7(200)
3C273* $dN/dE = .022E^{-1.55}$ $N_H < 2.2 \times 10^{21}$ cm^{-2}	> 19700	2820	484
Same spectrum renormalized to 10^{-12} ergs/cm^2s (2-10 keV)	> 180	25	4.4
Diffuse Background	17.4	2.4	0.4
Detector Background	24	2	2

*Worrall et al. 1979

ORIGINAL PAGE IS
OF POOR QUALITY

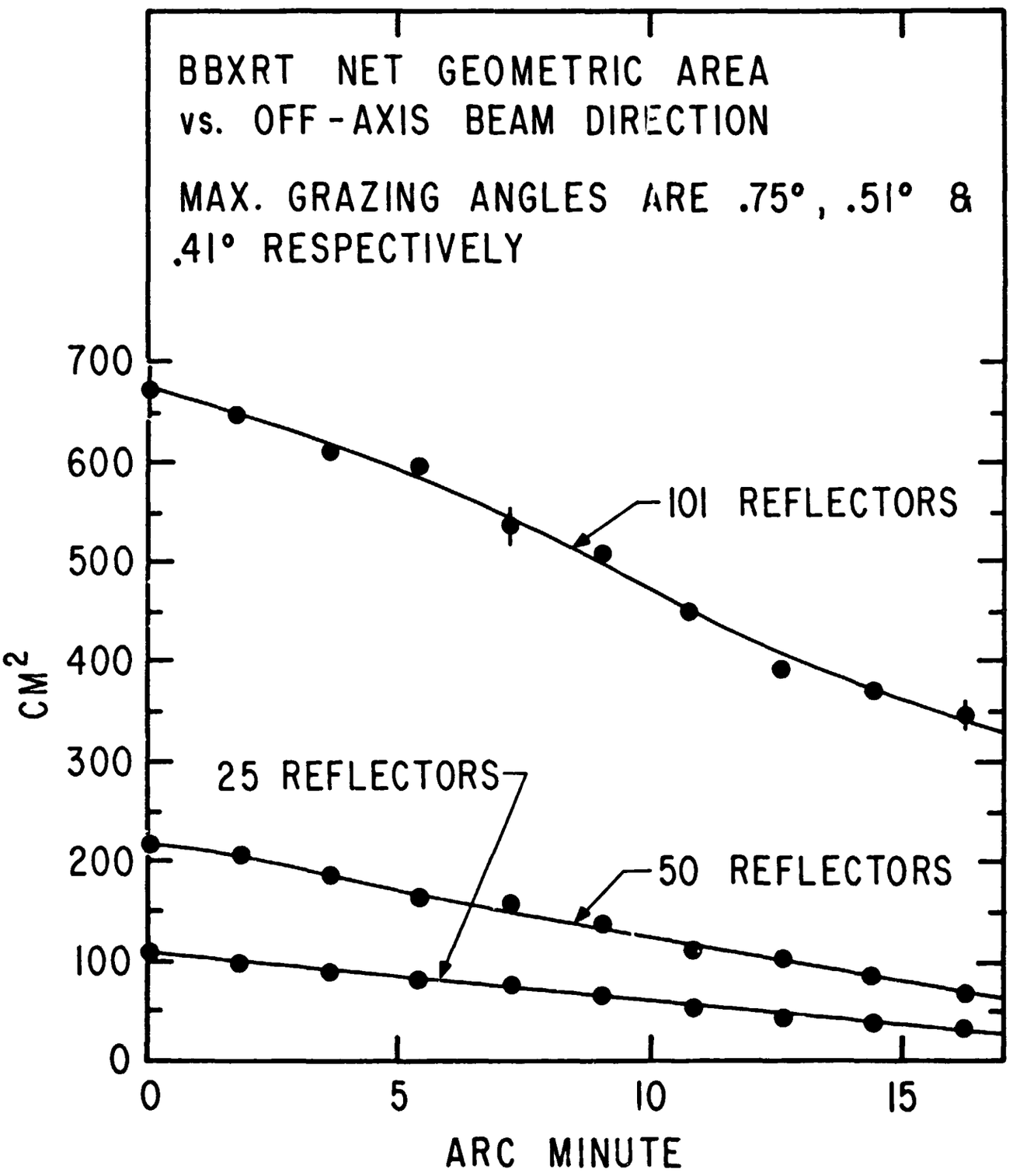

Figure 1

ORIGINAL PAGE
BLACK AND WHITE PHOTOGRAPH

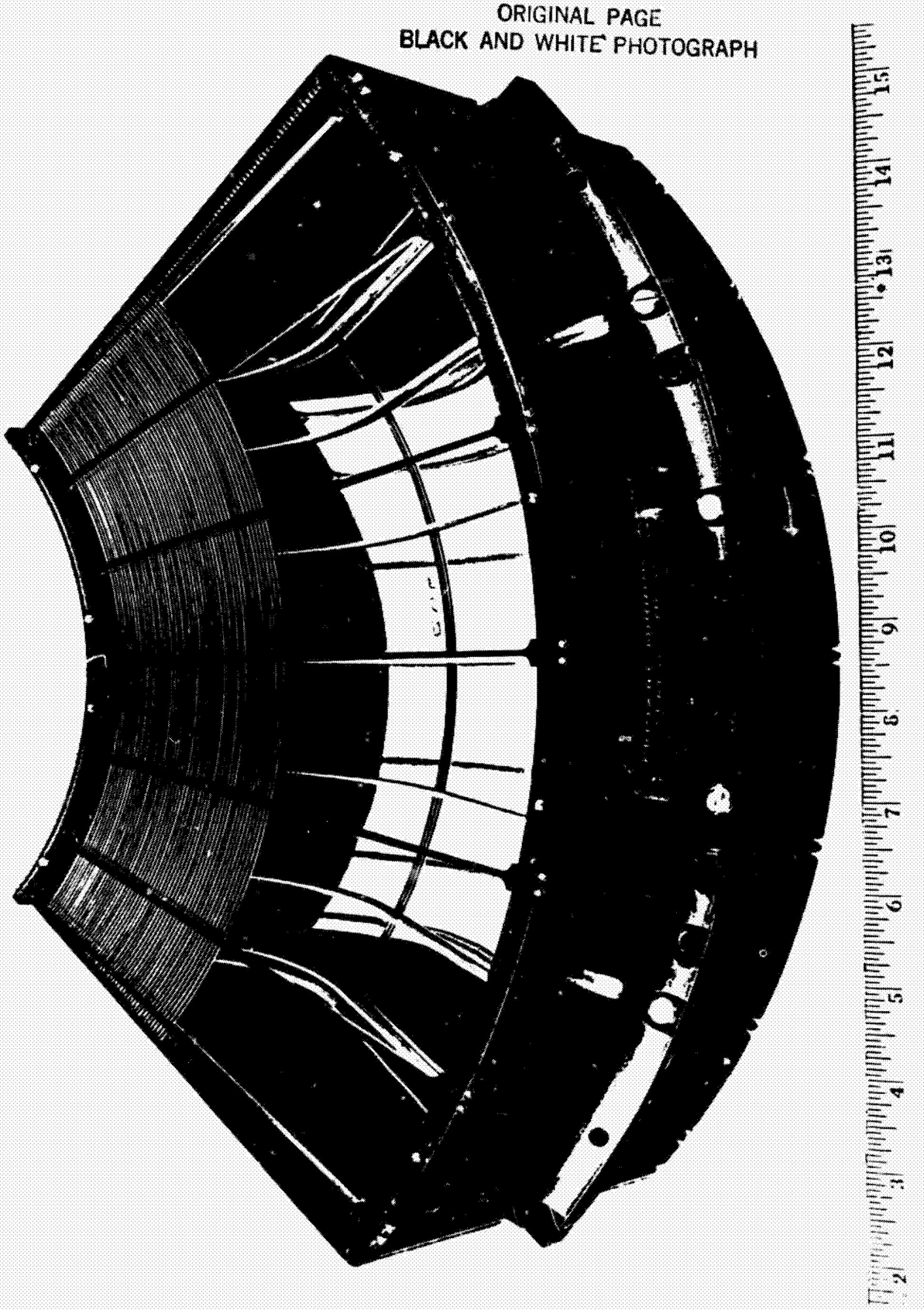

Figure 2

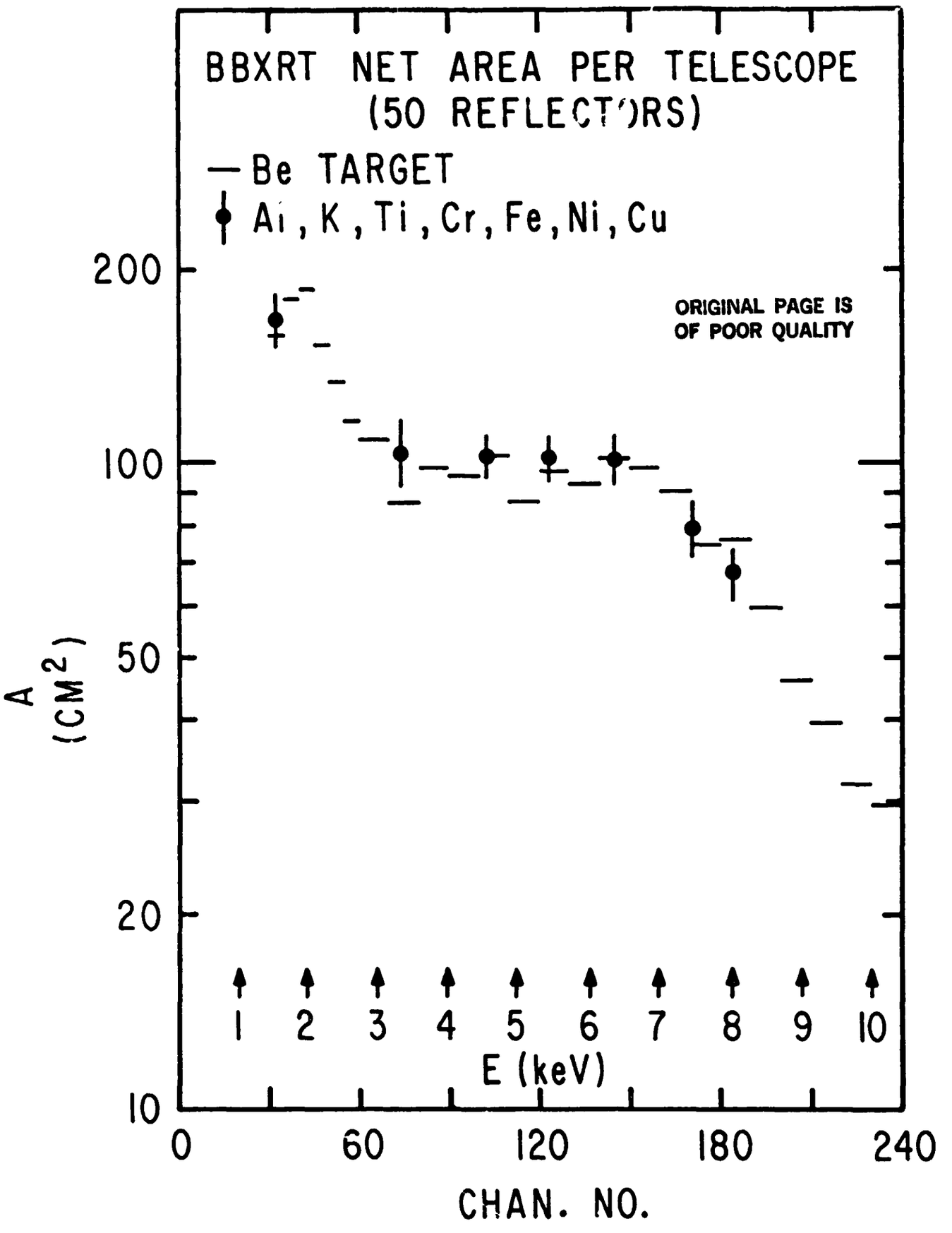
BBXRT NET AREA PER TELESCOPE
(50 REFLECTORS)
— Be TARGET
Al, K, Ti, Cr, Fe, Ni, Cu
ORIGINAL PAGE IS
OF POOR QUALITY
200
100
50
20
10
A
(CM²)
1 2 3 4 5 6 7 8 9 10
E (keV)
0
60
120
180
240
CHAN. NO.

Figure 3

ORIGINAL PAGE IS
OF POOR QUALITY

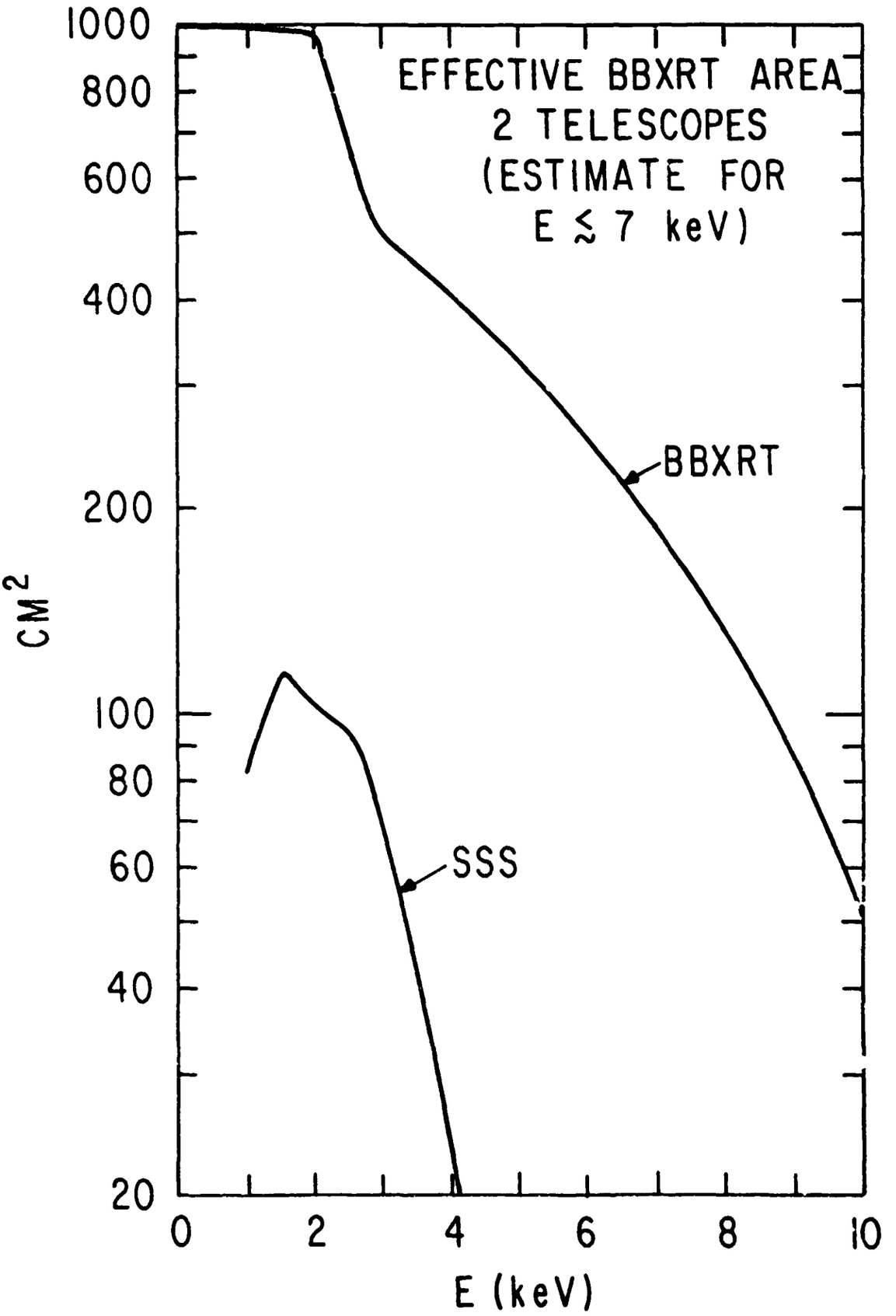

Figure 4

ORIGINAL PAGE IS
OF POOR QUALITY

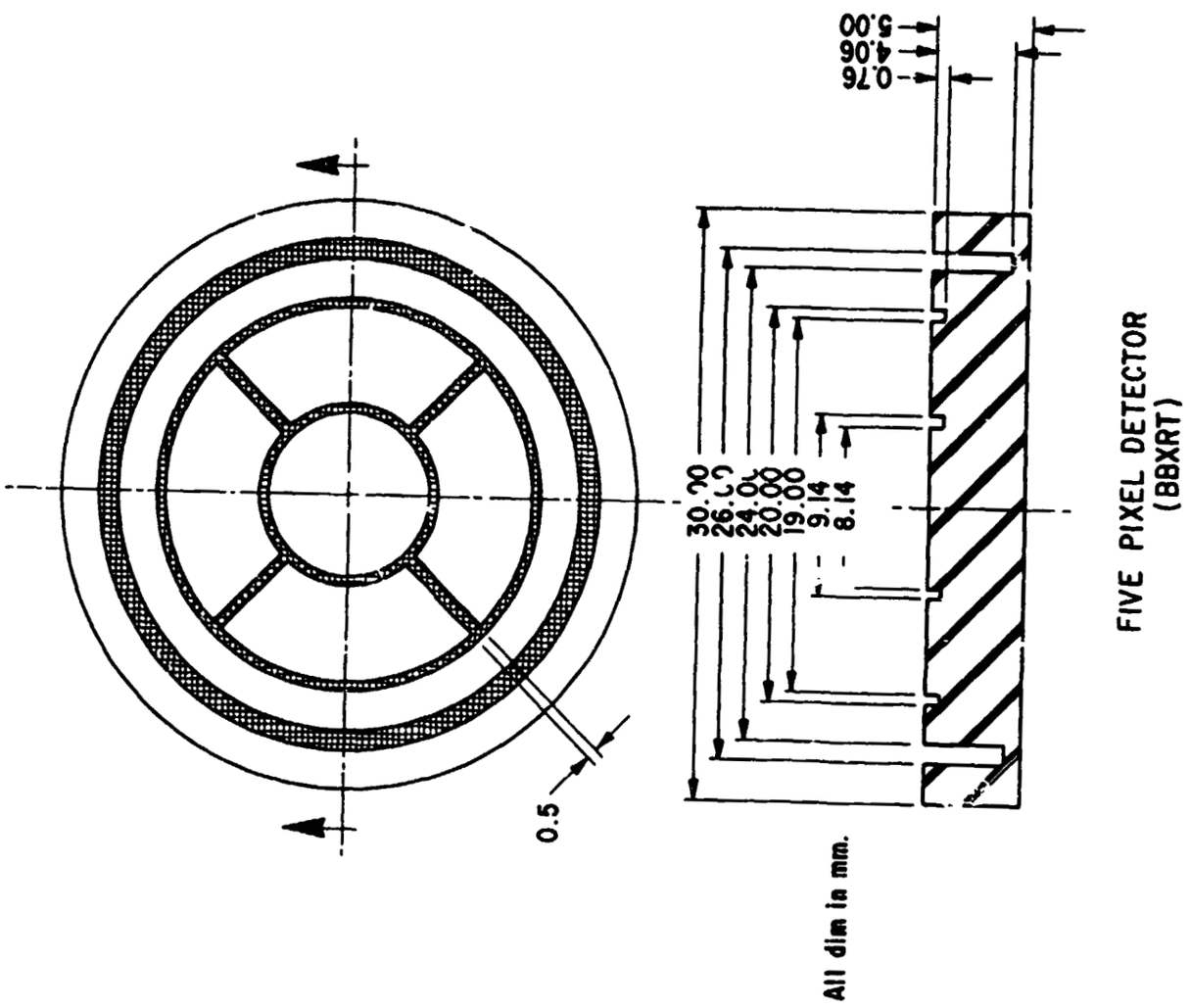

Figure 5

ORIGINAL PAGE IS
OF POOR QUALITY

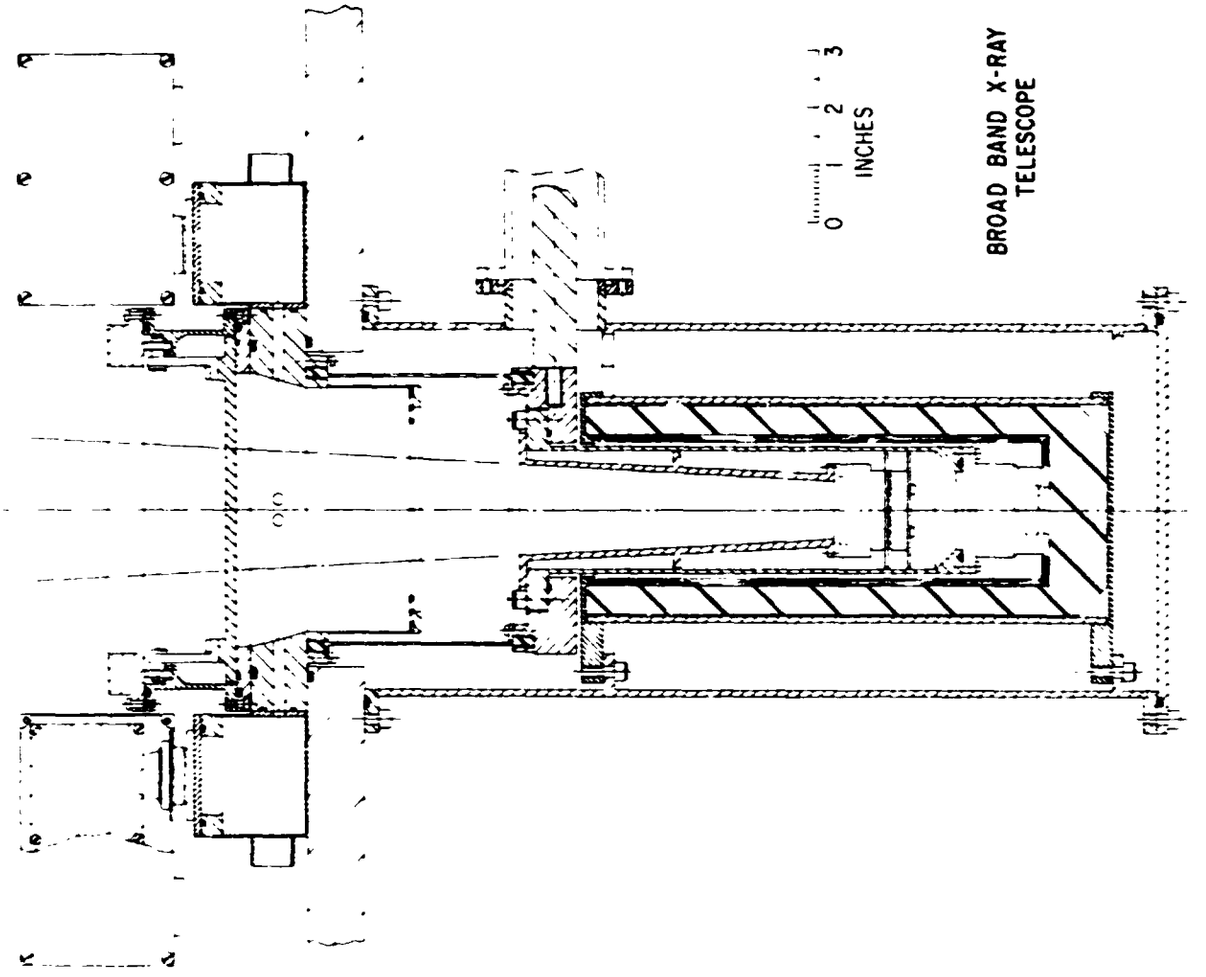

F gure o

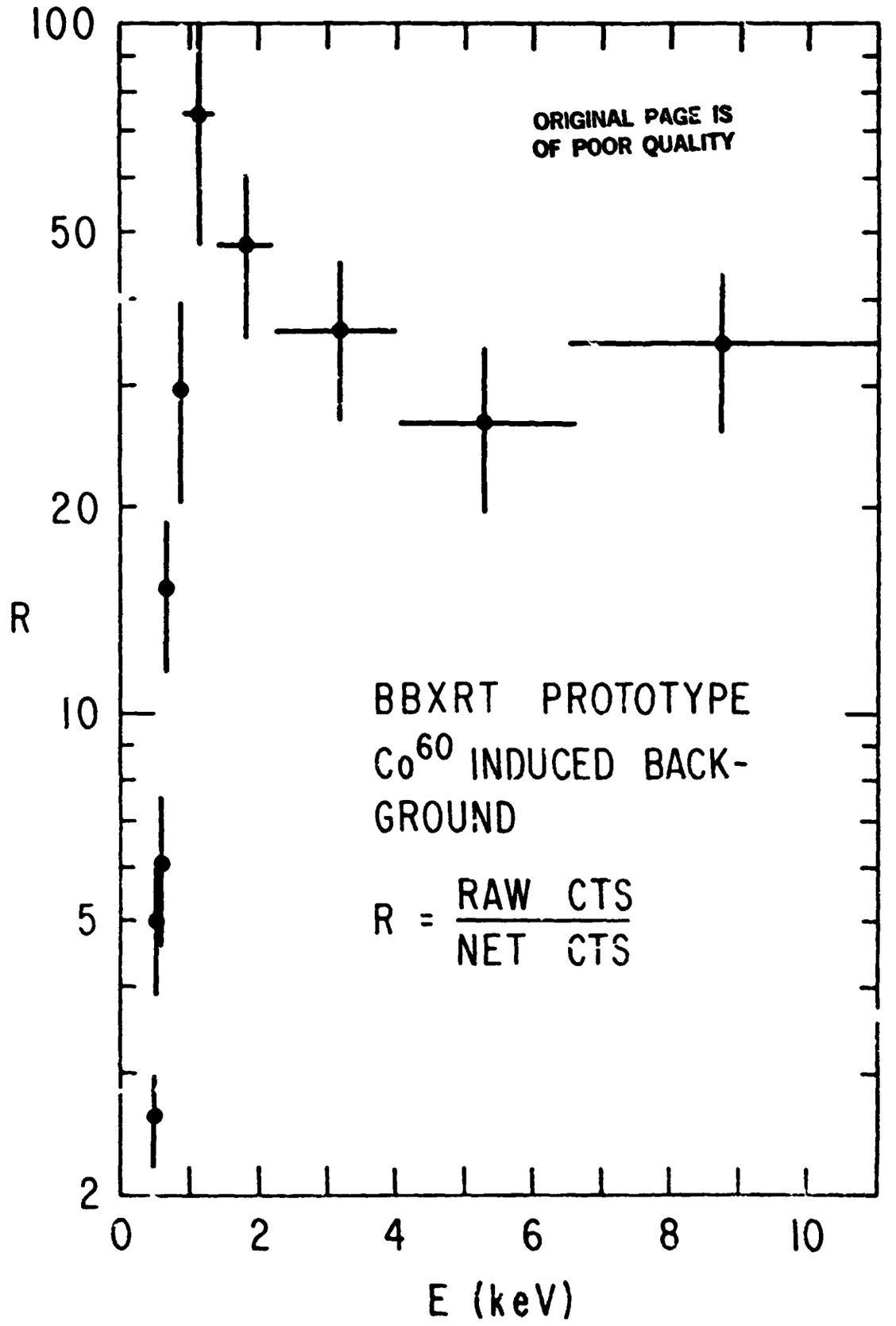
100
50
20
10
5
2
R
0
2
4
6
8
10
E (keV)
ORIGINAL PAGE IS
OF POOR QUALITY
BBXRT PROTOTYPE
Co60 INDUCED BACK-
GROUND
R = RAW CTS / NET CTS

Figure 7

N82 26078

D23

SOME OBSERVATIONAL TESTS OF X-RAY PULSAR EMISSION MODELS+

P. Mészáros*

NASA/Goddard Space Flight Center

Laboratory for High Energy Astrophysics

Code 665

Greenbelt, Maryland 20771

*Also at the University of Maryland. On leave of absence from

Max-Planck-Institut fur Physik und Astrophysik MPA, Garching.

+Paper presented at the NASA/GSFC Symposium on X-ray Astronomy, S.S. Holt, ed., Greenbelt, MD, 5-7 October 1981.

Abstract

Our understanding of neutron star physics relies heavily on knowing values of their mass, radius and magnetic field strength, and our only information about these comes from the surface radiation. There are however still major uncertainties about how this arises, concerning the nature of the mass exchange and the accretion flow, the magnetopause structure, the infall deceleration, the actual pulsation mechanism and the atmosphere geometry. We discuss the alternatives, and point out several possible observational tests.

ORIGINAL PAGE IS
OF POOR QUALITY

I. Some Outstanding Crucial Ambiguities

Out of the many unsolved questions about X-ray pulsars, there are three, connected with the actual emission mechanism, which are particularly irksome to the theoretician, but which appear to be within reasonable reach of observational solution. These are a) Is the mass exchange mechanism due to Roche lobe overflow, or due to (X-ray induced or spontaneous) wind transfer, and if the latter, will a disk form or not? ([1], [2], [3]). b) Is the pulsation mechanism due to intrinsic beaming at the polar caps ([4]), or to occultation at the Alfvén surface ([5], [6]), and if due to both, in what proportions? c) Is the deceleration of the infalling matter due to a collisionless shock ([7],[8]), or to binary coulomb encounters ([7],[9]) (besides radiation pressure contributions), that is, does the emitting polar cap atmosphere stick out significantly, emitting both across the field as well as along it, or is it mostly along it?

These questions, it is seen, tie into each other rather closely, and the reason why they are important is that their answer can have a significant effect on the determination of at least two crucial neutron star parameters, namely, the surface gravitational redshift and the magnetic field strength. The observed flux at earth F_x leads of course to a different estimate of the accretion efficiency $GM_xR_x^{-1}c^{-2}$, depending on the degree of beaming, that is even if we know M_x from doppler delay curves and eclipses, the value of R_x deduced depends crucially on the pulsation mechanism. This is of interest also for our understanding of the dynamics of the neutron star interior, via its effect on the calculation of the moment of inertia ([10]). The magnetic field strength, for its part, is either deduced from its effects on the rate of change of the pulsation period, $-\dot{p}/p$, for which the Alfvén geometry and the mass exchange mode is important, or is directly measured via cyclotron lines, the frequency of which is gravitationally redshifted and therefore affected by whether there is a shock which stands off above R_x or not. Spectroscopic

observations with a resolution $E/\Delta E \gtrsim 100$, as well as studies of the correlation of pulse shapes with the X-ray luminosity in different bands, may resolve these questions.

II. Mass Exchange Mechanism and Disk Question

In the X-ray domain, this boils down to resolving the dynamics of the flow at the Alfvén surface, located typically at

$$R_A(\mathrm{sph}) = \qquad (1)$$

$$10^8 (B/10^{12}\mathrm{G})^{4/7} (R_{ns}/10^6\mathrm{cm})^{12/7} (M/M_\odot)^{-8/7} (\dot{M}/1.3\ 10^{18}\mathrm{gs}^{-1})^{-2/7}\ \mathrm{cm},$$

for spherical infall, and at

$$R_A\ (\mathrm{disk}) = \qquad (2)$$

$$3\times10^7 (B/10^{12}\mathrm{G})^{40/69} (R_{ns}/10^6\mathrm{cm})^{120/69} (M/M_\odot)^{-13/69} (\dot{M}/1.3\ 10^{18}\mathrm{gs}^{-1})^{-16/69}\ \alpha^{18/69}\ \mathrm{cm}$$

for disk accretion, where α is the viscosity parameter of the disk ($\alpha < 1$). The Keplerian (~ free fall) and thermal velocities are

$$V_{kep}/c \approx V_{ff}/c = 6\ 10^{-2} (M/M_\odot)^{1/2} (r/10^8\mathrm{cm})^{-1/2}$$

$$V_{th}/c \approx 2\ 10^{-2}\ (T/10^6\mathrm{K})^{1/2} \qquad (3)$$

The Fe line observed in many X-ray pulsars very probably arises from this region ([11], [12]), and it could be used to trace the temperature and flow structure at the interface between the inflowing gas and the magnetic field, somewhat as the galactic

structure is studied in radio astronomy. If one could resolve the blue and red rotation components of the Fe line, this would confirm the existence of a magnetopause. Analysis of the outer shoulders of the pulse profiles could reveal whether most of the emitting matter is at a particular distance from the axis of rotation, which would argue for a disk, or whether it is spread out over a range of axial distances smaller than the maximum, which might indicate either a very well covered Alfven surface, fed from a disk, if the minimum velocity component is relatively very strong, or a more or less symetrical infall from all directions, if the emission strength at different velocities changes only very gradually. The strength and thermal width of the line might also give some clues as to the width of the Alfvén shell, providing valuable information about the viscosity at the field-plasma interface, and possible instabilities which might cause penetration of plasma into the magnetic cavity. The presence of several discrete velocity components might indicate either penetration of diamagnetic blobs, or strong non-dipole field components. Spectroscopic observations with $E/\Delta E \gtrsim 300$ would be the best for this, but $E/\Delta E \gtrsim 50$ would already be extremely useful.

III. Pulsation Mechanism

In order to test the possible contribution of the Alfvén shell as an occulting screen, one would want to know first the geometry and dynamics of the magnetopause flow, as described in II. This should be complemented by long term studies of the correlation of the X-ray luminosity with pulse shape in at least four bands,

$$E_s \lesssim 0.5 \ , \quad E_{ph} \sim 2\text{-}6 \ , \quad E_T \sim 8\text{-}12 \ , \quad E_T' \sim 15\text{-}25 \text{ keV} \qquad (4)$$

Here E_s is characteristic of screen reprocessing, E_{ph} is the band where photoabsorbtion may dominate; and E_T, E_T' are bands where scattering dominates. At least two of the latter are helpful, because the scattering opacity above 8 keV

should be frequency independent at the Alfvén shell and the pure screen mechanism would predict similar shapes at different energies. (The intensity Iν, originating at the surface of the star, could of course be different). If the screen mechanism dominates pulse formation, one would expect that a decrease in L_X (i.e. $\dot{M}$) would decrease screen opacity and therefore decrease the modulation factor (pulse throughs should fill in), while with increasing L_X, the pulse throughs should go down towards zero, i.e.

$$\text{Screen modulation} = \text{increasing function of } (L_X) \qquad (5)$$

On the other hand if the intrinsic beaming dominates pulse formation, very little change of the modulation with L_X is expected for either pencil or fan beams. For intrinsic fan beams, a change of the duty cycle or pulse width is expected to be correlated with L_X, while for intrinsic pencil beams the pulse multiplicity is expected to vary in a definite fashion with frequency, but not with luminosity, as discussed in the next section.

IV. Matter Deceleration and Geometry of the Emission Region

For luminosities $L_X \gtrsim 10^{37}$ erg s^{-1} radiation pressure plays a major role in the deceleration of the infalling matter at the polar caps, creating a smoothed-out radiation shock ([13]). In this case, the shock standoff distance varies from about $d_s \lesssim 0.1\ R_*$ to many times R_*, increasing approximately as $d_s \sim L_X^m$, with $m \sim 2/3$. The emitting atmosphere is the accretion funnel below the shock, sticking out above the stellar surface. The intrinsic beaming will be preferentially fan type, especially at the higher L_X, when the side surface largely exceeds the top surface of the column. The fan beam pulse width will be influenced by the amount of curvature of the side surface being sampled, this increasing with d_s and L_X. If a flat surface emits a narrow intrinsic beam, one can roughly estimate the angular

width of the actual beam from a curved surface as $\Delta\phi \sim$ channel width/height $\sim d_s^{3/2} d_s^{-1} \sim d_s^{1/2}$, where we used $a = a_0 [(R_\star + d_s)/R_\star]^{3/2}$ for the width of a dipole channel and took $d_s >> R_\star$. For $d_s \lesssim R_\star$ the dependence is not as strong, though still noticeable. Since in a radiation shock $d_s \sim L_x^{2/3}$, we expect

$$\Delta\phi \text{ (intrinsic pulse)} \sim L_x^{1/3}, \tag{6}$$

for $L_x \gtrsim 10^{37}$ erg s^{-1}. Thus, if the luminosity of the pulsar varies in time, so should the pulse width. Another quantity that may vary with L_x is the frequency of the cyclotron line feature, observed in some objects, if this arises near the shock. If the field is a dipole one would expect

$$\omega_H \sim (R^* + d_s)^{-3} \sim (1 + \text{const } L_x^{2/3})^{-3}, \tag{7}$$

For luminosities $L_x \lesssim 10^{37}$ erg s^{-1}, radiation pressure loses its importance, and one of the key uncertainties in deducing an atmosphere structure is whether a collisionless shock occurs, or whether the infalling protons are decelerated in the denser part of the stationary atmosphere by binary (coulomb or nuclear) encounters. In the absence of radiation pressure, the collisionless shock height (if present) would go as $d_s \sim n_e^{-1} \sim L_x^{-1}$, being given by the cooling or the coulomb exchange length. The collisionless shock would thus lead ([14]), by a reasoning similar to the high L_x case, to

$$\Delta\phi \text{ (intrinsic pulse)} \sim d_s^{1/2} \sim L_x^{-1/2}, \tag{8}$$

for $L_x << 10^{37}$ erg s^{-1}. This differs from the high L_x case treated before in equation (6). Similarly if the cyclotron feature arises near the shock, one would get

$$\omega_H \sim (R^* + d_s)^{-3} \sim (1 + \text{const}\, L_x^{-1})^{-3}, \qquad (9)$$

for $L_x << 10^{37}$ erg s^{-1}.

If no collisionless shock occurs (and theoretically, the physics of these shocks is largely unknown, so this is a distinct possibility) the stopping by binary encounters requires $y_0 \sim 5 - 50$ gm/cm^2, occurring in the dense part of the atmosphere. In this case the emitting region does not stick out significantly above the surface, and the beaming is essentially in a pencil pattern. In a magnetic field $B \sim 10^{12}$ gauss pointing perpendicular to the surface, the strong angular and frequency dependence of the cross sections leads to a very distinctive frequency behaviour of the pulse shapes. Detailed calculations ([15]) for homogeneous atmospheres indicate a rough rule of thumb for the pulse multiplicity in different frequency ranges (ω_H = cylcotron frequency), namely

$$\begin{aligned} &\text{single pulse:} && 10^{-1} \lesssim \omega/\omega_H \lesssim 1 \\ &\text{triple pulse:} && \text{few} \times 10^{-2} \lesssim \omega/\omega_H \lesssim 10^{-1} \\ &\text{double pulse:} && \omega/\omega_H \lesssim \text{few} \times 10^{-2}\ , \end{aligned} \qquad (10)$$

for pencil beam systems in which the magnetic axis is not too close to 90^0 away from the line of sight. These calculations also indicate that the spectrum is harder at midpulse, which observationally has been known to occur in some objects. Unlike in the shock cases, very detailed theoretical pulse profiles have been calculated for the pencil beam models ([15]), which would arise from binary particle deceleration. A refinement in progess now ([16]) consists in calculating the temperature and density profile of the coulomb decelerating atmosphere, which should provide more realistic spectra and pulse shapes to compare with observations.

References

1. Rappaport, S., Joss, P. C., 1977, Nature, 266, 683.
2. Ghosh, P., Lamb, F. K., 1979, Ap. J. 234, 296.
3. Kolykhalov, P. I., Sunyaev, R. A., 1979, Sov. A. J. Lett. 5, 180.
4. Gnedin, Yu. N., Sunyaev, R. A., 1974, Astron. Astrophys. 36, 379.
5. McCray, R., Lamb, F. K., 1976, Ap. J. 204, L115.
6. Basko, M. M., Sunyaev, R. A., 1976, Sov. A. J. 20, 537.
7. Zeldovich, Ya. B., Shakura, N. I., 1969, Sov. A. J. 13, 175.
8. Langer, S., Rappaport, S., 1981, Ap. J. in press.
9. Basko, M. M., Sunyaev, R. A. 1975, Astron. Astrophys. 42, 311.
10. Pines, D., 1979, in Procs. Wkshp. on Compact Galactic X-Ray Sources, F. Lamb and D. Pines, eds., U. Illinois, Urbana.
11. Ross, R., Weaver, R., McCray, R., 1978, Ap. J. 219, 297.
12. Basko, M. M., 1980, Astron. Astrophys 87, 330.
13. Basko, M. M., Sunyaev, R. A. 1976, M.N.R.A.S. 175, 395.
14. Mészáros, P., 1981, in Procs. Neutron Star Symposium, 5th European Physical Society General Meeting, Istanbul, Turkey.
15. Mészáros, P., Bonazzola, S., 1981, Ap. J. in press.
16. Harding, A. K., Mészáros, P., Kirk, J. G., Galloway, D., 1981, in preparation.

PRECEDING PAGE BLANK NOT FILMED

N82 26079

OBSERVABILITY OF ATOMIC LINE FEATURES IN STRONG MAGNETIC FIELDS[1]

G. WUNNER, H. RUDER, AND H. HEROLD
Institut für Theoretische Physik, Universität Erlangen-Nürnberg
West Germany

J. TRÜMPER
Max-Planck-Institut für Physik und Astrophysik,
Institut für Extraterrestrische Physik, Garching,
West-Germany

ABSTRACT

As an application of our comprehensive investigations of the physical properties of atoms in superstrong magnetic fields $B \sim 10^{10} - 10^{13}$ G, characteristic of neutron stars, we discuss the possibility of detecting magnetically strongly shifted atomic lines in the spectra of magnetized X-ray pulsars. Careful estimates of the relevant parameters lead us to the conclusion that it would be profitable to look for magnetically strongly shifted Fe XXVI Lyman lines in rotating neutron stars of not too high luminosity using spectrometers working in the energy range 10 - 20 keV, with sensitivities $\geq 10^{-4}$ photons per cm^2 and second, and resolution $E/\Delta E \sim 10\text{-}100$.

The observation of cyclotron features in the X-ray spectra of accreting neutron stars has confirmed the existence of superstrong magnetic fields of the order of $B \sim 10^{11} - 10^{13}$G (cf. Trümper et al. 1977). The discovery of further lines in the spectra of atomic origin for example, would provide an independent check on both the strengths of the magnetic fields and the assumptions of the physical conditions prevailing there. From the source temperatures $kT \sim$

[1]Research supported in part by the Deutsche Forschungsgemeinschaft (DFG).

ORIGINAL PAGE IS
OF POOR QUALITY

10 - 30 keV, derived from the observed spectra, it follows that the emitting matter is almost completely ionized, with a small fraction of hydrogen-like ions. The cosmic abundance of elements then implies that the lines with the largest possible energies and the highest intensities are members of the Lyman-series of Fe XXVI.

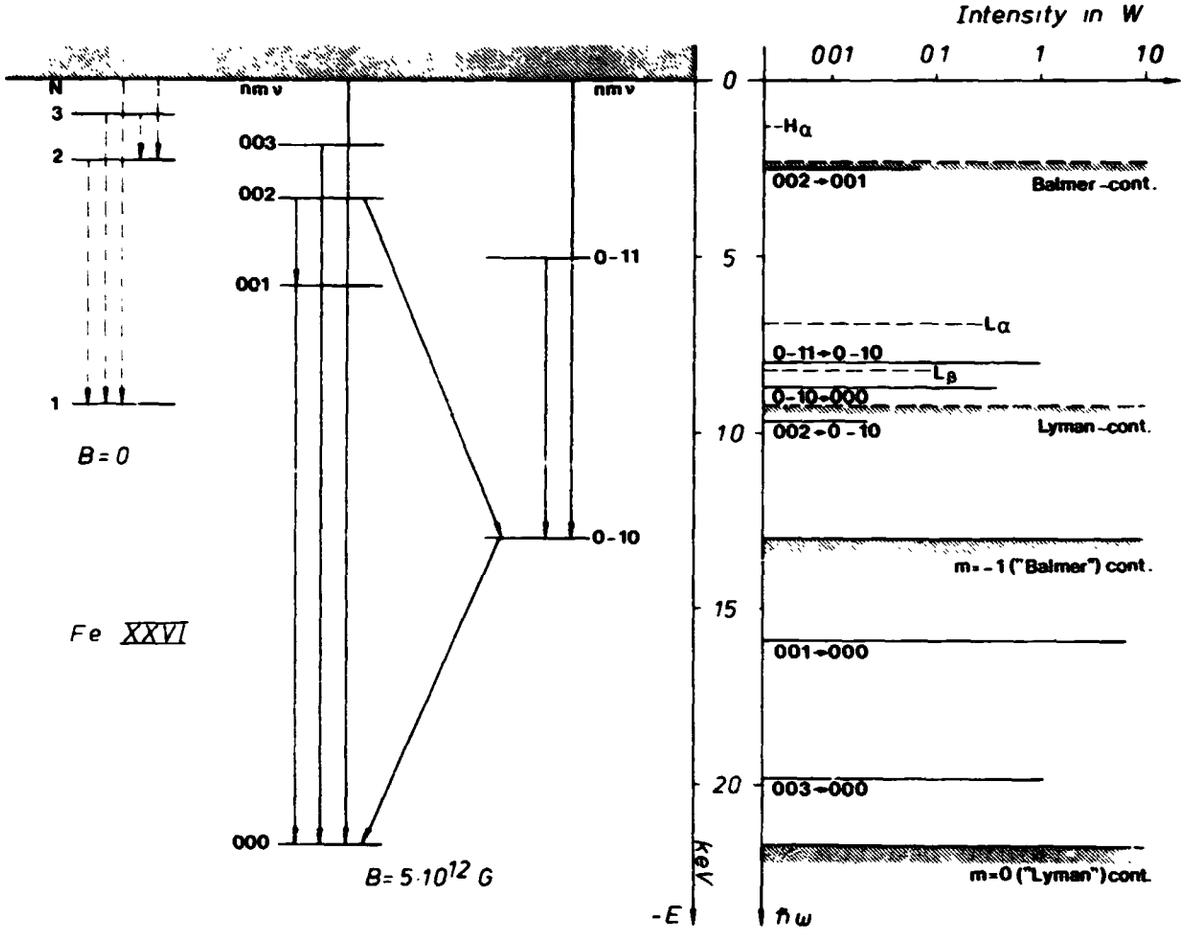

Fig.1. Level scheme for Fe XXVI and the photon spectrum resulting from the drawn transitions for B = $5 \cdot 10^{12}$G in comparison with B = 0 (dashed lines). The states are labelled by the usual field-free quantum numbers N,l,m, and by the quantum numbers n,m,ν of the adiabatic approximation. The intensities have been obtained assuming an average occupation number of one electron in the excited state. The onset of the continua is marked by hatching.

ORIGINAL PAGE IS
OF POOR QUALITY

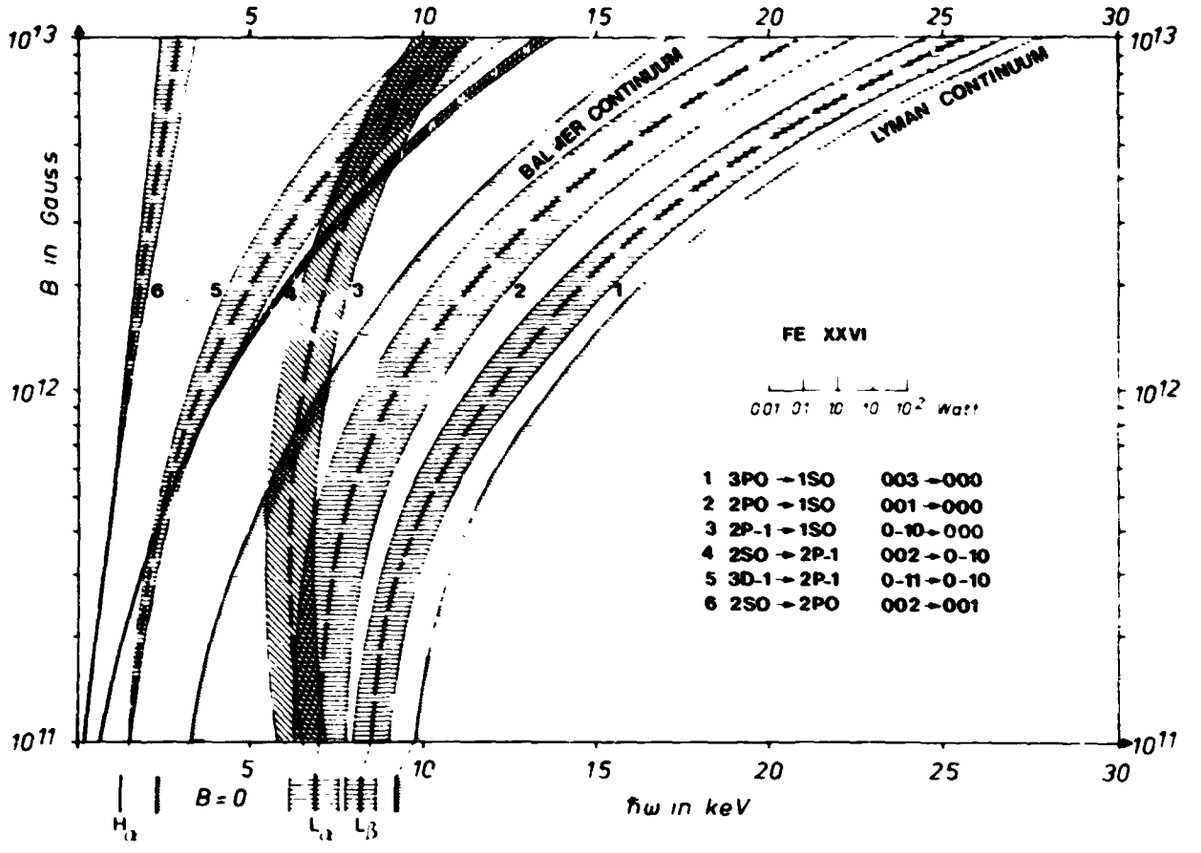

Fig.2. Energies and intensities of Fe XXVI lines as continuous functions of B in the range 10^{11} - 10^{13} G. The dashed lines represent the energetic positions of the lines, the widths of the corresponding corridors are proportional to the logarithms of the intensities in units of 10^{-2} W.

	B in Gauss							
	0	10^{11}	$5\cdot10^{11}$	10^{12}	$5\cdot10^{12}$	10^{13}	$5\cdot10^{13}$	10^{14}
Energies of γ's in keV	6.9	7.0	7.9	9.3	15.9	21.0	39.7	52.2
Numbers of γ's in 10^{15} s^{-1}	0.28	0.31	0.54	0.82	2.58	4.22	12.5	18.3

Tab.1. Energies and numbers of γ-quanta of the transition corresponding to L_α in the field-free case for Fe XXVI assuming one excited atom on the time average.

Using the scaling laws (Surmelian and O'Connell 1974, Wunner et al. 1981) of the one-electron energies E_m, $E_m(Z,B) = Z^2 E_m(Z=1,B/Z^2)$, (Z nuclear charge, m eigenvalue of the component of the angular momentum parallel to the magnetic field), and of the oscillator strengths, $f_{\tau\tau'}(Z,B) = f_{\tau\tau'}(Z=1,B/Z^2)$, the energy levels, oscillator strengths, transition probabilities, etc. of Fe XXVI in magnetic fields of arbitrary strength can immediately be derived from our comprehensive calculations (Wunner and Ruder 1980, Wunner et al. 1981) of the continuous B-dependence of these quantities for the H atom. Fig.1 shows the level schemes of Fe XXVI at B = 0 and $5 \cdot 10^{12}$ G and the resulting line spectra. The magnetic field dependence of both the energies and intensities of these lines over the whole regime of interesting field strengths can be seen from Fig.2. It is clearly exhibited that from $B \cong 10^{11}$ G onward for Z = 26 the magnetic forces begin to outweigh the Coulomb forces, to the effect that the structure of the spectrum changes from the field-free form to the magnetic-field-dominated shape. Furthermore one recognizes that L_α (asymptotically 001 → 000) remains the strongest transition. In Tab.1 we therefore provide, for this transition, the numerical values of the energies, and the numbers of γ-quanta emitted per second.

The observability of iron lines in the X-ray spectra of accreting magnetized neutron stars depends on a number of parameters such as plasma temperature and density, abundance of iron, source dimensions, magnetic field strength, and, of course, source distance. In addition, to be detectable the lines should be suffi-

ciently narrow ($\Delta E/E \lesssim 0.1$). Doppler broadening should be negligible for iron lines at the typical temperatures of these sources ($kT \sim 10$ keV), and collision broadening effects can be estimated to be less than ~ 1 keV at the prevailing temperatures and densities. However, a nontrivial condition is that the Thomson optical depth of the emitting plasma should be $\tau \lesssim 1$, in order to avoid too large line smearing by Comptonization.

The appropriate conditions may be found in accreting magnetic neutron stars of low luminosity, such as 4U900-40. Here one can expect that the interaction between the infalling gas and the radiation produced via Thomson scattering is small, and the material remains in free fall down to the stellar surface. If it is stopped there by Coulomb or nuclear collisions (Basko and Sunyaev 1975, Pavlov and Yakovlev 1976) the heated layer will have a thickness of 50 g/cm^2, viz., $\tau \sim 20$. However, recent computations by Kirk and Galloway (1981) show that plasma effects will considerably reduce the stopping length to values of the order of a few g/cm^2, which means $\tau \sim 1$ for the heated layer.

To arrive at a quantitative estimate, let us consider a radiating hot spot of area 10^{10} cm^2 and a thickness 2.5 g/cm^2 (corresponding to a total number of protons $1.5 \cdot 10^{34}$), a temperature of 10^8K, and $B = 5 \cdot 10^{12}$G. Starting from the Saha equation in a magnetic field (Gnedin et al. 1974), for these conditions the fraction of Fe XXVI ions in the first excited $m = 0$ state is calculated as $1 \cdot 10^{-4}$, which leads, together with the cosmic Fe abundance $3 \cdot 10^{-5}$, to $4.5 \cdot 10^{25}$ excited Fe ions on the time average. Using

Tab.1 and assuming a source distance of 1 kpc, we arrive at a line flux of iron L_α-photons of $1.0 \cdot 10^{-3}$ $cm^{-2}s^{-1}$, which should be detectable with X-ray spectrometers available at present. Actually, the iron line flux from the hot polar spot may be much higher than the above estimate, if the radiating plasma contains a substantial fraction of "stirred up" surface material, which should consist of pure iron.

Of course the detailed shape and width of the line feature are sensitively affected by the physical conditions in the accretion column (cf. Yahel 1981). For example it can be imagined that due to resonance scattering line trapping occurs, and a possible emission feature above the continuum background is changed into an absorption feature. At any rate, we conclude that it would be profitable in future X-ray explorer missions to look for magnetically shifted iron line features in magnetic neutron stars, using spectrometers working in the energy range 10 - 20 keV with sensitivities of $10^{-4}cm^{-2}s^{-1}$ and energy resolutions $E/\Delta E \sim 10\text{-}100$.

REFERENCES

Basko, M.M., and Sunyaev, R.A. 1975, Astron.Astrophys. 42,311
Gnedin, Yu.N., Pavlov, G.G., and Tsygan, A.I. 1974, Sov.Phys. JETP 39,20
Kirk, J.G., and Galloway, D.J. 1981, Mon.Not.R.astr.Soc. 195,45P
Pavlov, G.G., and Yakovlev, D.G. 1976, Sov.Phys. JETP 43,389
Surmelian, G.L., and O'Connell, R.F. 1974, Ap.J. 190,741
Trümper, J., Pietsch,W., Reppin, C., Sacco, B., Kendziorra, E., and Staubert,R. 1977, Ann. N.Y. Acad. Sci. 302,538
Wunner, G., and Ruder, H. 1980, Ap.J. 242,928
Wunner, G., Ruder, H., and Herold, H., 1981, Ap.J. 247,374
Yahel, R. 1981, presented at the 5th General Conference of the EPS, Istanbul

N82 26080 D25 477

A NEW METHOD FOR FOCUSING AND IMAGING X-RAYS AND GAMMA-RAYS WITH DIFFRACTION CRYSTALS

Robert K. Smither
Argonne National Laboratory
Received_____

ABSTRACT

The new method can focus monochromatic radiation from a point source or parallel beam down to a point image. Conversely, radiation from a point source can be focused into an outgoing parallel beam. The focusing to and from a parallel beam has never been achieved before with diffraction crystals. The method makes use of bent diffraction crystals in which the intercrystalline-plane spacing is varied as a function of position in the crystal. The Bragg angle for diffraction of monochromatic radiation will now vary as a function of position in the crystal and this new degree of freedom is used to obtain focusing and imaging of the diffracted beam. This new approach to focusing and imaging is applied to the design of a large-area, high resolution x-ray telescope that is also a high resolution monochromator with the unique feature that the width of the energy increment that is diffracted can be controlled and varied during the operation of the instrument. This makes it possible to first scan the field with a wide energy increment and ther switch to a narrow energy increment for the high resolution work. The new focusing system can be used with both transmission and reflection type diffraction crystals and is applicable to photons with energies from a few keV to 500 keV. High resoltion imaging (few arc sec) is possible even at the higher photon energies.

ORIGINAL PAGE IS
OF POOR QUALITY

I. INTRODUCTION

Diffraction crystals have been used for many years to focus a point or line source to a line image (Johnson, 1931) and in some special cases to focus a point source to a point image (Berreman, et al., 1954 and Berreman, 1955). A schematic drawing of the basic geometry used in these instruments is shown in Figure 1. The source, image, and bent crystal all lie on a focal circle whose

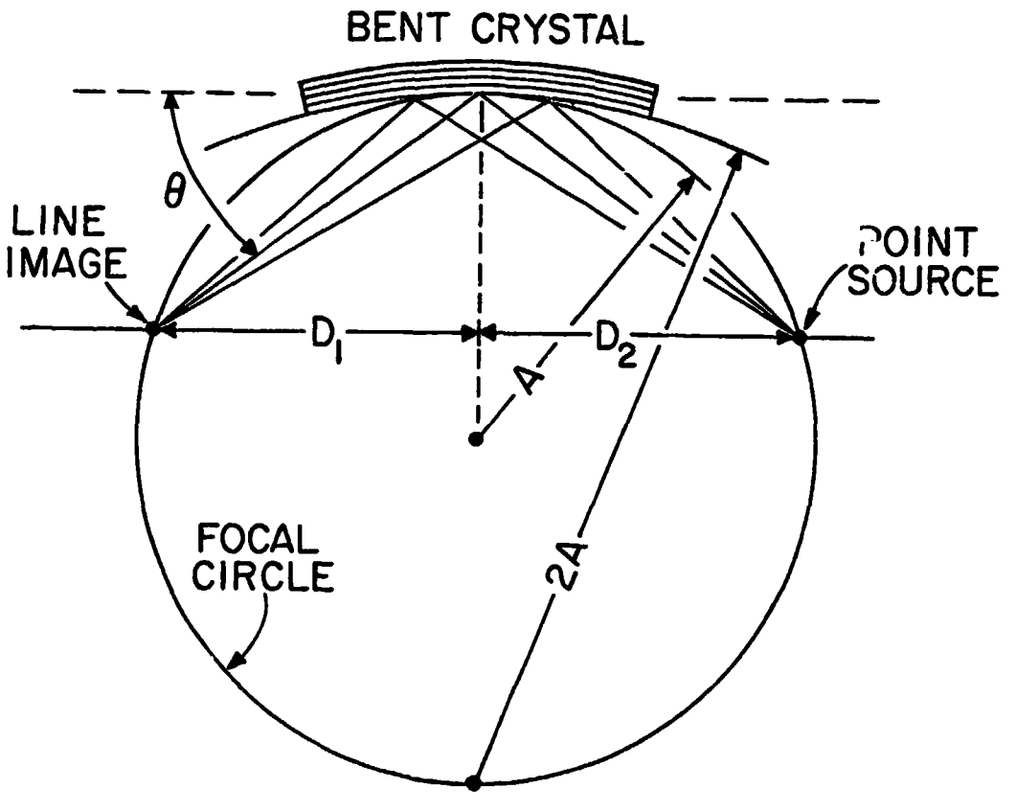

Fig. 1. Classic reflection-type focusing crystal-diffraction spectrometer. θ is the Bragg angles, "A" is the radius of the focal circle and "2A" is the radius of curvature of the bent-crystal. D_1 and D_2 are the image distance and the source distance, respectively

diameter is equal to the radius of curvature (2A) of the bent-crystal. D_1, the image distance in equal to D_2 the object distance. If the diffraction crysal is bent to a cylindrical shape the radiation will be focused to a line image. If the diffraction crystal is also bent in the direction perpendicular to the diffraction plane (the diffraction plane is the plane containing the incoming and outgoing rays) then it is possible to focus the radiation from a point source to a point image. The first type of focusing system works quite well in the laboratory when used with reasonable values for the diameter of the focal circle. A multiple crystal version of this type of instrument was used in conjunction with the grazing incidence x-ray telescope in the Einstien Observatory to do spectral analysis of the x-ray image (Canisares, et al. 1977).

ORIGINAL PAGE IS
OF POOR QUALITY

This type of instrument can not be extended for use with a point source at infinite because as D_2, the source distance increases the value of D_1, the image distance increase as well and in the limit when $D_2 \to \infty$, D_1 also approaches infinity and the bent crystal becomes a flat crystal ($2A \to \infty$). Thus the incoming parallel beam is diffracted as a parallel outgoing beam with no focusing in the diffraction plane. The use of a transmission type diffraction spectrometer does not help (see Figure 2). Here the diffracted beam is always

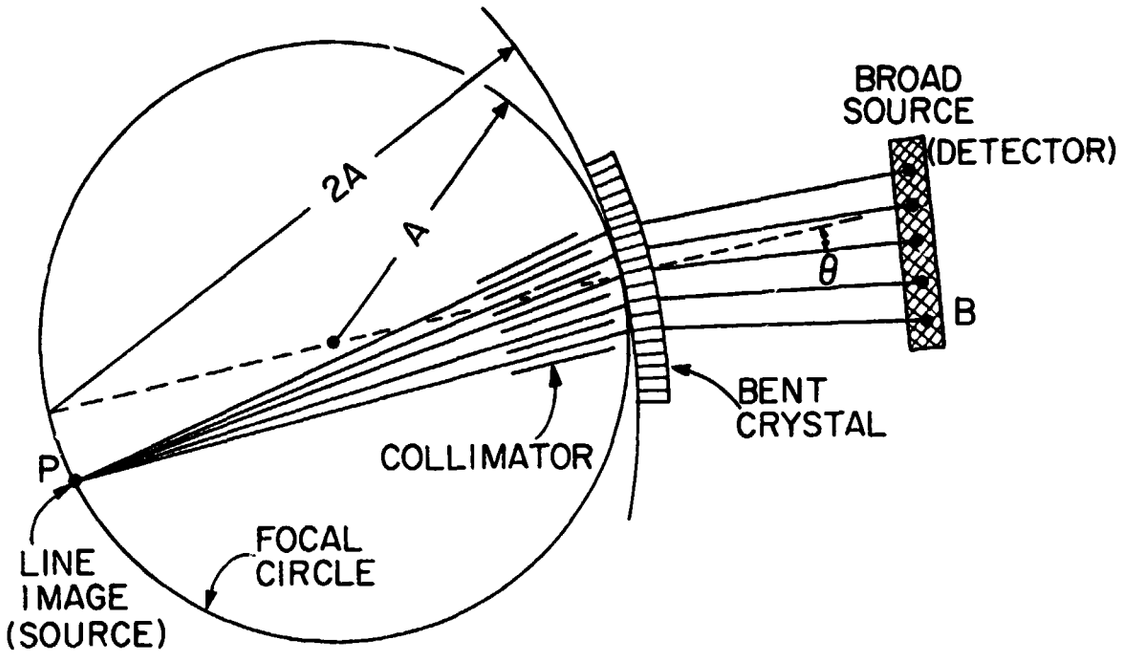

Fig. 2. Transmission-type crystal-diffraction spectrometer. "A" is the radius of the focal circle and "2A" is the radius of curveture of the bent crystal

defocused and approaches a parallel beam diffracted by a flat crystal when the source distance approaches infinity. In this mode of operation the diffraction crystal can be viewed as an excellent monochromatic collimator. Although this type of instrument is not very useful for imaging it could be used to make a spectra analysis of a large gas cloud or other extended sources. The different wavelengths would be focused at different places on the focal circle so the full spectrum could be recorded at the same time with a position sensitive detector

ORIGINAL PAGE IS
OF POOR QUALITY

II. NEW METHOD OF FOCUSING X-RAYS

The new focusing method is discussed in detail in a recent article in R.S.I. by R. K. Smither (1982). The basic approach is illustrated in Figure 3. Here a flat crystal is used to focus monochromatic radiation from a point or line source to a line image by varying the crystal "d" spacing in the diffraction crystal as a function of the distance, "x", from the baseline (line from source to image). A thermal gradient is used in this example to change the "d" spacing so that the Bragg condition:

$$n\lambda = 2d \sin \theta \tag{1}$$

is satisfied over the whole crystal surface for monochromatic radiation. If $D_1 = D_2$ this will automatically satisfy the focusing requirements as well.

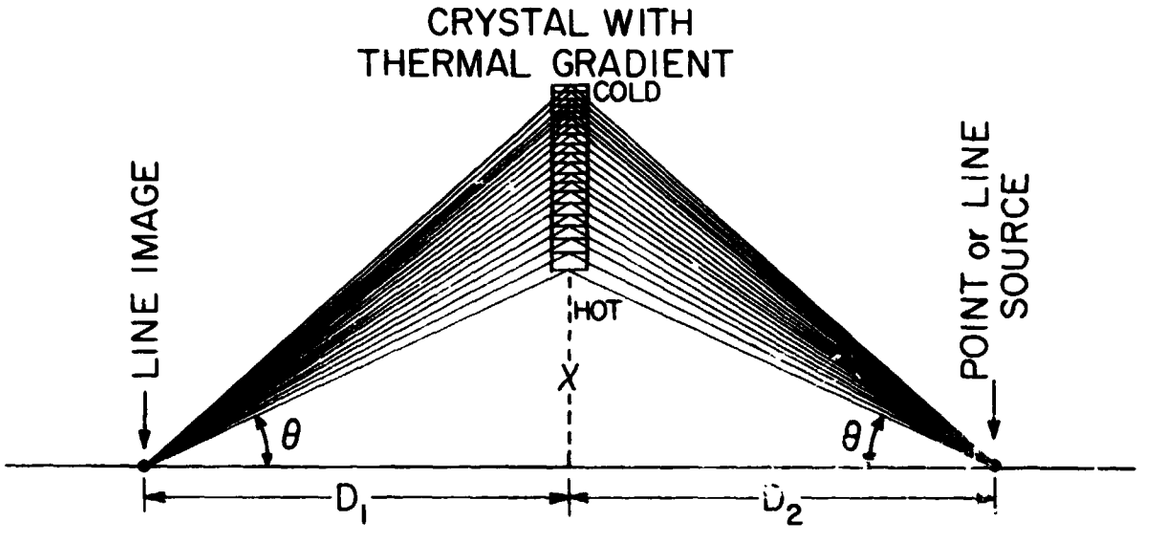

Fig. 3. New transmission type of crystal diffraction spectrometer using an unbent crystal with a thermal gradient applied to the crystal perpendicular to the diffraction planes with decreasing temperatures as x increases. The image distance, D_1, equals the source distance, D_2. D_1 must be equal to D_2 for the Bragg diffraction condition to be satisfied

The fractional change in the "d" spacing must match the fraction change in the value of sin θ. Thus:

$$\Delta d/d = \Delta \sin \theta / \sin \theta = \Delta\theta \cot \theta \tag{2}$$

where θ is the Bragg angle and d the "d" spacing in the crystal. In Eq. (1), λ is the wavelength and "n" the diffraction order.

The thermal gradient needed to achieve this diffraction focusing is given by Eq. (3)

$$\frac{\Delta t}{\Delta x} = \frac{1}{\alpha d} \cdot \frac{\Delta d}{\Delta x} = \frac{-\cos^2 \theta}{\alpha x} \tag{3}$$

where α is the coefficient of thermal expansion and $\Delta d/d = \alpha \Delta t$. The change in θ that can be focused is determined by the temperature differential, Δt, that is applied to the crystal. If the diffraction process uses the planes in quartz that are perpendicular to the optical axis, α is $1.34 \times 10^{-5}/°C$ and assuming a Δt of 200°C this gives $\Delta d/d = 2.7 \times 10^{-3}$. If $\theta = 20°$ then $\Delta\theta = 10^{-3}$ radians or 200 arc sec. This can be compared with the two arc sec for the rocking curve or acceptance angle of a good crystal without the presence of a thermal gradient. This results in an improvement of a factor of 100 for the diffraction intensity, while at the same time obtaining good convergence of the beam. The width of the image will be equal to the width of the source and will not reflect the mosaic structure of the crystal. This last effect leads to much better imaging than one might expect and comes about because most high quality crystals are composed of many small crystallite structures whose rocking curve or diffraction resolution is much better than the width of the mosaic structure which is a measure of the relative misalignment of these crystallites.

The more general case where D_1 is not equal to D_2 is shown in Figure 4. Both the transmission case (Figure 4a) and the reflection case (Figure 4b) lead to focusing so both large and small values of 6 can be handled with ease. The transmission case acts like a cylindrical lens (the first practical lens for high energy x-rays) and the reflection case like a cylindrical mirror. Both cases require that the diffraction crystal be bent. The radius of curvature, R_c, which controls the rate of change in the crystal plane tilt angle, ϕ, is given by Eq. (4) for the transmission case,

$$R_c = \frac{2R_1R_2}{(R_1-R_2)\cos\theta} \tag{4}$$

and Eq. (5) for the reflection case

$$R_c = \frac{2R_1R_2}{(R_2+R_1)\sin\theta} \tag{5}$$

where R_1 and R_2 are the distance from the image to the crystal and from the source to the crystal, respectively. ϕ is the angle between the crystal planes and the baseline. For a distant source D_2 and R_2 approach infinity as before but D_1 and R_1 remain finite and can be scaled up or down as one wishes so we now have two systems that will focus a parallel beam of radiation to a line image. The parallel beam focusing case is shown in Figure 5. The focal distance, D_1, in both cases is given by Eq. (6)

$$D_1 = x \cot 2\theta \tag{6}$$

ORIGINAL PAGE IS
OF POOR QUALITY

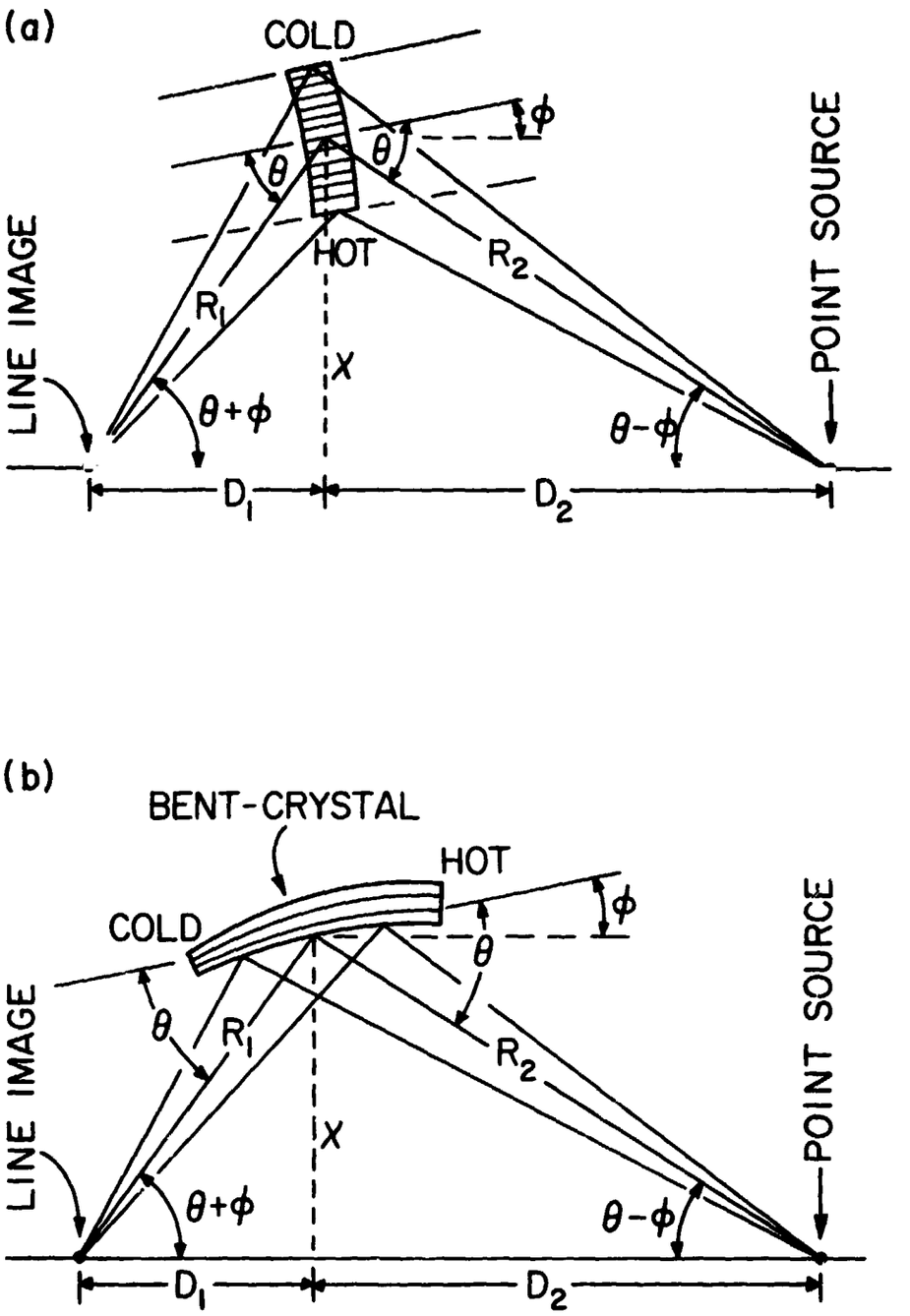

Fig. 4. (a) Transmission type and (b) reflection type diffraction spectrometer using thermal gradients and bent crystals for the general case when the image distance, D_1, is not equal to the source distance, D_2. ϕ is the angle of tilt of the crystal plane, x is the height of the crystal plane above the baseline, and R_1 and R_2 are the distances from the point of diffraction to the image and source, respectively.

ORIGINAL PAGE IS
OF POOR QUALITY

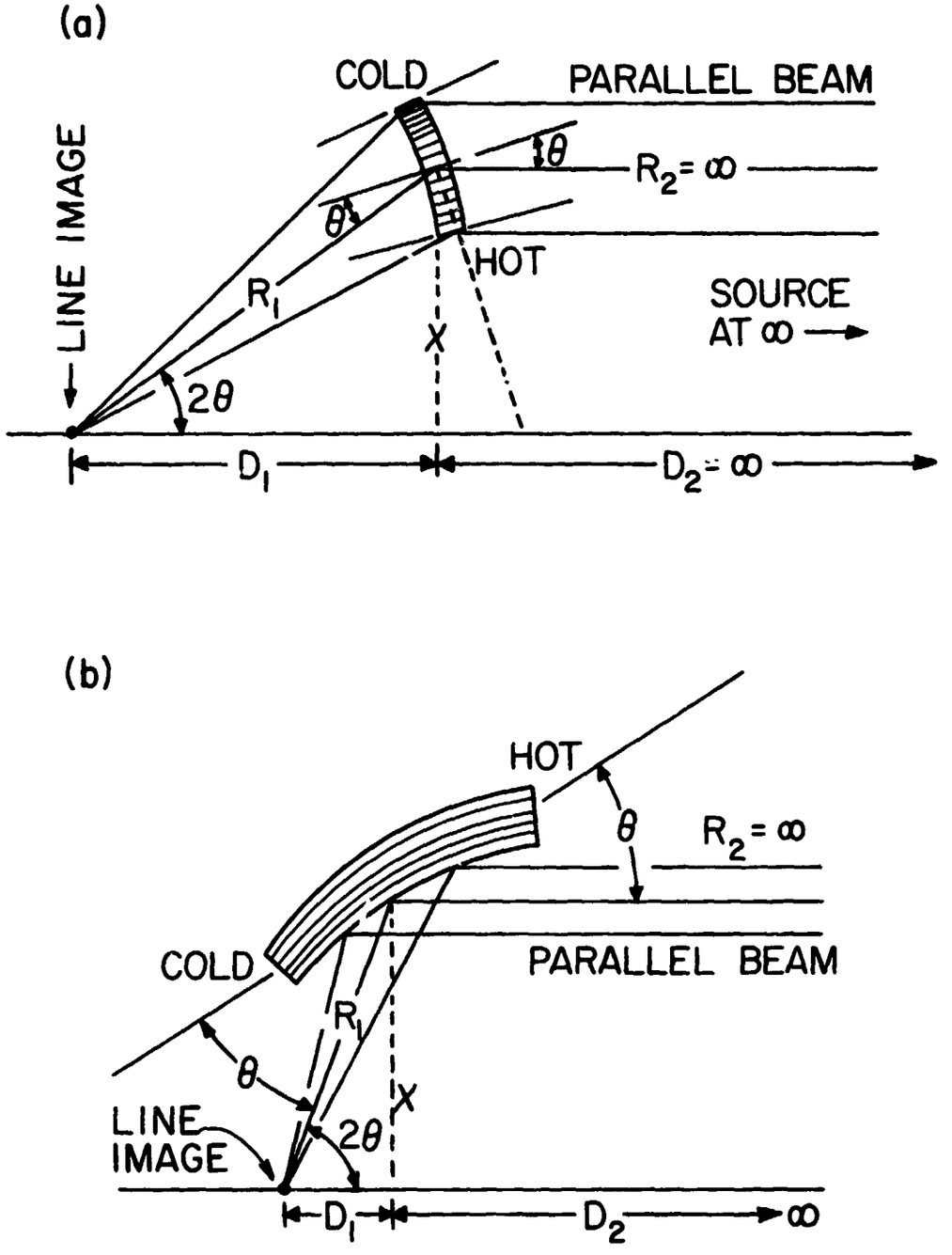

Fig. 5. Special case for parallel beams (source at inifinity) for the (a) transmission case and (b) reflection case of the new focusing method using bent crystals and thermal gradients. θ, x, D_1, D_2, R_1, and R_2 are the same as in Fig. 4

ORIGINAL PAGE IS
OF POOR QUALITY

If a point focus is required as it might in an imaging telescope then a second crystal-diffraction element will be required to focus the beam in the plane at right angles to the first focusing plane. This requires that the second crystal element be rotated by 90° around the axis of the beam as is shown in Figure 6.

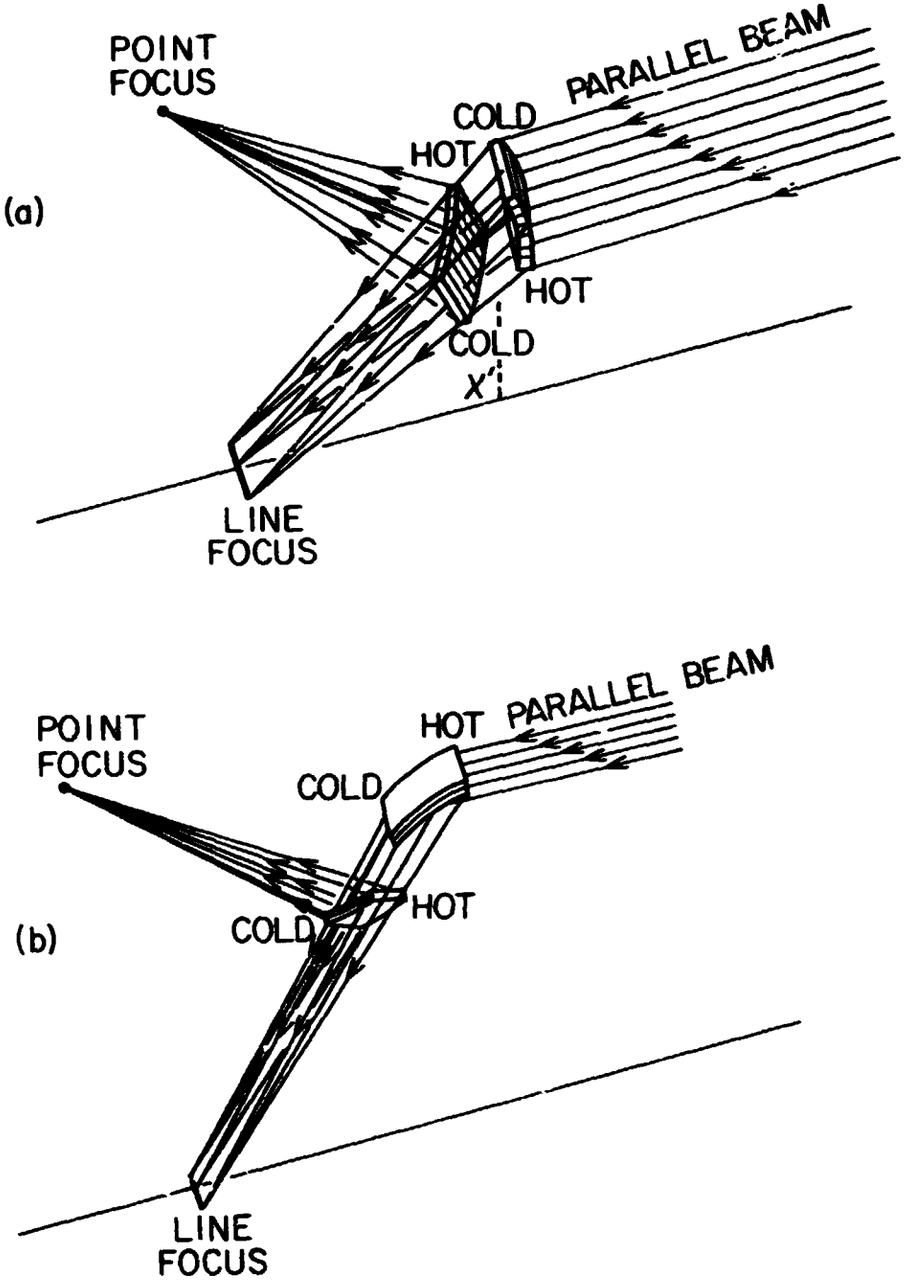

Fig. 6. Special case of double focusing of parallel beams for the (a) transmission case and (b) reflection case using the new bent crysta/thermal gradient method

ORIGINAL PAGE IS
OF POOR QUALITY

A more elegant but more complicated method can be found to obtain double focusing with the reflection type diffraction crystal (Berreman, 1955).

This approach is shown in Figure 7 where the diffraction crystal is also bent in a second direction, in the plane perpendicular to the diffraction plane. Either type of double focusing opens up the possibility of doing good imaging with a space telescope that uses some sort of position sensitive focal plain detector.

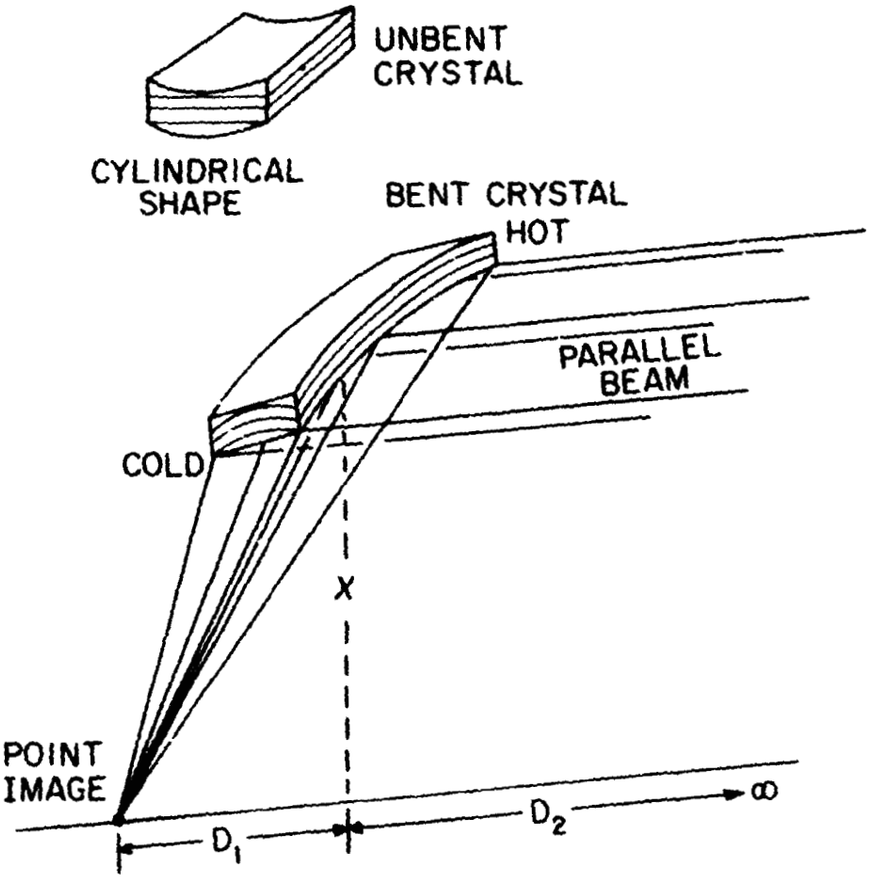

Fig. 7. Double focusing with a single crystal element that has been specially ground and shaped before bending and the application of a thermal gradient

In the parallel beam focusing case D_2 and R_2 approach infinity. This simplifies the expressions for R_c, $\Delta t/\Delta \ell$ or $\Delta d/\Delta \ell$ where $\Delta \ell$ is the distance along the surface of the crystal in the diffraction plane. R_c in the transmission case is given by Eq. (7)

$$R_c = \frac{2R_1}{\cos \theta} \tag{7}$$

and Eq. (8) in the reflection case

$$R_c = \frac{2R_1}{\sin \theta} \tag{8}$$

Also $\phi = \theta$ and the fractional change needed in the crystal spacing $\Delta d/d$ is given by Eq. (9) for the transmission case,

$$\frac{\Delta d}{d} = \frac{\cos^2 \theta}{2R_1 \sin \theta} \Delta \ell \tag{9}$$

and for the reflaction case, Eq. (10)

$$\frac{\Delta d}{d} = \frac{\cos \theta}{2R_1} \Delta \ell \tag{10}$$

The corresponding thermal gradient needed for the transmission is

$$\frac{\Delta t}{\Delta \ell} = \frac{\cos^2 \theta}{2\alpha R_1 \sin \theta} = \frac{\cos \theta}{\alpha x} \cdot \frac{\sin 2\theta}{2 \sin \theta} \tag{11}$$

and in the reflection case

$$\frac{\Delta t}{\Delta \ell} = \frac{\cos \theta}{2\alpha R_1} = \frac{\cos \theta}{\alpha x} \cdot \frac{\sin^2 \theta}{2} \tag{12}$$

For small values of θ the thermal gradient approaches a constant $(1/\alpha x)$ for the transmission case. In the reflection case the thermal gradient goes to zero as θ approaches zero or 90°. Note that the "d" spacing of the crystal does not enter into these equations so they are quite general. Also, the minimum value R_1 or x that can be used is set by the maximum value allowable for $\Delta t/\Delta \ell$ where $\Delta \ell$ is the length along the crystal surface in the diffraction plane. Thus the minimum size of the spectrometer is set by the maximum permissible value of the thermal gradient, $\Delta t/\Delta \ell$. For $\theta = 20°$ and $\alpha = 1.34 \times 10^{-5}$ (Quartz) and $\Delta t/\Delta \ell = 200°C/cm$, $x_{min} = 329.5$ cm in the transmission case and $x_{min} = 112.7$ cm in the reflection case. For a $\Delta t/\Delta \ell$ of 100°C/cm they will be twice as big, etc. This means that a spectrometer that relys on a thermal gradient to change the "d" spacing will be large, especially for small values of θ.

III. DIFFERENT METHODS FOR CHANGING THE CRYSTAL PLANE SPACING

The above discussion has used a thermal gradient to vary the "d" spacing in the diffraction crystals. The range of Bragg angles over which the crystal will focus monochromatic radiation is limited by how large a temperature difference can be applied to the crystal. In principle one could apply a Δt of 1000°C to a quartz crystal which would correspond to a $\Delta d/d = 1.34 \times 10^{-2}$ or 1.34%. In practice a Δt of 300°C (-100°C to +200°C) is all one would like to consider. This would give a $\Delta d/d = 4 \times 10^{-3}$ or 0.4%. As discussed in the previos section, the minimum value of x, the distance of the crystal from the axis or baseline is determined by t' maximum value attainable for $\Delta t/\Delta \ell$ [see Eq. (11) and (12)] and sets a minimum size for the spectrometer. An alternate method for changing the "d" spacing is to grow a crystal composed of two types of atomic like Si and B or Si and Ge (Pearson, 1967), (Pearson, 1972), and (Smither, 1982) and change the relative fraction of each type of atom as a function of position in the crystal. The lattice spacing in a Si-Ge mixed-element crystal can be changed from a value of d = 5.434 for pure Si to a value of d = 5.657 for pure Ge. This change in "d" of 4.1% corresponds to a $\Delta t = 10^4$°C for the thermal gradient method for varying "d". This approach has the advantage of giving large values of $\Delta d/d$ and $\Delta\theta$ and at the same time not requiring the power needed to maintain the thermal gradients needed in the examples cited, previously. The main disadvantage of this approach is that it does not have the ability to change the spacing gradient during the experiment and adjust for the focusing of different wave lengths or the ability to scan over a line in the spectrum by just changing the average temperature of the diffraction crystal. If the two approaches are combined, both the large $\Delta\theta$ and the variable $\Delta d/\Delta \ell$ can be retained. The use of at least some thermal gradient is also important because it retains the ability to control and change the increment of wavelength, $\Delta\lambda$, that is focused at one position on the focal plane. The narrowest value of $\Delta\lambda$ is obtained when the $\Delta d/\Delta \ell$ is matched to the changing Bragg angle needed for a perfect focus. If the system is detuned by using an incorrect value for the $\Delta d/\Delta \ell$ then a range of wavelengths will be focused at the image spot. This will allow a search mode to be used in the instrument if the energy of the line is not well known. After the line is located then the value of $\Delta\lambda$ can be adjusted to give the best sensitivity and/or resolution.

IV. APPLICATION TO A X-RAY TELESCOPE

A number of the special features of the new method, focusing monochromatic radiation, imaging, control of $\Delta\lambda$, line scanning, etc., could be quite useful in the design of an x-ray telescope. Although the method could be applied to the low energy x-ray region ($E_\gamma < 5$ keV) the considerable success of the grazing incident telescope like the one flown on the Einstein Observatory in this energy region make it more interesting to look at a telescope designed to look at radiation in the 10 keV to 200 keV range and the possibility of extending it to the 200-600 keV range. The fluxes at these higher energies are quite low so the collection area must be large, the order of square meters. This means that a large number of crystal elements will be needed that all contribute to the same focal spot. Figure 7 is a schematic

ORIGINAL PAGE IS
OF POOR QUALITY

drawing of a large area telescope where the individual diffraction crystals are located on a large ring structure. Assuming crystals of 6 cm length (Radial direction) and 0.5 cm wide mounted on a ring 20 m in diameter and assuming a 20% loss in area for the support structure then this one ring will have an entrance aperature for the telescope of $3.0 \times 10^4 \times \cos \theta$ (cm^2) for the transmission case and $3.0 \times 10^4 \times \sin \theta$ (cm^2) for the reflection case. For small values of θ the transmission case or large values of θ in the reflection case the entrance aperature would be about 2.5 to 2.2 m^2 and never need be lower than 2.1 m^2. If 5 such crystal rings are used then the entrance

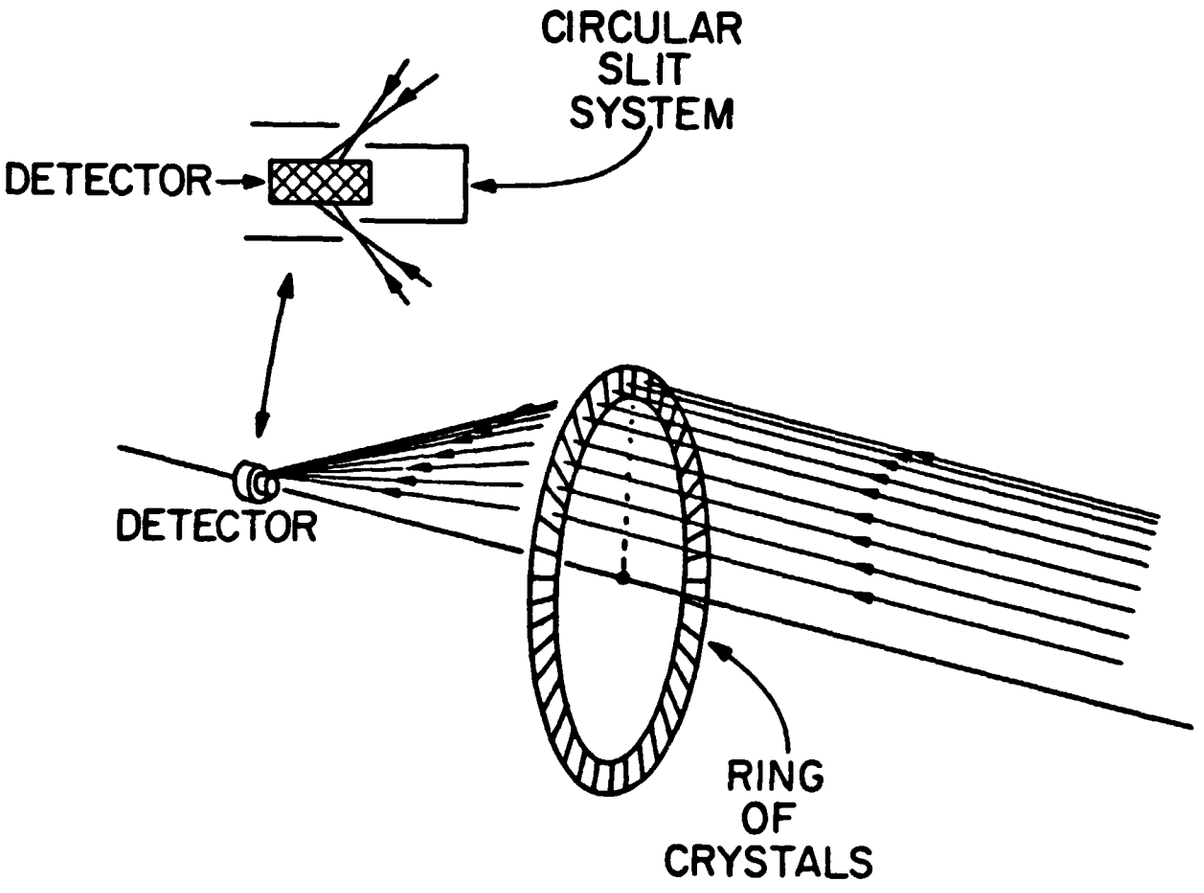

Fig. 8. Schematic drawing of a space telescope with a ring of diffraction crystals focusing a parallel beam into a circular slit. Details of the circular slit and detector are shown in the upper left

aperature will increase to 10.5 to 15 square meters or $\sim 10^5$ cm^2. If one uses high quality crystals then the through put of this system can be quite large due to the high reflectivity of the diffraction process. If one uses transmission crystals it is possible to select a thickness for the crystals that

maximizes the product of reflection of the crystal times the transmission through the crystal so that 30 to 40% of the incident monochromatic radiation is focused on the focal spot for any selected x-ray energy from 20 keV to 200 keV. At 500 keV the through put drops to 13%. Table I gives reflectivity and transmission coefficients for optimum thickness Quartz crystal based on measurements made on high quality quartz crystals at ANL. In principle, this

Table 1. Reflectivity and transmission coefficients for higher quality quartz crystal plates when used as transmission type diffraction crystals. The thickness of each plate has been optimized at each photon energy (E_γ) for the highest product of the reflectivity x transmission (Ref. x Trans.).

E_γ	Thickness (Opt.)	Reflectivity	Transmission	Ref. x Trans.
(keV)	(mm)	(%)	(I/I_o)	(%)
10.	0.04	45.5[a]	.825[a]	37.6
20.	0.22	48.2	.872	42.0
50.	1.45	48.5	.897	43.5
100.	4.50	46.6	.829	38.6
250.	20.0	42.7	.670	28.6
500	30.0	25.7	.499	12.8
1000.	50.0	13.0	.430	5.6

[a]Values extrapolated from data at higher energies.

approach could be extended down to 5 keV but the optimum thickness at these low energies becomes so thin that the crystals become difficult to handle and the use of reflection type crystals is more practical. A similar set of values can be obtained for the reflection case.Thus the effective collection area of the telescope for monochromatic radiation can be made the order of one third of the entrance aperature at any x-ray energy below 200 keV by choosing the right crystals and crystal thickness for the transmission case or by using the right crystals in the reflection case for x-rays with energies below 20 keV. This gives an effective collection area of 1.0 m^2 to 0.7 m^2 (10^4 to 7 x 10^3 cm^2) for one ring and 5 m^2 to 3.5 m^2 for the 5-ring assemble. These are large effective areas and assume single crystal diffraction elements. If the crystals are bent in only one direction as in Figure 5, then a line focus will be obtained and the focused radiation from a large ring (Figure 8) would be spread over an image spot whose diameter is equal to the width of the individual diffraction crystals. A 0.5 cm width gives an area of the image spot = 0.2 cm^2. For a focal distance (D_1) of 10 m this corresponds to a spot whose angular diameter is 100 arc sec.

Better angular resolution (~10 arc sec) and energy resolution can be obtained by focusing the crystals on a circular slit as shown in the upper left of Figure 8. This approach has the disadvantage in that it will not allow imaging of extended sources. If better imaging is desired than was obtainable with the cylindrically bent crystals discussed above then a doubly bent crystal element (see Figure 7) will have to be used or two singly-bent crystals (see Figure 6). If the later is used the maximum through put will be reduced from (30% to 40%) to (10% to 16%). The much better focus however will greatly increase the photons/cm^2 and the signal to background ratio. The spot size will now depend on the quality of the diffraction crystals used and could have a diameter of a few arc sec which corresponds to an image diameter of 0.2 mm for a focal length of 10 m and an angular width of 4 arc sec. The price that must be paid for this high resolution is that the instrument will be highly monochromatic and only a very narrow band of wavelengths will be diffracted at one time. The value of $E_\gamma/\Delta E_\gamma = 2 \times 10^4$ at 6 keV for a 4 sec width and a 2.57 Å "d" spacing (quartz, 110). This corresponds to a diffraction width of 0.3 ev. At 60 keV, the above example gives $E/\Delta E = 2 \times 10^3$ or a width of 30 ev. The doppler broadened line width (FWHM) of 6 keV line in a plasma with $T = 10^7$ K would be 2.2 ev and for a 60 keV line the broadened line width would be 22 ev. The 60 keV case is match in ΔE to the doppler broadening quite well and even if the plasma temperature was 10^8 K with the increased doppler width $\Delta\theta_D = 70$ ev, the loss would be less than a factor of 2. The resolution, ΔE, would also be the right order of magnitude to measure the temperature of the source by measuring the line width. The 6 keV line is not matched very well to the doppler broadening and it may help to detune the diffraction crystal by changing the thermal gradient so that the $\Delta\theta$ is 16 arc sec rather than 4 arc sec. This would give a ΔE for the diffraction process of 1.2 ev which would be a better match to the doppler broadened line. The total peak counting rate would however remain the same because the gain in reflectivity at one energy is balanced by the loss at another. The important feature of this type of ΔE control is that there is no loss in resolution either in the diffraction phase or in the plane perpendicular to the diffraction plane. If ΔE is increased by using a crystal with a large mosaic structure the loss occurs in both planes. If the mosaic structure of the diffraction crystal is increased from 4 sec to 16 sec then the reflectivity of the crystal for a single wavelength is decreased by a factor of 4 as it was before but there is also an increase in the image spot size in the direction perpendicular to the diffraction plane. This second expansion in the plane perpendicular to the diffraction plane is often neglected in efficiency calculation but it can seriously reduce the signal to background ratio in a focal plane detector. The expansion of the image in this sideways direction is given by Eq. (13)

$$\Delta\theta_\perp = \Delta\theta_M \tan 2\theta \qquad (13)$$

where $\Delta\theta_M$ is the width of the mosaic structure. For values of $\theta = 22°$ ($E_\gamma = 6.4$ keV in the above example) it becomes equal to the mosaic structure width. In the above example this effect would expand the image size further and decrease the photons per cm^2 in the image spot by an additional factor of 4. This additional spreading of the image will not only reduce the signal to backgrond ratio and thus the sensitivity of the instru-

ment but also seriously interfere with the resolution of two nearby images. This image broadening effect is discussed more throughly in the next section.

IV. IMAGING

The great success of the grazing incident telescope flown on the Einstien Observatory in generating high-resolution, two-dimensional images of extended sources has made everyone aware of the importance of imaging in x-ray astronomy. It is, therefore, of interest to see if the high resolution, monochromatic, x-ray telescope discussed above can be used to image extended sources. In most cases a diffraction crystal can be described as a collection of small nearly-perfect crystallites whose rocking curves or diffraction widths are much narrower than the width of the mosaic structure. In high quality quartz the diffraction width of these small crystallites can be the order of 0.1 arc sec for 50 keV radiation. The mosaic structure width is thus a measure of the misalignment of these small crystallites and for very monochromatic radiation from a distant point source only a small fraction of these crystallites will be available for diffracting the incoming beam. The rest will be orientated at angles that do not satisfy the Bragg condition. If the diffraction width of the crystallites were the only thing contributing to size of the image on the focal plane and the crystal had an overall mosaic structure ($\Delta\theta_M$) of 10 arc sec., then an image would be formed within this 10 arc sec range with 0.1 arc sec resolution. Unfortunately the crystallite diffraction width is not the only contributor to the image spot size. As was mentioned in the previous section the overall mosaic structure of the crystal spreads out the image spot in the direction prependicular to the diffraction plane. The amount of spreading is given by Eq. (13), where $\Delta\theta = \Delta\theta_M \tan 2\theta$. Even for small values of θ this spreading will be noticeable, ($\theta = 5°$, $\Delta\theta = 10 \times \tan 10° = 1.8$ arc sec) and for $\theta = 20°$ ($\theta = 22.5°$, $\Delta\theta = 10 \times \tan 45° = 10$ arc sec) or larger, the spread will be equal to or larger than the mosaic structure of the whole crystal and make it more difficult to resolve images in this direction. This effect is shown in Figure 9. The above examples assumed very monochromatic radiation. Most astronomical line sources have a finite line width either due to the life time of the x-ray or due to doppler broadening. In this case different subsets of crystallites will reflect different wavelengths at slightly different Bragg angles. This results in a spreading of the image spot in the diffraction plane. If the line is very broad then the spreading in this direction will approach the mosaic structure width. The image spot size for a range of values for θ is shown in Figure 10. Off-axis sources will also be imaged on the focal plane but with some distortion. For a single element focusing crystal like the one shown in Figure 7. The field of view is quite wide in the direction perpendicular to the diffraction plane (plane containing the source, center of the crystal and center of an axis image). For monocromatic radiation imaging in the diffraction plane is limited to an angular width similar to the mosaic structure. Images of sources with broad spectral lines will be formed in this off-axis direction within the range of angles that correspond to the spectral line width. If the telescope consists of a large ring of focusing crystals then some part of the ring will always be available for off-axis diffraction so large angular areas (10 min x 10 min) can be imaged with decreasing sensitivity as one moves farther off-axis. The distortion of these images will not be too great even if large diameter circular rings are used. For the case of a 20 m diameter ring, $\theta = 10°$, and an off-axis distance

ORIGINAL PAGE IS
OF POOR QUALITY

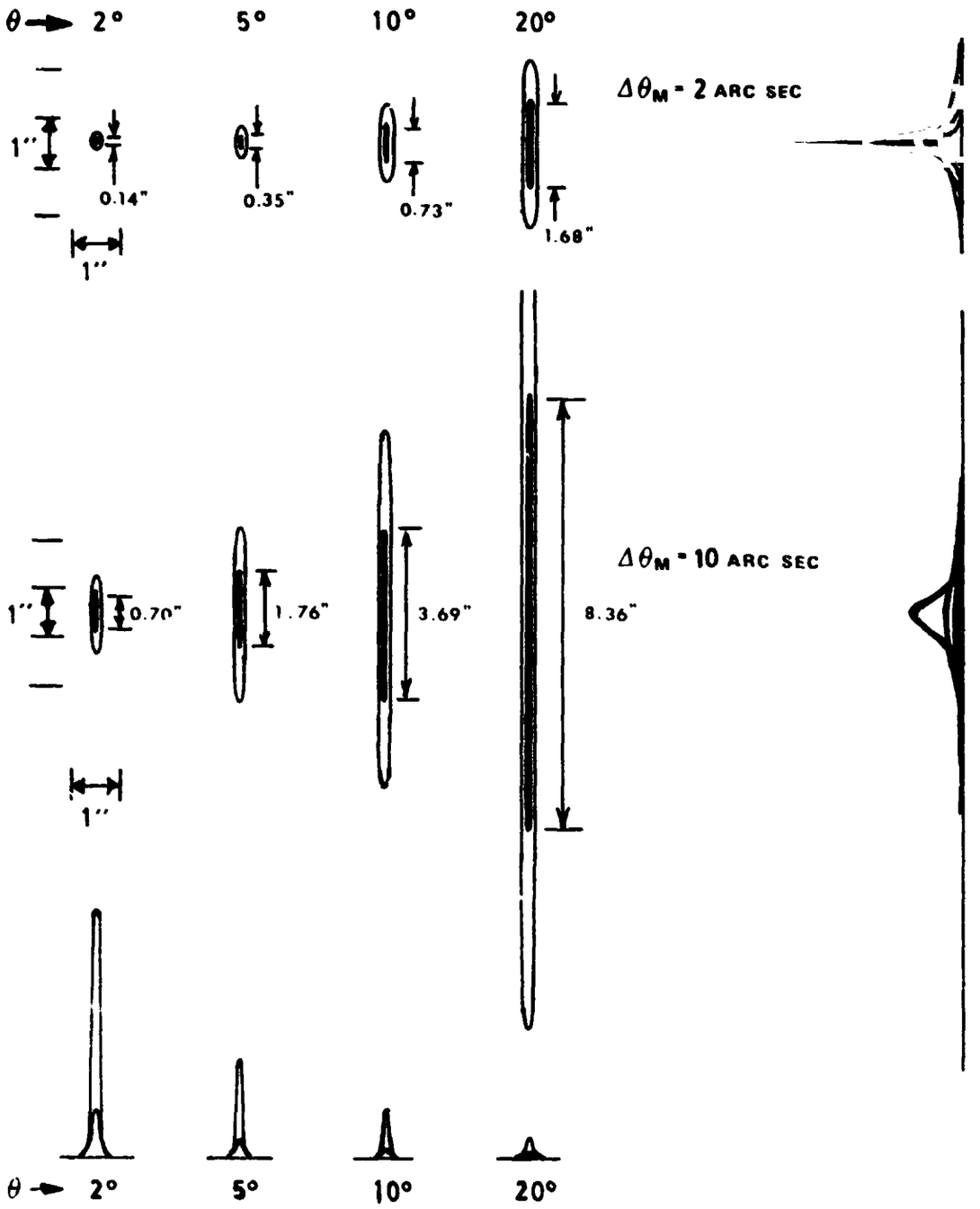

Fig. 9. Image spot size as a function of $\theta = 2°$, 5°, 10°, and 20° and mosaic structure width $\Delta\theta_M = 2$ sec and 10 sec for a double focusing single crystal system for a point source and monochromatic radiation. The solid filled area in the 50% height contour while the open line is the 10% height contour

ORIGINAL PAGE IS
OF POOR QUALITY

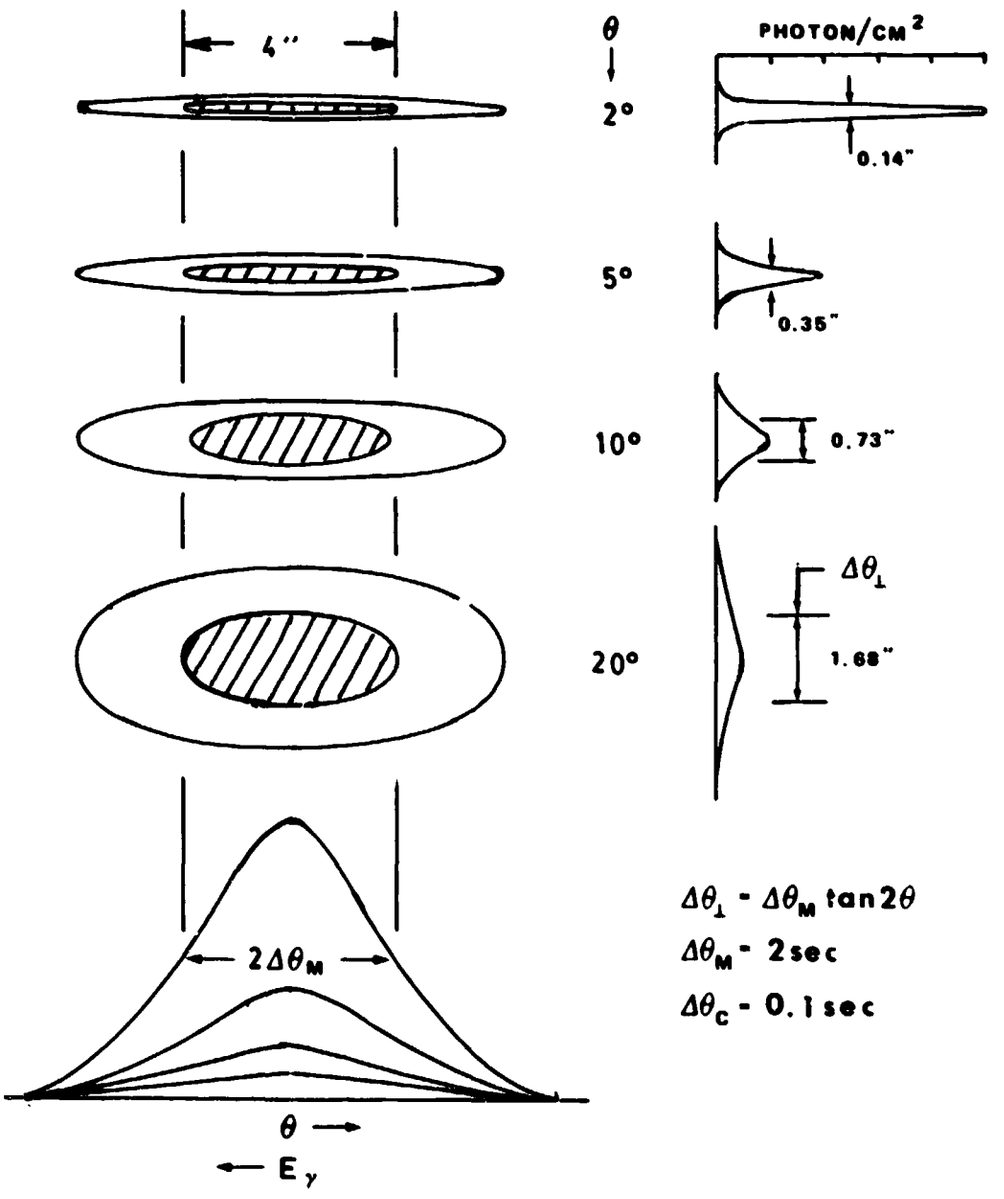

Fig. 10. Image spot size as a function of θ = 2°, 5°, 10°, and 20° for a single crystal system with a mosaic structure width $\Delta\theta_M$ = 2 sec when imaging continuum or very broad line sources from a distant point source. The shaded area is the 50% height contour while the outer ring is the 10% height contour.

of 20 arc sec the distortion of the image, $\Delta\psi_D$, is only 2.5 arc sec. In general $\Delta\psi_D$ given by Eq. (14)

$$\Delta\psi_D = \psi \sin 2\theta \tan 2\theta \qquad (14)$$

where ψ is the off-axis angle of the source. Note that the angular distortion is not a function of the size of the instrument or the focal length and the ratio of $\Delta\psi_D/\psi_D$ is only a function of the Bragg angle θ.

The use of a large circular ring of crystals generates an image spot that is a composite of the super imposed images from each crystal. This composite image can be generated from the single crystal images in Figures 9 and 10 by rotating these images through 360° aroung their centers. The off-axis images are generated in a similar way except that as the image rotates around its center, the center moves around a circle whose angular diameter ($\Delta\psi_D$) is given by Eq. (14). This distortion tends to disappear when the off-axis angle is large because the crystal elements responsible for the distortion are no longer at the right angle to diffract the beam. In many of the cases shown in Figures 9 and 10 the image is much larger in one dimension than the other and this rotation will generate an image with an appreciable larger area than the single crystal image. This will reduce the sensitive of the system and can considerably degrade the angular resolution. This image degradation can be partially eliminated by using narrow pie-shaped sectors covered with crystals rather than a continuous ring and focus each sector on a separate position sensitive detector. This would require the construction of sets of crystals with different average crystal spacings but it could improve the imaging at least in one direction by a factor of 5 to 10 depending on the angular width of the sectors (12° to 6°).

As mentioned above, if one increases $\Delta\theta_M$ in order to increase the range of wavelengths focused a spreading of the image in the direction perpendicular to the diffraction, $\Delta\theta_\perp$, also occurs. This loss in resolution and sensitivity can be avoided if one grows a reflection-type crystal so that the "d" spacing varies with depth into the crystal as well as with the position along the surface of the crystal. This variation of "d" with distance into the crystal has been used to increase the intregal reflectivity of a classical type instrument (see Figure 1) by varying the amount of Boron added to a silicon crystal grown epitaxially on a silicon crystal substrate (Fukuhara and Takano, 1980). The width of the diffraction peak was increased from a few arc sec for the undoped Si crystal to 80 sec for the epitaxial layer with graded Boron concentration that was 28 μm thick. This corresponds to fractional change $\Delta d/d = -10^{-3}$ and an enhancement of the rocking curve for the Cu K_α x-ray by a factor of 4 when using the 220 diffraction planes. The surface concentration of Boron was estimated to be 1.2×10^{26} atoms/m^3 (0.24%).

V. SUMMARY

The above discussion should not be considered as a formal proposal for an x-ray telescope but rather an illustration of the principals of the new focusing system and how it might be applied to the focusing and imaging of x-rays from a distant astronomical source. The real breakthrough for this application is the ability to image parallel beams (distant sources) of x-rays and the large con-

vergency angles that allow one to collect high energy x-rays from large areas without using impossibly long focal lengths.

The ability to change the width of the wavelength increment, $\Delta\lambda$, being diffracted without changing the image size and the ability to scan the line in wavelength without changing any of the physical dimensions of the instrument add to the attractiveness of this approach. The main design problems are how to apply thermal gradients to the bent crystals in a uniform and controllable manner and how to position and align a large array or ring of crystals to obtain the good resolution that is theoretically predicted.

REFERENCES

1. Berreman, D. W., DuMond, J. W. M., and Marmier, P. E., 1954, R.S.I., 25, 1219.

2. Berreman, D. W., 1955, R.S.I., 26, 1048.

3. Canizares, C. R., Clark, G. W., Bardar, D., and Markert, 1977, SPIE, 106, 154.

4. Fukahara, A. and Takamo, Y., 1980, J. Appl. Cryst., 13, 391.

5. Johnson, H. H., 1931, Z. Phys., 69, 185.

6. Pearson, W. B., 1967, A Handbook of Lattice Spacings and Structure of Metals and Alloys, (Pergamon, New York, Vol. 1, 1958 and Vol. 2, 1967).

7. Pearson, W. B., The Crystal Chemistry and Physics of Metals and Alloys, (Wiley-Interscience, New York, 1972).

8. Smither, R. K., 1982, R.S.I., (to be published in the Feb. 1982 issue).

ORIGINAL PAGE IS
OF POOR QUALITY

N82 26081

HIGH-RESOLUTION IRON-LINE SPECTROSCOPY

R.E. GRIFFITHS

Harvard-Smithsonian Center for Astrophysics

Cambridge, Massachusetts 02138

ABSTRACT

Methods of resolving the iron lines, the most common X-ray emission lines in both galactic and extragalactic X-ray sources, are briefly reviewed. A self-focussing crystal spectrometer is shown to be the most suitable instrument, and the optimum crystal geometry is spherical (Schnopper and Taylor 1980). The principles of operation of such a spherical crystal imaging spectrometer (SCIS) are briefly reviewed, and its sensitivity is shown to be two orders of magnitude better than a focal plane crystal spectrometer on AXAF. A Spacelab version of this payload would be very cost-effective.

PRECEDING PAGE BLANK NOT FILMED

ORIGINAL PAGE IS
OF POOR QUALITY

Introduction

The emphasis in this paper will be on high-resolution spectroscopy (the X-ray astronomer's definition: $\frac{E}{\Delta E} > 100$) of the iron lines in the 6-7 keV range. The first, and generally the strongest lines detected in proportional counter spectra of both galactic and extragalactic X-ray sources have been the iron lines in the 6-7 keV range. The reason for this line strength in optically thin plasmas is twofold: a) the high relative abundance of iron; and b) the ionization balance of elements at the temperatures typical of X-ray sources, i.e., 10^7 -10^8 K. Figure 1 is plotted from the tabulations of Raymond and Smith (1978) and shows theoretical calculations of the relative emissivities of the strongest iron lines between 3.10^7 and 10^8 K (not including satellite lines) and illustrates the reason that the Fe XXV/XXVI complex is so dominant in X-ray spectra - other elements are largely stripped out at lower temperatures. In particular, the effective temperature of intracluster gas in galaxy clusters, typically 8 x 10^7 K (see Mushotzky et al. 1978), is such that the iron complex forms the most useful diagnostic of cluster parameters.

The most common line observed in binary X-ray sources is the fluorescent iron line, for reasons of high fluorescence yield (a factor of 10 higher than any other element - see Table 1, taken from Pravdo 1978), coupled with the high relative abundance.

ORIGINAL PAGE IS
OF POOR QUALITY

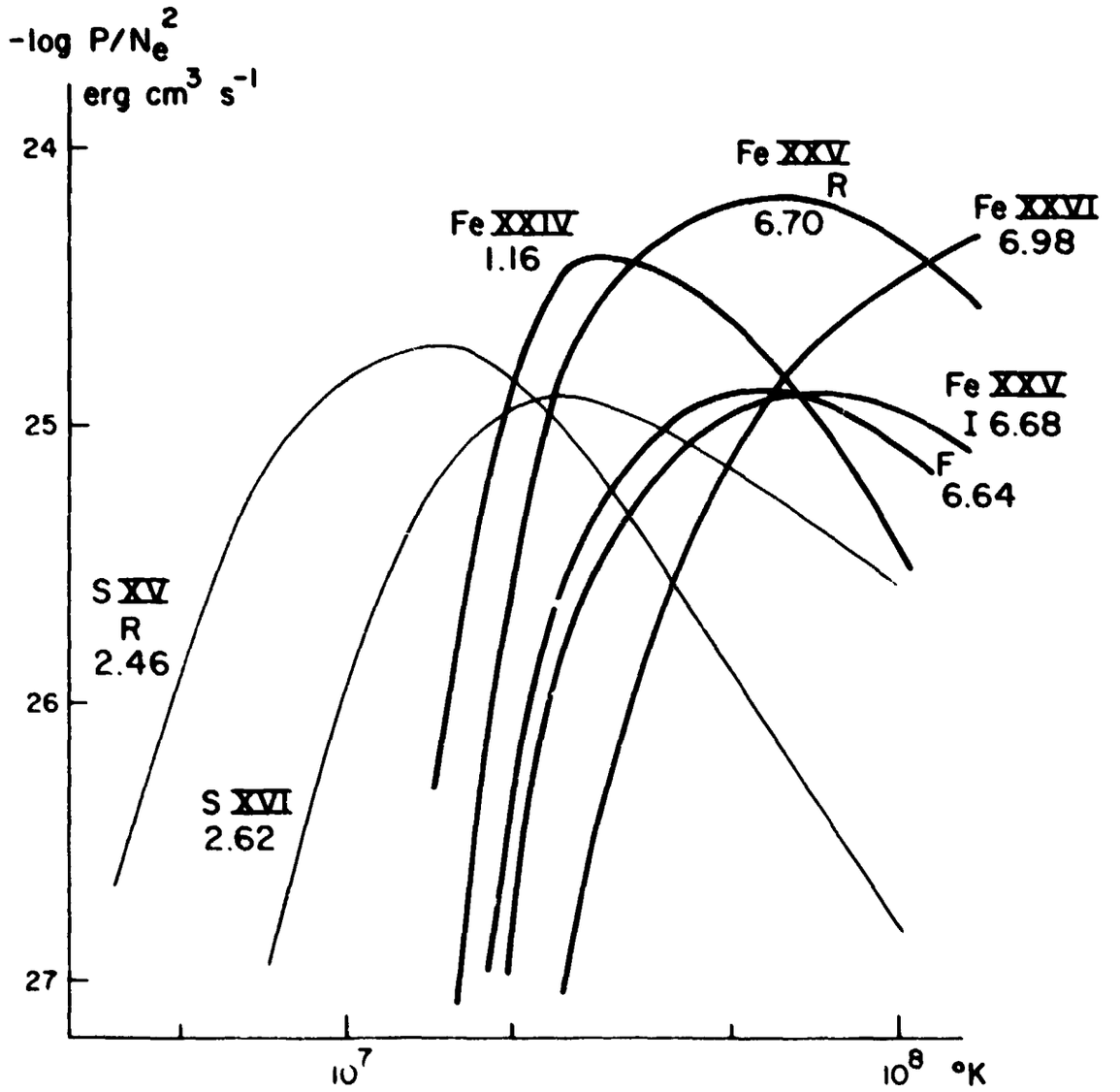

Figure 1 Relative emissivities of the strongest iron lines in a low-density plasma at temperatures between 3.10^7 and 10^8 K (not including satellite lines).

ORIGINAL PAGE IS
OF POOR QUALITY

TABLE 1

FLUORESCENCE EMISSION

Element	Relative Abundance	Fluor. Yield	Kα Energy	Rel. Equiv. Width (dN/dE^{-1})
Si	$3. \times 10^{-5}$	0.04	1.74	0.03
S	1.6×10^{-5}	0.08	2.31	0.03
Ar	$8. \times 10^{-6}$	0.13	2.96	0.03
Ca	$2. \times 10^{-6}$	0.16	3.69	0.01
Fe	$4. \times 10^{-5}$	0.35	6.40	1.00
Ni	$2. \times 10^{-6}$	0.41	7.47	0.07

Table 1 Relative fluorescence emission-line strengths (from Pravdo 1978)

ORIGINAL PAGE IS
OF POOR QUALITY

Dispersive Versus Non-Dispersive Spectroscopy

How can the iron line energy be reached for spectroscopy, and how can the iron lines be resolved for measurements of temperature, abundance, density and ionization balance?

Figure 2 illustrates the resolution typical of energy-dispersive devices (dashed lines) and those of dispersive devices (solid lines). Non-dispersive devices have been used almost exclusively thus far in the measurements of iron line strengths at 6-7 keV, but have insufficient resolution to separate the lines of Fe XXV from Fe XXVI. Gas proportional scintillation counters have twice the resolving power of the conventional gas proportional counters, but this is still insufficient to clearly separate Fe XXV from XXVI, or to resolve the Fe XXV triplet lines (note that lines of FE XXV, $1s^2$-1s2p and $1s^2$-1snp were recently resolved by a GPSC in the spectrum of Cas A - Andreser et al. 1981). The solid-state detector, of the kind flown on HEAO-2, (Holt, 1976), does have the resolution to separate Fe XXV from XXVI, and so, in principle, does a high-spatial resolution array of solid-state devices, i.e., the charge-coupled device. Considerable progress has been made in the development of a CCD with sufficient depletion depth for the 6 keV range (Griffiths et al. 1981; Peckerar et al. 1981), but solid-state performance equivalent to that from a conventional Si(Li) detector, has yet to be demonstrated from a full CCD array at this energy, although the lowest CCD noise levels are

ORIGINAL PAGE IS
OF POOR QUALITY

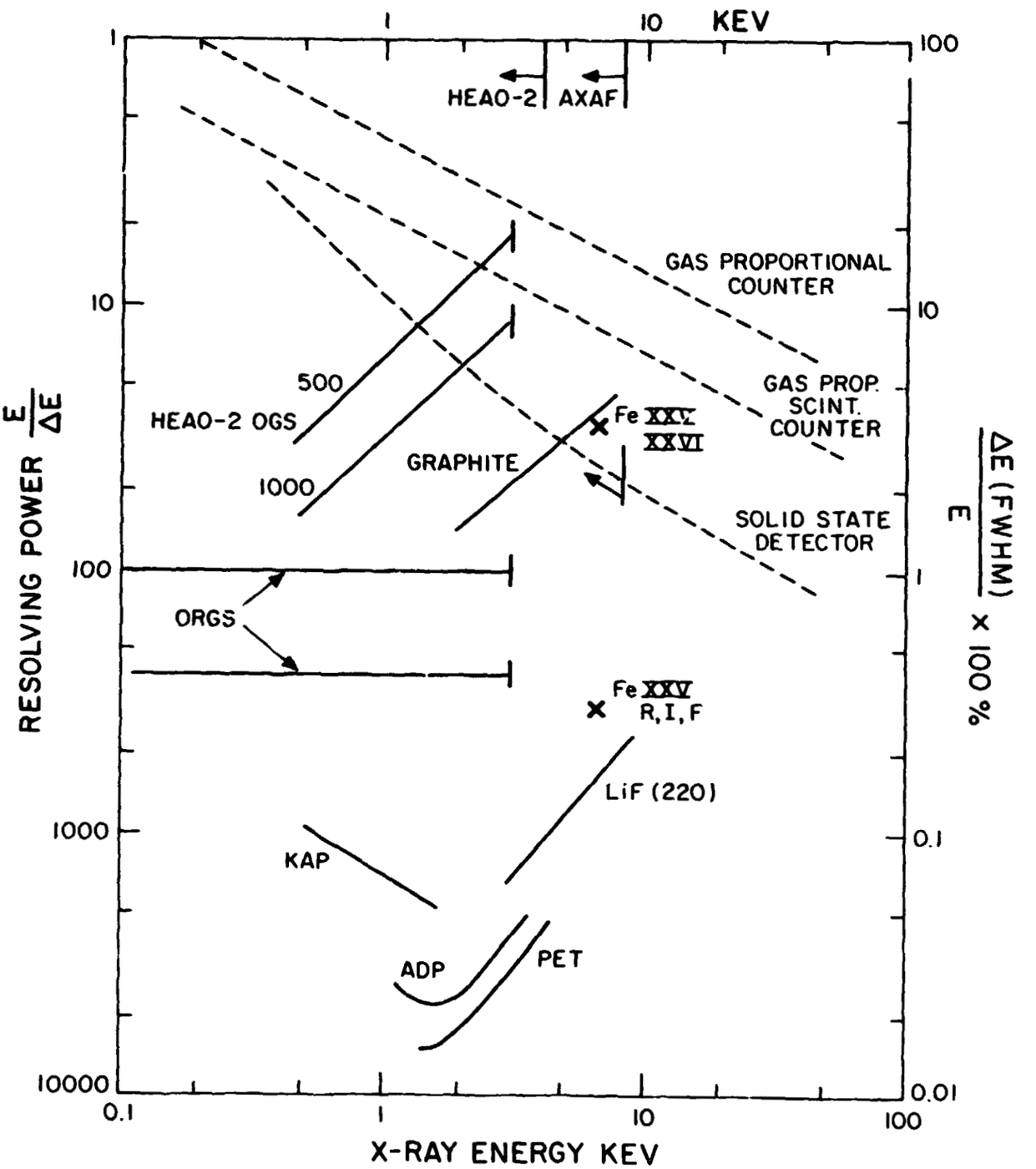

Figure 2 Energy resolution of non-dispersive devices (dashed lines) and dispersive devices (solid lines).

ORIGINAL PAGE IS
OF POOR QUALITY

comparable to or below that of the Si(Li) detector output. Both the conventional solid-state detector and the CCD have to rely on grazing-incidence optics for large collection areas, and in the case of HEAO-2, this resulted in no collection area at the 6 keV iron lines. For the proposed mirror design for AXAF, the effective collecting area at 6-7 keV will be about 200 cm^2 (Zombeck 1981).

To separate the Fe XXV triplet lines, the necessary resolving power is about 300, and this can be provided by crystal spectroscopy, lithium fluoride having a suitable 2d spacing (41^c Bragg angle for the atomic planes of LiF 220). In order to achieve high sensitivity, the particle background in the X-ray detector has to be effectively eliminated, so that the spectrometer is photon-limited for a large number of applications. Previous satellite-borne crystal spectrometers, on Ariel V, ANS, OSO-8 have been limited in sensitivity by their particle-induced background levels, concomitant on the flat crystal panels employed in each case. For large crystal areas and small detector sizes, some form of self-focussing is obviously required, and various geometries have been proposed, and some instruments flown, in recent years. The conical-segment spectrometer (Fig. 3a) was first proposed by Woodgate et al. (1973), and needs to be scanned over the required energy range. The convex version of this, described by Berthelsdorf et al. 1976 (Fig. 3b) is energy-dispersive along the detector axis, and has been employed on the solar maximum mission (Rapley et

ORIGINAL PAGE IS
OF POOR QUALITY

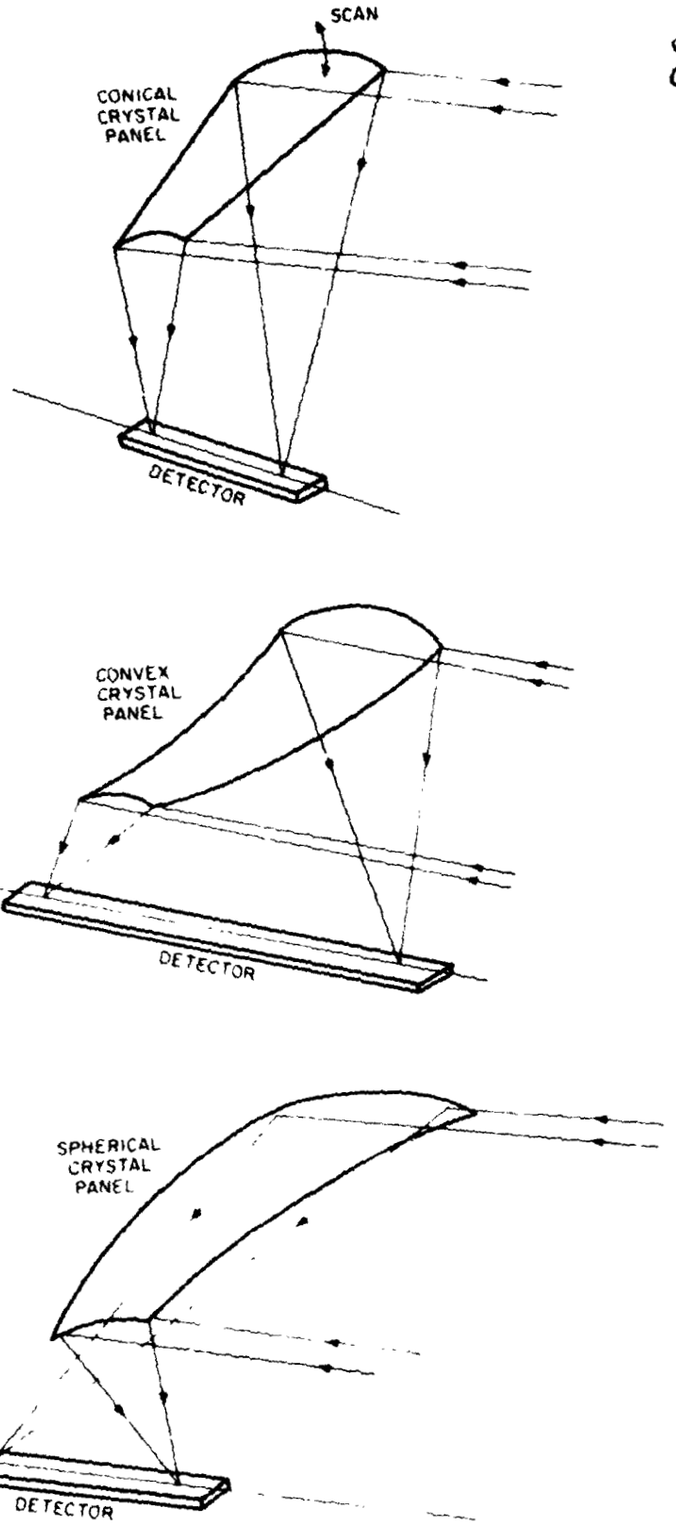

Figure 3 Self-focussing crystal spectrometers: a) conical spectrometer; b) convex spectrometer; and c) spherical spectrometer.

ORIGINAL PAGE IS
OF POOR QUALITY

al. 1977, Acton et al. 1981). The latter geometry leads to degraded performance for off-axis or extended sources, however, and the optimum geometry is the spherical case, fully described by Schnopper and Taylor (1981), and shown in Figure 3c. A brief description of the performance of this spectrometer will be repeated here.

Spherical Crystal Imaging Spectrometer

The axis of the spectrometer, along which the X-ray detector lies, is pointed at the target X-ray source. The operation of the instrument can be understood by reference to Figure 4, which shows the principle of operation in more detail. X-rays of energy E_1, incident in a cylindrical sheet on the top of the crystal panel, are focussed onto the detector at the point Z_1, and X-rays of energy E_2, incident in a similar sheet on the bottom of the panel, are focussed on the other end of the detector at Z_2. For a sphere radius of 2.5m, using lithium fluoride for the iron lines, the dispersion along the axis is about 0.4 mm per eV, or 2.4 mm for a 6 eV crystal-limited resolution element. Position sensitivity of 0.5 mm in the proportional detector is therefore sufficient for the energy-dispersive line focus. The position-sensitive detector reads out each X-ray event as it occurs, and the entire spectrum is thus recorded in a parallel fashion, with no mechanical scanning. The total energy range covered by the spectrometer is

ORIGINAL PAGE IS
OF POOR QUALITY

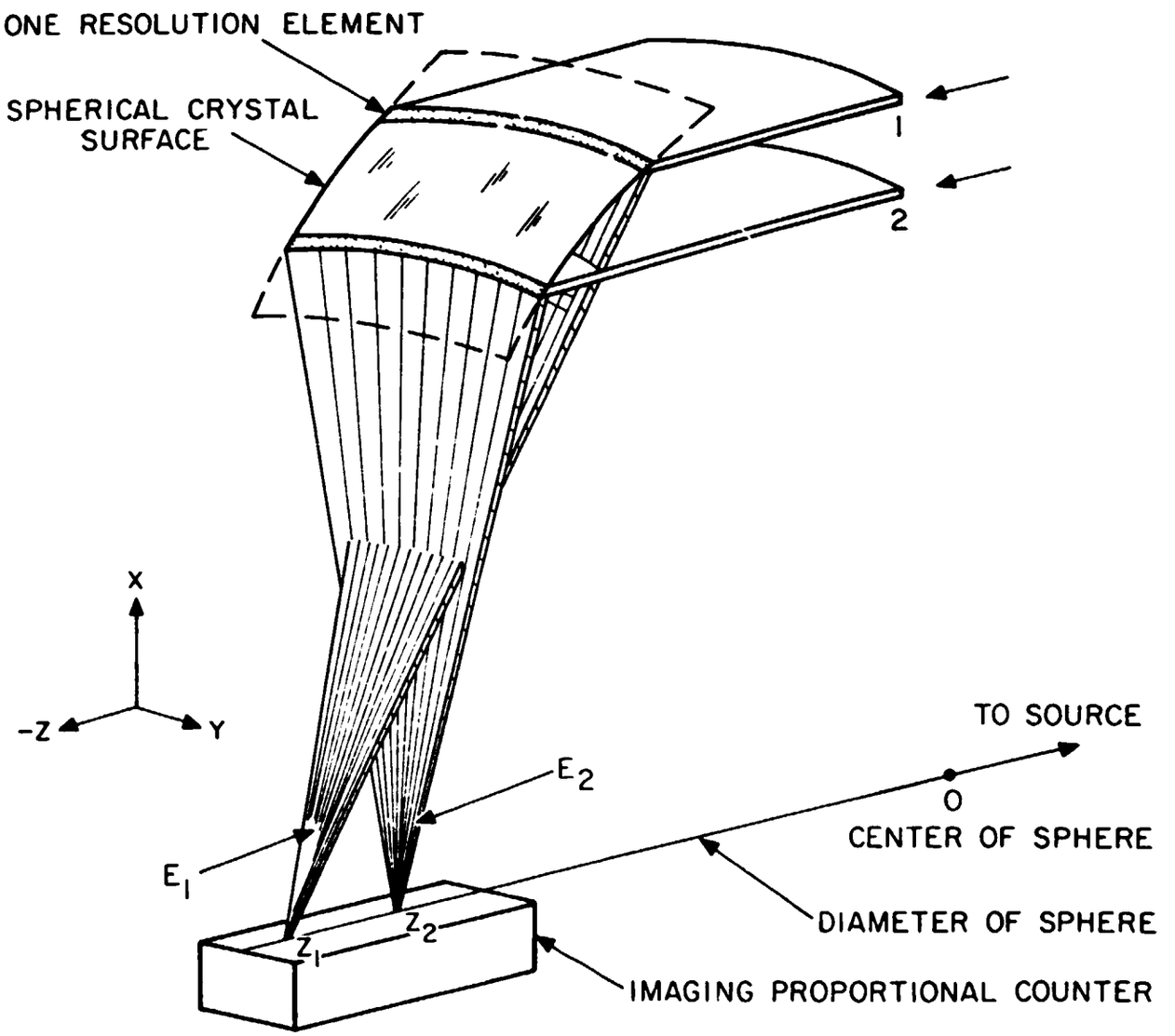

Figure 4 Basic operation of the spherical spectrometer.

ORIGINAL PAGE IS
OF POOR QUALITY

determined by the range of Bragg angles for X-rays incident at the extreme ends of the spherical section.

A real, imperfect crystal consists of a mosaic of individual perfect crystal blocks, on a microscopic scale, with a resultant increase in integrated reflectivity (James 1948). For the spherical spectrometer, the rocking curve width of the scanned flat crystal panel becomes a corresponding crystal-limited resolution element along the position-sensitive detector. For a Bragg angle of 45^{c}, the energy resolution in the spherical spectrometer case is the same as that for the scanned flat crystal panel. For Bragg angles much less than 45^{c}, there is some gain in the effective energy resolution with the spherical geometry, but the effective area of the crystal panel is reduced and the geometry does not use the available volume as efficiently as the 45^{c} case.

An extended X-ray source, or a spacecraft attitude error for a point source, will result in some slight degradation in performance, but it can easily be shown that the effects are almost negligible in terms of spectroscopic resolution. These effects are most easily understood by considering spacecraft attitude errors and a point X-ray source. It is obvious that, as the spacecraft and spectrometer rotate slightly around the center of the sphere, the spherical symmetry guarantees that the X-rays will still be focussed on the line joining the center to the X-ray source, with a small change in the energy range of the reflected X-rays. The detector will no longer be exactly on this

ORIGINAL PAGE IS
OF POOR QUALITY

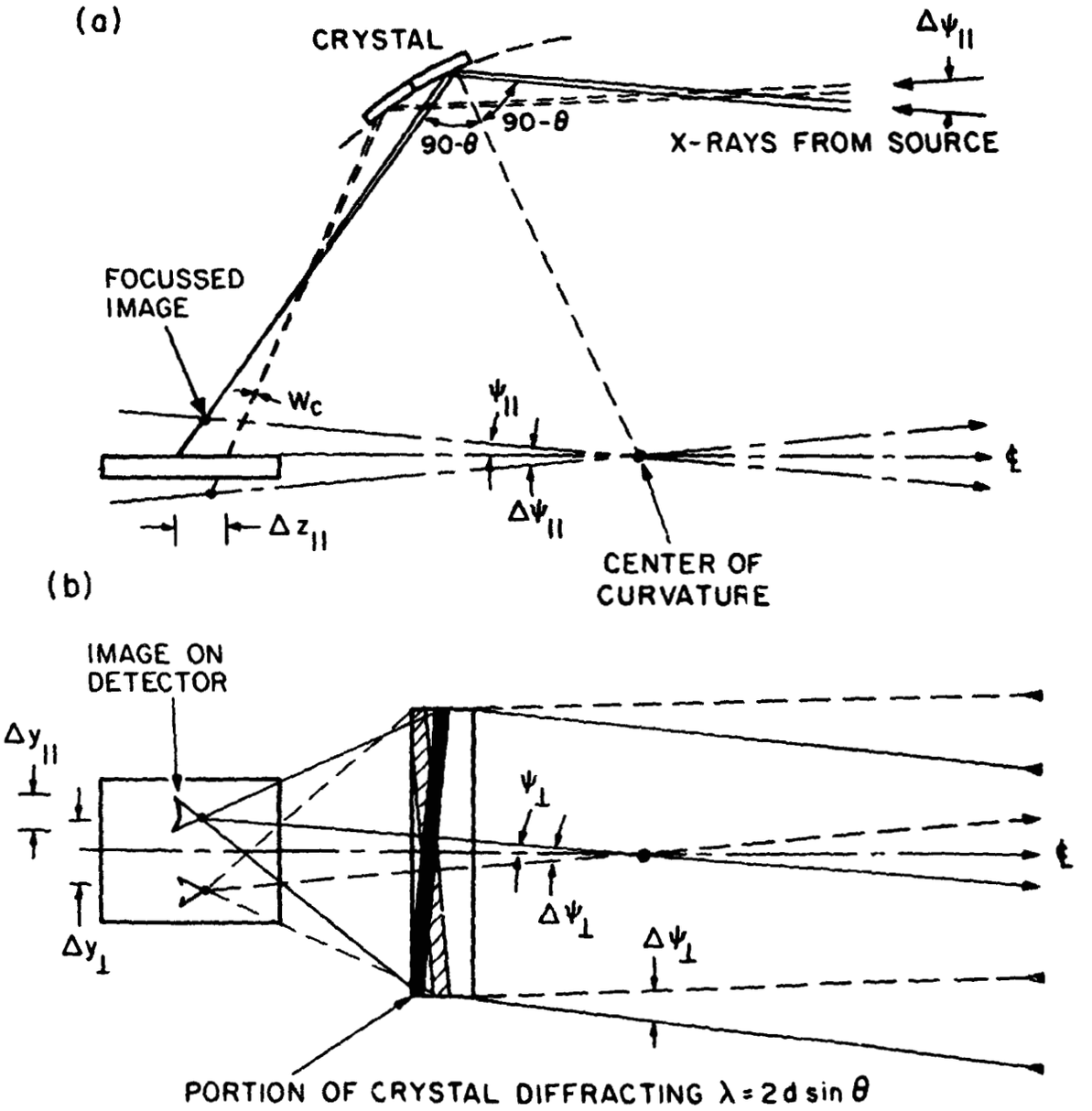

Figure 5 Effect of off-axis X-rays: a) in the plane of dispersion; and b) orthogonal to the plane of dispersion.

ORIGINAL PAGE IS
OF POOR QUALITY

line focus, however. It is most instructive to separate the pointing error into two components, one orthogonal to the plane of dispersion (Fig. 5b) and one in the dispersion plane. For the orthogonal pointing error, a stigmatic focus is formed on the detector, along an arc about the center of the sphere, where this arc is displaced in the manner shown (< 1 cm for a $0^{\circ}.5$ pointing error).

A pointing error in the plane of dispersion (Fig. 5a) results in a line focus lying slightly above or below the detector anode, and the image at any particular energy is formed in a hyperbolic arc on the detector, where the curvature of the arc causes an insignificant loss of energy resolution. The post-facto spacecraft or instrument aspect solution can be used to correct for the instantaneous size and position of the hyperbolic arc, so that the resulting spectrum is not significantly degraded. The pointing requirements for the spherical spectrometer are thus minimal, of the order of $\pm 0^{\circ}.1$.

The imaging of an extended source can best be considered in terms of point source components, where each off-axis point source is imaged into a short, hyperbolic arc, as described above. The energy resolution of the spectrometer in the plane of dispersion is slightly degraded by source extent, but this effect becomes important only for sources greater than $0^{\circ}.2$ in diameter, using lithium fluoride panels. In the plane orthogonal to the dispersion plane, the angular resolution is limited by the crystal rocking curve width of about 5 arc minutes.

ORIGINAL PAGE IS
OF POOR QUALITY

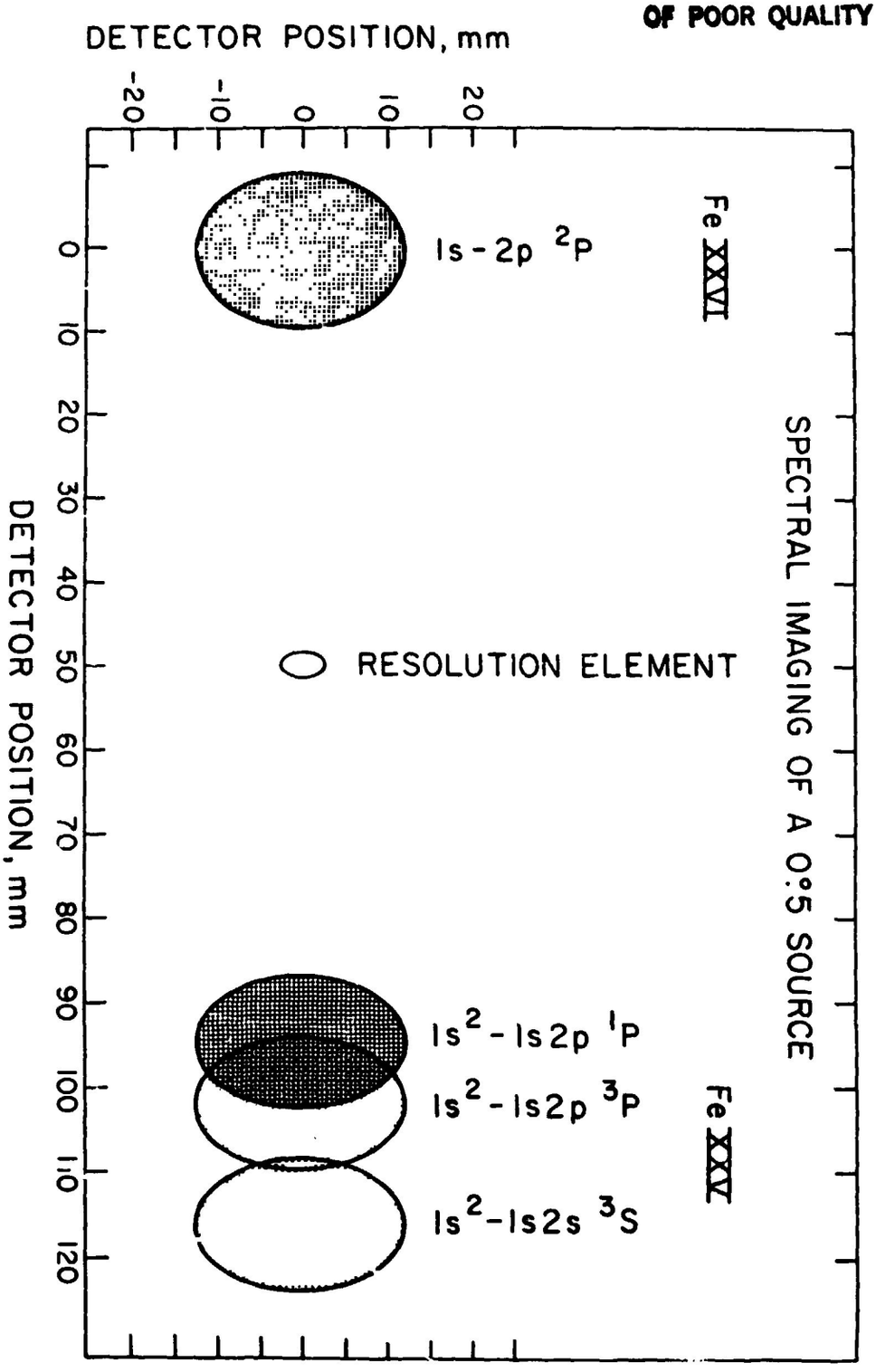

Figure 6 Idealized image of a cluster of galaxies of 0°.5 extent, showing shape of monochromatic images in lines of Fe XXV and XXVI.

ORIGINAL PAGE IS
OF POOR QUALITY

ORIGINAL PAGE IS
OF POOR QUALITY

Projected SCIS Performance

The combination of spectral and spatial resolution is illustrated in Figure 6, which shows an idealized image of a source about $0'.5$ in extent, emitting lines from hydrogen-like and helium-like iron. For this extreme source size (eg., the Virgo cluster), the helium-like triplet is slightly blended but still usefully resolved. The resolution element for a point X-ray source emitting narrow lines is also shown in Figure 6 for comparison purposes, and in this case the helium-like triplet is fully resolved.

The iron spectral features which can be covered by a 4° range in Bragg angle using lithium fluoride are summarized in Table 2, and extend from the neutral FeI absorption edge at 7.1 keV through the Fe XXV and XXVI transitions to a 10% red-shifted Fe XXVI line. The energy resolution of the LiF crystals is 6 eV.

The plasma diagnostics which can be performed with this energy range and resolution are indicated in Table 3, a list of necessary sensitivities and resolving powers for the iron lines, taken from the work of Pahcall and Sarazin (1978). These include the dielectronic satellite lines of helium-like iron, which may be at comparable fluxes to lines of the more usual transitions. Generally, it can be seen from the table that the resolving power of the crystal spectrometer described here is necessary for these plasma diagnostics.

ORIGINAL PAGE IS
OF POOR QUALITY

TABLE 2

IRON SPECTRAL FEATURES

Fe I K abs. edge	7.13 keV
Fe I Kβ	7.05
Fe XXVI 1s-2p	6.93
Fe XXV 1s^2-1s2p	6.70
1s^2-1s2p $^3P_2$	6.66
1s^2-1s2s ^3S	6.64
Fe I Kα_1	6.39
Fe XXVI 10% redshifted	6.30

Table 2 Iron spectral features in the 6-7 keV range

ORIGINAL PAGE IS
OF POOR QUALITY

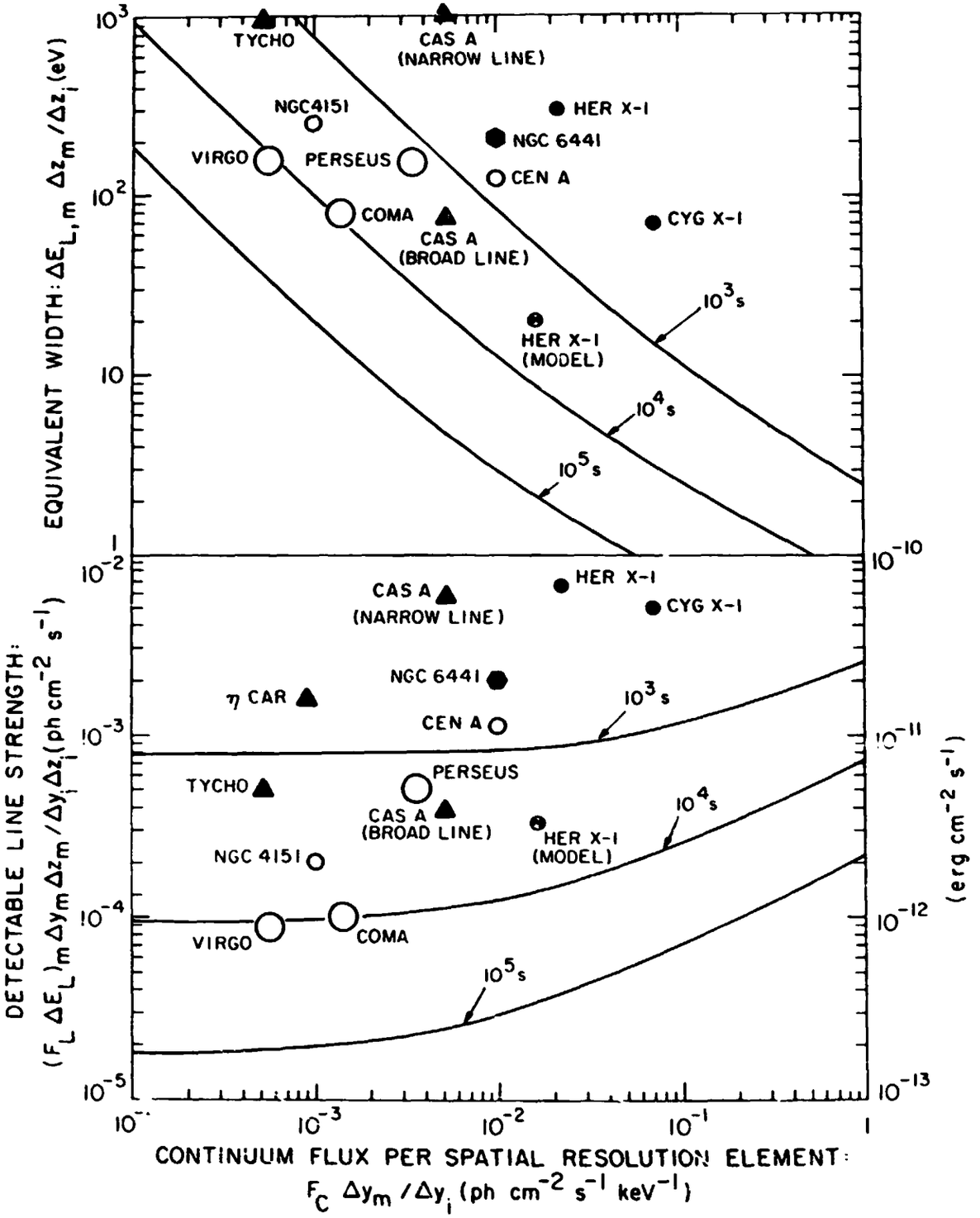

Figure 7 Minimum detectable equivalent widths and line strengths.

ORIGINAL PAGE IS
OF POOR QUALITY

The spherical crystal imaging spectrometer achieves high sensitivity by employing a large crystal area and a large concentration factor into a low background detector (the concentration factor is about 100, relative to the flat crystal case). The minimum detectable equivalent widths and line strengths, for an instrument with 0.4 m^2 projected area, are shown in Figure 7, which demonstrates that these sensitivities are a function of continuum flux for the stronger sources, but the spectrometer is photon-limited, i.e., limited by line count statistics, for most sources of interest in observation times of $\sim 10^4$s. With longer observation times, $\sim 10^5$s or longer, the instrument sensitivity becomes limited by detector background. Figure 7 also indicates some of the line strengths and equivalent widths of iron line features already detected by proportional counters on rocket and satellite experiments. In these cases where the source is extended, the observed strengths are shown per spatial-spectral resolution element of the proposed instrument (5 arc min^2 x 6 eV). It can be readily seen from these sensitivity curves that the instrument is sensitive to any of the plotted sources in an observation time of 10^4s, and for some, an observation time of only 10^2s is necessary. As an example, the instrument is sensitive, in a 10^4s observation of the Perseus cluster, to features with 30 eV equivalent width, in each resolution element. Such sensitivity is sufficient to measure the basic plasma parameters of temperature, relative abundance for iron, and ionization balance on a

ORIGINAL PAGE IS
OF POOR QUALITY

TABLE 3

PLASMA DIAGNOSTICS FOR CLUSTERS
(from Pancall and Sarazin 1978)

		Lines	Temp. Range 10^6 K	Necessary Sensitivity eV	Necessary Resolving Power $E/\Delta E$
	•	Fe XXV F/R	.3-2	40	200
Temperature		XXV $K\alpha/K\beta$	.1-.3	80	85
Determination		XXVII L_α/L_β	.2-.5	9	190
	•	XXV diel.	.2-1	100	210
	•	XXVI diel.	.4-2	8	210
Relative	•	Fe XXV + XXVI	.2-2	470	2
Abundance	•	XXV	.2-3	13	100
Determination	•	XXVI	.5-5	67	35
	•	Fe XXII inner shell	.1-.3	51	110
	•	XXIII inner shell	.1-.7	20	170
Ionization	•	XXIV inner shell	.1-1	46	340
Balance	•	XXVI/XXV	.2-4	20	85

Table 3 Necessary sensitivities and resolving powers for cluster plasma diagnostics (from Pancall and Sarazin 1978)

ORIGINAL PAGE IS
OF POOR QUALITY

spatially-resolved scale of 5 arc min over the extended cluster emission. The Virgo cluster line emission can similarly be detected in each 5 x 5 arc min spatial resolution element in 10^4s, and the combined data from the whole cluster would have a significance of about 15σ.

Line emission from supernova remnants is generally expected to be broadened by the expansion velocity profile, which has been measured in some cases for optical filaments, but not directly for the expanding X-ray shell. For CasA, the expansion may be estimated as ~400 kms^{-1} FWHM, and this expansion is expected to be observable as a broadened iron line covering about 15 resolution elements, with an average significance of about 6σ in each element. The sensitivity in the (unrealistic) non-expansion case and for the case of an expanding shell source are both shown in Figure 7.

In the optically-thick scattering plasma of accretion disks around compact objects, the narrow line emission is severely reduced from the optically-thin case (Felten and Rees 1972; Griffiths 1972). Ross et al. (1978) have modelled the line emission from Her X-1, and the narrow line core predicted by their model is plotted in Figure 8, i.e., the residual line core should be detectable in a 10^4s observation, with sufficient sensitivity to measure the relative strengths of the resonance, intercombination and forbidden lines of Fe XXV, giving a measure of density in the source. These residual line cores are an order of magnitude weaker than in the optically-thin case. Some of the

ORIGINAL PAGE IS
OF POOR QUALITY

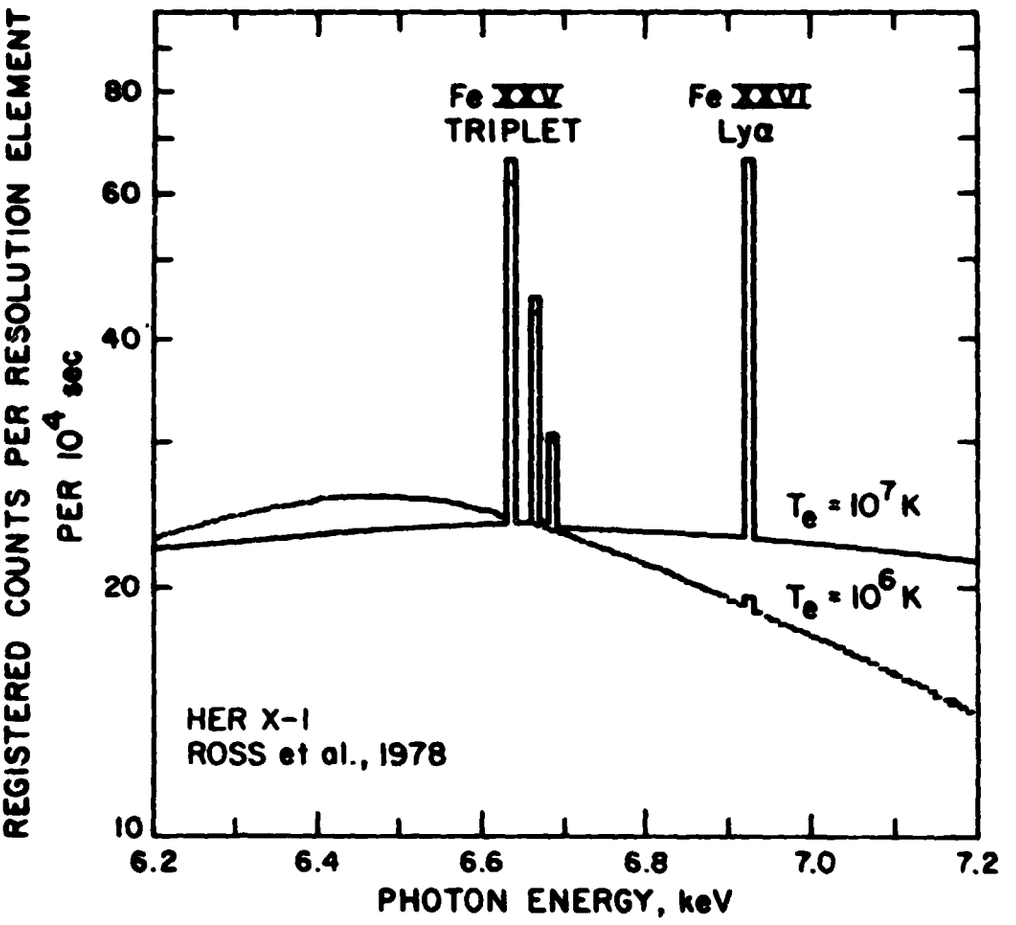

Figure 6 Calculation of counts from a 10^4s observation of Her X-1, using the residual line intensities from the model of Ross et al. 1978.

ORIGINAL PAGE IS
OF POOR QUALITY

fluorescence iron lines in binary X-ray sources are expected to be an order of magnitude stronger than these residual Fe XXV lines in Her X-1.

It is noteworthy that the sensitivity of an AXAF focal plane crystal spectrometer (i.e., the LiF crystal) would be about 10^{-2} ph cm^{-2} s^{-1} at the iron lines (Schnopper and Taylor 1981), two orders of magnitude worse than the instrument proposed here. The reason for this difference is simply one of area, with the realization that such spectrometers are photon-limited. The effective area of AXAF at 6.7 keV is between 100 and 200 cm^2, whereas the projected area of the crystal panels in the proposed SCIS is of the order of 10^4 cm^2. Considering high-resolution crystal spectroscopy alone, the use of grazing-incidence optics is clearly inefficient. The same argument remains valid, but to a lesser extent, at lower energies, where the AXAF effective area of ~1000 cm^2 can still be surpassed by a crystal panel with the appropriate atomic spacing for Bragg reflection and concentration of the silicon or sulphur lines, for example.

SCIS - Proposed Payload

The SCIS payload, as proposed for a Spacelab mission by SAO in collaboration with the Saclay group (Schnopper et al. 1978; Schnopper and Taylor 1980), is shown in a cut-away drawing in Figure 9. The large crystal panels are relatively cheap to fabricate, and a total payload cost has been estimated at around $2 million.

ORIGINAL PAGE IS
OF POOR QUALITY

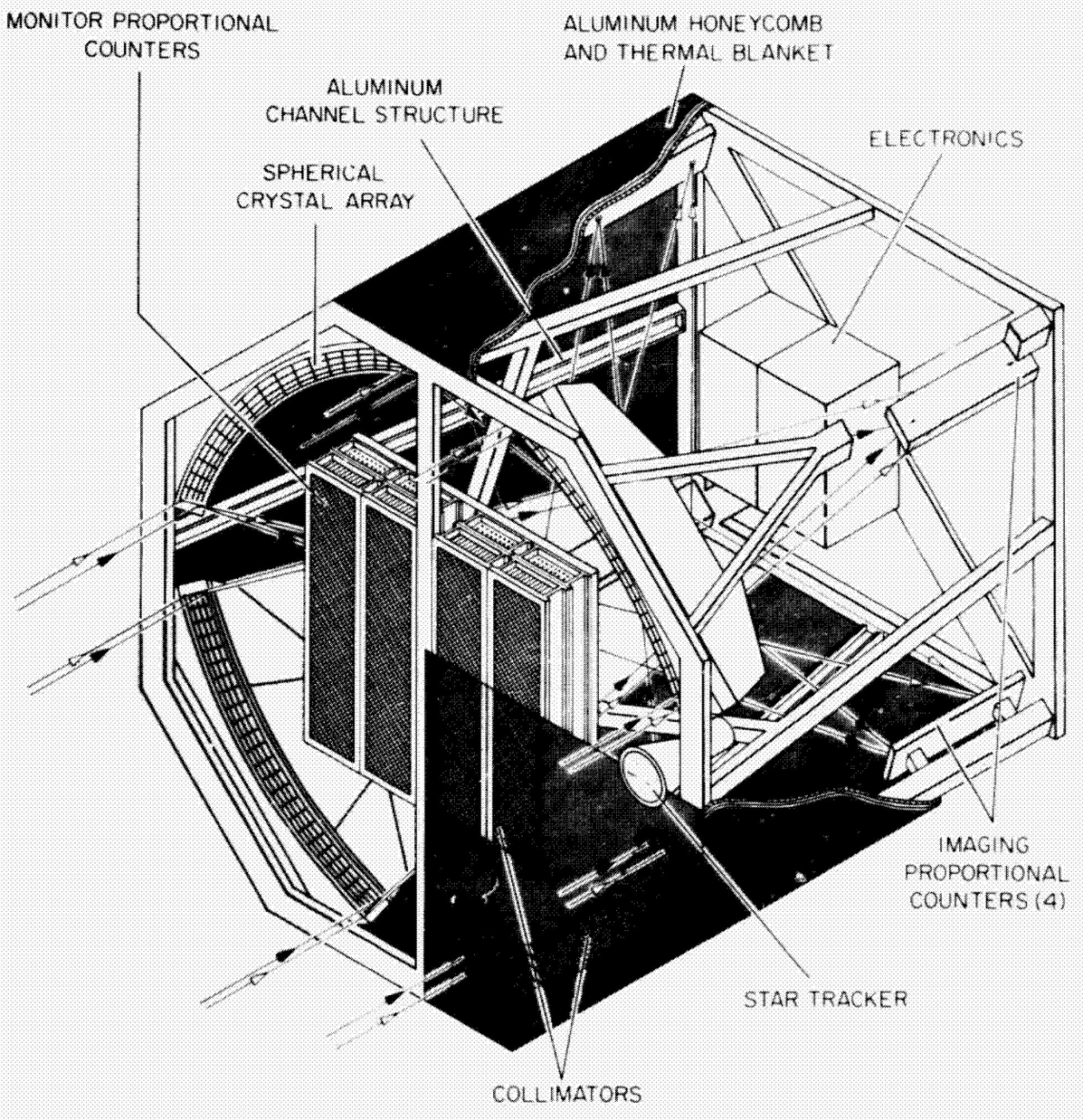

Figure 9 SCIS payload, as proposed for a Spacelab mission (Schnopper et al. 1978).

ORIGINAL PAGE IS
OF POOR QUALITY

The large central area is shown here filled with a monitor proportional counter for measurement of the overall spectrum of X-ray sources. A gas scintillation proportional counter would have twice the energy resolution and would better complement the crystal spectrometer. Ideally, the central area would be filled by an efficient grazing incidence collector, covering at least the ~1-8 keV range, with an array of solid-state devices in the focal plane.

Conclusions

The most efficient, and by far the most economical way of performing high-resolution spectroscopy of the 6-7 keV iron lines is by means of a spherical crystal imaging spectrometer. Such an instrument, of Spacelab-pallet proportions, would have a sensitivity two orders of magnitude better than an AXAF focal-plane crystal spectrometer, and would be sensitive in observation times of 10^4s or less, to all of the iron lines detected thus far by proportional counters.

ORIGINAL PAGE IS
OF POOR QUALITY

REFERENCES

Acton, L.W. et al. 1980, Solar Phys., 65, 53.

Andresen, R.D., Manzo, G., Peacock, A., Taylor, B.G., Catura, R.C., Culhane, J.L., and Berthelsdorf, R. 1981, Proc. 15th ESLAB Symposium, 'X-ray Astronomy', ESA.

Bahcall, J.N., and Sarazin, C.L. 1977, Ap.J. (Letters), 213, L99.

Bahcall, J.N., and Sarazin, C.L. 1978, Ap.J., 219, 781.

Berthelsdorf, R.F., Mitchell, R.J., and Culhane, J.L. 1976, Space Sci. Instr., 2, 349.

Felten, J.E., Rees, M.J., and Adams, T.F. 1972, Astron. and Astrophys., 21, 139.

Griffiths, R.E. 19 2, Astron. and Astrophys., 21, 97.

Griffiths, R.E., Polucci, G., Mak, A., Murray, S.S., and Schwartz, D.A. 1981, Proc. Soc. Photo-Opt. Instr. Eng. (SPIE), 'Solid-state imagers for astronomy', 290, 62.

Holt, S.S. 1976, Space Sci. Instr., 2, 205.

James, R.W., 1948, 'The Optical Principles of the Diffraction of X-rays', The Crystalline State, Vol. II, G. Bell and Sons, London.

Mushotzky, R.F., Serlemitsos, P.J., Smith, B.W., Boldt, E.A., and Holt, S.S. 1978, Ap.J., 225, 21.

Peckerar, M.C., McCann, D.h., and Yu, L. 1981, Rev. Sci.Instr., in press.

Pravdo, S.H. 1979, Proc. CCSPAR Symposium on X-ray Astronomy,

ORIGINAL PAGE IS
OF POOR QUALITY

Advances in Space Exploration (COSPAR), Vol. 3, p169, eds. W.A. Baity and L.E. Peterson.

Rapley, C.G., Culhane, J.L., Acton, L.W., Catura, R.C., Joki, E.G., and Bakke, J.C. 1977, Rev. Sci. Instr., 48, 1123.

Raymond, J.C., and Smith, B.W. 1977, Ap.J. Supp., 35, 419.

Ross, R.R., Weaver, R., and McCray, R. 1978, Ap.J., 219, 292.

Schnopper, H.W., and Taylor, B.C. 1980, App. Opt., 19, 3306.

Schnopper, H.W., Delvaille, J.P., Griffiths, R., Taylor, P.O., Koch-Miramond, L., Bergeron, J., Ilovaisky, S., Montmerle, T., Rocchia, R., and Rothenflug, R., 1978, Proposal to NASA, P 834-10-78.

Schnopper, H.W., and Taylor, B.C. 1981, App. Opt., in press.

Woodgate, B.E., Lowinger, T., and Schneider, M. 1973, Appl. Opt., 12, 2759.

Zombeck, M.V. 1981, Opt. Eng., 20, 297.

N82 26082

LABORATORY STUDIES ON A SPHERICALLY CURVED BRAGG SPECTROMETER FOR COSMIC X-RAY SPECTROSCOPY

M. Cantin, L. Koch-Miramond, B. Mougin, R. Rocchia
Centre d'Etudes Nucleaires de Saclay, France

ABSTRACT

A spherical array of twenty LiF 200 crystals has been built to test the performances of a freestanding, self-focussing spherical crystal cosmic X-ray spectrometer. Measurements presently available show that the size of the image for a point source at infinite distance would be 3mm(FWHM) along the focalisation axis and 2.1 mm (FWHM) along the dispersion axis. The mosaïc spread on individual crystals is less than 0.1 degree. A slightly systematic deviation from the ideal bending (0.1 degree) is observed at the edges of most crystals and this appears to be the major limitation to spectrometer performance.

I. INTRODUCTION

Precise piasma diagnostic on cosmic ray sources can only be obtained from measurements of line strength ratios with Bragg spectrometers. A free-standing Spherical Crystal Imaging Spectrometer (SCIS) similar to the one described by H. Schnopper and P. Taylor (1980) has been chosen for the ESA mission X 80 (L. Culhane, this Workshop). A free-standing spectrometer employs a curved array of crystals to simultaneously collect, focus and diffract the X rays emitted by a distant source. The concave spherical shape provides the minimum loss of spectral and spatial resolution which may result from source extent, spacecraft pointing and alignment errors (R. Griffith, this Workshop).

We began studies on spherically bent lithium fluoride crystals in 1979 to demonstrate the feasibility of the spectrometer we proposed to NASA in collaboration with the Smithsonian and Harvard Astrophysical Observatory (CFA). We describe hereafter the results obtained during this feasibility study. We will see that these results are directly applicable to the Bragg spectrometer of the ESA mission X 80 whose main design goals are :

- spectral resolution $E/\Delta E \simeq 10^3$ at 7 keV
- size (full width at half maximum) of the image of a distant point source : 2.5 mm along the dispersion axis and 4.5 mm along the focalisation axis for a radius of curvature of 2.5 m.

II. TYPES OF CRYSTALS

The following results were obtained with LiF 200 crystals which were proposed in the initial document (ref. ESA.SCL(79)3) for the observation of iron lines between 1.7 and 1.9Å. These crystals can be provided by cleavage or cut and polished. Cleavage along the 200 plane does not give very flat crystals : impurities produce cleavage steps of a few microns, even tens of microns. Polishing gives surfaces with very good quality which allows optical uses. It is note-worthy that polishing results in a bending of the crystal due to mechanical surface stress. For the tests we used square crystals (5 cm x 5 cm), 0.5 mm thick provided by Quartz et Silice. Other types of crystals (220 LiF, PET, TlAp) for further studies will be provided by the same manufacturer.*

III. TESTS AND SELECTION OF FLAT CRYSTALS

Planimetry

The flatness of each crystal is measured before bending. The required precision on the radius of curvature $\Delta R/R \simeq 5$-10% imposes a severe selection : to understand that we have to remind that a 2.5 m curvature radius produces a sagitta of only 125 microns on a 5 cm length. The surface of each crystal is scanned with a planimeter along several lines parallel to the X and Y axis. The two sides of each crystal are explored with an accuracy of 1 micron. Cleaved crystals with prohibitively

ORIGINAL PAGE IS
OF POOR QUALITY

high cleavage steps were excluded. Polished crystals exhibit a strong uniformity and no selection is required for these.

X-Ray tests

They are devoted to estimate the effect of the large scale mosaicity. The test bench consists of a point source, a crystal holder and a radiographic film. Mosaicity means that, at a given point on the crystal, crystalline lattice makes an angle with the upper surface. The different points on the crystal, satisfying the Bragg relation, contribute to the diffraction image on the film which consists in a single regular line for a perfect crystal and several portions of bent lines for actual crystals. The vertical spread ε of the diffraction pattern is proportional to the mosaicity W. Calibration gives $\varepsilon/W = 0.7$ mm/arc.min. The two lines $K\alpha_1$, $K\alpha_2$ of Copper are clearly seen for each scanning position. In most casesthe vertical spread is less than 3 to 4 mm corresponding to a mosaicity less than 0.1°. A few crystals only were rejected after this test.

IV. METHOD USED TO SPHERICALLY BEND THE LiF CRYSTALS

The LiF crystals are 0.5 mm thick and 50 x 50 mm^2 in area. The nominal radius of curvature is R = 2.50 m. Individual crystal holders 50 x 50 mm and 5 mm thick are made in aluminium alloy. They can be individually aligned by a classical optical method using the rear face. The front face is covered by a spherical deposit of STYCAST resin obtained by molding, the surface being polished against a convex spherical shape to remove any imperfection. Then the crystal is glued on the holder during 72 hours or more at room temperature under pressure of $\sim 7.10^5$ Pascals.

V. TESTS OF BENT CRYSTALS

Mechanical measurements

The same instrument as in sect.III was used to estimate the crystal sphericity. The profiles show slight cleavage steps. The set of tested crystals have radius clustered around the nominal value +5% with a maximum spread of about ± 8%.

X-ray tests

The equipment is shown in fig.1. It consists of an X-ray generator with a copper anticathode. The size of the X-ray source is 1 x 1 mm^2 ; after a trip of 6.5 meters in a tube filled with helium, X-rays reach the LiF crystal. The part of the radiation impinging the crystal with Bragg incidence is reflected and focussed, after another 6.5 meters trip in helium, on the sensor (film, PM, position sensitive proportional counter). For a perfect crystal, reflection should occur on a vertical line.

Fig.1 Test bench in X rays for spherical crystals.

Two tests were carried out :

(i) for a given position of the crystal the image is scanned along a vertical axis so as to estimate focussing properties. The image brightness is not gaussian in most cases and may exhibit some spikes or bumps. On the average the width with cleaved crystal is smaller than with polished ones, but the shape is not so smooth. This is probably due to small cleavage steps which give rise to different curvature radii.

(ii) The crystal is rotated around the curvature center. The detector is located so as to measure $K\alpha_1$ copper line only. Then the crystal is rotated around a vertical axis going through the theoretical curvature center. A perfectly bent crystal would give a constant reflection for a rotation of $\Theta = 75$ arc minutes. Most of the crystals show an increased reflection at the edges proving that they are not properly curved at those place ($R > R$ nominal). From the width and shape of the curves one can conclude that local angular deviations from a perfectly spherical surface is less than 0.1°. The reflectivity of polished crystals is about twice the reflectivity of cleaved ones.

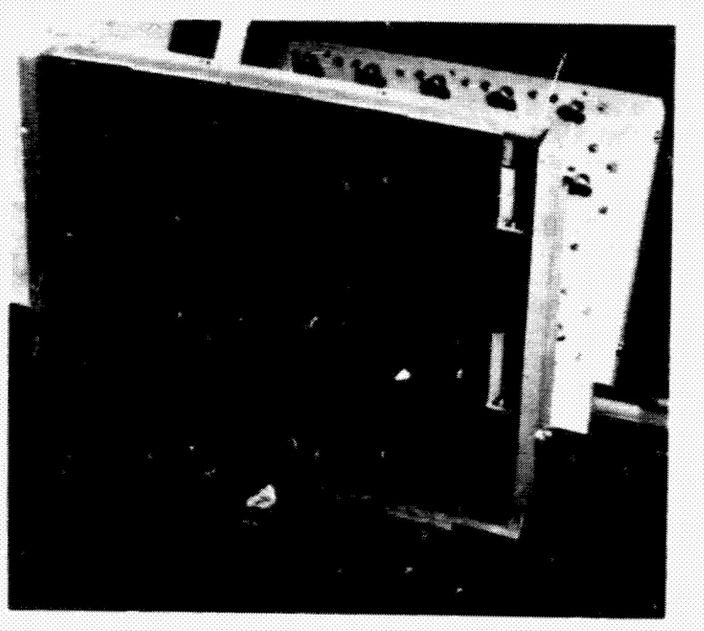

Fig.2 Mosaic array of 20 spherically curved LiF 200 crystals.

Testing of a mosaic array of spherically curved crystals

A mosaic array of 20 individual crystals is shown on fig.2. On this panel 4 crystals are cleaved, the other ones cut and polished.

First the panel is optically aligned on the test bench described on fig.1, his surface being perpendicular to the line joining the center of the panel to its center or curvature. Then each crystal is individually aligned using the reflection of a laser beam, all centers of curvatures are adjusted to coincide. The final alignment of individual crystals is obtained with the X-ray beam on the test bench : each crystal must focalise the diffracted beam on the line joining the source to the center of curvature of the crystal. When the whole panel is illuminated by X rays we can get the summation of diffracted beams coming from a row of 5 crystals. The figure 3 shows the X-ray intensity at the focus versus distance from the center of the image. The full width of the curve at half-maximum (FWHM) is 6 mm for 5 polished crystals. The composite image has a more gaussian shape for polished crystals.

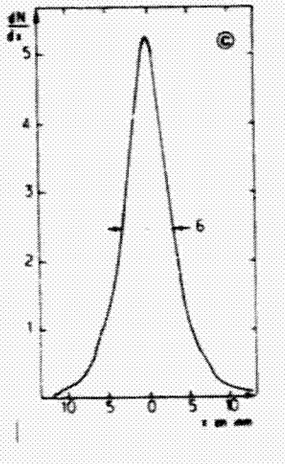

Fig.3 X-ray intensity distribution along the focussing direction versus distance from the center of the image.

ORIGINAL PAGE
BLACK AND WHITE PHOTOGRAPH

ORIGINAL PAGE IS
OF POOR QUALITY

Finally the whole panel is rotated around the center of curvature to test the response in the dispersion plane. Th[illegible]g.4 shows the received intensity versus angle of rotation for the whole panel. The upper curve corresponds to an aperture of 5 x 30 mm in front of the detector, the lower curve to an aperture of 5 mm diameter. The total diffracted intensity corresponds as expected to 4 times the mean intensity given by individual crystals. The imperfections of the curvature at the edges of the crystals explain the irregular shape of the curves. From the ratio of diffracted intensities between the upper and lower curves in fig.4 one deduces the size of the image in the dispersion plane : 4.2 mm (FWHM). During these tests we have monitored the focussing properties of the array which showed acceptable variations.

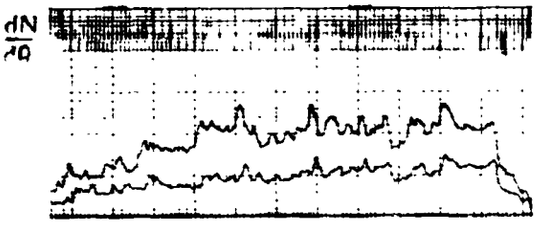

Fig.4 Diffracted X-ray intensity distribution along the dispersion direction versus rotation angle of the crystals around a vertical axis going through the theoretical curvature center.

VI. CONCLUSIONS

The results gathered with a limited size sample of twenty 200 LiF crystals (16 polished and 4 cleaved ones) show that :

- the focussing and dispersion curvatures are slightly better with cleaved crystals than with polished ones but reflection coefficient is increased by a factor two by polishing.

- a slightly systematic deviation from the ideal bending of less than 0.1° observed at the edges of most of the crystals is the major limitation of the spectrometer performance.

This deviation results in :
(i) A slight degradation of the energy resolution and focussing properties (non gaussian distribution, existence of wings).
(ii) A non-uniform energy range coverage.

The presently available measurements show that the size of the image for a point source at infinite distance (flight configuration) along the focussing direction would be 3 mm (FWHM) or 6 mm (FW at 1/8 max.). These figures are better than the estimated ones based on a mosaicity of W = 0.1° (5.4 mm FWHM or 7.8 mm at 1/8 max.). This proves that the mosaicity induced degradation has been, on the average of 5 crystals, overestimated. The effect of badly curved individual crystals does not show when considered in a set of several crystals (4 in the present case). The size of the image for a point source at infinite distance along the dispersion direction would be 2.1 mm (FWHM), better than the design goal. These results indirectly demonstrate that the energy resolution of 1000 at 7 keV is obtained together with a spatial resolution of 2.5 min of arc. This will be confirmed soon by measurements along the dispersion direction in a parallel X-ray beam. In these conditions point 2 appears to be the most severe limitation of the system but it can be overcome if we use staggered or alternative rows of crystals which produce the right overlapping for a nearly uniform energy range coverage.

Future tests will extend measurements to LiF 220, PET and TlAp.

The results obtained so far are surprisingly good and should be still better with an improved bending technique (increased curing time of the glue, optimization of the bending matrix shape).

References

Cantin, M., Koch L., Mougin B. and Rocchia R., 1981, CEA Report DPh.EP.Ap./81-11R.

European Space Agency Assessment Study, 1980, SCI (80)5

Schnopper H.W., Taylor P.O., 1980, App. Opt. 19, 3306

Schnopper H.W., Koch L., Mougin B., Rocchia R., Bethelsdorf R.F. and Culhane J.L. 1981, 15th ESLAB SYmposium X Ray Astronomy, Amsterdam.

*Quartz et Silice : 8, rue d'Anjou
75008 PARIS.

N82 26083

Cylindrical crystal imaging spectrometer (CCIS) for cosmic x-ray spectroscopy.

Herbert W. Schnopper
Danish Space Research Institute, Lundtoftevej 7, DK-2800 Lyngby

and

Paul O. Taylor
Harvard-Smithsonian, Center for Astrophysics, 60 Garden Street
Cambridge, MA. 02138, USA

ABSTRACT

We have developed a "stigmatic" focusing, Bragg crystal spectrometer that has been used for high spectral resolution x-ray emission line diagnostics on hot laboratory plasmas. Our concept can be applied at the focal plane of an orbiting x-ray telescope where it offers several advantages over conventional spectrometers, i.e., mechanical simplicity, high resolving power and sensitivity, simultaneous measurement of an extended segment of spectrum, and good imaging properties. The instrument features a simple, unambiguous, non-scanning spectrum readout that is not adversely affected by either spacecraft pointing error or source extent. We estimate the performance of the instrument in the context of the Advanced X-Ray Astrophysical Facility (AXAF) mission.

I. INTRODUCTION

Careful interpretation of precise spectral information obtained by the x-ray spectrometers on the Einstein Observatory (1) has established the role of spectroscopy in the understanding of the underlying physical phenomena that drive many cosmic x-ray sources. The increased collecting area associated with the use of a grazing incidence reflection telescope on the Einstein x-ray observatory has allowed powerful spectroscopic techniques commonly used in other branches of physics to be applied to many of the stronger x-ray sources. Numerous cosmic x-ray emitters, including binary sources, supernova remnants, active galaxies and the intercluster gas have thermal components and many have been found to exhibit characteristic line emission. Fe line or edge structures have been observed, but with very low resolution (proportional counter), in several of the brightest sources. Emission lines from several highly ionized elements (among them O, Si, S) have been observed by the solid state (1) and focal plane crystal spectrometers (1) on the Einstein Observatory. The future need is for more precise and higher resolution data that can be interpreted within the context of a particular model to provide information on temperature, density, relative abundance, ionization equilibria, mass motion, redshift or particle size distribution. Previously, detector sensitivity was the prime consideration in astrophysical observations. For future missions higher resolution ($>10^2$) will be desirable and, in many instances required to make a choise between various conflicting models, to obtain line shapes for measuring temperature broadening and bulk gas motion, and to discriminate against spurious features from redshifted or satellite lines.

Much of the quantitative information contained in the spectrum can be obtained only from precise ratios of line intensities. The simultaneous recording of the He-like triplet and/or lines of H-like or Li-like series and their satellite lines, will reduce inaccuracies that could result from serial observations of fluctuating cosmic plasmas in the presence of a varying charged particle induced detector background. Parallel recording of all spectral features will aid in line identification and charge state analysis and will also improve the efficiency of finding features with unknown redshifts, absorbtion edges, and continuum levels.

We have developed a high wavelength resolution, "stigmatic" focusing, Bragg crystal spectrometer for line shape diagnostics of hot laboratory plasmas. The concept has been studied previously (2-4), but rarely applied in practice. It employs a cylindrically bent crystal (Fig. 1) to intercept x-rays that diverge with

ORIGINAL PAGE IS
OF POOR QUALITY

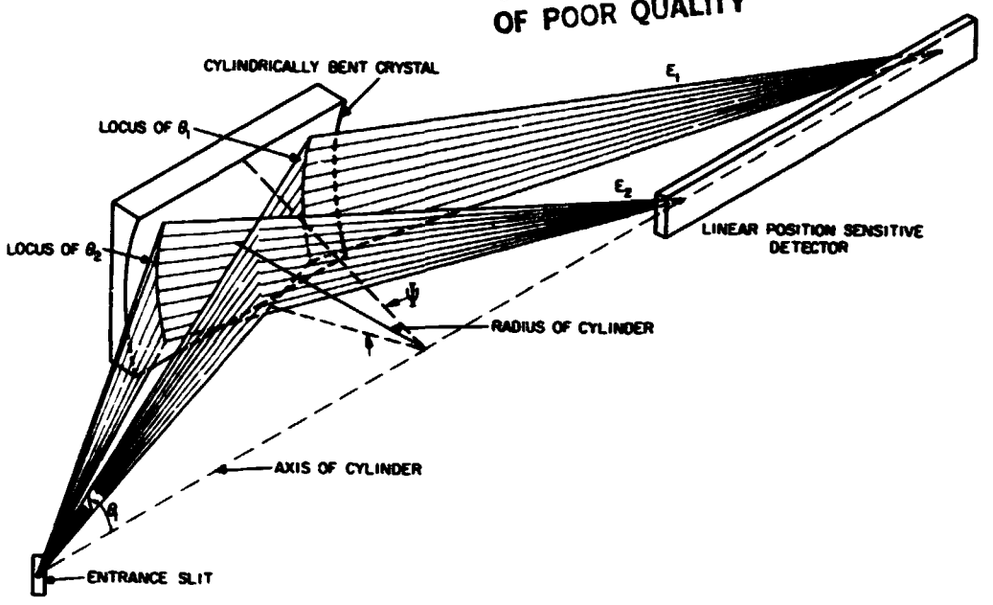

Fig. 1. CCIS concept; a cylindrical crystal surface gives exact point to point focus along the axis. Rays incident on the crystal at constant Bragg angle θ_1 define a conical surface about the axis with semi angle θ_1.

a broad range of Bragg angles θ from an entrance slit located on the axis of the cylinder. At each portion of the crystal those x-rays satisfying the local Bragg condition ($\lambda = 2d\sin\theta$, with d the lattice spacing) are reflected towards the axis where the dispersed spectrum is recorded on a position sensitive detector. This concept is to be contrasted with the more common Johann (5) design, cylindrical crystal spectrometer in which divergent x-rays are intercepted at almost constant Bragg angle. In the Johann design, a region of spectrum is scanned serially by changing the Bragg angle; hence, the relative position of focal point, crystal and detector must be adjusted repeatedly.

When the cylindrically curved imaging spectrometer (CCIS) is used at the focal plane of an x-ray telescope it can provide excellent imaging of an extended source. In the plane of the detector spatial information is displayed perpendicular to the cylinder axis while spectral information is displayed along the axis, and both can be recorded with a suitable two-dimensional, spatially resolving, detector. If, in some region of the spectrum, the predominent radiation is in an isolated narrow line, then then a two-dimensional image of an extended source will be recorded when the spectrometer is used without an entrance slit.

Finally, the unique focusing geometry of the cylindrical crystal makes it possible to exploit the greatly increased reflectivity of some mosaic crystals without a corresponding loss in resolution. With the inclusion of this benefit the cylindrically focusing spectrometer geometry will achieve a resolution and sensitivity equal to those of any current spectrometer design. In addition, the CCIS will have a large throughput since several hundred resolution elements are displayed simultaneously.

Our instrument has particular advantages for x-ray astronomy. The most important are:

1. An ability to measure simultaneously an extended segment of spectrum.
2. A spectrum integration mode in which scanning is unnecessary.
3. A simple unambiguous spectrum readout.
4. A minimal loss of energy resolution for extended or off-axis sources.
5. A high quality focus perpendicular to the dispersion plane.
6. A high resolving power, $E/\Delta E \gtrsim 10^2$.
7. A potential for increased sensitivity without loss of resolution if the high integrated reflectivity of mosaic crystals is exploited.
8. A geometry which does not require high resolution concentrating optics.

II. CCIS CONCEPT

A spectrometer concept in which the crystal is bent to a cylindrical surface that focuses and disperses the x-rays along the cylinder axis has been previously suggested (2,3) and its focusing properties and advantageous features have been examined in some detail (4).

The concept and geometry is illustrated in Figs. 1, 2, and 3. Rays from a point on the axis, incident on the cylindrically bent crystal at constant Bragg angle θ, define a conical surface about the cylinder axis with semi-angle θ (Fig. 1). We consider the crystal to be oriented at a central grazing angle θ_o with respect to the telescope axis about which the x-rays are diverging (Fig. 3).

ORIGINAL PAGE IS
OF POOR QUALITY

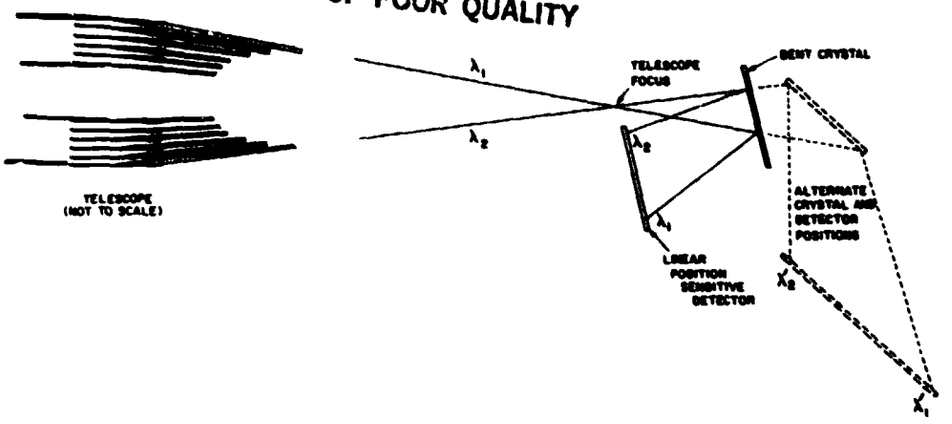

Fig. 2. CCIS at the focal plane of a grazing incidence telescope. Crystal and detector positions for two different wavelength bands are shown.

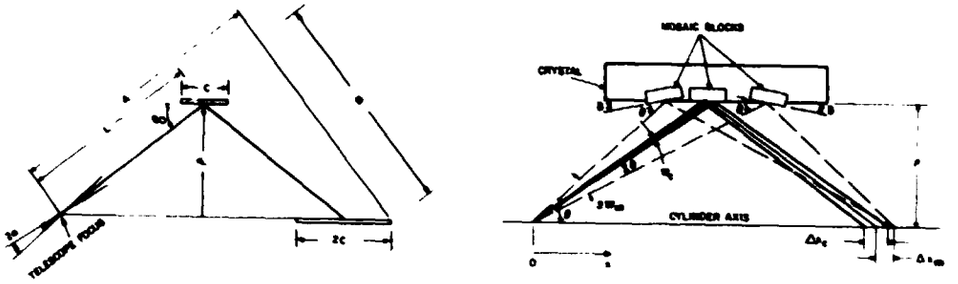

Fig. 3. Definition of spectrometer parameters.

Fig. 4. Effect of mosaic crystal structure on focus. Each block reflects over a range of angles W_c.

A. Wavelength dispersion.

X-rays of wavelength λ incident at Bragg angle θ are reflected in first order when $\lambda = 2d\sin\theta$, where d is the spacing of the diffracting crystal planes. If the crystal surface is a cylinder of revolution of radius ρ, rays originating on the cylinder axis are refocussed exactly onto that axis at a distance from the origin given by $x = 2\rho\cot\theta$. The wavelength dispersion along the x-axis is $\lambda = 2d/[1+(x/2\rho)^2]^{1/2}$ and the refocussed x-rays can be recorded by a linear, position sensitive, detector.

Relationships between detector spatial resolution x, angular resolution $\Delta\theta$, and energy ΔE, or wavelength resolution $\Delta\lambda$ are obtained by differentiating the expressions above. Thus,

$$dx = (2\rho/\sin^2\theta)d\theta \tag{1}$$

and

$$dE/E = d\lambda/\lambda = d\theta \cot\theta = (\sin 2\theta/4\rho)dx. \tag{2}$$

The crystal rocking curve width $\Delta\theta_c = W_c$ determines the limiting resolving power

$$S = (E/\Delta E)_c = \tan\theta/W_c, \tag{3}$$

and the corresponding limiting detector spatial resolution element

$$\Delta x_c = 4\rho/(S \sin 2\theta). \tag{4}$$

Several factors could degrade the angular or spectral resolution beyond the crystal limited value W_c and they have been analyzed in detail. Exact ray tracings indicate that no significant resolution loss will result from telescope aberations, pointing drift, or source extent.

The maximum telescope angular aperture 2α determines the crystal length C required to fully utilize that aperture (Fig.3);

$$C = \rho \sin 2\alpha/(\sin^2\theta_o - \sin^2\alpha) \simeq 2\alpha\rho/\sin^2\theta_o. \tag{5}$$

Assuming that there is a maximum convenient crystal size, then Eq. (5) sets an upper limit on ρ and on the other spectrometer parameters. The maximum fractional energy range which can be diffracted by one crystal at orientation θ_c is

$$(\Delta E/E)_\alpha \simeq 2\alpha \cot\theta_o, \tag{6}$$

which varies from 20% to 5% as θ_o is varied from 30° to 70°.

($2\alpha = 7^{o}$ for AXAF). This simultaneously diffracted energy band is sufficient to encompass the He-like triplet for all multiply charged ions (C to Fe) and, except for large θ_o, it also encompasses the H-like 2s - 2p/3p lines. When θ_o is reset to accommodate a specific energy band, the distance $L = \rho/\sin\theta_o$ (from slit to crystal, and from crystal to detector) must also be reset as is shown in Figs. 2 and 3. An instrument having L variable over nearly a factor of two and also having five or six interchangeable, cylindrically curved crystals available will accommodate the wavelength range from 25 Å to 1.5 Å, that covers all K lines and absorption edges from O to Fe.

B. Resolution

In this section we show that the spectral resolution of the cylindrical spectrometer is not significantly degraded by a mosaic crystal.

The probability $R(\theta,\lambda)$ of reflecting an x-ray of wavelength λ incident at an angle θ is sharply peaked about the Bragg angle. For a perfect crystal the full width at half maximum of this function is the single crystal diffraction width W_c. If the crystal is a mosaic of single crystal domains of appropriate microscopic size, then at each orientation of the crystal an x-ray can pass through many domains with slightly different orientations before being either absorbed or reflected. In this case, the "reflection window" or "half width" of the probability $R(\theta,\lambda)$ is the mosaic spread W_m which is generally larger than W_c.

Fig. 4 is a representation of this concept in the context of the cylindrical crystal geometry. A ray reflected at the Bragg angle from a mosaic block oriented parallel to the crystal surface will cross the crystal axis at a distance x given above. Rays of the same wavelength, however, incident on the surface at angles $\theta \pm \delta$, can reflect from mosaics tilted at angles $\pm \delta$ to the crystal surface, and will cross the axis at the distance

$$x = \rho\cot(\theta+\delta) + \rho\cot(\theta-\delta) \approx 2\rho\cot\theta\left[1+\delta^2/\sin^2\theta\right], \qquad (7)$$

which differs from the $\delta = 0$ position by

$$\Delta x_m - 2\rho\delta^2\cot\theta/\sin^2\theta. \tag{8}$$

The distribution of intensity in the image resulting from the mosaic effect is asymmetric with a peak at $x = 2\rho\cot\theta$ and a rapid fall-off towards larger x. Using $\delta = W_m$ as a measure of the resolution loss, we find that the mosaic broadening Δx_m, is equal to the single crystal diffraction limited resolution Δx_c given by Eq. (4) when

$$W_m = (W_c \tan\theta)^{1/2} = W_c S^{1/2} = \tan\theta/S^{-1/2}, \tag{9}$$

where S is given by Eq. (3). Mosaic spread orthogonal to the dispersion plane results in a large spatial blurring,

$$\Delta z_m = 2\rho\, W_m/(\sin\theta\cos\Psi), \tag{10}$$

where ψ is the half angle subtended by the crystal from a point on its axis (Fig. 1). An orthogonal tilt δ also results in a shift in Bragg angle of $\delta\theta = \delta^2\tan$. The associated spectral resolution loss will equal the diffraction limited value when

$$W_m = (2W_c\cot\theta)^{1/2} = 2S^{-1/2} \tag{11}$$

Thus, the maximum practical value for W_m is limited by Eq. (9) until $\tan\theta = 2^{1/2}$ and then by Eq. (11) and only if $W_m >> W_c$ will there be significant resolution loss resulting from the mosaic spread.

The efficiency of the spectrometer is, however, determined by the integrated reflectivity

$$R_c = \int_0^{\pi} R(\theta,\lambda)d\theta \tag{12}$$

which can be much greater for a mosaic crystal than a single crystal; roughly by the factor $W_m/W_c = S^{1/2}$.

Certain crystals can be prepared with domain structure that provides both a narrow diffraction width and a high integrated reflectivity. Two examples are graphite and lithium hydride which have theoretical single crystal resolving powers of ~ 5000 (2-5 keV) and ~ 0.5 to 1×10^5 (> 3.5 keV), respectively. Tolerable mosaic spreads are thus 0.8° for graphite at 2.5 keV and 0.4° for lithium hydride at 6.5 keV which are values typical of commercially available samples. Integrated reflectivities for ideal mosaic crystals are 18×10^{-4} for graphite and 35×10^{-4} for LiH; a factor of 10 or more higher than those for typical single crystals that might be chosen to reflect the same energy bands. This benefit of high integrated reflectivity together with high resolving power is not obtainable with scanning Bragg crystal spectrometers since, at each setting of the crystal, these instruments register on the detector the entire energy range determined by the rocking curve width W_m.

III. PERFORMANCE

A. Resolution

Design parameters for an instrument suitable for use at the focal plane of a large orbiting x-ray telescope are given in Table 1. Fig. 5 shows various spectrometer dimensions and Fig. 6 shows the resolving power limits imposed by telescope and spectrometer focusing and alignment aberrations. It is possible to have a very compact instrument without compromising on desired resolving power ($S \gtrsim 10^2$. If the spatial resolution of the detector is 0.2 mm x 3 mm it will impose a limiting spectral resolving power of S~4000 and a limiting transverse spatial resolution of 1 arcmin orthogonal to the dispersion plane. To accomodate the full range of Bragg angles ($2\alpha = 7^\circ$ and a field of view of 0.5°, the active area needs to be 20 cm x 10 cm (if $\rho = 20$ cm.).

TABLE 1

PARAMETERS OF AXAF TELESCOPE*

Effective area (wavelength dependent)	200-1000 cm^2
Pointing accuracy	± 30 arcsec
Aspect determination	± 1 arcsec
Focal length, F	10 m
Focal plane dispersion	50 m/arcsec
Focusing cone maximum angle, 2α	7
Resolution on axis	1 arcsec
7′ off axis	10 arcsec
15′ off axis	30 arcsec
20′ off axis	1 arcmin

PARAMETERS OF CYLINDRICALLY FOCUSING SPECTROMETER

Energy range, E	0.5 to 7.3 keV
Bragg angle range, θ_o	25^o to 70^o
Crystal length, C	100 mm
Crystal radius of curvature, ρ	200 mm
Detector pixel size	0.2 mm x 3 mm
Equivalent spatial resolution element	1 arcmin
Simultaneously recorded energy band $(\Delta E/E)_\alpha$	20% to 5%

*
These data are taken from AXAF Science Working Group Report, NASA TM-78285, May 1980.

ORIGINAL PAGE IS
OF POOR QUALITY

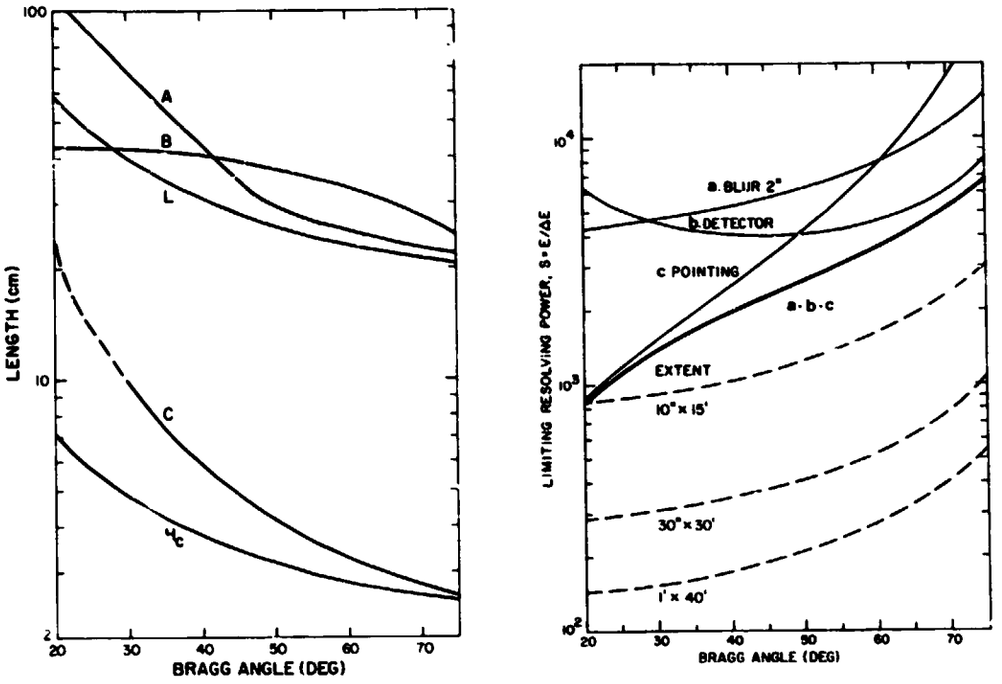

Fig. 5. Spectrometer dimensions corresponding to labels in Fig. 3: length A, bredth B, focal point to crystal distance L, minimum crystal length C, and crystal height H . All scale with the radius of curvature and have been computed for ρ = 200 mm.

Fig. 6. Spectral resolving power limits imposed by aspect drift (30 arcsec), telescope blur diameter (2 arcsec) and detector limiting spatial resolution (0.2 mm). The heavy curve combines these effects in quadrature and represents the geometric limit on resolving power for a point cosmic source. (Crystal resolving powers are shown in Fig. 7). The dashed curves show degraded resolving power due to source angular extent in the dispersion plane of 10 arcsec, 30 arcsec, 1 arcmin (corresponding to focal plane image widths of 0.5, 1.5 and 3 mm). Telescope blur diameter degrades approximately as the square of the off-axis angle and it is this effect, combined with abberations of the crystal focusing, which provided the indicated limits on source extent orthogonal to the dispersion plane.

Shown in Figs. 7 and 8 are resolving power and integrated reflectivities of several crystals (6-11) that can be used to cover the energy range from 0.5 to 7.3 keV. Spectrometer resolution can be limited by instrumental effects that must be combined with the crystal resolution. This is illustrated in the case of LiF (whose crystal resolving power is greater than 10^4) by showing in Fig. 7 the instrument resolving limit for a point cosmic source (from Fig. 6). The curves for ADP and RAP are similarly modified. When viewing an extended source a field of view of $1' \times 1^o$ will degrade the resolution to between 150 and 400.

B. Sensitivity

A spectral feature that contributes signal to a given detector pixel will be superimposed on an x-ray continuum (from bremsstrahlung, recombination, etc.) and a non x-ray background (from radiation belts, cosmic rays, etc). After an observing time t, the number of continuum photons recorded in a pixel of energy width ΔE_p from a point source contributing a flux $F_C(E)$ is

$$N_C = fF_C A_{eff} \Delta E_p t, \qquad (13)$$

where f is the fraction of the source imaged on the entrance slit and A_{eff} is the effective area $A_{eff} = (A/2\alpha)R_c \eta$ where $A/2\alpha$ is the average telescope collecting area per unit Bragg angle, and η is the proportional counter sensitivity. If n_b is non x-ray background count rate per detector pixel then the combined background is $N_B = N_C + n_b t$.

The response to a line of strength ($F_L \Delta E_L$) will be

$$N_L = f(F_L \Delta E_L) A_{eff} t/p. \qquad (14)$$

where it is assumed that the line covers p pixels. If the line is broad ($\Delta E_L >$ instrument resolution ΔE) then $p = \Delta E_L / \Delta E_p$; if the line is narrow $p = \Delta E / \Delta E_p$. The integrated line strength can be expressed in terms of the continuum, F_C and an equivalent line width, δE_L;

$$N_L = f(F_L \Delta E_L) A_{eff} t/p, \qquad (15)$$

ORIGINAL PAGE IS
OF POOR QUALITY

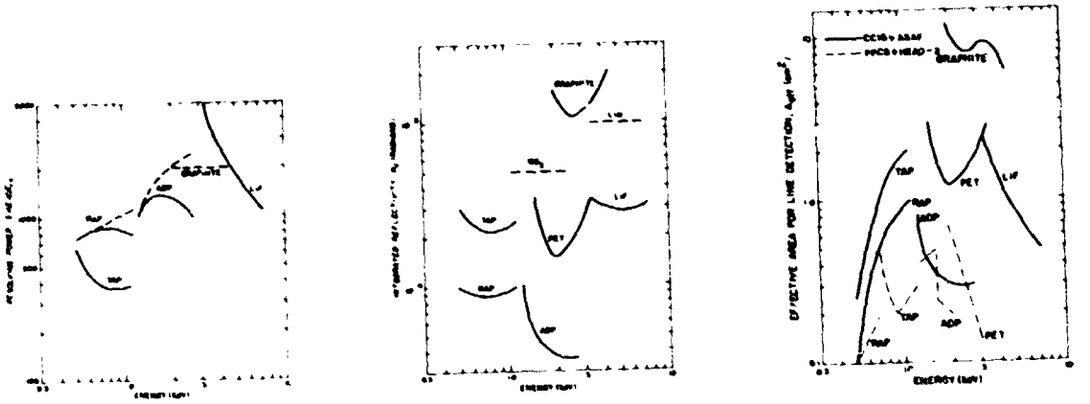

Fig. 7. Measured single crystal resolving powers for bendable crystals useful in the energy range 0.5 to 7 keV operating at Bragg angles $25^{o} < \theta_{o} < 70^{o}$. RAP TAP ; ADP (distorted crystal); Graphite ; LiF . In many cases the resolving power will be limited by instrumental effects (Fig. 6) as illustrated by the solid curves for LiF (whose crystal resolving power is greater than 10^{4}) ADP and RAP.

Fig. 8. Measured integrated reflectivities for crystal useful in the energy range 0.3 to 7 keV used at Bragg angles $25 < \theta_{o} < 70^{o}$. RAP, TAP, ADP ; PET ; LiF ; Graphite ; LiH, WS_2 (values for LiH and WS_2 are approximately one third the theoretical mosaic values).

Fig. 9. Expected effective detection areas, $A_{eff} = AR_{c}\eta/2\alpha$ for the proposed cylindrically focusing spectrometer at the focal plane of the AXAF. Effective area falls off at low energy due to proportional counter window transmission. For comparison equivalent effective areas for the HEAO-2 focal plane crystal spectrometer (FPCS) are shown (dashed curves).

If the line is detected in p channels, the minimum detectable number of counts signal $N_{L,m}$ can be written according to a 4σ criterion, $\rho N_{L,m}/\sigma(\rho N_{L,m}) = 4$, where $\sigma(\rho N_{L,m}) = \rho^{1/2}(N_{L,m}+N_B)^{1/2}$. It is assumed that the uncertainty in the background measurement is made negligible by sampling many background channels on either side of the line. Therefore for one channel

$$N_{L,m} = [8+(64+16\rho N_B)^{1/2}]/p \qquad (16)$$

The minimum detectable line flux is

$$F_L \Delta E_L = \rho N_{L,m}/(f A_{eff} t) \text{ photon cm}^{-2} \text{ s}^{-1}, \qquad (17)$$

and the minimum detectable equivalent width is

$$\delta E_{L,m} = \rho N_{L,m}/(f F_C A_{eff} t) \qquad (18)$$

The last quantity (a measure of signal to noise) is minimized by chosing p = 2 which is the smallest number of pixels consistent with proper sampling of the line width.

Sensitivities for three sample energies are calculated using the parameters listed in Table 2. We have set f = 1, p = 2, and used a $\Delta E_p < \Delta E = E/S$. Effective areas are shown in Fig. 9. They are used to calculate the minimum detectable line fluxes for a 1000 sec observation that are plotted in Fig. 10. Equivalent widths in keV can be obtained from the minimum fluxes by dividing by the corresponding continuum fluxes. The sensitivities are valid for line width $\Delta E_L < 2\Delta E_p$, but at low continuum flux levels (0.5 cm^{-2} s^{-1} keV^{-1}) the line sensitivity is signal limited and is valid for all line widths if the pixels are binned such that p = 2 effectively. For the Si line at ~ 2000 eV the gain in sensitivity using a mosaic graphite crystal versus a PET crystal is illustrated.

TABLE 2

PARAMETERS USED IN CALCULATING SPECTROMETER SENSITIVITIES

			FeXVII	SiXIII	SiXIV	FeXXV
Energy	E	(keV)	1.0	2.0	2.0	6.7
Disperser			TAP	PET	Graphite	LiF
Bragg Angle	θ_o	(deg)	28	45	67.5	27.5
Instrument Effective Area	A_{eff}	(cm^2)	1.8	1.2	12	0.5
Crystal Resolution	ΔE_c	(eV)	2.6	3*	1	<0.5
Instrument Resolution	ΔE	(eV)	2.6	3	1	6
Pixel Energy Width	ΔE_p	(eV)	1	1	1	3
Pixel Length		mm	1	0.4	0.6	0.4
Pixel Width**		mm	10	10	10	10
Background per pixel**	n_b	($10^{-4} s^{-1}$)	2.4	1.2	1.8	1
Simultaneous pixels	#		200	500	330	500
Extended Source Fraction	f		1			
Pixels per Line Width	p		2			
Radius of Curvature	ρ	mm	200			
Detector Length	2C	mm	200			

* Energy resolution for a mounted and vibrated PET crystal[7]; Best PET crystals show resolutions of 0.7 eV[7].

** The Einstein (HEAO-2) pixel area is about 1 cm^2 and backgrounds are scaled from reference 1.

ORIGINAL PAGE IS
OF POOR QUALITY

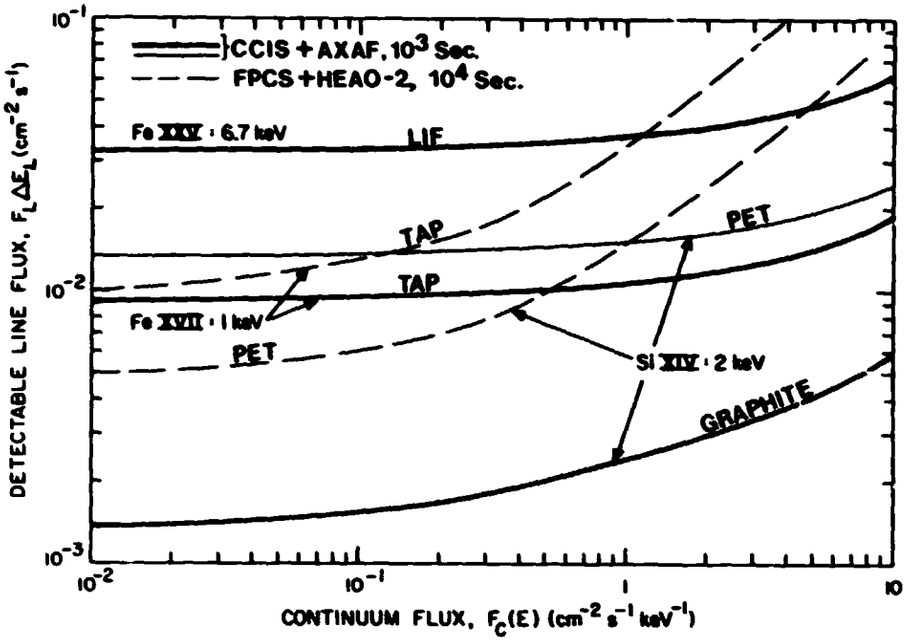

Fig. 10 Minimum detectable line fluxes at 4σ level for the proposed cylindrically focusing spectrometer at focal plane of AXAF (10^3 sec observation) and for the HEAO-2 focal plane crystal spectrometer (10^4 sec observation). These sensitivities can be compared directly since the AXAF telescope has about ten times the collection area of Einstein.

C. Comparison with Einstein Focal Plane Spectrometer.

Figs. 7 and 9 also show curves of resolving power and effective area for the Einstein focal plane spectrometer (12,13). The Einstein instrument suffers from severe focusing aberrations (12). It also has an order of magnitude worse resolution loss associated with drifting or extended sources and a more complicated spectrum readout. The crystal must be rocked and scanned during spectrum integration. CCIS, however, can achieve more uniform crystal limited resolving powers while still maintaining a large effective area per spectral resolution element. In Fig. 10 minimum detectable line fluxes for 10^4 sec Einstein observations are compared with our

predicted performance for a 10^3 sec observation with CCIS at the focus of the AXAF telescope. At 1 to 2 keV the AXAF telescope will have about 10 times the collection area of the Einstein telescope and, therefore, the curves may be taken as a comparison of the sensitivities of the two spectrometers. Thus, CCIS achieves comparable or better sensitivity per smaller resolution element while recording simultaneously several hundred channels of resolved spectrum thereby giving it a distinct throughput advantage.

IV. THE CONCEPT IN PRACTICE.

The components of a high resolution cylindrical focusing Bragg crystal spectrometer have been developed and fabricated. The instrument is currently operating at Alcator, the MIT tokamak, where it is used to obtain high quality, high resolution spectra emitted from the hot (approximately 2 keV) pulsed plasma. The instrument has a large (16.9 x 9.6 cm) PET crystal, (2d = 8.742 Å) bent to a radius of curvature of 60 cm, that is used at a Bragg angle of 34° to diffract MoL radiation near 2500 eV (4Å) with a dispersion of $\sim$2 mÅ/mm. The energy range detected by the 250 mm long position sensitive proportional counter is 350 eV. The resolution of the system is limited by the present detector to a value of $E/\Delta E = 400$. Data acquisition and analysis is controlled by a minicomputer that provides a real time plasma diagnostic. Test spectra covering a 300 eV range from a Mo target x-ray tube have been recorded on film and they show the expected line widths for MoL lines (Fig. 11). Spectra have been recorded for several different plasma conditions at Alcator A. The main spectral features in the region around 2.5 keV are MoL x-ray emission and K emission from Helium-like Cl and S. A typical spectrum is shown in Fig. 12. The strong doublet at 4.4Å is the resonance line $2p \rightarrow 1s$ from Helium-like Cl and the broader feature is a superposition of emission lines from Mo 24^+ to 30^+.

ORIGINAL PAGE IS
OF POOR QUALITY

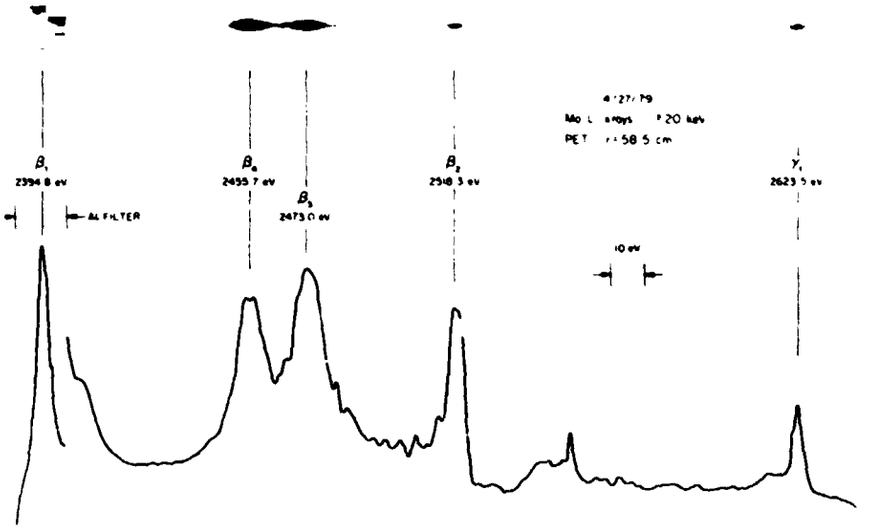

Fig. 11. Photographic plate and densitometer trace of a spectrum of a Mo target X-ray tube obtained with a cylindrically focusing spectrograph.

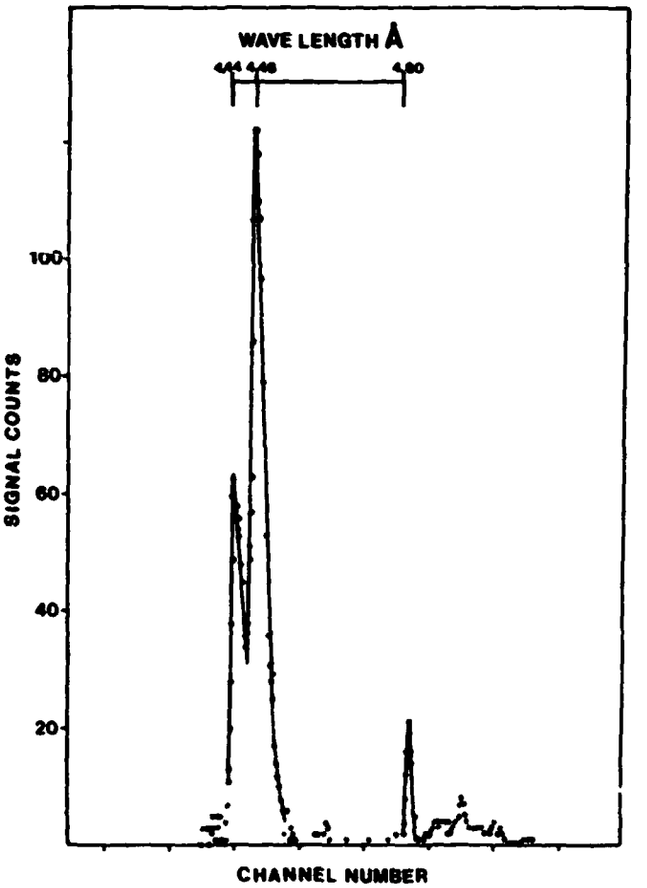

Fig. 12. Data from Alcator

ORIGINAL PAGE IS
OF POOR QUALITY

Photographic spectra (14) have also been obtained with a smaller (ρ = 5 cm) spectrometer using mica to disperse x-rays emitted in the 10 - 11Å range from glass microballoons imploded by a two-beam Nd: Glass laser system at the University of Rochester, Laboratory for Laser Energetics. The results are shown in Figs. 13 and 14. Of particular importance is the trace orthogonal to the dispersion direction shown in Fig. 14. It illustrates the excellent spatial resolution by displaying the brightening of the target poles caused by the two incoming laser beams perpendicular to the cylinder axis.

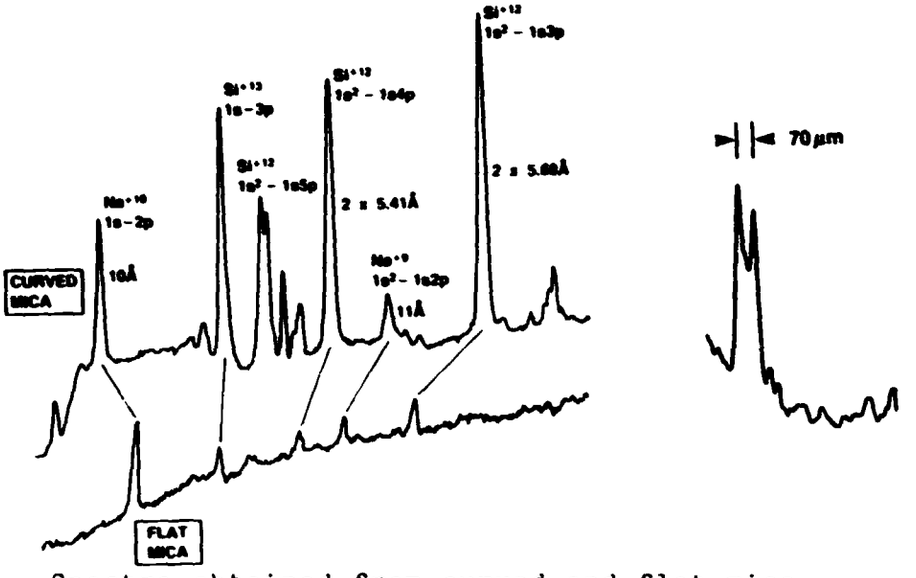

Fig. 13. Spectra obtained from curved and flat mica spectrographs. A comparison of collecting areas.

Fig.14 A trace orthogonal to the dispersion direction of a silicon line from a target of diameter 70μm.

These laboratory results show clearly the many advantages of the CCIS system and demonstrate its potential for cosmic x-ray spectroscopy.

V. CONCLUSIONS

The rich scientific yield from the spectrometer instruments carried by Einstein have emphasized the need to evaluate carefully the spectroscopic requirements of future missions. Throughput, spatial and spectral resolution, and wavelength range are variables in any combination of telescope focal plane spectrometer concept. For a given dispersing element

the question of throughput (i.e. sensitivity) is largely determined by the collecting area of the concentrating telescope. Resolutions, both spectral and spatial, are determined by the reflecting properties of the crystal and by the geometrical properties of the combined optical system. The upper limit on energy is usually set by the reflection efficiency of the telescope.

The dispersive spectroscopic systems on Einstein (transmission grating and Bragg spectrometer) require a high angular resolution telescope. As a result of the geometry of the optical system these instruments provide only modest spectral resolution and are almost totally ineffective when viewing extended sources. It is difficult to couple these instruments to any of the low resolution (1 arc min.) high throughput LAMAR systems without a severe degradation of performance.

The telescope/CCIS optical system is flexible with respect to both telescope resolution and source extent. In common with other good designs, CCIS will achieve crystal limited spectral resolution when it views the image of an on axis point source formed by a telescope having a high resolution. The distinguishing feature of CCIS is that it will achieve sufficient resolution to resolve the structure of the He-like emission structure when it views the image of an extended source formed by a telescope having only modest resolution and, in addition, it will provide simultaneously the intensity distribution across the source.

This work has been supported in part by the Smithsonian Institution and in part by the U.S. Department of Energy.

REFERENCES

1. R. Giacconi et al, Ap. J., 230, 540 (1979)

2. M. Guoy, Ann. Physique, 5, 241 (1916)

3. L. Van Hamos, Ann.d.Physik, 17, 716 (1933)

4. C.B. van der Berg and H. Brinkmam, Physica, 21, 85 (1955)

5. H.H. Johann, Z. Physik, 69, 185 (1931)

6. D.L. McKenzies, P.B. Landecker and J.H. Underwood, Space Sci. Instrum.,2, 125 (1976)

7. N.G. Alexandropoulos, Appl. Spectr., 28, 155 (1974)

8. J.P.R. Angel and M.C. Weisskopf, Ap. J., 75, 231 (1970)

9. D.B. Brown, M. Fatemi, and L.S. Birks, J. Appl. Phys., 45, 1544 (1974)

10. K.D. Evans, R. Hall, and M. Lewis, Space Sci. Instrum., 3, 163 (1977)

11. H.L. Kestenbaum, Appl. Spectr. , 27, 454 (1973)

12. H.W. Schnopper, J.P. Delvaille, A. Epstein, K. Kalata, and R. Sohval, Space Sci. Instrum., 2, 243 (1976)

13. C.R. Canizares, G.W. Clark, D. Bardas, and T. Market, SPIE, 106, 154 (1977)

14. B. Yaakobi, R.E. Turner, H.W. Schnopper, and P.O. Taylor, Rev. Sci. Instrum, 50, 1609 (1979)

PRECEDING PAGE BLANK NOT FILMED

N82 26084

SPECTROSCOPY IN THE 10 keV TO 10 MeV RANGE

JAMES L. MATTESON
Center for Astrophysics and Space Sciences
University of California, San Diego

ABSTRACT

Spectral lines in the 10 keV to 10 MeV range carry information of fundamental importance on many of the objects discussed at this workshop. Since the lines are directly related to specific physical processes this information is model independent and gives the physical conditions in the objects. At the sensitivities achieved to date, $\sim 10^{-4}$ to 10^{-3} ph/cm^2-sec for steady sources and $\sim 10^{-2}$ to 1 ph/cm^2-sec for transient sources, lines have been detected from the galactic center, gamma-ray bursts and transients, X-ray pulsators, the Crab pulsar and solar flares. Future instruments with a factor of $\sim$ 100 sensitivity improvement will allow detailed spectroscopic study of these classes of objects as well as supernova remnants, active galaxies and the interstellar medium. This sensitivity improvement can be obtained through the use of detector technology already proven in balloon and satellite instruments.

I. INTRODUCTION

Observations of spectral lines in the high energy range, 10 keV to 10 MeV, are directly related to the understanding of many of the classes of objects discusses at this workshop. Neutron stars, black holes, supernova remnants, the interstellar medium, the galactic nucleus and active galactic nuclei are known or predicted to be sources of spectral lines which can be studied with high-energy spectroscopy. Line forming processes with photon energies above 10 keV are a natural consequence of the $> 10^8$K temperatures and $> 10^{12}$ gauss fields which occur in or near these objects. The lines are due to electron-positron annihilation, cyclotron processes, radioactive decay, and nuclear deexcitation following inelastic collison or neutron capture. Since the lines are directly related to specific physical processes, they carry model-independent information on the physical conditions in the objects: temperature, density, bulk motion, abundance of isotopic species, the state of matter, the energy spectrum of particles and the mass of a central object. This information can be used to guide theoretical modeling and provide critical tests of models in order that the nature of the objects may be determined.

ORIGINAL PAGE IS
OF POOR QUALITY

The major difficulty in the development of the field of high energy spectroscopy has been the attainment of sufficient sensitivity. The early predictions by Morrison (1958) indicated line fluxes greater than 10^{-2} ph/cm^2-sec from steady sources. However, the strongest steady sources have now been observed to have fluxes of $\sim 10^{-3}$ ph/cm^2-sec and so their detection has only been possible with the improved instruments available in the last few years. Lines have now been detected in at least 41 different objects representing 6 classes of astrophysical phenomena. These include 9 impulsive solar flares (Chupp 1981) and 27 gamma-ray bursts (Mazets et al. 1981) where line features are characteristic rather than exceptional.

In this paper I review the line forming processes, the physical information carried by the lines and their energy distribution and expected widths. Then the observed and predicted fluxes are used to derive the instrumental sensitivities required for effective future observations. Finally, instrument concepts which can achieve these sensitivities are presented.

II. PHYSICAL PROCESSES OF 10 keV TO 10 MeV LINE FORMATION

In systems with effective temperatures greater than $\sim 10^8$K and/or magnetic fields greater than $\sim 10^{12}$ gauss line emission above 10 keV will occur by several processes. These have been reviewed by Ramaty (1978), Ramaty and Lingenfelter (1979) and Ramaty et al. (1981).

a) Cyclotron Processes

Cyclotron lines result from transitions between the Landau levels of electrons in strong magnetic fields. The $\sim$50 keV line in the binary X-ray pulsator Her X-1 is interpreted as due to either cyclotron absorption or emission and indicates a field of $\sim 5 \times 10^{12}$ gauss (Trümper et al. 1978). The shift of the line energy with phase of the 1.24 sec pulsation (Gruber et al. 1980) is apparently due to beamed emission from different field regions being responsible for the pulsed emission. Cyclotron absorption has been observed at $\sim$ 20 keV in the transient binary X-ray pulsator 4U0115+63, requiring a field of $\sim 2 \times 10^{12}$ gauss (Wheaton et al. 1980). The $\sim$ 50 keV absorption features observed in gamma-ray bursts have been interpreted as due to cyclotron processes indicating that highly magnetized neutron stars are the site of the bursts (Mazets et al. 1981). Since the cyclotron line width is a sensitive function of the magnetic field geometry (Bussard 1980), future high sensitivity spectroscopic observations will determine the magnetic field structure in the emission regions of all these objects and its temporal evolution in the case of

ORIGINAL PAGE IS
OF POOR QUALITY

gamma-ray bursts. A sensitive search for cylotron lines in X-ray bursters and galactic bulge sources could establish whether these objects contain highly magnetized neutron stars and determine their relationship to X-ray pulsators and gamma-ray bursts (Lamb 1981).

b) Electron-Positron Annihilation

Positrons are produced by pair production, inelastic collisions and radioactive decay of nucleosynthesis products. Since the 511.003 keV annihilation quanta have an exactly known energy in the rest frame, spectroscopic observations can provide a great deal of information. Line broadening would indicate the temperature and/or Keplerian or radial motion of the annihilation site. When positron lifetime information exists the line width could be used to determine the density of the positron slowing down region as well as limit the mass of a central object. A line centroid shift would indicate a gravitational redshift or a Doppler red- or blueshift. Figure 1 shows the galactic center 511 keV line measured by HEAO-3 (Riegler et al. 1981). The 2.5 keV limit on the line width and observation of variability in 6 months require $T < 7 \times 10^4$ K and a central mass $< 2 \times 10^7 M_\odot$. A remarkable feature of the galactic center annihilation radiation is that its luminosity, $\sim 5 \times 10^{4?}$ erg/sec, is a factor of $\sim$ 200 greater than that of the brightest 1-4 keV source in the GCX complex (Watson et al. 1981). Further theoretical and observational study of the annihilation radiation will be crucial to the understanding of the galactic nucleus.

The redshifted annihilation lines seen in the spectra of gamma-ray bursts at $\sim$ 400 keV can obtain up to 10 percent of the burst energy and can vary on shorter time scales than the total luminosity (Mazets et al. 1981) Ramaty et al. (1980) have interpreted the $\sim$ 400 keV line in the 5 March 1979 burst as due to annihilation of positrons produced by pair production in the radiation dominated, high temperature atmosphere of a neutron star which is heated to $T \sim 10^9$K and magnetically confined. Confinement is necessary to produce gravitationally redshifted rather than Doppler blueshifted annihilation radiation.

Pair production should occur when a radiation field's characteristic temperature exceeds $\sim 10^9$K. Since this is observed to occur in accretion fueled emission near black holes such as Cyg X-1 and those thought to exist at the centers of active galaxies, these objects should be sources of 511 keV photons (Lightman 1981). Observations of this radiation would significantly aid models of these objects and improve the understanding of their relationship to the galactic nucleus.

ORIGINAL PAGE IS
OF POOR QUALITY

c) Radioactive Decay

Gamma-ray lines are predicted to be produced by the radioactive decay of the products of explosive nucleosynthesis events in supernovae and novae (Clayton 1980, Woosley and Axelrod 1980). Although none of these lines has been discovered, the predicted fluxes are within the sensitivity of future instruments based on today's techniques. Since the gamma-rays' flux directly indicates the abundance of the relevant isotope, the abundance of synthesized material may be measured in a model independent manner. In contrast, the interpretation of atomic lines in the few keV range to determine abundances in an expanding supernova remnant is a model dependent procedure made particulary difficult since thermodynamic equilibrium does not occur. Earlier at this workshop Shull (1981) described these difficulties and the resulting large uncertainties in elemented abundances.

Gamma-ray lines can provide additonal important information. Used as tracers they can identify the positions of the galactic supernovae which have occurred in the past $\sim$ 300 years This does not appear to be possible in any other wavelength band. The Doppler broadening of the lines give the expansion velocity of the core of the supernova remnant, not the velocity of the shock-heated outer envelope which is measured optically. Ratios of gamma-ray lines give the density of the envelope which overlays the synthesized material (Clayton 1974). Long lived isotopes indicate the total rate and sites of galactic nucleosynthesis over the last $\sim 10^6$ years. These observations would provide detailed tests of the highly developed models of supernova and nova explosions and make the study of young galactic supernova available to other wavelength ranges.

d) Nuclear Deexcitation

Gamma-ray line production by nuclear deexcitation is expected whenever the particle energies exceed the threshold for nuclear reactions, typically a few MeV. The expected nuclear gamma-ray emissivities for temperatures in the 10^8-10^{12}K range have been calculated by Higdon and Lingenfelter (1977), Ramaty et al. (1979) and Ramaty et al. (1981). Since several hundred MeV/nucleon must be released in accretion onto a neutron star, it is expected that nuclear reactions should be a significant process near these objects. Neutrons would be produced by many of the reactions and interact themselves by inelastic scattering and neutron capture. The result of all these reactions would be excited nuclei which would produce characteristic nuclear gamma-rays. These indicate the composition of the medium as well as the energy spectrum of the fast particles. Line widths indicate the

ORIGINAL PAGE IS
OF POOR QUALITY

state of matter since large Doppler broadening occurs in lines from an ambient gas while small broadening occurs in dust and solids. Particle beaming results in a Doppler shift of the line energy due to the recoil of the excited nuclei. A gravitational redshift indicates the M/R value of the central object. Since the neutron thermalization time is density dependent, the time delay of neutron capture gamma-rays indicates the ambient density.

Nuclear gamma-rays have been observed in the 19 November 1978 gamma-ray burst at $\sim$ 740 keV, presumably due to gravitationally redshifted 847 keV gamma-rays from the first excited state of ^{56}Fe (Teegarden and Cline 1980). The 20-minute transient observed on 10 June 1974 from a balloon had a spectrum that consisted of four intense lines (Jacobson et al. 1978). Lingenfelter et al. (1978) have interpreted this event as due to episodic accretion onto a neutron star resulting in gravitationally redshifted ($z \simeq .20$ to .29) lines due to electron-positron annihilation (511$\rightarrow$413 keV) and neutron capture by hydrogen (2223$\rightarrow$1790 keV) and iron (7639$\rightarrow$5946 keV) as well as a non-redshifted line due to neutron capture by hydrogen (2223 keV).

Nuclear gamma-rays, as well as the electron-positron annihilation line, have also been observed in solar flares where protons are accelerated to several hundred MeV/nucleon and produce excited nuclei in the solar atmosphere by inelastic excitation and neutron capture (Chupp et al. 1973, Hudson et al. 1980). Recently the SMM Gamma-Ray Spectrometer has detected lines from 6 flares and the interpretation of these results indicate that electrons and ions are accelerated simultaneously during the impulsive phase of the flare and that this occurs even in relatively small impulsive flares (Chupp 1981).

Nuclear gamma-rays are predicted to be produced in the interstellar medium due to the interactions of cosmic-rays and the ambient medium. Ramaty et al. (1979) have calculated the line intensities and widths under various assumptions of composition and cosmic-ray energy. The ratios of the fluxes of various gamma-ray lines is a sensitive function of cosmic-ray energy at energies less than $\sim$ 100 MeV/nucleon. In addition, the lines indicate the spatial distribution and composition of the interstellar dust and gas. Figure 2 shows the predicted gamma-ray spectrum from the direction of the galactic center. The intensities and widths of these lines carry detailed information on 13 nuclides and the low-energy cosmic-ray spectrum.

ORIGINAL PAGE IS
OF POOR QUALITY

I. LINE ENERGIES AND WIDTHS

The energy distribution of the lines due to the processes described above are shown in Figure 3. Cyclotron lines occur in the 10 keV to 100 keV range, but could occur at higher energies if the magnetic field exceeds 10^{13} gauss. Electron-positron annihilation lines occur in the ~ 400 to 511 keV range and radioactive decay lines extend from ~ 10 keV up to a few MeV. Nuclear lines due to inelastic excitation occur in the 300 keV to ~ 10 MeV range and neutron capture lines occur from ~ 2 MeV to ~ 10 MeV. Also indicated in Figure 3 are the processes and line energies that have been observed or predicted in various objects. These lines span the entire 10 keV to 10 MeV range and it is clear that spectroscopic observations over the entire range are required to study these objects.

The widths of the various lines are shown in Figure 4. The distinction between resolved and non-resolved lines is important. When the line is resolved, i.e. its profile is measured, much additional information is obtained. The indicated width of non-resolved lines is an upper limit which results from low statistical significance and/or the inability to time-resolve a variable source. Also shown in Figure 4 are the energy resolution of NaI and Ge. These indicate that NaI is incapable of determining the width of most of the lines while Ge could do this for nearly all of them. Thus Ge detectors are required for spectroscopic observations in the 10 keV to 10 MeV range. Small HgI_2 detectors are now available and in the future they may also be suitable (Richer 1981).

IV. REQUIRED INSTRUMENT SENSITIVITY FOR FUTURE OBSERVATIONS

The required line sensitivity for effective spectroscopic studies can be determined from a consideration of the line fluxes of the objects detected to date. These are indicated in Figure 5. Because of the short duration of the gamma-ray bursts only very intense fluxes, ~ 1 ph/cm^2-sec, have been observed from them. Somewhat weaker fluxes, ~ .01-1 ph/cm^2-sec, have been observed from solar flares and the 20-minute transient detected from a balloon. The galactic center, X-ray pulsators, and the Crab pulsar produce quasi-steady lines in the 1 to 4 x 10^{-3} ph/cm^2-sec range. All these fluxes have been near the instrumental sensitivity limits so detections have typically been in the 3 to 10σ range. Although these have indicated the existence and flux of the lines, they have usually not given details on the lines' temporal behavior, width and exact energy.

ORIGINAL PAGE IS
OF POOR QUALITY

Also shown in Figure 5 are the instrument sensitivities achieved to date and those required for future instruments. The HEAO-3 instrument (Mahoney et al. 1980) used 4 large coaxial Ge detectors in an instrument optimized at $\sim$ 1 MeV. Below $\sim$ 60 keV the instrument was cut off due to detector dead layers. The sensitivity varied from $\sim 10^{-4}$ to 10^{-3} ph/cm^2-sec, depending on energy. Since HEAO-3 was a scanning spacecraft, $\sim$ 30 days were required to observe a source during which $\sim$ 100 hours of effective time on a point source occurred. The sensitivity that present balloon instruments which are optimized at $\sim$ 1 MeV can obtain in a single balloon flight (not shown in Figure 5) is a factor of $\sim$ 2 worse than that of HEAO-3. The sensitivity of present balloon instruments which are optimized at $\sim$ 60 keV, also shown in Figure 5, is 2 x 10^{-4} ph/cm^2-sec at 60 keV. Balloon instruments planned for the next 5 years will have a factor of $\sim$ 4 improvement over this sensitivity.

Gamma-ray lines have been observed from all the objects indicated in Figure 5 which have a flux $> 10^{-3}$ ph/cm^2-sec. However, the number of observations have been restricted to only the brightest objects in each class and therefore the scientific results have been limited. The predicted fluxes from galactic supernovae are $\sim 10^{-4}$ ph/cm^2-sec, just below present sensitivities. However, the predicted fluxes from extragalactic supernovae and the interstellar medium are a factor >10 lower, in the 3 x 10^{-6} to 7 x 10^{-5} ph/cm^2-sec range.

From these considerations of source fluxes one concludes that the potential of high energy spectroscopy will be realized when two basic conditions are fulfilled:

1. A sensitivity of 10^{-6} to 10^{-5} ph/cm^2-sec is achieved for (quasi-) steady sources and $\sim 10^{-4}$ to 10^{-2} ph/cm^2-sec for transient sources. This will allow the measurement of the predicted lines from galactic and extragalactic supernovae as well as the interstellar medium. It will also assure that detailed studies of lines will be performed on objects $\sim$ 10 times fainter than have been detected to date and that line features will be detected in objects that are $\sim$ 100 times fainter than those detected to date.

2. Observations are conducted from space and in missions with years of duration. This will assure that a large number of objects are studied in order to learn their class properties as well as discover line emission from unsuspected sources.

ORIGINAL PAGE IS
OF POOR QUALITY

The following examples indicated illustrate these requirements. The gamma-ray burst in which Teegarden and Cline (1980) detected redshifted line emission from ^{56}Fe at 3.5σ significance had a total energy flux of $\sim 3 \times 10^{-4}$ erg/sec. Since bursts of this intensity occur only $\sim$ once/year (Jennings and White 1980) both greater sensitivity and years of observation are required to obtain high quality spectroscopic data on a large number of gamma-ray bursts. At 100 times better sensitivity $> 20\sigma$ detections of the 847 keV Fe line would be expected in 10 to 20 bursts per year and detailed analysis could be performed on the class of gamma-ray burst sources. Similar considerations apply to steady sources. For example, the pulse-phase resolved study of the Her X-1 cyclotron line requires $\sim$ 10 times the present sensitivity and the opportunity to observe the entire 35-day cycle of Her X-1. A similar study of the $\sim$ 100 galactic objects brighter than a few UFU requires an additional factor of $\sim$ 10 sensitivity improvement.

V. CONCEPTS FOR FUTURE SPECTROSCOPY INSTRUMENTS

The sensitivity requirements developed above can be fulfilled by a combination of three instruments which are based on technology used in today's balloon and satellite instruments. Each instrument is optimized for a specific energy range and field of view. All the detectors would be germanium since it is capable of resolving nearly all the expected lines and is available today in large volume geometries, $\sim$ 150 cm^3. The objects for which the instruments are suited, their physical parameters and sensitivities are given in Table I. The sensitivities of the instruments are also indicated in Figure 5.

Instrument (1) is for the study of (quasi-) steady sources of lines in the 10 keV to $\sim$ 600 keV range. Optimum sensitivity would occur at $\sim$ 60 keV. A field of view of a few degrees would be provided by a passive collimator in order to reduce background and source confusion. Planar detectors would provide 40 times the collecting area of present instruments, an energy resolution of $\lesssim$ 1 keV and minimum background.

Instrument (2) is for the study of transient sources. It would cover the 10 keV to 10 MeV energy band and observe the entire sky. Since detector volume determines sensitivity above a few hundred keV, the volume would be $\sim$ 60 times that of the Teegarden and Cline (1980) detector. Unshielded coaxial detectors would be used in order to have good sensitivity above a few hundred keV.

Instrument (3) is for the study of (quasi-) steady sources of lines in the 100 keV to 10 MeV range. Optimum sensitivity would occur at a few MeV. The detector volume is 25 times that of HEAO-3 and very long observing times, $\sim$ 200 days, would be required to reach the desired sensitivity. Because of this, a wide field of view, $\sim 40^{\circ}$, with a coded aperture would be required to observe an acceptable number of objects during a several year mission. Heavily shielded coaxial detectors would be used in order to have minimum background and good sensitivity at the highest energies.

All the instruments would require cooling of the detectors to $\sim$ 90K. On HEAO-3 this was done with a solid cryogen refrigerator with lifetime of only $\sim$ 6 months. Mechanical refrigerators have also been used for germanium detector cooling in space (Nakano and Imhoff 1978), but have had problems with reduced efficiency in extended life also caused microphonic noise in the detector signal. The problems with mechanical refrigerators can be solved with a modest development program and in the 1990's they will be the preferred method of achieving the required detector temperatures.

Radiation damage was a problem with the p-type HEAO-3 detectors (Mahoney et al. 1981). However, the n-type detectors which are now commercially available are unaffected by radiation damage in a low earth orbit. These detectors also have a negligible dead layer, so they operate from < 10 keV to > 10 MeV.

VI. CONCLUSION

Future observations of spectral lines in the 10 keV to 10 MeV range will be of fundamental importance in our understanding of a wide variety of objects and phenomena which have been discussed at this workshop. These include neutron stars and black holes and processes near them, explosive nucleosynthesis and supernova remnants, solar flares, the interstellar medium, the galactic center and active galactic nuclei. Spectral lines have already been detected from many of these by the modest instruments that have been used to date. These have achieved a sensitivity of 10^{-4} to 10^{-3} ph/cm^2-sec for steady sources and 10^{-2} to 1 ph/cm^2-sec for transient sources. The instrument concepts presented here would achieve a factor of 100 sensitivity improvement, allowing detail study of many objects. Since the lines are directly related to specific physical processes, model independent information on the physical conditions in the objects results and the class properties and nature of the objects can be determined.

ORIGINAL PAGE IS
OF POOR QUALITY

The instrument concepts are based on detector technology that has already been developed for balloon and satellite instruments. Instruments using these concepts would easily be accommodated by a Shuttle-launched Explorer mission in the 1990's. Since the scientific return from such a mission would be both large and relevant to a wide variety of problems in high energy astrophysics it should be given the highest priority in the planning of future space missions.

ORIGINAL PAGE IS
OF POOR QUALITY

REFERENCES

Bussard, R.W. 1980, Ap. J., 237, 970.

Chupp, E.L., Forrest, D.J., Higbie, P.R., Suri, A.N., Tsai, C., and Dunphy, P.P. 1973, Nature, 241, 333.

Chupp, E.L., 1981, "Solar Energetic Photon Transients (50 keV-100 MeV)", in Gamma-Ray Transients and Related Astrophysical Phenomena, ed. R.E. Lingenfelter, H. Hudson and D. Worrall (New York: AIP) p. 363, in press.

Clayton, D.D. 1974, Ap. J., 108, 155.

Clayton, D.D. 1980, "Cosmic Radioactivity: A Gamma-Ray Search for the Origins of Atomic Nuclei", Max-Planck Institute für Kernphysik, Heidelberg, MPI H-1980-V8.

Gruber, D.E., Matteson, J.L., Nolan, F.P., Knight, F.K., Baity, W.A., Rothschild, R.E., Peterson, L.E., Hoffman, J.A., Scheepmaker, A., Wheaton, W.A., Primini, F.A., Levine, A.M., and Lewin, W.H.G. 1980, Ap. J. (Letters), 240, L127.

Higdon, J.C. and Lingenfelter, R.E. 1981, Ap. J. (Letters), 215 L53.

Hudson, H.S., Bai, T., Gruber, D.E., Matteson, J., Nolan, P.L., and Peterson, L.E. 1980, Ap. J. (Letters), 236, L91.

Jacobson, A.S., Ling, J.C., Mahoney, W.A., and Willet, J.B. 1978, in Gamma-Ray Spectroscopy in Astrophysics, ed. T.L. Cline and R. Ramaty (NASA TM-79619), p. 228.

Lamb, D.Q. 1981, this proceedings.

Lightman, A. 1981, this proceedings.

Lingenfelter, R.E., Higdon, J.C., and Ramaty, R. 1978, in Gamma-Ray Spectroscopy in Astrophysics, ed. T.L. Cline and R. Ramaty, (NASA TM-79619), p. 252.

Mahoney, W.A., Ling, J.C., Jacobson, A.S., and Tapphorn, R.M. 1980, Nucl. Inst. and Meth., 178, 363.

Mahoney, W.A., Ling, J.C., and Jacobson, A.S. 1981, JPL preprint, to be published in Nuclear Instruments and Methods.

Mazets, E.P., Golenetskii, S.V., Aptekar', R.L., Gur'yan, Yu.A., and Il'inskii, V.N. 1981, Nature, 290, 378.

ORIGINAL PAGE IS
OF POOR QUALITY

Morrison, P. 1958, Nuovo Cimento, 7, 858.

Nakano, G.H. and Imhoff, W.L. 1978, in Gamma-Ray Spectroscopy in Astrophysics, ed. T.L. Cline and R. Ramaty (NASA TM-79616), p. 529.

Ramaty, R. 1978, in Gamma-Ray Spectroscopy in Astrophysics, ed. T.L. Cline and R. Ramaty (NASA TM-79619), p. 6.

Ramaty, R., Bonazzola, S., Cline, T.L., Kazanas, D., Mészáros, P., and Lingenfelter, R.E. 1980, Nature, 287, 122.

Ramaty, R., Kozlovsky, B., and Lingenfelter, R.E. 1979, Ap. J. Supplement, 40, 487.

Ramaty, R., and Lingenfelter, R.E. 1979, Nature, 278, 127.

Ramaty, R., Lingenfelter, R.E., and Kozlovsky, B. 1981, "Gamma-Ray Lines from Solar Flares and Cosmic Transients", in Gamma-Ray Transients and Related Astrophysical Phenomena, ed. R. Lingenfelter, H. Hudson and D. Worrall, (New York: AIP), p. 211, in press.

Ricker, G. 1981, this proceedings.

Riegler, G.R., Ling, J.C., Mahoney, W.A., Wheaton, W.A., Willet, J.B., Jacobson, A.S., and Prince, T. 1981, Ap. J. (Letters), 248, L13.

Shull, M. 1981, this proceedings.

Teegarden, B.J. and Cline, T.L. 1980, Ap. J. (Letters), 236, L67.

Trümper, J., Pietsch, W., Reppin, C., Voges, W., Staubert, R., and Kendziorra, E. 1978, Ap. J. (letters), 219, L105.

Watson, M.G., Willingale, R., Grindlay, J.E., and Hertz, P. 1981, preprint, Center for Astrophysics, to be published in Ap J., 1 November 1981.

Wheaton, W.A., Doty, J.P., Primini, F.A., Cooke, B.A., Dobson, C.A., Goldman, A., Hecht, M., Hoffman, J.A., Howe S.K., Scheepmaker, A., Tsiang, E.Y., Lewin, W.H.G., Matteson, J.L., Gruber, D.E., Baity, W.A., Rothschild, R.E., Knight, F.K., Nolan, P., and Peterson, L.E. 1979, Nature, 282, 240.

Woosley, S.E., Axelrod, T.S., and Weaver, T.A. 1980, preprint UCRL-85118, to be published in Nuclear Particle Physics.

ORIGINAL PAGE IS
OF POOR QUALITY

TABLE I

HIGH-ENERGY SPECTROSCOPY INSTRUMENTS FOR THE 1990's

OBJECT/PHENOMENON	DETECTOR	SENSITIVITY
1. X-RAY PULSATOR PULSAR SUPERNOVA GALACTIC CENTER ACTIVE GALACTIC NUCLEUS BLACK HOLE	2000 CM^2 X 1.5 CM THICK PLANAR GE ARRAY FEW ^{0} FOV UP TO 30 DAY OBSERVATION 10 TO 600 KEV	$\sim 3x10^{-6}$ PH/CM^2-SEC @ 60 KEV. $\sim 3x10^{-5}$ PH/CM -SEC @ 511 KEV. SPECTRA OF > 1 UFU SOURCE. PHASE RESOLVED SPECTRA FOR > 10 UFU SOURCES. DISCOVER YOUNG GALACTIC SUPERNOVA VIA γ-RAY LINES < 600 KEV. DISCOVER 511 KEV EMISSION FROM ACTIVE GALACTIC NUCLEI.
2. GAMMA-RAY BURST (5 SEC) GAMMA-RAY TRANSIENT (20 MIN) SOLAR FLARE (20 MIN)	2000 CM^3 GE COAX ARRAY > 2π FOV 10 KEV TO 10 MEV	JUST DETECT FE LINE IN $3x10^{-6}$ ERG/CM^2 BURST (~150/YR). DETECT FE LINE @ $>20\sigma$ IN $>2x10^{-5}$ ERG/CM^2 BURST (~20/YR). $\sim 10^{-3}$ PH/CM^2-SEC @ 1 MEV FOR A 20 MIN EVENT. DETECT THE 20 MIN TRANSIENT'S LINES @ $\sim 60\sigma$ AND STRONG SOLAR FLARE'S LINES @ $\sim 300\sigma$.
3. SUPERNOVA INTERSTELLAR MEDIUM SEARCH FOR UNSUSPECTED SOURCES OF GAMMA-RAY LINES	10,000 CM^3 GE COAX ARRAY $\sim 40^0$ FOV $\sim 1^0$ POSITION DETERMINATION SENSITIVE TO POINT AND DIFFUSE SOURCES 200-DAY OBSERVATION 100 KEV TO 10 MEV	$\sim 5x10^{-6}$ PH/CM^2-SEC @ 1 MEV. MEASURE > 100 KEV GAMMA-RAY LINES FROM GALACTIC AND EXTRAGALACTIC SUPERNOVAE. MEASURE AND MAP THE INTERSTELLAR GAMMA-RAY LINES. DISCOVER UNSUSPECTED SOURCES OF GAMMA-RAY LINES.

ORIGINAL PAGE IS
OF POOR QUALITY

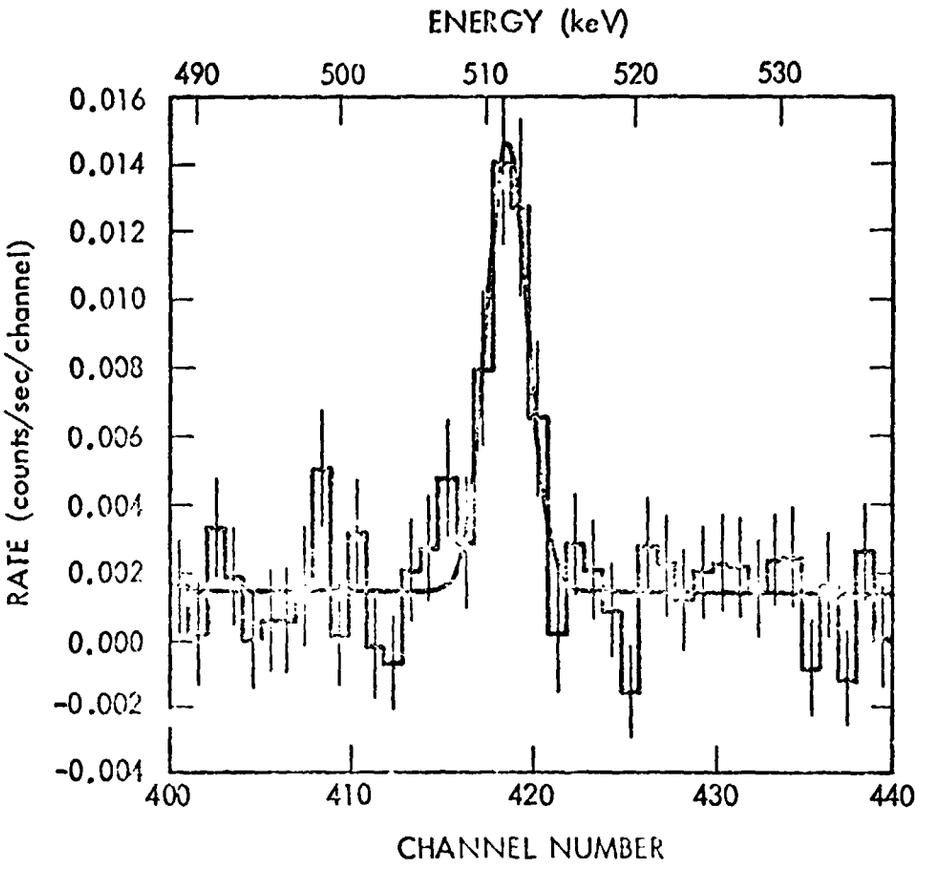

Figure 1. The spectrum of the galactic center region measured by HEAO-3 in Sept/Oct 1979 (Riegler et al. 1981). The 511 keV electron-positron annihilation line flux, $(1.8 \pm .2) \times 10^{-3}$ ph/cm^2-sec, was found to be a factor of 3 lower when HEAO-3 reobserved the galactic center 6 months later. The observed line width is due to the 2.7 keV FWHM energy resolution of the detectors. These data constrain the galactic center line width to less than 2.5 keV (1σ) and 3.4 keV (2σ).

ORIGINAL PAGE IS
OF POOR QUALITY

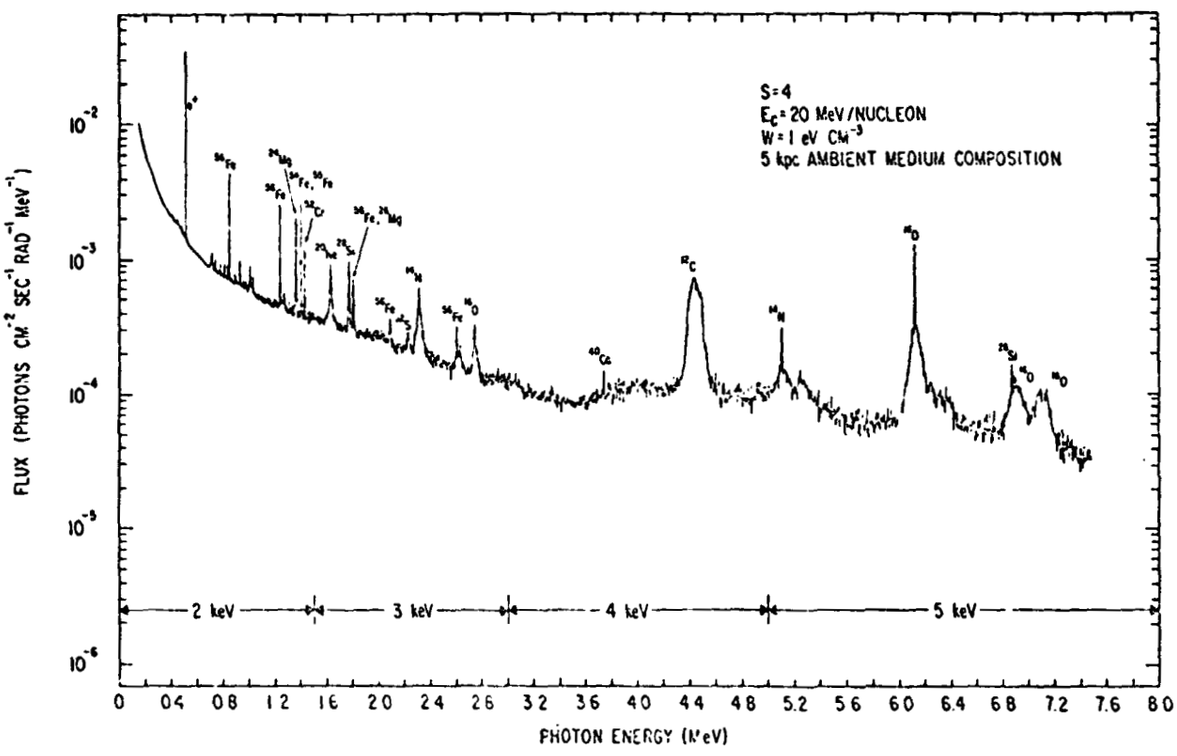

Figure 2. The predicted spectrum of gamma-ray lines and bremsstrahlung from the direction of the galactic center (Ramaty et al. 1979, Figure 30). Narrow lines are due to the excitation of nuclei in grains and wide lines are due to the excitation of nuclei in gas. The short lifetime of the 4.438 MeV level of ^{12}C, 5×10^{-14} sec, results in a broad line at this energy in both cases. The fluxes are typically $\sim 10^{-5}$ ph/cm^2-sec-rad, a factor of $\sim$20 below the best sensitivity achieved to date, but within the capabilities of the future instruments discussed in this paper.

ORIGINAL PAGE IS
OF POOR QUALITY

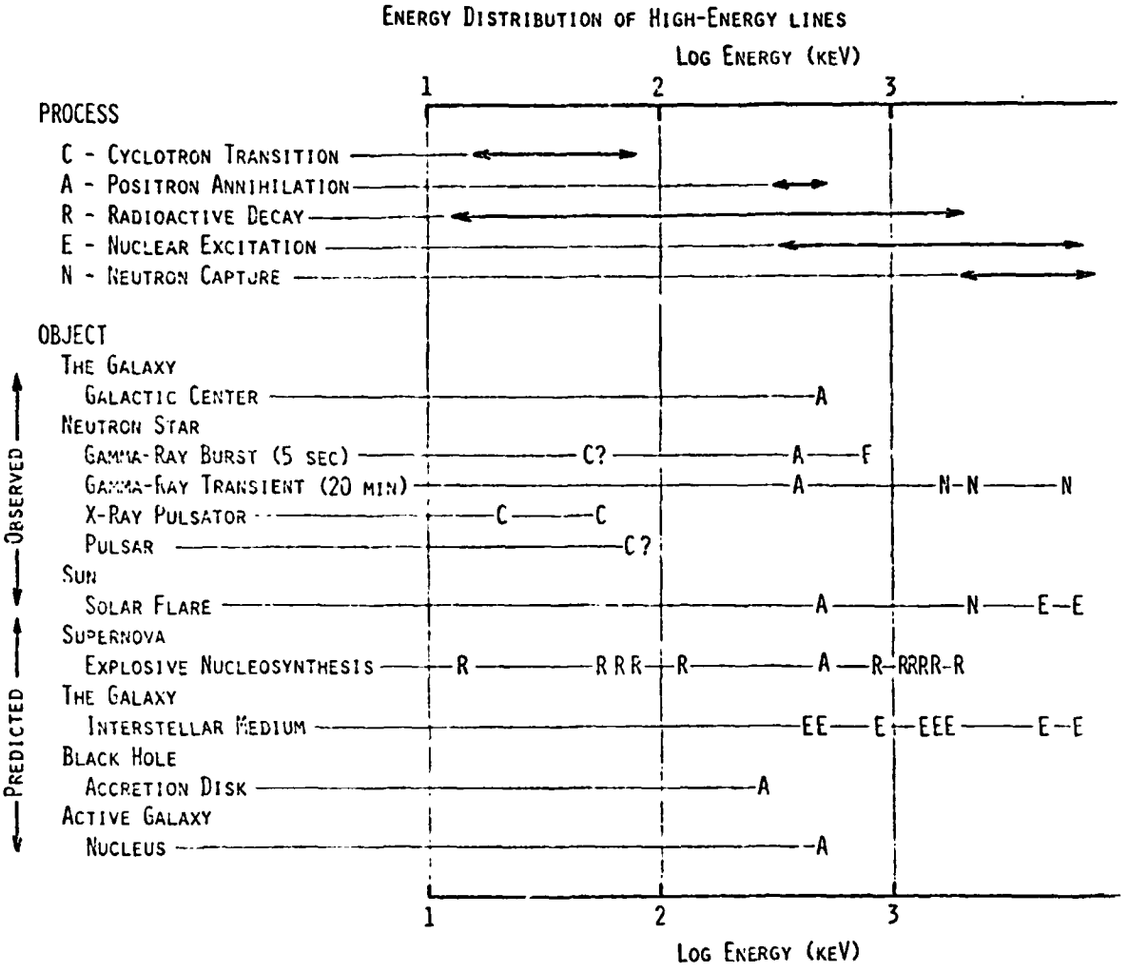

Figure 3. The energy distribution of lines produced by the processes discussed in the text. Also shown are the processes and energies of lines observed and predicted in a variety of astronomical objects.

ORIGINAL PAGE IS
OF POOR QUALITY

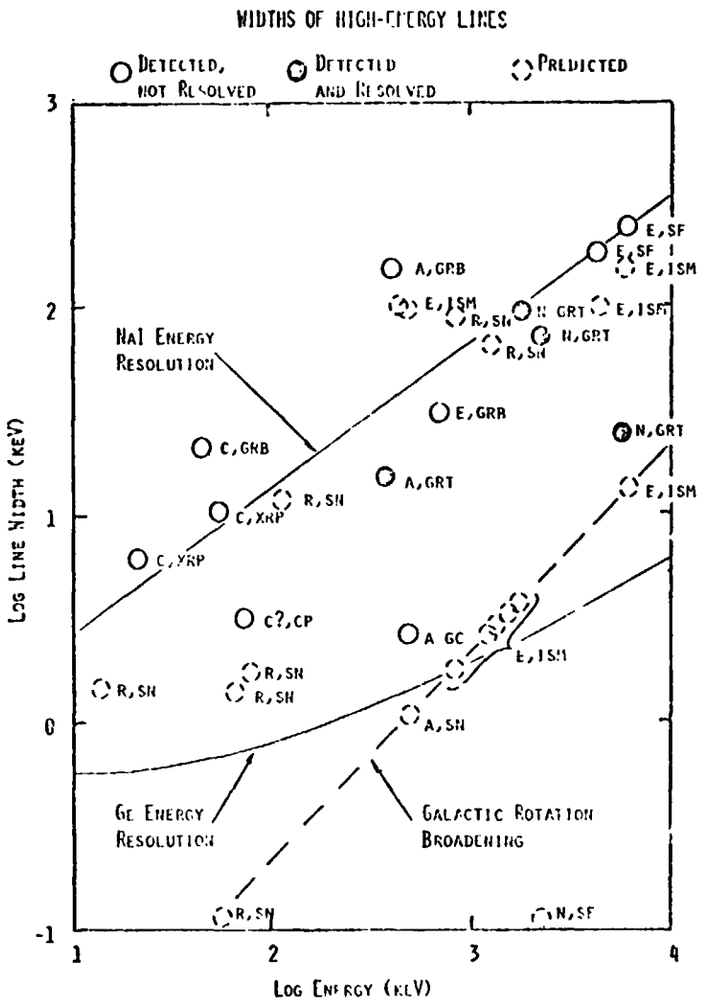

Figure 4. The widths of lines produced by the processes discussed in the text. The plotted width of a detected, but not resolved line is an upper limit to the line's true width. The energy resolution of Ge and NaI detectors are also plotted. It is obvious that Ge is required for detailed studies which measure the widths and profiles of lines. The processes and sources of the lines are indicated by the notation X,Y, where X = process and Y = source, as given below.

Process		Source	
C	Cyclotron	GC	Galactic center
A	Electron-positron annihilation	GRB	Gamma-ray burst
R	Radioactive decay	GRT	20-min gamma-ray transient observed from a balloon
E	Inelastic excitation of nuclei	SF	Solar flare
N	Neutron capture	ISM	Interstellar medium
		SNR	Supernova remnant, i.e. explosive nucleosynthesis
		XRP	X-ray pulsator
		CP	Crab pulsar

ORIGINAL PAGE IS
OF POOR QUALITY

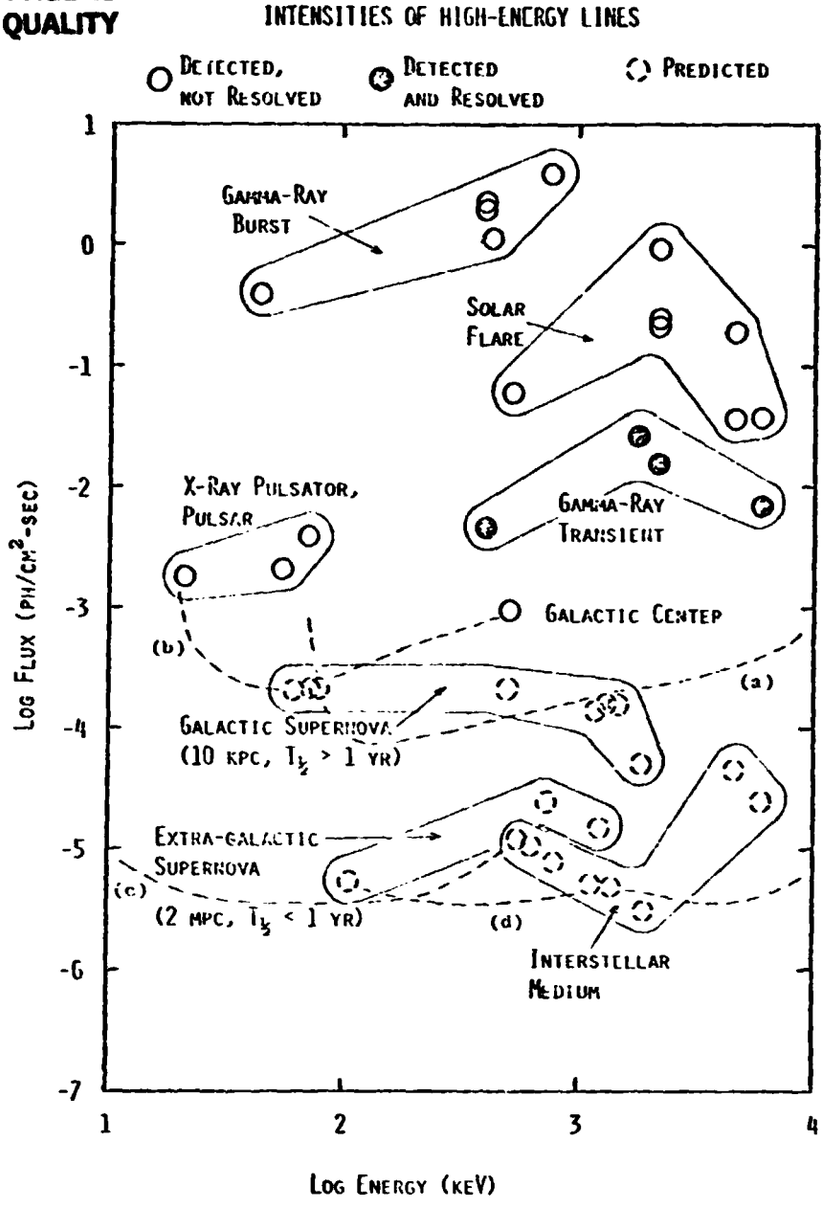

Figure 5. The intensities of high-energy lines. The most intense lines of each class of object are plotted. Also plotted are the sensitivities of several instruments.

(a) HEAO-3: 400 cm^3 coaxial Ge detector array, 30-days of scanning observation.

(b) Present balloon instrument: 50 cm^2 Ge detector array, 6 hour pointed observation.

(c) Future space instrument: Instrument (1) from the text, 2000 cm^2 planar Ge array, 30-day pointed observation.

(d) Future space instrument: Instrument (3) from the text, 10,000 cm^3 coaxial Ge array, 200-day observation.

N82 26085 D30 567

SPECTROSCOPY FROM 2 to 200 keV

David J. Helfand, Gary A. Chanan, and R. Novick

Columbia Astrophysics Laboratory, Columbia University

Crawford J. MacCallum

Sandia Laboratories

and

Marvin Leventhal

Bell Telephone Laboratories

ABSTRACT

The astrophysical processes responsible for line and continuum emission in the spectral range 2 keV to 200 keV are examined from the viewpoint of designing a spectrometer which would operate in this regime. Phenomena considered include fluorescent line radiation in X-ray binaries, magnetically shifted iron lines and cyclotron emission from neutron star surfaces, line emission from cosmically abundant elements in thermal plasmas, and nuclear deexcitation lines in fresh nucleosynthetically produced matter. An instrument consisting of a ~100 cm^2 array of planar germanium detectors surrounded by a large sodium-iodide anticoincidence shield is described and detailed consideration of projected background rates and sensitivities are presented. A sample observing program for a two-day Shuttle-based mission is included as an example of the wide range of scientific questions which could be addressed by such an instrument.

I. INTRODUCTION

From the serendipitous discovery of the first celestial X-ray source less than 20 years ago, X-ray astronomy has catapulted to the forefront in many of the most exciting areas of current astrophysical research: neutron stars, black holes, supernovae and their remnants, quasars and other galactic nuclei, the interstellar medium, and cosmology. The detection and identification of numerous classes of X-ray emitters, along with the recognition and interpretation of the wide variety of temporal variability they exhibit, constituted the driving force behind the early growth of the field. More recently, the launch of the Einstein Observatory extended sensitivites by a factor of $\sim 10^3$ and provided the capability for imaging X-ray emitters with spatial resolution comparable to that achievable in the radio and optical regimes. Major missions planned for the future include a larger soft X-ray telescope facility and a satellite dedicated primarily to detailed timing studies of bright galactic sources.

The development of cosmic X-ray spectroscopy has been slower than that of spatial and temporal studies, although recent advances indicate that this field holds great potential for providing important new insights into many areas of astrophysical research. Lines from silicon, sulfur, neon, oxygen, and other cosmically abundant elements have been detected from thermal plasmas in a variety of settings with the spectrometers on Einstein. Iron line emission has been discovered in the spectra of galaxy clusters, confirming the hypothesis that these X-rays arise from partially processed material. At higher energies, cyclotron features have been seen in the spectra of several

galactic X-ray sources thought to contain magnetized neutron stars including Her X-1 and other binaries, the Crab pulsar, and γ-ray bursters.

A wide variety of radiation processes are involved in producing the high energy photons we detect from celestial objects and X-ray spectroscopy is an essential tool in identifying these mechanisms and characterizing the physical environments in which they operate. Hot thermal and nonthermal plasmas produce the intense continuum and line emission we observe from X-ray binary stars, supernova remnants, and clusters of galaxies. Synchrotron radiation and inverse Compton emission are thought to be responsible for the energy output of active galactic nuclei (e.g., Seyferts, BL Lac objects, and quasars), while cyclotron radiation is dominant in the region of intense magnetic fields near the surface of a neutron star. Explosively produced radioactive nuclei from novae and supernovae as well as excited nuclei produced via the interaction of cosmic rays with the interstellar medium are expected to emit characteristic X- and gamma-ray lines. Finally the radiation from all of these processes is modified by the material through which it passes, both in the near source environment and along our line of sight to the source.

The instrumental limitations encountered thus far in X-ray spectroscopy can be summarized as the need to make unsatisfactory tradeoffs among three fundamental parameters: the resolution of the instrument, its sensitivity to line and continuum emission, and the total range of energies over which it can operate. Traditional proportional counters (with which the iron emission features in clusters have been detected) have good sensitivity and reasonable spectral range, but inherently poor resolution. On the other hand, the high resolution obtainable with crystal spectrometers requires severe sacrifices in sensitivity and spectral range, while scintillation detectors (such as the one

used to discover the Her X-1 cyclotron line) are limited in resolution and, thus, in their sensitivity to narrow lines. Finally, any spectrometer located at the focus of a grazing incidence telescope is limited to the spectral regime below ~8 keV. For instruments flown to date, the cutoff has been ~4 keV.

We have designed a wide-band germanium X-ray spectrometer capable of obtaining high resolution spectra over two decades of energy in the region of the spectrum most crucial to our understanding of the origin of both the line and continuum emission from celestial X-ray sources. At the lower end of the instrument's spectral range, it offers an improvement in energy resolution of a factor of 3 over traditional proportional counter experiments, while in the hard X-ray region (50 keV to 200 keV) it provides a gain in sensitivity and resolution of more than an order of magnitude over existing instruments. It is this unique combination of sensitivity, resolution, and spectral range which would allow one to carry out, in the brief period available on a Shuttle mission, an extensive, variegated observational program addressing many important questions of current astrophysical interest. Below, we discuss several of the sources of X-ray line emission which would be detectable with this instrument (§II) including a summary of previous work and estimates of the observing time required to meet various objectives. In §III, we describe the instrument design and develop detailed estimates of the backgrounds expected and the sensitivities achievable. In the final section, we comment briefly on the place such experiments might occupy in the space science program of the future.

II. SPECTROSCOPY FROM 2-200 KEV

a) Lines from Thermal Plasmas

Emission lines from highly ionized species of iron in the energy range from 6 to 7 keV have been discovered in the spectra of a wide variety of celestial X-ray emitters including supernova remnants (Charles et al. 1978), clusters of galaxies (Mushotzky et al. 1978), cataclysmic variable stars (Swank et al. 1978), and binary X-ray sources (Pravdo 1978). The latter sources are particularly interesting in that their continua cannot be characterized simply as thermal emission from an optically thin hot plasma; a superposed source of fluorescing material is required to account for the line emission. Potential locations for this material include the atmosphere of the companion star, a shell at the Alfven surface of the neutron star, and an accretion disk (Pravdo 1978). Evidence for a dependence of line energy and intensity on pulse and orbital phases has been reported for several sources including Her X-1 and Cyg X-3 (Becker et al. 1977; Becker et al. 1978). In addition, iron-abundance determinations for the binary sources indicate an enhancement of metal-rich material in these systems over that found in the thermal sources (supernova remnants and clusters of galaxies). This may, however, be more indicative of our crude knowledge of the excitation and emission mechanisms involved than of an overabundance of high-Z matter.

A wealth of information can be obtained from the determination of precise line energies and the measurement of high-resolution line profiles. The exact species responsible for the emission can be determined, with the relative contributions of each yielding information on the ionization balance of the emitting region. In addition, more reliable abundance determinations become

possible, and kinematic conditions in the source can be explored. Such information is crucial, for example, in choosing among the various models proposed for the source of the fluorescing plasma in X-ray binaries.

Most of the existing iron-line measurements have been made with proportional counters which have typical energy resolutions at 6 keV of ~1 keV. Thus, in many cases, the intrinsic line widths are unknown and, even in the few sources where resolved features are seen, the detailed structure of the line cannot be determined. The resolution of the proposed spectrometer is ~370 eV at 6 keV; this represents nearly a factor of 3 improvement over most proportional counter experiments and will allow one to pursue many of the important questions outlined above. The sensitivity of the instrument is such that in less than three hours' observing time, we could obtain high signal-to-noise ($\gtrsim$10 σ iron lines), high-resolution spectra for all of the eight binary X-ray sources known to exhibit iron features, easily resolving emission due to neutral iron (Kα at 6.4 keV) from that of various highly ionized species (e.g., Fe XXV at 6.7 keV and Fe XXVI at 6.93 keV). In 12 hours, we could detect these same lines (at the 5 σ level) from a dozen thermal sources including four supernova remnants, six clusters of galaxies, and two cataclysmic variable stars. Observations over one complete 4.8 hour binary orbit of Cyg X-3 would yield high resolution iron-line profiles (at the 20 σ level) in each of 30 orbital phase intervals. A six-hour observation of any one of the brighter X-ray binaries could lead to the first detection of the nucleosynthetically important nickel line at 7.5 keV.

Similar duration pointings would detect the strong sulfur, silicon, and neon lines observed in several galactic SNR with the Einstein Solid State Spectrometer (SSS), albeit with nearly a factor of 2 worse resolution. How-

ever, the wider field of view of the Germanium experiment will yield total spectra of the larger remnants (e.g., Vela, Puppis A, and the Cygnus Loop) for the first time. In addition, the simultaneous determination of the line strengths for iron and the silicon group elements will be invaluable in sorting out some of the abundance anomalies found in the SSS data. Such broad spectral coverage of both the line and continuum radiation is required for determinig the run of temperatures and the resulting ionization distribution in these objects.

b) Line Emission from Magnetic Neutron Stars

The exciting possibility of studying the intense magnetic fields (10^{12} to 10^{13} gauss) at the poles of a neutron star via X-ray spectroscopy was first pointed out by Gnedin and Sunyaev (1974) and Basko and Sunyaev (1975). Electrons in the ionized plasma accreting onto the surface of X-ray pulsars will undergo cyclotron motion in the magnetic field. Transitions between discrete Landau levels can occur, giving rise to a series of X-ray lines at the fundamental cyclotron frequency and its harmonics. Observations of these lines constitute a direct measurement of the magnetic field intensity, and a determination of the line profiles could yield important new information about the spatial distribution of the field and the accreting matter. Recently, the observation of such a line from Her X-1 at 55 keV was announced by Trumper et al. (1977) and Coe et al. (1977). The line emission is reportedly pulsed, with a flux of $\sim 10^{-3}$ photons $(cm^2\ s)^{-1}$ and an instrumentally determined width of $\lesssim 12$ keV. The implied magnetic field in the line-forming region is 4.6×10^{12} gauss.

The existing observations are insufficient even to determine whether the line is seen in emission at 55 keV or in absorption around 45 keV. High

spectral resolution data are the only way to choose between these two possibilities and to provide the input required in modeling kinematic and plasma conditions in and around the source. If the reported line from Her X-1 is intrinsically narrow (~1 keV), it will appear as a 40 σ detection in a 12-hour observation with the proposed instrument (a 10 keV wide line will yield a 30 σ result). The entire 40-70 keV continuum will be measured at a resolution of 1 keV and both the second (reported at 110 keV) and third cyclotron harmonics should be detectable.

The amount of line broadening due to Doppler (1978) and self-absorption effects (Meszaros 1978) helps to determine the angle between the magnetic field and the observer's line of sight. The proposed instrument will be able to specify this angle unambiguously, and its variation as a function of pulse phase could provide an important clue to the geometry of the emitting region and the relative orientation of the star's magnetic and rotation axes. The relativistic fine structure (Daugherty 1978) of the proposed line emission provides another estimate of the viewing angle. More importantly, however, the splitting of the fine structure levels ($\omega_{1,0}$, $\omega_{2,1}$, $\omega_{3,2}$, etc.) is related to the field strength; thus, a measurement of this splitting provides a determination of the field strength which is <u>independent</u> of the line energy. This in turn allows one to calculate the gravitational redshift at the emitting region, locating it precisely above the surface of the neutron star (whose mass is known from observations of its binary companion). Such a result is well within the capabilities of the proposed spectrometer and would yield the first firm upper limit on the radius of a neutron star (an extremely important input for calculations of the equation of state for matter at ultra-high densities) as well as providing a wealth of information on the magnetospheric

structure at the base of the accretion column (Meszaros 1978).

The radiative transfer calculations of Weaver (1978) and others indicate that a large fraction of the cyclotron-line radiation should be scattered to lower energies. Detailed line and continuum shapes can choose between models in which the line photons escape through holes in the circumstellar shell above the magnetic poles of the star and those in which the radiation passes directly through the shell. Thus, the line can also be used as a probe of plasma conditions at the Alfven radius of the star, yielding data relevant to the problems of the soft component of the X-ray emission from Her X-1 and the overall accretion process.

Observations of other pulsating X-ray binaries such as Cen X-3, Vela X-1, and the transient source 4U0115+63 (in which evidence for a 25 keV line has been reported) as well as of isolated neutron stars such as the Crab pulsar (in which a transient 77 keV emission feature was seen [Strickman, Kurtess, and Johnson 1981] could extend the usefulness of this sensitive probe to other objects. A feature ten times weaker than the reported Her X-1 line would be easily detected in Vela X-1 in half a day's time. These observations would, of course, all be simultaneous with those examining plasma conditions in these systems farther from the neutron star via high-resolution spectroscopy of the iron lines as discussed above.

Recently, it has been suggested that atomic lines of iron, strongly shifted by the intense magnetic field, might also be detectable from neutron star surface regions. Energies and strengths of the Lyman lines have been calculated by Ruder et al. (1981) for a variety of surface temperatures, abundances, and field strengths. The detection of these lines would yield the first direct observation of neutron star surface material, and would add

substantially to our knowledge of plasma conditions in the region where the accreting material impacts the star and the primary radiation is produced. Wunner et al (this volume), have calculated the requirements of a spectrometer necessary to observe such lines: 10 keV $\lesssim$ E $\lesssim$ 20 keV; $E/\Delta E \sim 10$ to 100 ; and line sensitivity of $\gtrsim 10^{-4}$ ph cm^{-2} s^{-1} . All of these specifications are exceeded by this proposed instrument.

c) Explosive Nucleosynthesis in Supernovae

The modern era of theoretical nucleosynthesis may be dated from 1957 with the publication of the classic paper Burbidge et al. (1957) (B^2FH). Set down therein is the basis for the currently held belief that the elemental abundances as we know them derive from stellar evolutionary processes rather than being a primordial arrangement of matter. These workers gave, for the first time, a characterization of the specific physical processes (r-, s-process, etc.) which lead to the formation of different classes of isotopes. In a sense, most of the research in this field for the past 25 years represents a search for the astrophysical sites of these processes, originally delineated by B^2FH. From the beginning, with the advocation of the californium hypothesis (Baade et al. 1956) to explain their light curves, supernovae were believed to play an important role in nucleosynthesis. During the latter part of the 1960s and early 1970s, large, fast computers became available for general use. This made it possible to follow phenomenologically the complex nuclear reaction matrix that takes place when a highly evolved star explodes and hydrodynamically expands. The calculations of Arnett, Cameron, Clayton, Colgate, Fowler, Schramm, Tinsley, Truran, Woosley, and others (Schramm and Arnett 1973) led to the remarkable result that many of the elements can be produced explosively in the correct cosmic abundance. This conclusion lent

great credence to the theories of explosive nucleosynthesis. An important objective of a germanium spectrometer would be to provide an observational basis for these theories. Many of the stable species are first produced as unstable radioactive elements which then decay, often with the emission of characteristic X-ray and gamma-ray lines (Clayton 1973). The unequivocal detection of even a single line from explosively produced radioactive matter would represent a fundamental breakthrough in this area of research.

Predictions of line fluxes to be expected from radioactive species produced in the various shells of a presupernova star have been pursued most actively by Clayton, Colgate, and Fishman (1969), Clayton (1973, 1974, 1975), and Ramaty and Lingenfelter (1977). Several lines of particular interest fall within the spectral range of our proposed instrument: three lines from the $^{57}Co \rightarrow {}^{57}Fe$ decay at 14 keV, 122 keV, and 136 keV, the 59 keV line from the $^{60}Fe \rightarrow {}^{60}Co \rightarrow {}^{60}Ni$ chain, and a doublet at 68 keV and 78 keV from the reaction $^{44}Ti \rightarrow {}^{44}Sc \rightarrow {}^{44}Ca$. These decay schemes have average lifetimes t_{av} of 1.1 years, 4.3×10^5 years, and 68 years, respectively. (See Table 1 for a summary of potential sources and required observing times.) At a time t following the supernova explosion, the flux F observable in lines such as these is given by

$$F = \frac{N \eta \exp(-t/t_{av})}{4\pi \, t_{av} \, D^2} \qquad (1)$$

where N is the number of nuclei produced in the explosion, η is the number of photons produced per disintegration, and D is the distance to the source. Using some typical values for these quantities, equation (1) becomes:

$$F = 2.6 \times 10^{-1} \left(\frac{N}{10^{51}}\right) \left(\frac{\eta}{1.0}\right) \left(\frac{1\ \mathrm{yr}}{t_{av}}\right) \left(\frac{1\ \mathrm{kpc}}{D}\right)^2 e^{-t/t_{av}} \text{ photons } (\mathrm{cm}^2\ \mathrm{s})^{-1} \quad (2)$$

To observe a gamma-ray line from the short-lived process $^{57}Co \rightarrow {}^{57}Fe$, a very young ($t < 10$ years) supernova remnant is required. Current estimates of galactic supernova rates range from one per five years to one per fifty years (Tamman 1977; Clark and Stephenson 1977; Manchester and Taylor 1977), with some recent results (Jones 1975; Taylor 1978) tending to favor the higher rate. Thus, it is not at all unlikely that a remnant less than 5 to 10 years old exists somewhere in the Galaxy; such an object would prode a 122 keV line flux of 4×10^{-4} photons $(\mathrm{cm}^2\ \mathrm{s})^{-1}$ at 20 kpc. With our $1^{\circ}.5$ field of view pointed along the galactic plane, we could search over 75% of the entire volume of the Galaxy in which supernova remnants are known to exist ($R < 12$ kpc; $|z| < 150$ pc) to this level of sensitivity in less than two days. The only excluded regions would be within a few kiloparsecs of the earth within which we are quite certain no such recent event has occurred.

While the prospect of detecting such a young remnant is an exciting one indeed, the initial program for such a spectrometer would probably concentrate on the other two disintegration chains noted above, since their longer half-lives allow us to search for these lines in known objects. The ^{44}Ca doublet will be detectable with our instrument in a three-hour integration if it is present in the Cas A remnant at the expected level. These searches for nuclear lines from the explosively produced matter can, of course, be carried out simultaneously with the detailed study of the atomic spectra of both the ejected and swept-up material via the 6-7 keV iron and nickel lines.

Although less energetic by several orders of magnitude, galactic novae are also thought to be the site of significant nucleosynthesis, and their

frequent occurrence (>25 per year in the Galaxy) makes them an important potential target. Assuming a yield of unstable nuclei of $10^{-3.5}$ times that for supernovae (Lingenfelter and Ramaty 1978), we could easily detect both the ^{57}Co and ^{44}Ti lines from a nova 3 kpc away for the first year or two after its outburst. In addition, the potentially quick response time of the Shuttle suggests the exciting possibility of observing one of the most abundant of the iron peak isotopes (^{56}Ni, 163 keV) despite its short lifetime of ~10 days (a launch within 3-4 months of the outburst of a nearby [~2 kpc] nova would be required). In conclusion, then, our spectrometer offers the first opportunity to put the so-far brilliantly successful theory of explosive nucleosynthesis to a direct test at the sources of the created material.

d) Continuum Spectra

No instrument has every been flown which covers the entire energy range from soft X-rays to soft gamma-rays. Consequently, all of the currently available X-ray source spectra are composites of data taken with different instruments and, more importantly for these variable sources, at different times. Detailed continuum spectra are a valuable discriminant among various emission and radiative transfer models, and with the current observational situation, progress in understanding these sources has been slow.

An obvious by-product of the spectral line observations proposed above is the determination of source continuum spectra over the spectrometer's range of 2 to 200 keV. The high resolution available over the entire band will enable us to pinpoint spectral breaks and absorption edges, and will provide data which will be most useful in studying detailed models for source emission components. Assuming a Crab-like spectrum and a 1 keV resolution element, we can detect in three hours all sources brighter than 15 Uhuru counts out to 50

keV and all sources brighter than 300 Uhuru counts (~25 sources) out to 200 keV.

e) Solar Physics

High resolution solar spectra have never been obtained in the energy range from 50 to 200 keV and standard, free-flying spacecraft constraints often preclude solar observations entirely. Thus, the closest object in the universe of interest to high energy astrophysicists remains an enigma. The relationship of radio noise storms and bursts to the energetic particles evident in X-ray flares is not well understood, and detailed continuum shapes are required to make progress in the theories of particle acceleration and storage mechanisms. Lines from the hot thermal plasma of the corona will be easily observable. Jacobsen (1977) has reported the detection of a 73 keV line which may have originated in the quiet Sun, and although theoretical estimates of their strengths are quite low, lines from the deexcitation of nuclei produced in surface nuclear reactions and in the spallation of the thermal nuclei of the photosphere by the high energy flare particles might well be detected. Detailed line shapes can yield kinematic and positional information about the emitting particles. By following the time development of the spectrum through a solar flare, densities and temperatures in the emitting volume can be obtained (see, for example, Parkinson 1975). Although solar astronomy would probably not be the primary objective of the initial flight of the proposed instrument, its spectral range and resolution make it an obvious candidate for use in studying the Sun. We have included a solar observation of a few hours in our sample observing plan to obtain the first high resolution spectrum of the quiet Sun available in this energy regime. If an active region is present at launch time, we could specify a more extended

pointing in an attempt to obtain a flare spectrum which would contribute substantially to our knowledge of the energetic phenomena taking place on our closest star.

f) Sample Observing Program

In Table 2 we present a sample c' .erving program that could be carried out with this instrument in two days of pointed observations on a Shuttle mission. We have assumed that on-source data will be collected during only 40% of our observing time and have based our integration time requirements on the sensitivity calculations found in §III.f. A wide range of targets is possible in this short time, and there are manifest advantages in being able to combine search program (e.g., for cyclotron and nuclear deexcitation lines) with observations which we are confident will yield positive, important results (the high-resolution spectroscopy of the 6 keV iron lines and the detailed continuum spectra).

III. EXPERIMENT DESCRIPTION

a) Overall Design

The Wide-Band Germanium X-Ray Spectrometer is illustrated in Figure 1. The detector package, consisting of 19 planar germanium crystals and their associated low-noise preamplifiers in a vacuum cryostat, is surrounded by a massive active Polyscin (NaI) shield/collimator and its associated complement of phototubes. The two-section collimator provides each detector with a $1.^{\circ}5$ FWHM field of view, and includes two movable shutters used in acquiring background data, along with an aluminum filter to allow solar observations. A solid Argon refrigerator sits at the base of the unit, providing sufficient

cooling capacity to maintain the detector cryostat at $T \lesssim 90$ K for a period of up to five weeks. This experiment will provide the first single-instrument coverage of this entire energy range, a factor of 3 improvement over the resolution of proportional counters in the 6-7 keV iron-line region, and more than an order of magnitude increment in both resolution and line sensitivity in the 30 to 200 keV region. The design details for each of the system's components, along with questions of sensitivity and background rates, are discussed below.

b) Detector Package

The detector itself consists of a hexagonal close-packed array of 19 planar high-purity germanium crystals of 1 inch diameter (5 cm^2). These individual intrinsic detectors are readily available commercially in a variety of thicknesses; we have chosen 10 mm as the optimum value for energy range and resolution (but see §III.g below). The quantum efficiency of the detectors is greater than 80% from 3 to 90 keV and remains greater than 25% between 1.5 and 200 keV; the resolution is better than 400 eV at the low end of this energy range and degrades only slowly to a value of ~650 eV (0.4%) at the upper end. The detectors are mounted on a cold plate to minimize thermal generation of electron/hole pairs and to increase the mobility of the pairs created by the ionizing X-rays from the source.

Each crystal is equipped with a low-noise FET preamplifier which resides inside the detector cryostat. The preamplifier output signals are sent to the electronics box mounted beneath the shield assembly where they are amplified, shaped, and processed in a pulse-height analyzer. Four multiplexed 12-bit analog-to-digital converters (one for each five detectors) assign each event to one of the 4096 50-eV wide energy channels. The data are serially

transferred to the Shuttle telemetry system through a buffer; anticoincidence triggers recorded by the phototubes and other secondary science and housekeeping data are subcommutated with the primary data stream by a microprocessor.

c) Shield/Collimator System

In the low-energy X-ray regime (< 20 keV), large anticoincidence scintillator shields have not traditionally been employed, since the instrument background is typically dominated by diffuse X-ray emission. At high energies, however, the spectrum of the diffuse background steepens, and the charged particle background becomes the sensitivity-limiting factor. In addition, passive collimators become increasingly difficult to build as the energy increases above 40 keV. In the proposed spectrometer, the shield allows for good collimation over the entire spectral range, diffuse background-limited observations out to nearly 50 keV, and remarkably low [$\sim 10^{-3}$ counts $(s\ keV)^{-1}$] total background rates throughout the hard X-ray portion of the spectrum.

The shield/collimator assembly consists of four pieces of sodium iodide housed in nermetically sealed containers with glass windows for their associated phototube arrays. The shield design assures that the path to any detector from the outside world is at least 4 inches. The sodium iodide pieces surrounding the detector box on the bottom and sides are each viewed through symmetrical arrays of six 5-inch ruggedized phototubes. The 18-inch high collimator section on top of the detector is a honeycomb of nineteen 1-inch holes (one above each detector) and requires a dozen phototubes for effective light collection. Similar drilled collimators have been flown successfully with solid-state detectors in several experiments (e.g., on OSO-7 and HEAO-1). The forward collimator section with its own set of 3-inch photo-

tubes resides 18 inches above the top of the instrument to provide a reduction of a factor of 2 over the unprecollimated field of view to $1.^{\circ}5$ FWHM (5.4×10^{-4} ster).

With an effective geometric area of ~4000 cm^2, the instrument should experience incident background rates of $\sim 4 \times 10^4$ events s^{-1}. A bilevel anti-coincidence trigger mechanism will provide a short (1-2 μs) gate for normal background events and a wider (~50 μs), adjustable gate for those events that deposit very large amounts of energy in the shield ("stars"). The dead time from the normal events will be ~5%; we estimate that there may be 10^3 "stars" per second, leading to an additional 5% dead time. Since the rate of "stars" is difficult to predict accurately, the exact veto width of the "star" gate can be uplinked once the background orbit is determined.

d) Background Shutters

Mounted atop the main collimator are two motor-driven interlocking shutters, each with its own phototube. They can be commanded closed individually or together to cover either 9, 10, or all 19 of the detectors for the purposes of obtaining simultaneous background data while the source is in the field of view. Such simultaneity may be required to extract, for example, the weak nuclear deexcitation lines from the strong, time-varying background spectrum. For most observations, however, we will be able to obtain sufficient background data during portions of the orbit when the source of interest is not accessible (e.g., Earth occultation) and thus will utilize the full effective area of the detectors for source observation.

e) Background Calculations

The calculated instrument background spectrum is shown in Figure 2. The following background components have been included in our considerations:

(1) The diffuse X-ray background (both inside the field of view and incident on the remainder of the instrument)

(2) Cosmic gamma-ray-induced spallation in the germanium crystals

(3) Trapped gamma-ray-induced spallation in the germanium crystals

(4) Charged particle-induced radioactivity in the NaI shield, and

(5) Neutron activation in the germanium.

We have taken the diffuse background spectrum dF_{bl}/dE from Schwartz (1978); for our 95 cm^2 detector with its $1.^{o}5$ field of view, this implies

$$\frac{dF_{bl}}{dE} = \begin{cases} 0.50\ E^{-1.4} & (1 < E < 21\ \text{keV}) \\ 9.90\ E^{-2.38} & (21 < E\ \text{keV}) \end{cases}$$

This contribution dominates the instrument background up to ~40 keV and then is rapidly swamped by the non-X-ray background, contributing less than 10% above 95 keV. Due to the thick NaI shield which completely surrounds the detector, the contribution to the background from the isotropic diffuse flux incident on the instrument is negligible; calculations indicate it can be neglected completely below ~400 keV.

We have performed detailed Monte Carlo simulations using the computer codes at Sandia Laboratories[1] to estimate the contribution to the background from long-lived (compared to the veto time gate width) radioactivity induced in the germanium crystals from both cosmic rays and trapped protons. The cosmic-ray proton flux was taken from Figure 17 of Webber's review (1967),

---

[1] We wish to acknowledge the invaluable assistance of Jim Morel and John Halbleib of Sandia Laboratories for performing these important simulations.

using the values for sunspot maximum. The South Atlantic Anomaly protons ad electrons were treated using Proton Model AP8 Max (Sawyer and Vette 1976) and solar maximum models AE4 and AE6 (Teague, Chan, and Vette 1976). The trapped proton flux was calculated for a time corresponding to one orbit after the last South Atlantic Anomaly passage on the tenth day of the mission. The simulations were performed for shield geometries closely approximating our present design and with minimum shield thicknesses of 8 cm and 12 cm. There were no statistically significant differences between the two runs, although the assumption of neglecting the noncollimated diffuse radiation begins to break down for thinner shields.

In principle, one can calculate the background contribution due to charged particle-induced radioactive spallation products in the NaI shield itself with the same detailed procedures used above for the germanium. However, since the vast majority of these nonvetoed events leave the instrument without interacting in the detector, a vast number of particle and photon histories must be followed before statistically meaningful results are achieved, and the computing costs become prohibitive. Thus, we have modeled this contribution to the background by calculating the particle and photon flux out of the surface of a block of NaI with the appropriate amount of induced, nonvetoed radioactivity. This has then been treated as an isotropic background bathing the Ge crystals and can be converted to a background counting rate by simply multiplying by the isotropic efficiency of each detector and summing over all detectors. This contribution turns out to be roughly comparable to that from the spallation in the germanium over most of the energy range of interest (see Fig. 2).

In addition to the continuous background produced by charged particles

and diffuse X-rays, several sharp lines typically appear in the background spectrum of germanium detectors due to transitions in the crystals induced by incident neutrons. While a massive active NaI shield is effective in rejecting charged-particle and uncollimated X-ray events, it is not particularly useful in reducing the flux of these neutrons. Earth albedo and spacecraft-generated neutrons ranging in energy from a fraction of a keV to >100 keV contribute in two ways to the production of a metastable excited state of ^{73}Ge: (1) neutron capture in ^{72}Ge, and (2) inelastic scattering off ^{73}Ge. Two of the strong background lines produced by the decay of this metastable state occur at inauspicious locations in the spectrum: at 54 keV (near the Her X-1 cyclotron line) and at 67 keV (near the 68 keV nuclear deexcitation line of ^{44}Ti). The high gain stability and attention to obtaining background data inherent in the instrument design will allow the accurate subtraction of such background features.

f) Instrument Sensitivity

The minimum line flux F_L detectable at an M-sigma level in orbit time t is given by

$$F_L = \frac{M\ (2B\ \Delta E)^{1/2}}{A\ \varepsilon_A (\varepsilon_t \cdot t)^{1/2}} \quad ,$$

where ΔE (keV) is the instrumental resolution or the intrinsic line width (whichever is greater), A (cm^2) is the geometric area of the detector with efficiency ε_A, ε_t is the fraction of orbit time in which good data are collected, and B is the background counting rate, consisting of both the non-X-ray counting rate plus the diffuse X-ray background, dF_b/dE, and the source

continuum flux, dF_c/dE, in the vicinity of the line (in counts [cm^2 s keV]$^{-1}$). Thus, the time to detect a feature of known strength is given by

$$t = \frac{M^2}{\varepsilon_t \cdot F_L \cdot A \cdot \varepsilon_A} \left(1 + \frac{2\frac{dF_b}{dE}\Delta E}{F_L \cdot \varepsilon_A} + \frac{2\frac{dF_c}{dE}\Delta E}{F_L}\right) \quad .$$

The geometric area of the detector is 95 cm^2 and the resolution in the iron line region of the spectrum is ~400 eV. We have assumed that useful data will be obtained during 40% of our observing time (i.e., $\varepsilon_t = 0.40$). Note that for many of the strong X-ray binary targets, the source continuum is the dominant contribution to the "background" counting rate. In estimating the observing times requried for the observations of bright binary sources discussed in §II.a), we have used the 6 keV continuum fluxes reported in the references from which the line fluxes were taken and have extrapolated these values to the sulfur, argon, and nickel energies using an E^{-1} power law spectrum (a good approximation of these objects over this narrow spectral range [Pravdo 1978]).

Using these parameters, the 3-σ sensitivity obtainable in 10^4 s of orbit time is approximately

$$F_{L(min)} \simeq 6 \times 10^{-4} \left(\frac{dF_b}{dE}\right) + \left(\frac{dF_c}{dE}\right)^{1/2} \text{ photons } (cm^2\ s)^{-1} \quad ,$$

implying line sensitivities of $\lesssim 10^{-4}$ photons $(cm^2\ s)^{-1}$ and $\lesssim 4 \times 10^{-5}$ photons $(cm^2\ s)^{-1}$ at 6 and 60 keV, respectively.

g) Other Detector Configurations

The detector system described above was chosen to optimize sensitivity and resolution while extending the useful spectral range down to 2 keV. In view of the extensive spectroscopic results from the Einstein SSS in the 2-4

keV range, it is useful to consider other possible detector configurations which deemphasize this soft X-ray regime. One such possibility would be to substitute thicker germanium crystals for those in the baseline design to provide increased sensitivity at the higher energies. For example, 1.6 cm planar crystals retain 10% of their efficiency up to 550 keV. Thus, a 19-element array would provide ~10 cm^2 of effective area in the region of the 511 keV position annihilation line which has been observed from the direction of the galactic center. The narrow field of view and high spectral resolution of this experiment would provide new information on the source of this line. The price of such a change is a worsening of the resolution in the 6-7 keV iron line region by nearly a factor of two (to ~10%, i.e., comparable to that achievable with gas scintillation proportional counters - see Hailey et al. and Culhane, this volume). Alternatively, the complexity of the detector and shield assemblies could be reduced considerably by choosing an array of seven 15-cm^2 crystals in place of the nineteen 5-cm^2 array in the current design. Again, however, the resolution is degraded from 360 eV to 560 eV at 6 keV. Detailed scientific/engineering tradeoff studies are currently under way to determine the optimum configuration for a flight design.

IV. CONCLUSIONS

A number of outstanding astrophysical problems require critical inputs from moderate-to-high resolution X-ray spectroscopy in the 2-200 keV band and beyond. A large number of the atomic, nuclear, and cyclotron transitions that occur in the regime offer unique probes of the physical conditions which

obtain in sources ranging from neutron star binaries to clusters of galaxies. We have designed a planar germanium spectrometer which would operate in this rich spectral domain to address such questions as the structure of neutron star magnetospheres and accretion disks and the origin of the chemical elements. With the elimination of the germanium spectrometer on the Gamma Ray Observatory, no currently planned NASA mission will be able to meet the patent need for such a spectrometer.

The sample observing program displayed in Table 2 illustrates that a substantive scientific program can be carried out by such an experiment in the brief observing time available on a week-long Shuttle flight. As the cost of a free-flying mission escalates past $100 M and the funds available for new starts declines precipitously, it is perhaps appropriate to reexamine the premises on which the space science program of the past decade was built. Ten experiments of the class described here and elsewhere in this volume can all be built for half the cost of one free-flyer in less than half the time. The continued existence of an American program in high energy astrophysics may well turn on which of these options is chosen.

This work was supported by the National Aeronautics and Space Administration under Contract NAS 5-26041. This is Columbia Astrophysics Laboratory Contribution No. 216.

ORIGINAL PAGE IS
OF POOR QUALITY

TABLE 1

Nuclear Deexcitation Lines from the Sites

of Explosive Nucleosynthesis

Nuclei	Energy (keV)	Life-time (yr)	Nuclei Produced per Event	Photons per Decay	Source	Dis-tance (kpc)	Time Required* (hr)
$^{57}Co \rightarrow ^{57}Fe$	14,122	1.1	7×10^{52}	0.88	5 yr SNR	20	0.34
	136	1.1	7×10^{52}	0.11			4.8
$^{57}Co \rightarrow ^{57}Fe$	14,122	1.1	2×10^{49}	0.88	1 yr Nova	3	0.61
	136	1.1	2×10^{49}	0.11			14
$^{60}Fe \rightarrow ^{60}Co \rightarrow ^{60}Ni$	59	4.3 $\times10^{5}$	5×10^{50}	1.0	Sof: X-Ray loop	0.2	38
$^{44}Ti \rightarrow ^{44}Sc \rightarrow ^{44}Ca$	68, 78	68	6×10^{51}	1.0	Cas A	2.8	2.4
$^{56}Ni \rightarrow ^{56}Co \rightarrow ^{56}Fe$	163	0.025	9×10^{50}	0.85	1 mo Nova	3	0.01
					3 mo Nova		5.9

*To detect a 3 σ detection based on line strength calculations discussed above.

ORIGINAL PAGE IS
OF POOR QUALITY

TABLE 2

Sample Observing Program for Two Days' Observing Time

Source	Time (hr)	Objectives: Fe Line (≥6 σ)	Ni Line (4 σ)	Other Lines (3 σ)	Continuum Spectra	Cyclotron Lines (>10 σ)	Nuclear Lines (3 σ)
X-Ray Binaries							
Cyg X-3*	5	✓	✓	✓	✓	✓	...
Cen X-3	0.1	✓	...	...	✓	...	...
Vela X-1	6	✓	✓	✓	✓	✓	...
Her X-1	12	✓	✓	...	✓	✓	...
GX 301-2	0.1	✓	...	...	✓	...	...
1626-67	0.1	✓	...	...	✓	...	...
Cir X-1	0.3	✓	...	...	✓	...	...
Supernova Remnants							
Cas A	20	✓	✓(6 σ)	...	✓	...	✓
GX 287.8-0.5	1	✓	...	...	✓	...	...
Recent nova	0.2	...	...	...	✓	...	✓
Clusters of Galaxies							
Perseus	0.15	✓	...	...	✓	...	...
Virgo	0.25	✓	...	...	✓	...	...
Coma	0.8	✓	...	...	✓	...	...
0251+41	1.0	✓	...	...	✓	...	...
The Sun	3	...	...	✓	✓	...	✓
Total	50						

*One complete orbit.

REFERENCES

Armstrong, T. W., Chandler, K. C., and Barish, J. 1973, J. Geophys Res., 78, 2715.

Baade, W. et al. 1956, P.A.S.P., 68, 296.

Basko, M. M., and Sunyaev. R. A. 1974, Astron.Ap., 42, 311.

Becker, R. H., Boldt, E. A., Holt, S. S., Pravdo, S. H., Rothschild, R. E., Serlemitsos, P. J., Smith, B. W., and Swank, J. H. 1977, Ap. J., 214, 879.

Becker, R. H., Rothscild, R. E., Boldt, E. A., Holt, S. S., Pravdo, S. H., Serlemitsos, P. J., and Swank, J. H. 1978, preprint.

Burbidge, E. M., Burbidge, G. R., Fowler, W. A., and Hoyle, F. 1957, Rev. Mod. Phys., 29, 597.

Charles, P. A., Mason, K., Cash, W., Lampton, M., and Bowyer, S. 1978, Bull. A.A.S., 10, 420.

Clark, D. H., and Stephenson, F. R. 1977, M.N.R.A.S., 179, 878.

Clayton, D. D. 1973, in Explosive Nucleosynthesis, eds. D. N. Schramm and W. D. Arnett, (Texas: U. Texas Press), and references therein, p. 264.

Clayton, D. D. 1973, in Explosive Nucleosynthesis, eds. D. N. Schramm and W. D. Arnett, (Texas: U. Texas Press), and references therein, p. 265.

Clayton, D. D. 1974, Ap. J., 188, 155.

Clayton, D. D. 1975, Ap. J., 198, 151.

Clayton, D. D., Colgate, S., and Fishman, G. J. 1969, Ap. J., 155, 75.

Coe M. J. et al. 1977, Nature, 268, 509.

Daugherty, J. K. 1978, "Gamma Ray Spectroscopy in Astrophysics," NASA Technical Memorandum 79619, p. 364.

Dyer, C. S. 1977, "Assessment of Background Radiation Effects in Low-Energy Gamma Ray Astronomy," 1977 Gamma-Ray Symposium, Frascati, Section 7.

Gnedin, Y. N., and Sunyaev, R. A. 1974, Astron. Ap., **36**, 379.

Hess, W. N., Canfield, E. H., and Lingenfelter, R. E. 1961, J. Geophys. Res., **66**, 665.

Hess, W. N., private communication.

Jacobsen, A. S. 1977, "High Resolution Gamma Ray Spectroscopy," invited paper presented at Spring Meeting of APS.

Jacobsen, A. S. et. al. 1975, N.I.M., **127**, 115.

Jones, E. M. 1975, Ap. J., **201**, 377.

Kanbach, G., Reppin, C., and Schonfelder, V. 1974, J. Geophys. Res, **79**, 5159.

Lingenfelter, R. F., and Ramaty, R. 1978, Physics Today, **31**, 40.

Manchester, R. N., and Taylor, J. H. 1977, Pulsars (San Francisco: Freeman), 160.

Meszaro , P. 1978, Astron. Ap., **63**, 19.

Meszaros, P. 1978, in "Gamma-Ray Spectroscopy in Astrophysics," NASA Technical Memorandum 79619, p. 425.

Mushotzky, R. F., Serlemitsos, P. J., SMith, B. W., Boldt, E. A., and Holt, S. S. 1978, preprint.

Parkinson, J. H. 1975, Solar Phys., **42**, 183.

Pravdo, S. H. 1978, presented at the 21st COSPAR Plenary Meeting, Innsbruck, Austria.

Preszler, A. M., Sinett, G. M., and White, R. S. 1974, J. Geophys. Res., 79, 17.

Ramaty R., and Lingenfelter, R. E. 1977, Ap. J. (Letters), 213, L5.

Ruder, H., Wunner, G., Harold, H., and Trumper, J. 1981, Phys. Rev. Lett., 46, 1700.

Sawyer, D. M., and Vette, J. I. 1976, NSSDC/WDC-AR&S 76-06, National Space Science Data Center, NASA GSFC, Greenbelt, Maryland.

Schramm, D. N., and Arnett, W. D. eds., 1973, Explosive Nucleosynthesis (Texas: University of Texas Press), and references therein.

Schwartz, D. A. 1978, presented at 21st COSPAR Plenary Meeting, Innsbruck, Austria.

Swank, J. H., Boldt, E. A., Holt, S. S., Pravdo, S. H., Rothschild, R. E., and Serlemitsos, P. J. 1978, Bull. A. A. S., 23, 581.

Tamman, G. A. 1977, Proceedings of Eighth Texas Symposium on Relativistic Astrophysics, Ann. N. Y. Acad. Sci., 302, 61.

Taylor, J. H. 1978, private communication.

Teague, M. J., Chan, K. W., and Bette, J. I. 1976, NSSDC/WDC-AR&S 76-04, National Space Science Data Center, NASA GSFC, Greenbelt, Maryland.

Trumper, J. et al., 1978, "Gamma-Ray Spectroscopy in Astrophysics," NASA Technical Memorandum 79619, p. 331.

Weaver, R. P. 1978, "Gamma-Ray Spectroscopy in Astrophysics," NASA Technical Memorandum 79619, p. 418.

Webber, W. R. 1967, Handbuch der Physik, 46, (Springer-Verlag).

White, R. S. 1973, Rev. Geophys. and Space Phys., II, 595.

FIGURE CAPTIONS

FIG. 1 - Schematic diagram of Wide-Band Germanium X-Ray Spectrometer.

FIG. 2 - Background counting rates for the Wide Band Germanium X-Ray Spectrometer as a function of energy including contributions from nonvetoed charged-particle events in the detectors (Ge) and shield (NaI), and the diffuse X-ray background.

ORIGINAL PAGE IS
OF POOR QUALITY

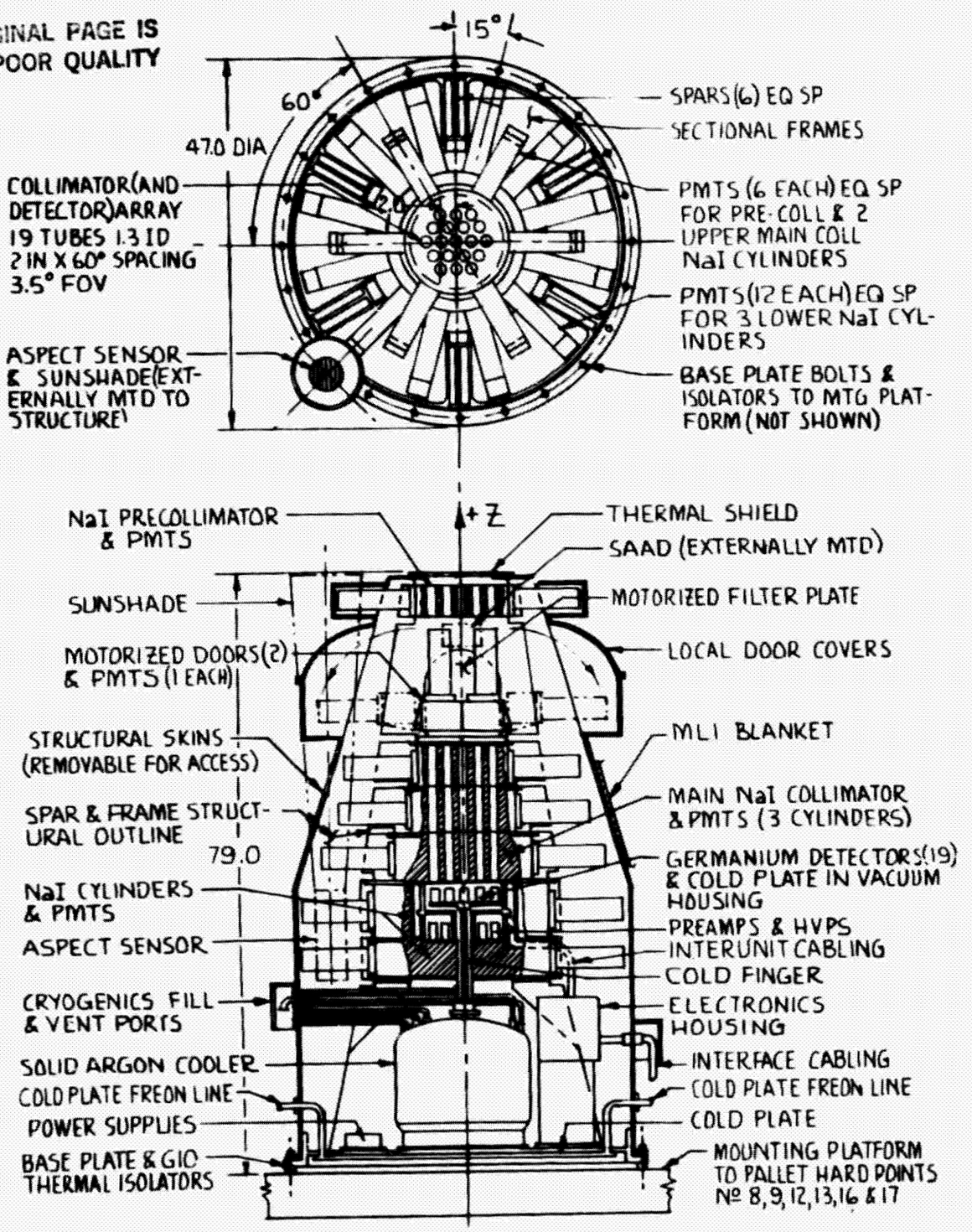

GENERAL ARRANGEMENT
WIDE-BAND GERMANIUM X-RAY SPECTROMETER
SCALE: APPROX 1/16

FIGURE 1

ORIGINAL PAGE IS
OF POOR QUALITY

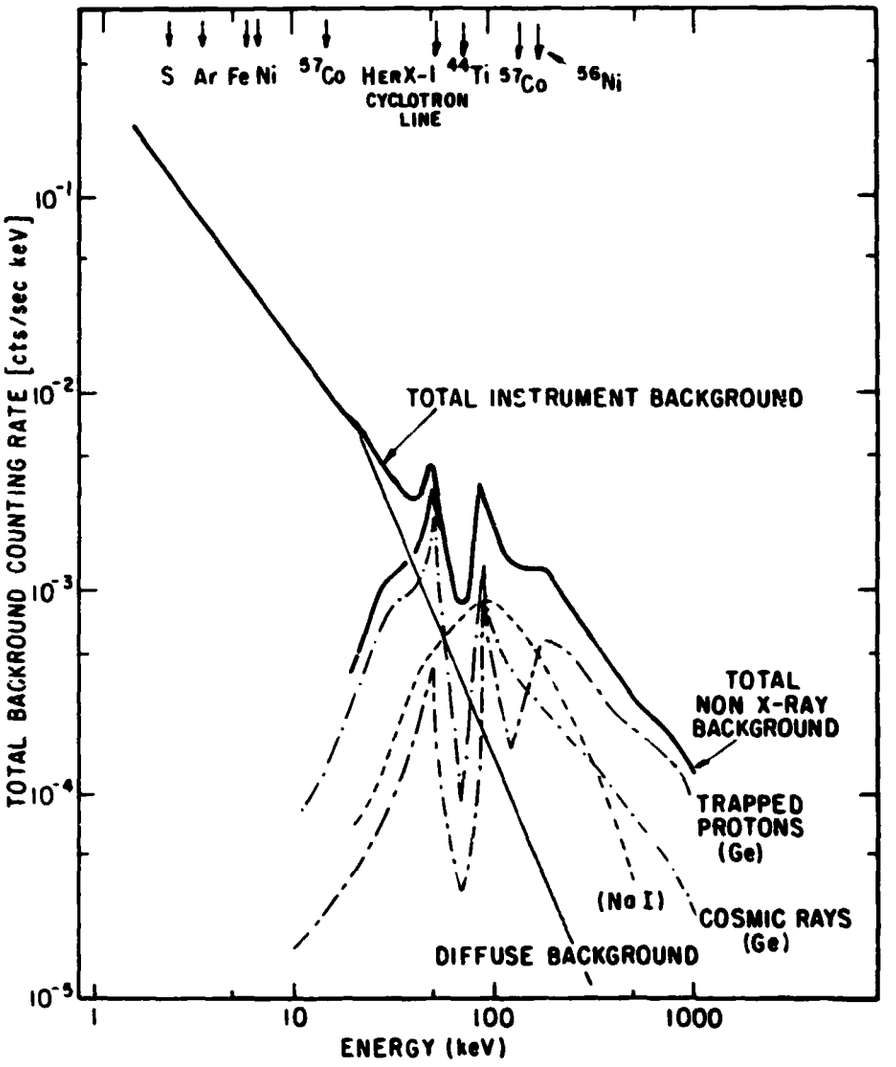

FIGURE 2

ORIGINAL PAGE IS
OF POOR QUALITY

N82 26086

HARD X-RAY ASTROPHYSICS

Richard E. Rothschild
University of California, San Diego

While many people have come to this workshop to promote various instruments of interest, I have come to promote a specific area of observations. Hard x-ray astrophysics includes observations above 20 keV and up to hundreds of keV, and it can provide much valuable information on the astrophysics of cosmic sources. A review of past hard x-ray and lower energy satellite instruments is in order and is given below.

NAME	AREA (cm^2)
Hard X-Ray Instruments (> 20 keV)	
OSO-3	10
OSO-7	64
Ariel-V	8
OSO-8	28
HEAO-1 A4	220
HEAO-3 C1	85
Hakucho	49
XTE (Proposed)	2000
X-Ray Instruments (2-20 keV)	
UHURU	840
OSO-7	70
Copernicus	18
Ariel-V	580
SAS-3	300
OSO-8	244
HEAO-1 A1	6400
HEAO-1 A2	2400
Einstein	667
Hakucho	210
XTE	10000

Hard x-ray instruments reached one-fourth of the *UHURU* area with the A4 instruments aboard the *HEAO-1* satellite, even though the measured signal for hard x-ray observations is generally down by three orders of magnitude from that in the *UHURU* energy range. The small areas devoted to hard x-ray astrophysics have forced observers to deal with signal-to-background ratios less than one if they wished to study anything other than the brightest sources. *HEAO-1* and recent balloon results show that sources can be detected with conventional techniques at the few per cent of background level. This translates to being able to detect sources at the 1 *UFU* level at 100 keV with a few thousand square centimeters of detector area in a few days. Hence, the pre-Einstein catalog of x-ray sources (*i.e.* > 1 *UFU* sources) can be available for detailed study.

Now that we are in the shuttle era, weight and power are no longer the real factors in experiment

ORIGINAL PAGE IS
OF POOR QUALITY

design that they were years ago (money is !), and arrays of scintillation counters are no longer at a disadvantage with respect to gas counters. It is possible today to fly thousands of square centimeters of scintillator with no technical development necessary.

In order to calculate possible sensitivities of future arrays, the efficiencies of a one atmosphere-inch gas counter (the *HEAO-1* A-2 xenon-filled HED3) and a 3 mm phoswich scintillator (the *HEAO-1* A-4 NaI LED1) are compared in Figure 1. Above 15 keV the scintillator is more efficient. In order to translate this into sensitivities, 10,000 cm^2 and 100,000 seconds livetime have been assumed, and Figure 2 shows the 3σ minimum detectable flux for both detector types, plus the spectrum of a one *UFU* (or 1.24 μJy) E^{-2} source. Clearly, astrophysics above 20 keV can be better served by a scintillator. In a similar comparison germanium detectors' sensitivity is not much different from that for scintillators, except at high energies where the sensitivity would remain flat and not rise with the loss of efficiency.

Since large area detectors have the sensitivity to measure one *UFU* sources, what about the hard x-ray sky? Is there anything there to see? Figure 3 shows the representation of the preliminary findings of the *HEAO-1* 40-80 keV SKYMAP (Levine, *et al.* 1979). Over 50 sources are presented to a limiting sensitivity of about 3 x 10^{-5} photons/cm^2 s keV, or about 10 *UFU* for an E^{-2} spectrum. Within this sample are active galaxies, clusters of galaxies, a possible quasar, x-ray binaries, radio pulsars, globular clusters, bulge sources, and even a nova. Hence, a wealth of sources are available to study astrophysical problems. I shall now address myself to some of these questions.

PHYSICS OF ACTIVE GALAXIES AND THE DIFFUSE BACKGROUND

Many aspects of testing the massive black hole model of the power source in active galaxies are related to the total luminosity (Lightman 1981). Measurements of this luminosity must be made in the hard x-ray range, where most of the power resides in the case of active galaxies. The lower energy 2-20 or 0.5-5 keV spectra cannot be extrapolated to higher energy arbitrarily , since a break in the hard x-ray spectrum at something like the characteristic energy must occur. In the past, breaks at 40 keV were predicted, based on the break in the diffuse background spectrum. Figure 4 shows the mean *HEAO-1* 2.1-165 keV spectrum of 10 active galaxies -- the majority of which are Seyfert 1 galaxies -- and no 40 keV break is seen (Rothschild, *et al.* 1981). Fitting the data confirms what is apparent -- that is, no break is seen up to 100 keV. Breaks around 100 keV have been invoked in the *HEAO-1* analysis of Cen A (Baity, *et al.* 1981a) and NGC 4151 (Baity, *et al.* 1981b). Other published results have claimed breaks in Seyferts as high as 3 MeV (Perotti, *et al.* 1979). The break energy must be measured, not hypothesized. Otherwise, only upper limits to system parameters will be obtained.

Another important hard x-ray astrophysical question relates to the relationship between active galaxies, including quasars, and the diffuse x-ray background. In the lower energy 2-40 keV regime no one class of discrete distant objects contributes more than half of the observed background in the form of unresolved point sources. Quasars are 30-40% (Giacconi, *et al.* 1979), Seyferts are about 20% (Mushotzky, *et al.* 1980), and clusters are less than 10% (McKee, *et al.* 1981). Hence, comparison of spectral shapes of classes of extragalactic objects to that of the diffuse background yields little information about its nature.

Above 40 keV things change drastically. The diffuse background, shown in Figure 5 and measured by the *HEAO-1* instruments from 2-400 keV (Marshall, *et al* 1980; Matteson, *et al* 1979) and by others above this energy (Trombka, *et al* 1977; Fichtel, *et al* 1977), starts to drop rapidly about 40 keV. Classes of objects with soft spectra, like clusters of galaxies, become unimportant at these high energies. The fraction of the x-ray background due to the remaining classes of objects must increase rapidly with energy if their spectral shapes remain unchanged. Our results mentioned above indicate that the active galaxy power law spectral index holds out to at least 100 keV, and the dashed line in Figure 5 shows their contribution. Active galaxies make up about 40% at 100 keV, and could be responsible for 100% by 250 keV. Active galaxies may also be responsible for the slope change in the diffuse x-ray background spectrum at 300 keV to 3 MeV. If the active galaxies are responsible for the diffuse background at 250 keV and beyond, what has happened to the quasar contribution seen at lower energies? The quasar spectrum then must break before 250 keV, and this has yet to be

ORIGINAL PAGE IS
OF POOR QUALITY

observed. If the quasar spectra do indeed break before the active galaxy spectra do, this might be evidence for evolutionary effects in quasar spectra.

PHYSICS OF BLACK HOLES

Black holes were not mentioned in the theoretical papers at this workshop, but a great amount of interest still exists in the study of these bizarre and fundamental objects. This is another area in which hard x-ray measurements can yield information on the pressing questions in astrophysics. Cyg X-1 is almost unique among galactic x-ray sources due to its $\geq$ 50 keV emission. The spectrum of a thermal process as described by Sunyaev and Titarchuk (1980) or by Guilbert and Fabian (1981) would be cutoff at an energy determined by the maximum temperature. Our *HEAO-1* spectrum of Cyg X-1, spanning the broad energy range of the A2 and A4 instruments, 10 keV-8 MeV, are shown in Figure 6. The model shown is the Sunyaev-Titarchuk type which fits quite well up to a few hundred keV, and indicates a temperature near 30 keV for a single thermal or ones near 15 and 40 keV for a dual temperature model. Andy Fabian has indicated that his non-equilibrium model describes this data well also with a temperature near 100 keV As you can see, there is an excess to the model at high energies. Figure 7 displays this excess more clearly, and a broad (640 keV FWHM) 511 keV line has been added to the previously mentioned model. Note, however, that most any additional type of model would fit the excess with the uncertainties involved, and the GRO mission should be able to investigate this in more detail in the future.

We can further study the emission process near black holes by investigating the temporal aspects of the scattering of photons by the hot plasma. Since the higher energy photons may be the result of more scatterings in the plasma than the lower energy photons, one would expect a time delay between the emergence of the low and high energy photons after the injection of some soft photons into the plasma. If such a time delay were confirmed, not only would we be more confident of our understanding of black hole accretion disks, but we might be able to measure the size of the emitting region. *HEAO-1* results (Nolan, *et al.* 1981) indicate a possible 10 ms lag between 20 and 60 keV photons. Instruments aboard the Ariel VI spacecraft have observed a 7 ms lag at lower energies (Fabian, private communication). Future instruments must be able to accomplish this study over as broad an energy range as possible, in order to establish the energy dependence of this time delay, and to determine the physics of the emission region.

Ultrafast temporal variability -- on the order of milliseconds or less -- may contain vital information on both the accretion process and the angular momentum of the black hole itself. General considerations of black holes show that the orbit time for the innermost stable orbit is much shorter for Kerr metrics as opposed to the Schwarzschild metric (Novikov and Thorne 1973). If the energy spectrum of the ultrafast variability is flatter than that of the overall emission above 20 keV, hard x-rays would yield a clearer signal of the bursts and thereby be more able to study the fast temporal behavior. Studying the temporal/spectral variability will, first-of-all, indicate if the millisecond bursts arise from the same process as the slower variable emission. Secondly, it will determine if a time delay occurs between the bursts as a function of energy? Finally, it may answer whether or not the time structure, or of lack of it, persists at higher energies. Such investigations will guide us in formulation of theories of black hole accretion and may link the millisecond bursting to the slower, more persistent, variability.

PHYSICS OF RADIO PULSARS

No totally consistent picture of radio pulsar x-ray emission has yet emerged. Pulsars are spinning neutron stars, but that is about all we are sure of Presently only a handful of pulsars are seen in x-rays, and only the Crab pulsar is seen to pulse. Yet in the future this will change with the use of more sensitive instruments.

Pulse phase spectroscopy, or more properly, phase resolved spectroscopy, has revealed a new

ORIGINAL PAGE IS
OF POOR QUALITY

component in the Crab pulsar spectrum. Starting with the lower energy work of Pravdo and Serlemitsos (1981) with OSO-8 data, Knight (1981) has shown from *HEAO-1* hard x-ray data that the interpulse region of the Crab light curve (shown in Figure 8) is significantly different from the peak regions. The two peaks' spectra are nearly identical and are seen over a wide range of energies (Figure 9). The peak emission has been described in terms of the synchrotron process involving high energy electrons in the pulsar magnetic field, and polarization measurements confirm this. The interpulse spectrum, shown in Figure 10, is significantly different. It is flatter and appears to break around 200 keV, possibly indicative of the emission process energy (perhaps the cyclotron energy). Attempts to model this have included a 150 keV thermal bremsstrahlung process, Compton scattering of low energy photons by 25 keV plasma of Thomson depth 5, and scattered radiation from a thick atmosphere in a strong magnetic field. Considerations, such as emission region size, temperature, and field strength pose problems with all these models. Undoubtedly, however, a new component has been revealed -- perhaps originating from quite close to the neutron star itself. Further study of this spectra in the hard x-ray range is essential to a better understanding of radio pulsars.

PHYSICS OF X-RAY PULSARS

Naturally, the most exciting aspect of the hard x-ray astrophysics of neutron stars presently is the prospect of measuring their magnetic field strength by observing the cyclotron features in their spectra. Theoretical work as presented at this workshop is advancing on predicting the size and shape of these features as a function of field strength. Her X-1, shown in Figure 11, is the most prominent example of this phenomenon, and others include 4U0115+63 (Wheaton, *et al.* 1979) and numerous gamma-ray bursts (Mazets, *et al.* 1981). The *HEAO-1* results (Gruber *et al.* 1980) of model fitting the Her X-1 data reveal the cyclotron feature to be broad (28 keV, if in emission) and occuring around 45 keV. (The energy of the centroid depends upon whether it is in emission [48 keV] or absorption [39 keV].) The feature's centroid varies with pulse phase, at least during the pulsed portion of the light curve, as is shown in Figure 12. A 15% or 30% variation is seen, depending upon emission or absorption. We are unable to follow the feature through the "off-pulse" phase region due to inadequate detector area, but the variability is not enough to cause the breadth of the feature. This changing centroid energy is probably a result of viewing the specific geometry of the Her X-1 system from different angles, and thus the geometry is open for study.

Even for those x-ray pulsars without an obvious cyclotron feature, information on their magnetic field strength is available in the form of the hard x-ray spectrum (Boldt, *et al* 1976). As shown in Figure 13, the spectrum conforms to a power law with index around one until about 20 keV, where it breaks to a steeper spectral form. This is caused by the complex interplay of cyclotron and scattering processes in the accretion plasma in the strong magnetic field. Several x-ray pulsars display this behavior and we are confident that this may allow understanding the processes involved and may lead to further measurements of neutron star magnetic field strengths and distributions.

Her X-1 is just the prime example of a class of x-ray binaries. The Hard X-ray and Low Energy Gamma-Ray Experiment aboard *HEAO-1* has discovered long term variability (~ weeks), similar to that seen in Her X-1 (Gorecki, *et al.* 1981), in two other eclipsing binary pulsars: LMC X-4 (Lang, *et al.* 1981) and SMC X-1 (Gruber, *et al.* 1981). This now increases the class of pulsing, eclipsing binaries with additional longer term "on/off" activity to three. The LMC X-4 light curve and the SMC X-1 light curve are shown in Figures 14 and 15. Hence, the x-ray community can begin the detailed study of this class of objects (and hopefully XTE will) in order to determine which characteristics are unique to individual sources and which can be related to the class in general. In order to accomplish this detailed study of accretion onto magnitized neutron stars, large detector areas are necessary. Figure 13 shows the spectrum of Her X-1 and that of SMC X-1. The latter source is about ten times weaker than the former, and consequently, ten times the sensitivity is necessary to study it at the same level as *HEAO-1* studied Her X-1. Perhaps the SMC X-1 spectrum has a cyclotron feature, but we will not know without the higher sensitivity.

A possible source of collimation of the x-ray pulsar beam is the hole in the magnetosphere near the neutron star magnetic poles through which the accretion plasma reaches the x-ray emission region. If this hole

ORIGINAL PAGE IS
OF POOR QUALITY

is responsible for the overall x-ray pulse shape, the observed pulses should broaden by about 10% as one goes to higher energy due to the change in the Compton cross section with energy. If this effect is not seen, the collimation must be due to the source region. Hence, further information on the pulse formation in x-ray pulsars is available at hard x-ray energies.

PHYSICS OF CLUSTERS OF GALAXIES

Clusters of galaxies are believed to contain an intracluster magnetic field. This basic cluster parameter can be measured by observing the weak hard x-ray component in cluster x-ray spectra (Lea and Holman 1978), due to the microwave photons inverse Compton scattering off of the intracluster electrons that are spiralling around field lines and generating radio emission. This x-ray component will reflect the shape of the electron power law spectrum, and its magnitude will be directly related to the field strength. Thus, even upper limits to the high energy flux will set lower limits to the magnetic field. Hard x-ray spectral components have been detected by the Hard X-Ray and Low Energy Gamma-Ray Experiment aboard *HEAO-1* from the Perseus (Primini, *et al.* 1981) and Virgo clusters and upper limits from Abell 2142 (Lea, *et al.* 1981) were also determined (see Figure 16). The Perseus hard tail is due, however, to the active galaxy NGC 1275 at its center, and thus the limits to the inverse Compton component are even lower. In the case of the Virgo cluster it is questionable whether or not the galaxy M 87 at the cluster core is responsible. In any event we have $B \geq 5 \times 10^{-7}$ Gauss (Virgo), $B \geq 10^{-7}$ Gauss (Perseus), and $B \geq 5 \times 10^{-8}$ Gauss (Abell 2142). These results indicate that the magnetic fields in cluster radio sources must be close to the equipartition values.

CONCLUSIONS

I would like to emphasize the importantance of further research in hard x-ray astrophysics. These investigations could utilize large scintillator arrays, large cooled germanium arrays, coded apertures, Bragg concentrators, etc. Measurements above 20 keV extending to hundreds of keV must be made to attack some of the major identified astrophysical questions before us. Correlated analyses over as broad an energy range as possible is very important for distinguishing between competing models for a given source and for the general knowledge of the phenomonology of cosmic x-ray sources.

ORIGINAL PAGE IS
OF POOR QUALITY

REFERENCES

Baity, *et al.* 1981a, Ap. J., *244*, 429.
Baity, *et al.* 1981b, in preparation.
Boldt, *et al.* 1976, Astron. Astrophys., *50*, 161.
Fichtel, *et al.* 1977, Ap. J., *217*, L9.
Giacconi, *et al.* 1979, Ap. J., *234*, L1.
Gorecki, *et al.* 1981, Ap. J., submitted.
Gruber, *et al.* 1980, Ap. J., *240*, L127.
Gruber, *et al.* 1981, in preparation.
Guilbert, P. W. and Fabian, A. 1981, preprint.
Knight, F. K. 1981, PhD dissertation, UCSD.
Lang, *et al.* 1981, Ap. J., *246*, L21.
Lea, S. M. and Holman, G. D. 1978, Ap. J., *222*, 29.
Lea, *et al.* 1981, Ap. J., *246*, 369.
Levine, *et al.* 1979, B.A.A.S., *11*, 429.
Lightman, A. 1981, Workshop on X-Ray Astronomy and Spectroscopy, GSFC.
Marshall, *et al.* 1980, Ap. J., *235*, 4.,
Matteson, *et al.* 1979, B.A.A.S., *11*, 653.
Mazets, *et al.* 1981, Nature, *290*, 378.
McKee, *et al.* 1980, Ap. J., *242*, 843.
Mushotzky, *et al.* 1980, Ap. J., *235*, 377.
Nolan, *et al.* 1981, Ap. J., *246*, 494.
Novikov, I. D. and Thorne, K. S. 1973, Black Holes, (Gordon and Breach:New York), 343.
Perotti, *et al.* 1979, Nature, *282*, 484.
Pravdo, S. and Serlemitsos, P. 1981, Astron. Astrophys., submitted.
Primini, *et al.* 1981, Ap. J., *243*, L13.
Rothschild, *et al.* 1981, in preparation.
Sunyaev, R. A. and Titarchuk, L. G. 1980, Astron. Astrophys., *86*,121.
Trombka, *et al.* 1977, Ap. J., *212*, 925.
Wheaton, *et al.* 1979, Nature, *282*, 240.

ORIGINAL PAGE IS
OF POOR QUALITY

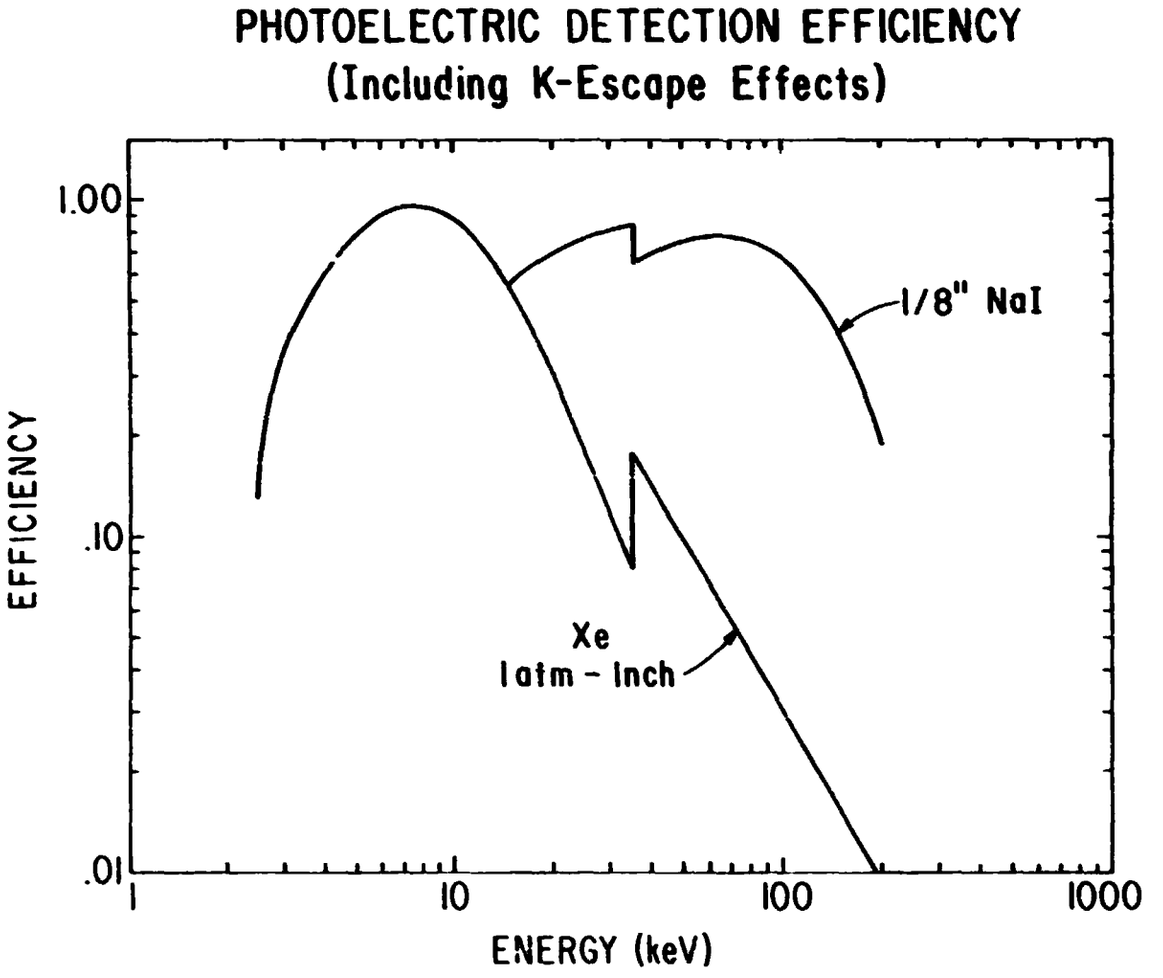

Figure 1: X-Ray efficiencies, including K-escape effects, for a xenon proportional counter and a NaI phoswich scintillation counter.

ORIGINAL PAGE IS
OF POOR QUALITY

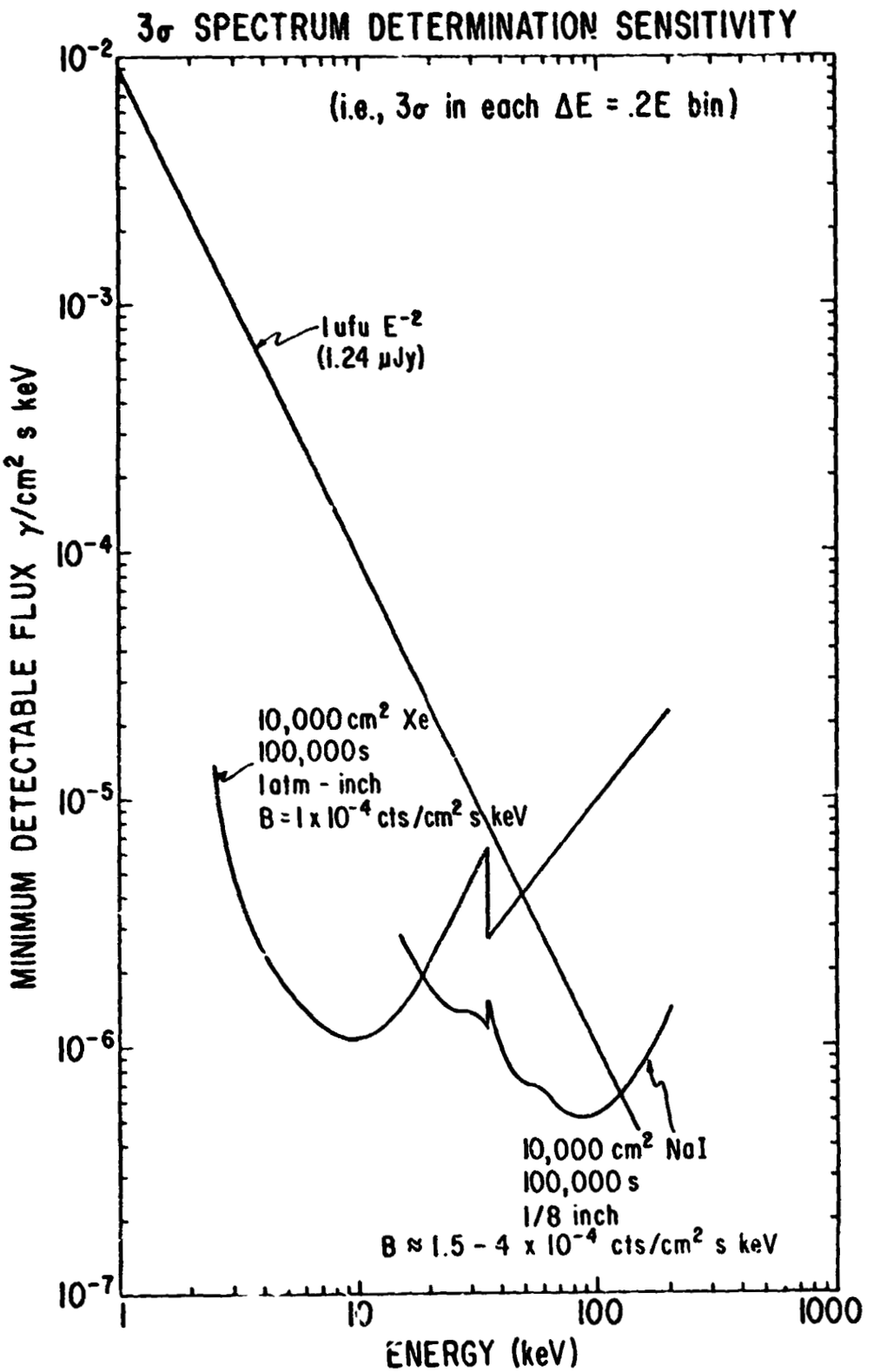

Figure 2: Sensitivities (3σ) for a xenon proportional counter and a NaI phoswich scintillation counter for 10,000 cm^2, 100,000 s and ΔE = 0.20 E. The spectrum of a 1*UFU* E^{-2} source is also shown.

40-80 KEV FLUX
> 2.6×10^{-5} PH/CM^2-SEC-KEV
(≃ 1/84 CRAB)
(≃ 11 UFU) for E^{-2} spectrum

HEAO-1 UCSD/MIT SKY SURVEY: 40-80 keV
(PRELIMINARY; LEVINE, et al. 1980, B.A.A.S., 12, 463)

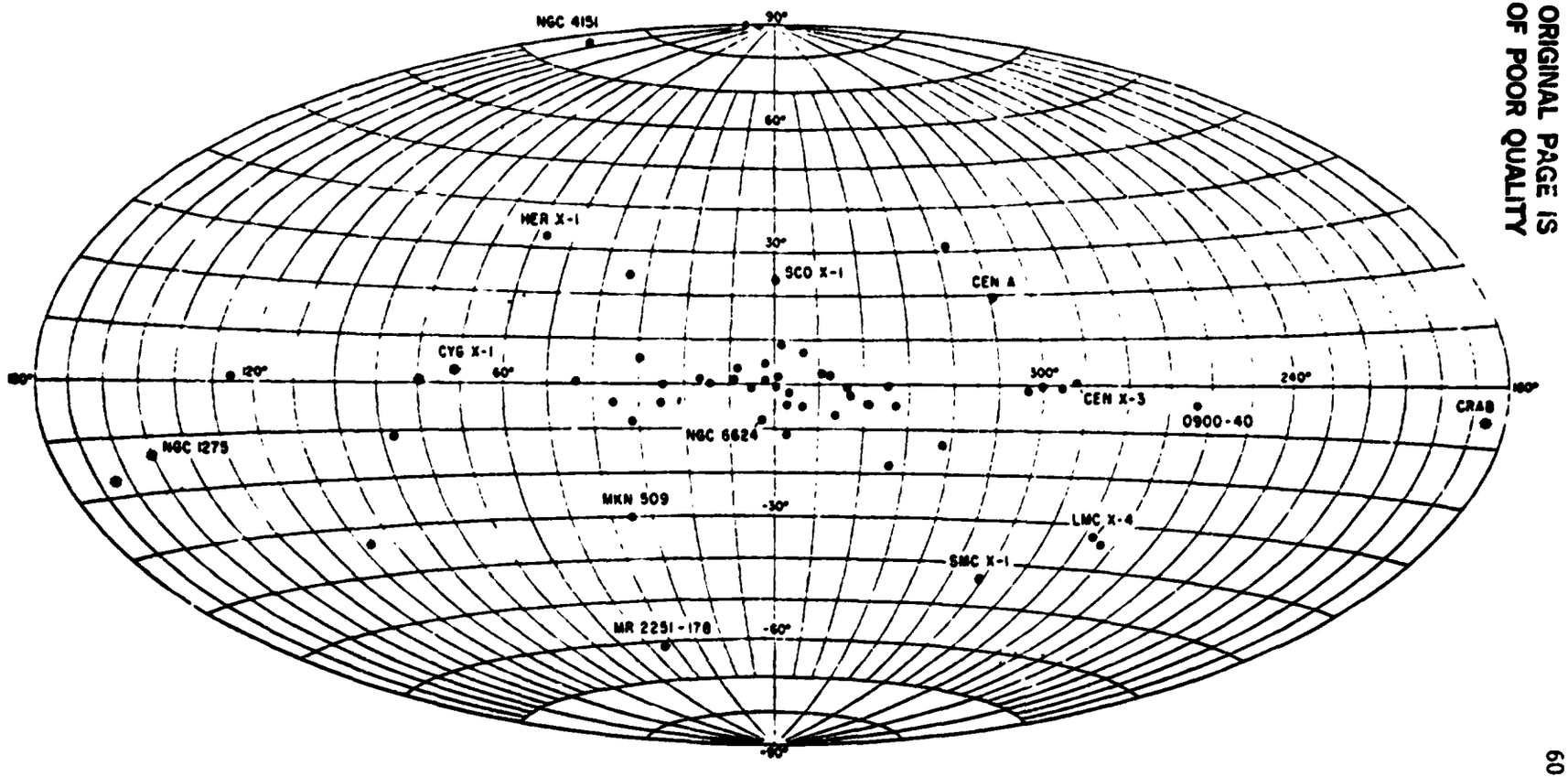

Figure 3: The *HEAO-1* 40-80 keV SKYMAP.

ORIGINAL PAGE IS
OF POOR QUALITY

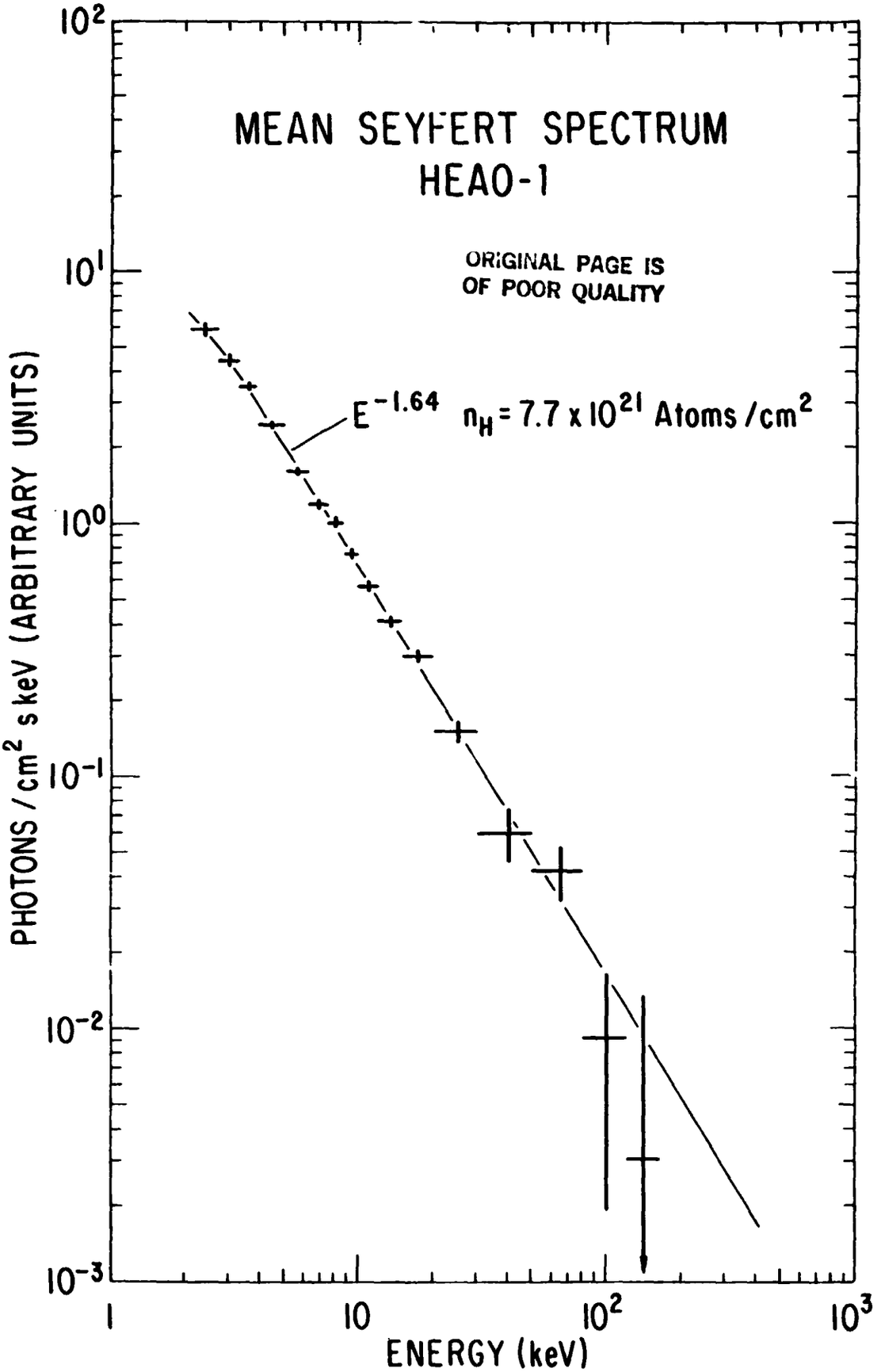

Figure 4: The mean *HEAO-1* spectrum of active galaxies.

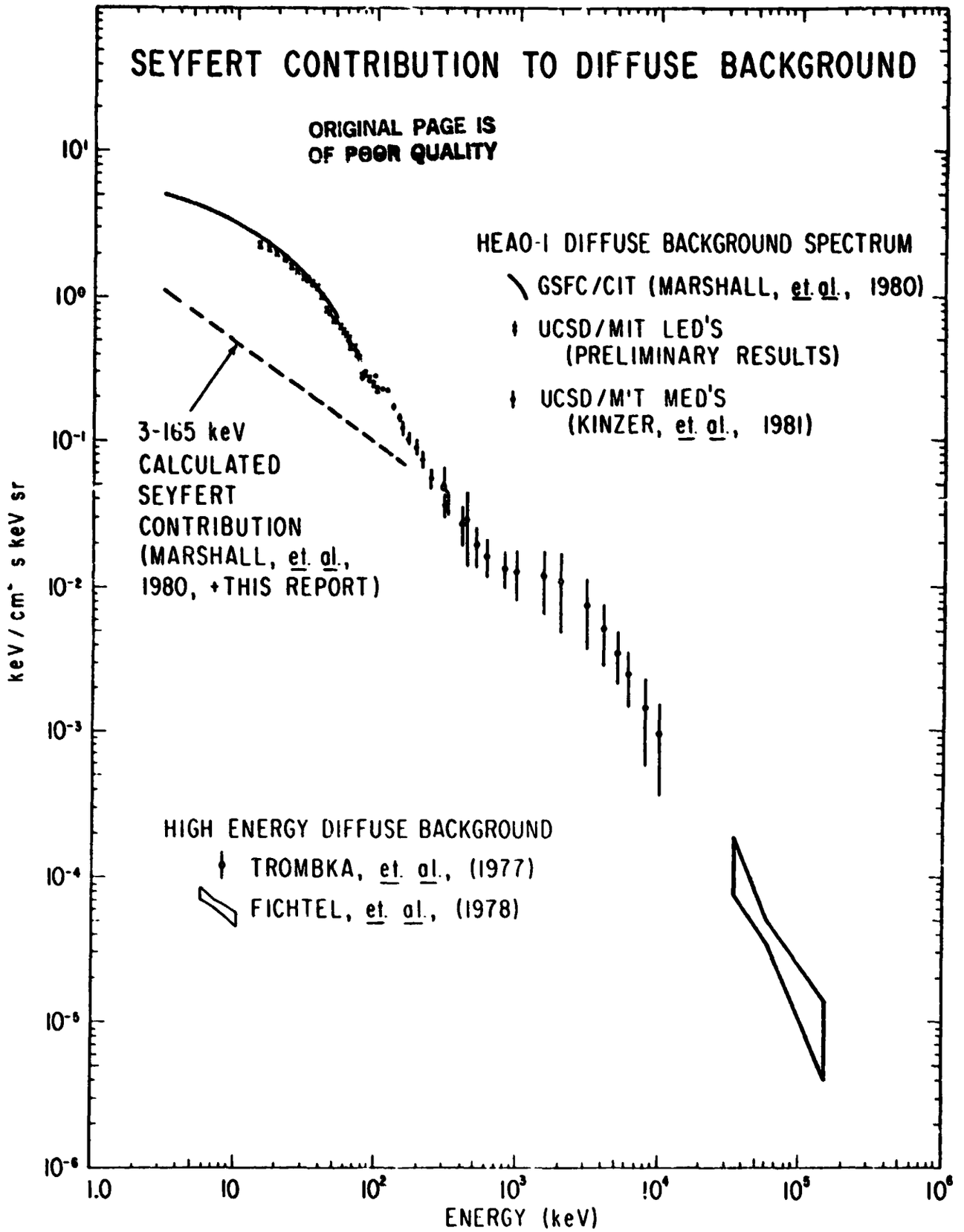

Figure 5: The diffuse x-ray background, along with the contribution of active galaxies

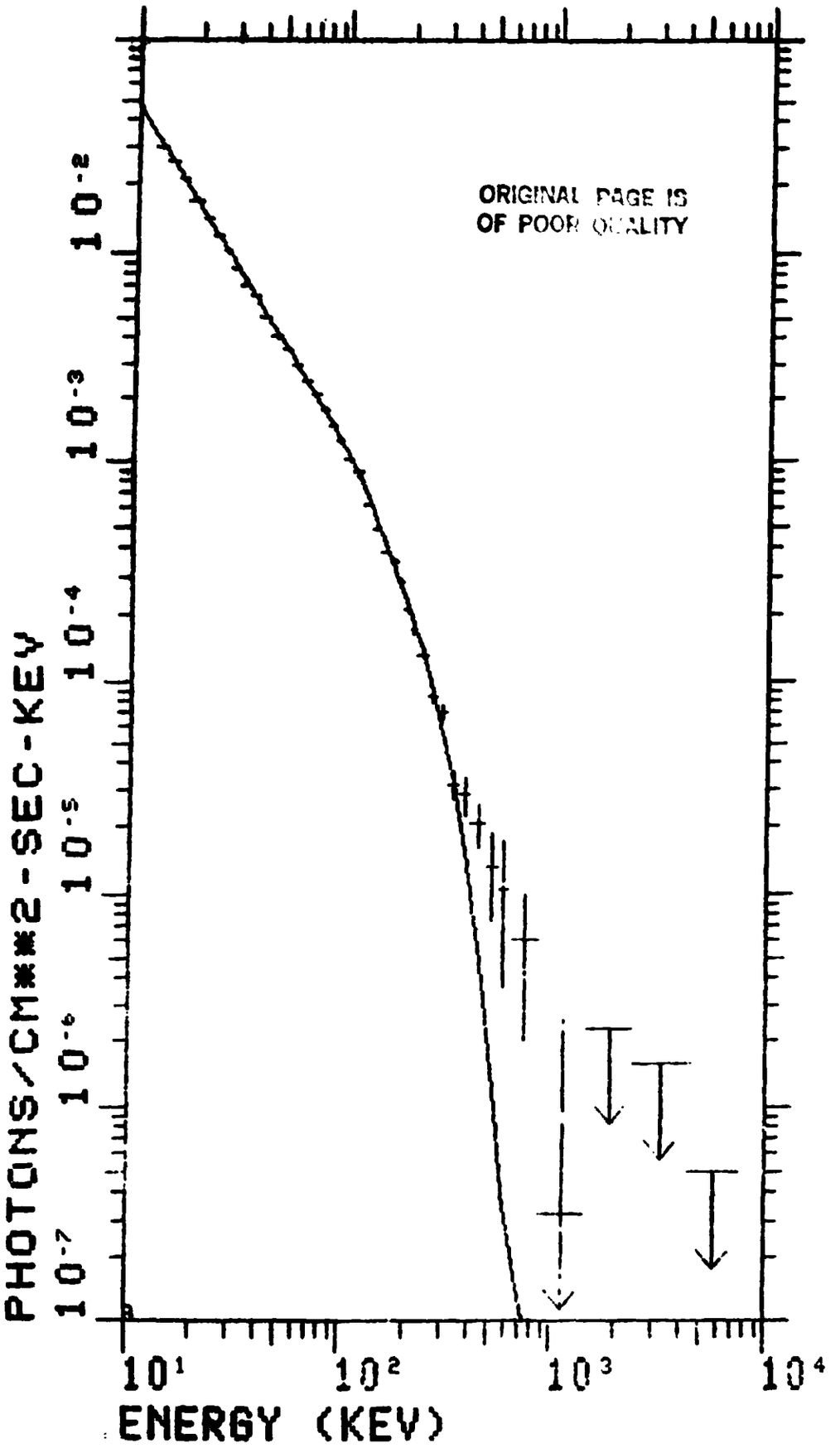

Figure 6: The *HEAO-1* spectrum of Cyg X-1.

ORIGINAL PAGE IS
OF POOR QUALITY

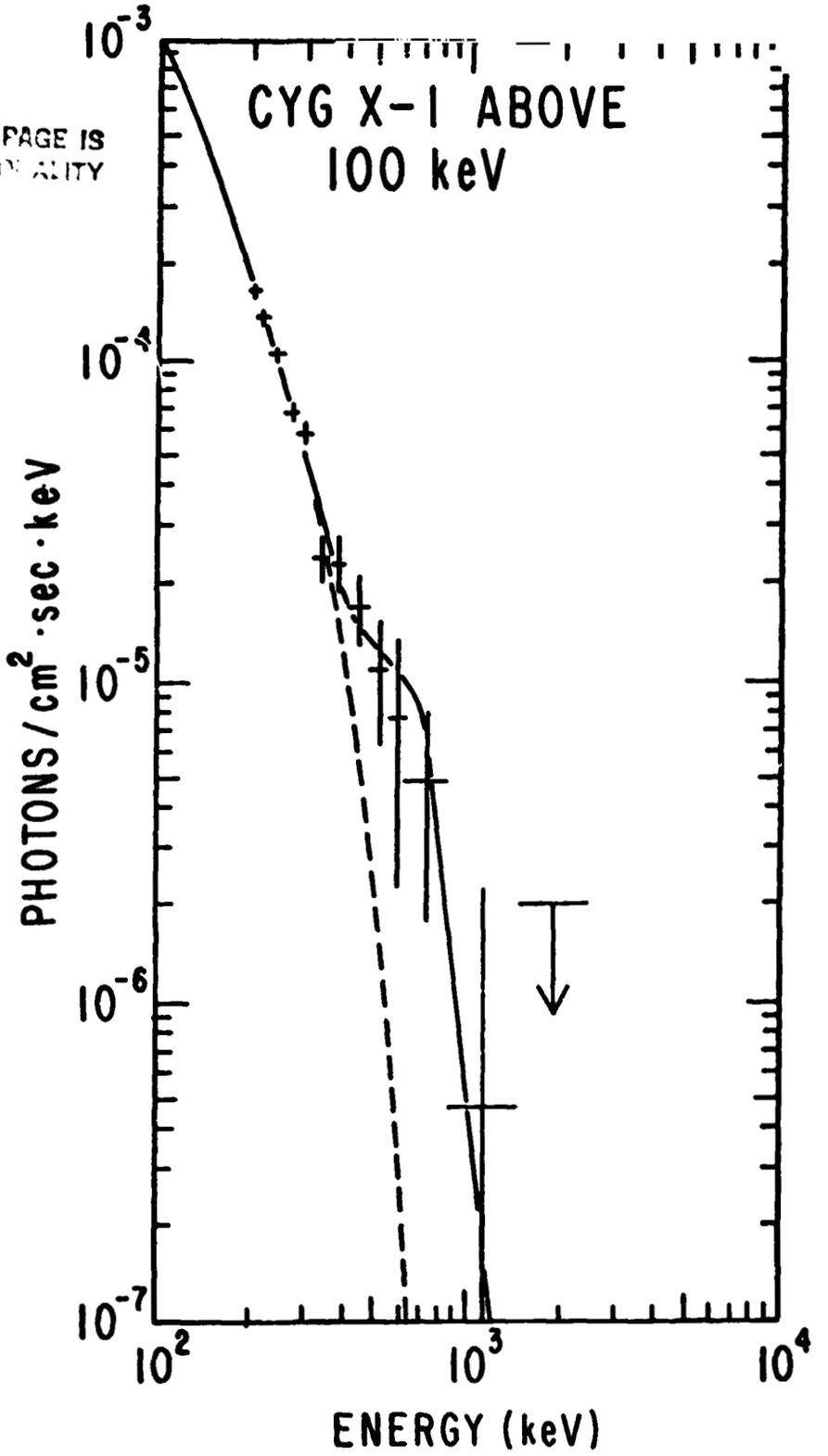

Figure 7: The *HEAO-1* spectrum of Cyg X-1 at high energies.

ORIGINAL PAGE IS
OF POOR QUALITY

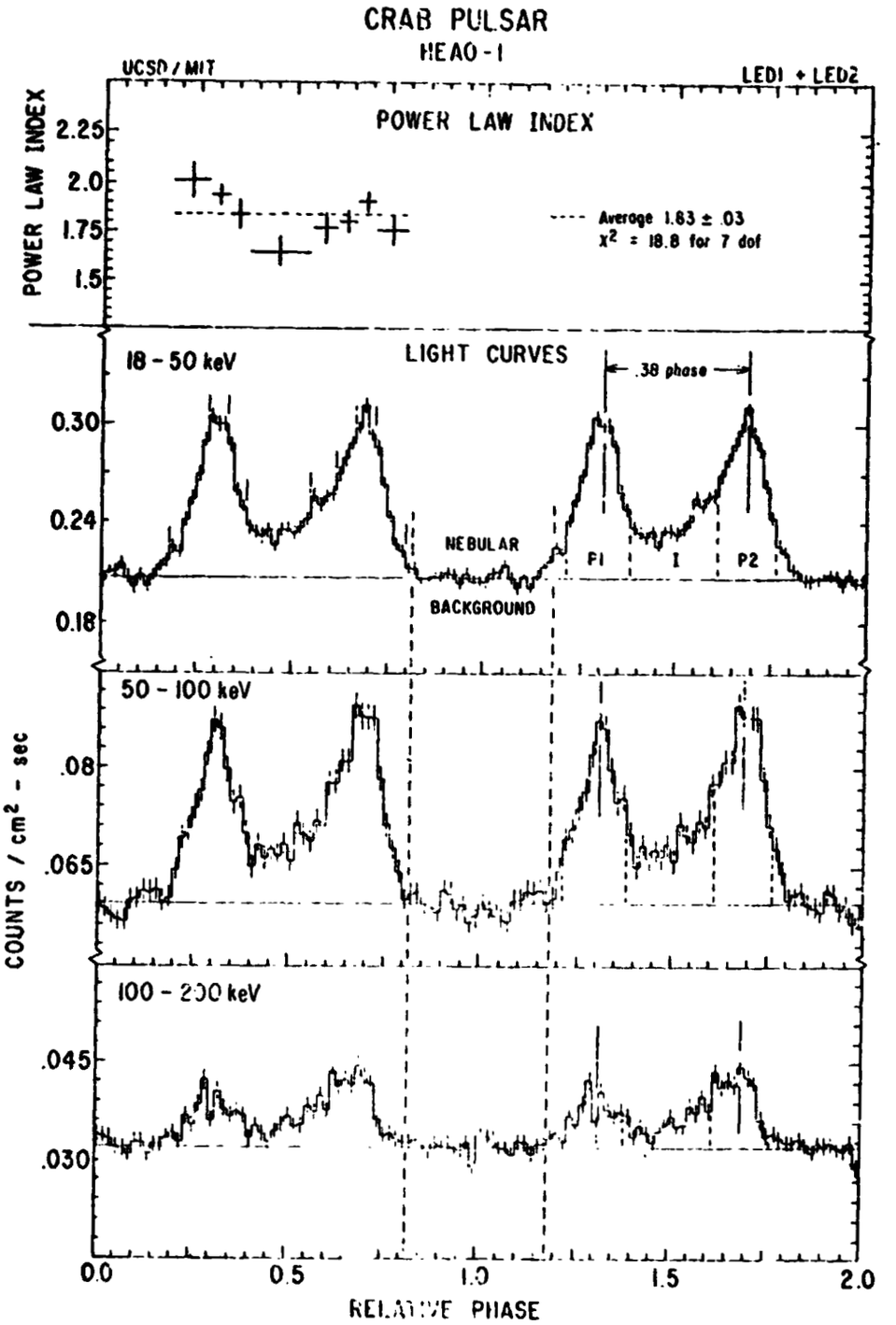

Figure 8: The *HEAO-1* Hard X-Ray and Low Energy Gamma-Ray Experiment light curve for the Crab nebula pulsar. The interpulse region of phase is denoted by " I ".

ORIGINAL PAGE IS
OF POOR QUALITY

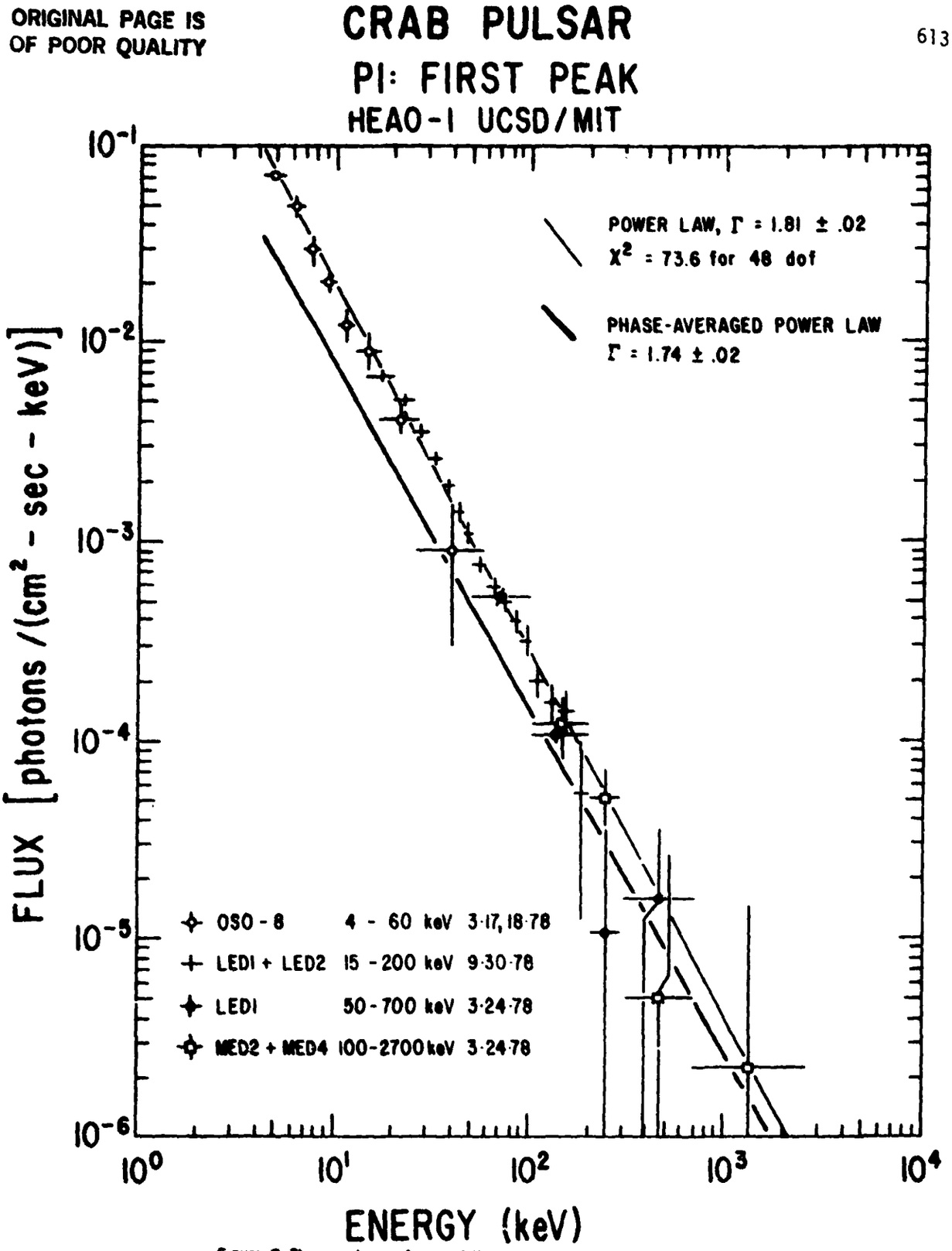

Figure 2: The spectrum of one of the peaks in the Crab nebula spectrum from the Hard X-Ray and Low Energy Gamma-Ray Experiment aboard *HEAO-1*.

8/81 FKK 2883

ORIGINAL PAGE IS
OF POOR QUALITY

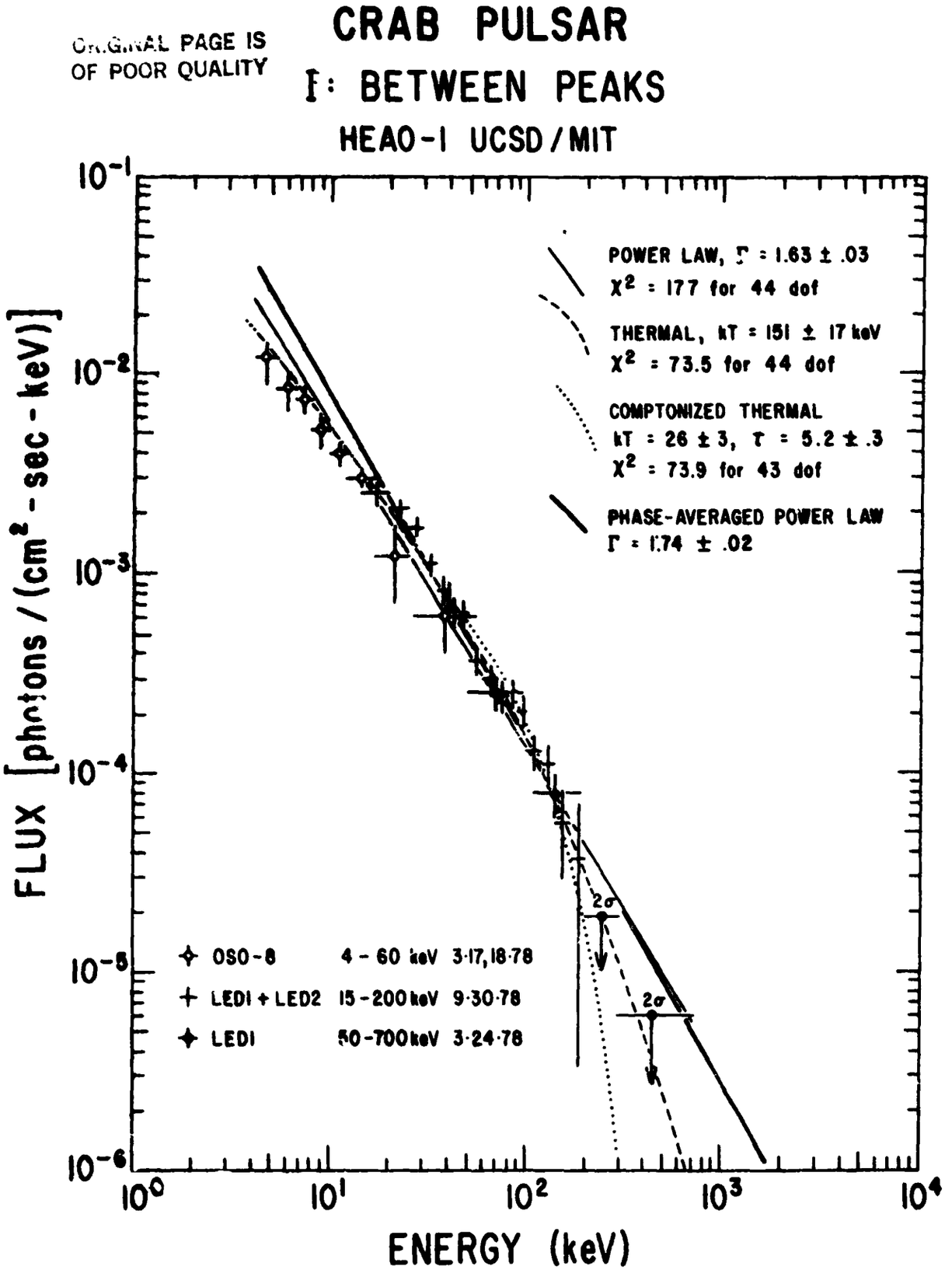

Figure 10: The interpulse spectrum of the Crab nebula from OSO-8 and *HEAO-1*.

3/26/81 FKK 2883

ORIGINAL PAGE IS
OF POOR QUALITY

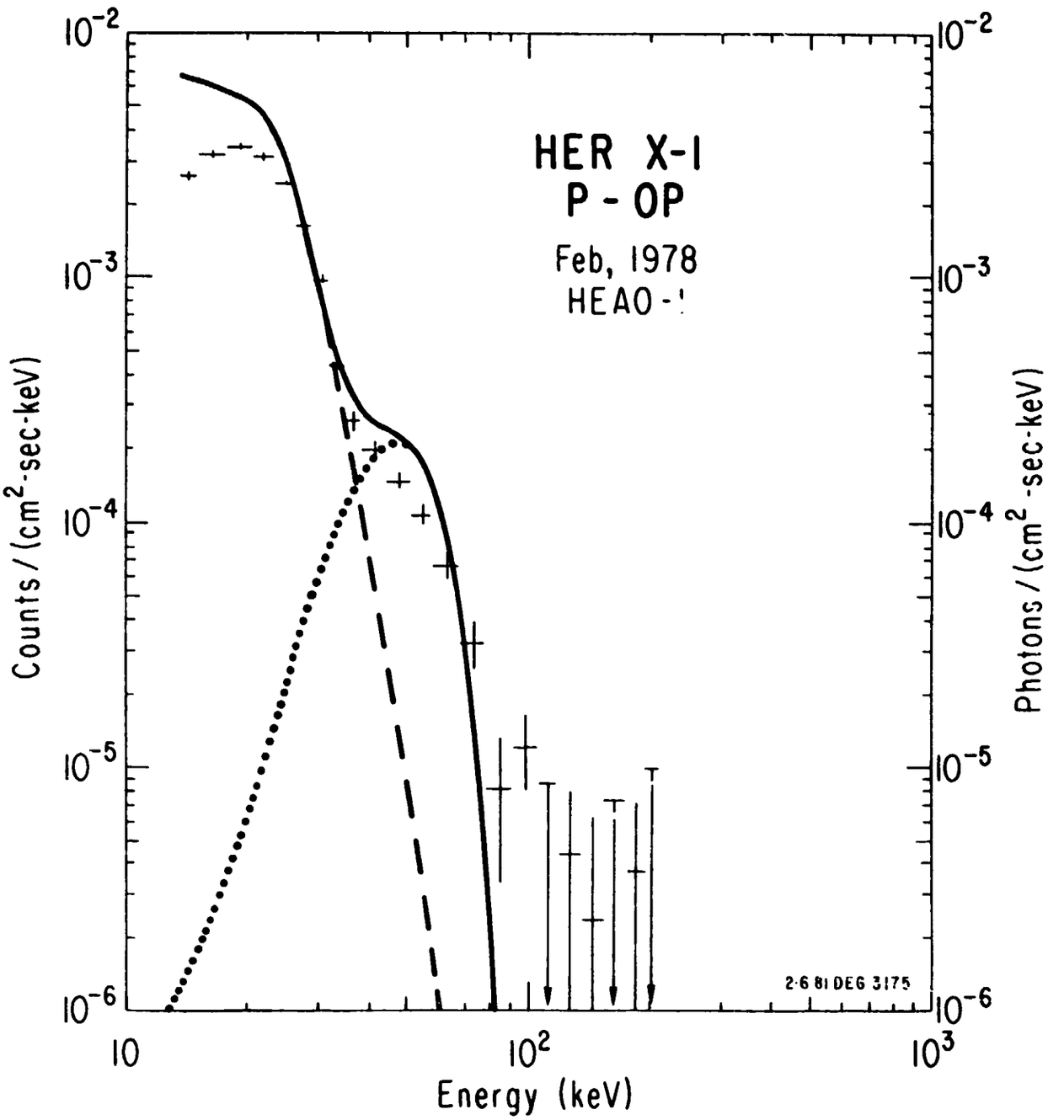

Figure 11: The spectrum of Her X-1 from *HEAO-1*. The model shows both the continuum and the modelled line in emission.

ORIGINAL PAGE IS
OF POOR QUALITY

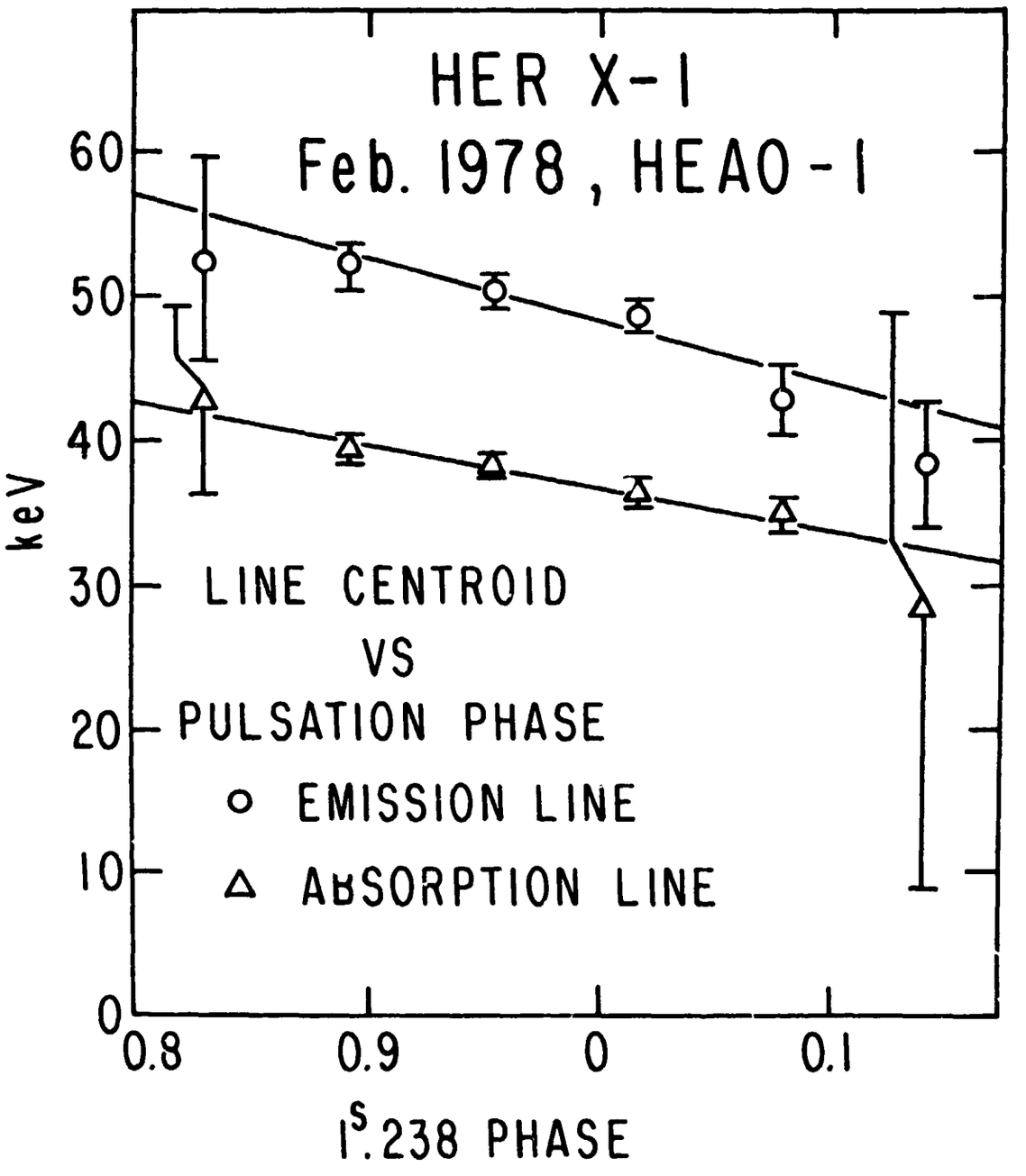

Figure 12 Variation of the centroid of the cyclotron feature in Her X-1 as measured by *HEAO-1*.

ORIGINAL PAGE IS
OF POOR QUALITY

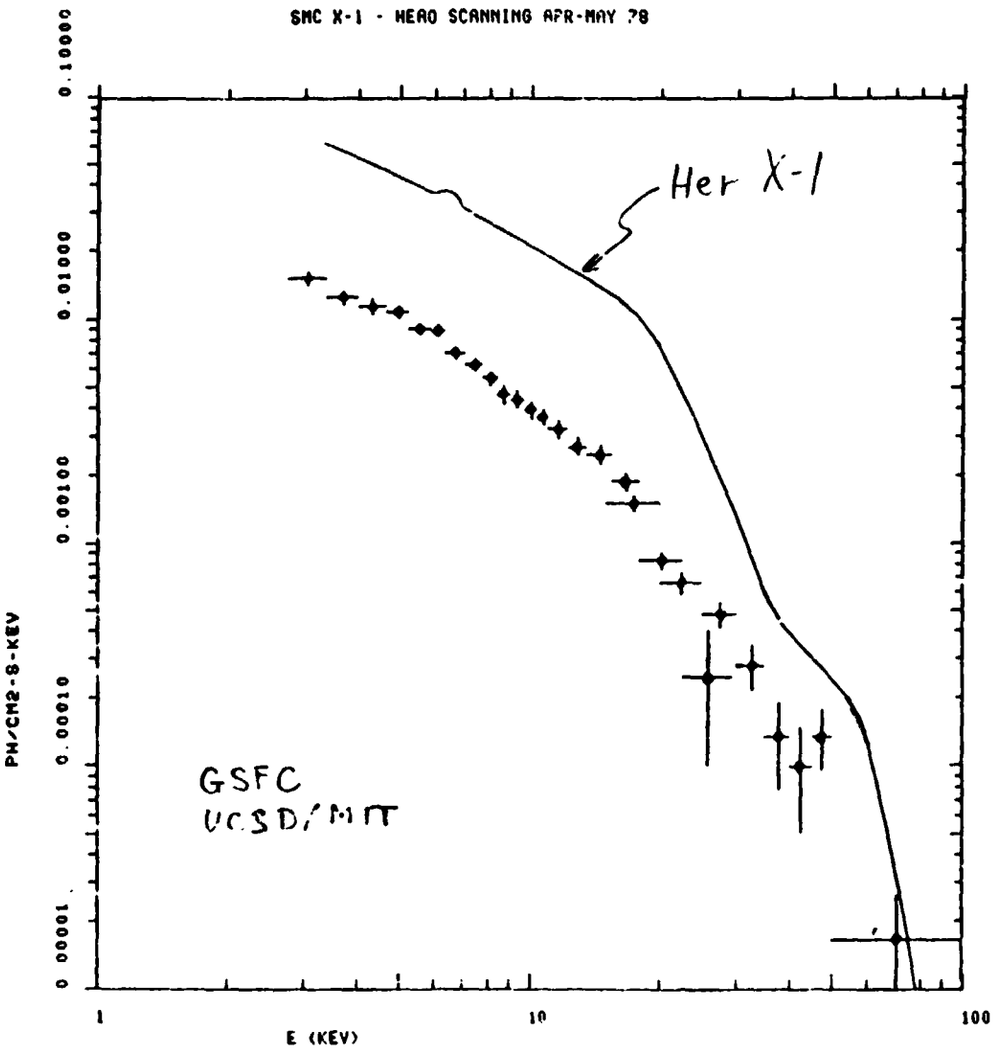

Figure 13: The spectrum of Her X-1 and SMC X-1 from *HEAO-1*. The solid line represents the best-fit model to the Her X-1 data and the data points are for *HEAO-1* observations of SMC X-1.

ORIGINAL PAGE IS
OF POOR QUALITY

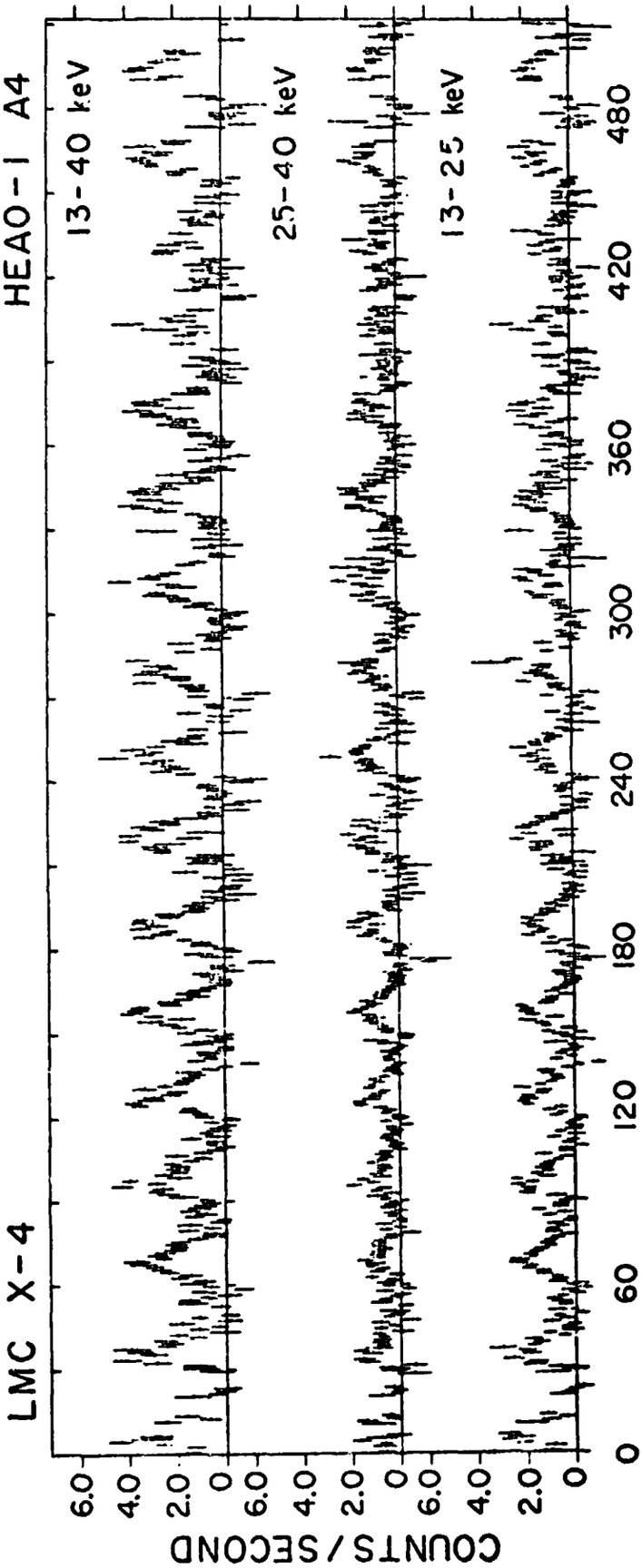

Figure 14: The *HEAO-1* light curve of LMC X-4 above 12 keV.

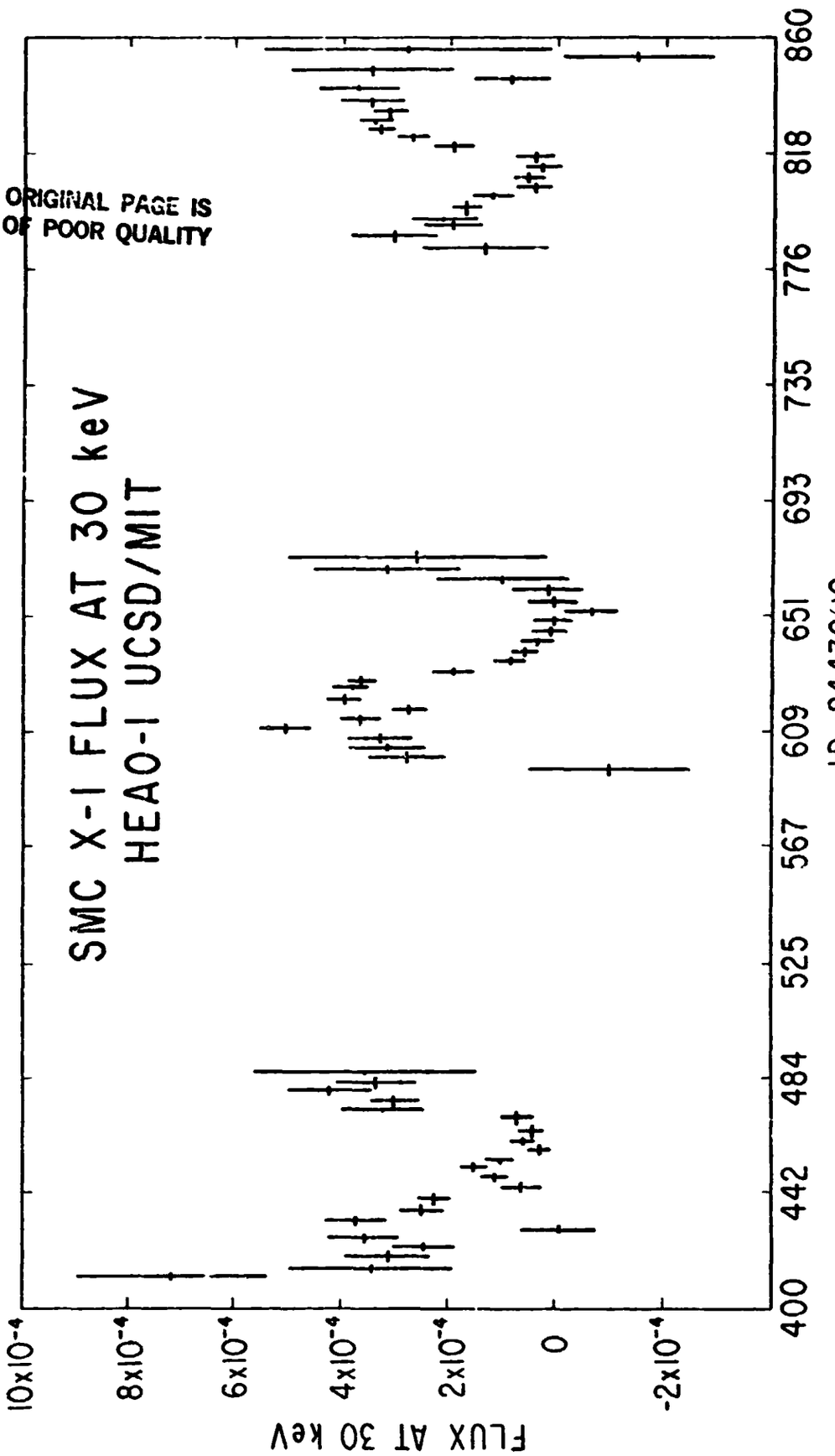

Figure 15: The *HEAO-1* light curve of SMC X-1 at 30 keV.

ORIGINAL PAGE IS
OF POOR QUALITY

ORIGINAL PAGE IS
OF POOR QUALITY

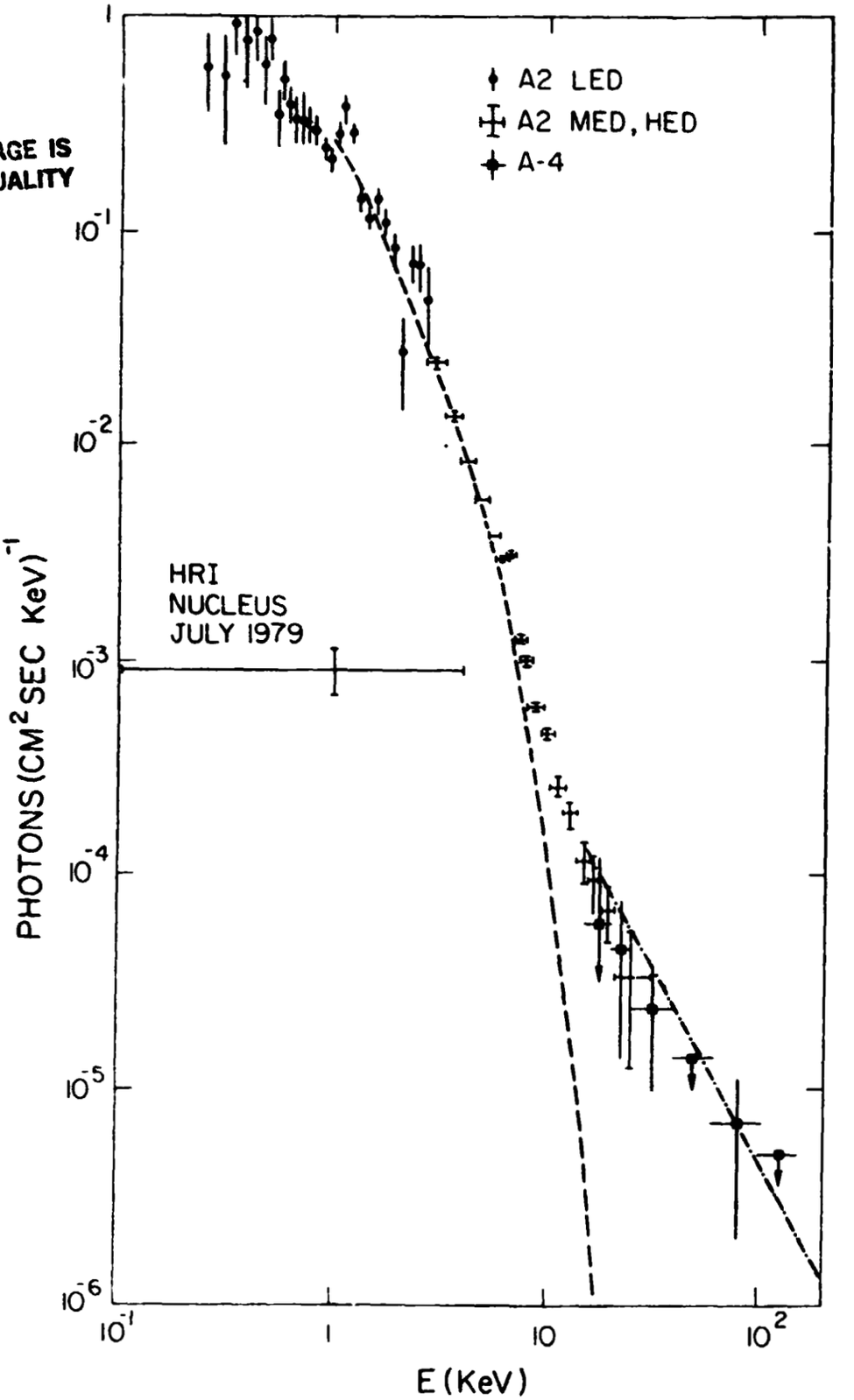

Figure 16: The *HEAO-1* spectrum of the Virgo cluster.

LIST OF PARTICIPANTS

Lorin W. Acton
Code 602.6
NASA/GSFC
Greenbelt, MD 20771

B. Aschenbach
Max Planck Inst
Garching 8046
Munich, WEST GERMANY

J.H. Beall
Code 4152.2
Gamma Ray Astrophysics
Naval Research Lab
Washington, DC 20375

Elihu Boldt
Code 661
NASA/GSFC
Greenbelt, MD 20771

Stuart Bowyer
Astronomy Department
Univ. of California
Berkeley, CA

Hale Bradt
37-581
M.I.T.
Cambridge, MA 02139

Alan N. Bunner
Perkin Elmer Corp
MS 979
100 Wooster Heights Road
Danbury, CT 06810

Claude R. Canizares
Institute of Astronomy
Univ. of Cambridge
Madingly Road
Cambridge CB3 0HA
ENGLAND

Webster Cash
LASP
Univ. of Colorado
Boulder, CO 80309

R.C. Catura
Bldg. 255, Dept. 5212
Lockheed Research Lab
3251 Hanover Street
Palo Alto, CA 94304

George W. Clark
MIT
Room 37-611
Cambridge, MA 02146

Len Cowie
MIT
Cambridge, MA 02139

J. Len Culhane
Mullard Space Sci. Lab.
Holmbury St. Mary
Dorking, Surrey
UNITED KINGDOM

Linda Dressel
Code 661
NASA/GSFC
Greenbelt, MD 20771

Andy Fabian
Institute for Astronomy
Madingly Road
Cambridge
UNITED KINGDOM

Gilbert G. Fritz
Code 4129
Naval Research Lab
Washington, DC 20375

Gordon P. Garmire
504 Davey Lab
Pennsylvania State Univ.
University Park, PA 16802

Riccardo Giacconi
Director
Space Telescope Science Inst.
Homewood Campus
Baltimore, MD 21218

Paul Gorenstein
Harvard/Smithsonian Center
for Astrophysics
60 Garden Street
Cambridge, MA 02138

Richard E. Griffiths
Harvard/Smithsonian Center
for Astrophysics, B-440
60 Garden Street
Cambridge, MA 02138

Jonathan Grindlay
Harvard/Smithsonian
60 Garden Street
Cambridge, MA 02138

Herbert Gursky
NRL
Code 4100
Washington, DC 20375

Andrew Hamilton
Leander McCormick Obs.
P.O. Box 3818
Univ. Station
Charlottesville, VA 22903

David J. Helfand
Columbia Astrophysics Lab
538 W 120th Street
New York, NY 10027

Steve Holt
Code 661
NASA/GSFC
Greenbelt, MD 20771

Esther Ming Hu
Code 661
NASA/GSFC
Greenbelt, MD 20771

Hugh Hudson
CASS, C-011
UCSD
La Jolla, CA 92093

James Imamura
Dept. Astronomy
University of Virginia
P.O. Box 3818
University Station
Charlottesville, Va 22903

Lou Kaluzienski
Code SC
NASA Headquarters
Washington, DC 20546

Fred Knight
Code 4153.4
Naval Research Laboratory
Washington, DC 20375

Lydie Koch
CEN, B.P. No. 2
91190 Gif Sur Yvette
Saclay
FRANCE

William Ku
538 West 120th Street
Columbia Astrophysics Lab
New York, NY 10025

Nikolaos D. Kylafis
Institute for Advance Study
School of Natural Sciences
Princeton, NJ 08540

Don Q. Lamb
D-?22
Center for Astrophysics
60 Garden Street
Cambridge, MA 02138

Fred K. Lamb
Dept. Physics
Univ. of Illinois
Urbana, IL 61801

Steven Langer
Dept. of Astronomy
Univ. of Illinois
Urbana, IL 61801

Alan M. Levine
MIT, 37-601
Cambridge, MA 02139

Margaret Lewis
Univ. of Leicester
X-ray Astronomy Group
Leicester LR1 7RH
UNITED KINGDOM

Alan P. Lightman
Center for Astrophysics
60 Garden Street
Cambridge, MA 02138

Jeff Linsky
Univ. of Colorado
LASP
Boulder, CO 80309

Knox S. Long
Columbia Astrophysics Lab
538 W 120th Street
New York, NY 10027

Frank Marshall
Code 661
NASA/GSFC
Greenbelt, MD 20771

Franklin D. Martin
Code SC
NASA Headquarters
Washington, DC 20546

James L. Matteson
CASS, Code C-011
Univ. California, San Diego
La Jolla, CA 92093

Dan McCammon
Dept. of Physics
6207 Chamberlin Hall
1150 University Avenue
Madison, WI 53706

Jeff McClintock
MIT
Bldg. 37-521
Cambridge, MA 02139

Richard McCray
JILA
Univ. of Colorado
Boulder, CO 80309

John F. Meekins
Code 4125
Naval Research Lab
Washington, DC 20375

Peter Meszaros
Code 665
NASA/GSFC
Greenbelt, MD 20771

George Newton
Code SC
NASA Headquarters
Washington, D.C. 20546

Patrick Nolan
CASS, C-011
UCSD
La Jolla, Ca 92093

Robert Novick
Columbia Astrophysics Lab
538 West 120th Street
New York, NY 10027

Jonathan Ormes
Code 661
NASA/GSFC
Greenbelt, MD 20771

Robert Petre
M.I.T., Rm 37-576
77 Massachusetts Ave.
Cambridge, MA 02139

Raymond Proctor
CASS, C-011
Univ. California, San Diego
La Jolla, CA 92093

Saul Rappaport
37-551 CSR
MIT
Cambridge, MA 02139

G.R. Ricker
M.I.T., Rm 37-527
77 Mass Ave.
Cambridge, MA 02139

Guenter R. Riegler
M.S. 169-327
Jet Propulsion Lab
Pasadena, CA 91109

Richard Rothschild
CASS, C-011
UCSD
La Jolla, CA 92093

Julia Robinson-Saba
Code 661
NASA/GSFC
Greenbelt, MD 20771

Herbert W. Schnopper
Danish Space Res. Inst.
Lundtoftevej 7
DK-2800 Lyngby
DENMARK

Dan Schwartz
SAO
60 Garden Street
Cambridge, M A 02138

Peter J. Serlemitsos
Code 661
NASA/GSFC
Greenbelt, MD 20771

Gerald Share
Code 4152
Naval Research Lab
Washington, DC 20375

J. Michael Shull
Univ. of Colorado
JILA
Boulder, CO 80309

Robert Smither
Argonne National Lab
9700 S. Cass
Argonne, IL 60439

Jean Swank
Code 661
NASA/GSFC
Greenbelt, MD 20771

Andy Szymkowiak
Code 661
NASA/GSFC
Greenbelt, MD 20771

Yasuo Tanaka
Institute of Space and
Astronautical Science
6-1, Komaba 4-Chome
Meguro-ku
Tokyo 153
JAPAN

Harvey Tananbaum
Center for Astrophysics
60 Garden Street
Cambridge, MA 02138

Allyn Tennant
Code 661
NASA/GSFC
Greenbelt, MD 20771

Melville P. Ulmer
Dept. Physics & Astron.
Northwestern University
Evanston, IL 60201

Hugh M. Van Horn
Dept. Physics & Astronomy
Univ. of Rochester
Rochester, NY 14627

Giuseppe S. Vaiana
Center for Astrophysics
60 Garden Street
Cambridge, MA 02138

Ira Wasserman
Center for Radiophysics &
Space Research
Cornell University
Ithaca, NY 14853

Michael Watson
Univ. of Leicester
Leicester LR1 7RH
UNITED KINGDOM

Nick White
Code 661
NASA/GSFC
Greenbelt, MD 20771

Richard White
Code 661
NASA/GSFC
Greenbelt, MD 20771

Bruce Woodgate
Code 681
NASA/GSFC
Greenbelt, MD 20771

Guenter Wunner
Institut f. Theoretische
Physik der Universitaet
Glueckstr 6, D-8520
Erlangen
WEST GERMANY

PRECEDING PAGE BLANK NOT FILMED

INDEX OF CONTRIBUTORS